University of Reading

Understanding the regional and seasonal influences of the stratospheric contribution to tropospheric ozone

PhD Atmosphere, Oceans and Climate

Department of Meteorology, School of Mathematical and Physical Sciences

Ryan Scott Williams

April 2021

Declaration of Authorship

I confirm that this is my own work and the use of all material from other sources has been properly and fully acknowledged.

Ryan Williams

12 April 2021

Acknowledgements

In producing this work, I owe many thanks to my three supervisors: Dr Michaela Hegglin and Dr Nicolas Bellouin of the University of Reading, UK, as well as Dr Brian Kerridge of the Rutherford Appleton Laboratory (RAL). Michaela (my lead supervisor) has continually overseen my research progression and personal development throughout my time as a PhD student in the Department of Meteorology at the University of Reading. Without her support, I would not be where I am today. She has supported me throughout the highs and lows and steered me to realising my potential. I have thoroughly enjoyed my time as a research student in the department and I therefore also give credit to the community and supportive environment within for my success. I have made many new friends and acquired a number of research contacts along the road, which I hope will pave way to an exciting career in meteorological science and research. I would also like to extend my thanks to all my family and friends for their continued support throughout my time studying for a PhD.

I would also like to acknowledge the SCENARIO doctoral training partnership and the Natural Environmental Council (NERC) for funding my research over the last four years. I am also grateful for receiving additional financial support from the Rutherford Appleton Laboratory (RAL) during this time, courtesy of their involvement in my research as the project industrial case partner. I have enjoyed regular interaction with Brian and colleagues on a regular basis throughout my PhD, along with occasional visits to their working group on Harwell Campus, Didcot. I am incredibly lucky to have had access to their knowledge and expertise and I am grateful for all their support.

Abstract

Tropospheric ozone (O_3) is the third most important greenhouse gas (GHG) and as an air pollutant, constitutes one of the major contributors to ~7 million premature deaths (WHO, 2019) annually worldwide and also to ecosystem damage. Furthermore, ozone determines hydroxyl (OH) radical levels, which serves to breakdown various pollutants and GHGs. Despite its significance, regional and seasonal variations in tropospheric ozone are poorly understood. Ozone in the troposphere is formed from various precursor species (e.g. CO, NO_x and VOCs), which have both natural and anthropogenic sources, as well as transported down from the stratosphere. The relative importance of each influence has been the subject of intense debate in recent decades. Using a combination of in situ (ozonesonde) and satellite (GOME-2A and OMI) observations, in conjunction with state-of-the-art chemistry climate models (EMAC and CMAM), comprehensive quantification of the regional and seasonal variability in tropospheric ozone is here provided, including recent changes and source attribution using the models' stratospheric-tagged ozone tracers. This combined approach is necessary to overcome the shortcomings of individual datasets. The realism of each dataset is first rigorously evaluated and limitations identified. A significant source of retrieval error is identified in the satellite measurements, which will serve to retrospectively improve existing datasets. Using both models, it is quantified that the stratospheric influence is larger than found in previous studies; exceeding 50 % near the surface during winter in the extratropics. Finally, the influence of midwinter Sudden Stratospheric Warmings (SSWs) in relation to upper troposphere/lower stratosphere (UTLS) composition and stratosphere-troposphere exchange (STE) of ozone is presented, as a potential source of interannual variability. Approximately half of all SSWs result in significant, prolonged perturbations in UTLS composition, with implications for STE of ozone at lead times of ~50 days. The radiative and air quality implications are subsequently discussed.

Table of Contents

Chapter 1

An overview of this research project, in the context of the wider subject area, is here provided in this chapter. The fundamental importance of ozone as a trace gas in Earth's stratosphere is first outlined, before the contrasting importance of the small component by mass of tropospheric ozone is then summarised. Tropospheric sources and sinks, together with influx of ozone-rich air from the stratosphere, are subsequently discussed in influencing the regional and seasonal variability in the climatological distribution of tropospheric ozone. Atmospheric modes of interannual variability are also outlined as modulating influences. The relative importance of the stratospheric influx, versus in situ tropospheric production, has been the subject of a longstanding debate in determining the tropospheric ozone burden, owing to difficulty in isolating and quantifying each influence. The evolution of tropospheric ozone since pre-industrial times (before 1850) is lastly synthesised. Recent trends are also discussed in the context of possible changes in the attribution of the stratospheric influence.

Research questions arising from this overview are outlined at the end of this chapter. The motivation for the work undertaken in this thesis is reflected by these and the objectives within each of the main scientific research chapters (Chapters 4 to 6 inclusive) are here provided. The contents and structure of the thesis as a whole is additionally presented at the end of this chapter.

Introduction

Ozone (O_3) is a molecule composed of three oxygen atoms and was first postulated to exist in the upper atmosphere by Walter Noel Hartley in 1880. It was later confirmed, by French physicists Charles Fabry and Henry Buisson in 1913, that ozone indeed blankets Earth within a region of atmosphere between ~15 to 35 km and has since been referred to as the 'ozone layer'. The importance of the ozone layer for the evolution of all life on Earth has since been recognised, as this chemical species effectively filters incoming solar radiation in biologically harmful wavelengths within the UV region (~200-315 nm) of the electromagnetic spectrum. Whilst ozone in the atmosphere is primarily confined to this region, comprising ~85-90 % of ozone by mass, an additional ~10-15 % resides in the troposphere, with typical mixing ratios ranging from ~20 to 100 ppbv (Fishman et al., 1990; Salawitch et al., 2019).

Tropospheric ozone has wide-ranging implications for air quality, radiative forcing of Earth's climate and the oxidation capacity of the troposphere (Fiore et al., 2002a; Myhre et al., 2013). It is a contributing cause of some 7 million premature deaths annually worldwide due to air pollution (WHO, 2019); of second most importance after particulate matter (Paoletti et al., 2014). The global distribution of the respiratory mortality rate due to prolonged ozone exposure is exemplified in Figure 1.1, with a global hotspot of attributable deaths over India (> 100 per 100,000 people). These estimates were derived based on a relative risk approximation (defined by Turner et al., 2016), adjusted for NO_2 exposure and both near-source and regional PM2.5, using the annual average daily maximum 8-h ozone concentration as the exposure metric (Malley et al., 2017). High ozone levels may furthermore be detrimental to ecosystems, limiting photosynthesis and carbon sequestration (Paoletti, 2007; Monks et al., 2015), with an estimated $14-16 billion (US dollars; 2009) of crop yield losses annually worldwide (Van Dingenen et al., 2009). Ozone also serves as a primary source of the hydroxyl (OH) radical which acts to cleanse the troposphere by breaking down a large number of pollutants, along with some greenhouse gases (Seinfeld & Pandis, 2006; Cooper et al., 2010; Lelieveld et al., 2016). Ozone is also a greenhouse gas itself, exerting its largest radiative forcing in the upper troposphere due to the inherent low temperatures in the upper troposphere (Lacis et al., 1990). Ozone was estimated in the Intergovernmental Panel for Climate Change Fifth Assessment Report (IPCC AR5) to exert a total globally averaged radiative forcing of +0.35 (0.15 to 0.55) W m^{-2}, with a contribution of +0.40 (0.20 to 0.60) W m^{-2} from the troposphere and -0.05 (± 0.10) W m^{-2} from the stratosphere (Myhre et al., 2013), but with

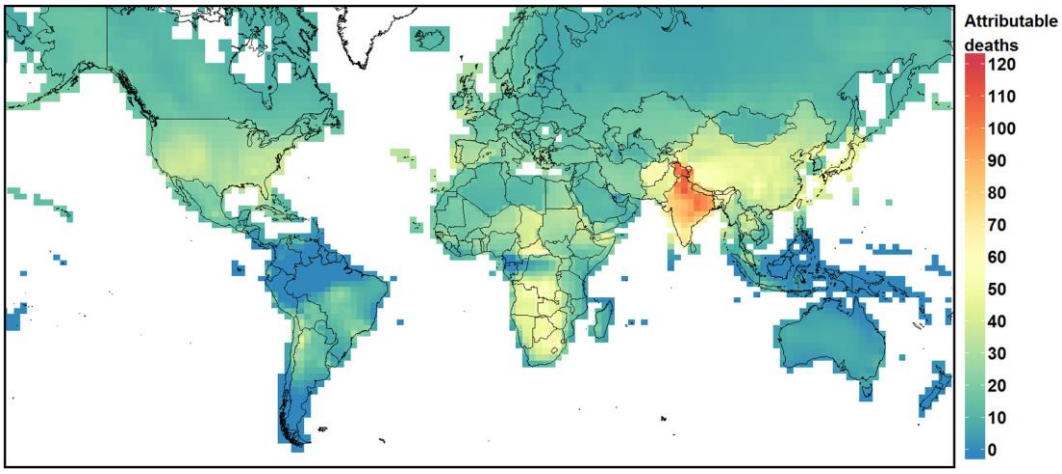

Figure 1.1 – Estimated number of respiratory deaths (per 100,000 people) attributable to long term ozone (O_3) exposure in 2010 for adults ≥ 30 years of age. Exposure to other pollutants (e.g. PM2.5 and NO_2) are accounted for in the estimates, which utilise the annual average daily maximum 8-h O_3 concentration metric to represent level of O_3 exposure. Adapted from Figure 1 in Malley et al. (2017).

significant latitudinal variation in this forcing since pre-industrial times (Checa-Garcia et al., 2018). The sign and magnitude of the ozone radiative forcing as a function of latitude is dependent upon the opposing influence of stratospheric ozone depletion (which promotes stratospheric cooling), with respect to the general background increase in tropospheric ozone (leading to warming). The study by Checa-Garcia et al. (2018), which derives historical tropospheric and stratospheric ozone radiative forcing estimates using the Coupled Model Intercomparison Project phase 6 (CMIP6) ozone dataset, highlights the increasing prevalence of cooling due to ozone (negative radiative forcing) over the Southern Hemisphere high-latitudes between the 1970s and 2000s, due to the dominance of stratospheric ozone depletion and relative small change in tropospheric ozone burden. This contrasts with the increasing, peak (positive) response in ozone radiative forcing over the subtropics (particularly in the Northern Hemisphere), due to the proximity to the primary source regions of tropospheric ozone precursors, during this time. Such a marked overall increase in tropospheric ozone since pre-industrial times is estimated to be equivalent to approximately 25 % of the forcing from carbon dioxide (CO_2) (Forster et al., 2007).

Since ozone has a relatively short global mean lifetime in the troposphere (~3 weeks), along with spatially and temporally highly varying sources and sinks (Lelieveld et al., 2009), it is not well mixed compared with longer-lived gases like carbon dioxide (CO_2) or nitrous oxide (N_2O), with large spatial and temporal variations in ozone abundance as a result over seasonal, interannual and decadal timescales. This is reinforced by the strong dependence on sunlight as well as precursor emissions, necessary for the formation of ozone, which have both natural and anthropogenic sources. The lifetime of ozone is however much shorter in the planetary boundary layer (PBL) due to the rapid breakdown by chemical reactions and surface deposition (Cooper et al., 2014). Subsequently, it is unsurprising that our knowledge of the global distribution and abundance of tropospheric ozone is poorly constrained, particularly on a regional and seasonal basis. This is illustrated in Figure 1.2 from both a trajectory-mapped ozonesonde dataset (TOST) and multiple satellite inferred maps of tropospheric column ozone, in which significant regional disparities are evident despite broad overall agreement.

A large fraction of the ozone in the troposphere is formed through photochemical reactions of precursor molecules such as carbon monoxide (CO), nitrogen oxides (NOx), methane (CH_4) and non-methane volatile organic compounds (VOCs) (The Royal Society, 2008; Monks et al., 2009). Natural ozone precursor emission sources include wildfires,

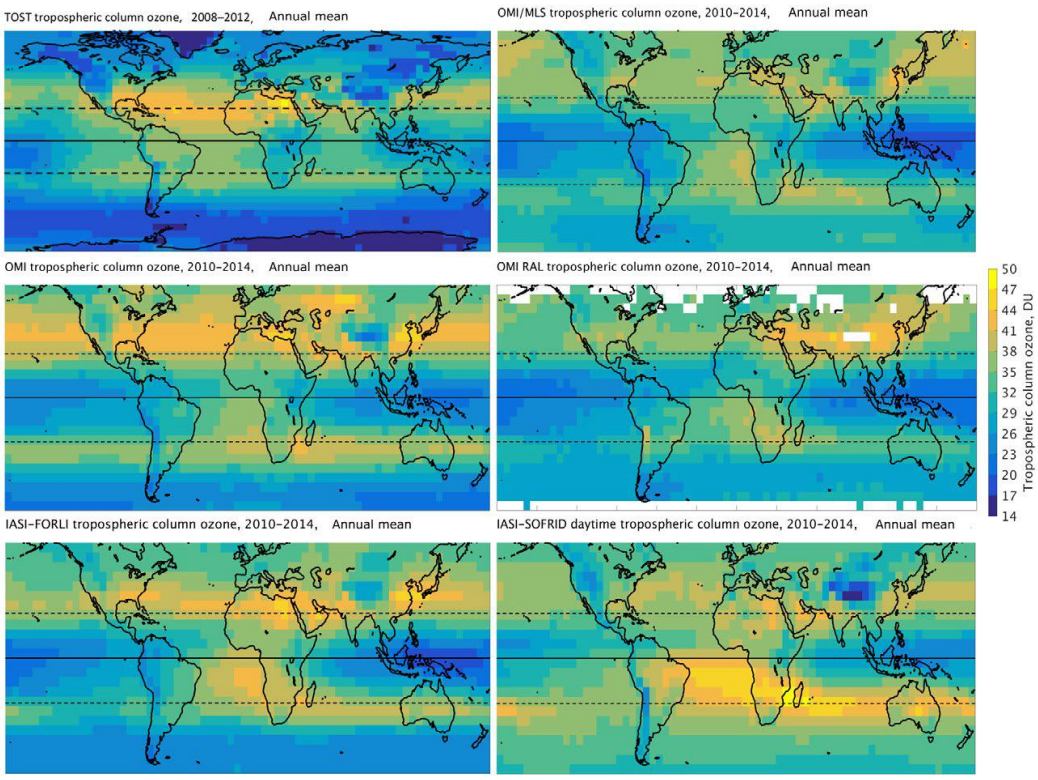

Figure 1.2 – Maps of annual mean tropospheric subcolumn ozone (O_3) (Dobson Units, DU) derived from ozonesondes (TOST) (top left) and five different satellite products: OMI/MLS (top right), OMI-SAO (middle left); OMI-RAL (middle right); IASI-FORLI (bottom left) and IASI-SOFRID (bottom right). The TOST data is averaged over the period 2008-2012, whereas the five satellite products are averaged over the period 2010-2014, gridded at 5° x 5° horizontal resolution. Taken from Figure 10 in Gaudel et al. (2018).

biogenic hydrocarbon emissions, lightning NO_x and biogenic NO_x from soils, whilst anthropogenic source contribution arises from activities such as crop burning, biofuel and fossil fuel burning (Cooper et al., 2014). Whilst the contribution of biomass burning to the formation of ozone precursor emissions due to human activities in each hemisphere is relatively even (Lelieveld and Dentener, 2000), some 90 % of fossil fuel produced NO_x emissions originate from the Northern Hemisphere. Ozone may be produced either in situ or remotely to precursor source regions, as determined by the prevailing synoptic meteorological conditions, with the potential for long-distance advection prior to photochemical destruction or deposition (Lelieveld et al., 2009). An additional source of tropospheric ozone is that of exchange of stratospheric and tropospheric air, which leads to a net downward flux of ozone (Holton and Lelieveld, 1996; Lamarque et al., 1999; Lelieveld and Dentener, 2000; Stohl et al. 2003), especially in mid-latitude regions (Miles et al., 2015). Known as stratosphere-troposphere exchange (STE), this flux is ultimately determined by a mean meridional residual circulation in the stratosphere (the Brewer-Dobson Circulation (BDC): see section 2.2), which also explains the latitudinal pattern of

ozone and other tracers in the stratosphere (Haynes et al., 1991; Holton et al., 1995). The relative importance of the stratospheric influence, versus in situ formation from tropospheric ozone precursors, has been a subject of extensive debate over the decades and remains poorly understood, particularly at a regional level and on a seasonal basis. At one end of the spectrum, up to nearly 90 % of the tropospheric ozone burden has been attributed to in situ photochemical formation from ozone precursors in recent model and observational constrained studies (e.g. Kalabokas et al., 2017), whilst many other studies highlight the importance of the stratosphere in sometimes rivalling the contribution from this influence (e.g. Lelieveld and Dentener, 2000; Banarjee et al., 2016). The contribution of each influence thus warrants further quantitative, comprehensive evaluation.

The seasonal cycle in tropospheric ozone abundance is generally larger in the Northern Hemisphere and is dominated here by photochemical processes. Although photochemistry also governs the seasonality over the Southern Hemisphere to a large extent, STE has a significant influence on the seasonal cycle at background locations especially (Lelieveld and Dentener, 2000). In the extratropics, a springtime peak in tropospheric ozone has long been known to occur (Bojkov, 1986; Linvill et al., 1980; Lisac and Grubišić, 1991; Perl, 1965; Feister and Warmbt, 1987), largely in phase with the seasonal cycle in the STE. In the Northern Hemisphere mid-latitudes for example, a maximum in STE occurs in February-March, with a subsequent maximum in surface ozone over a month later (Lelieveld and Dentener, 2000). A tendency towards a broadened and extended spring-summer tropospheric ozone maximum has however been widely reported in recent decades, principally due to the influence of anthropogenic pollution, although a shift back towards a springtime maximum is already in evidence at more rural sites in regions where reductions in ozone precursor emissions are already proving successful (Cooper et al., 2014). The characteristics of the seasonal cycle in lower tropospheric ozone (750 hPa), from both models and observations, is illustrated in Figure 1.3 for both the Northern and Southern extratropics and tropics. It should however be noted that the seasonality of tropospheric ozone also varies significantly from region to region. During summertime, regions such as Eastern Mediterranean and Middle East (EMME) are particularly prone to high levels of tropospheric ozone that also impact surface air quality (up to 80 ppbv or 160 μg m^3). Such 'hotspots' in tropospheric ozone occur naturally in part due to preferential stratosphere-to-troposphere transport (STT) pathways, associated with high tropopause fold activity in regions of strong subsidence (Lelieveld et al., 2009; Zanis et al., 2014; Akritidis et al., 2016; 2019), in conjunction with

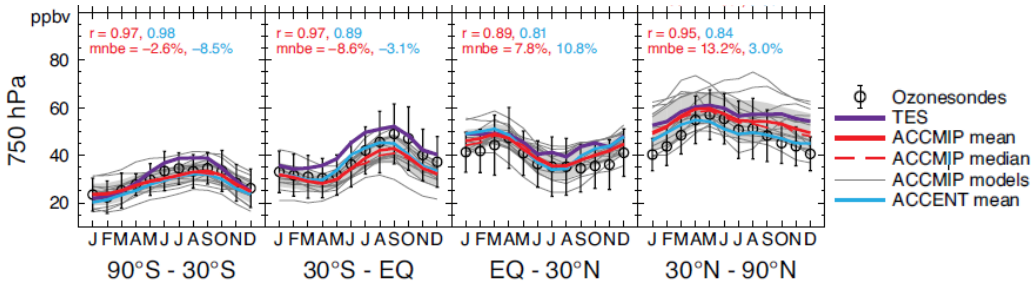

Figure 1.3 – The seasonal cycle in lower tropospheric ozone (750 hPa) as resolved from ozonesondes, the Tropospheric Emission Spectrometer (TES), and as simulated by two independent chemistry-climate model (CCM) intercomparison projects from a year 2000 time-slice mean (independent models represented by thin grey lines in the case of ACCMIP). The seasonality is shown for (**left to right**) the Southern Hemisphere extratropics, Southern Hemisphere tropics, Northern Hemisphere tropics and Northern Hemisphere extratropics. Uncertainty is represented by error bars (average interannual standard deviation) for the station observations and the grey shaded region (± standard deviation) for the ACCMIP ensemble mean. Correlation (*r*) and mean normalised bias error (mnbe) values for both the ACCMIP (red) and ACCENT (blue) ensemble means provide quantification of the level of model-measurement agreement. Adapted from Figure 4 in Young et al. (2013).

favourable meteorological conditions for the photochemical production of ozone from abundant precursor emissions that together favour exceedances of the 60 ppbv European air quality standard (Kalabokas et al., 2017; EEA, 2018). This contrasts with other subtropical regions that have an ozone maximum closer to wintertime such as over the South Atlantic region, where biomass burning over western Africa is prevalent during the dry season and is advected offshore (Mauzerall et al., 1998).

Regional and seasonal tropospheric ozone levels also exhibit significant interannual variability and have been linked to the major modes of internal variability such as the El Niño Southern Oscillation (ENSO). Attendant reorganisation of the distribution of tropical upwellling and adjacent regions of subsidence leads to basin-wide anomalies in tropospheric ozone abundances across the tropical Pacific (e.g. Olsen et al., 2016). ENSO may also act as a teleconnection to the dynamical state of the extratropics via both tropospheric and stratospheric pathways (Zeng and Pyle, 2005; Doherty et al., 2006). Although not fully understood, it is known that ENSO can induce shifts in both the subtropical and mid-latitude eddy-driven jet streams as a result of changes to the wave propagation pathways of Rossby waves, most notably over the Pacific sector (Langford, 1999; Trenberth et al., 2002). These perturbations can however propagate downstream, influencing the location and amplitude of mid-latitude ridges and troughs, in turn, modulating tropospheric ozone and STE (Olsen et al., 2016). Another important driver of tropospheric ozone variability, through modulation of STE principally, is the Quasi-

Biennial Oscillation (QBO) which has implications for the strength of the BDC in conjunction with the phase of ENSO (Hsu and Prather, 2009; Neu et al., 2014; Tripathi et al., 2014). Although the easterly phase of the QBO is known to favour an enhanced BDC (Garfinkel et al., 2012; Tripathi et al., 2014), and in turn the seasonal build-up of ozone in the LMS (Krebsbach et al., 2006), the impacts on STE of ozone may be much more complex. Whilst some studies indeed show an enhancement in STE under such conditions (Neu et al., 2014), other studies find the opposite tendency due to other competing factors. For instance, Hsu and Prather (2009) find evidence for an unfavourable dynamical condition for mixing in the mid-latitude, lower stratosphere during the easterly QBO phase which can hinder STE. In conjunction with other modes of variability, tropospheric ozone levels and the STE ozone flux can thus be impacted on a global scale, although such mechanisms are difficult to ascertain and disentangle due to the complex interplay between different drivers and potential chemical-dynamical feedbacks.

Since the late 19th century, changes or trends in the tropospheric ozone burden can be largely attributed to anthropogenic precursor emissions. This had led to a significant increase in baseline (HTAP, 2010; Cooper et al., 2014), and also background (Fiore et al., 2002b; Zhang et al., 2008; Stevenson et al., 2013) ozone volume mixing ratios (VMRs), where baseline concentrations are considered to be the amount measured at sites unaffected by recent, locally produced anthropogenic pollution, whereas background ozone levels refer to the atmospheric concentration due to natural sources alone and are purely a model construct. There is however a large element of uncertainty over the magnitude of such an increase. Whilst a typical increase on the order of 25-50 % in the burden of tropospheric ozone since 1900 is acquired from atmospheric chemistry models (e.g. Young et al., 2013), direct measurements imply increases in surface ozone mixing ratios of up to 300 % (Volz and Kley, 1988; Marenco et al., 1994; Pavelin et al., 1999), albeit with an uncertain level of accuracy. Other observational studies however support the range of tropospheric ozone increase from models (Yeung et al., 2019). The largest increases are simulated in the Northern Hemisphere mid-latitudes (although it should be noted that this attribution is derived purely from modelling studies). In pre-industrial times (before 1850), surface ozone mixing ratios were estimated to be around ~30 ppbv during the springtime seasonal maximum, but are widely in exceedance of 40 ppbv across the Northern Hemisphere during summertime (the peak of the photochemically active season) in the present day (Vingarzan, 2004). Moreover since the 1970s, the climatology of tropospheric ozone has increasingly diverged in mid-latitudes between each

hemisphere (Cooper et al., 2014), which was not apparent before this decade (Fabian and Pruchniewicz, 1977).

Recent trends in tropospheric ozone are regionally and seasonally complex however and are strongly influenced by changing emissions of ozone precursors. In recent decades, the largest increases in surface ozone are found over East Asia (Ding et al. 2008; Wang et al., 2009; Li et al., 2010; Lin et al., 2010; Parrish et al., 2012; Oltmans et al., 2013), which contrasts with recent decreases or a levelling off in regions such as the eastern US during summer (Lefohn et al., 2010) and background sites over western Europe (Tarasova et al. 2009; Gilge et al., 2010; Logan et al. 2012; Parrish et al. 2012; Derwent et al., 2013; Oltmans et al. 2013). This picture is consistent with recent declines in ozone precursor emissions across Europe and North America and increases over East Asia (Granier et al., 2011), with a shift of emissions more generally from high to low latitudes in the Northern Hemisphere (Parrish et al., 2014). Modelling studies show that changes in both long-range transport and STE are also influential in explaining observed regional and seasonal trends, with each factor varying in magnitude with height, region and season, which is corroborated by observations. For instance, tropospheric ozone levels across western North America are particularly susceptible to increasing Asian emissions due to long-range transport across the Pacific (Hudman et al., 2004; Zhang et al., 2008; Cooper et al., 2010; Lin et al., 2014; 2015) and the increasing contribution of the stratosphere to the tropospheric ozone burden has been noted in recent years (Ordóñez et al., 2007; Hess and Zbinden, 2013; Lin et al., 2012; 2015). Whilst many studies find evidence for an increase in STT of ozone under anthropogenic-induced climate change (Hegglin and Shepherd, 2009; Neu et al., 2014; Akritidis et al., 2019), such finding is highly sensitive to the choice of metric as illustrated in a study by Oberländer-Hayn et al. (2015). The complication of a rising tropopause under climate change may reduce the overall STE mass flux, across this specific reference surface, whilst the STE of ozone flux may indeed increase (as STT becomes more ozone-enriched).

This research project aims to advance our understanding and knowledge of the influences on tropospheric ozone, specifically the role of STE with respect to in situ formation from ozone precursor emissions, as resolved both regionally and seasonally using contemporary models and measurements in a combined approach. To help address this, the following research questions are here outlined:

(1) *"What are the limitations of satellite-retrieved tropospheric ozone measurements from UV-nadir sounders? What are the sources of potential retrieval error that may contribute towards such limitations? How can such retrieval errors be mitigated, thus reducing associated uncertainty and retrospectively improving the accuracy of the satellite datasets?"*

(2) *"What are the regional and seasonal characteristics of tropospheric ozone, according to both models and measurements? How does the role of the stratosphere compare with influence from in situ formation of ozone? What are the recent changes in tropospheric ozone and how is this influenced by changes in STE?"*

(3) *"What are the sources of interannual variability in tropospheric ozone and STE? Which teleconnections or drivers are understudied in relation to such impacts? What are the radiative implications of resultant composition changes in response to such sources of internal variability? What are the ramifications for STE of ozone and tropospheric ozone, including potential impacts on surface air quality?"*

As a first step (1), the limitations of observational data from UV-nadir sounding instruments will be evaluated using ancillary datasets (ozonesondes and chemical reanalysis data) in this thesis. A fundamental understanding of the uncertainty range associated with the retrieval of tropospheric column ozone in this configuration will be important when using such data for later validation of model and other independent data (e.g. ozonesondes). As a long term goal beyond the scope of this research project, development of a geophysically meaningful bias correction scheme, that can be applied on a profile-by-profile bias, would help to greatly constrain the uncertainty range associated with the satellite measurements. As a first step towards achieving this however, an attempt to identify and quantify the effect of the main factors leading to retrieval error, here, will be useful when undertaking evaluations in the next phase of work presented in this thesis. The regional and seasonal characteristics of tropospheric ozone will be investigated (2); providing an update to earlier studies (e.g. Lamarque et al., 1999) using new available measurements, state-of-the-art chemistry climate models (CCMs), and additional model diagnostics. Recent changes in tropospheric ozone will be evaluated, together with the changing influence of the stratosphere during the most recent climatological period (1980-2010). The interannual variability in tropospheric

ozone will additionally be assessed, and subsequently following on from this work, the role of a largely neglected component of variability in the extratropical stratosphere (3), specifically sudden stratospheric warmings (SSWs) (see section 2.4.6), in influencing the STE of ozone flux will be explored. The decision to investigate SSWs in relation to STE and tropospheric ozone was informed from an in depth synthesis of the literature surrounding the drivers of interannual variability (section 2.4). Having addressed the broader questions concerning the stratospheric influence on tropospheric ozone in (2), it became clear that the same tools could be used to investigate such element of interannual variability in more detail. Investigation of the radiative importance of chemical composition changes in the upper-troposphere lower-stratosphere (UTLS) however constitutes an additional aspect that is explored, on the premise that such changes can have potentially important impacts on Numerical Weather Prediction (NWP) skill following such events, with implications for predictability on sub-seasonal timescales.

Chapter 2 will cover the theoretical background to the present-day distribution of atmospheric ozone, as well as the mechanisms of STE and modulating influences. Details of the different data sources used will be outlined in Chapter 3, including intricacies of the UV-nadir instrument retrieval algorithms and the methods by which these satellite measurements can be directly compared with both models and in situ observations. A brief idealised assessment of the impact of model biases on limiting the effectiveness of model-measurement comparisons of tropospheric ozone using such methods will then be presented. Chapter 4 will first comprise quantitative evaluation of the agreement of observations from the Global Ozone Monitoring Experiment-2 (GOME-2A) and Ozone Monitoring Instrument (OMI) UV-nadir satellite instruments, with respect to an independent observationally constrained dataset, the Copernicus Atmospheric Monitoring Service (CAMS) reanalysis. This comparison will then be expanded by quantifying the relationships of the differences as a function of different co-retrieved geophysical and instrumental variables, to elucidate the leading causes of retrieval error. This exercise will constitute a pre-requisite to development of a profile-by-profile, geophyiscally meaningful bias correction scheme that could retrospectively improve the accuracy of the GOME-2A and OMI tropospheric ozone datasets. An updated assessment of the regional and seasonal characteristics of tropospheric ozone will then be presented in Chapter 5, with quantification of the stratospheric influence and its contribution to recent changes using the CCMs. The models are however first tested for robustness and constrained using the findings of a model-measurement comparison. The influence of

sudden stratospheric warmings (SSWs), which constitute the largest deviations in the Northern Hemisphere extratropical stratosphere from the mean climatological background state, on the distribution of Arctic UTLS ozone and water vapour is next investigated in Chapter 6, together with the implications for the STE of ozone flux. Transient radiative impacts based on such chemical perturbations are calculated, alongside results of some sensitivity evaluations for artificially imposed biases in UTLS ozone and/or water vapour. Quantification of background and episodic enhancements in tropospheric ozone over mid-latitudes are also later derived. Finally, a synthesis of the findings in this thesis is given in Chapter 7 and the wider implications of the research are discussed.

Chapter 2

A comprehensive, in depth synthesis of the chemical and dynamical drivers of tropospheric ozone is presented in this chapter. The distribution of ozone in Earth's atmosphere is first summarised, followed by an overview of the photochemical controls of ozone in both the stratosphere and the troposphere respectively. The fundamental importance of the stratospheric Brewer-Dobson circulation in determining the stratosphere-troposphere exchange (STE) of ozone flux is then reviewed. The mechanisms of STE are then discussed and explored in relation to regional and seasonal variability in STE and resultant tropospheric ozone levels. Finally, the role of the primary modes of interannual variability within Earth's climate system, in determining interannual variability in STE and tropospheric ozone, are reviewed in turn. This extensive review culminated in the identification of an understudied source of interannual variability in this context (sudden stratospheric warmings), which is subsequently the basis of investigation in Chapter 6.

Background

Ozone is a trace gas in Earth's atmosphere, ranging from ~20-100 ppbv in the troposphere (Fishman et al., 1990) and up to ~10 ppmv in the stratosphere, in conjunction with the ozone layer. This is depicted in Figure 2.1 in the form of mean vertical profiles in ozone concentration and (volume) mixing ratio, which are two important but fundamentally different quantities as a measure of the abundance of ozone. Whilst concentration (or number density) is a measure of the amount of ozone within a unit volume of air, hence units are typically expressed as molecules cm^{-3} or $\mu g\ m^{-3}$, mole fraction or (volume) mixing ratio constitutes the ratio of ozone molecules to all air molecules (typically expressed in units of mol mol^{-1} or ppmv respectively), yielding such difference in vertical profile shape as air density falls with altitude. Profiles of trace gases such as ozone are also commonly expressed as a partial pressure, in which the pressure exerted by all molecules of species is calculated if all other gases of a mixture are removed (Jacob, 1999). For this reason, the vertical distribution of ozone partial pressure closely matches that of ozone concentration (number density).

In the stratosphere, variations in ozone abundance are fairly uniform, but significant meridional and seasonal gradients exist. Although the highest ozone concentrations are found locally around 10 hPa (~30-35 km) in the tropics, total and stratospheric columns

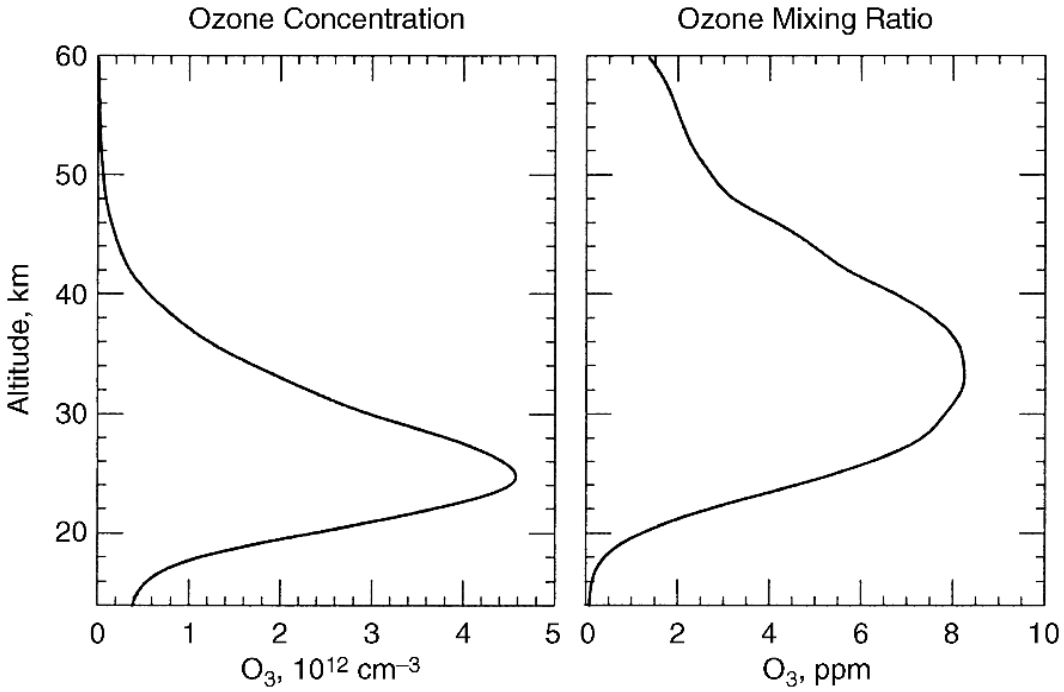

Figure 2.1 – Vertical O_3 profile through the stratosphere, as measured by the satellite Jet Propulsion Laboratory Fourier transform infrared (FTIR) spectrometer in September 1996 for the Northern Hemisphere mid-latitude (35°N). Note the difference in the altitude peak of the molecular concentration and mixing ratio profiles. Taken from Figure 2.6 in Seinfeld and Pandis (2006).

exhibit the lowest values here due to intense tropical upwelling in association with the Brewer-Dobson Circulation (BDC); a global wave-driven, meridional residual circulation within the stratosphere (see section 2.2). This contrasts with much higher values in the extratropics in each hemisphere (particularly in wintertime) as this circulation leads to the poleward transport and accumulation of ozone in this region. This is despite the primary photochemical production of ozone at low-latitudes, which is testament to the importance of dynamically-induced transport given the long lifetime of ozone in the stratosphere. A major seasonal anomaly (most notably in the Southern Hemisphere) is the annual occurrence of an 'ozone hole' due to photochemical depletion aided by extremely low polar stratospheric temperatures. Although such depletion occurs naturally to some extent, this has been exacerbated in recent decades due to anthropogenic emissions of chlorofluorocarbons (CFCs) which lead to the catalytic destruction of ozone in such environment. The spatiotemporal evolution of ozone in the troposphere is much more complicated and is produced from ozone precursor emissions from both natural and anthropogenic sources, together with downward transport of ozone from the stratosphere. Given the relatively short lifetime in the troposphere (~3 weeks), the abundance can be highly variable over short distances and vary significantly over periods of hours to days, particularly towards the earth's surface. This chapter aims

to cover the important influences over the regional and seasonal characteristics of tropospheric ozone, with particular emphasis on the stratospheric contribution. Ozone photochemistry is first presented in section 2.1, followed by a synthesis of the BDC in section 2.2. The relation of the BDC to the occurrence of stratosphere-troposphere exchange (STE) is then discussed in section 2.3 before the role of teleconnections, in terms of influencing STE and tropospheric ozone on interannual and intraseasonal timescales, is covered finally in section 2.4.

2.1 Ozone in the Atmosphere

2.1.1 Stratospheric Ozone Photochemistry

The majority (~90 %) of atmospheric ozone is found in the stratosphere (~10-50 km), with the largest abundances within the ozone layer (~15-35 km), with a peak mixing ratio abundance of ~12 ppmv (Seinfeld and Pandis, 2006). This peak occurs around ~30-35 km, which is above the region of peak ozone concentration (number density) as shown previously in Figure 2.1, between approximately 20 and 30 km (Holloway and Wayne, 2010). The arrival of relatively short wavelength ultraviolet radiation from the sun (λ < 242 nm) leads to the photolysis of oxygen (O_2) in the stratosphere to yield atomic oxygen:

$$O_2 + h\nu \rightarrow O + O \qquad \lambda < 242\,nm \tag{2.1}$$

With $h\nu$ the product of the Planck constant and the frequency of light at wavelength λ.

Produced atomic oxygen then readily combines with O_2 molecules in the presence of a third, inert species *M* to form ozone (O_3):

$$O + O_2 + M \rightarrow O_3 + M \tag{2.2}$$

Where *M* (usually N_2 or O_2) serves as a collision partner that has the role of removing excess energy, which leads to the eventual dissipation in the form of heat (Jacob, 1999). Equation 2.2 constitutes the sole ozone formation reaction applicable to the entirety of Earth's atmosphere, although production of ozone in the stratosphere is largely confined to an altitude of ~25-30 km or above. Ozone is primarily produced in the tropical mid-stratosphere, before being transported poleward and downward by the BDC toward the polar lower stratosphere. As observed by Dobson in the 1930s (Dobson, 1963), the circulation subsequently results in the largest abundances of vertically integrated total column ozone across the mid- to high-latitudes; most notably during winter when the BDC is strongest (Baldwin et al., 2019). Due to strong absorption of ozone in the 240-320 nm

wavelength range however (the Hartley bands), where it is the dominant absorbing chemical species, ozone is subject to decomposition (photolysis) to form again O_2 and O which strongly increases with altitude. For altitudes below 30 km, ozone photolyses at longer wavelengths (in the Chappuis bands) with the rate largely independent of altitude (Seinfeld and Pandis, 2006):

$$O_3 + h\nu \rightarrow O + O_2 \qquad \lambda\,(400 - 600\,nm) \qquad (2.3a)$$

$$O_3 + h\nu \rightarrow O(^1D) + O_2 \qquad \lambda < 320\,nm \qquad (2.3b)$$

These photolysis reactions constitute the primary sink of ozone. In the case of reaction 2.3b, $O(^1D)$ (an oxygen atom in an excited state) is readily quenched to ground-state atomic oxygen which can then combine with additional O_3 molecules to reform two oxygen molecules:

$$O + O_3 \rightarrow O_2 + O_2 \qquad (2.4)$$

Lastly, atomic oxygen atoms may also react together in the presence of a third species *M* to yield oxygen:

$$O + O + M \rightarrow O_2 + M \qquad (2.5)$$

The ozone reaction sequence above (Equations 2.1-2.5) is known as the Chapman mechanism, as proposed by Chapman (1930). However, it was later realised that the equilibrium for an equatorial profile cannot be adequately explained by a simple box model (Seinfeld and Pandis, 2006). This is because catalytic reaction cycles involving NO_x and HO_x were needed to explain the observed values. The influx of ozone depleting substances (ODSs), such as chlorofluorocarbons (CFCs), from surface anthropogenic emissions as early as the 1960s however, as demonstrated in Shepherd et al. (2014), subsequently lead to the formation of an additional catalyst (ClO_x) which further disturbed the equilibrium balance of the stratospheric ozone layer. These substances are long-lived and are extremely stable, only photolysing under intense UV in the stratosphere where chlorine is released, which acts to destroy ozone in catalytic reaction cycles. This photochemistry is illustrated in Figure 2.2, together with a depiction of the global nature of resultant impacts on stratospheric ozone due to the BDC. A positive trend in surface CFC-12 during the 1990s in both hemispheres further highlights the long residence times within the atmosphere. The various destructive catalytic cycles are contained within Table 1 of Solomon (1999). ODSs are generally highly stable and inert, but can photolyse to yield free chlorine radicals in the stratosphere under intense

incoming UV solar radiation from the sun. The destruction of ozone in a second step involving catalytic reaction cycles can then ensue. Very short lived species (VSLS), which are an important subset of ODSs with lifetimes typically less than six months, also contribute to stratospheric halogen loading (Sturges et al., 2000; Laube et al., 2008). The very short lifetime means that efficient transport mechanisms, such as deep tropical convection, are necessary for rapid transport from the surface to the tropical tropopause; the entry point for air into the stratosphere (IUP Bremen, n.d.). Bromine substances usually originate from natural sources such as seaweed and phytoplankton, whereas chlorine substances are typically emitted from anthropogenic sources (Hossaini et al., 2015). VSLSs such as methyl bromide (CH_3Br) have a relatively longer lifetime of up to a year (Yvon-Lewis and Butler, 2015).

Ozone depletion in the stratosphere was first confirmed from measurements at the Halley British Antarctic Survey station during austral springtime (Farman et al., 1985). A clear indication of an ozone hole over the continent during Antarctic spring was soon realised from a combination of ozonesonde measurements at other Antarctic stations (e.g. Komhyr et al., 1986), observations from satellites (Stolarski et al., 1986), as well as other remote sensing measurements, including both in situ infrared (Farmer et al., 1987) and visible spectroscopy (Mount et al., 1987) measurement techniques. This “hole” was later

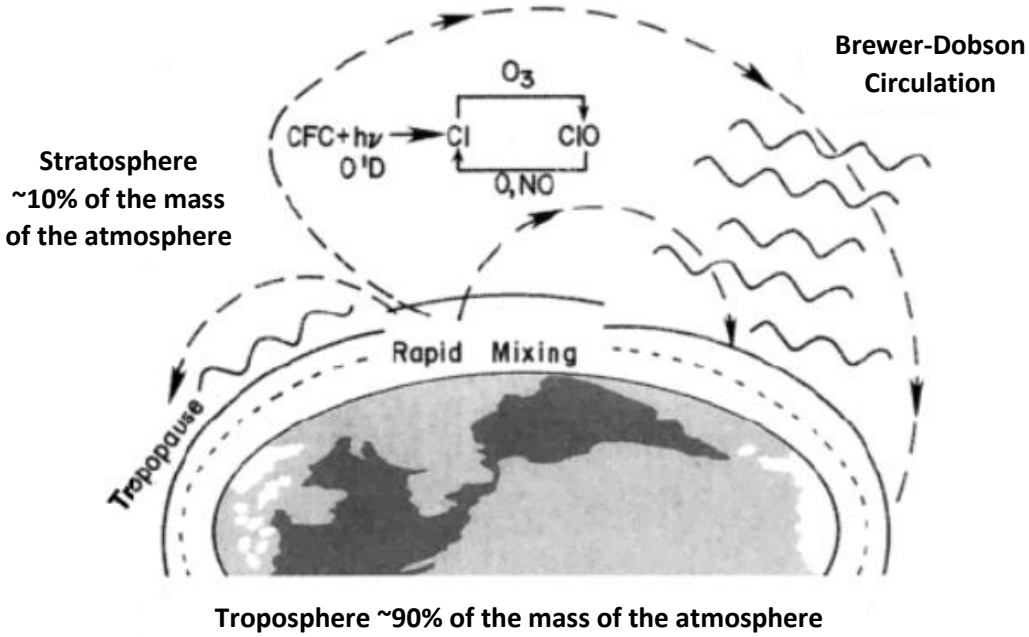

Figure 2.2 – Schematic depicting the depletion of middle and upper stratospheric ozone induced by the breakdown of CFCs and the resultant catalytic destruction. The fundamental dynamical pathways for trace gas transport (including CFCs) are also indicated in association with the BDC. Adapted from Figure 2 in Solomon (1999).

noted to coincide broadly with the expanse of the wintertime stratospheric polar vortex (SPV) (Holton et al., 1995). The importance of heterogeneous chemical depletion of ozone on so-called Polar Stratospheric Clouds (PSCs), which only form when temperatures fall below ~-85°C (Austin et al., 2003) as found during early spring in the polar stratosphere between ~12 and 25 km, has since been recognised in explaining such "ozone hole" feature (e.g., Solomon et al. 1986; McElroy et al. 1986; Tung et al. 1986; Molina and Molina 1987; Anderson et al. 1989).It is important to note however that stratospheric ozone depletion has not only been confined to polar regions, but has also occurred to a lesser extent worldwide without the additional influence of such heterogeneous reactions. Between 1979 and 1997 for instance, when ODSs were increasing to their highest concentrations before the intervening regulations imposed by the Montreal Protocol in 1987, stratospheric ozone declined at a rate of approximately -7 % per decade in the upper to middle stratosphere of the Northern Hemisphere mid-latitudes according to satellite observations (WMO, 2014). It is anticipated from interactive chemistry-climate models (CCMs) that total ozone levels will however return to pre-1980 levels before 2050, with the exception of Antarctica where this is expected 10 years later (Dhomse et al., 2018; Langematz and Tully, 2018).

2.1.2 Tropospheric Ozone Photochemistry

In contrast to the stratosphere, where ozone is formed entirely naturally due to the photodissociation of O_2 molecules, ozone in the troposphere is photochemically produced via ozone precursors, which are emitted from both natural and anthropogenic ground-based sources. Chemical species such as carbon monoxide (CO), volatile organic compounds (VOCs) and hydrocarbons (RH), are oxidised in the presence of nitrogen oxides (NO_x = NO + NO_2), which act as a catalyst, to form ozone photochemically in the troposphere. The principal RH oxidation sequence within the atmosphere involves the rapid photolysis of NO_2 at wavelengths < 424 nm (Lelieveld and Dentener, 2000; Seinfeld and Pandis, 2006; Doherty et al., 2006):

$$RH + OH\ (+ O_2) \rightarrow\ RO_2 + H_2O \tag{2.6}$$

$$RO_2 + NO\ (+ O_2) \rightarrow\ NO_2 + HO_2 + CARB \tag{2.7}$$

$$HO_2 + NO \rightarrow\ NO_2 + OH \qquad \lambda < 424\ nm \tag{2.8}$$

$$2[NO_2 + h\nu\ (+ O_2) \rightarrow\ NO + O_3] \qquad \lambda < 420\ nm \tag{2.9}$$

$$Net: \quad RH + hv + 3O_2 \rightarrow 2O_3 + H_2O + CARB \tag{2.10}$$

Where CARB refers to carbonyl compounds. This reaction sequence is initiated by hydroxyl (OH) radicals formed in a reaction step (as part of the HO_x cycles) following Equation 2.3b (Lelieveld and Dentener, 2000; Doherty et al., 2006):

$$O(^1D) + H_2O \rightarrow 2OH \tag{2.11}$$

Ozone is produced in the oxidation sequence (Equations 2.6 to 2.10) from conversion of NO to NO_2, with OH regenerated in the process, whilst the photodissociation of carbonyl compounds (aldehydes in particular) also leads to the formation of CO and additional O_3 (Lelieveld and Dentener, 2000). The lifetime of ozone can be highly variable in the troposphere, ranging from days to months (Wang and Jacob, 1998; Law, 2010), but is typically around ~3 weeks in the free troposphere (Lelieveld et al., 2009). Due to the quiescence of photochemistry in winter, the lifetime of ozone and its precursors is longest during this season (Hauglustaine et al., 1998). There is also a strong altitudinal dependence in the lifetime of ozone within the troposphere; ranging from just a few days in the tropical planetary boundary layer (PBL), where surface deposition and chemical reactions readily act to destroy ozone (Cooper et al., 2014), to as much as a year in the upper troposphere (IPCC, 2013). Since pre-industrial times, it is estimated that the globally averaged ozone lifetime has decreased by ~20 % due to the predominance of ozone increases in the lower troposphere, where the lifetime is much shorter than in the upper to middle troposphere (Wang et al., 1998c). Thus, although the chemical production of ozone has more than doubled since then, the burden of tropospheric ozone is only 63 % greater (Wang and Jacob, 1998).

Again, photolysis is the primary sink of ozone in the troposphere (as in Equation 2.3b) and is followed by subsequent reaction with water vapour (H_2O) molecules as in Equation 2.11. This reaction is one of the main sources of OH in the atmosphere, which serves to regulate the oxidation capacity of the troposphere. Levels of pollution from CO and VOCs, as well as the potent greenhouse gas methane (CH_4), are controlled via sink reactions involving OH radicals (Fishman et al., 1979).

2.1.2.1 Precursor Emission Sources

Tropospheric ozone precursor emissions originate from both anthropogenic (e.g. fossil fuel burning) and natural sources (biomass burning, lightning, soils, wetlands etc.) (Sauvage et al., 2007; Monks et al., 2009). Quantitative estimates for emissions (Tg yr^{-1})

Source Category	CO, TgC yr^{-1}			NMHC, Tg yr^{-1}			NO_x, TgN yr^{-1}		
	1860	1993	2025	1860	1993	2025	1860	1993	2025
Energy use									
fossil fuel combustion	2	112	142	1	37	67	0.3	24.4	41.1
fossil fuel production				0	26	65			
biofuel combustion	22	83	83	8	32	32	0.4	1.3	1.3
aircraft							0	0.5	1.6
Industrial processes	6	15	18	0	56	102	0	1.5	2.8
Biomass burning									
savannah burning	24	77	95	5	15	17	0.9	3.1	3.6
tropical deforestation	8	48	71	1	8	12	0.2	1.1	1.6
temperate wildfires	90	46	50	7	4	4	1.6	0.8	0.9
agricultural waste burning	36	89	156	5	16	19	0.9	2.2	3.9
Agricultural soils							0	2.2	4.5
Natural vegetation/soils	115	115	115	403	403	403	3	3	3
Lightning							5	5	5
NO_y from stratosphere							0.6	0.6	0.6
Natural	205	161	165	410	407	407	10.2	9.4	9.5
Anthropogenic	98	424	565	20	190	314	2.7	36.3	60.4
Total	303	585	730	430	597	721	12.9	45.7	69.9

Here Tg = 10^{12} g. Data are from J. A. Van Aardenne et al. (A high-resolution data set of historical anthropogenic trace gas emissions for the period 1890–1990, submitted to *Global Biogeochemical Cycles*, 1999). NMHC is nonmethane hydrocarbons.

Table 2.1 – Annual estimates for three main O_3 precursor emissions for the pre-industrial (1860), end of the 20th century (1993) and as projected in the near-future (2025). Taken from Table 1 in Lelieveld and Dentener (2000).

of three main ozone precursor species (carbon monoxide (CO), non-methane hydrocarbons (NMHC) and nitrogen oxides (NO_x)) are shown in Table 2.1 for the pre-industrial (1860), end of the 20th century (1993) and as expected in the year 2025, with respect to the various different source categories diagnosed in Lelieveld and Dentener, 2000. Note that methane (CH_4) is an additional important species, but was not the subject of a detailed budget analysis in this study, which used a global transport-chemistry model driven by European Centre for Medium-Range Weather Forecasts (ECMWF) reanalysis data, hence its omission here. The ratio of the production of both CO and NMHC are of approximately equal magnitude for all three reference years, where they collectively constitute the bulk of the tropospheric ozone precursor species burden, with NO_x emissions only a relatively small component in each instance. Despite this, NO_x is understood to exert a dominant control over the in situ formation of tropospheric ozone, as it serves as a catalyst for production from CO and hydrocarbons (Crutzen, 1988). NOx is estimated to influence photo-oxidation of CO, methane (CH_4) and NMHC by as much as 90 % (Lelieveld and Dentener, 2000). A sharp increase is evident for each species from pre-industrial times to the near present-day (2025) estimates, on the order of ~80-125 % for CO and NMHC, but as much as ~500 % for NO_x. For CO and NO_x, the partitioning of the production from both natural and anthropogenic sources dramatically shifts from a dominant natural input to a dominant anthropogenic input. For NMHC, the anthropogenic input is initially small but almost rivals the natural input in terms of magnitude for the 2025 estimate.

2.1.2.2 Tropospheric Ozone Budget

Multiple chemical species are strongly coupled with ozone (O_3) in the troposphere, including NO_x, HO_x (OH and HO_2), CO and hydrocarbons, with the implication that ozone chemistry in the troposphere is highly non-linear. Subsequently, the ambient state of the troposphere imposes a nonlinear control over the tropospheric chemical response to STE (Lamarque et al., 1999). It may therefore be reasonably assumed that the effect of STE, in terms of the net impact on the tropospheric ozone burden, also has a nonlinear dependence on its magnitude, together with its spatial and temporal distribution. As noted in Lamarque et al. (1999), the evolution of O_3 in the troposphere may be quantified using the following equation:

$$\frac{d}{dt}\,O_3 = p - l \cdot O_3 - d \cdot O_3 + s_{STE} \tag{2.12}$$

Where *p* is the photochemical production rate, *l* is the photochemical loss rate, *d* is the deposition rate and s_{STE} is the source of O_3 from STE. The ambient tropospheric ozone chemistry then determines the ozone production and loss rate once a stratospheric intrusion has mixed into the troposphere. After an STE event, it therefore stands to reason that the steady-state equilibrium *p/(l+d)* of O_3 is approached along a trajectory with the chemical timescale *1/(l+d).* It is found by Hauglustaine et al. (1998) that this timescale, or tropospheric mean ozone lifetime, is on the order of ~19 days in the Northern Hemisphere and ~23 days in the Southern Hemisphere. However, these annually averaged hemispheric lifetimes mask significant seasonality; the Northern Hemisphere lifetime has been found to range between 15 days in summer to 30 days in winter overall for example. In turn, Equation 2.12 can be re-written in an integrated form over the depth of the troposphere (Lamarque et al., 1999):

$$[O_3] = \frac{[p] + [S_{STE}]}{\langle l \rangle + \langle d \rangle} \tag{2.13}$$

Where $[O_3]$ is the integrated tropospheric column amount of ozone, $[S_{STE}]$ is the integrated source from the stratosphere, *[p]* is the integrated tropospheric production and <*l*> and <*d*> represent the appropriate tropospheric average O_3 loss and surface deposition respectively. The total contribution to the tropospheric O_3 burden contribution from the stratosphere is therefore represented by $[S_{STE}]/(\langle l \rangle + \langle d \rangle)$. A transient ozone perturbation would simply arise in the event that <*l*> or *[p]* were to remain unaffected by STE. The stratospheric contribution to tropospheric ozone would subsequently be quantifiable

through the accumulated effect of these transient perturbations. In reality however, STE can modulate both *<I>* and *[p]*, inducing a nonlinear tropospheric response to STE, as the system is invariably more complicated (Lamarque et al., 1999).

2.2 Brewer-Dobson Circulation (BDC)

The Lagrangian-mean meridional overturning circulation in the stratosphere is known as the Brewer-Dobson Circulation (BDC); consisting of a meridional cell in each hemisphere with ascending motion in the tropics and subsequent poleward and downward movement of air in middle and high latitudes to ensure mass continuity (see Figure 2.3). At higher altitudes, the circulation however reverts to a one-cell circulation with rising motion in the summer hemisphere and sinking motion in the winter hemisphere (Rosenlof, 1995; Brasseur and Solomon, 2005). Brewer and Dobson were the first to describe the general features of the circulation and proposed the two-cell BDC structure, in order to explain early observations of stratospheric ozone (O_3) and water vapour (Brewer, 1949; Dobson, 1956). As a by-product of atmospheric testing of nuclear weapons around this time, additional evidence for such circulation was derived from patterns of radioactive fallout (Sheppard, 1963). Based on stratospheric heating and cooling rates, Murgatroyd and Singleton (1961) were also able to reproduce a remarkably consistent "diabatic circulation" to that deduced from observations of chemical tracers. The circulation is however a residual one; air flow around each hemisphere is typically zonal, with disturbances to this flow from planetary waves in the extratropics which induce a slow meridional drift (Haynes et al., 1991; Rosenlof and Holton, 1993; Newman et al., 2001; Plumb, 2002). This mechanism been described by Holton et al. (1995) as an 'extratropical pump' and as a 'Rossby-wave pump' by Plumb (2002). This leads to the gradual poleward transport of tracers, on timescales of up to a few years from the tropical tropopause entry point to the polar lowermost stratosphere (LMS) (Waugh and Hall, 2002), but such circulation is subsequently not directly observable. A fluid dynamical explanation for this circulation was later presented independently by both Andrews and McIntyre (1976, 1978a,b,c) and Boyd (1976) (see section 2.2.1).

The BDC is principally a wave-driven circulation; waves propagate upwards from the troposphere, depositing westward angular momentum and energy in the stratosphere as they dissipate (Shepherd, 2007). Planetary wave driving can be described by the convergence of the Eliassen-Palm (EP) flux (Weber et al., 2011):

$$-\vec{\nabla} \cdot \vec{F} \qquad (2.14)$$

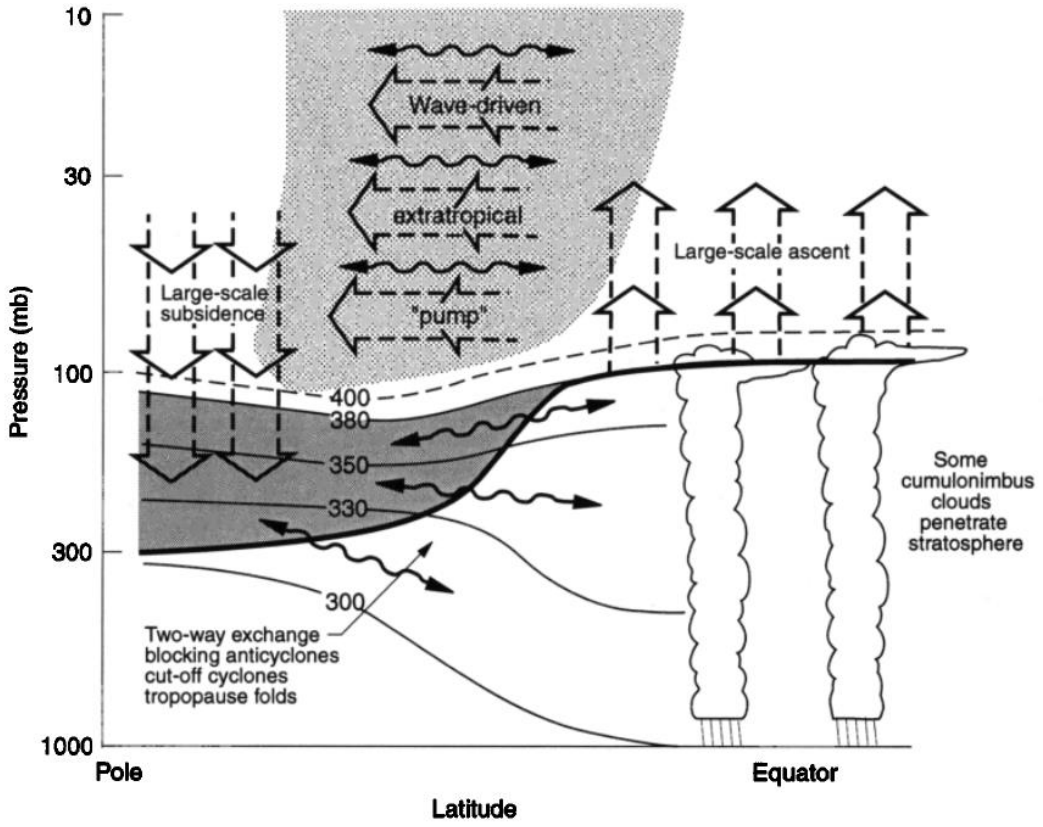

Figure 2.3 – Schematic depicting the dynamics of the BDC and STE processes. The shaded area denotes the 'lowermost stratosphere', which is bounded by the 380 K isentrope and the tropopause (thick black line) in the extratropics. The significance of this region is that isentropic surfaces intersect the tropopause, which facilitates quasi-isentropic exchange of air, in conjunction with tropopause folding mechanisms. The atmosphere above the 380 K isentrope is sometimes referred to as the 'overworld', characterised by the extratropical 'pump' in which a residual poleward flow is instigated by wave-induced forces. This induces large-scale ascent over the tropics and large-scale subsidence over the polar regions. Eddy-driven, two-way exchange in the meridional plane is denoted by double-headed arrows. Adapted from Figure 3 in Holton et al. (1995).

This quantity is a measure of the easterly momentum deposited, which directly acts to decelerate the wintertime westerly zonal flow (Newman et al., 2001). As required under geostrophic balance, a small meridional flow component constitutes the residual 0meridional circulation (Andrews et al., 1987). The process leading to the resultant circulation shown in Figure 2.3 has been described as "gyroscopic pumping" (Holton et al., 1995). It has been recognised that even small wave forcing close to the equator can be as important as wave driving in the extratropics (Plumb and Eluszkiewicz, 1999). In addition to the EP flux convergence, the eddy heat flux ($\overline{v'T'}$) can also be used to describe variations in the BDC wave driving. The eddy heat flux is proportional to the vertical component of the EP flux vector (F_z), serving as a measure of vertical wave propagation up from the troposphere (Weber et al., 2011).

This transfer of angular momentum is subsequently balanced by a Coriolis torque associated with a poleward mass flux within the stratosphere (Shepherd, 2007; Cohen et al., 2014), which constitutes the transient response to an imposed wave-induced forcing. The BDC is characterised by both a shallow and deep branch, which collectively determines ozone abundances in the LMS region (Albers et al., 2018); defined as the region between the dynamical tropopause (taken as 2PVU or 4PVU: PV unit = 10^{-6} K m^2 kg^{-1} s^{-1}) and the 380 K isentropic surface (Hoskins, 1991; Holton et al., 1995) as shown in Figure 2.3. Concerning the build-up of the LMS ozone reservoir over winter, Haynes et al. (1991) outlined a 'downward-control' principle in which the diabatic mass flux across a given isentropic surface is solely dependent upon the distribution of a quasi-steady zonal force above that surface. Subsequently, the downward transport component (diabatic vertical velocity) of the BDC in middle to high-latitudes is determined by eddy dissipation above the layer of concern, resulting from the dissipation of upward propagating planetary waves from the troposphere. Satellite observations of temperature and ozone, together with a radiative transfer scheme, indicated that this principle explains ~80 % of the effective control in the real atmosphere below 40 km altitude. The implication of this key finding is that this dynamical response explains, to a leading order, the amount of ozone available to be entrained into the troposphere via STE mechanisms. Notably, this includes tropopause folding but it is important to recognise that such activity does not represent a control over the stratosphere-to-troposphere transport (STT) mass flux (Haynes et al., 1991).

The BDC has a pronounced seasonal cycle, with a maximum strength in winter and minimum in summer, which yields a seasonal peak in LMS ozone during early springtime (Ray et al., 1999; Konopka et al., 2015; Hegglin et al., 2006). Since the strength of the circulation is closely related to the magnitude of stratospheric wave driving, interannual variability in the abundance of springtime extratropical LMS ozone must in part depend on the cumulative strength of this wave driving over the course of the preceding winter; with differences in the deep versus shallow component also critical in determining the seasonal build-up of this ozone reservoir (Albers et al., 2018). Typically, a strengthening of the upper branch of the BDC leads to enhanced ozone abundances in this LMS reservoir, whereas a decrease in ozone values occurs due to an enhancement in the shallow branch circulation due to an opposing difference in the meridional gradient of ozone in the upper and lower stratosphere respectively (Pan et al., 1997; Rood et al., 2000; Shepherd, 2007; Hegglin and Shepherd, 2007; Bönisch et al., 2009; Butchart, 2014;

Neu et al., 2014). The deep branch of the BDC always prevails over the shallow branch during winter however due to both the presence of a strong transport barrier in the subtropics (Haynes and Shuckburgh, 2000; Shuckburgh et al., 2009) and the seasonal maximum of stratospheric planetary wave driving during winter (Charney and Drazin, 1961; Randel et al., 2002). Both factors diminish thereafter, which results in the seasonal 'flushing' of the ozone reservoir (Hegglin and Shepherd, 2007; Bönisch et al., 2009) and the annual peak in STT. Heterogeneous chemical destruction of ozone can also modulate the LMS ozone reservoir amount to a lesser extent, which is most important during spring when the polar lower stratosphere is coldest (e.g. Manney et al., 2011).

2.2.1 Transformed Eulerian Mean (TEM) Residual Circulation

Quantitative estimates of the strength of the BDC are inherently difficult to obtain as the circulation cannot be measured directly. However, derivation of the Transformed Eulerian Mean (TEM) residual circulation can serve as a reasonable proxy for the circulation strength (Rosenlof, 1995), which indeed provides the dynamical framework for understanding the BDC (Cohen et al., 2014). Through this formulation of equations, the pioneering work of Andrews and McIntyre (1978a,b,c) and Boyd (1976) was able to show that a balance between the angular momentum budget and the contribution from wave momentum fluxes could be attained, which is physically consistent with the single cell characteristics of the circulation in each hemisphere. Ambiguities and inconsistencies in the description of the BDC were present in earlier work due to this apparent imbalance, prior to derivation of the TEM set of equations (Baldwin et al., 2019). Ordinarily, a two-dimensional description of stratospheric transport is impeded by an eddy-mean flow cancellation problem, in which the meridional transport by the mean circulation cannot be determined without separation of the eddy transports (fluctuations about the zonal mean). Subsequently, a mathematical formalism (a set of TEM equations) is required that describes the zonally averaged atmospheric structure, in which these two components are separated more meaningfully (Brasseur and Solomon, 2005). As suggested by Dunkerton (1978), a practical approach is to directly derive the net mean circulation from the diabatic heating rate ($\bar{q}$) using the simplified expression from the thermodynamic equation:

$$\frac{\partial \bar{\theta}}{\partial t} + \frac{\bar{v}}{a}\frac{\partial \bar{\theta}}{\partial \phi} + \bar{w}\frac{\partial \bar{\theta}}{\partial z} \simeq \bar{q} - \left[\frac{1}{a\cos\phi}\frac{\partial}{\partial \phi}\left(\overline{v'\theta'}\cos\phi\right) + \frac{1}{\rho_0}\frac{\partial}{\partial z}\left(\rho_0\overline{w'\theta'}\right)\right] \qquad (2.15)$$

This relation implies that both the eddy heat flux divergence and the vertical advection of the mean potential temperature are approximately balanced for small diabatic effects

($\overline{q} \simeq 0$) (non-acceleration theorem). It can be assumed that the terms highlighted in red are small or negligible in Equation 2.15 and can thus be neglected to leave the remaining approximation (terms in black). This simplified equation can subsequently be transformed to obtain the TEM or residual circulation, in the form of the net mean meridional ($\bar{v}^*$) and vertical ($\overline{w}^*$) velocities:

$$\bar{v}^* = \bar{v} - \frac{1}{\rho_0}\frac{\partial}{\partial z}\left(\frac{\rho_0 \overline{v'\theta'}}{\partial z}\right) \tag{2.16}$$

$$\overline{w}^* = \overline{w} + \frac{1}{a\cos\phi}\frac{\partial}{\partial \phi}\left(\frac{\overline{v'\theta'}\cos\phi}{\partial z}\right) \tag{2.17}$$

These TEM equations of motion state that the average net drift of air parcels can be approximated by subtraction of the component of the Eulerian circulation due to eddy heat transport from the Eulerian average (Rosenlof, 1995). Further simplifying the thermodynamic equation by neglecting the eddy heat flux divergence term (small under quasi-geostrophic scaling) and using the steady state approximation for the continuity equation, the residual circulation can also be expressed in terms of the diabatic circulation to a good approximation (Brasseur and Solomon, 2005; Butchart, 2014). The two circulations are very similar and therefore upward TEM motions in the latitude-height plane generally coincide with regions of net positive diabatic heating (Q) with downward motion largely occurring in regions of net negative Q. Estimation of the diabatic circulation from these two simplified equations is however conditional to a priori knowledge of the temperature distribution (Brasseur and Solomon, 2005). Despite this, full consideration of the zonal momentum budget, in addition to the thermodynamic and continuity equations, can yield a self-consistent mean meridional circulation. The TEM formalism shows that the circulation is driven by a non-local momentum forcing resulting from wave dissipation – the extratropical "fluid-dynamical suction pump" (Holton et al., 1995).

2.2.2. Future Trends

A consistent projection of stratosphere-resolving GCMs and CCMs is for an acceleration or intensification of the stratospheric BDC under anthropogenic-driven climate change (Rind et al. 1990; Butchart and Scaife 2001; Butchart et al. 2006; Garcia and Randel 2008; Li et al. 2009; Calvo and Garcia 2009; McLandress and Shepherd 2009; Butchart et al. 2010; Okamoto et al. 2011; Bunzel and Schmidt 2013; Oberländer et al. 2013). This is despite no clear observational evidence yet for a long-term strengthening of the circulation, as inferred indirectly from changes in trace-gas distributions (Engel et al. 2009;

Bönisch et al., 2011; Diallo et al. 2012; Seviour et al. 2012; Hegglin et al., 2014). It is again important to note that since the stratospheric meridional overturning circulation is of some two orders of magnitude smaller than in the troposphere, the BDC cannot be directly measured. Therefore, a common metric in quantifying this change within a model framework is the integrated tropical upward mass flux (F_{trop}) across a fixed stratospheric level (e.g. 70 or 100 hPa) (Oberländer-Hayn et al., 2016). Future trends in F_{trop}, dependent on greenhouse gas forcing scenarios, are in the range of + 2.0-3.2 % dec^{-1} (Baldwin et al., 2019). An alternative quantity to assess changes in BDC-driven transport, together with changes in eddy-driven mixing, is that of the stratospheric mean age of air (AoA) (Kida, 1983; Hall and Plumb, 1994). This concept, introduced in the 1990s, is a metric for the mean transit time of air from the entry point (tropical tropopause layer) to any given location in the stratosphere. A reduction in the mean AoA (i.e. younger air) is indicated by climate models, equating to shortened transit times (Butchart and Scaife, 2001).

Another anticipated consequence in response to climate change is the lifting of the circulation as features such as the tropopause rise. Indeed, an overall increase in tropopause height in recent decades (e.g. Xian and Homeyer, 2019) has been attributed to both increasing greenhouse gas (GHG) emissions and stratospheric ozone depletion, that has resulted in a pattern of tropospheric warming and stratospheric cooling (Santer et al., 2003a,b). Projected trends in tropopause height for the period 1960-2100 were estimated to be around ~-7 hPa per century in the tropics (~20°S-20°N) and ~-20 hPa per century in the polar regions (~60°-90°N/S) in the multi-model mean study by Gettelman et al. (2010). Although no coherent changes the overall strength of the BDC have been recently observed, there is indication of a weakening of the deep branch and a compensatory strengthening of the shallow branch of the circulation (Bönisch et al., 2011). Assuming both tendencies are a consistent response to the forcing to be imposed by anthropogenic-induced climate change over the coming century, such changes in the two branches of the BDC may also reflect how wave driving in the stratosphere will respond. Whilst the strength of upward propagation of waves responds, in part, to changes in the troposphere, it is known that the stratospheric background state strongly influences how upward propagating waves interact with the mean-flow, through both onward propagation (e.g. Bell et al., 2010) and momentum deposition (e.g. Lubis et al., 2018). On balance however, the response of both the relative changes in planetary wave forcing (zonal wavenumbers 1-3) and synoptic-scale wave activity (zonal wavenumbers 4+), which drive the deep and shallow branches of the BDC respectively, to climate change

is extremely uncertain (Plumb, 2002). Regardless, changes in the BDC would have implications for the STE flux of ozone from the stratosphere (e.g. Zeng and Pyle, 2003; Hegglin and Shepherd, 2007; Meul et al., 2018), although changes in the strength of each branch are known to have an opposing influence (Pan et al., 1997; Rood et al., 2000; Heggin and Shepherd, 2007; Bönisch et al., 2009; Butchart, 2014; Neu et al., 2014).

2.3 Stratosphere-Troposphere Exchange (STE)

Stratosphere–troposphere exchange (STE) of air is governed non-locally by the wave-driven large-scale meridional circulation, the BDC (Holton et al., 1995; Shepherd, 2007; Butchart, 2014). The BDC induces preferential troposphere-to-stratosphere transport (TST) in the tropics, in contrast to mid- to high-latitude regions where STT must prevail to conserve mass continuity (Holton et al., 1995). The BDC, and thus STE, exhibits strong seasonality in both hemispheres with the circulation strongest during wintertime, but especially in the Northern Hemisphere where the largest wave-forcing occurs (Holton et al., 1995). Given a photochemical lifetime of several months in the lower stratosphere, analogous to transport timescales, seasonality in the BDC results in a significant enrichment of ozone and other chemical tracers in the extratropical LMS over winter (Hegglin et al., 2006; Krebsbach et al., 2006); with the largest VMRs achieved close to the tropopause in early summer (Prather et al., 2011; Škerlak et al., 2014). The enrichment of ozone in the LMS is important in determining the magnitude and variability of the STT flux of ozone as such air is entrained in stratospheric intrusions that can mix ozone downward into the troposphere (Shapiro, 1980; Holton et al., 1995; Gettelman et al., 2011).

Whilst it is recognised that the STE flux of ozone in the extratropics reaches a seasonal maximum in late spring and early summer (Yang et al., 2016), this incidentally coincides closely with the seasonal minimum in the downward STE mass flux of air (Škerlak et al., 2014; Yang et al., 2016). This strongly implies that the ozone VMR at the tropopause controls the seasonality in the downward ozone flux. Staley (1962) was the first to note that it is in fact the displacement of the tropopause altitude seasonally in each hemisphere that primarily governs the downward mass flux: maximum in spring as the tropopause rises and minimum in autumn as the tropopause falls relative to the mean state. Analysis of deep STE events, where direct entrainment of stratospheric air into the PBL occurs, indicates that the downward transport of ozone is primarily controlled by the mass flux for these events, with a peak in early spring (Škerlak et al., 2014).

Air mass exchange between the troposphere and stratosphere is maximised in mid-latitudes, where the height of the tropopause exhibits significant spatiotemporal variability in association with both the eddy-driven (Vaughan et al., 1994; Beekman et al., 1997) and subtropical jet streams (Baray et al., 2000) in the UTLS. This is primarily facilitated through tropopause folding or stratospheric intrusion events as depicted in Figure 2.4. Throughout the extratropics, it has been determined from aircraft campaign measurements (e.g. Zahn et al. 2004; Engel et al. 2006; Pan et al., 2007) that there exists a mixing layer, known as the extratropical transition layer (ExTL), between the stratosphere and the troposphere due to individual mixing processes (Baldwin et al., 2019). This includes different PV nonconservative processes including turbulent mixing, radiative heating and cooling, and convective erosion, which can all lead to irreversible mixing (Pan et al., 2007). Although this layer has been confirmed to be globally extensive from satellite observations (Hegglin et al., 2009), a deeper ExTL is typically present in the Northern Hemisphere relative to the Southern Hemisphere, which is consistent with the enhanced frequency of Rossby wave breaking events which is closely associated with the thickness of this layer (Hitchmann and Huesmann, 2007). Whilst mixing processes associated with tropopause folding have been long identified for their importance in facilitating STE (Reed and Danielsen, 1959), other mechanisms are known to be important, including aforementioned seasonal shifts in the height of the tropopause (Stanley, 1962) and turbulent mixing more generally (e.g. Libby, 1959). Aircraft campaign data from the 1980s and 1990s later provided more comprehensive evidence however that the first-order mechanisms for STE include turbulent mixing processes in association with tropopause folds and cut off lows (Shapiro, 1980; Ebel et al., 1991; Vaughan et al., 1994; Browell et al., 1998). Additionally, downward mixing of stratospheric air into the upper troposphere has also been associated with thunderstorm activity in connection with mesoscale convective systems (Poulida et al., 1996).

Tropopause folds, or so called ‘stratospheric intrusions’, may be on the order of up to ~4000 km for synoptic scale systems (Danielsen, 1968). An example of this is shown in Figure 2.4 over western North America, based on ECMWF reanalysis data, with STT confirmed from air parcel trajectories calculated using the Lagrangian Analysis Tool (LAGRANTO) at the locations indicated (black crosses). They are commonly associated and formed as a result of Rossby wave breaking (Sprenger et al., 2003; Tang and Prather, 2012; Albers et al., 2018); typically occurring on the rear-flank of attendant extratropical cyclones (cyclonic side of the jet) in conjunction with a dry descending air stream that

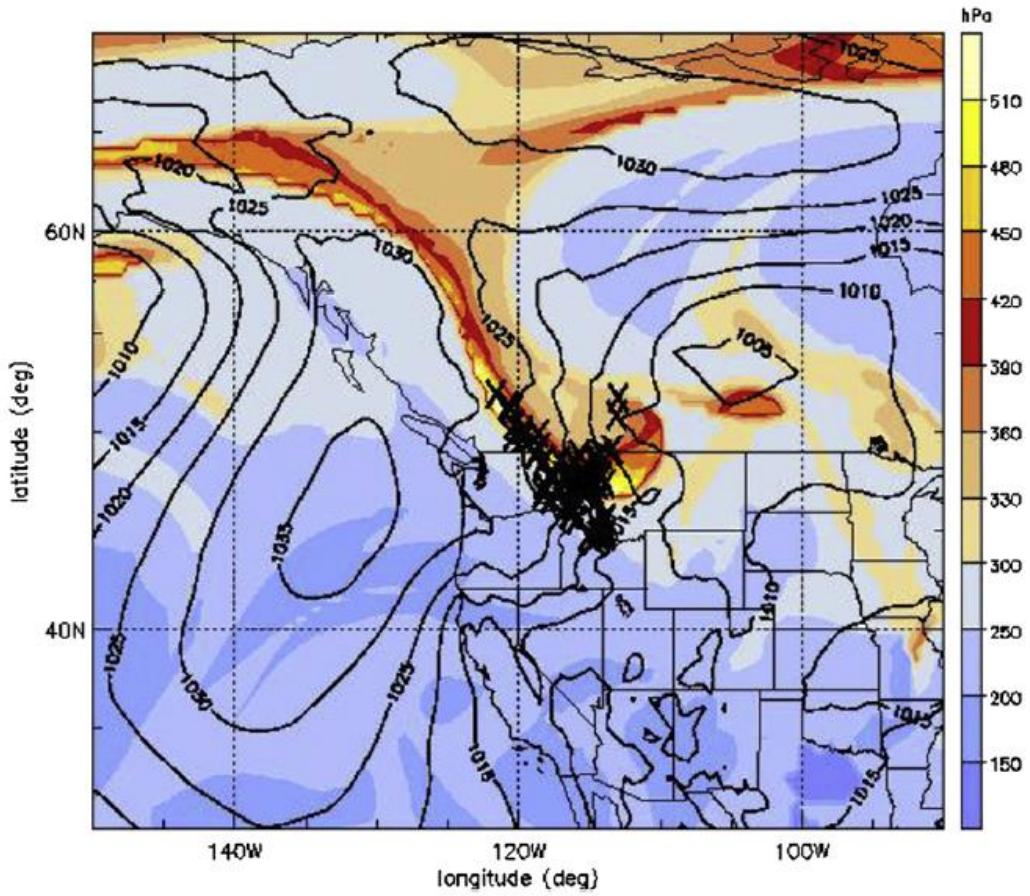

Figure 2.4 – Example of a synoptic-scale (≥ 1000 km) tropopause fold (stratospheric intrusion) over western North America on 2 May 2006 06 UTC. A marked lowering of the tropopause pressure (see colourbar) signifies the extent of this fold. Black symbols denote the occurrence of STT and air parcel trajectory analysis provided clear evidence of stratospheric contribution to a pronounced peak in surface O_3. Adapted from Figure 4 in Lefohn et al. (2011).

favours STT, with TST conversely dominant on the forward-flank of such systems in association with an airstream known as a warm conveyor belt (Wernli and Davies, 1997; Reutter et al., 2015). Favourable regions for STE include regions typically located downstream of strong jet regions such as the North Atlantic and North Pacific (Stohl et al., 2003; Sprenger and Wernli, 2003; Škerlak et al., 2014). A detailed description of the structure of stratospheric intrusions in association with synoptic-scale systems can be found in Danielsen (1968; 1980). Downward and equatorward transport of air, in conjunction with an upper level jet, from the stratosphere into the troposphere typically wraps around the cyclonic flow. These intrusions are often aligned with the passage of frontal boundaries as descent of stratospheric air occurs and filaments or streamers break off and irreversibly mix into the troposphere (Sprenger et al., 2003). This relationship with synoptic systems however varies from region to region as exemplified in a Southern Hemisphere case study by Greenslade et al., 2017. Although low pressure activity, frontal

systems and cut off lows were generally closely related to STT across different regions of the Southern Ocean in this study, such sources of upper-tropospheric turbulence were not observed to be a necessary condition for STT and tropopause folding beneath the stratospheric polar vortex (SPV).

In addition to large tracer gradients, stratospheric intrusions may be obviously identified as tongues of high potential vorticity (PV) air, or low water vapour mixing ratios characteristic of the stratosphere, that may descend to low altitudes. Elongation of such features leads to filamentation, instigating irreversible mixing of such dynamical structures and associated chemical tracers. Additional STT pathways include deep overshooting convection (Poulida et al., 1996; Frey et al., 2015), entrainment of stratospheric air associated with tropical cyclone activity (Das et al., 2016) and resulting from synoptic-scale disturbances in mid-latitudes (e.g. Stohl et al., 2003). In particular, extratropical cyclones that become detached from the mid-latitudes westerlies, so-called cut off lows, are recognised to lead to significant STE in middle to subtropical latitudes (Price and Vaughan, 1993; Wirth, 1995). Such systems are typically associated with the equatorward advection of polar air masses which favour convection. Associated diabatic heating in the upper troposphere can subsequently instigate cross-isentropic transport as such systems, together with the locally lowered tropopause, radiatively decay. This leads to irreversible entrainment of stratospheric air into the troposphere as the tropopause reforms at a higher altitude (Wirth, 1995). Whilst cross-isentropic processes can lead to STE, particularly on synoptic spatial and temporal scales, quasi-isentropic transport mechanisms largely govern the seasonal mean mass flux across the tropopause. Such processes operate over longer timescales and spatial scales in conjunction with the "downward-control principle" outlined by Haynes et al. (1991), which is intrinsically related to zonal-mean eddy-induced forcing in the middle atmosphere (Holton, 1990; Rosenlof and Holton, 1993).

Irreversible mixing in association with both STE and strong anticyclonic subsidence has been identified as the dominant causal factor that gives rise to regions prone to high background levels of tropospheric ozone, with significant source attribution from the stratosphere. It should be noted that anticyclonic subsidence also provides favourable conditions for the in situ photochemical formation of ozone from tropospheric emission precursors, which is another mechanism that gives rise to regions of tropospheric ozone maxima, principally in subtropical latitudes. A prime example is the eastern Mediterranean and Middle East (EMME) region (Richards et al., 2013; Zanis et al., 2014;

Akritidis et al., 2016; Dafka et al., 2020), where summertime ozone-mixing ratios average 2.5-3 times higher than the background hemispheric average within both the PBL and up to 4 km altitude (Lelieveld et al., 2002). Thus, regional weather patterns and stratospheric mixing are both important in understanding STT (Greenslade et al., 2017). In the context of surface air quality especially, it is important to distinguish between episodic, direct enhancements from STT processes and background enhancements from the entrainment of ozone-rich air into the free troposphere, which is later transported downwards towards the PBL (Lefohn et al., 2011).

During pre-industrial times, it is believed that STE processes constituted the primary contribution to even surface ozone due to a seasonal maximum that widely occurs in spring (Stohl et al., 2003a), several months prior to the peak in potential photochemical production from tropospheric precursor sources. Although the sharp increase in anthropogenic precursor emissions since ~1850 complicates such assessment, a range of studies demonstrate that the stratosphere provides a significant contribution to ground level ozone, principally during springtime and in the Northern Hemisphere mid-latitudes, at both high and low elevation surface monitoring sites (e.g. Lefohn et al., 2011). However, direct entrainment of stratospheric intrusions of ozone-rich air into the planetary boundary layer (PBL) is thought to be extremely limited, with the exception of some elevated regions (Trickl et al., 2010), with the PBL acting as a barrier to downward transport of air from the free troposphere. A large number of studies however show such propagation of such features down to just above the PBL, with corresponding high ozone concentrations within the lower troposphere of predominantly stratospheric origin (Ott et al., 2016). In order for STE to contribute to near-surface ozone levels, it is recognised that vertical transport associated with turbulent mixing within the PBL at the mesoscale level must be important to explain such significance (Lefohn et al., 2011).

2.3.1 Contribution of Ozone (O_3) STT to Tropospheric Ozone (O_3) Budget

Estimates from models for the globally integrated STT ozone flux range widely from ~400-800 Tg yr^{-1}, as shown in Table 2.2 from the 2013 IPCC AR5 report. This quantity represents a small contribution to the total source of tropospheric ozone, which is on the order of 3000-5500 Tg yr^{-1} from in situ chemical formation and constitutes a factor of 7-15 times that of the flux from the stratosphere, with an attribution of ~30 % from human activity downward flux of ozone from the stratosphere is of major importance in determining the tropospheric ozone burden once chemical loss and dry deposition (tropospheric ozone

Burden	Production	Loss	Deposition	STE	Reference
Tg	Tg yr^{-1}	Tg yr^{-1}	Tg yr^{-1}	Tg yr^{-1}	
Modelling Studies					
337 ± 23	4877 ± 853	4260 ± 645	1094 ± 264	477 ± 96	Young et al. (2013); ACCMIP
323	N/A	N/A	N/A	N/A	Archibald et al. (2011)
330	4876	4520	916	560	Kawase et al. (2011)
312	4289	3881	829	421	Huijnen et al. (2010)
334	3826	3373	1286	662	Zeng et al. (2010)
324	4870	4570	801	502	Wild and Palmer (2008)
314	N/A	N/A	1035	452	Zeng et al. (2008)
319	4487	3999	N/A	500	Wu et al. (2007)
372	5042	4507	884	345	Horowitz (2006)
349	4384	3972	808	401	Liao et al. (2006)
344 ± 39	5110 ± 606	4668 ± 727	1003 ± 200	552 ± 168	Stevenson et al. (2006); ACCENT
314 ± 33	4465 ± 514	4114 ± 409	949 ± 222	529 ± 105	Wild (2007) (post-2000 studies)
N/A	N/A	N/A	N/A	515	Hsu and Prather (2009)
N/A	N/A	N/A	N/A	655	Hegglin and Shepherd (2009)
N/A	N/A	N/A	N/A	383–451	Clark et al. (2007)
Observational Studies					
333	N/A	N/A	N/A	N/A	Fortuin and Kelder (1998)
327	N/A	N/A	N/A	N/A	Logan (1999)
325	N/A	N/A	N/A	N/A	Ziemke et al. (2011); 60S–60N
319–351	N/A	N/A	N/A	N/A	Osterman et al. (2008); 60S–60N
N/A	N/A	N/A	N/A	449 (192–872)	Murphy and Fahey (1994)
N/A	N/A	N/A	N/A	510 (450–590)	Gettelman et al. (1997)
N/A	N/A	N/A	N/A	500 ± 140	Olsen et al. (2001)

Table 2.2 – Estimates of the global budget of tropospheric ozone (O_3), including sources (STE, chemical production), sinks (chemical loss, dry deposition) and resultant burden. Uncertainties shown correspond to 1 standard deviation (68 % confidence interval). Adapted from Table 8.1 in Chapter 8 of the IPCC AR5 Climate Change 2013 report (Working Group I: The Physical Science Basis).

sinks) are both accounted for. Observational estimates for the stratospheric influx are to the present-day burden of tropospheric ozone (Young et al., 2013). Despite this, the much more limited but are in broad agreement with these values, despite similarly uncertainties around these values. In the 2013 IPCC AR5 Report, the estimate from observations (550 ± 140 Tg yr^{-1}) (Solomon et al., 2007) is very close to that estimated from a suite of 26 state-of-the-art atmospheric chemistry models in the study by Stevenson et al. (2006). Although within the range of the uncertainties from both estimates, the globally integrated stratospheric influx was calculated in Škerlak et al. (2014) to be lower from ERA-Interim at 420 Tg yr^{-1} between 1979 and 2011. In this global climatology study, a seasonal maxima in the STT ozone flux was found in June (23.3 Tg month^{-1}) and January (18.9 Tg month^{-1}), and a seasonal minima in December (14.0 Tg month^{-1}) and June (14.6 Tg month^{-1}), in the Northern Hemisphere and Southern Hemisphere respectively.

Important in explaining the wide ranging estimates of STE in Table 2.2, and associated large uncertainty ranges in the case of multi-model comparison studies for instance, is the way in which STE is diagnosed within a model or observational framework. A critical aspect of this is the exact definition of the tropopause that is implemented (IPCC, 2013), as STE estimates are very sensitive to the sharp vertical gradient in ozone close to this

boundary. In terms of the globally and annually averaged tropospheric ozone burden (estimated to be 337 ± 23 Tg, 1-σ according to most recent models; IPCC, 2013), Wild (2007) notes that the differences in tropopause definition can account for 10 % of inter-model variations. For the 26 models as part of the Atmospheric Composition Change: the European Network of excellence (ACCENT) European Union project (Stevenson et al., 2006), the STE influx estimates were derived indirectly using a residual approach (STE = L + D – P), as diagnosed in each model and summed over the tropopause. Thus, the tropopause definition used has a potentially significant impact on the resultant STE estimates. A later multi-model comparison study by Young et al. (2013), as part of the Atmospheric Chemistry and Climate Model Intercomparison Project (ACCMIP) addressed this issue by diagnosing the tropopause as the 150 ppbv ozone contour, with the benefit that it is simple to apply across all models. The same indirect residual approach (budget closure) was again adopted and the resultant STE estimates were more tightly constrained (ACCMIP: 477 ± 96 Tg yr^{-1} versus ACCENT: 552 ± 168 Tg yr^{-1}). Of course, calculating STE estimates within the same models using a different approach, for instance using model diagnostics in a direct manner, would likely have yielded somewhat different results (e.g. Sanderson et al., 2007). Observational-based estimates (e.g. Olsen et al., 2001) of STE are made possible through measurement of chemical gradients and tracer-tracer correlations (McLinden et al., 2000). In the case of ozone, the flux can be derived from observation of the NO_y/O_3 ratio in the LMS, in conjunction with knowledge of the known steady-state lifetime of species chemical species such as N_2O. Measurement uncertainty, as well as drifts in the steady-state lifetime of different chemical constituents, therefore manifest as the main limiting factors in diagnosing STE using observational data.

2.3.2 Understanding the Influence of STE on Tropospheric Ozone (O_3)

The current understanding of the seasonal and regional climatology of tropospheric ozone is severely constrained by the paucity of in situ measurements from ozonesondes and aircraft measurements, which are spatially and temporally biased, although the advent of satellite remote-sensing platforms in recent years for the inference of global tropospheric ozone abundance has reduced uncertainty to a significant extent (Parrish et al., 2014). Relatively long (decadal) global satellite datasets of tropospheric ozone now exist from several platforms (e.g. the Ozone Monitoring Instrument, OMI; the Tropospheric Emission Spectrometer, TES; the Total Ozone Mapping Spectrometer, TOMS; the Infrared Atmospheric Sounding Interferometer, IASI) that have been extensively validated with respect to in situ and ground-based remote-sensing

measurements as well as intersatellite comparisons. Nonetheless, there are inherent limitations with retrieving tropospheric ozone from spaceborne instruments, and this has implications for the accuracy of resultant satellite-based climatologies (Gaudel et al., 2018). Tools such as chemistry-climate models (CCMs), which offer sensitivity simulations and specific diagnostic variables that are not available from observations alone, are however required to elucidate the drivers of variability and longer-term changes in the global distribution of tropospheric ozone, which includes the quantification of the stratospheric influence. Additionally, CCMs can be used to assess and quantify the causes of tropospheric ozone features through the analysis of photochemical production and loss rates, together with transport tracer simulations. The latter can serve to identify the relative importance of in situ photochemical production, long-range transport and stratospheric influence. Nonetheless, such simulations are subject to a number of constraints, including limitations in model horizontal and vertical resolution, complexity of the implemented chemistry scheme, and the realism of simulated transport characteristics. Above all, however, the largest unknown by far is the accuracy of the precursor emission inventories used in CCM simulations (Hoesly et al., 2018).

2.3.2.1 Model Estimates

Whilst it is accepted that STE is an important and significant source of upper-tropospheric ozone (e.g. Holton et al., 1995), the influence on near-surface ozone levels is poorly understood. Although the important role of photochemistry is well established, the relative influence of the stratosphere between present-day global CTMs and CCMs is highly contested (Wu et al., 2007). Overall, there is a consensus that photochemistry exerts a larger influence over the background tropospheric ozone burden (Crutzen et al., 1999; Lelieveld and Dentener, 2000), although the significance of STT in regions favourable for subsidence within the middle to upper troposphere, as well as episodically in the lower troposphere in association with deep stratospheric intrusions, is nonetheless recognised (Roelofs and Lelieveld, 1997; Sprenger and Wernli, 2003; Akritidis et al., 2010). Globally, Lamarque et al. (1999) estimated that STE increases the average tropospheric column amount by only a modest ~11.5 % using a three-dimensional global chemistry transport model. However, on a monthly resolved basis, this influence was shown to increase to ~10 %–20 % in the lower troposphere and ~40 %–50 % in the upper troposphere. More recent modelling studies, however, show a much larger influence. The annual mean estimated influence of the stratosphere is shown to range between 25 % and 50 % in the lower and middle extratropical troposphere, with the largest influence in

the Southern Hemisphere where other sources of ozone provide a smaller contribution to the tropospheric ozone budget, according to various modelling studies (e.g. Lelieveld and Dentener, 2000; Banerjee et al., 2016). Hess and Zbinden (2013) found from observations that lower-stratospheric (150 hPa) ozone explains nearly 70 % of the variance in mid-troposphere (500 hPa) ozone trends and variability over Northern Hemisphere midlatitude regions, including Canada, the eastern US and Northern Europe. Over North America, the influence of interannual variability in stratospheric ozone has been demonstrated to significantly impact ozone in both the upper and lower troposphere, as elucidated through the use of a stratospheric ozone tracer in the high resolution (0.5° x 0.5°) Goddard Earth Observing System, Version 5 (GEOS-5) model: ~60 % and 66 % at 400 hPa and ~11 % and 34 % at 700 hPa during winter and spring respectively (Liu et al., 2020).

Furthermore, a number of mid-latitude case studies have demonstrated that STT events may provide a much larger contribution to surface ozone in some seasons (typically spring) and more locally on timescales of hours to days given favourable meteorological conditions. Over a 3-month period between April and June 2010, Lin et al. (2012) concluded that the stratosphere was the source of 20 %-30 % of surface O3 across the western US using the high-resolution (~50 × 50 km^2) GFDL AM3 CCM, with episodic enhancements of some 20-40 ppbv of the surface maximum 8h average (MD8A) ozone estimated from 13 identified stratospheric intrusion events. Similarly, model-based studies find evidence for a significant stratospheric contribution to the pronounced tropospheric summertime ozone maximum over the eastern Mediterranean and the Middle East (EMME) (Zanis et al., 2014; Akritidis et al., 2016; Dafka et al., 2020) and the Persian Gulf (Lelieveld et al., 2009), with influence as far down as the PBL where near-surface ozone levels are known to frequently exceed EU air quality standards. In relative terms, it is obvious that STE constitutes a strong contributor to tropospheric O_3 levels where photochemistry is relatively quiescent (Lelieveld and Dentener, 2000).

2.3.2.2 Observational estimates

Observationally based studies show a wide range in the level of stratospheric influence. In conjunction with a beryllium (Be)-based mixing model, Dibb et al. (1994) showed that the stratosphere has a maximum influence during spring in the Canadian Arctic of a mere 10 %-15 % at the surface. Greenslade et al. (2017) also found only a small stratospheric contribution (1 %-3.5 %) to the mean tropospheric ozone burden for three sites

neighbouring the Southern Ocean, although with exceedances of 10 % during individual events. A number of Europe-focussed studies highlight the significance of the stratosphere during episodic events, particularly over Alpine regions where elevated regions are sometimes directly impacted by stratospheric intrusions (e.g. Stohl et al., 2000; Zanis et al., 2003; Colette and Ancellet, 2005). This influence is typically largest in winter and spring (smallest in summer), although the seasonality exhibits greater complexity at some high-altitude locations, which is largely site dependent. Significant enhancements in surface ozone, in association with stratospheric intrusions, have also been detected across the Himalayas during winter especially (up to 25 % contribution), in direct contrast to minimal influence during the summer monsoon season (e.g. Cristofanelli et al., 2010). Summertime ozonesonde campaign measurements over the north-eastern US (Thompson et al., 2007a, b) imply a stratospheric contribution of ~20 % to 25 % to the tropospheric column ozone during summer 2004, which is comparable to the budget inferred from European profiles (Colette and Ancellet, 2005). A similar level of influence is found on average in the middle and upper troposphere for 18 North American sites based on summer ozonesonde campaign data between 2006 and 2011 (Tarasick et al., 2019). Ozonesonde measurements from all seasons between 2005 and 2007 reveal a larger influence still (34 % or 22 ppbv) over south-eastern Canada, decreasing to 13 % (5.4 ppbv) and 3.1 % (1.2 ppbv) in the lower troposphere and boundary layer respectively, with typical occurrence of STT of 2-3 days (4-5 days) during spring and summer (autumn and winter). It is important to note that most observational estimates of STE are derived from local to regional based case studies, which makes evaluation of model estimates challenging over longer timescales and larger spatial scales.

2.4 Sources of Interannual Variability

Linkages between changes in the weather across widely separated regions of the world are known as teleconnections (AMS, 2012). The most notable example is that of the El Niño Southern Oscillation (ENSO), in which the near-surface temperatures of the tropical Pacific Ocean either warm or cool between ~1°c and 3°C on timescales of two to seven years (Bellenger et al., 2014). These temperature changes have a subsequent impact on the global atmospheric circulation, leading to large-scale changes in the positioning of features such as jet streams and storm tracks, with attendant implications for regional temperatures and precipitation around the world. Such influence also extends to the distribution of non-well mixed trace gases such as ozone, methane and nitrogen oxides

(Pope et al., 2018). A synthesis of the influence of such drivers on tropospheric ozone and STE of ozone is provided here.

2.4.1 El Niño Southern Oscillation (ENSO)

Variations in the temperature of the near-surface waters of the tropical Pacific Ocean are known to lead to significant changes in tropospheric circulation. Over the Pacific Ocean basin, sea surface temperature (SST) anomalies influence the location of both regions of convective, cyclonic upwelling and anticyclonic downwelling, which subsequently invoke changes in tropospheric chemistry, including ozone. During El Niño conditions, a decrease (increase) in tropospheric ozone is observed over the central and eastern (western) tropical Pacific, in association with enhanced (suppressed) convection (Olsen et al., 2016). These tendencies are reversed for La Niña conditions in a largely antisymmetric pattern (DeWeaver and Nigam, 2002). Such anomalies in tropical tropospheric ozone are apparent from satellite observations (e.g., Chandra et al., 1998; Thompson et al., 2001; Ziemke et al., 2010, 2015), ground-based instruments (e.g., Fujiwara et al., 1999; Lee et al., 2010) and both chemical transport models (CTMs) driven by observed meteorology and free running models (e.g., Sudo and Takahashi, 2001; Zeng and Pyle, 2005; Doherty et al., 2006; Oman et al., 2011). However, the net effect of El Niño (La Niña) leads to an overall decrease (increase) in upper tropospheric ozone, when a zonal mean is constructed (Neu et al., 2014). The ozone response to ENSO has further been found to be consistent with changes in the Walker Circulation (e.g. Oman et al., 2011); the atmospheric component of the response but not limited to just over the Pacific Ocean basin. These propensities also apply to the partial tropical tropospheric column of ozone, with a decrease (increase) on the order of 4 DU (1-2 DU) during strong El Niño (La Niña) conditions according to observations (Leventidou et al., 2018). Whilst the strongest relationship of ozone with the Niño 3 index is highest with a zero month lag in the tropics, the relationship is stronger globally with a six month lag (Doherty et al., 2006).

It has furthermore been demonstrated that interannual variability in tropospheric ozone precursors, including lightning NO_x and isoprene (C_5H_8), are highly correlated with ENSO changes (Stevenson et al., 2005). Globally, variability in lightning activity (in terms of both intensity and location) has been shown to be associated with ENSO time scales, with the largest impacts evident at latitudes characterised by the dry, descending air stream in conjunction with the Hadley circulation (Sátori et al., 2009). Wildfire or biomass burning activity is also strongly influenced by ENSO phase, particularly within the Indo-Pacific

region due to regional changes in precipitation (e.g. Chandra et al., 2009), which further modulates regional tropospheric ozone levels in addition to ENSO-related dynamical effects. The production, destruction and dry deposition fluxes of ozone have a relationship with ENSO that is stronger after a lag of six months in both the tropics and extratropics, indicating that the fluxes in ozone are driven by ENSO-modulated variations in the climate of the lower troposphere and the surface, although a higher correlation at a zero month lag occurs for the net ozone chemical production (Doherty et al., 2006). It therefore follows, however, that the fast atmospheric response to ENSO over the Pacific Ocean, with subsequent establishment of circulation anomalies, has a greater influence over the timing of the tropospheric ozone response within the tropics (i.e. stronger relationship at a zero month lag), as opposed to such chemical modulation effects. The relative importance of ENSO-driven dynamical and chemical modulation effects are on the other hand less clear in the extratropics, which both lag behind changes in ENSO. It is therefore clear that ENSO can influence tropospheric ozone levels in and around the tropical Pacific Ocean basin, with evidence for such modulation via both dynamical and chemical mechanisms.

Modulation of the tropospheric circulation remote to the tropical Pacific Ocean basin, and in turn tropospheric ozone, may also arise due to changes in the propagation of Rossby waves which can alter the positioning of jet streams, storm tracks and anticyclones (e.g. Langford, 1999; Trenberth et al., 2002; García-Herrera et al., 2006). For instance, seasonal ozone levels at the Mauna Loa Observatory, Hawaii are sensitive to changes in ENSO via modulation to long-range transport pathways of ozone-rich air masses from Eurasia across the Pacific, also captured by atmospheric circulation indices such as the Pacific-North American (PNA) pattern (Lin et al., 2014). An increase (decrease) in springtime ozone is observed here following El Niño (La Niña) conditions. During El Niño, an equatorward shift and eastward extension of the subtropical jet stream is attributed to enhance long-range transport of Asian pollution to this region. Beneath the Northern Hemisphere climatological position of the subtropical jet, Neu et al. (2014) found evidence of an increase in mid-tropospheric ozone from the Tropospheric Emission Spectrometer (TES) during the 2009-10 El Niño event and a decrease during the 2007-08 La Niña event that would agree with this finding. A consistent response in the upper tropospheric ozone burden (due to changes in ENSO) over the western US has also been noted, albeit with a greater frequency of springtime stratospheric intrusions (SIs) (that have the capacity to reach the surface) following strong La Niña winters (Lin et al., 2015).

Attendant changes in convection and tropopause height, as a consequence of ENSO-modulated circulation changes, have been demonstrated to significantly influence the magnitude of such deviations in tropospheric ozone with respect to the climatological average (Olsen et al., 2016). Whilst many studies find that ENSO explains a significant proportion of the variance in extratropical tropospheric ozone (e.g. Ebojie et al., 2016), a number of observational and modelling studies show no robust relationship (e.g. Hess et al., 2015; Vigouroux et al., 2015), which may imply that such non-local influence is relatively weak or geographically confined (Olsen et al., 2016; Wespes et al., 2016).

Additionally, ENSO is an important driver of changes in the stratospheric circulation, in conjunction with the Quasi-Biennial Oscillation (QBO), which is discussed next in section 2.4.2. Over a 5-year period (2005-2010), Neu et al. (2014) estimated that interannual variations in the strength of the stratospheric Brewer-Dobson circulation of ~40 % are largely governed by ENSO and the QBO. This modulation can thus influence stratospheric ozone levels from low to high latitudes, and in turn the STE flux of ozone according to models (Zheng and Pyle, 2005; Hsu and Prather, 2009; Voulgarakis et al., 2011). The deep branch of the BDC must be the principal pathway for such mechanism since a strengthening of the lower branch of the circulation would lead to mixing of lower tropical ozone abundances in the extratropical lower stratosphere, and since ENSO/QBO-driven anomalies in tropical lower stratospheric ozone tend to be of opposite sign to that in mid-latitudes (Neu et al., 2014). The dynamical interplay between ENSO and the QBO is also critical in determining interannual variability in stratospheric water vapour (Garfinkel and Hartmann, 2007; Taguchi, 2010; Wang et al., 2020), aside from annual cyclic variations in association with the 'tape recorder' (Mote et al., 1996; Glanville and Birner, 2017). During El Niño conditions, an anomalously cold tropical UTLS region is observed (e.g. Trenberth and Smith, 2006) in response to enhanced adiabatic cooling of the tropical stratosphere that occurs as a result of intensified upwelling. This favours anomalously low ozone amounts in the tropical lower stratosphere (Randel et al., 2009), but also increased lower stratospheric water vapour (Hu et al., 2016; Avery et al., 2017; Diallo et al., 2018). Although this tendency may seems counterintuitive with the freeze-drying mechanism, as air ascends through the cold-point tropical tropopause (Jensen and Pfister, 2004), the lower stratosphere warms locally over the western Pacific region during El Niño where most of the upward mass flux from the troposphere enters the stratosphere. This enhanced upwelling is associated with a strengthening of the BDC, driven by increased extratropical Rossby wave breaking during El Niño (Sassi et al., 2004; Taguchi and

Hartmann, 2006), which furthermore induces anomalously warm Arctic stratosphere conditions (Garfinkel and Hartmann, 2007). The inverse is observed during La Niña conditions. Linkages between ENSO extremes, the Walker Circulation and the BDC have also been explored in relation to stratospheric ozone, principally east of the international dateline (Manatsa and Mukwada, 2017). It stands to reason that variability in the Walker Circulation, in addition to ENSO alone, may influence STE of ozone in both the tropics and extratropics (via interaction with the BDC) with subsequent implications for interannual variability in tropospheric ozone.

The net downward flux of stratospheric ozone into the troposphere has been shown to be affected by ENSO, with indication of an approximate lag of six months from the peak of an ENSO event to the most pronounced changes in STE (Zeng and Pyle, 2005; Doherty et al., 2006). With respect to the Southern Oscillation Index (SOI), Zeng and Pyle (2005) shows that STE is strongly anticorrelated with such lag (e.g. r = -0.6 over the 1990-2001 period); such that STE is enhanced (suppressed) in La Niña (El Niño) years. This finding is consistent with an earlier study by Langford et al. (1998), with a subsequent study (Langford, 1999) using observations above Colorado, USA, attributing such relationship regionally to atmospheric circulation changes in the vicinity of the eastern Pacific subtropical jet exit region, in response to ENSO. Resultant changes to the tropospheric ozone burden of the extratropics via STE can be thought of as the stratospheric pathway contribution from ENSO, which may either amplify or dampen any changes induced by ENSO via tropospheric pathways. However, other studies find little evidence that ENSO correlates with global or hemispheric STE of ozone fluxes, even when isolating influence from the QBO (Hsu and Prather, 2009). Indeed, the QBO is widely reported to exert a larger control over total column (TCO) and stratospheric ozone variability compared to ENSO. For instance, Camp et al. (2003) found by performing Empirical Orthogonal Function (EOF) analysis on the monthly mean Merged Ozone Dataset (MOD) that the QBO explains 75 % of the tropical total ozone variability, which contrasts with just 3 % due to ENSO. Despite this, stratospheric circulation changes due to both ENSO and the QBO are highly correlated and are to a large part inseparable (Neu et al., 2014), which hinders our understanding of the role of each subsequent component on STE and resultant tropospheric ozone abundances. It has been shown in Diallo et al. (2018) however that the effects of these two drivers can be disentangled through established methods such as multiple linear regression. Nevertheless, this study shows the combined effects ENSO and the QBO have in explaining anomalies in stratospheric water vapour, due to the regulatory

effect of tropical cold point tropopause temperatures, can be particularly challenging to understand. This combined influence is however discussed further in section 2.4.2 below.

2.4.2 Quasi-Biennial Oscillation (QBO)

The QBO is a cyclic variation in the zonal winds of the equatorial stratosphere (between ~20°S-20°N and 5-100 hPa), with of a somewhat irregular periodicity of between ~24 and 30 months, that is characterised by alternating, downward propagating easterly and westerly winds (Baldwin et al., 2001; AMS, 2012). This oscillation is primarily driven by the upward propagation of eddy fluxes from equatorially trapped Kelvin waves, excited by convection, which interact with the stratospheric mean flow (Lindzen and Holton, 1968; Tripathi et al., 2015). The QBO is the main component of the dynamics of the tropical stratosphere (Chipperfield et al., 1994; Chipperfield, 2003; Randel and Wu, 1996, 2007; Logan et al., 2003; Tian et al., 2006; Fadnavis and Beig, 2009; Hauchecorne et al., 2010). Local to the tropics and in conjunction with the phase of ENSO, tropical upwelling is modulated which gives rise to changes in ozone (O_3) and stratospheric water vapour (H_2O); the latter of which is controlled by the temperature of the cold-point tropical tropopause (Yulaeva et al., 1994; Flury et al., 2013). Anomalously cold temperatures manifest during the easterly QBO phase as enhanced upwelling invokes stronger radiative cooling, as well as negative anomalies in tropical lower stratospheric ozone and water vapour. The opposite occurs during the westerly phase, although horizontal transport and mixing of chemical tracers and aerosols poleward is enhanced (Plumb and Bell, 1982; Trepte and Hitchman, 1992). A QBO signal can also be extracted from this record in the tropical troposphere, with maximum changes of between 2 and 7 DU (Ziemke and Chandra, 2012). Limited in situ (ozonesonde) data confirms such signals extending down into the mid-troposphere (~10-20 % of typical values), albeit with different regional response time lags and disparities in the sign of changes in tropospheric ozone, in response to both the QBO and ENSO (Lee et al., 2010). This highlights the importance of dynamical horizontal transport processes in influencing the response; the effects of which has been asserted to be a critical factor (Ziemke and Chandra, 1999), such as the role of deep convection modulated by the QBO in tropical regions especially (Collimore et al., 2003). Modulation of upper tropospheric photochemistry in response to QBO-induced stratospheric ozone anomalies is however also known to be an important factor. Despite this, other observational studies report that the overall mean interannual variability in tropical tropospheric ozone is largely unaffected by the QBO, as well as the solar cycle (e.g. Leventidou et al., 2018).

Like ENSO, it has been shown that the QBO acts to modulate the strength of the stratospheric BDC (Baldwin, 2001; Calvo et al., 2010; Tripathi et al., 2014), and subsequently the distribution of stratospheric ozone (Holton and Tan, 1982; Gray and Pyle, 1989; Oman et al., 2013; Wespes et al., 2016). In low to mid-latitudes, the modulation of the stratospheric circulation directly explains anomalies in lower stratospheric ozone, whereas the response at high latitudes is also influenced by modification of upward propagating wave activity from the troposphere (Kinnersley and Tung, 1999), which is known as the Holton-Tan Mechanism (Holton and Tan, 1980). The phase of the QBO is known to exert a control over where the EP flux is absorbed and in turn where residual mean motion is induced (Holton and Tan, 1980; McIntyre, 1982). In the easterly QBO phase, mean meridional motion is focussed poleward, together with anomalous downwelling and adiabatic warming in the winter hemisphere, which leads to a warmer SPV and increased polar stratospheric ozone (Gray and Pyle 1989; O'Sullivan and Salby 1990; O'Sullivan and Young 1992; Tung and Yang 1994). The opposite tendency occurs during the westerly QBO phase. Salby et al. (2011) showed from 3D modelling integrations of stratospheric dynamics and photochemistry that the QBO has a larger role over anomalous and temperature structure poleward of 40°N later in winter, whilst anomalous EP flux from the troposphere is dominant during early winter. This influence increasingly competes with the modulation effect of the QBO as winter progresses, in terms of influencing structural anomalies in temperature and ozone.

The influence of the QBO on the stratospheric circulation is illustrated in Figure 2.5 in terms of both the induced tropical stratospheric temperature changes, in response to anomalous changes in vertical motion, and perturbations to the meridional ozone transport during each of the respective QBO phases. There is observational evidence that the QBO is the primary source contribution to the interannual variability of stratospheric ozone, with the most coherent signal for this over the Southern Hemisphere where total column ozone variability of ~30-40 DU is present in the Aura OMI and Aura Microwave

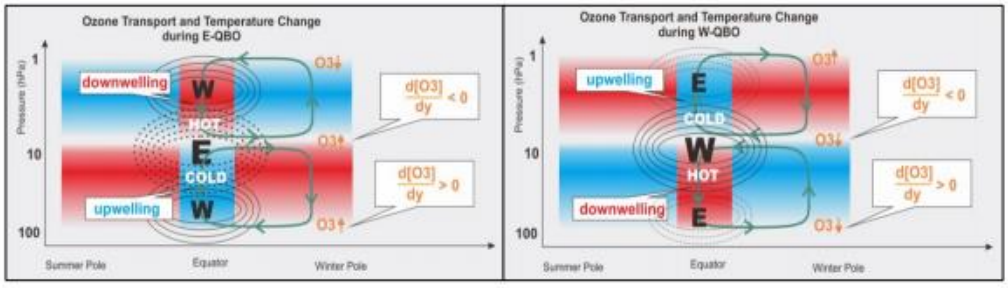

Figure 2.5 – Depiction of ozone transport and temperature changes associated with the phase of the QBO. Adapted from Figure 8 in Kusuma et al. (2019).

Limb Sounder (MLS) satellite record (Ziemke and Chandra, 2012). Nevertheless, the high level of correlation between ENSO and the QBO makes disentanglement of each individual influence highly challenging (Calvo et al., 2009; Neu et al., 2014), albeit not impossible as demonstrated by Diallo et al. (2018). A stronger BDC is observed during east phase events as planetary waves are directed more towards the equatorward flank of the polar night jet (reduced wave refractive index), where subsequent dissipation decelerates the zonal flow around the wintertime stratospheric polar vortex (Garfinkel et al., 2012; Tripathi et al., 2014).

This response is synonymous with El Niño and the two are more frequently in phase; together they have been postulated to favour an enhancement in the downward flux of ozone from the stratosphere into the troposphere (Neu et al., 2014). A robust QBO signal on the distributions of other tropospheric trace gases (N_2O, CFC-11 and CFC-12) via this mechanism, in relation to interannual variability in the BDC strength, has also been demonstrated on a regular and persistent basis (from both model output and measurements) that extends down to the surface (Ray et al., 2020). Despite this, other studies investigating the role of the QBO on STE of ozone find a different tendency to the phasing of the QBO. A maximum positive (negative) STE ozone flux response was found for instance by Hsu and Prather (2009) over mid-latitudes during the QBO west (east) phase, in antiphase with the midlatitude QBO signal in total column ozone. Such variability in STE was however quantified to be a relatively small, albeit potentially significant, fraction of the global average value of ~1.2 g m^{-2} a^{-1}, peaking around 0.2 g m^{-2} a^{-1} which equates to ~>15 %. The inference is that the downward flux of ozone into the troposphere over mid-latitudes is limited by some dynamical constraint during the easterly QBO phase, in association with induced sinking of the overturning circulation in the subtropics (Hsu and Prather, 2009). The interannual variance in the hemispheric STE ozone flux was been quantified to be on the order of 20 % and 45 % in the Northern Hemisphere and Southern Hemisphere respectively, implying that the QBO is nonetheless likely to be an important driver of changes in STE.

2.4.3 11-Year Solar Cycle

The influence of solar activity on Earth's climate has been documented for over 100 years, with longstanding observations of variations in the solar output. A combination of ground-based and satellite observations, together with breakthroughs in modelling and theoretical understanding, have served to develop our knowledge of the importance of

solar variability, particularly involving the stratosphere (Baldwin et al., 2019). Statistical relationships between solar activity and a variety of surface meteorological parameters, such as air temperature and precipitation, were already being identified during the 19th and early 20th century (see citations within Helland-Hansen and Nansen, 1920), with an expansion of the number of correlated variables (ozone, temperature and tropopause pressure) as upper-air data became available in subsequent decades (Pittock, 1978). A response of the high-latitude stratosphere to the 11-year solar cycle has been demonstrated in both climate models and reanalysis datasets in recent years (e.g. Kuroda and Kodera, 2002; Matthes et al., 2006; Ineson et al., 2011; Mitchell et al., 2015).

Beginning with the advent of direct spectral measurements of the sun's output from satellites in 1978, quantification of the total solar irradiance (TSI) – the variation in solar insolation from the solar (sunspot) minimum to solar (sunspot) maximum – was found to be typically only ~1 W m^{-2} (Fröhlich, 2006); oscillating around a baseline value of ~1366 W m^{-2}. The corresponding relative change in the solar power available to the Earth's system, once an albedo of ~0.3 is taken into account, was determined to be a mere ~0.07 %. However, significantly larger observed changes in climate on a regional scale especially, related to variability associated with the 11-year solar cycle, imply that more complex mechanisms can influence the Earth system (Gray et al., 2010). For instance, an observed lag of ~3 years in the climate response of the North Atlantic to solar variability may be largely attributable to atmosphere-ocean coupling (Scaife et al., 2013). The subsequent realisation, however, that significantly larger variations in the sun's output occur across the shorter spectral wavelengths during the 11-year solar cycle (Gray et al., 2010), principally in the UV, was recognised to be a likely explanation for the apparent solar-climate connections. The fractional changes between solar maximum and solar minimum conditions were reported to be > 6 % in the UV spectral region (Ermolli et al., 2013). The mechanisms still remain unclear even in the present day but are thought to consist of a bottom-up mechanism, possibly involving SST changes and subsequent tropospheric feedbacks (e.g. Meehl et al., 2008; Misios et al., 2019), as well as a top-down mechanism that involves modulation of stratospheric ozone levels, and thus ozone heating (Haigh, 1994), in addition to the dynamical stratospheric background state that may impact planetary wave propagation, and in turn, stratosphere-troposphere coupling (Kuroda and Kodera, 2002). For instance, the formation of ozone is impacted by modulation of incoming solar irradiance between 100-240 nm and the destruction of ozone is affected by changes in the 240-350 nm region (Gray et al., 2010). On top of this, solar activity

changes also impact energetic particle precipitation (EPP) that may lead to the formation of reactive nitrogen in the thermosphere, which can influence ozone levels if transported down into the stratosphere (Solomon et al., 1982). For this reason, the 'top-down mechanism' may be further split into the modulation resulting from UV effects, as well as EPP effects, since they both invoke changes in temperature, ozone and the circulation of the upper stratosphere. Subsequent tropospheric and surface impacts may then result as anomalies propagate down via stratosphere-troposphere coupling mechanisms (e.g. Gray et al., 2013; 2016). The range of mechanisms and connections between variability associated with the 11-year solar cycle and climate are displayed in the schematic diagram produced by Gray et al. (2010) in Figure 2.6.

The typical modulation of total column ozone due to the 11-year solar cycle has been quantified to be between ~1 and 2 %, with the bulk of this occurring in the lower stratosphere (altitudes < 28 km) according to Solar Backscattered Ultraviolet (SBUV)/SBUV-2 data (Hood, 1997). Using multiple regression methods, it is shown that total ozone, lower stratospheric temperatures and geopotential heights are most sensitive to solar variability in the Northern Hemisphere, peaking at around 30°N. This sensitivity is further maximised over the Pacific region (between 160°E and 110°W), with

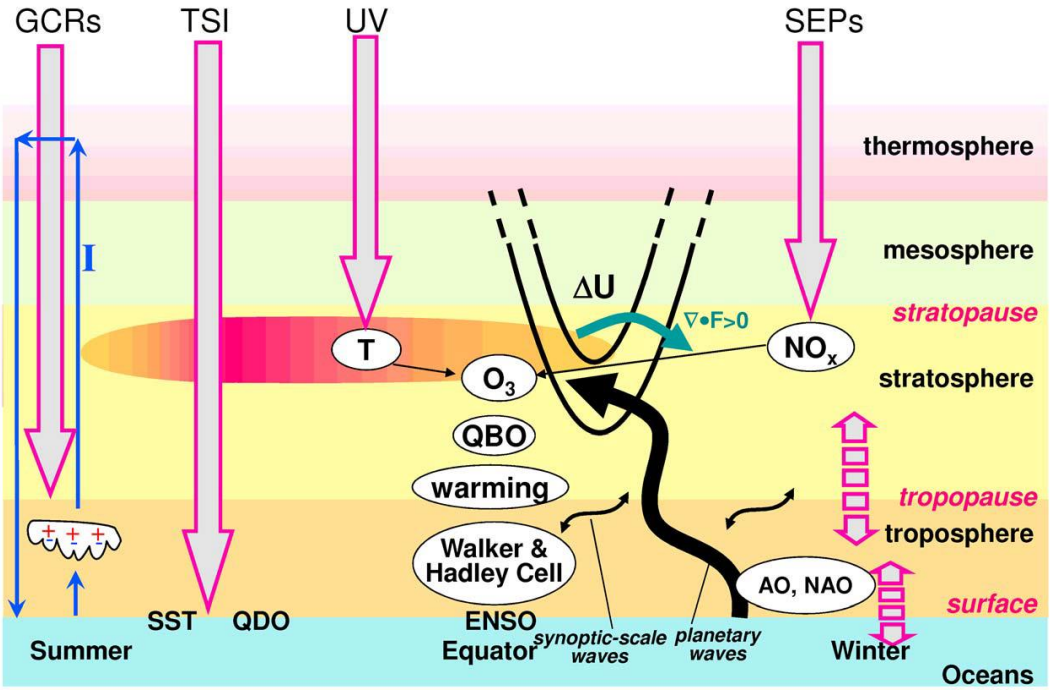

Figure 2.6 – Schematic diagram of solar modulation on climate produced by Gray et al. (2010), based on the earlier work of Kodera and Kuroda (2002). Both direct and indirect effects are shown through changes in solar irradiance (TSI and UV), in addition to corpuscular radiation effects (energetic particles and galactic cosmic rays), with respect to solar (sunspot) maximum conditions. Atmosphere-ocean and stratosphere-troposphere coupling is denoted by the dashed arrows.

maximum changes between solar maximum and solar minimum of 11 DU in total ozone, 0.8 K temperature change at ~100 hPa and 60 m geopotential height variation at 50 hPa. This location of maximum latitudinal sensitivity of ozone is confirmed also by Shindell et al. (1999), with increases of wintertime lower stratospheric ozone of ~1-2% between 25°N and 30°N from solar maximum to solar minimum conditions, which contrasts with a decrease of 0.5-1.5% between 35°N and 50°N. In the middle atmosphere, increases of ~2-4 % were modelled during Northern Hemisphere winter, which is larger compared to the Southern Hemisphere for the same season due to the mitigating effects of increased chemical destruction. Similar findings are made by Haigh (1994) and Soukharev and Hood (2006). Ozone production is enhanced as additional oxygen photolysis occurs at wavelengths less than 242 nm due to enhanced irradiance during solar minimum conditions (Maycock et al., 2016).

2.4.4 Annular Modes

Interannual variability in the internal atmospheric dynamics of the mid- to high-latitudes can be described by so-called annular modes, which describe anomalous hemispheric flows irrespective of the seasonal cycle (Thompson, n.d.). The Northern Annular Mode (NAM) is the dominant mode of climate variability from daily to seasonal timescales in the Northern Hemisphere (Thompson and Wallace, 2000; Baldwin and Dunkerton, 2001). Closely related to both the North Atlantic Oscillation (NAO) and Arctic Oscillation (AO), the NAM index is a measure of the pressure differential between the Arctic and the surrounding lower latitudes (Thompson and Wallace, 2000). The positive phase is characterised by an enhanced meridional pressure gradient, associated with a stronger, more isolated SPV, with a weaker pressure gradient and SPV inherent features of the negative phase (Kiesewetter et al., 2010). Total column ozone variability has been shown to be profoundly influenced by the annular modes (e.g. Orsolini and Doblas-Reyes, 2003), with much of the variability in high-latitude ozone found to be attributable to variations in the NAM (Kiesewetter et al., 2010). This relationship with the NAM index is closely linked to variability in the strength of the BDC, with some 80 % of interannual variability in middle to high-latitude stratospheric column ozone related to variations in BDC wave driving; with changes due to chemistry accounting for the remaining 20 % (Fusco and Salby, 1999; Salby and Callaghan, 2002; Weber et al., 2011). In March however, Arctic ozone depletion has been estimated to explain up to 50 % of ozone variability between 50 and 70 hPa (Kivi et al., 2007). Subsequently, long term potential changes in the BDC may therefore be inferred from long-term changes in the NAM or AO index (Fusco and

Salby, 1999; Randel et al., 2002). However, other studies put more emphasis on the combined importance of both dynamics and chemistry in explaining long term ozone trends (e.g. Weber et al., 2011), as well as interannual variability in the spring-to-autumn polar total ozone ratios and winter polar ozone loss (Weber et al., 2003; Tegtmeier et al., 2008).

A robust relationship between planetary wave driving, as quantified using the 100 hPa winter eddy heat flux proxy, and observed polar-cap ozone is found for both hemispheres, albeit this is modulated by the influence of heterogeneous chemical losses (Weber et al., 2011). The role of chemistry in influencing ozone variability is amplified in the Southern Hemisphere, due to a climatologically stronger SPV and concurrently weaker BDC and planetary wave driving (Holton et al., 1995). Moreover, the influence of chemistry became more significant during the latter half of the 20th century, particularly during springtime, due to increased stratospheric halogen loading in response to CFC emissions (Solomon, 1999; Weber et al., 2011). This tendency has since reversed but is still likely to be an important factor for several more decades as the residence time of CFCs is relatively long. This factor has primarily been associated with the near linear decreases in springtime Antarctic total ozone during the 1980s, and not as a result of measured changes in planetary wave activity over this period. On the other hand, a much closer correspondence between planetary wave driving and Southern Hemisphere total ozone variability is apparent in satellite observations from the mid-1990s onwards (Weber et al., 2011).

Winters dominated by persistently negative NAM states have been linked to years in which the springtime reservoir of ozone in the LMS has been anomalously large, with subsequent implications for the enrichment of ozone exchanged into the troposphere, and thus the net seasonal STT flux of ozone (Albers et al., 2018). This finding can be related to an anomalously strong BDC (and attendant strong wave driving) in such winters which leads to the accumulation of high ozone abundances in the extratropical LMS, mediated to an additional extent by loss of ozone to the troposphere due to STT over winter and the presence of any anomaly residuals in the system residing from the previous year (e.g. Fioletov and Shepherd, 2003; Tegtmeier et al., 2010; Weber et al., 2011). The relationship between the strength of the BDC and the seasonal build-up of ozone in the LMS may however be complicated by the opposing meridional gradients in ozone within both the shallow and deep branches of the circulation, as discussed earlier in section 2.2.

Tropospheric ozone interannual variability in connection with the annular modes is well documented in the literature, particularly across the Northern Hemisphere mid-latitudes. In terms of the AO, regional modulations of ozone concentrations of up to 5 ppbv have been noted in the troposphere during springtime (Hess and Lamarque, 2007). The NAO, as a regional manifestation of the hemispheric AO over the Atlantic sector, has also demonstrated by Pausata et al. (2012) to impact surface ozone concentrations over south-western, central and northern Europe in all seasons except autumn. This study demonstrated that NAO+ conditions may lead to advection of ozone-rich maritime air from the Atlantic Ocean, with positive anomalies of up to 10 ppbv over the UK, central Europe and Scandinavia. Conversely, negative ozone anomalies exceeding 10 ppbv may occur during NAO- conditions over the western and central Mediterranean Sea due to entrainment of ozone-poor air masses from the African continent. Li et al. (2002) found that the strongest correlation of ozone transport over the Atlantic to the NAO occurs in spring, in both the free troposphere and the boundary layer. Creilson et al. (2005) found a greater sensitivity of tropospheric ozone to AO variability in the Atlantic region, compared to the Pacific region, with a statistically significant correlation evident between the AO and the distribution of tropospheric ozone over the north-eastern Atlantic from satellite observations. Over North America, up to 50 % of the lower tropospheric ozone interannual variability can be attributed to the AO during springtime, as verified from ozonesondes (Lamarque and Hess, 2004). Consistent with recent trends in Northern Hemisphere lower tropospheric ozone, Kivi et al. (2007) related an increase in free tropospheric ozone of 11.8 ± 1.8 % (16.0 ± 3.1 % between January to April) between 1989 and 2003 primarily to long-term changes in the AO. Furthermore, pronounced anticorrelations between tropospheric ozone and the AO have been reported by Liu et al. (2020) during winter, with the impact larger over North America compared with Europe. The strength of the anticorrelation typically increases towards the surface over North America, maximising near 90°W, whereas a modest increase from 400 to 700 hPa over Europe sharply reverses below 700 hPa.

The AO influence can be separated into a stratospheric component, in which STT of ozone is impacted, and a tropospheric component in which transport of ozone and its precursors are affected. The former component is shown to be most influential over northern Canada and the Arctic in Hess and Lamarque (2007), whilst modulation of the tropospheric component governs the response over the Atlantic, Europe and eastern Siberia. Indeed, the role of stratospheric subsidence in association with changes in the AO has been

concluded to be larger over North America compared with Europe, due to climatologically lower tropopause and geopotential heights (Liu et al., 2020). The variations associated with the tropospheric component of the influence from the NAO during winter over Europe and the Atlantic region have been extensively quantified in the observational and modelling study by Pope et al. (2018). Unlike primary pollutants such as nitrogen oxides (NO_2) and carbon monoxide (CO), ozone as a secondary pollutant responds inversely to NAO changes such that ozone is enhanced (reduced) during NAO+ (NAO-) conditions over continental Europe. Nonetheless, modulation of both STE and transport of tropospheric produced ozone in response to the AO and NAO has been simulated by models over each of the three main populated centres (North America, Europe and Asia) across the Northern Hemisphere (e.g. Lamarque and Hess, 2004). In a climatological study (1979-2013) by Sprenger and Wernli (2003), less (more) STE has been shown to occur during the NAO+ (NAO-) phase, due to the enhanced (reduced) frequency in anticyclonic conditions over the Atlantic Ocean basin. This tendency can be related to the important role of synoptic-scale and meso-scale processes, in association with the jet positioning and cut off low formation, in facilitating STT of ozone-enriched air masses. Creilson et al. (2003) separated both the role of tropospheric circulation and STE as a function of the NAO. The conclusion of their study was that the strength of the prevailing westerly zonal flow had a much greater influence over the amount of tropospheric ozone above the Atlantic Ocean and Europe. Variability in STE due to the NAO was inferred to be greatest in spring but the relative magnitude of this influence becomes more limited during this time, as tropospheric ozone levels attain an annual maximum.

2.4.5 Sudden Stratospheric Warmings (SSWs)

The variability of the extratropical stratosphere is influenced by various external forcings (Baldwin et al., 2001), including sea surface temperatures (SSTs), the 11-year solar cycle and the QBO which are also thought to influence the likelihood of major midwinter sudden stratospheric warmings (SSWs) (Harada et al., 2010). SSWs are defined by a reversal of the meridional temperature gradient poleward of 60°N and a reversal of the 10 hPa zonal mean wind at 60°N from westerly to easterly (e.g. Andrews, 1987; Manney et al., 2008b). SSWs, first observed by Scherhag (1952), are abrupt and occur over the course of just a few days. Such events occur on average six times a decade in the Northern Hemisphere with only one such event ever observed in the Southern Hemisphere (Thompson et al., 2005; Charlton et al., 2007; Butler et al., 2015). SSWs constitute the largest deviations from the mean climatological state in the Northern Hemisphere

wintertime stratospheric circulation (Andrews, 1987). They are characterised by disturbances of the wintertime stratospheric polar vortex due to the upward propagation of planetary waves from the troposphere, which break and dissipate at a certain level (Matsuno, 1971), in association with upper tropospheric weather systems (e.g. Coy et al., 2009) and blocking ridges (Martius et al. 2009; Castanheira and Barriopedro 2010; Woolings et al. 2010; Nishii et al. 2011). This deposition of momentum leads to the slowing or reversal of the westerly circulation at increasingly lower levels in the stratosphere as waves break at the critical level above which vertical propagation is inhibited by the downward propagating flow reversal (Matsuno, 1971). The impact on the zonal-mean meridional circulation beneath regions of sustained anomalous wave driving, represented by the Eliassen-Palm (EP) flux divergence, later formed the basis of the "downward control" principle proposed by Haynes et al. (1991).

The tropospheric circulation can thus be modulated by SSWs that propagate down to the tropopause through stratosphere-troposphere coupling. It has however been demonstrated that the relationship between vertical wave propagation into the stratosphere and upper tropospheric blocking is complex, with blocking in some localities such as the western Pacific and the Far East leading to a suppression in stratospheric wave activity (Nishii et al., 2011). The deceleration of the stratospheric zonal flow arises due to a reduction in the meridional temperature gradient under thermal wind balance, as a result of a strengthening in the poleward residual circulation. Upward propagating waves impart westward momentum as they dissipate, although the enhanced influence of Coriolis force on the anomalous induced poleward residual circulation (acting orthogonal to the axis of the eddy forcing) offsets this. To ensure continuity however, enhanced descent (ascent) poleward (equatorward) of the eddy forcing region must occur in association with an enhanced poleward residual circulation, giving rise to the reduced meridional temperature gradient as a result of the adiabatic temperature changes that subsequently occur. Thus, the polar stratosphere is subject to an abrupt increase in temperature due to enhanced polar descent and associated adiabatic warming (Limpasuvan et al., 2004), that is necessary in maintaining quasigeostrophic balance as vorticity weakens due to imposing anticyclonic regions (Matsuno, 1971).

2.4.5.1 Event Type Classifications

An SSW can be dynamically distinguished as either a vortex displacement or vortex split event as illustrated in Figure 2.7, which is typically forced by a primary wave-1 or wave-2

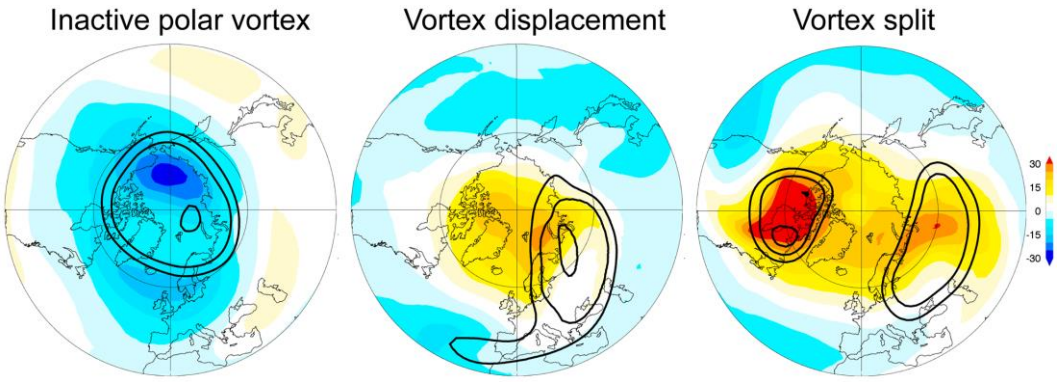

Figure 2.7 – A depiction of a vortex displacement (23 January 1987) (centre) and vortex split event (24 January 2009) (right) in relation to an inactive (strong) state of the wintertime stratospheric polar vortex (~9 January 2009) (left) from the MERRA2 reanalysis. Contours denote PV at 550 K (for 75, 100 and 125 PVU) and shading represents temperature anomalies (K) at 10 hPa. Taken from Figure 1 in Butler et al. (2017).

perturbation to the zonal westerly flow respectively. Events may further be classified as those which propagate into the troposphere and those that have no direct influence on the troposphere (Nakagawa and Yamazaki, 2006). A key difference in the upward propagation of waves into the stratosphere is found for 51 different events in ECMWF reanalysis data (1957-2002) for tropospheric warm and cold events, classified using the 30-day polar mean temperature anomaly at 500 hPa after the key-day (the day at which the warming rate is maximised at 10 hPa), in the composite analysis study by Nakagawa and Yamazaki (2006). The EP flux is directed upward and poleward (equatorward) in warm (cold) events, which has implications for wave forcing and subsequent residual circulation anomalies in the troposphere. Whilst warm events are characterised by a continuation of the strong downward residual motion from the stratosphere towards the surface, the tropospheric wave forcing in cold events opposes the strong downward residual circulation in the stratosphere which inhibits propagation into the troposphere. A similarly defined distinction is made based on the two leading empirical orthogonal functions (EOFs) of daily-mean polar-cap (70-90°N) temperature anomalies integrated over the middle atmosphere column, with so-called Polar-night Jet Oscillation (PJO) events identified where the SSW temperature anomaly (as projected onto these two EOFs) is maximised at ~60 hPa, so long as the anomaly is sufficiently strong (Kuroda and Kodera, 2004; Hitchcock et al., 2013). Such distinction is related to the depth to which the warming descends through the stratosphere, which is closely associated with the magnitude of upward and poleward directed wave forcing. PJO events are noted for the subsequent strength of their signal in the lower stratosphere, in contrast with non-PJO events where any response is largely statistically insignificant (de la Cámara et al., 2018b).

Regardless, the complexity and high interannual variability in the state of the troposphere from year to year results in a unique character and evolution of each event.

2.4.5.2 Tropospheric Response

Variations in the SPV strength have a typical downward propagation timescale into the troposphere of several weeks and such influence may last for up to two months (Baldwin and Dunkerton, 1999; 2001). A surface response can however occur within just 2-3 days of the onset of split events, which account for about 50 % of cases (Kidston et al., 2015). The typical manifestation is that of a negative AO/NAO pattern (Limpasuvan et al., 2004), although it was found that a weak positive AO pattern followed non-propagating SSWs in the study by Nakagawa and Yamazaki (2006). A NAO- like response in near-surface geopotential height fields is also found to follow stratospheric final warming (SFW) events, which is often preceded by extended periods of NAO+ conditions in the weeks prior to the SFW (Black et al. 2006). Such a precursor signal is not clearly discernible however prior to midwinter SSWs (Limpasuvan et al., 2004). In the model-based study by (Kidston et al., 2015), negative temperature anomalies over Europe (of up to 3 K) and positive temperature anomalies (> 1.5 K) over eastern North America are shown to correlate with split SSW events in a surface pattern that resembles a strong NAO- pattern. An increased incidence of cold air outbreaks over North America is found following displacement events, albeit such signal is weaker and delayed due to a slower downwelling response compared with split events (Mitchell et al., 2013). Associated hemispheric circulation changes in the troposphere arise due to weakening of the stratospheric circumpolar jet stream, which leads to an equatorward displacement in the location of the extratropical storm tracks. An equatorward deflection of planetary waves, due to the inhibition of vertical propagation into the stratosphere following an SSW, is also found to be a contributing factor in observed subtropical and tropical circulation changes (Gómez-Escolar et al., 2014). Modelling studies show that synoptic wave variability is a key component of the response in the tropospheric jet prior to an SSW event. Domeisen et al. (2013) shows that anomalous equatorward synoptic eddy momentum fluxes are fundamental to the persistence of a displaced jet for up to three months, which is consistent with that seen in observations (e.g. Lorenz and Hartmann, 2003). An important role of tropospheric eddy feedbacks has furthermore been demonstrated to explain the downward coupling of NAM anomalies (Song and Robinson, 2004; Kunz and Greatbatch, 2013) and wave anomalies (Lubis et al., 2018) into the troposphere, in both numerical modelling and unambiguous observations of the surface

impacts of stratospheric variability, although straightforward theoretical mechanisms of such tropospheric effects remain elusive (Baldwin et al., 2019). Despite the uncertainties regarding stratosphere-troposphere coupling mechanisms in explaining the influence of SSWs on the state of the troposphere, it is clear that the build-up and onset of such events provides a significant source of predictability on sub-seasonal timescales (e.g. Sigmond et al., 2013).

The key dynamical processes associated with stratosphere-troposphere coupling are understood to be dependent on the linkages between variability in the zonal flow of the lower stratosphere and tropospheric wave activity (waves smaller than wavenumber-3) (Limpasuvan et al., 2004). An equatorward jet shift is also found when separating out both weak vortex and strong vortex regimes, with a weak vortex state associated with downward propagation of negative Northern Annular Mode (-NAM) conditions and an increase in the likelihood of AO- and NAO- conditions within 60 days of an anomalous state in the wintertime stratospheric polar vortex (Baldwin and Dunkerton, 2002).

2.4.5.3 Stratospheric Chemical Composition Changes

Changes in the chemical (trace gas) composition of the stratosphere during the evolution of an SSW are also well documented in the literature (e.g. Manney et al., 2009a; 2009b; Tao et al., 2015). Typical changes around the SSW onset include enhanced meridional transport and accelerated polar descent in the stratosphere, which leads to an increase in stratospheric ozone (O_3), as well as a breakdown in the polar vortex mixing barrier that leads to a flattening of tracer gradients in species such as water vapour (H_2O), carbon monoxide (CO), methane (CH_4) and nitrogen dioxide (N_2O) due to enhanced mixing across the weakened polar vortex edge. Using ERA-Interim reanalysis and Whole Atmosphere Community Climate Model (WACCM) simulations, de la Cámara et al. (2018b) showed that a weaker residual circulation and enhanced isentropic mixing establishes (for more than two months in the lower stratosphere), with a stronger and more persistent response for PJO events of up to three months. PJO-composite anomalies in isentropic mixing are found to be almost twice as large throughout the stratosphere, whereas any enhanced mixing within the lower stratosphere during non-PJO events is largely statistically insignificant. The potential impact of SSW events on STE and resultant tropospheric chemical composition is an aspect that has however received very little attention so far, despite some earlier work on the influence resulting from longer term variations in the NAM and Southern Annular Mode (SAM) indices (see section 2.4.5).

The radiative effect of both O_3 and H_2O is known to be significant in the UTLS region (e.g. Randel and Wu, 2010; Gilford et al., 2016) and changes in such radiatively active trace gas species in this region are known to have the largest relative impact on surface temperatures (Riese et al., 2012). Indeed, pronounced surface climate impacts across the Southern Hemisphere have been unambiguously detected in recent decades, as a consequence of both radiative and dynamical effects of the Antarctic ozone hole (Thompson et al., 2012; Kidston et al., 2015). Such changes largely project onto the SAM, with the most robust impacts occurring in austral summer (Thompson and Solomon, 2002), and have involved a poleward displacement of the tropospheric jet (Arblaster and Meehl, 2006). This leads to modification of air-sea fluxes through perturbed wind stresses (Cagnazzo et al., 2013), with implications for the carbon ocean uptake (Lenton et al., 2009) and perhaps also the Atlantic thermohaline circulation (Reichler et al., 2012). The importance of interactive chemistry for accurate model representations of stratosphere-troposphere coupling has been further demonstrated in the context of stratospheric extreme events, which namely includes SSWs (Haase and Matthes, 2019; Oehrlein et al., 2020). This study found that inclusion of interactive ozone chemistry is pertinent to adequately reproducing the characteristics of such events, in terms of both the mean state and variability, and in explaining more prolonged surface impacts as a possible result of feedbacks between ozone and dynamics during such events when advection of ozone-rich air into polar latitudes occurs.

Chapter 3

This chapter commences with an overview of our understanding of the distribution and abundance of atmospheric ozone, as it has evolved over the last ~140 years, from different observational sources. A description of the different data sources used in this thesis, including two UV-nadir sounders (GOME-2A and OMI), ozonesondes, chemical reanalysis data (CAMS) and simulations from two state-of-the-art chemistry-climate models (CCMs), is thereafter provided. Aspects covered include the theoretical basis for satellite retrievals, instrument or dataset specifications, as well as the constraints and limitations of each information source. Finally, a common approach to comparing models and measurements of tropospheric ozone, through the use of satellite averaging kernels (AKs) which represent the satellite observation geometry, is presented. As an addition to this, the sensitivity of applying satellite AKs to comparison (model or ozonesonde) datasets is evaluated, including cases where biases in lower stratospheric ozone maybe inherently present in models.

Data and Methodology

Our first knowledge of the importance and distribution of ozone in Earth's atmosphere originated from the discovery of the stratosphere by both Teisserenc de Bort (1902) and Assmann (1902). Temperature observations from balloon flights indicated the presence of an isothermal layer above ~10-12 km that extended up to at least ~17 km, which marked the limit of most balloon-borne sondes at this time (Hoinka, 1997). It is today known that a pronounced temperature inversion is found from these altitudes, extending up to ~45-50 km which marks the stratopause (the boundary between the stratosphere and mesosphere), and is a direct result of the vertical distribution and abundance of atmospheric ozone. Such knowledge was developed gradually over approximately a quarter of a century, beginning with initial indications for a temperature inversion in the recently discovered stratosphere from meteor trail observations by Lindemann and Dobson (1923) and culminating with rocket measurements during World War II, which provided confirmation of this feature in real-time (via telemetry), as inferred from both in situ pressure information and radar observations of rocket altitude and speed (Best et al., 1947).

Although the presence of ozone in the upper atmosphere was inferred by Hartley (1880), before knowledge of the existence of the stratosphere, it was a few decades before observation of the incoming solar spectrum led to the inference of the ozone layer by French Physicists (Charles Fabry and Henri Buisson) in 1913. The first measurements of ozone came about in the 1920s, when Dobson and colleagues developed a network of ground-based Dobson spectrophotometers across Europe. This instrumentation was however limited to measuring only the total abundance of ozone through the earth's atmosphere, and not its vertical distribution, although vertical profile information could be derived in conjunction with the Umkehr method developed by Götz et al. (1934). Knowledge of stratospheric ozone chemistry was soon derived thereafter, first outlined in the work of Chapman (1930), but the important role of the Brewer-Dobson Circulation (BDC) in explaining the global distribution of stratospheric ozone and other chemical species took several more decades to understand.

Over subsequent decades, the network of ground-based spectrophotometers progressively expanded, particularly following the International Geophysical Year (IGY) in 1957-58 when a concerted effort to systematically monitor ozone and other chemical constituents worldwide was established (Solomon et al., 2005; Baldwin et al., 2019). Additional observations that also yielded such height-resolved information, using both ground-based and airborne remote sensing techniques, became increasingly available in the post-World War II era. These techniques included differential optical absorption spectroscopy (DOAS), Fourier-transform infrared spectroscopy (FTS) and microwave radiometry, as examples of passive remote sensing methods, together with differential absorption lidar as an example of an active remote sensing technique. Profiles of ozone through different regions of the atmosphere are made possible through the differential absorption or emission properties of ozone with respect to wavelength, which can be exploited to discriminate ozone amounts along the line of sight (Baldwin et al., 2019). The first in situ vertical profile measurements of ozone however began in the 1960s in the form of balloon-borne ozonesondes (Solomon et al., 2005), many years after the advent of balloon-borne temperature observations (radiosondes) in the 1930s. Ozone soundings on either a weekly or bimonthly basis were first limited to a few select sites across the Antarctic but are now routinely undertaken worldwide at least once a week, although large spatial inhomogeneities remain in both spatial and temporal sampling. Both in situ aircraft and sonde measurements have been instrumental in the identification and understanding of LMS transport pathways. For instance, the tropically controlled

transition region (Grant et al., 1994; Rosenlof et al., 1997), characterised by isentropic exchange of air in the region above the subtropical jet (Volk et al., 1996), was inferred from trace gas correlations (e.g. N_2O versus O_3) to lead to the seasonal "flushing" of the LMS ozone reservoir during summer, involving the poleward transport of ozone-poor tropical air masses into the extratropics (Hegglin et al., 2006). Such observations were also key to understanding the connection between Antarctic stratospheric ozone depletion and levels of reactive chlorine monoxide (ClO) (Anderson et al., 1989). Facilitated by polar stratospheric clouds (PSCs), which act as surfaces for heterogeneous chemical reactions to occur, severe, catalytic destruction of ozone was found to occur annually during Antarctic spring in the lower stratosphere (Fahey et al., 1990, 2001).

The first spaceborne inferences of atmospheric ozone originated from the Backscatter Ultraviolet (BUV) experiment, aboard the Nimbus-4 satellite that was launched in April 1970 (Heath et al., 1973), shortly followed by the Solar Backscatter Ultraviolet and Total Ozone Monitoring Spectrometer (SBUV/TOMS) aboard Nimbus-7 in 1978 (NASA, 2020). From the 1980s onwards, a number of additional satellite observing platforms increasingly served to fill in the gaps in our understanding of the regional and seasonal variability of atmospheric ozone, as well as other chemical tracers, across the world. Together with earlier nadir-viewing platforms (e.g. BUV and SBUV/TOMS), vertical profiling of stratospheric temperature and chemical constituents by limb-sounding was subsequently pioneered through use of the Limb Radiance Inversion Radiometer (LRIR) on Nimbus 6 (Sissala, 1975; Gille et al., 1980); the Limb Infrared Monitor of the Stratosphere (LIMS) (Gille and Russell, 1980); and the Stratospheric and Mesospheric Sounder (SAMS) (Jones et al., 1986) on NIMBUS-7, which for the first time elucidated the combined effects of both transport and chemistry in shaping the distributions of stratospheric trace gases (Jones and Pyle, 1984). The advent of limb-viewing instruments, with the capability to probe the chemical composition of the atmosphere from the UTLS upwards at fine vertical resolution, supplemented the limitations of nadir-viewing sounders, namely coarse vertical resolution, to greatly enhance knowledge of the spatiotemporal evolution of ozone and other chemical tracers. Progress in understanding phenomena such as the QBO in the 1990s and 2000s was, in part, derived from the observed oscillation in the vertical distribution and slow downward propagation of tropical stratospheric ozone anomalies from satellite limb sounder observations, alongside rapid advances in the theoretical understanding of stratospheric dynamics (Gray and Pyle, 1989). Knowledge of other features and phenomena acquired with the aid

of satellite-retrieved long-lived trace gas distributions, include planetary wave breaking within the wintertime polar vortex surf zone region (Leovy et al., 1985; Randel, 1993); the subtropical transport barrier, that delineates tropical and extratropical air masses (Neu et al., 2003); and the occurrence of SSWs through the resultant signature in total column ozone (Varotsos, 2002). Therefore, it is clear that satellite observations were invaluable in identifying transport processes and dynamical modes of interannual variability, with trace gases distributions still used to benchmark transport (as well as chemistry) in CCMs (Garcia et al. 1992; Prather and Remsberg 1993; Eyring et al. 2006; Hegglin et al. 2010; Strahan et al. 2011).

Historically, a number of UV-nadir viewing sensors have measured both atmospheric partial and total column atmospheric ozone, including BUV, SBUV, TOMS, SBUV-2, GOME, SCIAMACHY, OMI and GOME-2A, with typical accuracies in the range of 0.5 to 2 % (e.g. Klenk et al., 1982; Loyola et al., 2011; van Roozendael et al., 2012). A timeline of the different UV-nadir sounding instruments since the 1970s (including future planned missions) for ozone is shown in Figure 3.1. The derivation of partial or subcolumn ozone data has enabled the reconstruction of ozone profiles (e.g. Bhartia et al., 1996), albeit at

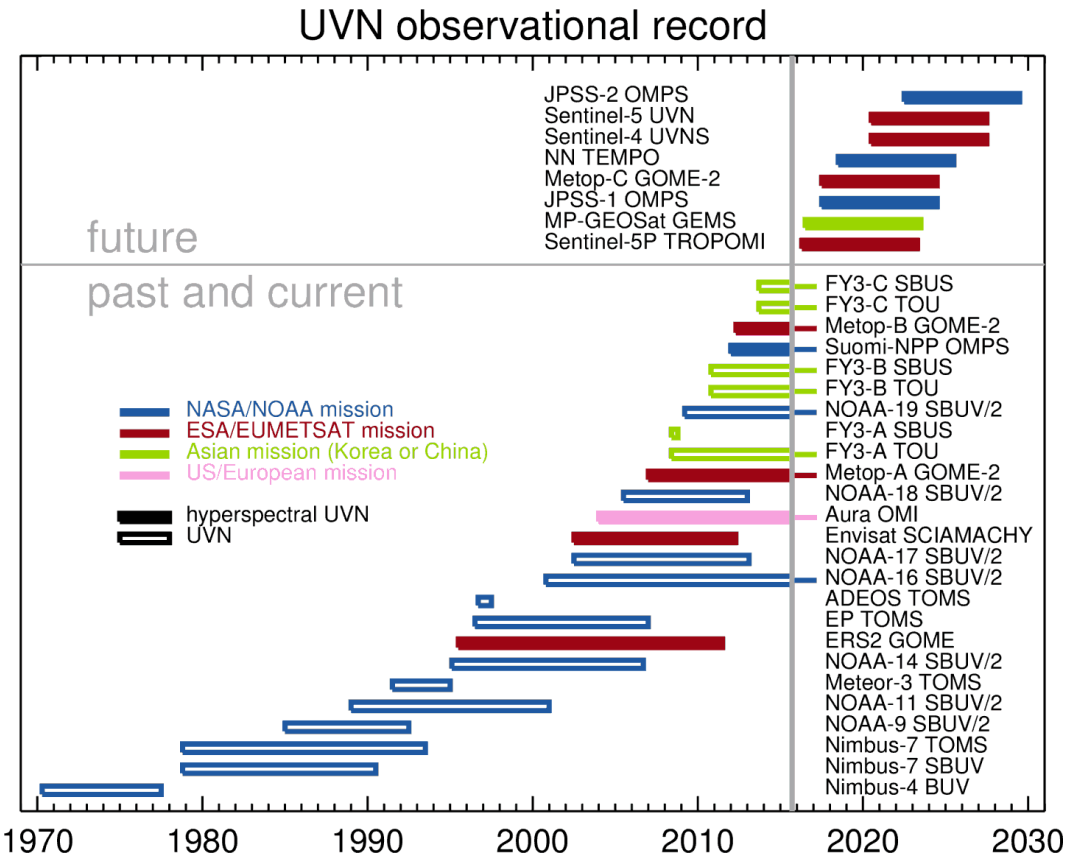

Figure 3.1 – A timeline of UV-nadir (UVN) sounding missions from the 1970s to the 2010s, together with future planned missions. Figure taken from ESA (2020) (https://earth.esa.int/web/sppa/recover).

limited vertical resolution, but estimates of tropospheric ozone have long remained problematic due to the intervening stratospheric ozone layer. As opposed to direct methods of detection, subtraction of an estimated stratospheric component from the measured total column can yield information on the tropospheric ozone column amount. This residual technique entails assumptions of the ozone profile shape and knowledge of the tropopause height (Fishman and Larsen, 1987; Schoeberl et al., 2007; Ziemke et al., 2011). Accurate knowledge of the tropopause pressure or altitude is paramount in limiting retrieval uncertainty. Thus, global climatology studies, such as that by Ziemke et al. (2012) that use the OMI/MLS tropospheric ozone residual method, extract the tropopause pressure (altitude) from reanalysis data in real-time. However, uncertainty may arise from using datasets such as MLS, which are less measurement sensitive with increasing pressure (decreasing altitude) in the UTLS. Thus, estimates using this approach are less precise in the extratropics, particularly as the tropopause pressure is lower at the latitudes. As quantification of this, root-mean square errors of stratospheric ozone columns derived from MLS v3.3 ozone data was calculated to be 0.03 ppmv for retrievals extending down to 261 hPa, increasing to 0.05 ppmv if data is used down to 316 hPa (Ziemke et al., 2011). Whilst day-to-day variability in tropospheric height is large in mid-latitudes, as a result of strong modulation by frontal system activity, the variation in the tropics is much smaller, such that construction of monthly averages can however further reduce uncertainty in the retrieval (Jensen, 2012).

Discrimination of tropospheric ozone amounts in the tropics has also been facilitated from comparisons of the derived total column ozone between adjacent cloud-free and convective cloud-filled satellite pixels; known as the convective-cloud-differential (CCD) method (Ziemke et al., 1998; Valks et al., 2003; Valks et al., 2014). Over regions of convective cloud cover, where cloud tops reach up to the tropopause, only the stratospheric column of ozone can be retrieved. Resultant products are usually only meaningful, however, when compiled into monthly-means for applications such as trend analysis, due to the sparseness and irregularity of such cases. As a significant limitation of this approach however, is that effective cloud top pressure measurements as retrieved by the satellite instrument, for instance GOME-2 in Valks et al. (2014), often reside ~100 hPa lower than the true tropopause altitude (~100 hPa in the tropics). This is supported by other studies which imply that convective cloud tops instead usually reach only to the bottom of the tropical transition layer (TTL), several km below the tropopause (e.g. Folkins et al., 1999; Fueglistaler et al., 2009).

In addition to such observational knowledge, advances in numerical modelling have enabled a quantitative understanding of the role of different chemical and dynamical processes in determining the regional and seasonal characteristics of atmospheric ozone distribution and abundance. In particular, for assessment of the stratospheric contribution to tropospheric ozone, the development and improvement of stratosphere-resolving general circulation models (GCMs) (e.g. Pawson et al., 2000; Gerber et al., 2012), CCMs (e.g. Eyring et al., 2005; SPARC, 2010) and reanalyses (e.g. Iwasaki et al., 2009; Seviour et al., 2012) has been critical for such progress. These developments have been facilitated through increased computing power, which has translated into significant enhancements in model horizontal and vertical resolution needed to more accurately simulate the suite of dynamical, radiative and chemical processes at work, as well as in understanding inherent atmospheric phenomena that are highly non-linear (e.g. the QBO) (Baldwin et al., 2019). Model development has led to new and improved theoretical understanding, which has in turn informed the best use of additional computational resources for further model advances. This is particularly relevant in the case of stratosphere-troposphere coupling, as it has only been recognised relatively recently that the stratosphere can have a profound role over the dynamics of the troposphere. This was first postulated by Scherhag (1952) from limited observations that SSWs could impact surface dynamics, but it was not until the 1980s that model simulations could show a circulation response in the troposphere due to variations in the strength of the SPV (e.g. Boville, 1984; Hoskins et al., 1985). Subsequently, increasing computational resources have been targeted towards improving the representation of the stratosphere in models, as well as increasing the model top (lid) height (Charlton-Perez et al., 2013; Baldwin et al., 2019).

The properties and limitations of the different data sources used for evaluations in this thesis are discussed in this chapter. In section 3.1, in situ measurements provided by ozonesondes (collated into a global database) are first covered, before measurements from two UV-nadir satellite instruments (GOME-2A and OMI) are discussed in section 3.2, including generalities of the retrieval basis. Details of chemical reanalysis data from the Copernicus Atmospheric Monitoring Service (CAMS) are next presented in section 3.3, followed by a description of CCM simulations used from both the European Centre for Medium-Range Weather Forecasts – Hamburg (ECHAM)/Modular Earth Submodel System (MESSy) Atmospheric Chemistry (EMAC) and the Canadian Middle Atmosphere Model (CMAM) finally in section 3.4. Lastly, the approach to comparing both models and

measurements for assessments of tropospheric ozone is then detailed in section 3.5, together with discussion of the limiting factors.

3.1 In Situ Measurements (Ozonesondes)

Vertical ozone profile data over the period 1980-2010 were derived from the World Ozone and Ultraviolet Radiation Data Centre (WOUDC); an archive of balloon-borne in situ measurements of ozone, together with other variables such as temperature, humidity and pressure. Ozonesondes typically provide a vertical resolution of ~150 m from the surface up to a maximum altitude of approximately 35 km, although not in all cases (Worden et al., 2007; Nassar et al., 2008). Most sonde stations launch ozonesondes on a weekly basis, but a number of European sites provide measurements 2-3 times a week (Worden et al., 2007). The WOUDC archive contains measurements from primarily electrochemical concentration cell (ECC) sondes, but also from two other instruments: the Brewer-Mast (BM) and the Japanese ozonesonde (KC) (SPARC, 1998), which all yield measurements of ozone equivalently. A map of all observations sites contributing to the WOUDC measurement network is shown in Figure 3.2. The accuracy of sonde measurements is typically estimated to be within the range of ± 5 % in the troposphere (WMO, 1998), depending on various factors. Precision between the different sonde types is estimated to be within ± 3 %, with systematic biases of less than ± 5 % within the lower to middle stratosphere (12-27 km altitude range), provided that profile measurements

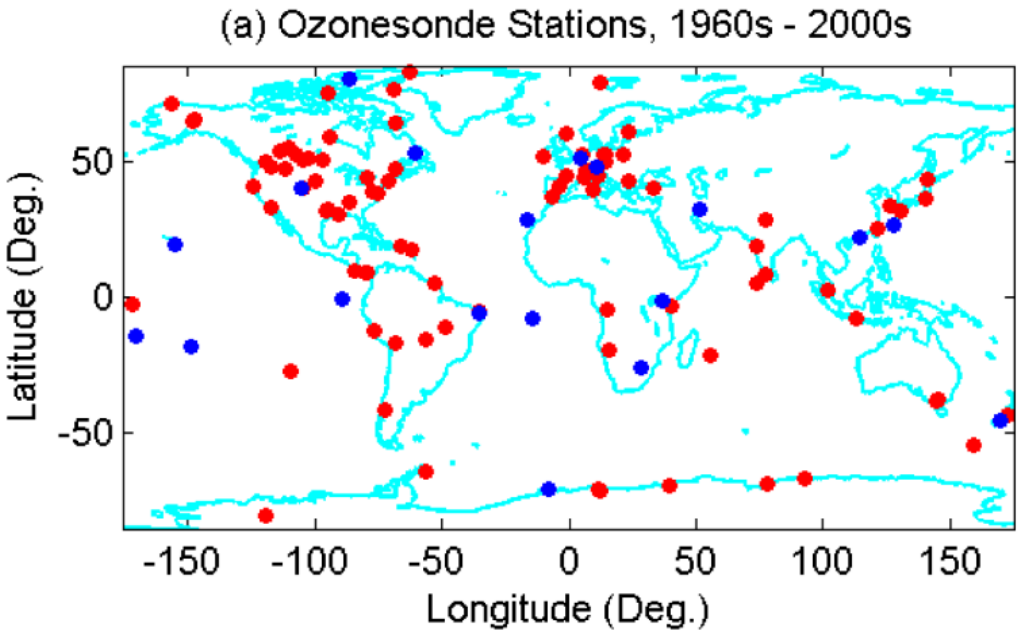

Figure 3.2 – Global map of ozonesonde stations contributing to the WOUDC database between the 1960s and 2000s. Blue dots represent sites used for validation in Liu et al. (2013) of a derived global ozone product, involving a domain-filling trajectory approach. Taken from Figure 1a in Liu et al. (2013).

have been normalised with respect to ground-based total ozone measurements (SPARC, 1998). Although such normalisation (correction) may help improve accuracy, experimental evidence indicates that this should not be implemented in the case of ECC sondes for tropospheric ozone profile measurements. Despite this, such procedure can be effective in filtering out dubious profiles, with the caveat however that such screening does not eliminate the possibility of erroneous profile cases (WMO, 1998).

Uncertainties are, however, much larger in the troposphere due to lower ozone VMRs, yielding a relatively low signal-to-noise ratio, which increases the susceptibility to both instrumental errors and instrumental variability. Sonde performance can additionally be affected by other air pollutants, which can further enhance measurement uncertainty. Systematic differences in ozone concentration measurements between different instruments in the troposphere were estimated to be between 10 and 15 % in various inter-comparison campaigns between 1970 and 1990 (Beekman et al., 1994; Smit et al., 1998). There is evidence that the ECC sondes have greater precision and consistency than either the BM or KC sondes (e.g. WMO-III and JOSIE campaigns), i.e. a precision of ±5-10 % for ECC compared with a range of ± 10-20 % for BM and KC. A small positive bias of 3 % is noted for ECC with no evidence of biases exceeding ± 5 % for BM and KC (Smit and Straeter, 2004a, b). Whilst ozonesondes are thus considered to provide near-truth information on the vertical distribution of ozone at fixed locations, and are therefore suited for validation of model and satellite observations, it should be noted that they may not provide a reliable indicator of the accuracy of a model or satellite product in depicting spatial distributions of ozone over large-scale regions, or indeed globally (Miles et al., 2015). This caveat can however be mitigated by carefully sampling model datasets to achieve collocation with observations in both space and time.

3.2 UV-Nadir Satellite Datasets

3.2.1 Theoretical Basis

The first satellite observations of ozone, from the NIMBUS-4 Backscatter Ultraviolet (BUV) Atmospheric Ozone Experiment (Heath et al., 1973; Bhartia, 2009), used measurements of solar backscattered radiation at a discrete set of UV wavelengths. Ozone information is retrieved from UV reflectances, obtained through division of the earth radiance by the incoming solar irradiance at the same set of wavelengths measured by the same instrument, as stated in equation 3.1 below:

$$R = \pi I/(\mu_\sigma E) \tag{3.1}$$

Where *R* is the reflectance, *I* is the earth radiance, μ_σ is the cosine of the solar zenith angle and *E* is the solar irradiance (W m^{-2}). Retrieval algorithms applied to modern instruments with contiguous rather than discrete spectral coverage start by obtaining this reflectance spectrum (Levelt et al., 2006), as depicted in Figure 3.3. Ozone absorption at the peak of the Hartley band (~254 nm) restricts backscattered photons to the upper stratosphere and mesosphere. As ozone absorption decreases monotonically with increasing wavelength, photons can be scattered back to the instrument from progressively lower altitudes and in the Huggins bands (325-350 nm), which is characterised by low absorption of ozone, a significant proportion of solar photons are reflected at the surface and re-emerge at the top of the atmosphere (TOA). Exploiting this wavelength-dependence enabled height resolved distributions and total columns of ozone to be retrieved (Heath et al., 1973; Bhartia, 2009).

Modern instruments afford contiguous spectral coverage at comparatively high resolution (~0.5 nm), extending through the visible and near-IR. The strong Fraunhofer absorption lines (~390 nm) in the solar spectrum, where irradiances (and Earth radiances) are extremely low, are usually excluded when fitting the reflectance spectrum. Rotational Raman scattering, which entails inelastic scattering (wavelength changes), however has the effect of widening all absorption lines through the atmosphere, including the Fraunhofer lines, such that retrievals should account for small spectral features that are retained in the reflectance spectrum. This is known as the Ring Effect (Grainger and Ring, 1962; Vountas et al., 1998), which leads to infilling of the Fraunhofer lines (wavelengths at which the sun is a blackbody) as species such as nitrogen (N_2) and oxygen (O_2) absorb

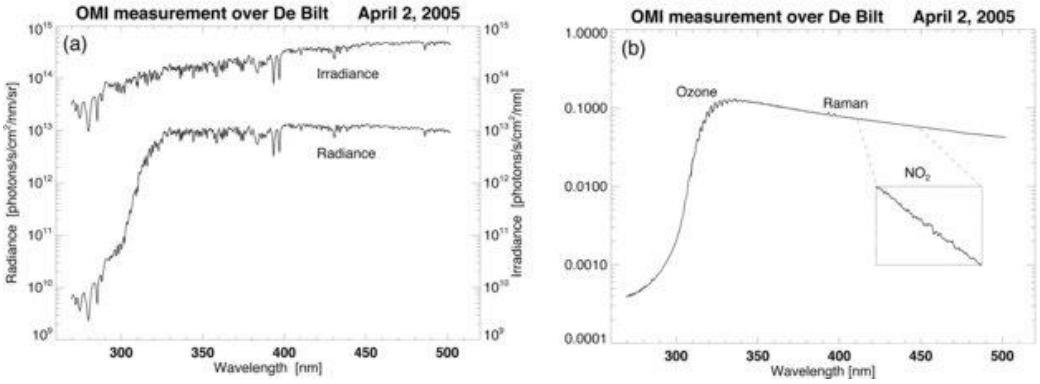

Figure 3.3 – An example of (**a**) the irradiance and radiance spectra for OMI on a cloudless day over the Netherlands and (**b**) the resultant ratio spectrum, which clearly shows the absorption peaks of ozone spanning the Hartley and Huggins bands (270-330 nm. Raman lines from the Calcium Fraunhofer lines are evident as a double peak around 390 nm, with very small absorption features corresponding to NO_2 between 410 and 450 nm also visible (inset). Adapted from Figure 7 in Levelt et al. (2006).

and re-emit light at slightly different wavelengths. Also required in retrieving ozone vertical information is the transmittance of the atmosphere, which is dependent upon the solar radiation incident on the atmosphere. UV-nadir instruments typically contain a solar viewing port, located on the flight-direction side of the instrument, to measure this quantity (Munro et al., 2016). For the retrieval of ozone, stratospheric profile information can be retrieved from the Hartley band region (254-310 nm), whereas temperature-dependent spectral structure in the region between 320 and 345 nm (the Huggins band) contains information to extend retrieval of ozone downwards into the troposphere, although a high precision fit (< 0.1 % RMS) is required to extract this information (Miles et al., 2015). Whilst the presence of other trace gases can pose slight interference when retrieving height-resolved information on atmospheric ozone, the limiting effects of atmospheric radiative transfer are largely governed by other factors such as radiometric calibration, which are also affected by different instrumental variables.

Retrieval of height-resolved information from nadir-viewing satellites is an example of an ill-posed problem (i.e. there is no mathematically unique solution), which Optimal Estimation (OE) algorithms seek to address by combining measurement information with a priori information (Rodgers, 1976) (e.g. GOME-2A, Miles et al. 2015), in order to provide the high accuracy of such measurements, as verified through validation with ozonesondes. In the case of the OMI instrument, both an operational OMO3PR algorithm developed by KNMI (Kroon et al., 2011), with a vertical resolution of 6-7 km, and a NASA developed scientific algorithm (Liu et al., 2010) have been used, which differ in terms of the radiometric calibration, radiative transfer models, vertical grids and a priori covariance matrices implemented in each algorithm (Mielonen et al., 2015). Measurements errors can arise from a number of different sources and vertical sensitivity is also variable, thus it is important that profiles are characterised on a pixel-by-pixel basis (Miles et al., 2015). Although both instruments have relatively high sensitivity to the troposphere, sensitivity is much weaker near the surface due to the limited penetration of photons and subsequent reduced signal in the backscattered radiance spectrum (Sellitto et al., 2011). Factors such as surface albedo and aerosols in the PBL can also result in additional interference (Liu et al., 2010). In particular, large disparities between UV-nadir sounders and ozonesondes often become apparent for the lower troposphere during high ozone events, whilst consistency is generally maintained in the mid-troposphere (Wang et al., 2012).

The Rutherford Appleton Laboratory (RAL), based in Didcot, UK, have also developed an independent ozone profile OE retrieval scheme, that is specifically tailored to the inference of tropospheric ozone (Miles et al., 2015). This retrieval scheme is further different from both the KNMI and NASA retrieval schemes; the latter of which use ozonesonde information to tightly constrain the tropospheric profile, inhibiting any deviation of this part of the retrieval, thus greatly limiting any new information the retrieval can provide in this region. The RAL scheme is a refinement of earlier work which first demonstrated the method by which tropospheric ozone can be observed from space (Munro et al., 1998). Vertical profiles of ozone are retrieved using a three-step sequential approach: (1) a Band 1 (B1) retrieval that extracts information from the long-wave tail region of the Hartley Band (~266-307 nm) window to derive the stratospheric profile; (2) a measurement of the effective surface albedo, using wavelengths that are less sensitive to atmospheric ozone (~336 nm), that corresponds to each pixel used in the next retrieval step; (3) a Band 2 (B2) retrieval from the Hartley band region (~323-335 nm) window which is used to extend the retrieval down into the UTLS and troposphere region. In this final step, the B1 retrieval in (1), associated error covariance matrix and the effective surface albedo retrieved in (2) are used as prior information. The logarithm of the ozone (VMR) on a fixed pressure grid (surface pressure, 450, 170, 100, 50, 30, 20, 10, 5, 3, 2, 1, 0.5, 0.3, 0.17, 0.1, 0.05, 0.03, 0.017, 0.01 hPa) provides the basis for the retrieved profiles (Miles et al., 2015). This approach has consistently shown to yield a relatively high degree of sensitivity to the troposphere region, as quantified through persistence in a high number of degrees of freedom for signal (DFS) (Miles et al., 2015). This strength led to the RAL retrieval algorithm being selected as the provider for the ESA Climate Change Initiative (CCI), following an independent comparison with the GOME-2 operational ozone profile scheme (Keppens et al., 2014). Additional information regarding the RAL ozone retrieval scheme is later included in Chapter 4.1.

3.2.2 Global Ozone Monitoring Experiment-2A (GOME-2A)

The Global Ozone Monitoring Experiment-2A (GOME-2A) instrument (pictured in Figure 3.3) is a nadir-viewing UV-VIS spectrometer, launched aboard the European Space Agency's (ESA's) Metop satellites, that measures the daytime earth reflectance for ground pixels of 40 x 80 km across a swath of ~2200 km (Foret et al., 2014). The Metop satellites operate from an altitude of approximately 820 km in a sun-synchronous orbit, as part of the EUMETSAT Polar System, with an equatorial crossing time of 09:30 local time (LT) in the descending node (Munro et al., 2016). GOME-2A provides contiguous spectral

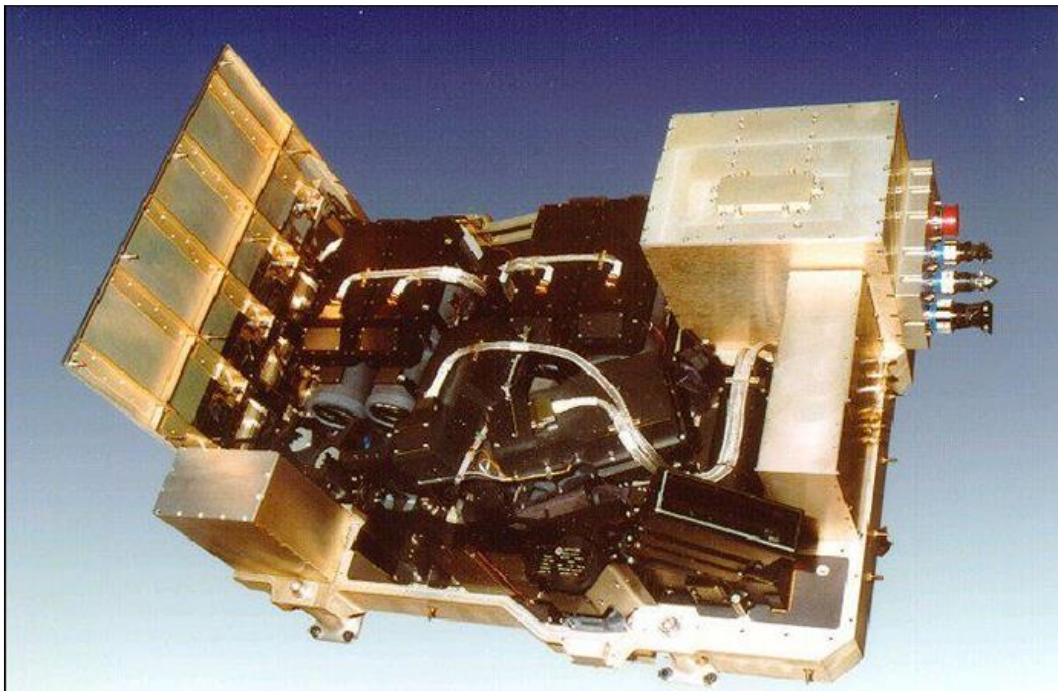

Figure 3.3 – Image of the GOME-2 instrument on board ESA's Metop satellites. Taken from Figure 1 in Munro et al. (2016).

sampling of 0.11-0.22 nm at a spectral resolution of 0.24-0.53 nm, across four bands spanning the 240-790 nm interval (Callies et al., 2000), after convolution by the instrument response function (Foret et al., 2014). Across-track scanning at nadir, along with sideways viewing for full polar coverage and instrument characterisation measurements using the moon, is all made possible through the use of the scan mirror which feeds the optical spectrometer (Callies et al., 2000). The polarisation state of the incoming light is measured in real-time by onboard devices, which is necessary for calibrating the intensity of light for this instrument, which is polarisation-sensitive. Although measurement of polarisation is performed at lower spectral resolution, sub-pixel cloud cover can be determined through observation at higher spatial resolution (Munro et al., 2016). As explained previously in section 3.2.1, the ozone retrieval exploits two microwindows (the Hartley and Huggins bands) in the UV (~270-336 nm) to obtain an estimate of the vertical profile. In addition to vertical profile and total column information on atmospheric ozone, the recorded spectra from GOME-2A also provides accurate knowledge of the total column amount of nitrogen dioxide (NO_2), sulphur dioxide (SO_2), water vapour (H_2O), oxygen (O_2), bromine oxide (BrO), together with other trace gases, aerosols and cloud optical properties (Munro et al., 2016).

Close agreement between GOME-2A ozone (retrieved by the RAL scheme) and the TOMCAT chemistry transport model (CTM) has been demonstrated for lower

tropospheric ozone, with a correlation of 0.66 and a model bias of just 0.7 DU for cloud-free monthly mean GOME-2A pixels (Miles et al., 2015). Furthermore, geographical features such as the regional summertime ozone maximum over the Mediterranean are accurately captured (Richards et al., 2013), as well as aspects such as the shape of the seasonal cycle. This was particularly found to be the case across the US and eastern China, in which a double peak was captured by both the model and the retrieval (not apparent in the a priori estimate) in the GOME-2A validation study by Miles et al. (2015). Despite this, validation with respect to ozonesondes after applying satellite AKs, necessary to account for the limited vertical sensitivity associated with the satellite retrieval (see later section 3.5.1 for specifics), revealed an overall retrieval bias for lower tropospheric ozone of around 1.5 DU (6 %). This bias has been determined to be strongly latitude dependent, ranging from an underestimation of ~1-3 DU (15-20 %) in the Southern Hemisphere to an overestimation of ~2 DU (10 %) in the Northern Hemisphere (Miles et al., 2015).

3.2.3 Ozone Monitoring Instrument (OMI)

The Ozone Monitoring Instrument (OMI) is a Dutch-Finnish UV-visible nadir-viewing solar backscatter spectrometer aboard the NASA-Aura satellite launched in July 2004. The satellite has a retrograde, sun-synchronous polar orbit (inclination of 98.2°) at an altitude of 705 km, providing some 14 orbits a day with a local equatorial crossing time in the ascending node of 13:45 local time (Levelt et al., 2006). The viewing geometry is illustrated in Figure 3.4. OMI operates in the 270–500 nm spectral range and has a spectral resolution of 0.42–0.63 nm (Foret et al., 2014). OMI is the first of a generation of instruments which use 2-D detector arrays, providing concurrent sampling at all across-track positions, as opposed to platforms which use a 1-D detector array to scan across track. OMI supplements the observational knowledge of ozone from other longstanding satellite platforms, such as NASA's SBUV/TOMS instrument and ESA's GOME class of instruments, at a much enhanced spatial resolution (e.g. 13 km × 24 km for OMI compared with 40 km × 320 km for GOME in the along-track and across track directions nominally at nadir). The across track resolution, however, becomes significantly coarser away from nadir; reaching 13 km × 150 km towards the edge of the swath (corresponding to an angle of 57° from nadir). The swath is 2600 km wide at the surface resulting from a wide field of view of 114°, with a near-global coverage time of 1 day (Levelt et al., 2006; Foret et al., 2014).

Individual profile measurements (Level-2; L2), and globally gridded (Level-3; L3) data from

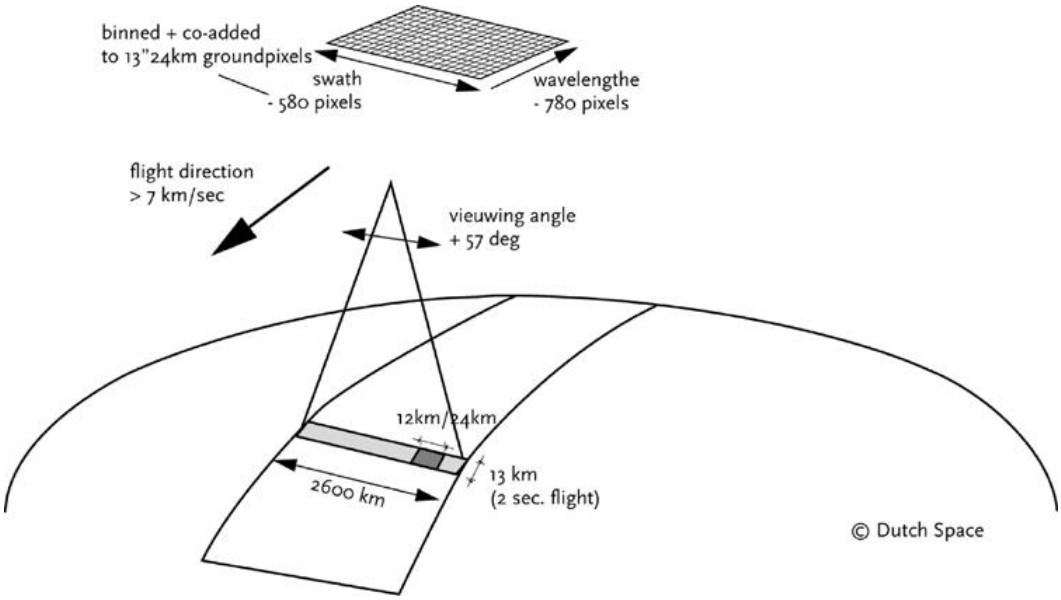

Figure 3.4 – The retrieval principle for the ozone monitoring instrument (OMI) as shown in Figure 4 of Levelt et al. (2006).

OMI is here used; in particular surface-450 hPa (~0-5.5 km) retrieved subcolumn ozone, as derived using the RAL height-resolved OE profiling scheme (Miles et al., 2015; Gaudel et al., 2018). For scientific evaluations in Chapter 5, the version of OMI data used is first averaged onto a monthly-mean 2.5° × 2.5° (~275 km) grid (L3 data) between 2005 and 2010. This resolution is more comparable with the resolution of the CCM simulations used in this study for model comparisons (see section 3.4). As for the GOME-2A sensor, systematic biases with respect to independent observations can be attributed to inaccuracies in the radiative transfer modelling, which are partially rectified through the use of a priori information to shift the erroneous retrieved profiles towards the true values (Mielonen et al., 2015). An additional monthly-mean, (linearly interpolated) latitude-dependent bias, identified with respect to the global ozonesonde ensemble, was also corrected for in the OMI data for evaluations in Chapter 5. Other filtering criteria used to enhance the quality of the dataset include omission of observations with a cloud fraction greater than 0.2 and a solar zenith angle exceeding 80°. This estimation differs from other techniques such as cloud slicing (e.g. Ziemke and Chandra, 2012) and residual methods such as total-column ozone (TCO) from OMI minus vertical profile measurements from the MLS (e.g. Ziemke et al., 2011). In comparison with the OMI-MLS method, the OMI-RAL profiling scheme is more (less) sensitive to the lower (upper) troposphere (Gaudel et al., 2018).

OMI is regarded as a very stable instrument, with the radiometric degradation during the instrument's lifetime estimated to have been just ~2 % in the UV and ~0.5 % in the visible

channel, which is significantly lower than other comparable instruments (Levelt et al., 2018). Despite this, the quality of radiance data began to decline from 2007 onwards (but particularly starting from 2009) across all wavelengths in a progressively larger number of across-track views, corresponding to rows in the 2-D detector arrays, suspected to be blocked by insulation blankets covering the instruments which have become damaged. This one main anomaly is subsequently referred to as the row anomaly (Schenkeveld et al., 2017).

3.2.4 Limitations

The primary limitation of UV-nadir sounders for observation of tropospheric ozone is the requirement to first retrieve the stratospheric profile above with very high accuracy. However, such viewing geometry imposes a significant constraint over the vertical resolution of measurement profiles. By contrast, limb-viewing instruments such as the Microwave Limb Sounder (MLS), can elucidate vertically resolved structure of abundances in ozone and other chemical constituents in the stratosphere, but are unable to probe much below the tropopause due to the rapid increase in pressure broadening (due to water vapour and clouds) (Olsen et al., 2016). A schematic of these two main viewing geometries is illustrated in Figure 3.5 for visual reference. Other inherent issues to retrieving lower tropospheric ozone information from space by UV sounding are Rayleigh scattering and photometric precision. This often precludes detailed observation of local-scale features such as pollution plumes, except on occasion for isolated urban centres and when aggregating over longer (e.g. monthly) timescales (Kar et al., 2010).

A suite of thermal infrared (TIR) sensors, including the Tropospheric Emission Spectrometer (TES) (Worden et al., 2007) and the Infrared Atmospheric Sounding Interferometer (IASI) (Clerbaux et al., 2009), can also offer vertical information on ozone in the troposphere. For IR-nadir sounders, sensitivity is relatively higher in the mid- to upper-troposphere but much weaker in the lower troposphere compared with UV-nadir

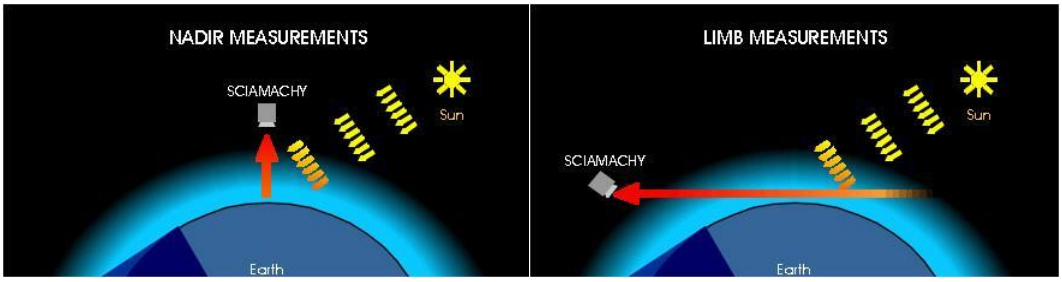

Figure 3.5 – Schematic of nadir versus limb viewing geometries for the SCIAMACHY instrument. Figure adapted from IUP Bremen at https://www.iup.uni-bremen.de/sciamachy/instrument/modes/.

sounders, except where substantial thermal contrast between the air and the ground arises (B. Kerridge, personal communication). Instruments such as IASI, also aboard the Metop satellites, have the added benefit of providing considerably enhanced sampling density across its swath with respect to GOME-2A. Not only can IASI provide information at finer spatial resolution therefore (e.g. 12 x 25 km pixels for IASI at nadir), but enhanced thermal contrast associated with photochemical pollution plumes can also increase measurement sensitivity near the surface. Despite this, lower tropospheric sounding of ozone by IR-nadir sensors has its own inherent challenges concerning surface spectral emissivity, surface temperature, temperature profile, dust and spectroscopy. It has subsequently been demonstrated therefore that combining information from both UV and TIR sensors has the potential to further enhance retrieval accuracy from the troposphere region, through mitigation of individual sensor and retrieval scheme limitations. Such a multispectral synergistic approach has already been adopted in recent studies. For instance, Cuesta et al. (2013) found that a multispectral retrieval using both IASI (TIR) and GOME-2A (UV) adequately captured ozone plumes below 3 km altitude, as validated using the CHIMERE regional CTM. Overall very good agreement of IASI + GOME-2A retrievals was also noted with respect to ozonesondes (mean biases < 1 % and variability within ± 10 %). Increased sensitivity and improved consistency was also yielded in a study by Fu et al. (2013) for measurement of ozone from the surface to the UTLS region, which used a combined TES (TIR) and OMI (UV) approach. Further improvements in the detection of near-surface ozone may additionally be possible through exploitation of information available within the Chappuis band within the visible (VIS) spectrum (Chance et al., 1997), which has been confirmed experimentally using a neural network approach entailing satellite observation (Sellitto et al., 2012). Thus, a multispectral retrieval approach that combines information from each of these three bands (UV, VIS and TIR), may further enhance signal-to-noise ratio throughout the troposphere.

3.3 Copernicus Atmospheric Monitoring Service (CAMS) Chemical Reanalysis

The Copernicus Atmospheric Monitoring Service (CAMS) is the latest European-based global atmospheric composition reanalysis dataset (alongside the US-based Modern-Era Retrospective Analysis for Research and Applications version 2; MERRA-2), spanning the period 2003-2018 to date, which now supersedes the earlier Monitoring Atmospheric Composition and Climate (MACC) and CAMS-interim (CAMSira) reanalyses (Inness et al., 2019). A reanalysis product objectively combines observations and numerical modelling to comprehensively simulate weather, climate or composition-related variables, based on

a synthesised estimate of the state of the Earth's atmosphere. The development and insights gained from the earlier datasets enables the CAMS dataset to more accurately simulate the evolution of multiple chemical species within the atmosphere, at enhanced horizontal (~80 km), vertical (60 levels), and temporal resolution (3-hourly forecast fields and hourly surface forecast fields). Simulated meteorological fields are taken from the ECMWF Reanalysis 5th Generation (ERA-5). Smaller biases and greater temporal consistency are found in the simulated fields of ozone (O_3), carbon monoxide (CO), nitrogen dioxide (NO_2) and aerosol optical depth (AOD), with respect to both MACC and CAMS-interim reanalyses, using the latest, updated cycle of the 4D-var assimilation cycle of the ECMWF Integrated Forecasting System (IFS) framework which ingests satellite observations from multiple sources (Inness et al., 2019), as shown in the timeline provided in Figure 3.6. However, the evolution in tropospheric ozone simulated by CAMS is subject to weaker observational constraints due to the indirect assimilation of this information, which entails derivation from subtraction of the stratospheric column from the total column amount of ozone. This is achieved for instance by differencing total column information from OMI with respect to MLS observations; the latter of which does not provide information much below the tropopause due to the instrument observation geometry, to infer tropospheric column ozone as a residual. Given the importance of NO_2 for tropospheric ozone photochemistry, which is also more weakly constrained compared with stratospheric ozone and CO, this further reduces the constraint on tropospheric ozone (Wang et al., 2020), which is additionally exacerbated by the short lifetime of tropospheric NO_2 (Inness et al., 2015).

The representation and performance of the CAMS reanalysis is routinely validated with respect to a range of observations from satellites (which includes both limb and nadir sounders as shown in Figure 3.6), ground-based remote sensing, in situ measurements, ozonesondes and commercial aircraft measurements by the CAMS validation team, orchestrated by KNMI through the CAMS-84 contract (Eskes et al., 2015; 2018; Christophe et al., 2019). In the stratosphere, CAMS estimates of ozone are closely correlated with these assimilated observations globally, with the exception of the ozone hole period over Antarctica when a systematic overestimation is found (on the order of 25 % on average with respect to ozonesondes for instance). Despite weaker observational constraints for ozone in the troposphere, biases in free tropospheric ozone (which are taken as the region between 200 hPa and 750 hPa in the tropics or 350-750 hPa elsewhere), with respect to both MOZAIC-IAGOS, Global Atmospheric Watch (GAW) programme and ozonesonde

measurements, have been determined to be close to zero (mean bias within ±10 %) in mid-latitudes and the Arctic throughout the year (Eskes et al., 2018; Christophe et al., 2019). A mean positive bias of ~10-20 % is however found in the tropics, which contrasts with an approximately proportional negative bias at high latitudes. Despite such overall good agreement, a seasonal dependence in the free tropospheric ozone bias (negative in winter and positive in summer) developed after a change in assimilated SBUV-2 data was implemented in 2013 (Christophe et al., 2019). The temporal evolution of the biases in CAMS free tropospheric ozone for four different regions is shown in Figure 3.7, as quantified from ozonesonde measurements, shows the mean biases resolved for different regions (the Arctic, northern mid-latitudes, the tropics and Antarctica) between 2003 and 2019. Whilst CAMS evidently represents ozone well in the Arctic free troposphere, the representation is noticeably poorer over Antarctica, with significant interannual variability in the magnitude and sign of the bias beyond 2013.

In the upper troposphere (100-200 hPa in the tropics or 300-350 hPa elsewhere), a systematic positive bias has been observed, perhaps related to the assimilation procedure of satellite observations, but improved agreement with observations has been detected over (Northern) Europe compared with the MACC reanalysis during winter-spring (Eskes et al., 2018). Verification of the performance of CAMS near the surface is more difficult to ascertain, due to higher spatial heterogeneity owing to spatial variations in ozone sources and sinks, but In-service Aircraft for a Global Observing System (IAGOS) observations

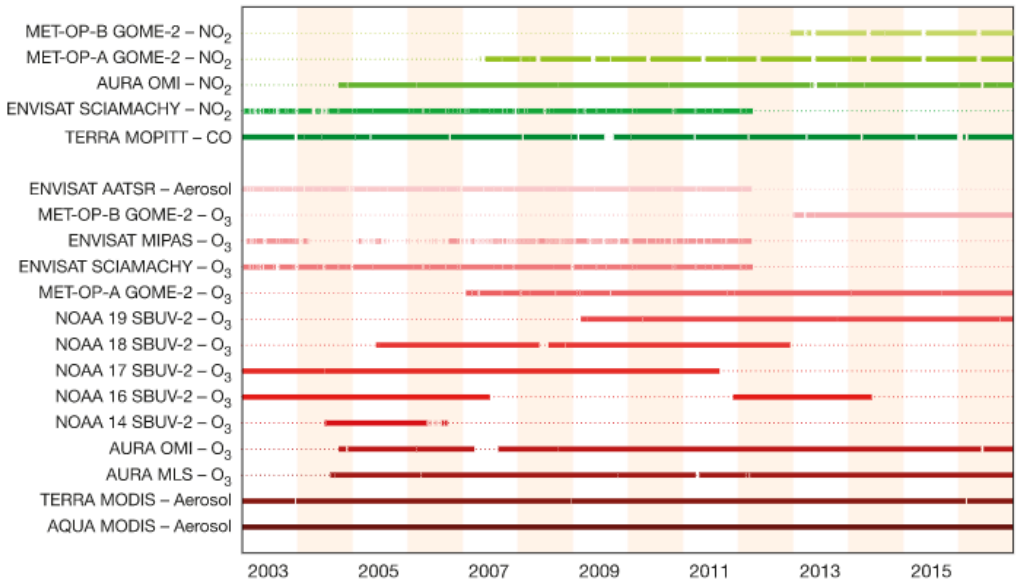

Figure 3.6 – Timeline of the different assimilated data sources used in CAMS over the period 2003-2016. Taken from Inness et al. (2019) - https://ecmwf.net/en/newsletter/158/meteorology/new-cams-global-reanalysis-atmospheric-composition.

indicate that the reanalysis realistically represents surface and boundary layer ozone. Despite this, biases in CAMS ozone against GAW site measurements vary considerably from location to location (time correlations ranging from 0.3 to 0.9) (Eskes et al., 2018). Across Northern and Central Europe at least, there is however evidence for a significant improvement in the representation of surface ozone compared with the earlier MACC reanalysis, according to European Monitoring and Evaluation Programme (EMEP) and AirBase European Background observations, particularly between July and September. A notable negative bias however remains across the high latitudes over Europe during winter-spring (Christophe et al., 2019).

In validating the performance of the CAMS reanalysis, measurements from multiple airborne field campaigns (INTEX-A, INTEX-B, NEASQS-ITCT, ITOP, AMMA, ARCTAS, VOCALS, YAK-AEROSIB, HIPPO and KORUS-AQ) have also been used as a source of independent observational data. It has been found that CAMS adequately reproduces the observed concentrations and distributions of these chemical species, with biases in O_3 and CO of < 20 % (Wang et al., 2020). The biases are lowest in the lower troposphere and are generally greater in the middle, and particularly upper, troposphere. A systematic overestimation is observed (although widely less than 15 %), which is largest in regions such as the tropics and the Arctic (~30 %) as well as in the free troposphere (as high as 50 % over the Pacific Ocean basin). Comparisons of the vertical profiles of CAMS estimated tropospheric ozone with ARCTAS campaign measurements for the Arctic region, including the use of a control version of CAMS with no assimilated observations, clearly indicates that the observational constraint imposed forces the reanalysis towards the true state; an underestimation in ozone above ~1km altitude (but particularly above 6 km) in the control

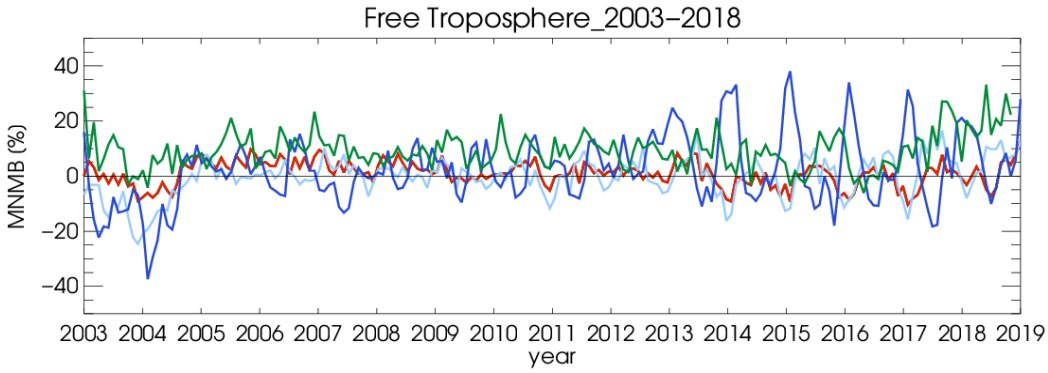

Figure 3.7 – Ozonesonde validation of the CAMS reanalysis (2003-2019) in the free troposphere for Antarctica (dark blue), the Arctic (light blue), northern mid-latitudes (red) and the tropics (green), as quantified using the ozone modified normalised mean bias (MNMB). The free troposphere is defined here as the altitude range 750-350 hPa, except in the tropics where 750-200 hPa is used. Adapted from Figure S.3 in Christophe et al. (2019).

case (~20 %) is largely removed in the operational reanalysis. Despite this, an overestimation near the surface (concentrations of approximately double that from aircraft data) remains, due to the likely negligence of halogen chemical loss from Bromine chemistry on snow during Arctic spring. On a global scale, ozone biases in CAMS are substantially more uniform than in the control case and an overall slight improvement in the calculated ozone fields is achieved through data assimilation, as quantified from squared correlation coefficient (R^2) values (increase from 0.89 to 0.93) (Wang et al., 2020). It is obvious that aircraft campaign data, in contrast to long-term operational monitoring, has the benefit of providing new insights when evaluating such datasets. The intensive nature of data collection over small spatial areas is better tailored to answering specific science questions surrounding process-orientated mechanisms. The concentrations of chemical species not operationally monitored may also be measured in such airborne campaigns, further supporting assessments of model performance, in particular the representation of complex chemical and physical processes (Emmons et al., 2000).

3.4 Chemistry-Climate Model (CCM) Simulations

General circulation models (GCMs) that include interactive chemistry, enabling the study of the chemistry and dynamics of the stratosphere and troposphere, are known as chemistry-climate models (CCMs). They constitute important tools in understanding past and predicting future changes in the chemical composition of the stratosphere-troposphere system, through their comprehensive representation of dynamical, chemical and radiative processes (Eyring et al., 2006). Whilst the inclusion of interactive chemistry is still computationally expensive, and thus neglected in many climate simulations (Taylor et al., 2012; Kravitz et al., 2013), it is a necessary addition in understanding and quantifying coupled feedbacks between dynamics and chemistry. The importance of interactive chemistry for climate modelling more generally is however becoming increasingly recognised,) with some participating models in CMIP6 now accommodating for this (e.g. Collins et al., 2017). Compared with CCMs, chemical transport models (CTMs), which are another main tool used to study atmospheric chemistry (which can but generally do not assimilate chemical species), but cannot be used to investigate feedbacks between chemistry and dynamics. CTMs are instead tailored for evaluation of chemical drivers, particularly in the troposphere, as they are driven by assimilated meteorological fields. This acts as a strong dynamical constraint which is either not imposed or imposed more weakly in CCMs, through nudging (Newtonian relaxation) to specify dynamics, thus constituting the main difference between these two model classes. Since ozone exerts a

primary control over the radiative properties of the stratosphere, the inclusion of the radiative-dynamical feedback in CCMs makes them invaluable tools for depicting chemistry-climate coupling (World Meteorological Organization/United Nations Environment Programme (WMO/UNEP), 2003).

Where CCM hindcast simulations are nudged towards meteorological reanalyses (e.g. ERA-Interim), they are referred to as specified-dynamics simulations, with those unconstrained known as free-running simulations. Whilst specified-dynamics simulations enable the role of large-scale circulation changes, in understanding recent changes and interannual variability in chemical constituents, to be effectively elucidated, they may be less dynamically consistent due to disparities in the method of implementation of the nudging (Orbe et al., 2020). With respect to free-running simulations, internal model dynamical biases and differences in variability between models and reanalyses, and in turn their impacts on chemical composition, can be evaluated (Morgenstern et al., 2017). A framework of the different components within a CCM is shown in Figure 3.8, which includes inputs (e.g. emission sources and climate drivers), the four main interactive schemes (chemistry, transport, dynamics and radiation), outputs (e.g. trends and model diagnostics), together with model output validation which may ultimately feedback into future model developments.

Hindcast specified-dynamics reference simulations (RefC1SD) (Plummer et al., 2014) conducted for phase 1 the Chemistry Climate Model Initiative (CCMI-1) (Hegglin and Lamarque, 2015; Morgenstern et al., 2017) are here used, of both ozone (O_3) and stratosphere-tagged tracer ozone (O_3S) for the period 1980-2010 inclusive from two state-of-the-art CCMs: EMAC (Jöckel et al., 2016) and CMAM (Scinocca et al., 2008). These two models were primarily selected due to the close similarity in the O_3S tracer definition (detailed in section 3.4.3), which is either absent or defined differently in other CCMI models. This diagnostic is fundamental to the quantification of the stratospheric influence and attribution to recent changes in tropospheric ozone undertaken in Chapter 5. O_3S decays according to the same reactions used in the O_3 simulations, although the reactions leading to photochemical production of ozone are omitted for the O_3S tracers (Roelofs and Lelieveld, 1997). In each simulation, the prognostic variables: temperature, vorticity and divergence as well as (the logarithm of) surface pressure for ECHAM only (the coupled general circulation model in EMAC) from the ERA-Interim reanalysis dataset have been used to nudge each CCM towards the observed atmospheric state through Newtonian relaxation, with corresponding relaxation times of 24, 6, 48 and 24 h respectively for

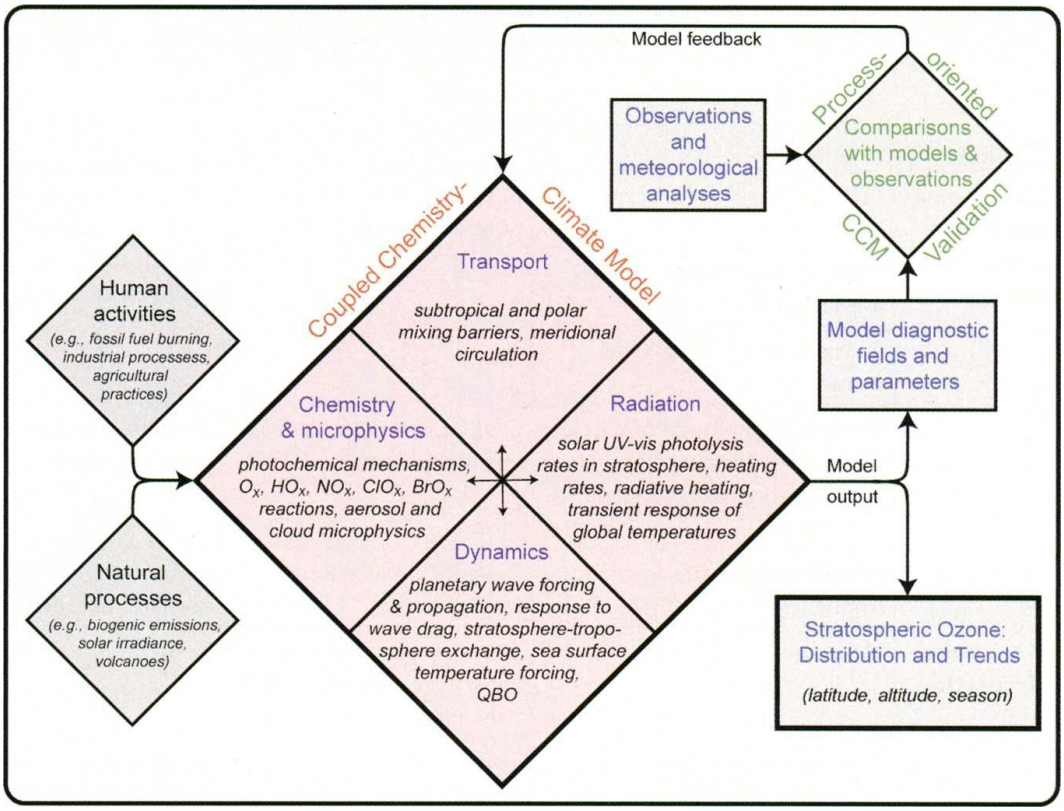

Figure 3.8 – A framework for validating CCMs (as incorporated in the CCMVal evaluation approach). Included within a CCM are four primary process categories (transport, chemistry & microphysics, dynamics and radiation) which are fundamentally interdependent and interactive. Inputs required include knowledge of human activities and natural processes, which are essential in quantitatively defining atmospheric processes and expectations for future changes. Model outputs associated with the four different process categories, include an array of parameters and diagnostics. A special case highlighted separately is the distribution and trends in stratospheric ozone, because of the recent interest in halogen-based ozone depletion and subsequent recovery in recent decades. Critical to process-oriented CCM validation, is the comparison of model diagnostics and other outputs with meteorological analyses and other atmospheric observations. The results of this work provide essential feedback on the representation of these processes in CCMs, thus elucidating priorities for future model development. Adapted from Figure 3 in Eyring et al. (2005).

EMAC (Jöckel et al., 2016) and 24 h for all three variables in CMAM (McLandress et al., 2013). Variability in sea surface temperatures (SSTs) and sea ice concentration is directly prescribed in both EMAC and CMAM from ERA-interim and HadISST (provided by the UK Met Office Hadley Centre) respectively (Rayner et al., 2003; Morgenstern et al., 2017).

Furthermore, each model includes either prescribed decadal emissions or lower boundary conditions of anthropogenic and natural greenhouse gas (GHG) and ozone precursor emissions (which act as a forcing) from the MACCity inventory, which is based on the Coupled Model Intercomparison Phase 5 (CMIP5) inventory and representative concentration pathway (RCP) projections (Lamarque et al., 2010), alongside variability

induced by other natural forcings such as solar activity and volcanic eruptions in most simulations (Brinkop et al., 2016). All simulations used are compliant with the CCMI experimental designs specified by the International Global Atmospheric Chemistry (IGAC) and Stratosphere-troposphere Processes And their Role in Climate (SPARC) communities (Eyring et al., 2013). The stratospheric influx for CCMI models ranges from ~400 to 650 Tg yr^{-1}, which is within the range estimated from observational studies (IPCC, 2013). For full details of the model chemistry treatments and emission inventories used, the reader is directed to the CCMI review paper by Morgenstern et al. (2017) as well as Jöckel et al. (2016) for EMAC and section 2 of Pendlebury et al. (2015) for CMAM. The main difference between the two models is the complexity of the tropospheric chemistry scheme, namely that CMAM simulates no non-methane hydrocarbon chemistry, with additional differences in the model transport schemes, the treatment of heterogeneous chemistry, and accounting for NO_x and isoprene emissions and representation of the Quasi-Biennial Oscillation (QBO). A brief overview of the two models and these differences is provided below (section 3.4.1 and 3.4.2).

3.4.1 EMAC

The European Centre for Medium-Range Weather Forecasts – Hamburg (ECHAM)/Modular Earth Submodel System (MESSy) Atmospheric Chemistry (EMAC) model is an interactively coupled state-of-the-art CCM (Jöckel et al., 2016). RC1SD-base-10 simulation results (without nudging of the global mean temperature) are used, which have a T42 triangular spectral resolution, equating to a quadratic Gaussian grid of ~2.8° by 2.8° and 90 vertical hybrid sigma pressure levels up to 0.01 hPa (Jöckel et al., 2016). EMAC uses the flux-form semi-Lagrangian (FFSL) transport scheme for chemical constituents, water vapour, cloud liquid water and cloud ice (Lin and Rood, 1996), with the chemistry submodels MECCA (Sander et al., 2011) and SCAV (Tost et al., 2006) describing the kinetic systems in the gaseous and aqueous or ice phase respectively. Comprehensive atmospheric reaction mechanisms that include basic O_3, CH_4, HO_x and NO_x chemistry, non-methane hydrocarbon (NMHC) chemistry up to C_4 and isoprene, halogen (Cl and Br) chemistry, and sulfur chemistry is all included in the chemical scheme. Relevant for the representation of heterogeneous chemistry in the stratosphere, deviations from thermodynamic equilibrium are accounted for, which has implications for the distribution of polar stratospheric clouds (PSCs) and associated ozone depletion. In the troposphere, an offline representation of aerosol (dust, sea salt, organic carbon, black carbon, sulfates and nitrates) provides surfaces for heterogeneous chemistry. Emissions of lightning NO_x,

soil NO_x and isoprene (C_5H_8) are parameterised online for EMAC using the submodel ONEMIS (Kerkweg et al., 2006; Jöckel et al., 2016). The model provides a consistent handling of the photolysis (submodel JVAL; Sander et al., 2014) and shortwave radiation schemes (submodel FUBRAD; Kunze et al., 2014), including variability associated with the 11-year solar cycle (Morgenstern et al., 2017). The QBO is internally generated by the model, although zonal winds near the Equator are nudged towards a zonal wind field (Brinkop et al., 2016) with a 58-day relaxation timescale to ensure realistic simulation of the QBO magnitude and phasing (Jöckel et al., 2016).

For the RC1SD-base-10 specified dynamics simulations evaluated in this thesis, spanning the period 1980-2013, the key elements of the global, annually averaged tropospheric ozone budget is calculated to be:

- Total column ozone: 312 DU
- Tropospheric column ozone: 36 DU
- Tropospheric ozone production: 5269Tg yr^{-1}
- Tropospheric ozone destruction: 4637 Tg yr^{-1}
- Ozone deposition : 867 Tg yr^{-1}

The production and loss terms were calculated from the centred time derivative of the accumulated ozone production (PRODO3) and ozone loss (LOSSO3) tracers (from the 10-hourly output). By then diagnosing the actual tropopause, it was therefore possible to compute the production and loss rate (kg s^{-1}) at every 10-hour model timestep. Averaging this quantity between January 1980 and December 2013, the above estimates could then be derived.

3.4.2 CMAM

The Canadian Middle Atmosphere Model (CMAM) is a CCM based on an upwardly-extended version of the Canadian Centre for Climate Modelling and Analysis (CCCma) third-generation atmospheric GCM (Beagley et al., 1997; Scinocca et al., 2008). Simulations from the atmosphere-only version of the model are used here with a T47 spectral resolution (equivalent to ~3.75° by 3.75°) on the linear Gaussian grid used for the physical parameterisations in CMAM, with 71 vertical hybrid sigma pressure levels which extend to 0.01 hPa (Hegglin et al., 2014; Pendlebury et al., 2015). The model uses spectral advection of “hybrid” moisture for transport (Merryfield et al., 2003) and a similar spectral advection of “hybridized” tracers for chemically active tracers exhibiting strong horizontal

gradients (Scinocca et al., 2008). Whilst a representation of heterogeneous chemistry on PSCs is provided, the model does not account for nitric acid trihydrate (NAT) or polar stratospheric cloud (PSC) sedimentation (resulting in denitrification). Heterogeneous chemistry calculations are also made in the troposphere through prescribing sulfate aerosol surface area densities. Chemistry is calculated throughout the troposphere, although the only hydrocarbon considered is methane. To account for isoprene (C_5H_8) oxidation in CMAM, an additional 250 Tg-CO yr^{-1} in emissions (including an additional 160 Tg-CO yr^{-1} from soils) is included, distributed as Guenther et al. (1995) isoprene emissions. Unlike EMAC, soil NO_x emissions are not calculated online for CMAM and are instead prescribed, with lightning NO_x emissions parameterised from the Allen and Pickering (2002) updraft mass flux scheme (Morgenstern et al., 2017). In contrast to EMAC, consistency in the radiation and photolysis schemes has not specifically been imposed. Although CMAM does not generate a QBO internally, a representation of the QBO is induced in the specified-dynamics simulations through nudging to ERA-Interim.

The annually averaged tropospheric ozone budget in CMAM is given below:

- Total column ozone: 289 DU
- Tropospheric column ozone: 32 DU
- Tropospheric ozone production: 6008 Tg yr^{-1}
- Tropospheric ozone destruction: 5746 Tg yr^{-1}
- Ozone deposition : 777 Tg yr^{-1}

Based on the residual to close the tropospheric ozone budget, an estimate for the STE of ozone in the CMAM model can be derived. From the diagnosed quantities above, this estimate is approximately 515 Tg yr^{-1}. The photochemical production and destruction was calculated in-line by the model, integrated up to the WMO thermal tropopause (2K km^{-1} definition; WMO, 1957), from a timeslice run in year 2000 conditions (D. Plummer, personal communication, 2021).

3.4.3 Stratospheric-tagged ozone (O_3S) tracers

For each model, an additional stratospheric-tagged ozone tracer (O_3S) simulation is made available for use as a diagnostic. For tracing stratospheric ozone, the O_3S tracer is reset to the standard ozone tracer above the tropopause. To delineate this, the World Meteorological Organization (WMO) thermal definition is used in EMAC equatorward of 30°N/S and the 3.5 potential vorticity unit (PVU) dynamical tropopause definition

threshold is implemented poleward of 30°N/S, as defined in every model time step. By comparison, the O_3S tracer in CMAM uses the WMO thermal tropopause definition as the threshold for tagging ozone as stratospheric across all latitudes, with an additional criterion that the tropopause must be < 0.7 in hybrid-sigma coordinates to prevent erroneous identification at high latitudes, during winter especially. In EMAC, the O_3S tracer is nudged by Newtonian relaxation in the stratosphere, with the model timestep length the determinant of the relaxation time, ensuring that ozone is conserved within the stratosphere. The O_3S tracer can be transported across the tropopause, where it becomes subject to the tropospheric ozone sink reactions. The corresponding chemical loss of O_3S (LO_3S) is diagnosed and integrated and, in addition to its dry-deposition, provides a direct measure for the STE of ozone (Jöckel et al., 2006, 2016). Subsequently, dLO_3S/dt (the time derivative) directly corresponds to the ozone influx by STE into the troposphere. The O_3S loss reaction mechanisms used in EMAC are given in Roelofs and Lelieveld (1997) (see equations R5 to R9). A similar but subtly different treatment is used in CMAM. At every time step, the O_3S tracer is set equal to the model ozone above the tropopause, while below the tropopause the O_3S tracer has an imposed first-order loss rate equal to the model calculated first-order chemical loss rate of O_x defined as:

$$O_x = O_3 + O(^1D) + O(^3P) + NO_2 + HNO_4 + 2NO_3 + 3N_2O_5 \quad (3.3)$$

The O_3S tracer also undergoes dry deposition at the surface with the same dry-deposition velocity as calculated for ozone. However, the definition of the photochemical production and loss terms, to yield the tropospheric ozone budget estimates shown in section 3.4.2, is not identical for the O_3S tracer. Whilst both are based on broad definitions of O_x, they differ in terms of the assumptions made to treat some of the loss processes. Nevertheless, a comparison of the two definitions has been performed for each simulation (O_3 and O_3S individually), revealing very similar estimates in each case. Thus, it is reasonable to assume that the two simulations are comparable in this regard (D. Plummer, personal communication, 2021).

The overall lifetime of stratospheric ozone in the troposphere (O_3S) is largely governed by transport between the extratropical tropopause (the primary source region of stratospheric influx) and the subtropical lower troposphere, where the ozone photochemical loss rate is largest due to high insolation and humidity levels (Kentarchos and Roelofs, 2003). Tropospheric amounts of O_3S increase during wintertime as photochemical activity is quiescent in the presence of low solar insolation, and thus, the

chemical destruction of ozone is outweighed by the influx of O_3S. The opposite occurs during spring and summer as O_3S influx reduces and the efficiency of photodissociation increases, which leads to a minimum in O_3S abundance in the troposphere in late summer. The regional to seasonal variation in O_3S lifetime is difficult to ascertain and quantify within CCMs such as EMAC and CMAM due to complexity of the model specifications. Studies involving simpler climate models such as in Kentarchos and Roelofs (2003), which uses the ECHAM4 climate model, however arise at a mean lifetime of O_3S in the troposphere broadly ranging between ~1.5 to 2 months in the wintertime Northern Hemisphere to less than a month during summer. Although the O_3S tracer definition used in their study was defined similarly to that used in either of the EMAC or CMAM CCMs, it should be noted that their estimates might be inflated by the relatively coarse model vertical resolution, combined with an overly diffusive semi-Lagrangian transport scheme. Both factors may lead to an overestimation of the efficiency to which stratospheric ozone is transported down into the troposphere (Meloen et al., 2003; Cristofanelli et al., 2003).

3.4.4 Limitations

Whilst both CCMs are inferred to reasonably well simulate the mean residual circulation and downward STE, in terms of the multi-mean spread (see SPARC CCMVal 2010, chapter 10; Butchart et al., 2011), the coarse resolution (typically several hundreds of kilometres) does hinder the adequate spatiotemporal representation of the corresponding distribution and flux of STE across the tropopause (Lamarque et al., 1999). The timing, strength and location of synoptic-scale mixing processes is fundamental to such accurate representation, which are largely associated with tropopause folds (Danielsen, 1968; Shapiro, 1980) and cut off lows (Price and Vaughan, 1993; Wirth, 1995). Furthermore, small-scale stratospheric intrusions are typically not resolved by such coarse resolution CCMs (Lin et al., 2012) and remain highly challenging to simulate (e.g. Elbern et al., 1998; Roelofs et al., 2003; Trickl et al., 2010; 2014). Realistic simulations of low-level increases in ozone associated with stratospheric intrusions have however been demonstrated for global CCM simulations at high resolution (~50 km) but these remain computationally expensive to run (Lin et al., 2012). Whilst regional air quality models may supplement our understanding of the impact of stratospheric intrusions on background lower tropospheric ozone levels and surface air quality, offering high-resolution over limited domains of interest, the chemical and dynamical environment from which stratospheric intrusions develop may not be represented, as such features are linked with the development of large-scale synoptic patterns (Ott et al., 2016). The ability of CCMs to

accurately simulate distributions of ozone and other chemical tracers may be limited by disparities between models and observations, particularly in multi-model comparisons where disagreement may be large between models (Eyring et al., 2006). This is because the level of agreement between models and measurements is an important metric in evaluating the success to which models can represent the relevant radiative, chemical and dynamical processes which influence the regional and seasonal characteristics of trace gases in the atmosphere. Multi-model validation efforts have been undertaken in the stratosphere (e.g. Butchart et al., 2011), extratropical UTLS (e.g. Hegglin et al., 2010), the tropics (e.g. Gettelman et al., 2010) and in terms of representation of dynamical parameters (e.g. Butchart et al., 2010).

For simulation of heterogenous ozone chemistry, temperature biases are also an important limitation as chemical reaction rates may be highly temperature dependent. An obvious example is the catalytic destruction of stratospheric ozone due to CFCs, that is accentuated through the presence of PSCs when temperatures fall below ~-85°C (Austin et al., 2003). An inherent issue in the lower Southern Hemisphere stratosphere, common to many CCMs, is a "cold-pole" bias, particularly during winter and spring. Efforts to address this problem have included developments in gravity wave parameterisations (e.g. Garcia et al., 2017), which were first shown in McLandress et al. (2010) to be under-represented in the Southern Hemisphere. This leads to a delayed breakdown of the wintertime SPV by approximately 2-3 weeks (Eyring et al., 2006; SPARC CCMVal 2010, chapter 4). This has the effect of prolonging conditions that are conducive to stratosphere ozone loss, whilst also leading to a postponement of mixing in of ozone-rich air masses from lower latitudes.

Deficiencies in model transport are another important factor that can preclude accurate simulation of non-well mixed trace gases, including ozone. This not only applies to the species of interest, but also other chemical constituents that are rudimentary to their chemical budgets (e.g. NO_x, VOCs and CH_4 as examples of tropospheric ozone precursors or Cl concentrations as a stratospheric ozone destruction precursor) (Eyring et al., 2006). In terms of the large-scale stratospheric BDC, in which accurate representation is required in correctly modelling the observed distributions of different trace gas species, it is clear from model inter-comparisons that gaps in our understanding of the competing mechanisms that drive the circulation remain. For instance, indicated changes in the BDC from observations over recent years have not been predicted from models, which supports this argument (e.g. Butchart, 2014; Mahieu et al., 2014). Accurate

representation of the BDC in models is inherently difficult as the circulation cannot be observed directly and is complicated by the existence of two distinct branches (Plumb, 2002; Birner and Bönisch; 2011), which have different effects on the resultant stratospheric trace gas distributions (as discussed previously in section 2.2), thus contributing to a wide spread in inter-model biases of various stratospheric chemical constituents.

In hindcast CCM simulations, nudging (or Newtonian relaxation) of the large-scale temperature and dynamical fields towards the observed state of the atmosphere, as estimated from reanalyses, can help to overcome model transport deficiencies (McLandress et al., 2014; Shepherd et al., 2014). For free-running (observationally unconstrained) simulations, direct model-measurement comparisons of chemical species are not possible, due to the chaotic evolution of the atmosphere on a day-to-day basis, and thus nudged (specified-dynamics) simulations serve to circumvent this issue through by removing the influence of model internal variability (Kolonjari et al., 2017). Instead previous multi-model validation studies of free-running simulations have focussed on evaluation of climatological fields (typically multi-year monthly means) (e.g. Hegglin et al., 2010; Gettelman et al., 2010; Butchart et al., 2010; 2011), which are also important for disentanglement of chemistry and dynamics. Despite this, dynamics at smaller sub-scales than the nudged reanalysis, together with implemented physical parameterisations that may exhibit similar sub-scale behaviour, still remain unconstrained and can even imprint onto the large-scale dynamical fields (Pendlebury et al., 2015). On a more local scale, transport errors arise due to erroneously high numerical diffusion, which is an inherent unavoidable issue as models operate on a discrete grid. Subsequently, specially designed transport schemes are employed in models to minimise numerical diffusion, although in some cases the imposition of explicit diffusion may be necessary to ensure stability of model simulations (Morgenstern et al., 2017). This issue disproportionately impacts the simulation of fine-scale structures and processes such as tropopause folds and mixing associated with planetary-scale waves related to cross-tropopause transport, at even the highest model resolutions (Pendlebury et al., 2015).

3.5 Model-measurement comparison methods

3.5.1 Satellite Averaging Kernels (AKs)

For model and ozonesonde profile comparisons to be made on a like-for-like basis against observations from UV-nadir sounders, it is necessary to account for the smoothing of

information that inherently occurs in the satellite measurements in the vertical plane. This occurs due to both the satellite observation geometry and the sub-optimal information content of the retrieval (ill-posed problem). In the case of the lower tropospheric subcolumn (surface-450 hPa), for GOME-2A and OMI measurements retrieved using the RAL OE scheme, vertical sensitivity does extend into the overlying, ozone-rich stratosphere. This is illustrated using monthly-mean layer OMI AKs for a typical extratropical profile in Figure 3.9 (red line). Although AKs are first derived for each

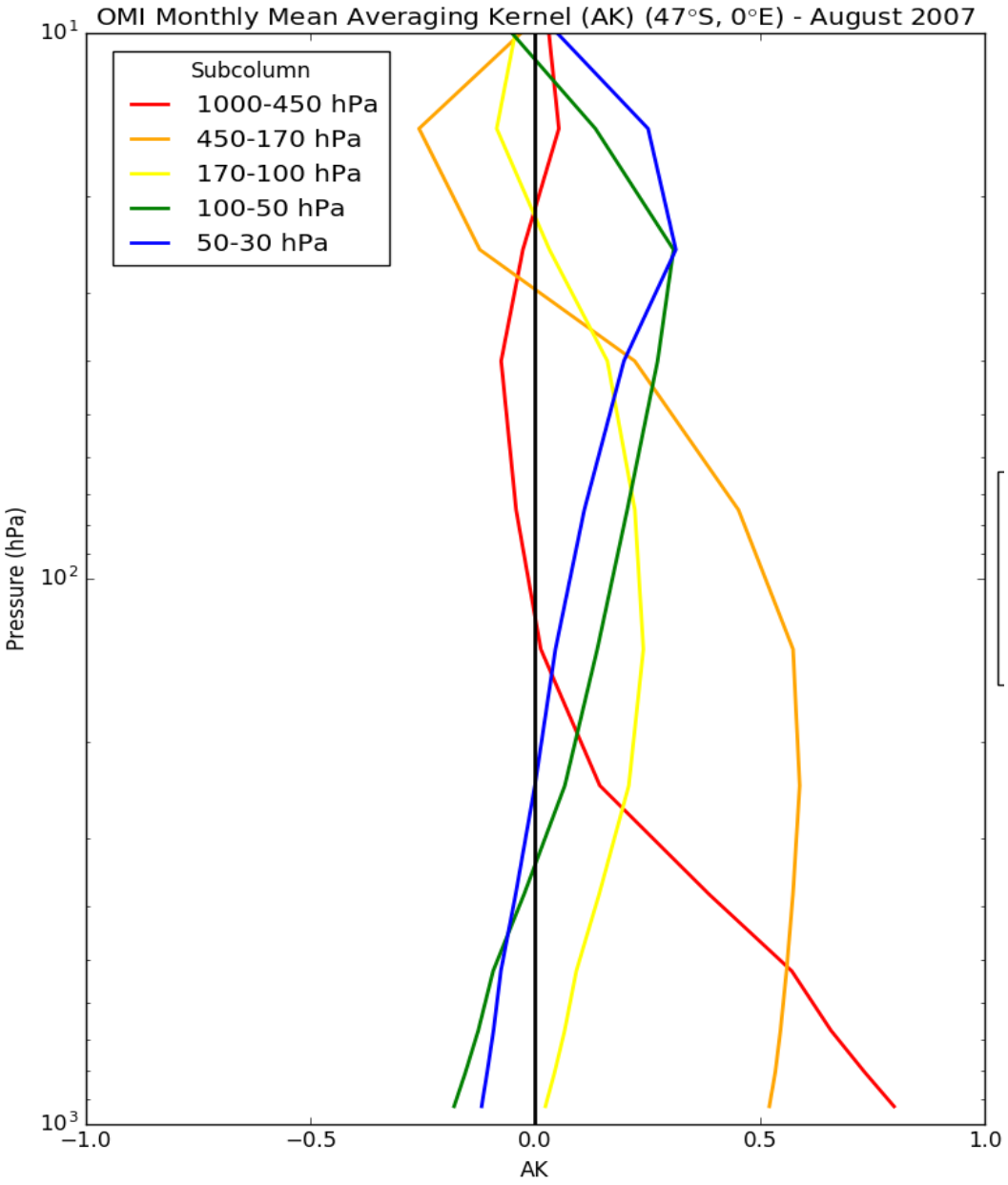

Figure 3.9 – Example of monthly-mean OMI averaging kernels (AKs) used to convolve model and ozonesonde subcolumn profiles to ensure a like-for-like comparison with OMI. The red line (AK for the surface-450 hPa subcolumn) for instance, shows sensitivity to influence from primarily the 450-100 hPa region. Application of this AK leads to a systematic increase in surface-450 hPa subcolumn ozone in mid- to high-latitudes due to contamination with higher ozone above the tropopause (which is typically within this pressure range).

Volume Mixing Ratio (VMR) to Dobson Units (DU) Unit Conversion

Direct model comparisons of tropospheric ozone were undertaken against the subcolumn measurements from OMI, between 1000 and 450 hPa (0-5.5 km), since the amount of height resolved information is much more limited from the satellite measurements. Both CCM simulations store ozone volume mixing ratio (VMR) data on a hybrid-sigma pressure grid, necessitating a conversion to the subcolumn integrated amount (DU). This was calculated for every model grid cell for each monthly timestep using the equation below (Ronald, 1999):

$$\mathrm{COLUMN} = 10 \cdot \frac{RT_0}{g_0 p_0} \cdot \sum_{i=1}^{N-1} 0.5\left(VMR(i) + VMR\,(i+1)\right)(p_i - p_{i+1}) \qquad (3.3)$$

Where g_0 is the rate of gravitational acceleration at mean sea level (9.8 m s^{-2}), T_0 the standard temperature (273.15 K), p_0 the standard pressure (1013.25 hPa) and $R = \frac{kN_A}{M_A}$ the specific gas constant for air (287.3 J kg^{-1} K^{-1}). k denotes the Boltzmann's constant (1.38 x 10^{-23} J K^{-1} $molecule^{-1}$), N_A the Avogadro Number (6.022 x 10^{23}) and M_A the mean mass of air (28.94 x 10^{-3} kg). For outstanding notations, p is the pressure in hPa, VMR is given in ppmv and resultant column is in DU. For model analyses of ozone VMR on fixed pressure levels, the model fields were transformed onto a regular pressure grid using a model specific equation stored in the file metadata. The same vertical pressure levels (n = 63) from a similar CMAM simulation (but on a fixed pressure grid) were selected as a reference for these transformations.

individual profile, and are sensitive to the tropopause height, clouds, the vertical profile in temperature, ozone and other chemical constituents, they may be averaged over to reflect the retrieval vertical sensitivity in a broader sense (smoothing out any small-scale, transient structure). Nonetheless, the RAL scheme is advantageous in that stratospheric contamination of tropospheric ozone retrievals is reduced compared with other retrieval schemes, as sensitivity is maximised in the lower troposphere. The broadness of the 450-170 hPa layer (orange line in Figure 3.9) furthermore depicts the inherent difficulty of the retrieval in resolving the sharp gradient in ozone that occurs near the tropopause (which typically resides within this layer). A retrieval's vertical sensitivity is represented by its AK, as briefly introduced earlier in section 3.2.2. The mathematical derivation and formulation of AKs is detailed in Rodgers (2000). If not accounted for in comparisons with models (or correlative ozonesonde) data, biases are likely to result; particularly so in the case of tropospheric ozone due to the much larger ozone concentrations in the stratosphere. It is therefore necessary to apply the profile retrieval layer AKs, in order to assess the agreement between satellite and model or ozonesonde datasets on a like-for-like basis.

The AK is a matrix of weighting information which should be multiplied against the comparison dataset. This effectively modifies each profile to account for cross-layer contamination. To obtain the equivalent retrieved model subcolumns, an additional a priori contribution needs to be added:

$$MOD\_AK\_HR_j = APR_{ij} + AK_{RT\,ij} \times MOD\_HR_j \quad (3.2)$$

Where *MOD_AK_HR* is the model or ozonesonde equivalent data (fitted with AKs) to be directly compared with the satellite retrieved profile, *APR* the a priori contribution to be added to the matrix product term, *AK_RT* the AK of the retrieved subcolumn with respect to the true subcolumn and *MOD_HR* the model or ozonesonde profile at higher vertical resolution without AKs fitted. The *i* denotes that the application of satellite AKs, and addition of the a priori term, for each subcolumn *j* is applied as a function of all AK resolved levels throughout the vertical profile. Although the RAL ozone scheme is retrieved on 19 fixed retrieval (pressure) levels (j = 19), the AKs used to convolve with models are provided with a few additional levels in the troposphere to capture the tropospheric structure better (i = 23). An example of the resultant modification to the vertically integrated subcolumn amounts (DU) for CAMS, used here as the comparison dataset to which the OMI AKs are applied, is also shown in Figure 3.10 for another extratropical case. The effect of applying the AKs is an enhancement in lower troposphere

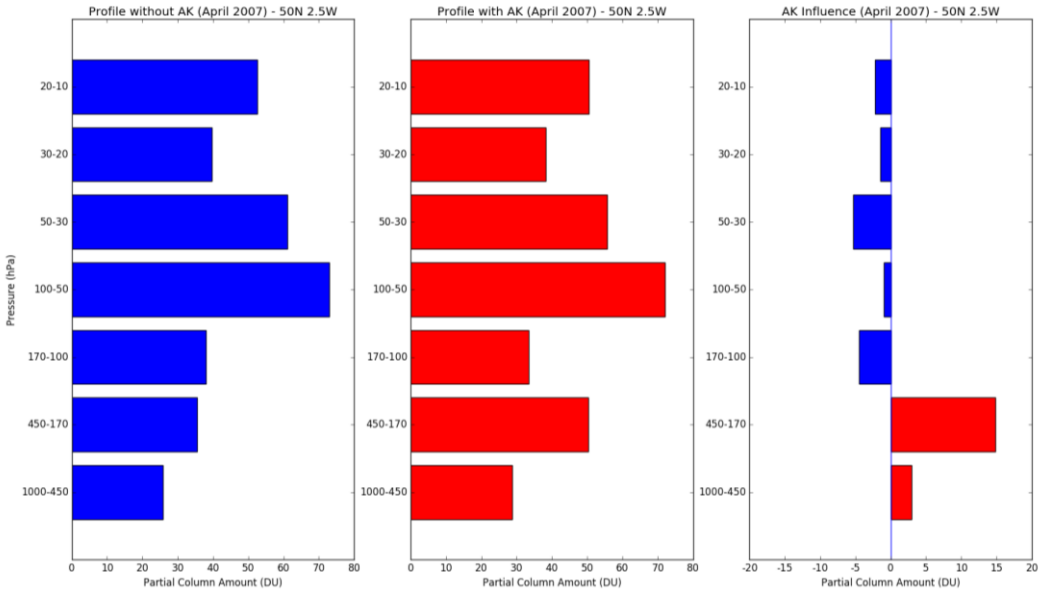

Figure 3.10 – An example of the change in CAMS ozone (DU), integrated for equivalent subcolumns to that retrieved by OMI, after applying the satellite AKs. Imposing the constraint of limited vertical resolution to the model profile, results in vertical smearing of information. This leads to a reduction of stratospheric ozone layer amounts and an enhancement in 450-100 hPa and surface-450 hPa subcolumn ozone amounts.

(surface-450 hPa) and UTLS (450-170 hPa) ozone, which contrasts with smaller reductions to the several, overlying stratospheric layer ozone amounts.

3.5.2 AK Sensitivity: Tropospheric Ozone

As explained previously in section 3.5.1, the standard procedure for comparing vertically well-resolved model or ozonesonde profiles with satellite-derived tropospheric ozone subcolumn amounts from UV-nadir satellite instruments, is to first convert to the corresponding integrated measure (typically from VMRs or MMRs to DU) over the retrieved layer. Satellite AKs, which account for vertical transfer of information that inherently occurs across layers (as governed by the atmospheric radiative transfer), must then be subsequently applied to the comparison dataset to ensure a direct comparison. For the OMI and GOME-2A lower tropospheric subcolumn (surface-450 hPa) measurements, it is important to note that the AKs are sensitive to the distribution of overlying stratospheric ozone. This can be appreciated from examination of the corresponding AK (see Figure 3.9), as a height-resolved indicator of retrieval sensitivity, which shows a pronounced tail above the tropopause region (~250-300 hPa) that is characteristic of the extratropical regions. Additionally, a priori information (derived from climatology) must be accounted for in the case of ozone profile retrievals from UV-nadir sounders, as the measurement is ill-posed by nature. In conjunction with the RAL optimal estimation (OE) scheme, this constraint is also applied to the comparison dataset when making like-for-like comparisons. The RAL retrieval scheme uses standard OE algebra to solve this non-linear problem as detailed in Rodgers (2000) and Miles et al. (2015). Briefly, this entails combining information from both measurement and prior information, as quantified from the corresponding error covariance matrix for each, to derive an estimate of the state vector.

In the case of models however, inherent biases in lower stratospheric ozone may exist due to relatively large differences in the simulated strength and dominance of the two branches of the BDC, together with inaccuracies in cross-tropopause mixing (e.g. numerical diffusion) and, in the case of CCMs, the interactive model chemistry schemes used. These limitations and others were discussed in detail in section 3.4.5. Through the induced smearing of vertically-resolved model ozone information, when AKs are applied for model-measurement comparisons of tropospheric ozone, such biases may complicate assessment of the level of agreement that exists. In certain cases, caution may be advocated when applying the satellite AKs for this application, particularly where a large

bias in stratospheric ozone is known to be present in the comparison model used and/or the representation of tropospheric ozone in the model is known to be particularly good.

To investigate this issue further, a series of idealised experiments were conducted using the CAMS reanalysis dataset for the period 2005-2016; resolved as a function of latitude intervals (10°) and month of the year. In these experiments, the amount of UTLS (450-100 hPa) ozone was perturbed systematically by different increments. Additionally for each perturbation increment applied, a series of eight different sub-experiments were performed (Table 3.1), in which the artificially imposed bias was applied to different pressure (altitude) ranges within the UTLS region (450-100 hPa). This experimental design was intended to elucidate the altitudinal sensitivity to an imposed bias, in terms of the contaminating effect on the troposphere when satellite AKs are applied. Although the ozone abundance increases sharply with altitude in this region (tropopause transition region), the surface-450 hPa AK is more sensitive with increasing pressure (decreasing altitude) as shown earlier in Figure 3.9, and thus anticipating the altitude sensitivity as a function of latitude and month is not straightforward.

Evaluation of the two CCMs used in this project (EMAC and CMAM) with respect to OMI observations, in later section 5.1, led to the realisation of a potential methodological issue with this generally established method of comparison, when later diagnosing large biases in lower stratospheric ozone with respect to ozonesonde measurements. A summary of the quantitative results from this idealised evaluation is presented here, that would be of strong interest to the CCM community, when undertaking model-measurement analyses of tropospheric ozone. Such assessment would enable users to better understand the complicating influence a potential UTLS ozone bias may have, through modulation of the AK influence, on the model simulated tropospheric ozone columns to be compared

Experiment	450-310 hPa	310-170 hPa	170-100 hPa
CTRL			
L	**x**		
M		x	
U			**x**
LM	**x**	**x**	
MU		**x**	**x**
LU	**x**		**x**
LMU	**x**	**x**	**x**

Table 3.1 – The series of experiments applied for each ozone perturbation value, selected in quantifying the OMI and GOME-2A AK sensitivity for the tropospheric subcolumn (surface-450 hPa) derived from the CAMS reanalysis dataset (2005-2016). Black crosses denote the pressure ranges above this layer, in which an artificial bias is implemented for each experiment.

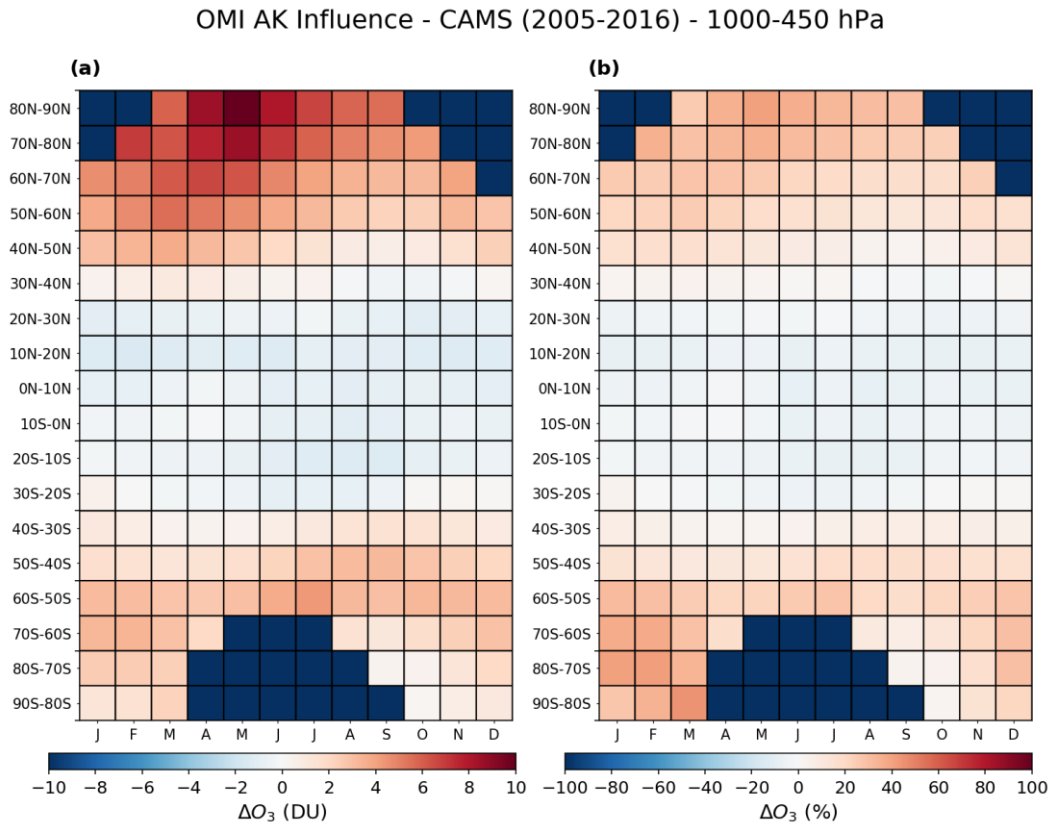

Figure 3.11 – (**a**) Absolute (DU) and (**b**) relative (%) change in CAMS vertically integrated) surface-450 hPa layer ozone after applying OMI AKs, resolved on a latitude band (10°) versus month basis over a common baseline period (2005-2016). It represents the CAMS x AK – CAMS difference.

directly with satellite measurements. This in turn would enhance interpretations of the level of tropospheric ozone model-measurement agreement.

The CAMS reanalysis dataset (2005-2016) is selected for this analysis as it constitutes an observationally constrained model. Although not free from bias, as input observations may be pre-processed prior to assimilation to ensure consistency with the model or may be affected by discontinuities (see section 3.3), this dataset is driven by assimilated satellite observations in a mathematically optimal way. The default modification to the CAMS surface-450 hPa subcolumn amount (CAMS x AK – CAMS), due to the influence of the OMI AKs, is shown in Figure 3.11 in both absolute (DU) and relative (%) terms for the control (CTRL) or unperturbed experiment on a latitude band (10° intervals) versus month basis. Application of AKs is seen to increase the surface-450 hPa layer amount ubiquitously across the extratropics throughout the year, largest in absolute terms across the Northern Hemisphere high-latitudes during late spring (up to ~10 DU which equates to 40-50 % of the initial tropospheric subcolumn amount), and during austral summer in the Southern Hemisphere polar region in relative terms (~50-60 % but equating only to 2-4 DU due to the lower ozone abundances here). This contrasts with decreases to the initial

surface-450 hPa subcolumn amount across the tropics (30°S-30°N), on the order of ~2-3 DU or 10-20 %, with evidence for a seasonal migration of this region towards the summer hemisphere.

Ozone perturbations of between -50 and +50 % were subsequently then applied for each series of sub-experiments (n = 8, shown in Table 3.1) at 5 % intervals, to quantify the change in this modification due to the AKs as a function of imposed biases in the abundance of UTLS (450-100 hPa layer) ozone. It is later shown in Chapter 5 (Figure 5.4) that seasonally varying model biases (at least in EMAC and CMAM) in UTLS ozone of up to and over ±50 % can occur over mid-latitude regions, as verified against ozonesondes. A sample of these results is included in Figure 3.12 and Figure 3.13 for the LMU experiment. The absolute difference (DU) in the AK influence for a -50 %, -25 %, +25 % and a +50 % perturbation applied, versus the unperturbed (control) case shown in Figure 3.11a, is shown in Figure 3.12 as a function of latitude interval (10°) and month of the year. The resultant impact on the AK influence for these different experiments is then shown for comparison in Figure 3.13.

A reduction in the UTLS (450-100 hPa) layer ozone for the LMU experiment is shown to have the largest impact on the AK-induced vertical smearing into the surface-450 hPa layer over the Northern Hemisphere high latitudes in boreal springtime (MAM), as shown in Figure 3.12a-b. For the -50% perturbation (Figure 3.12a), the resultant impact to the AK influence (as quantitatively shown in Figure 3.11) is between -6 and -8 DU in such case. Increased sensitivity to the AK can also be discerned over the Southern Hemisphere mid-latitudes for this perturbation case (Figure 3.12a; largest during austral spring where the change in the AK influence is up to -5 DU during late austral winter (JAS). Note that the reduction in the AK influence is muted over both the tropics and Southern Hemisphere high latitudes, where the AK influence was already found to be much smaller in the unperturbed (control) case (Figure 3.11), and could thus have been expected.

This modification to the AK influence manifests as a sharp contraction of the region affected by an increase in surface-450 hPa layer ozone, which spanned much of the extratropics in the unperturbed case (Figure 3.12), to include largely only high latitudes for the 50 % UTLS (450-100 hPa) ozone reduction case (Figure 3.13a). On the contrary, the area characterised by a decrease in the surface-450 hPa layer amount due to the AK, which was confined largely to the tropics in the control (unperturbed) case, has expanded

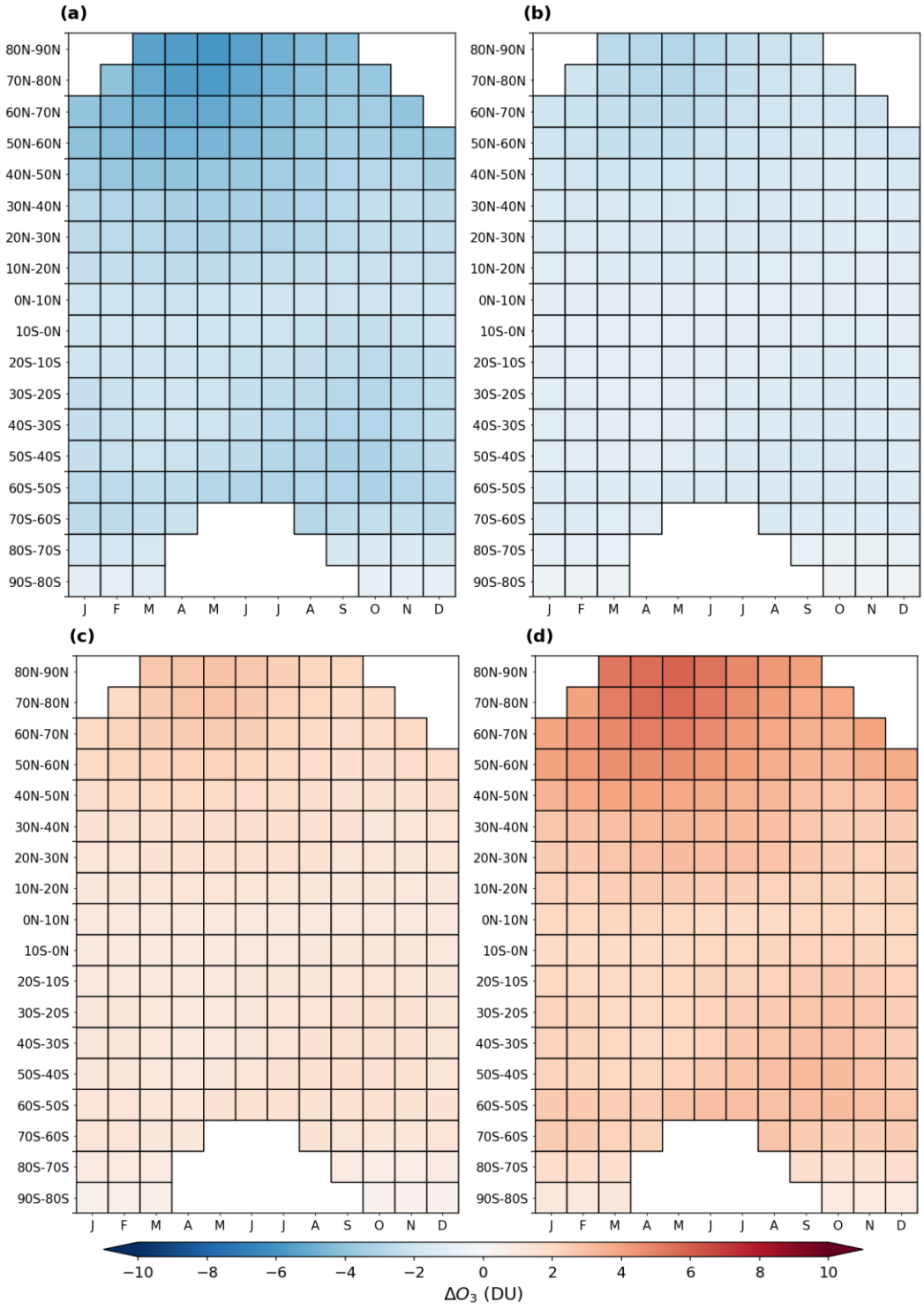

Figure 3.12 – The difference in the absolute (DU) change in CAMS surface-450 hPa layer ozone after applying OMI AKs, relative to that shown in Figure 3.11a for the unperturbed (control) case, for (**a**) a -50 %, (**b**) a -25 %, (**c**) a +25 % and (**d**) a +50 % perturbation in UTLS ozone (experiment LMU: 450-100 hPa).

across into mid-latitudes and intensified in magnitude (~-4 to -6 DU for the -50 % perturbation experiment over the tropics compared, with less than -2 DU in the control case). It is worth noting also that the austral springtime Antarctic ozone hole means that the AK influence changes readily changes sign as the UTLS ozone amount is reduced

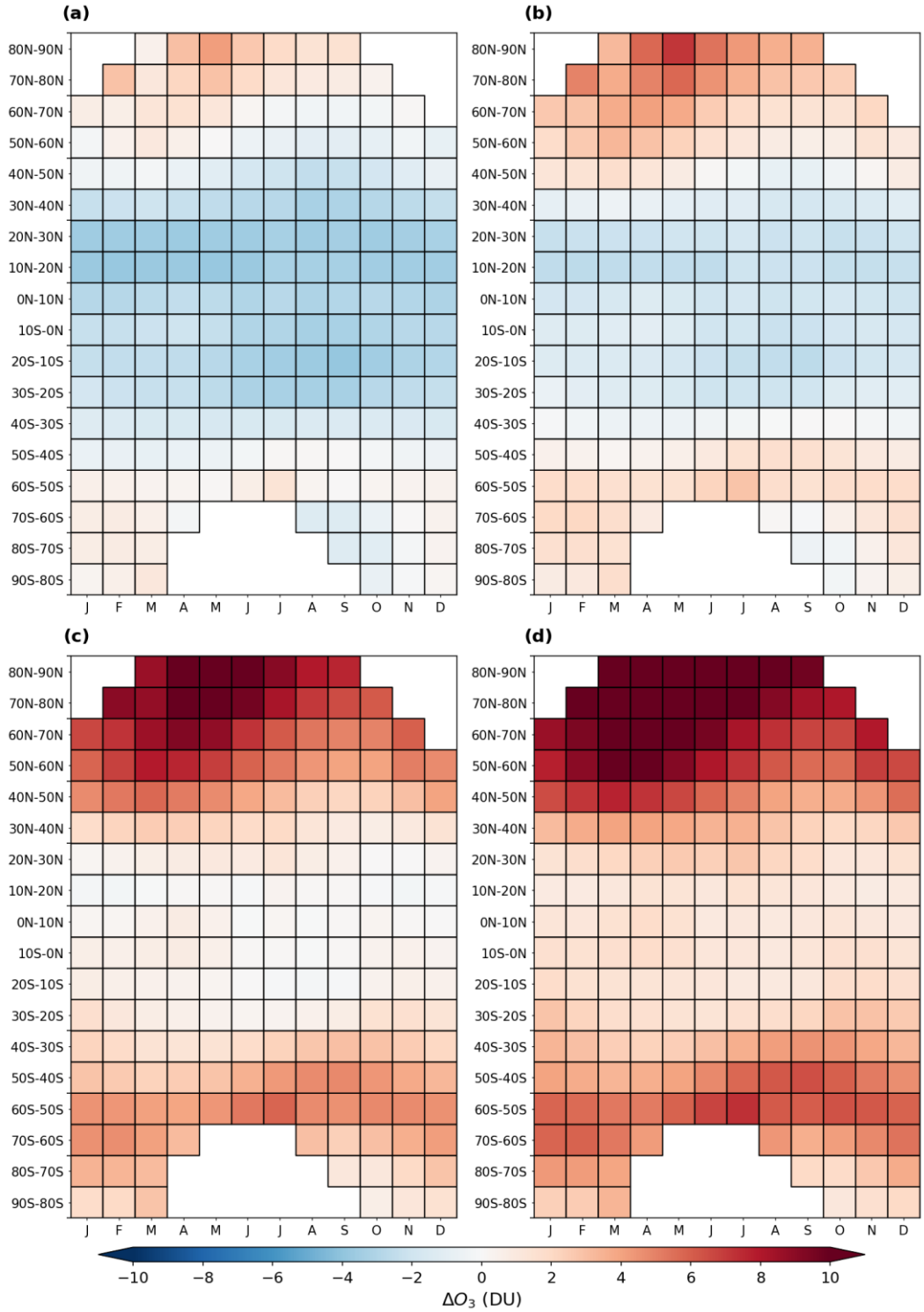

Figure 3.13 – The absolute (DU) change in CAMS surface-450 hPa layer ozone after applying OMI AKs for (**a**) a -50 %, (**b**) a -25 %, (**c**) a +25 % and (**d**) a +50 % perturbation in UTLS ozone (experiment LMU: 450-100 hPa).

(shown in Figure 3.13a-b), leading to a decrease in the surface-450 hPa layer amount due to the AK (as opposed to a slight increase in the unbiased case shown earlier in Figure 3.11). The patterns or changes noted here for the -50 % perturbation case in both Figure 3.12a and Figure 3.13a also apply to the -25 % perturbation case (Figure 3.12b and Figure 3.13b), albeit the magnitude of these shifts is smaller. In fact, the changes to the AK

influence are relatively modest for the -25 % perturbation case compared with the -50 % perturbation case. This reflects the increasing importance a UTLS ozone bias may have for a larger negative perturbation, as the default influence of the AK (in the unperturbed or control case) becomes less dominant.

For the corresponding positive ozone LMU perturbation experiment results, shown in both Figure 3.12c-d and Figure 3.13c-d, the changes noted for the negative experiments are largely consistent but are of course opposing in sign. The largest change to the default AK influence (in the unbiased case in Figure 3.11) is again evident over the Northern Hemisphere high latitudes during spring of comparable magnitude (~6 to 8 DU increase for the +50 % perturbation case), with a less pronounced maxima in this change over Southern Hemisphere mid-latitudes during late austral summer (up to +5 DU for a 50 % enhancement in UTLS ozone). The smallest changes to the AK influence are again apparent over the tropics and Southern Hemisphere high-latitudes, coinciding with the regions least sensitive to the AK influence (as was earlier evident in Figure 3.11).

The impact to the AK influence is subsequently shown in Figure 3.13c-d. The predominance of an increase in the surface-450 hPa layer amount due to the AK over much of the extratropics in the control case (Figure 3.11) is seen to extend entirely across the tropics in the case of a +50 % perturbation. However, the magnitude of the increase due to the AK over the tropics is still small (< 2 DU) but has importantly changed in sign. In the case of a +25 % perturbation, the change due to the AK is smaller still (between ± 1 DU). Over the extratropics, the AK influence is increased significantly in magnitude for the +50 % perturbation especially (widely > 10 DU in Northern Hemisphere spring and summer over mid- to high-latitudes and between 6 to 8 DU between 40°S and 70°S). This reflects the combined influence of the AK ordinally, together with the additional smearing of higher ozone from the UTLS region, as a result of the artificially imposed positive bias applied in this region. The results are consistent for a smaller +25 % perturbation but as noted for the equivalent negative perturbation experiments, a bias in UTLS ozone can be inferred to have an increasingly larger impact on the AK influence for higher increments. This is because the change due to the bias in the AK influence (Figure 3.12) for a ± 25 % perturbation is less than half that shown for a ± 50 % perturbation.

As mentioned, the UTLS (450-100 hPa) region was divided up into three constituent parts for these sensitivity evaluations: lower (L) (450-310 hPa), middle (M) (310-170 hPa) and upper (U) (170-100 hPa), to assess the level of AK sensitivity to these different sub-layers.

Resultant experiments therefore involved perturbing either none, only one or two, or all three of these sub-layers. Whilst, the lower tropospheric subcolumn (surface-450 hPa) AK has a stronger weighting to information with increasing proximity to the upper bound of this layer (as was previously demonstrated for an extratropical example in Figure 3.9, section 3.5.1), the sharp vertical gradient in ozone abundance, in association with the transition from a tropospheric to a stratospheric regime (tropopause region), means that the L sub-layer does not necessarily have the greatest impact on the influence of the AK. Indeed the influence has been found to be highly variable both spatially and temporally from this set of experiments analysed. Further work is required however to quantify and summarise such information in an effective manner, that would be invaluable to the CCM community for applied studies involving model comparisons of tropospheric ozone with UV-nadir satellite measurements.

Chapter 4

In this first of three scientific working chapters, retrieval biases in OMI and GOME-2A for the different retrieved subcolumns using the Rutherford Appleton Laboratory (RAL) scheme are first investigated using the Copernicus Atmospheric Monitoring Service (CAMS) reanalysis dataset. Following a brief overview of the retrieval vertical sensitivity to the troposphere, the rationale for this choice of comparison dataset is first outlined and demonstrated to agree well with limited, sparse ozonesonde observations which can be considered the 'real truth'. The CAMS reanalysis is next used to infer biases that arise in the stratosphere, where this part of the retrieval is determined by nuances in the backscattered radiances within the Hartley band, of which this constitutes the first step of the RAL ozone retrieval. The implications this has for the retrieval in the second step, which corresponds with the Huggins band involving extraction of signal from the troposphere region, are then inferred and discussed. Dependencies of the retrieval – CAMS differences are then finally presented as a function of solar zenith angle (SZA), latitude and scattering angle, as associations are found with respect to these factors. A summary of the chapter findings are then provided, together with recommended next steps for future work that would make retrospective reconciliation of the existing UV-nadir datasets of tropospheric ozone possible.

Reconciliation of UV-Nadir Satellite Tropospheric Ozone Datasets

4.1 Retrieval Sensitivity to Tropospheric Ozone

As mentioned in Chapter 3 (section 3.2), the RAL ozone profiling scheme for UV-nadir sounders, including both the GOME-2A and OMI instruments, is performed using a three-step sequential approach. The first step entails retrieval of the mid- to-upper stratospheric ozone profile using spectral information from the long-wave tail of the Hartley band region (266-307 nm), which is facilitated by the strongly decreasing ozone absorption and Rayleigh scattering coefficient with increasing wavelength across this interval (Miles et al., 2015). This first stage is known as the Band 1 (B1) retrieval step, in which height-resolved information retrieved from the ratio of backscattered (radiance) and direct-sun (irradiance) spectra (Munro et al., 1998; Gaudel et al., 2018). Before fitting sun-normalised (reflectance) spectra, the natural logarithm is taken, since this quantity depends linearly on atmospheric (i.e. ozone) optical depth at all wavelengths along this

interval. Additionally, a low order polynomial is subtracted from both measured and calculated reflectance spectra prior to fitting to minimise sensitivity to scattering and reflecting media (Munro et al., 1998). Spectral features in the sun normalised radiance, arising from the fine-scale structure in the solar irradiance spectra, are corrected for using a co-retrieved wavelength mismatch parameter (between Earth radiance and direct sun irradiance spectra). Additionally, a derived wavelength-independent Lambertian effective surface albedo and detector (dark) leakage (in raw signal units) parameter serve an important role in calibrating the retrieval (Munro et al., 1998; Miles et al., 2015). A scaling factor for the theoretical calculation of the infilled spectrum by the (singly scattered) Ring effect (modelled in the approach of Joiner and Bhartia 1995), to correct for Rotational Raman scattering, is additionally retrieved in the B1 step (Miles et al., 2015).

An effective surface albedo is then retrieved at 336 nm in band 2 (B2), where ozone absorption is very low, for use in the second ozone retrieval step. Due to the differing fields of view, this step is necessary as the effective albedo retrieved at the longest wavelengths in B1 (< 307 nm) is not suited for the B2 fit (which operates on wavelengths in B2 between 323 and 335 nm). Collectively, the 336 nm effective albedo, together with the B1 retrieved ozone profile and error covariance matrix, serve as the prior information for the fit in the Huggins bands (323-335 nm) in the final step (Miles et al., 2015), of which the spectral coverage has been recently extended to 321.5-334 nm (Gaudel et al., 2018). Information in this stage is derived from ozone absorption in the troposphere region, but requires high-precision fitting (< 0.1% RMS) to extend the retrieval down from the stratosphere to the surface (Miles et al., 2015; Gaudel et al., 2018). To achieve this, coarse-scale spectral artefacts, which may arise due to un-modelled features in UV surface sun-normalised radiance or due to radiometric miscalibration, must be removed to yield fine-scale differential spectral structure due to the presence of ozone. Use of both the logarithm of the sun-normalised radiance and a subtracted fourth order polynomial in wavelength, enables wavelength-dependent structure from differential vibration-rotational behaviour due to ozone absorption (as a function of temperature) to be fitted as part of the B2 retrieval (Miles et al., 2015).

The state vector for the retrieved ozone profile is given as the volume ozone mixing ratio on a fixed pressure grid (surface, 450, 170, 100, 50, 30, 20, 10, 5, 3, 2, 1, 0.5, 0.3, 0.17, 0.1, 0.05, 0.03, 0.017, 0.01 hPa), with radiative transfer calculations performed on a finer grid (at approximately 2 km intervals throughout the profile) by the forward model (Miles et al., 2015). Based on the known pressure-altitude relation (Equation 2 in Miles et al., 2015)

the pressure levels quoted correspond to approximate altitudes of 0, 6 and 12km, with subsequent 4 km increments up to 80 km thereafter. With respect to the information content of each instrument, the retrieval grid oversamples the profiles which subsequently necessitates constraint from other sources. This a priori information for the B1 step is taken from an ozonesonde based climatology, resolved by both latitude and month (McPeters et al., 2007). Both the B1 retrieved profile and the associated error covariance matrix are subsequently used as the a priori profile for the B2 step. To yield an adequate photometric signal-to-noise ratio in B1, the GOME-2A sensor requires averaging over eight pixels (consisting of two across-track and four along-track) (Miles et al., 2015). This yields a composite B1 pixel of 160 x 160 km which reduces noise by a factor of ~1/√8. A version of the GOMETRAN++ radiative transfer model (Rozanov et al., 1997) is used in the forward model and scalar/vector look-up tables from LIDORT, as provided by BIRA (C. Lerot, personal communication, 2012), are utilised to correct for polarisation. Additional sources of information include the solar reference spectrum (Chance and Kurucz, 2010), ozone absorption cross-sectional information (Daumont et al., 1992; Brion et al., 1993, 1998; Malicet et al., 1995), together with temperature and pressure information retrieved from ERA-Interim reanalysis data (Miles et al., 2015). A typical precision of ~4 DU is yielded for surface-450 hPa (~0-5.5 km) layer information from an individual ozone sounding (Gaudel et al., 2018). Since Miles et al. (2015), treatment of rotational Raman scattering in ozone absorption lines is now height-resolved and modifications to the 2D detector array of OMI have been implemented in place of the across-track scanning performed by GOME class sensors (Gaudel et al., 2018).

4.2 Analysis of Satellite UV-Nadir Sounder Biases: Ozonesondes and CAMS

Given the inherent difficulty in retrieving vertical information from UV-nadir spaceborne instruments below the stratospheric ozone peak, particularly near the tropopause where there is an abrupt change in gradient and in the troposphere where only ~10% of the column resides, efforts to quantity and eventually reduce potential biases that may exist in the resultant satellite datasets are extremely important. At present, monthly biases in the GOME-2A (2007-2018) and OMI (2004-2018) missions, have been derived for different latitude bands, with respect to ozonesondes from the World Ozone and Ultraviolet Radiation Data Centre (WOUDC) global database (R. Siddans, personal communication). These are shown for GOME-2A in Table 4.1 for the tropospheric subcolumn (surface-450 hPa or ~0-5.5 km), and can be corrected for (note that the equivalent values for this version of OMI data, which uses a linear retrieval scheme, are

not available at the time of writing). Applying empirically-derived bias corrections is considered necessary although not a satisfactory solution. In principle, it would be preferable to identify the underlying cause(s) of height-dependent retrieval bias and implement improvements to the retrieval scheme to avoid the need to do so. Potential shortcomings with the retrieval could be associated with a host of different geophysical and instrumental variables.

The WOUDC global database of ozonesonde profiles is nonetheless highly limited in terms of spatial and temporal sampling for such an application. Although subject to its own biases associated with modelling, assimilation scheme and observations assimilated, the CAMS reanalysis (as described in Chapter 3.3) constitutes the most advanced and extensively validated dataset of its kind. The dataset provides height-resolved ozone data for all locations and days as sampled by the satellites, spanning the duration of the GOME-2A and OMI missions. Assessment of the UV-nadir biases with respect to this dataset is therefore a suitable option for diagnosing factors that may limit retrieval accuracy, albeit with some caveats concerning its own inherent accuracy. Notably, shortcomings in the CAMS dataset arise from differences in the observations assimilated through time, with sharp discontinuities apparent where changes to the assimilated data source abruptly occur (Christophe et al., 2019; Inness et al., 2019). Another important caveat is that the CAMS reanalysis dataset cannot be considered wholly independent of the OMI and GOME-2A measurements compared with here. Both GOME-2A and OMI total column ozone information are assimilated in CAMS, along with other satellite UV sounders, although height-resolved information is assimilated only from OMI. However, it should be emphasised that the representation of ozone in CAMS is more strongly influenced spatially by assimilated limb sounder information (see Figure 3.6 in section 3.3). Furthermore, bias corrections are derived and applied to GOME-2A, OMI and all other data prior to assimilation in CAMS, and the treatment of ozone production, transport and loss processes within the Composition Integrated Forecasting System (C-IFS) has a large impact on both tropospheric and stratosphere analyses of ozone in this product. Therefore, the suitability of CAMS for examining biases in the non-biased corrected OMI and GOME-2A satellite datasets, retrieved using the RAL ozone scheme, is still of considerable value.

The retrieval minus ozonesonde (Ret – Sonde x AK) differences over the time period 2007-2018 are plotted in Figure 4.1 for GOME-2A, for the five layers shown. Note that the

translation of the subcolumn bounds from pressure to geometric height is approximate moving forwards. Corresponding differences between GOME-2A and the CAMS reanalysis dataset (Ret – CAMS x AK) are shown for the same time period, and equivalent OMI versus CAMS (Ret – CAMS x AK) differences are shown for the 2004-2018 mission period. Cross-correlations between the different levels in each case are summarised in Table 4.2 (top and middle). Strikingly good agreement between the Ret – Sonde x AK and Ret – CAMS x AK differences is shown for the surface-450 hPa layer (Figure 4.1), with reasonable consistency apparent for the four higher layers. However, the Ret – Sonde x AK differences show more inter-seasonal variability, with more gradual changes in the Ret – CAMS x AK differences evident from month to month and with latitude. This enhanced variability appears to also manifest as weaker correlations (r values) with each respective higher level, when compared with those shown for Ret – CAMS x AK. This is likely related, in part, to inhomogeneous spatial sampling and the extremely small sample sizes for the in situ (ozonesonde) measurements that are aggregated in each bin, compared to CAMS. The comparison for the higher subcolumns is also limited by the termination of ozonesonde measurements; typically around 35 km but sometimes much lower (Worden

LB	J	F	M	A	M	J
60-90°N	+0.44	+1.79	+3.69	+8.33	+10.29	+7.04
30-60°N	+1.93	+3.55	+2.62	+0.42	+0.19	+0.33
0-30°N	+2.26	+0.95	-0.27	-1.55	-2.27	-1.78
0-30°S	+0.47	-0.75	-1.62	-2.61	-2.58	-2.59
30-60°S	+0.05	-1.29	-2.41	-3.00	-1.55	-0.63
60-90°S	+1.55	+2.43	+3.23	+0.55	-0.81	-0.65
LB	**J**	**A**	**S**	**O**	**N**	**D**
60-90°N	+5.07	+5.24	+6.71	+2.68	+0.65	+1.54
30-60°N	+0.55	+1.75	+2.64	+2.87	+2.66	+1.86
0-30°N	-0.60	+0.88	+1.28	+2.57	+3.55	+3.56
0-30°S	-1.41	-0.73	-0.14	+0.40	+1.19	+0.91
30-60°S	+0.23	+1.48	+2.07	+2.77	+1.82	+0.98
60-90°S	+0.50	+0.71	-0.06	+0.81	+1.26	+1.21

Table 4.1 – GOME-2A minus ozonesonde (Ret – Sonde x AK) monthly mean differences (DU) of tropospheric subcolumn ozone (surface-450 hPa) calculated over the period 2007-2017 for 30° latitude bands (LBs). These differences are subtracted from the OMI L3 data for later scientific evaluations (Chapter 5), as a simplistic approach to correct for biases in the data arising from potential issues with the retrieval.

et al., 2007; Nassar et al., 2008). A general negative bias in GOME-2A is evident for both the 450-170 hPa (5.5-12 km) and the 170-50 hPa (12-21 km) subcolumns, which contrasts with an overall positive bias for the 50-20 hPa (21-27 km) and the 20-5 hPa (27-37 km) subcolumns. Of particular note, is the pronounced anticorrelation between the patterns of positive and negative for the 450-170 hPa (5.5-12 km) layer, with respect to the 100-50 hPa (21-27 km) layer especially, particularly in the extratropics. A Pearson correlation coefficient (r) value of -0.390 is calculated between these two subcolumns for the Ret – Sonde x AK differences, but a much greater value of -0.935 is calculated for the Ret – CAMS x AK differences. When factoring in the inhomogeneities associated with the use of ozonesondes, it is reasonable to conclude that a fairly strong inverse relationship between the bias patterns for these two layers likely exists.

The equivalent differences between OMI and CAMS (Ret – CAMS x AK) are shown in the right panels of Figure 4.1 for direct comparison with the GOME-2A versus CAMS (Ret – CAMS x AK) residuals, together with the different cross-correlations between layers in Table 4.2 (bottom). Overall, it is obvious that the latitude versus month biases with respect to CAMS are significantly smaller for OMI compared to GOME-2A. This is particularly the case for the stratospheric (Hartley band regime) part of the retrieval, as evidenced in the 170-50 hPa (12-21 km), 50-20 hPa (21-27 km) and the 20-5 hPa (27-37 km) Ret – CAMS x AK layers. Although there are pros and cons with regard to the configuration of each instrument, such as the scan mirror and sampling technique (see details in section 3.2.2 and section 3.2.3 for GOME-2A and OMI respectively), an instrument-specific shortcoming for the GOME-2A can be inferred from this evaluation. In contrast, the deviations for the surface-450 hPa (0-5.5 km) layer, between the retrieval and CAMS (Ret – CAMS x AK) for each instrument, are of similar magnitude, albeit each sensor is characterised by very different seasonal and latitudinally varying patterns. Whilst the bias patterns for each instrument are seemingly unrelated for this tropospheric layer, some similarities are observed for the four overlying subcolumns. Of particular note is the presence of a strong anticorrelation between the 450-170 hPa (5.5-12 km) and the 50-20 hPa (21-27 km) layers for OMI – CAMS x AK (r = -0.823), as was commented on for GOME-2A. The possible role of the atmospheric temperature profile in explaining that anticorrelation is discussed in section 4.3.2. Whilst the GOME-2A versus CAMS biases are characterised by a general negative beneath a general positive residual, the OMI versus CAMS biases are generally opposite in sign and significantly smaller in magnitude (by as much as half). Whilst the bias patterns are strongly latitudinally and seasonally dependent

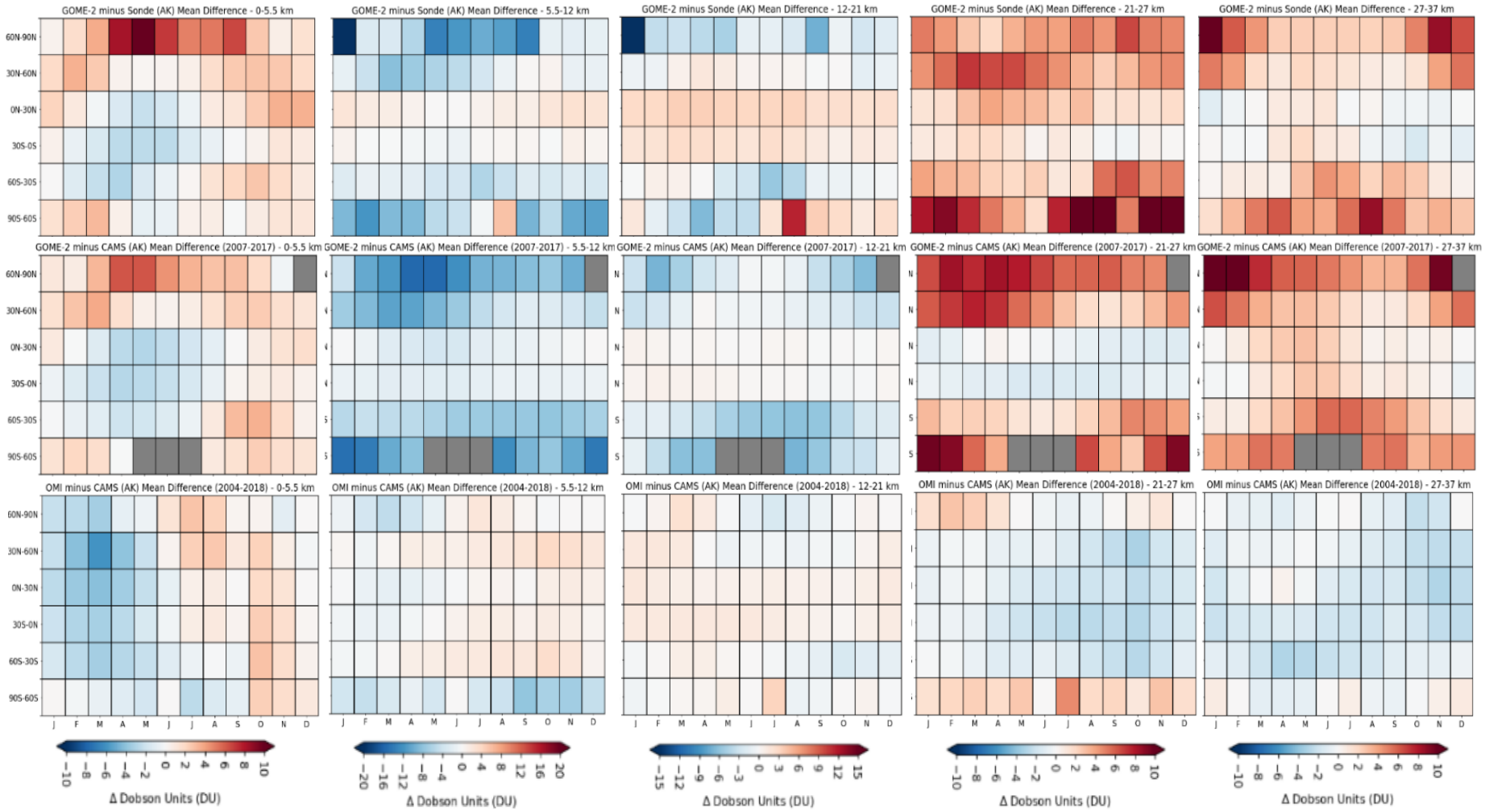

Figure 4.1 – A comparison between the (**left row**) GOME-2A minus ozonesonde (GOME-2A – Sonde x AK), (**middle row**) GOME-2A minus CAMS (GOME-2A – CAMS x AK) and (**right row**) OMI minus CAMS (OMI – CAMS x AK) retrieved integrated amount of ozone (DU) for (**left to right**) the surface-450 hPa (0-5.5 km); the 450-170 hPa (5.5-12 km); the 170-50 hPa (12-21 km); the 50-20 hPa (21-27 km) and the 20-5 hPa (27-37 km) subcolumn, as resolved on a 30° latitude band versus month basis. Note the different scale ranges between each subcolumn.

Subcolumn	0-5.5 km	5.5-12 km	12-21 km	21-27 km	27-37 km
0-5.5 km	1.000	-0.399	-0.319	0.152	0.120
5.5-12 km	-0.399	1.000	0.678	-0.390	-0.474
12-21 km	-0.319	0.678	1.000	0.114	-0.538
21-27 km	0.152	-0.390	0.114	1.000	0.550
27-37 km	0.120	-0.474	-0.538	0.550	1.000

Subcolumn	0-5.5 km	5.5-12 km	12-21 km	21-27 km	27-37 km
0-5.5 km	1.000	-0.597	-0.288	0.662	0.336
5.5-12 km	-0.597	1.000	0.594	-0.935	-0.760
12-21 km	-0.288	0.594	1.000	-0.559	-0.796
21-27 km	0.662	-0.935	-0.559	1.000	0.719
27-37 km	0.336	-0.760	-0.796	0.719	1.000

Subcolumn	0-5.5 km	5.5-12 km	12-21 km	21-27 km	27-37 km
0-5.5 km	1.000	0.274	-0.550	-0.315	-0.101
5.5-12 km	0.274	1.000	-0.263	-0.823	-0.537
12-21 km	-0.550	-0.263	1.000	0.147	-0.237
21-27 km	-0.315	-0.823	0.147	1.000	0.568
27-37 km	-0.101	-0.537	-0.237	0.568	1.000

Table 4.2 – Matrix of the Pearson correlation coefficients (r) between each layer for (**top**) the Ret – Sonde x AK differences and (**middle**) the Ret – CAMS x AK differences for the GOME-2A instrument, as well as (**bottom**) the Ret – CAMS x AK differences for the OMI instrument.

for both instruments, the OMI minus CAMS x AK residuals show greater complexity than for GOME-2A minus CAMS x AK.

These findings are indicative that likely deficiencies in the RAL retrieval scheme for each instrument, in the B1 or stratospheric part of the retrieval, result from both sensor-specific issues and issues common to the retrieval method for UV-nadir sounders. The role of the B1 step of the retrieval (Ret(B1) – CAMS), in contributing to the observed Ret – CAMS differences observed for each instrument is next assessed in section 4.3.1. In section 4.3.2, the possible role of the atmospheric temperature profile in explaining the anticorrelation between the 450-170 hPa (5.5-12 km) and the 50-20 hPa (21-27 km) layers for each sensor will be illustrated. Additional influence from the shape of the respective

AKs for each layer will also be inferred. The B1 versus B2 contributions to the layer biases will also be examined with respect to different geophysical variables, that include the solar zenith angle (SZA), latitude, scattering angle and the Rayleigh scattering phase function, which have been found to herald some promising initial insights (section 4.3.3). The causes for the biases in the lower troposphere region (surface-450 hPa) are much more difficult to speculate upon at this stage, but could involve propagation of potential errors in the B1 step of the retrieval, as well as issues local to this layer (i.e. deficiencies relating to the Huggins band or B2 stage of the retrieval).

4.3 Analysis of Hartley and Huggins Bands Steps in UV-Nadir Sounder Retrieval Bias

Comparing the Ret – CAMS and the Ret(B1) – CAMS differences will not only help to elucidate the role of the B1 influence, but also the role of the remaining secondary Band 2 (B2) step of the retrieval, which concerns inference of vertically-resolved ozone information in the troposphere region from the Huggins Band (320-345 nm). The geophysical and instrumental variables that were then subsequently examined in relation to the Ret – CAMS x AK differences are listed in Table 4.3, but are by no means exhaustive (notable parameters that have not been covered include temperature and aerosol, which would be anticipated to influence such biases). Note that for the instrumental and remaining geophysical variables investigated, no clear insights can yet be gained. Nonetheless, there are indications that these variables can influence the Ret – CAMS x AK profile differences, at least on an individual profile basis, and further tests have been identified as future work (see discussion in section 4.4). Since the variables which have been covered are all profile dependent, ungridded level-2 (L2) subcolumn ozone data, which consists of all filtered individual profiles from GOME-2A over the 2007-2017 time period (~4.8 million) and OMI over the 2004-2018 period (~168 million), are used in these evaluations. Standard filtering includes omission of all profiles in which the solar zenith angle (SZA) > 80° and the effective cloud fraction (ECF) > 0.2, defined as:

$$ECF = \frac{CF\ x\ CT}{5} \tag{4.1}$$

Where CF is the cloud fraction and CT is the cloud top height (km). An additional filter applied is the B1-fail flag, which is triggered when the B1 step of the retrieval is unsuccessful. This condition is met almost exclusively over the region affected by a known anomaly in the Earth's geomagnetic field; the South Atlantic Anomaly (SAA) region. The B2 step is still performed in these circumstances because the prior for the B1 retrieval is propagated as the prior for B2. However, the retrieval quality is slightly degraded.

Instrumental Variable	Description
B1COST	Retrieval cost from Band 1 step
B1FCAL	Scale factor for Band 1 radiometric gain
B1LEAK	Dark current signal offset in Band 1
B1RING	Scale-factor for Ring Effect cross-section applied in Band 1
B1SALB	B1 surface albedo
SLIT	Scaling factor for Band 2 slit-width
MISR	Mis-registration between Earthshine and direct-sun spectrum
B2COST	Retrieval cost from Band 2 step
B2LEAK	Dark current signal offset in Band 2
B2RING	Scale-factor for Ring Effect cross-section applied in Band 2
B2SALB	B2 effective surface albedo
B2GAIN	Scale factor for Band 2 radiometric gain
Geophysical Variable	**Description**
LAT	Latitude
LON	Longitude
SZA	The solar zenith angle at the time of each vertical profile retrieval
LZA	The 'line-of-sight' viewing angle of the instrument with respect to the vertical plane
CP	The cloud-top pressure, where clouds are present.
CF	The cloud cover fraction with respect to clear-sky
ECF	Effective cloud fraction
SCAT	The scattering angle (between line of sight and the sun in degrees (°))
RSCAT PF	The Rayleigh scattering phase function
DoM	Day in satellite mission

Table 4.3 – A description of the different instrumental and geophysical variables examined that may influence the observed UV-nadir retrieval minus CAMS (Ret – CAMS) differences found for each subcolumn.

4.3.1 Retrieval Minus CAMS x AK versus Retrieval Band 1 (B1) Minus CAMS x AK

In Figure 4.2, mean differences between the GOME-2A retrievals and CAMS for the five layers, with the addition of the total column (0-80 km), are shown for the B1 step and for the B2 step, both with and without the AKs applied to CAMS. GOME-2A minus CAMS x AK (Ret – CAMS x AK), GOME-2A minus CAMS (Ret – CAMS) and GOME-2A B1 minus CAMS (Ret(B1) – CAMS) differences are shown in the top, middle and bottom rows of Figure 4.2 respectively. The patterns of mean difference in stratospheric layers (< 170 hPa) for the B1 step are clearly seen to propagate onto the B2 retrieval, as evident from the B2 (centre panels) and B1 (right panels) plots in which the satellite AKs have not been applied. This is because height-resolved information down to the stratospheric ozone peak comes from the strong wavelength-dependent absorption in the Hartley band. The impact of applying AKs is then shown by the transition from the centre to left panels for B2 in Figure 4.2. The effect of applying the satellite AKs to the comparison dataset (CAMS) can be seen to be quite marked. The proportionately largest effect is evident for the 170-50 hPa (~12-21 km) subcolumn, in which the AK leads to a reduced negative bias at high latitudes and largely eliminates the large positive bias in low- to mid-latitudes. The AK for this layer is considerably broader and shallower than for higher layers (as was shown earlier in Figure 3.9 In section 3.5.1). Bias structure in the layers above, where AKs are better behaved, is retained after their application.

Agreement between the GOME-2A and CAMS total columns is extremely good, with a degree of resemblance to the bias pattern for the troposphere (~0-5.5 km), particularly in the Northern Hemisphere. Together with the strong anticorrelation between bias structures in the 5.5-12km and 21-27km layers (r = -0.916 for the Ret – CAMS x AK differences; see Table 4.4), the evidence that bias introduced in the stratosphere by the B1 step is being compensated to an extent in the 5.5-12km layer is robust. The B2 bias in the 0-5.5km layer is therefore a residual of stratospheric bias in B1 which has not been compensated in the 5.5-12km layer or higher layers, in combination with bias intrinsic to (Earthshine radiance spectra divided by a direct-sun irradiance spectrum), it is nonetheless susceptible to errors in radiometric calibration. Degradation in optical coatings over time due to their exposure to UV sunlight during flight has to be accounted for explicitly in the RAL processing schemes for GOME-2A, since this affects Earth views and solar views differently. Radiometric errors due to factors such as stray-light or dark current correction become increasingly significant at low light levels, so are dependent on the SZA and therefore latitude and season. Errors in Hartley band forward

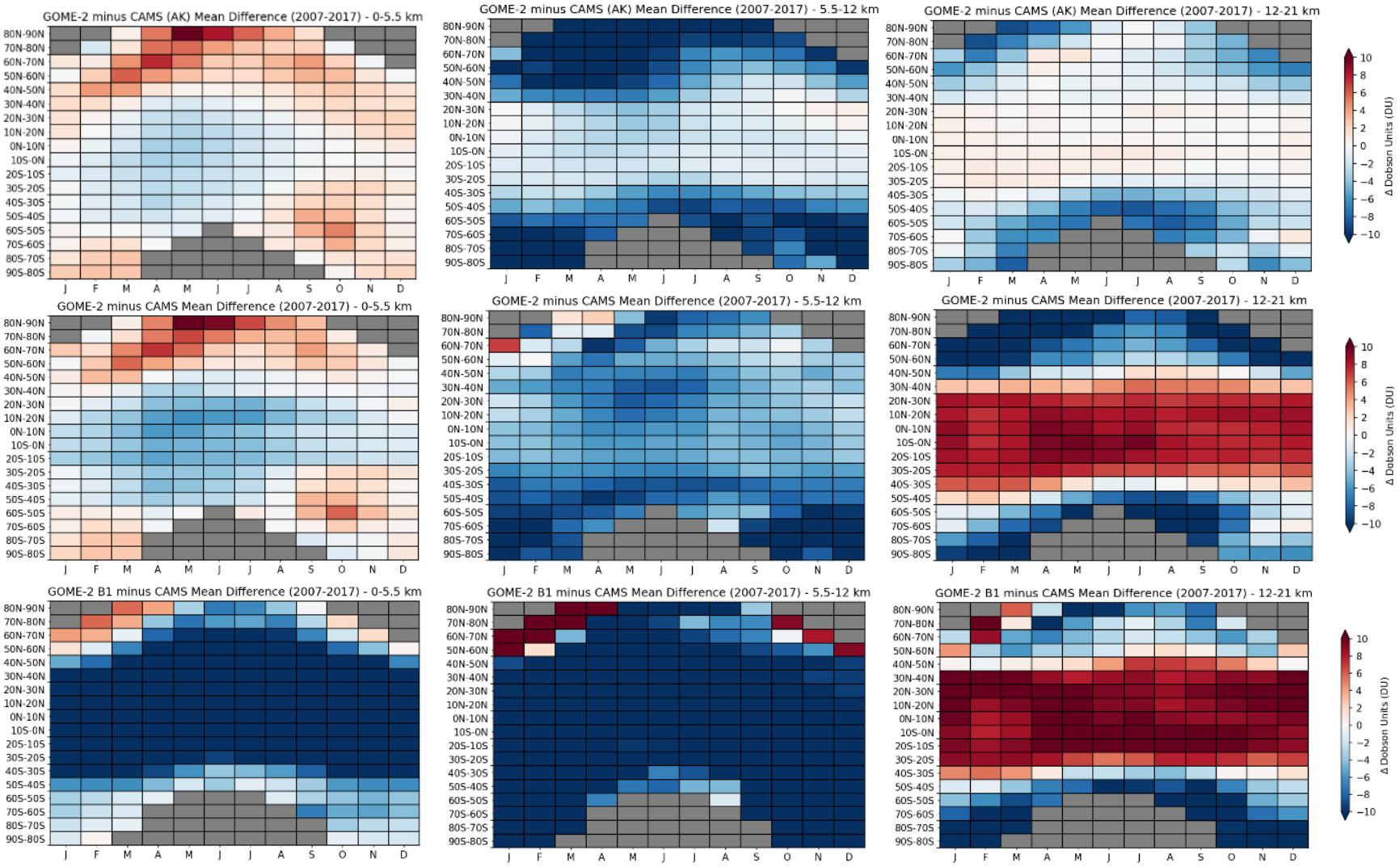

Figure 4.2a – Latitude band (10° intervals) versus month mean differences in subcolumn ozone for (**top row**) GOME-2A minus CAMS x AK; (**middle row)** GOME-2A minus CAMS; and (**bottom row**) GOME-2A B1 minus CAMS for **(left to right)** surface-450 hPa (0-5.5 km); 450-170 hPa (5.5-12 km); 170-50 hPa (12-21 km).

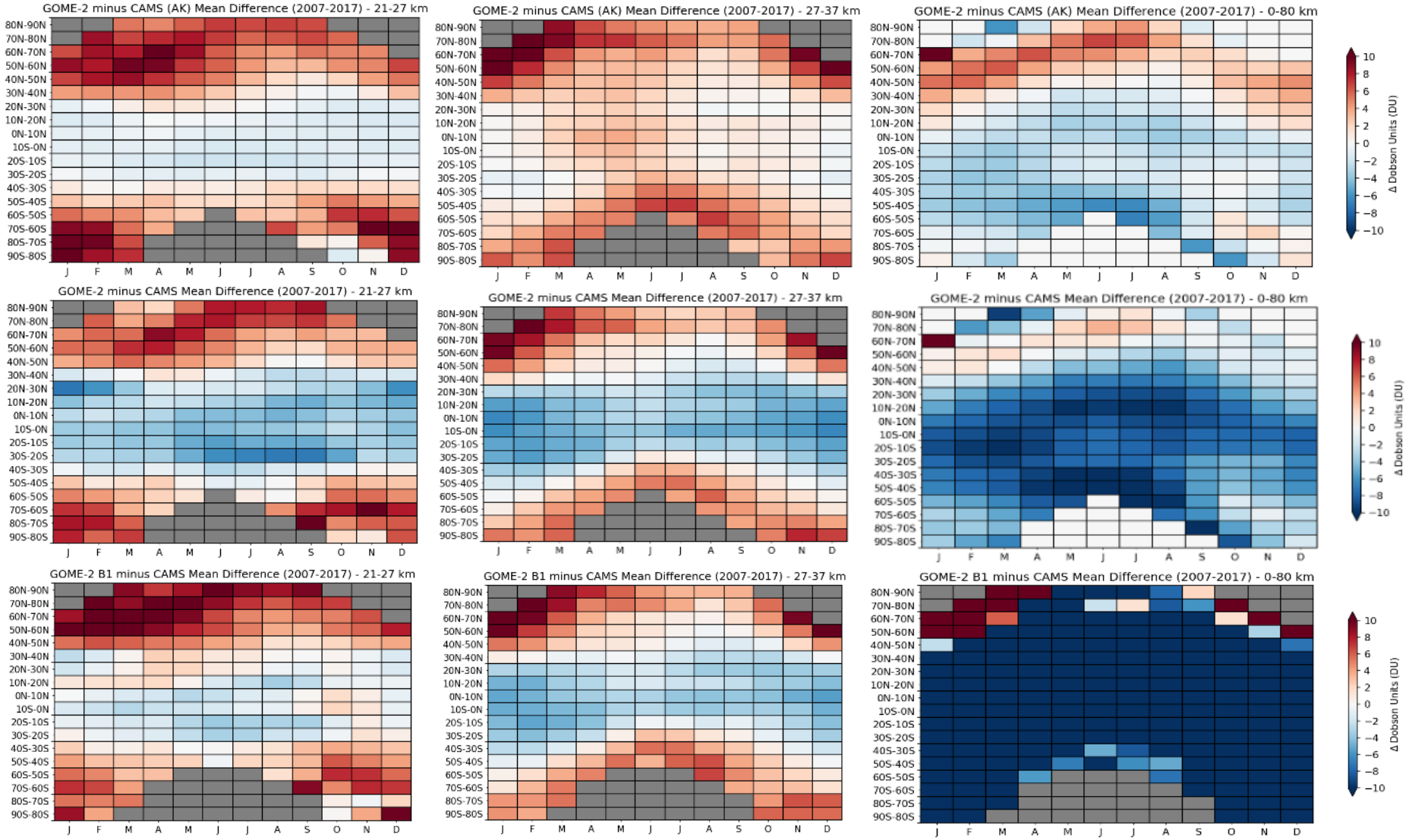

Figure 4.2b – Latitude band (10° intervals) versus month mean differences in subcolumn ozone for (**top row**) GOME-2A minus CAMS x AK; (**middle row)** GOME-2A minus CAMS; and (**bottom row**) GOME-2A B1 minus CAMS for **(left to right)** 50-20 hPa (21-27 km); 20-5 hPa (27-37 km) and the total column (0-80 km).

Subcolumn	0-5.5 km	5.5-12 km	12-21 km	21-27 km	27-37 km
0-5.5 km	1.000	-0.553	-0.289	0.611	0.275
5.5-12 km	-0.553	1.000	0.578	-0.916	-0.743
12-21 km	-0.289	0.578	1.000	-0.487	-0.773
21-27 km	0.611	-0.916	-0.487	1.000	0.669
27-37 km	0.275	-0.743	-0.773	0.669	1.000

Subcolumn	0-5.5 km	5.5-12 km	12-21 km	21-27 km	27-37 km
0-5.5 km	1.000	0.031	-0.727	0.709	0.567
5.5-12 km	0.031	1.000	-0.006	-0.329	-0.095
12-21 km	-0.727	-0.006	1.000	-0.804	-0.917
21-27 km	0.709	-0.329	-0.804	1.000	0.731
27-37 km	0.567	-0.095	-0.917	0.731	1.000
Subcolumn	**0-5.5 km**	**5.5-12 km**	**12-21 km**	**21-27 km**	**27-37 km**
0-5.5 km	1.000	0.284	-0.758	0.634	0.864
5.5-12 km	0.284	1.000	0.307	0.128	0.322
12-21 km	-0.758	0.307	1.000	-0.599	-0.685
21-27 km	0.634	0.128	-0.599	1.000	0.703
27-37 km	0.864	0.322	-0.685	0.703	1.000

Table 4.4 – Matrix of the Pearson correlation coefficients (r) between each layer for (**top**) the Ret – CAMS x AK differences, (**middle**) the Ret – CAMS differences and (**bottom**) the Ret(B1) – CAMS differences for the GOME-2A instrument.

modelling are also likely to be associated with solar and viewing geometries, and hence latitude and season along with surface reflectance and other factors. A contribution (residual error) from deficiencies in the B1 step of the retrieval, that principally impact the overlying layers, in conjunction with additional errors specific to the Huggins band (Band 2; B2) stage of the retrieval are likely to explain spatiotemporal variations in the surface-450 hPa (0-5.5 km) tropospheric subcolumn biases.

Figure 4.3 shows the multi-year global annual mean differences, spatially resolved on a 1° x 1° grid, between GOME-2A and CAMS to be strongly zonally symmetric, except for the surface-450hPa layer and the total column (0-80 km) where there is some association with surface type, and the influence of B1 on the B2 retrieval in the stratosphere is seen to be

similarly evident. In the extratropics, large-scale variability can in part be related to undulations in the tropopause height, in association with the climatological positioning of planetary (Rossby) waves. The appearance of this feature in part highlights the relatively poorer performance of the satellite retrieval in the extratropical regime, compared with the subtropical or tropical regime (elevated, less variable tropopause variability). However, the differences can be expected to be relatively larger in the extratropics, as column ozone abundances are greater than in the tropics (as also apparent from inspection of the total column in Figure 4.3). For the tropospheric subcolumn (surface-450 hPa), variability is much more complex, albeit with a clear indication of some degree of association with the distribution of land and sea, particularly in the Northern Hemisphere. Given that the surface reflectance in the UV between land and sea does not vary greatly, such association may point towards a bias in the CAMS reanalysis; for instance ozone surface deposition, which would constitute a major ozone sink. Indeed, the bias in CAMS simulated tropospheric ozone has been shown in a recent validation study by Huijnen et al. (2020) to increase towards the surface, which becomes more complicated to model as ozone exhibits strong local dependence with factors such as precursor emissions, deposition, vertical mixing and chemistry (Sekiya et al., 2018), and the constraint by the assimilated satellite observations reduces with decreasing altitude.

Corresponding latitude versus month plots of the mean differences between the OMI minus CAMS x AK (Ret – CAMS x AK), OMI minus CAMS (Ret – CAMS) and OMI B1 minus CAMS (Ret(B1) – CAMS x AK) are compared in Figure 4.4. Similarly to the GOME-2A comparison (Figure 4.2), a strong anticorrelation in patterns is again seen between both the 450-170 hPa (5.5-12 km) and the 50-20 hPa (21-27 km) subcolumns (r = -0.790 for the Ret – CAMS x AK differences; see Table 4.5). Biases induced in the B1 stage of the retrieval strongly propagate onto the Ret – CAMS, and in turn the Ret – CAMS x AK, differences for each of these five subcolumns. However the application of the AK to CAMS (the comparison dataset) significantly attenuates the magnitude of the Ret – CAMS differences, particularly with decreasing altitude. For the 450-170 hPa (5.5-12 km) layer, the effect of the AK is significant enough to alter the sign of the biases, as evidenced in the transition from the Ret – CAMS (centre) to the Ret – CAMS x AK (left) difference panels. This exact behaviour was also noted for GOME-2A, but the overall sign of the biases between these two opposing regions is largely inverse for OMI; a general negative bias exists for 50-20 (21-27 km) and the 20-5 hPa (27-37 km) subcolumns and an overall positive bias is apparent for both the 450-170 hPa (5.5-12 km) and 170-50 hPa (12-21 km)

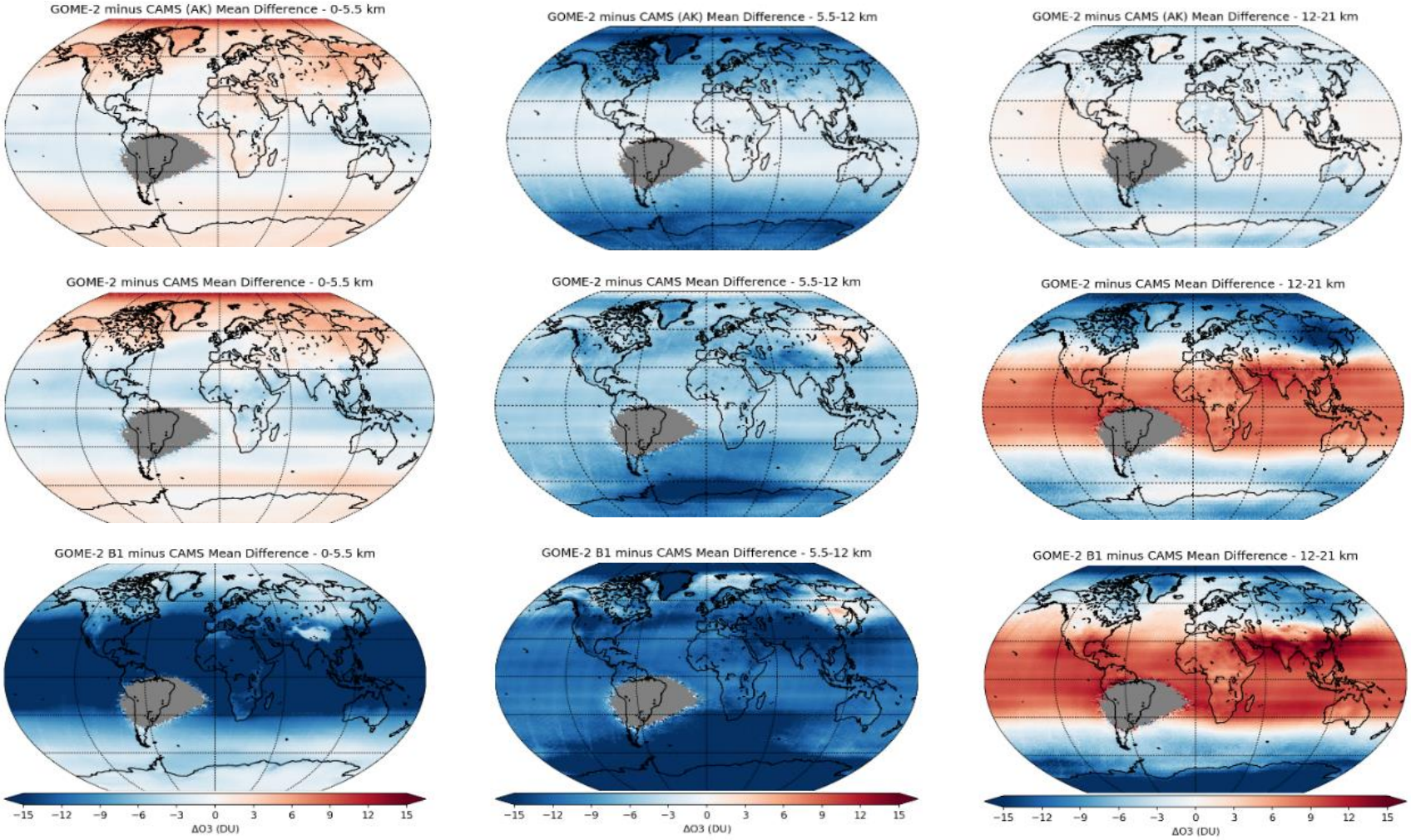

Figure 4.3a – Global annual mean differences in subcolumn ozone for (**top row**) GOME-2A minus CAMS x AK; (**middle row)** GOME-2A minus CAMS; and (**bottom row**) GOME-2A B1 minus CAMS for (**left to right**) surface-450 hPa (0-5.5 km); 450-170 hPa (5.5-12 km); 170-50 hPa (12-21 km). The grey shaded region denotes the region affected by the SAA, which is subsequently filtered by the B1-fail flag.

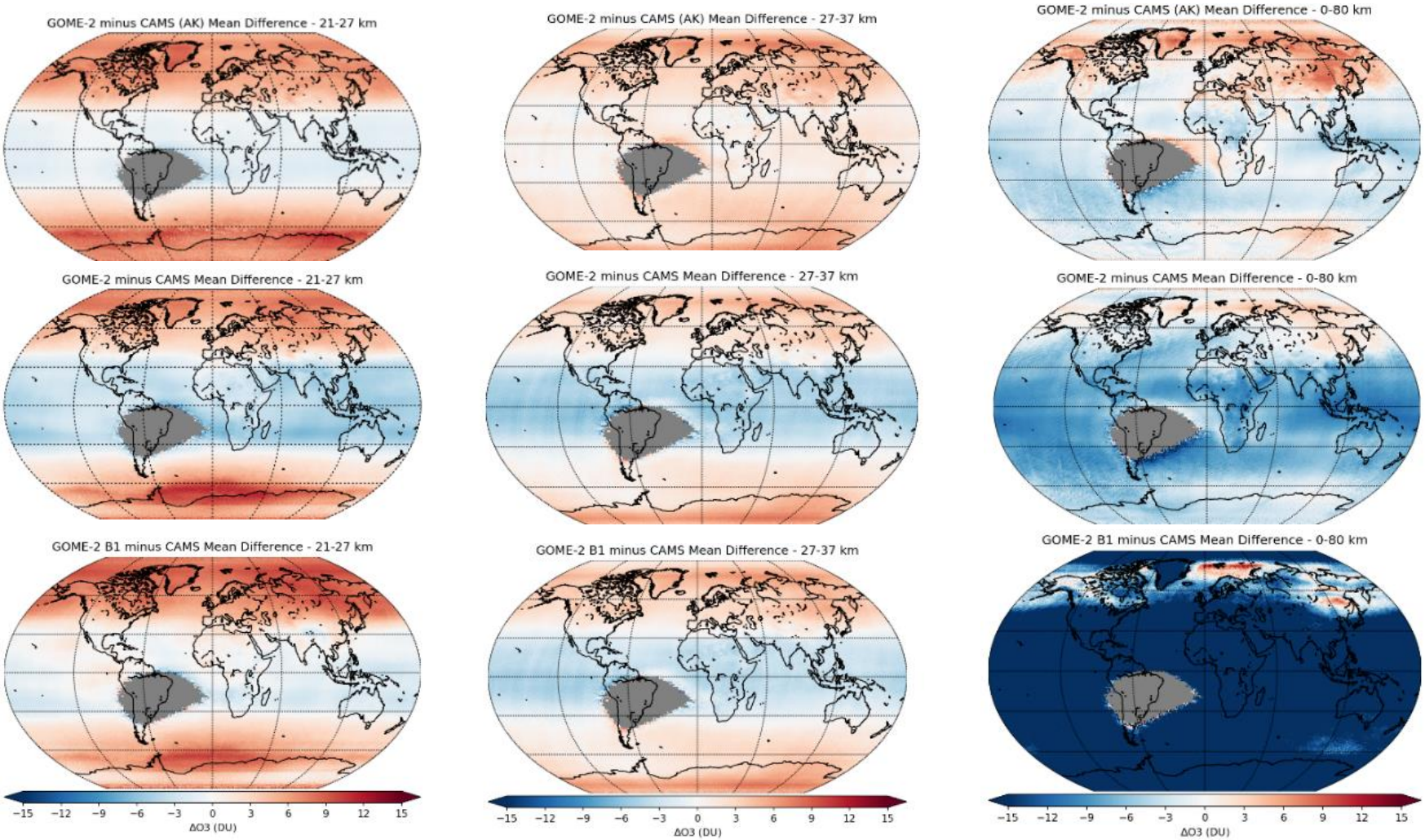

Figure 4.3b – Global annual mean differences in subcolumn ozone for (**top row**) GOME-2A minus CAMS x AK; (**middle row)** GOME-2A minus CAMS; and (**bottom row**) GOME-2A B1 minus CAMS for (**left to right**) 50-20 hPa (21-27 km), 20-5 hPa (27-37 km) and the total column (0-80 km). The grey shaded region denotes the region affected by the SAA, which is subsequently filtered by the B1-fail flag.

layers. However the same latitudinal and seasonal structure remains for both UV-nadir sounders; a tendency towards a negative (positive) difference is favoured at low (high) latitudes for both the 50-20 hPa (21-27 km) and the 20-5 hPa (27-37 km) subcolumns, with reversed tendencies for the 170-50 hPa (12-21 km) subcolumn.

As previously identified in section 4.2, the residuals are lower overall for OMI compared with GOME-2A, particularly within the stratospheric part of the retrieval. Although this would appear to signify that OMI more accurately captures the true vertical distribution of ozone if CAMS is assumed to a be a representative estimate of the true state, particularly in the B1 (Hartley band) step, the performance of each instrument cannot be evaluated conclusively here due to differences in the measurement implementation as eluded to earlier (e.g. scan mirror and sampling technique). Nonetheless, an instrument specific limitation for GOME-2A again seems likely from this evaluation. Smaller biases for OMI may however contribute to enhanced seasonal variability in the sign of the biases, which is most complex for the tropospheric (surface-450 hPa) subcolumn. Despite this, the seasonal evolution of a generally negative bias early in the calendar year, maximising in boreal spring across most latitudes, which shifts to a positive bias later in the year, again reaching a peak across most latitudes during boreal autumn, may be indicative of an instrumental origin. The consistency of this seasonal evolution in both hemispheres strongly suggests that geophysical factors are likely of lesser importance in explaining the tropospheric (surface-450 hPa) subcolumn Ret – CAMS biases for the OMI instrument. It is again noted here for OMI, that partial association between the bias pattern for the tropospheric subcolumn (0-5.5 km) and the total column (0-80 km) highlights significant compensation of biases induced in the B1 step between layers. This results in a bias pattern that is derived from both propagation of residual biases induced in the B1 step, as well as induced by potential deficiencies in the B2 in the retrieval step (concerned with the tropospheric part of the retrieval) that collectively imprint onto the total column biases.

The equivalent mean differences between the OMI minus CAMS x AK (Ret – CAMS x AK), OMI minus CAMS (Ret – CAMS) and OMI B1 minus CAMS (Ret(B1) – CAMS x AK) are further resolved globally on a 1° x 1° spatial resolution in Figure 4.5. The relative increase in longitudinal variability in both the sign and magnitude of the Ret – CAMS biases, as quantified here on an annual mean basis, with decreasing altitude is again noted for OMI as identified previously for GOME-2A (Figure 4.3). Similar bias spatial patterns are furthermore apparent for the total column, again reflecting earlier assertion that inferred

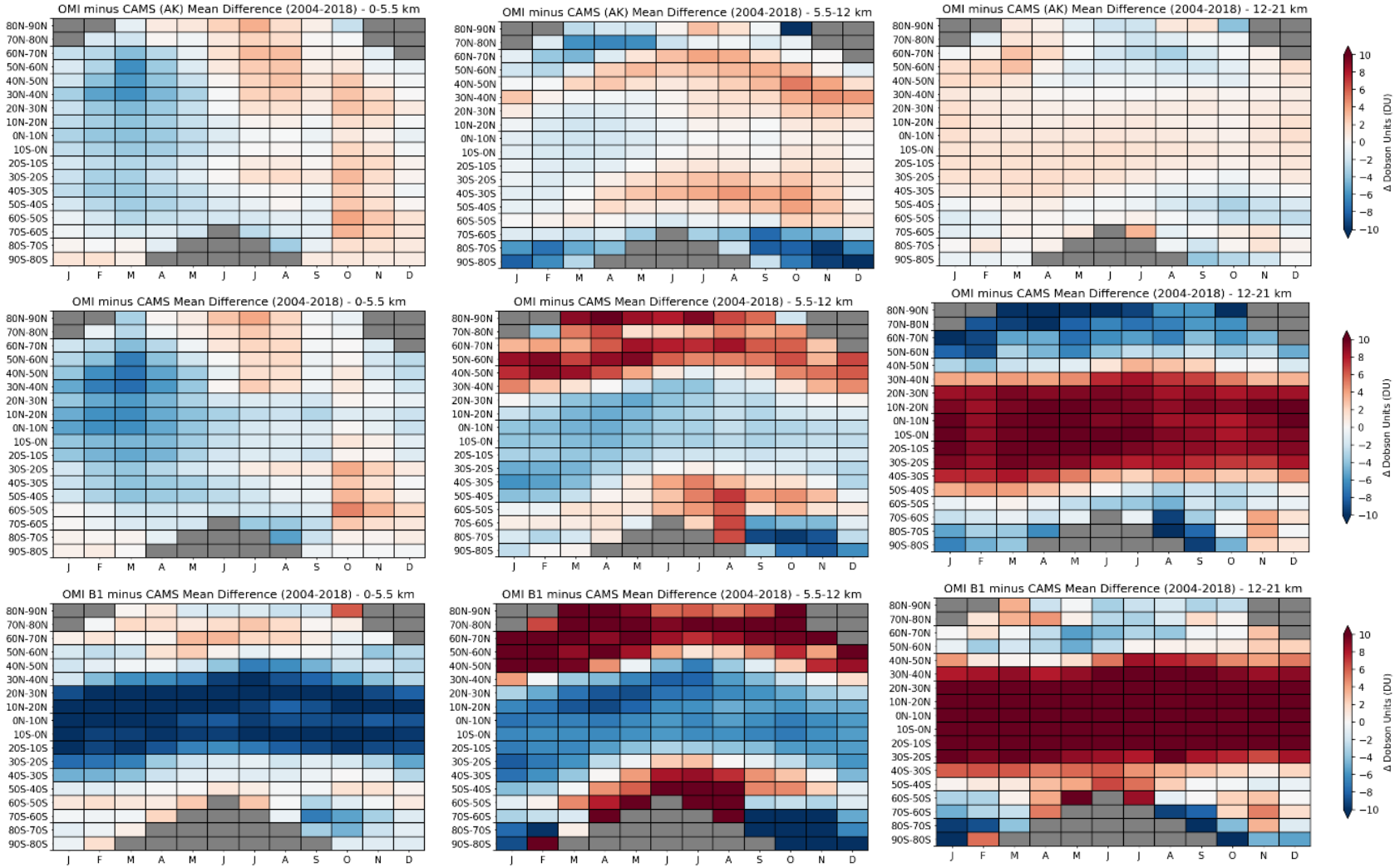

Figure 4.4a – Latitude band (10°) versus month mean differences in subcolumn ozone for (**top row**) OMI minus CAMS x AK; (**middle row)** OMI minus CAMS**;** and (**bottom row**) OMI B1 minus CAMS for (**left to right**) surface-450 hPa (0-5.5 km); 450-170 hPa (5.5-12 km) and 170-50 hPa (12-21 km).

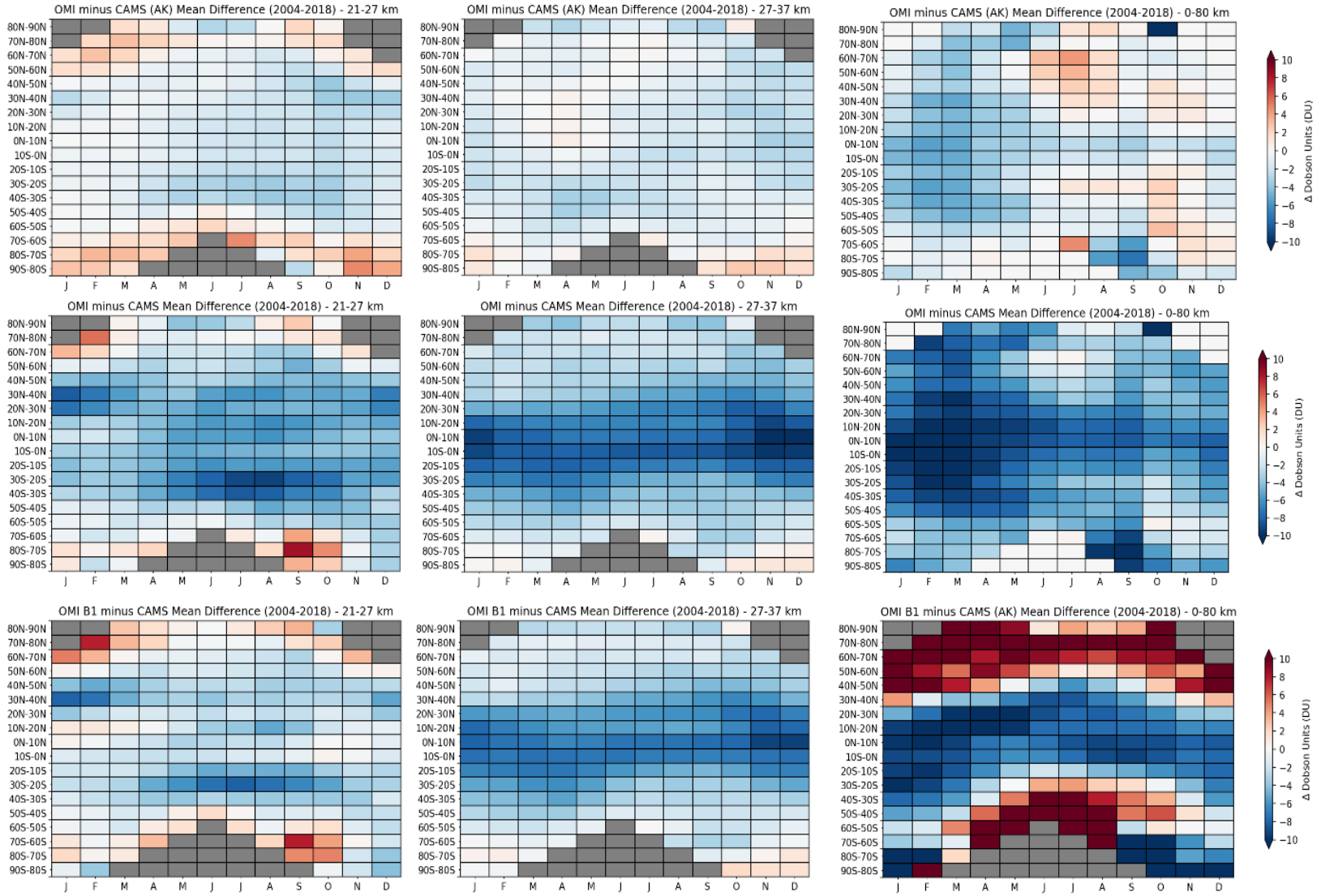

Figure 4.4b – Latitude band (10°) versus month mean differences in subcolumn ozone for (**top row**) OMI minus CAMS x AK; (**middle row)** OMI minus CAMS**;** and (**bottom row**) OMI B1 minus CAMS for (**left to right**) 50-20 hPa (21-27 km); 20-5 hPa (27-37 km) and the total column (0-80 km).

Subcolumn	0-5.5 km	5.5-12 km	12-21 km	21-27 km	27-37 km
0-5.5 km	1.000	0.210	-0.472	-0.230	-0.060
5.5-12 km	0.210	1.000	-0.098	-0.790	-0.528
12-21 km	-0.472	-0.098	1.000	0.072	-0.388
21-27 km	-0.230	-0.790	0.072	1.000	0.481
27-37 km	-0.060	-0.528	-0.388	0.481	1.000

Subcolumn	0-5.5 km	5.5-12 km	12-21 km	21-27 km	27-37 km
0-5.5 km	1.000	0.123	-0.295	0.115	0.307
5.5-12 km	0.123	1.000	-0.676	0.046	0.351
12-21 km	-0.295	-0.676	1.000	-0.663	-0.763
21-27 km	0.115	0.046	-0.663	1.000	0.583
27-37 km	0.307	0.351	-0.763	0.583	1.000

Subcolumn	0-5.5 km	5.5-12 km	12-21 km	21-27 km	27-37 km
0-5.5 km	1.000	0.704	-0.755	0.155	0.830
5.5-12 km	0.704	1.000	-0.346	0.185	0.491
12-21 km	-0.755	-0.346	1.000	-0.413	-0.811
21-27 km	0.155	0.185	-0.413	1.000	0.259
27-37 km	0.830	0.491	-0.811	0.259	1.000

Table 4.5 – Matrix of the Pearson correlation coefficients (r) between each layer for (**top**) the Ret – CAMS x AK differences, (**middle**) the Ret – CAMS differences and (**bottom**) the Ret (B1) – CAMS differences for the OMI instrument.

deficiencies in the B1 step of the retrieval, particularly between 21-27 km, are compensated for further down (primarily within the 5.5-12 km layer). Thus, deficiencies in the B2 (Huggins band) step manifest more strongly when the column differences are integrated over the full depth of the atmosphere, as supported by a fair degree of association with the tropospheric subcolumn (surface-450 hPa) biases. Similarly to the GOME-2A instrument, the sine-wave signature associated with the climatological Rossby wave pattern in the extratropics is again apparent for OMI in the lowest three subcolumns. However this feature is less discernible after AKs are applied to CAMS, implying that the AK compensates for any differential handling of the two different profile

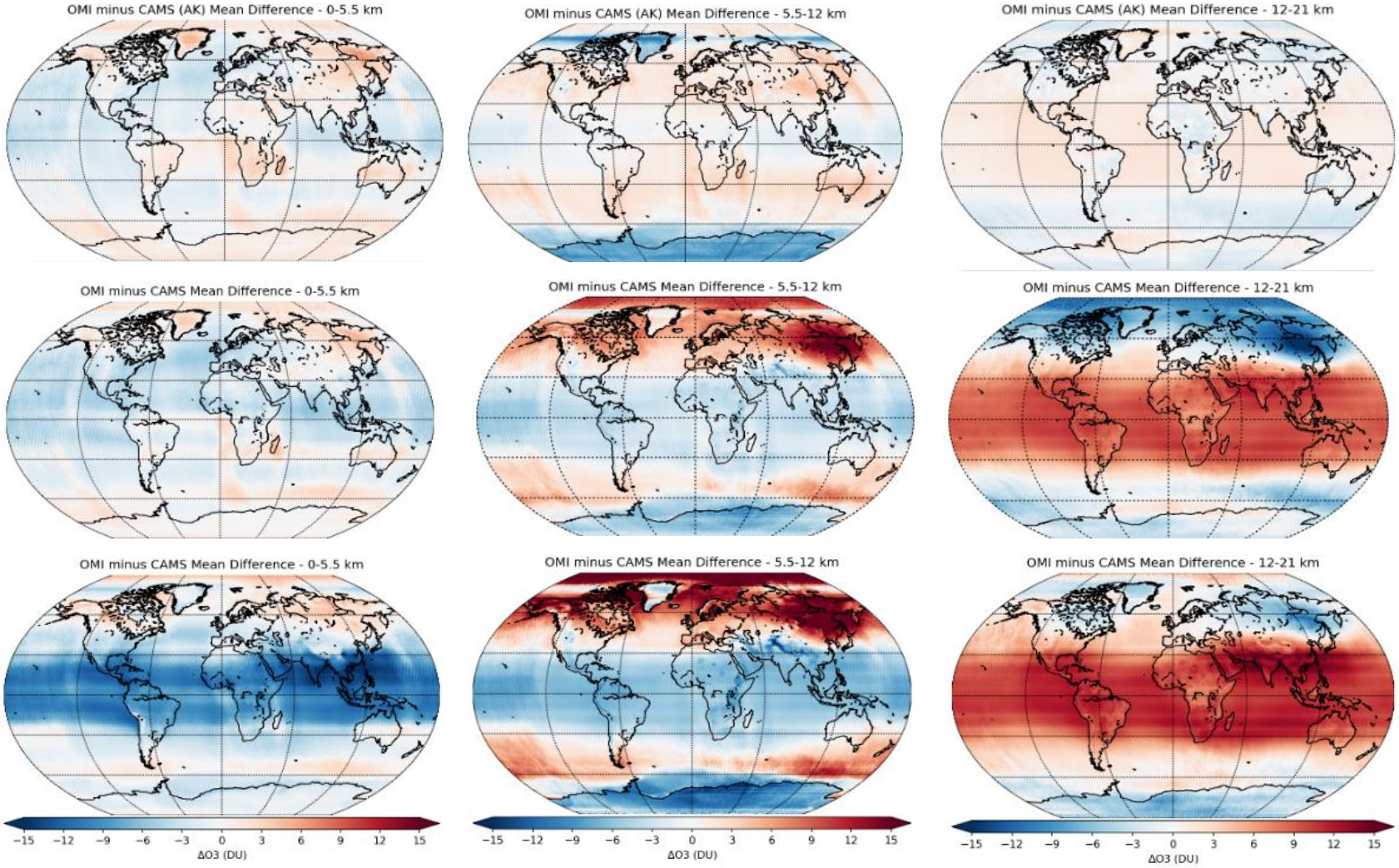

Figure 4.5a – Global annual mean differences in subcolumn ozone for (**top row**) OMI minus CAMS x AK; (**middle row)** OMI minus CAMS; and (**bottom row**) OMI B1 minus CAMS for (**left to right**) surface-450 hPa (0-5.5 km); 450-170 hPa (5.5-12 km) and 170-50 hPa (12-21 km).

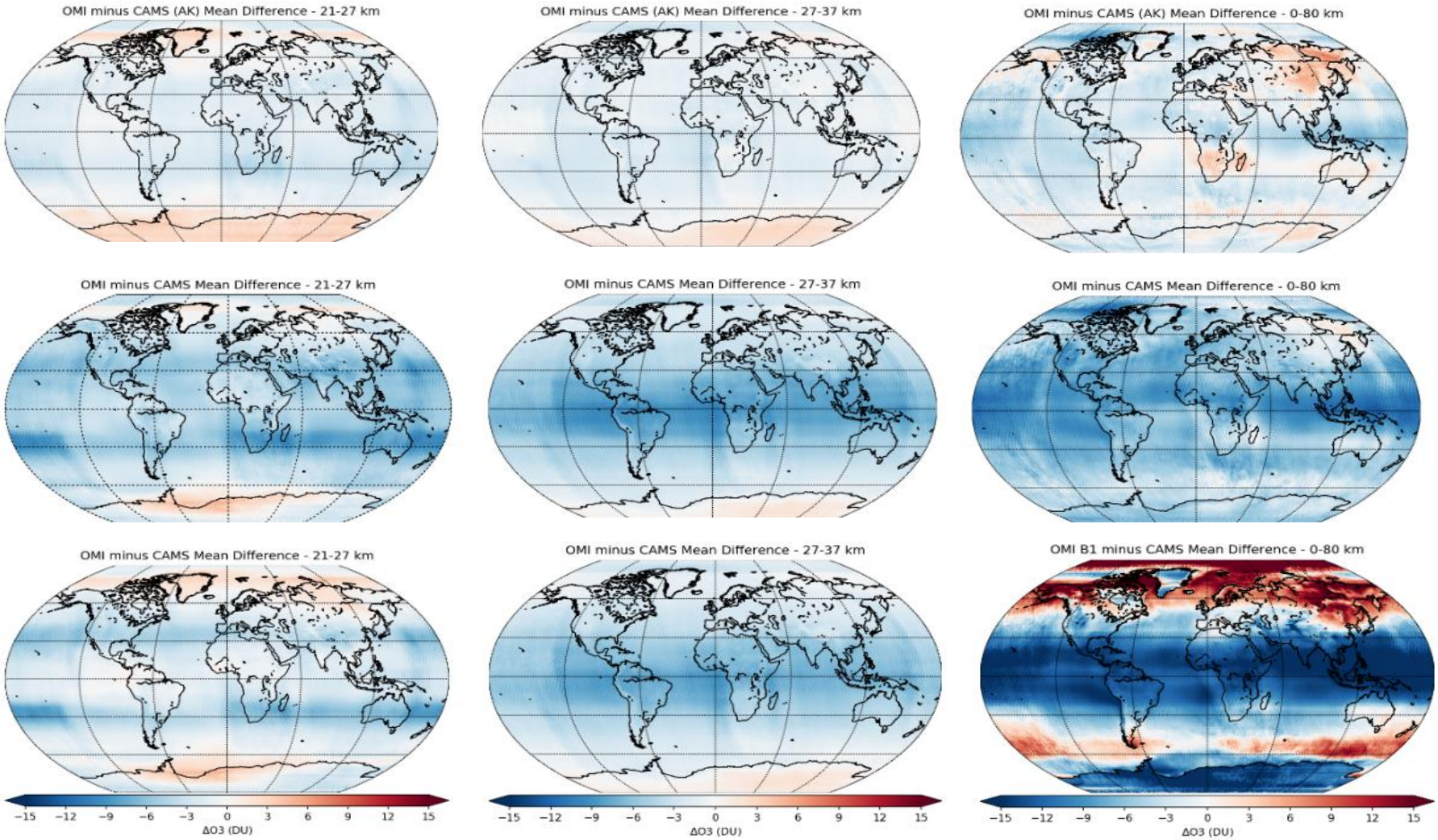

Figure 4.5b – Global annual mean differences in subcolumn ozone for (**top row**) OMI minus CAMS x AK; (**middle row)** OMI minus CAMS; and (**bottom row**) OMI B1 minus CAMS for (**left to right**) 50-20 hPa (21-27 km) and 20-5 hPa (27-37 km) and the total column (0-80 km).

regimes (extratropics versus sub-tropics/tropics) which gives rise to this bias pattern. Unlike for the GOME-2A instrument however, the presence of structures in the bias distributions for all subcolumns that are extensive in the meridional plane, across the suite of Ret – CAMS x AK, Ret – CAMS and Ret(B1) – CAMS differences, are noticeable. This is highly likely to be artefacts of the retrieval, and most probably in relation to the instrument sampling technique. Whilst GOME-2A uses a 1-D detector array for across-track scanning, OMI uses a 2-D detector array which provides simultaneous sampling at all across-track positions (Levelt et al., 2006; Foret et al., 2014). Thus, it is reasonable to assume that some dependency between the Ret – CAMS x AK differences might be present as a function of viewing geometry (angle between line-of-sight and the nadir position of the satellite). Biases for the tropospheric subcolumn (surface-450 hPa) once again show the greatest spatial complexity and warrant particularly close investigation to determine potential causal factors. Resemblance between the spatial patterns of the globally resolved surface-450 hPa (0-5.5 km) layer biases (Figure 4.3 for GOME-2A and Figure 4.5 for OMI), particularly over regions such as East Asia, may however point towards potential shortcomings associated with the CAMS reanalysis, which would further complicate the picture.

In summary, biases induced during the B2 step of the retrieval, which concerns discrimination of ozone in the tropospheric (0-5.5 km) layer, and in part within the UTLS region (5.5-12 km), are inferred for each instrument. Differences in the bias patterns for the surface-450 hPa (0-5.5 km) layer and the total column (0-80 km) for each instrument implies that residual bias propagation from the B1 step must infiltrate down to these levels. This is despite clear evidence for compensation effects of the anticorrelation between the 450-170 hPa (5.5-12 km) and 50-20 hPa (21-27 km) layers. Thus, the origin of biases in the surface-450 hPa (0-5.5 km) and 450-170 hPa (5.5-12 km) layers stems from a combination of these two competing influences, which would require further in depth investigation to be able to quantify and disentangle each effect. The physical basis for the inherent difficulty in retrieving vertical information on atmospheric ozone for these UV-nadir sounders will next be illustrated in section 4.3.2, and discussed in its relation to the biases shown for the 0-5.5 km layer.

4.3.2 B2 Bias Compensation

To illustrate the likely geophysical reasons for the B1 contamination influence into the B2 step, the atmospheric temperature profile for a typical extratropical case is shown, together with the layer AKs which depict layer retrieval sensitivity throughout the depth of the atmosphere in Figure 4.6. Firstly, it is evident that a similar temperature regime exists in both the upper portion of the 450-170 hPa (5.5-12 km) and 50-20hPa (21-27 km) layers, which means they are not distinguishable via temperature dependence of the Huggins band spectral signature and is the cause of anticorrelation. An additional factor is that of the vertical shape of the satellite AKs, which depicts the individual layer retrieval sensitivity throughout the atmosphere, which could impose a further limitation in the accuracy of the retrieved vertical profiles. In particular, the width of the 450-170 hPa (5.5-12 km) AK (orange line in right panel) is notable, with significant sensitivity to both stratospheric layers (up to ~50 hPa) and the tropospheric or surface-450 hPa (0-5.5 km) subcolumn, as indicated by the deviance of the line from zero. The former presents a particular issue, as information from the stratospheric ozone peak may significantly contaminate the retrieved ozone abundances from the 5.5-12 km layer.

More generally, significant variability in the temperature regime between 450 hPa and 170 hPa for any given profile, with respect to a monthly averaged profile (which would be expected, on average, to follow the environmental lapse rate of ~-6°C km^{-1} up to the tropopause in this environment) may also impose a further constraint. These fluctuations in temperature on a profile-by-profile basis may also serve as a limiting factor when

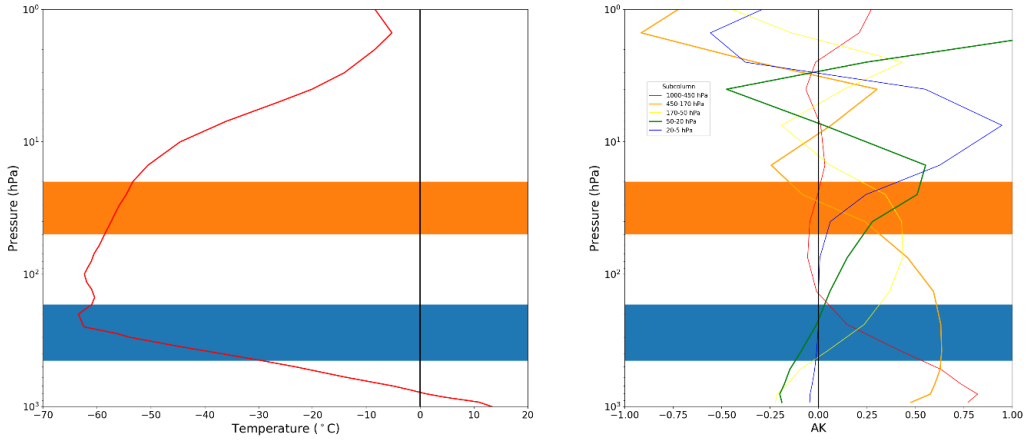

Figure 4.6 – An example of (**left**) a typical extratropical air temperature (°C) profile (45°N, 0°E) taken from the EMAC model, together with (**right**) the satellite AKs for this location (here taken from OMI) which provide indication of layer retrieval sensitivity throughout the atmosphere.

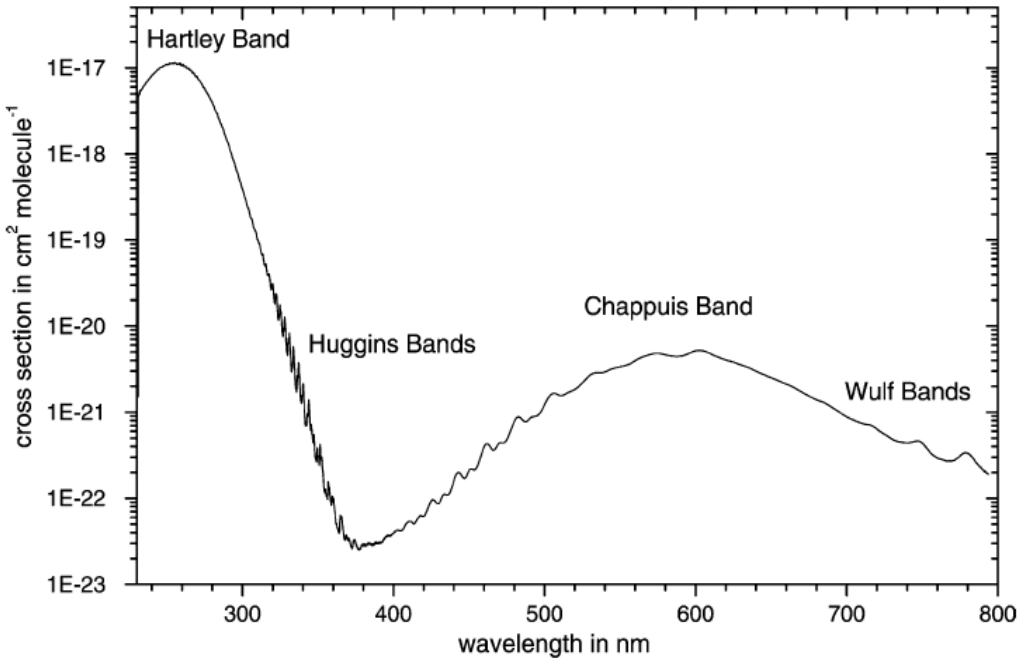

Figure 4.7 – The spectrum in ozone (O_3) as measured at room temperature. Taken from Figure 1 in Orphal (2003).

evaluating the surface-450 hPa (0-5.5 km) and the 450-170 hPa (5.5-12 km) subcolumns of ozone from either the GOME-2A or OMI instruments, as the retrieval is very sensitive to the temperature dependence of the spectral structure in the Huggins band window (320-345 nm), as further shown in Figure 4.7 for the cross-section of molecules within this region. The structure in this region is temperature dependent and thus the ability to discriminate lower layers from stratospheric layers, where ~90% of absorption takes place, is governed by the difference in temperature between layers.

4.3.3 Retrieval Minus CAMS x AK Geophysical Variable Dependencies

The dependencies of all filtered individual profile Ret – CAMS x AK differences, for both the GOME-2A (2007-2017) and OMI (2004-2018) instruments over their respective missions, were investigated with respect to the suite of geophysical and instrumental variables listed and detailed earlier (Table 4.3). Some results are shown here for four different geophysical variables (SZA, latitude, scattering angle and the subsequent derived Rayleigh scattering phase function) that provide some insights into the causes of instrument biases identified in sections 4.2 and 4.3.1 with respect to the CAMS reanalysis.

4.3.3.1 Solar Zenith Angle (SZA)

Figure 4.8 first shows the Ret – CAMS x AK density distributions versus SZA for GOME-2A, for the seven retrieved subcolumns between the surface to ~0.5 hPa, in addition to the total column. Note that a minority of profiles (outliers) extend beyond the scale range of

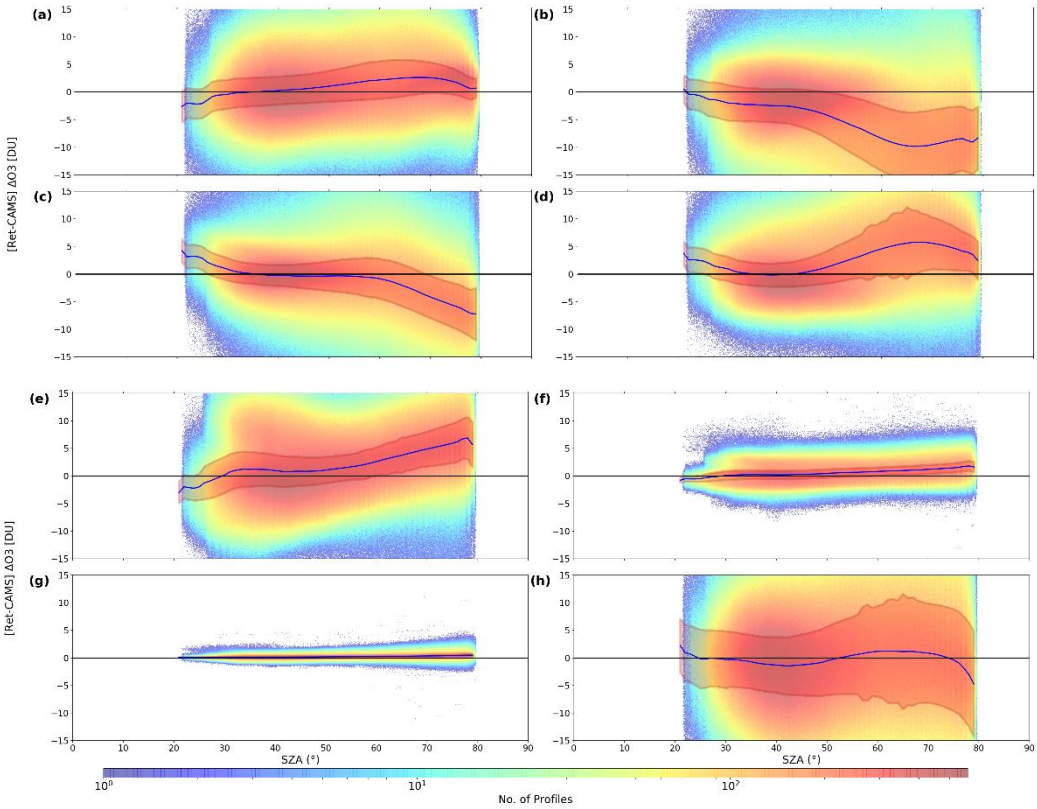

Figure 4.8 – Cloud density plots of the GOME-2A Ret – CAMS x AK tropospheric ozone (0-5.5 km) differences (y-axis) versus the GOME-2A (Ret) SZA (x-axis) for (**a**) the 0-5.5 km layer, (**b**) the 5.5-12 km layer, (**c**) the 12-21 km layer, (**d**) the 21-27 km layer, (**e**) the 27-37 km layer, (**f**) 37-43 km layer, (**g**) 43-53 km layer and (**h**) the 0-80 km (total column) layer. The mean variation in the GOME-2A Ret – CAMS x AK differences as a function of SZA (°), as resolved on a 1° basis, is additionally overlaid (solid blue line) together with the standard deviation (1σ) calculated over all profiles (red shading).

that shown here (as is also the case for all remaining evaluations presented in this chapter), as the focus of this investigation is very much concerned with identification of general dependencies as a function of variables such as SZA. For this reason, the mean dependency (solid blue line) and standard deviation (red shading) is additionally overlaid for each layer examined to highlight trends more clearly. For the GOME-2A sounder, all layers reveal some dependency on SZA over the observed range (20° to 80°), although this is not monotonic. An overall tendency for an increase in layer bias between GOME-2A and CAMS is apparent with increasing SZA. This applies to both the main clustering of profiles (n profiles > 10^3), which initially are tightly clustered around zero for a SZA of 20°, as well as the distribution of outlier profiles (n profiles < 10^1). Whilst the overall Ret – CAMS x AK differences become increasingly positive for the troposphere (0-5.5 km), up to ~2-3 DU for a SZA of ~60-80°, a general negative tendency is evident for the 450-170 hPa (5.5-12 km) layer. The presence of outliers increases substantially for SZAs > 50°, particularly in the latter case where the number of positive outliers also increases despite the overall

negative tendency. For this subcolumn, the mean difference between the Ret – CAMS x AK is up to -10 DU for SZAs > 60° (~1σ between -2 and -15 DU), which is significant in the context of the measured range of ozone abundances for this layer (~0-100 DU). Whilst the 170-50 hPa (~12-21 km) layer also shows a similar bias distribution, the 50-20 hPa (~21-27 km), and to a lesser extent the 20-5 hPa (~27-37 km) layer, sharply differ in this respect. Indeed, a dependency with respect to SZA of an opposing nature is evident, such as an overall tendency towards positive Ret – CAMS x AK values with increasing SZA (mean Ret – CAMS x AK differences of ~+5-10 DU for SZAs > 60° (~1σ above 0 DU), which compares with GOME-2A measured range of ozone amounts for this layer of ~40-120 DU) but a much greater number of negative outliers for SZAs between 50° and 80°. This is consistent with the identified anticorrelation between these two layers, and suggests that error in the B1 step (21-27 km layer) might be associated with SZA, which is compensated for in the 5.5-12 km layer (B2 step). For the 5-2 hPa (37-43 km) and 2-0.5 hPa (43-53 km) layers, the retrieval appears to be generally well behaved across the range of SZAs (absence of any significant outliers), albeit with a very slight overall positive bias for the GOME-2A instrument with respect to CAMS emerging for SZAs > ~60°. The reduced scatter for these layers could be explained by the high level of correspondence with the a priori at these altitudes in the retrieval.

For the total column (0-80 km), the Ret – CAMS x AK differences are overall very close to zero for a SZA ranging between 20° and 80°. Despite this, the spread of the density distribution markedly increases for higher SZAs (as also illustrated by the 1σ range), implying that SZA is an important variable in terms of explaining the potential for error to account for large differences in the satellite measurement versus the CAMS estimate of the true state, even when integrated over the full depth of the atmosphere. The fundamental reason for this is that the backscattered intensity of UV light that reaches each sensor is low at high SZAs, due to the ozone absorption path length increasing with sec(SZA) in the path from the sun to the scattering point. At the highest SZAs furthermore, the sphericity of the Earth also becomes important in determining absorption path length. With respect to lower SZAs, signal-to-noise ratios fall as factors such as dark current, photometric noise and stray-light from lower wavelengths become increasingly important, in association with the reduced UV photon flux received. Nonetheless, the high level of consistency in the density field for the total column corroborates the assertion that deficiencies in the B1 step, which manifest as large differences in the Ret – CAMS x AK differences for the 21-27 km and 27-37 km layer, are by and large

compensated for in the 5.5-12 km layer (and to a lesser extent the 12-21 km layer) in terms of opposing sign and magnitude.

The corresponding density fields of the Ret – CAMS x AK differences for the OMI instrument are shown for comparison in Figure 4.9, with respect to the measurement SZA. The profile biases are generally smaller for OMI than for GOME-2A, with more consistent clustering of profiles around zero throughout the range of measurement SZAs (20° to 80°), with significantly fewer large residual outliers evident. Nevertheless, some association of the mean bias especially, with respect to the SZA, is clear and some intriguing structures (unlike those seen for GOME-2A) emerge.

For the tropospheric subcolumn (0-5.5 km), mean biases are close to zero over the full range of SZAs, with the exception of a slight negative bias at low SZAs (> 30°) of up to ~2 DU. It should be noted however that a relatively small number of profiles (beyond the scale range shown here) exhibit a much larger difference with respect to CAMS for SZAs > 60°. Given that both instruments observe in a sun-synchronous orbit, albeit with

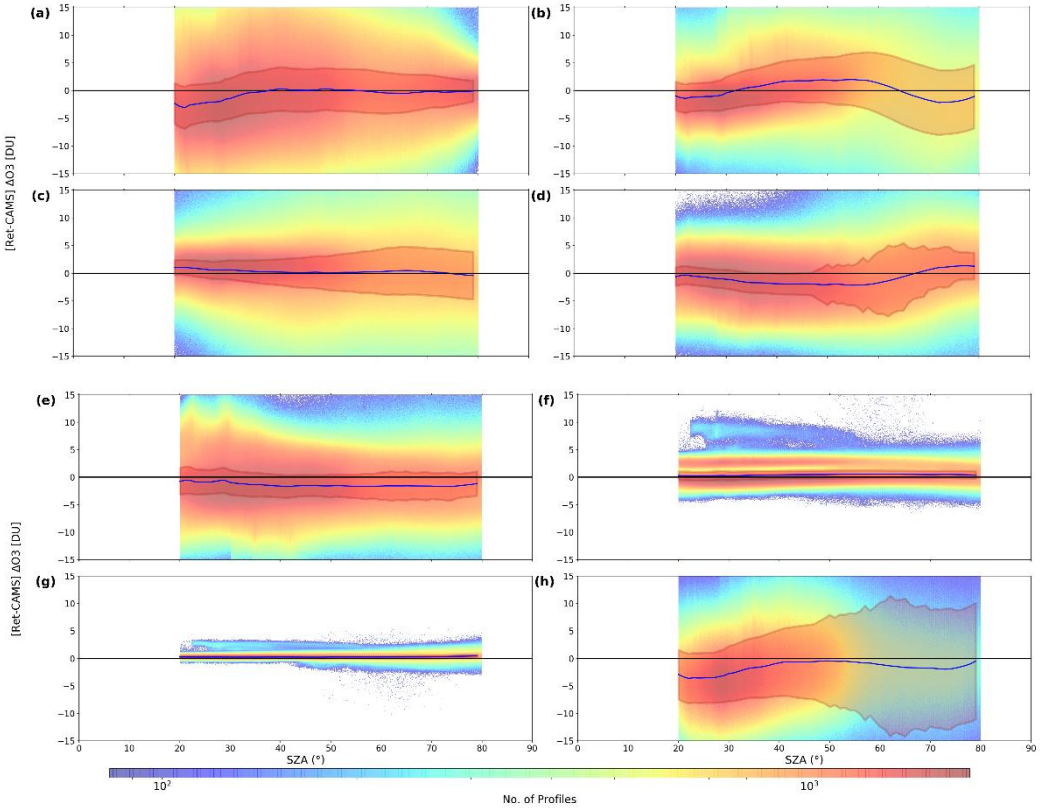

Figure 4.9 – Cloud density plots of the OMI Ret – CAMS x AK tropospheric ozone (0-5.5 km) differences (y-axis) versus the OMI (Ret) SZA (x-axis) for (**a**) the 0-5.5 km layer, (**b**) the 5.5-12 km layer, (**c**) the 12-21 km layer, (**d**) the 21-27 km layer, (**e**) the 27-37 km layer, (**f**) the 37-43 km layer, (**g**) the 43-53 km layer and (**h**) the 0-80 km (total column) layer. The mean variation in the OMI Ret – CAMS x AK differences as a function of SZA (°), as resolved on a 1° basis, is additionally overlaid (solid blue line) together with the standard deviation (1σ) calculated over all profiles (red shading).

differing local solar viewing times (~9:30 for GOME-2A and ~13:30 for OMI at the equator), it is obvious that these profiles are strongly associated with observation at high latitudes. Overall similar density distributions are observed for the overlying 450-170 hPa (5.5-12 km) and 170-50 hPa (12-21 km) layers, with the latter subcolumn in particular exhibiting increased incidence of outliers with increasing SZA, whilst the former is characterised by a greater number of positive outliers (particularly for SZAs > 40°). This scatter in the 450-170 hPa (5.5-12 km) layer appears to be related to increased negative scatter in the 50-20 hPa (21-27 km) layer, which would be consistent with the anticorrelation between the biases observed between those two regions. A small, opposing mean bias is also evident between these two layers which, interestingly, is largest for intermediate SZAs (~40-60°). Nonetheless, both aspects are not as obvious as for GOME-2A, but would be in agreement with the overall much smaller differences between these two layers for the OMI instrument. It is worth noting for OMI, that the retrieval appears well constrained for SZAs < 40° (differences almost uniformly less than ± 10 DU) but spread increases substantially for larger SZAs (~10^2 profiles of up to ± ~30 DU), despite close consistency for the majority of profiles.

Whilst the 20-5 hPa (27-37 km) layer shows lesser dependence with SZA, a secondary cluster of profiles emerges from the main distribution for the 5-2 hPa (37-43 km) layer. This is most pronounced for relatively low SZAs (~20-30°), with a positive bias of ~5-10 DU in layer, whilst profiles re-merge into the main cluster for SZAs of ~50-60 DU. A very small number of outliers is additionally evident for this layer at relatively high SZAs (~50-70°). A similarly structured feature is moreover apparent in the 2-0.5 hPa (43-53 km) layer, which is consistent with the vertical extension of this influence. This feature is unlike that seen for GOME-2A and therefore likely originates from an instrumental, sensor-specific cause. It however seems likely that such deficiency has minimal impact on the handling of the rest of the profile in these cases, given the absence of any corresponding structures for other layers, albeit this small, systematic bias is evidently not compensated for by any other layers. Finally and similarly to GOME-2A, the total column (0-80 km) bias distribution implies that the OMI retrieval is overall well behaved, and unsurprisingly both sensors exhibit a wider bias spread for higher SZAs. Despite this, a low bias of up to ~3-4 DU (1σ mostly below 0 DU) for SZAs between 20° and 40° can be discerned (similarly to as observed for the 0-5.5 km layer), but this is likely to be unrelated to SZA as issues associated with increased absorption path length only become relevant at higher SZAs. The inspection of layer dependencies in the Ret – CAMS x AK differences against SZA for

each instrument enable a principle cause of bias relating to deficiencies in radiative transfer modelling to be largely ruled out, together with effects relating to sphericity which become relevant at the highest SZAs. A much more pronounced dependence for GOME-2A instead points towards a potential issue with B1 spectroradiometry at low signal levels for this sensor.

4.3.3.2 Latitude

In the same manner as section 4.3.3.1, the distribution of the individual Ret – CAMS x AK profile differences for each sensor, with respect to the observation latitude, is again presented here in the form of density plots. This is first shown for GOME-2A in Figure 4.12. Of first note is that scatter in the GOME-2A subcolumns with respect to latitude is typically greater and more wide ranging in the extratropics versus the tropics on the whole. Whilst scatter exhibits a relatively wide spread outside of the tropics for almost all layers, spread within the tropics is confined to certain layers. This applies to the tropospheric subcolumn (0-5.5 km), even though the retrieval is inferred to be best constrained here, particularly in the Northern Hemisphere tropics. A systematic tendency towards a positive mean bias in the Northern Hemisphere extratropics is found, maximising between ~5-10 DU poleward of 60°N, whilst the Southern Hemisphere is affected by a region of greater spread between ~20°S and 45°S, and poleward of 60°S (despite no overall mean bias in the retrieval with respect to CAMS over all latitudes). The former feature can be attributed to the South Atlantic Anomaly (SAA) in Earth's geomagnetic field, in which charged particles striking the detectors substantially increases dark-current noise in the UV, leading to an increase in error in the retrieval of the stratospheric ozone profile (B1 step). Despite application of a B1-fail flag filter, this and peripheral regions are still adversely affected. Increased scatter (not shown) over the Antarctic continent is however skewed towards significant positive values (> 30 DU in a small number of cases) for the surface-450 hPa (0-5.5 km) layer.

The 450-170 hPa (5.5-12 km) differences with respect to latitude show much increased spread outside of the tropics (poleward of 30°N/S), as well as an overall negative tendency towards the polar regions (with a ~-5 to -10 DU mean difference here). A significant number of positive outliers are also present for this layer over Antarctica (up to ~+80 DU). Remarkable closeness between the retrieval and CAMS is also present for the 170-50 hPa (12-21 km) layer in the tropics, with similar association to the 450-170 hPa (5.5-12 km) layer evident in the extratropics, although mean differences in the polar regions are

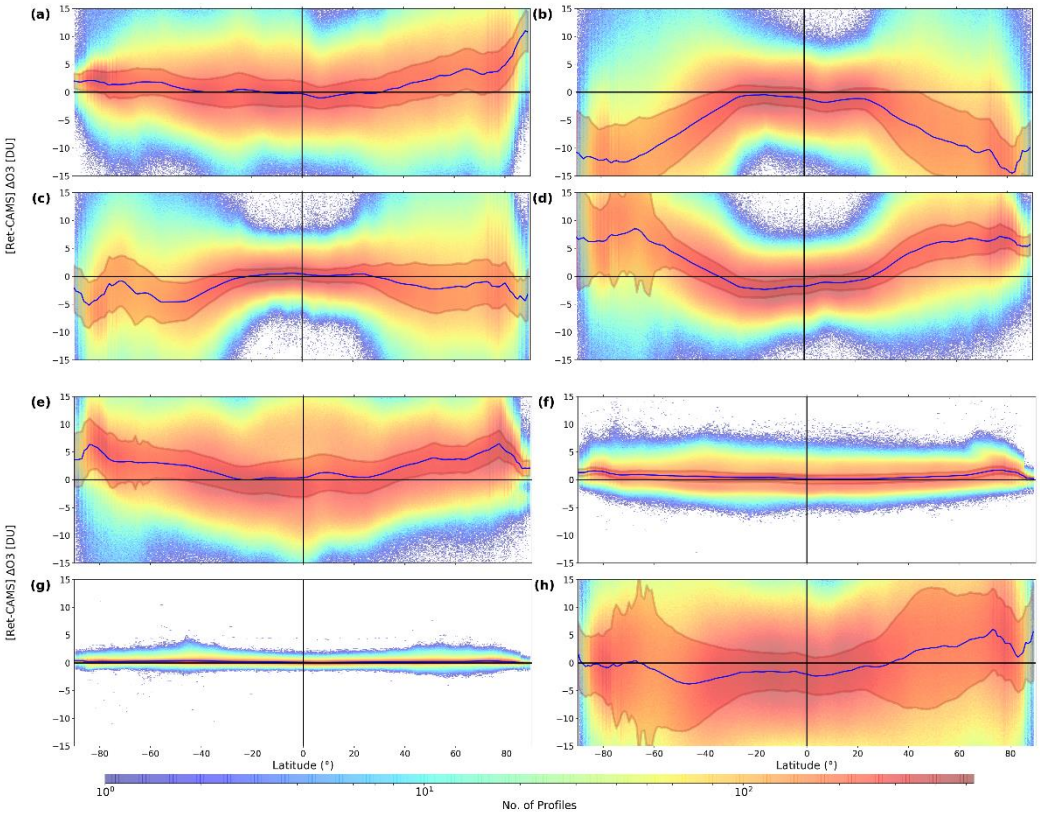

Figure 4.10 – Cloud density plots of the GOME-2A Ret – CAMS x AK tropospheric ozone (0-5.5 km) differences (y-axis) versus the GOME-2A (Ret) latitude (x-axis) for (**a**) the 0-5.5 km layer, (**b**) the 5.5-12 km layer, (**c**) the 12-21 km layer, (**d**) the 21-27 km layer, (**e**) the 27-37 km layer, (**f**) the 37-43 km layer, (**g**) the 43-53 km layer and (**h**) the 0-80 km (total column) layer. The mean variation in the GOME-2A Ret – CAMS x AK differences as a function of latitude (°), as resolved on a 1° basis, is additionally overlaid (solid blue line) together with the standard deviation (1σ) calculated over all profiles (red shading).

smaller (~0 to -5 DU). Compared with the 450-170 hPa (5.5-12 km) layer especially, the 50-20 hPa (21-27 km) layer shows opposing latitudinal association. Whilst mean differences and spread in the tropics remains small, an overall positive tendency is apparent in the extratropics with increasing latitude (~5 to 10 DU). Furthermore, a significant number of negative outlier profiles were present over Antarctica (up to ~-80 DU) that tallies with the minority of positive outliers commented upon for the 5.5-12 km layer. To a lesser extent, this feature extends up to the 20-5 hPa (27-37 km) layer, whilst the overall mean differences between the retrieval and CAMS show a slightly weaker dependency with latitude of up to ~5 DU, with much smaller residuals evident within the tropics. The 5-2 hPa (37-43 km) layer further follows suite, with indication of only a very slight dependency in the mean at high latitudes (~+2 DU). A slight dependency with latitude is evident also for the 2-0.5 hPa (43-53 km) layer, but only in terms of scatter and not in a mean sense, which is most pronounced for a minority of profiles between ~30°S and 50°S (again consistent with the latitude of the SAA region). For the total column (0-

80 km), spread in the Ret – CAMS x AK differences greatly increases once more outside of the tropics (1σ spanning both sides of the zero lines), but is generally largest in mid-latitudes. This reflects the cancellation of the large outlier differences for the 21-27 km layer across Antarctica further down in the 5.5-12 km layer especially. In contrast, individual layer dependencies over mid-latitudes appear to arise as a result of factors that are not necessarily exclusive to any particular altitude range, or indeed specifically to the B1 or B2 step of the retrieval. An overall mean bias for the total column of up to ~+5 DU is found at Northern Hemisphere high-latitudes, which contrasts with a small mean negative bias in the tropics and Southern Hemisphere mid-latitudes (~-2 to -3 DU). This tendency is very similar to that seen for the 0-5.5 km layer, which further supports the notion that the errors in the stratospheric retrieval associated with the B1 step are largely compensated for in lower layers.

The same Ret – CAMS x AK dependencies are subsequently shown for the OMI instrument in Figure 4.11, with the mean dependency and 1σ shading overlaid as before for each layer. The latitudinal dependencies of the spread of the distributions are overall very similar to GOME-2A, which reflects the latitudinal distribution of ozone subcolumns (for a given fractional error, there would be a larger subcolumn error (DU) in the extratropics than the tropics). Also, the same retrieval scheme has been applied to both sensors so its deficiencies are common to both sensors. Whilst the overall spread is increased for the tropospheric subcolumn (0-5.5 km) with respect to GOME-2A, likely due to a much larger number of samples in the distributions and increased noise at low UV signal levels associated with high SZAs, there is very little latitude dependence in the mean bias for this instrument. Nevertheless, spread does increase in the extratropics, which may be related to factors such as the SZA that has been shown, in section 4.3.3.1, to be associated with dependencies in the Ret – CAMS x AK differences. Beyond the scale range shown here, a few noteworthy outliers (~10^1 profiles) were found over Antarctica for this subcolumn (mostly positive, but with a few that are negative close to ~60°S), as well as over the Arctic region (~70-80°N). Similarly to GOME-2A, the 450-170 hPa (5.5-12 km) layer residuals are consistently small throughout the tropics, but are much more wide ranging in the extratropics. A mean negative bias of up to ~5-10 DU (1σ of the mean below zero) is visible over Antarctica and between ~70-80°N. Overall spread appears to be largest in mid-latitudes for this layer, with the exception of a small minority of very large positive Ret – CAMS x AK differences over the Antarctic region (up to ~100 DU). This further applies to the 170-50 hPa (12-21 km) layer, albeit with a sharp reduction in the

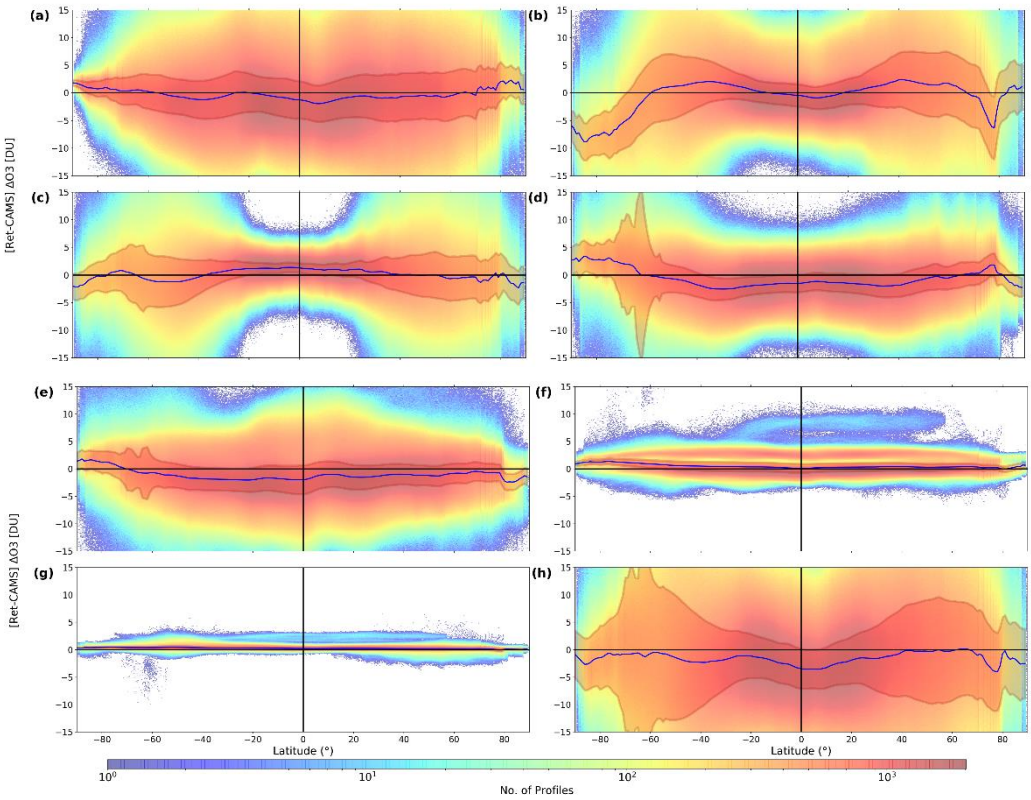

Figure 4.11 – Cloud density plots of the OMI Ret – CAMS x AK tropospheric ozone (0-5.5 km) differences (y-axis) versus the OMI (Ret) Latitude (x-axis) for (**a**) the 0-5.5 km layer, (**b**) the 5.5-12 km layer, (**c**) the 12-21 km layer, (**d**) the 21-27 km layer, (**e**) the 27-37 km layer, (**f**) the 37-43 km layer, (**g**) the 43-53 km layer and (**h**) the 0-80 km (total column) layer. The mean variation in the OMI Ret – CAMS x AK differences as a function of latitude (°), as resolved on a 1° basis, is additionally overlaid (solid blue line) together with the standard deviation (1σ) calculated over all profiles (red shading).

number of outliers and reduced overall spread for all latitudes, but particularly within the tropics. This is additionally the case for the 50-20 hPa (21-27 km) layer, but with increased scatter prevalent over the Antarctic continent region. The Ret – CAMS x AK differences for these outliers are significantly negative (up to -100 DU), which again compensates for outliers of up to ~+100 DU for this region within the 5.5-12 km layer. A slight mean positive (negative) bias is apparent over Antarctica (low- to mid-latitudes), which is largely anti-correlated against the 450-170 hPa (5.5-12 km) region.

For the layers 20-5 hPa (27-37 km), 5-2 hPa (37-43 km) and 2-0.5 hPa (43-53 km), the dependency with latitude becomes much smaller in the same vain as GOME-2A, in both a mean sense and in terms of the overall density scatter. However, an interesting bimodal structure begins to emerge for the 37-43 km layer in particular, even trimodal between ~30°S to 50°N, in which the retrieval either underestimates (~1-2 DU) or overestimates slightly (~2-3 DU) with respect to CAMS. This would need to be examined further but could be explained by the relatively low photon flux, and thus signal-to-noise ratio, received for

the retrieval at these altitudes (in the shortest wavelengths of the Hartley band region). Therefore sensitivity to radiometric offset error, such as caused by stray-light, is increased. A dependency with respect to time through the mission might be anticipated as optical degradation inevitably occurs during the mission lifetime. A smaller density of profiles between ~30°S and 50°N are also shown to have Ret – CAMS x AK differences of up to ~+10 DU. Such intriguing structures were not evident for GOME-2A, but similar behaviour was noted with respect to SZA (for relatively low SZAs) in section 4.3.3.1, indicating potential association with SZA for this region as a function of a likely instrument-specific issue. Finally, the total column (0-80 km) differences show the same behaviour as GOME-2A, with maximum spread in the Ret – CAMS x AK differences across mid-latitudes (but locally largest around the periphery of Antarctica where 1σ encompasses a Ret – CAMS x AK difference of between ± 25 DU) and closest agreement in the tropics, reflecting the latitudinal variation of the total column, and extremely close agreement in the mean with CAMS. The mean bias on the other hand is very small across all latitudes, with a slight negative overall bias however shown at low-latitudes. Analysis of the outlier profiles beyond the scale range shown here, indicate that the erratic behaviour of a small number of outliers for individual stratospheric layers in the B1 retrieval is largely compensated for in the B2 retrieval. It is worth noting that these cases significantly increase in number when standard filtering is not applied, suggesting that these profiles only just surpass accepted limits for inclusion in the evaluations shown (such as peripheral areas around the SAA region).

4.3.3.3 Scattering Angle Dependence

Dependencies in the Ret – CAMS x AK differences are subsequently shown in this sub-section with respect to the scattering angle of the Earthshine reflectance for each sensor. Evaluation of this quantity, together the computed Rayleigh scattering phase function, will help to elucidate possible deficiencies associated with polarisation effects, which are induced as trace gases such as ozone scatter light back towards each instrument in the UV. Figure 4.12 firstly shows the Ret – CAMS x AK dependence over the range of scattering angles measured by the GOME-2A for the same seven subcolumns as before, together with the total column. As in the previous section, the mean dependency and one standard deviation interval (spread) as a function of scattering angle are additionally shown (solid blue line and red shading respectively), as resolved on a 1° basis. Although considerable scatter extends beyond the vertical scale range shown here, the main clustering of profiles

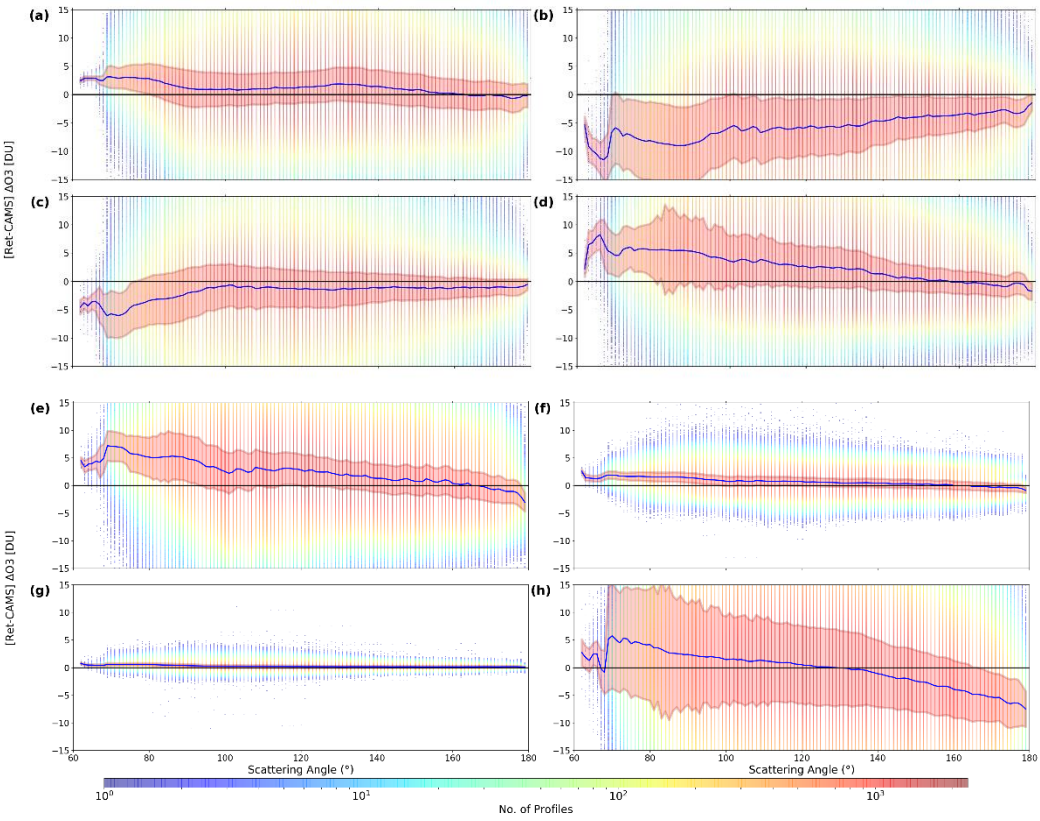

Figure 4.12 – Cloud density plots of the GOME-2A Ret – CAMS x AK (0-5.5 km) differences (y-axis) versus the GOME-2A (Ret) scattering angle (°) (x-axis) for (**a**) the 0-5.5 km layer, (**b**) the 5.5-12 km layer, (**c**) the 12-21 km layer, (**d**) the 21-27 km layer, (**e**) the 27-37 km layer, (**f**) the 37-43 km layer, (**g**) the 43-53 km layer and (**h**) the 0-80 km (total column) layer. The mean variation in the GOME-2A Ret – CAMS x AK differences as a function of the scattering angle (°), as resolved on a 1° basis, is additionally overlaid (solid blue line) together with the standard deviation (1σ) calculated over all profiles (red shading).

with respect to the scattering angle (between the solar path and the line-of-sight) is relatively close to zero in each case across the range of scattering angles recorded.

However, a small mean dependency is evident for most layers at low scattering angles more especially. For the surface-450 hPa (0-5.5 km) subcolumn, a small positive mean bias of up to 3-4 DU is evident for scattering angles between 60° and 90°. However this feature is not likely of significance as it is confined to the edge of the distribution range. For the 450-170 hPa (5.5-12 km) layer however, the magnitude of the earlier identified underestimation of the retrieved values with respect to CAMS exhibits some dependence with scattering angle. At acute scattering angles (< 90°), when the atmospheric path length is relatively short, the mean difference is up to -10 DU (1σ range confined below zero), which reduces gradually for obtuse angles (> 90°) (although the 1σ range remains almost exclusively below zero). For scattering angles approaching 180°, when light is scattered in the forward direction (as can occur at high SZAs), the mean difference is much smaller (~-1-2 DU). In contrast, the mean differences are close to zero (up to ~-5 DU) for

obtuse (acute) angles within the 170-50 hPa (12-21 km) layer. In connection with the established anticorrelation between the 50-20 hPa (21-27 km) and 450-170 hPa (5.5-12 km) layers, the mean scattering angle dependency for 21-27 km strongly mirrors that seen for 5.5-12 km in an inverse fashion. This is somewhat true also for the 20-5 hPa (27-37 km) layer. Both the 5-2 hPa (37-43 km) and 2-0.5 hPa (43-53 km) subcolumns show close agreement throughout, although a very obvious dependence is found for the total column (0-80 km). At lower scattering angles, a mean positive Ret – CAMS x AK bias of up to ~5 to 8 DU is found (albeit the 1σ range is large), which converges around zero for angles between ~100° and 140°, before falling to ~-5 to -8 DU for angles approaching 180°. As a fraction of the total column however, such differences are only very small which negates the significance of this dependency to an extent. It should be noted that the dependencies commented on here for GOME-2A are strongly associated with that seen for SZA and latitude, as all three variables are intrinsically related.

The Ret – CAMS x AK dependence as a function of scattering angle measured by the OMI instrument is next shown for comparison in Figure 4.13.. Again, the mean bias appears to exhibit little dependency with scattering angle for each layer, although significant structure is presenr for the scatter of outlier points beyond the vertical scale range shown here, as identified earlier for OMI with respect to SZA and latitude. Nevertheless, such consistency points to an origin of the biases principally not involving scattering/polarisation effects. For the surface-450 hPa (0-5.5 km) layer, a low bias of ~5 DU exist for scattering angles less than ~30° and a high bias exceeding 5 DU for scattering angles larger than 80°, with close agreement for intermediate scattering angles. A similar pattern is also evident for the 450-170 hPa (5.5-12 km) layer, which is supportive of influence intrinsic to the Huggins band (B2 step) regime. Indeed, the dependence of the Ret – CAMS x AK mean bias is well behaved for the 170-50 hPa (12-21 km) layer, albeit with more variance for intermediate scattering angles (as also reflected by the 1σ shaded region). This follows also for the 50-20 hPa (21-27 km) and the 20-5 hPa (27-37 km) subcolumn, although a systematic negative bias emerges for this layer at relatively high scattering angles (> 80°) of up to ~-3 to -4 DU. For the layers 5-2 hPa (37-43 km) and 2-0.5 hPa (43-53 km), the mean difference cannot be distinguished from the zero line, as agreement is very close (with the exception of a small number of positive values associated with the bimodal structure identified with respect to SZA and latitude in sections 4.3.3.1 and 4.3.3.2. For the total column (0-80 km), the mean bias with respect to scattering angle is very closely associated with that seen for the troposphere or surface-

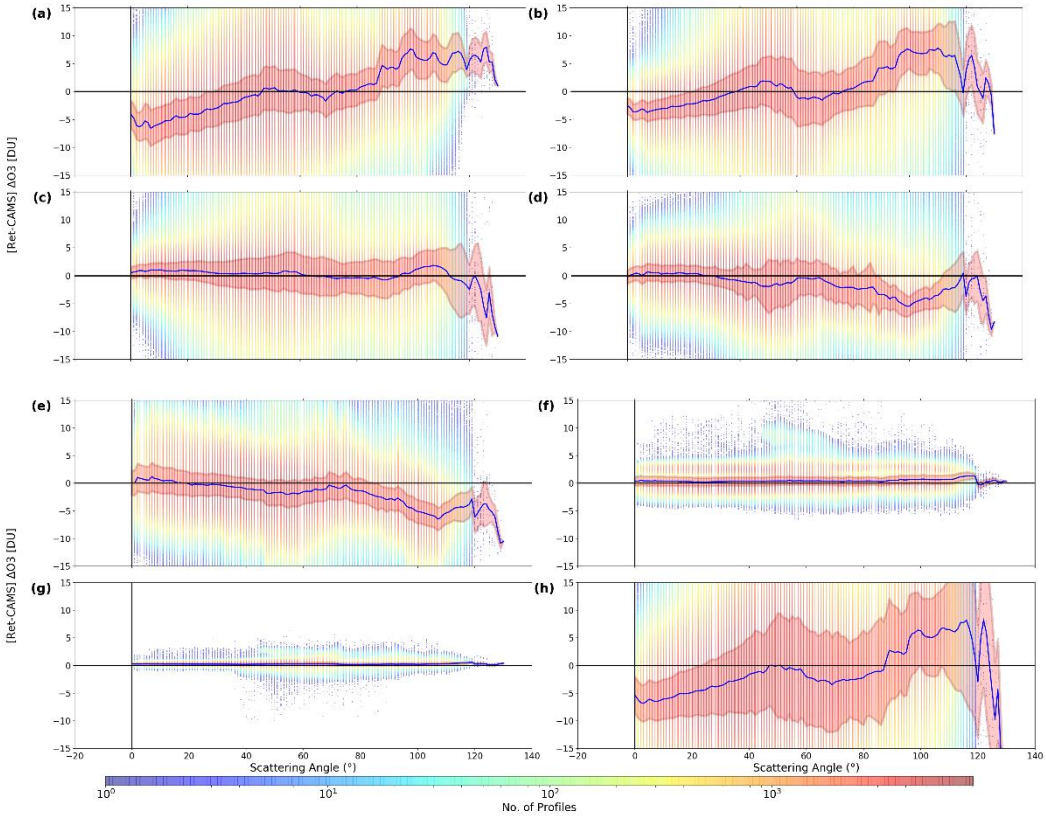

Figure 4.13 – Cloud density plots of the OMI Ret – CAMS x AK tropospheric ozone (0-5.5 km) differences (y-axis) versus the OMI (Ret) scattering angle (°) (x-axis) for (**a**) the 0-5.5 km layer, (**b**) the 5.5-12 km layer, (**c**) the 12-21 km layer, (**d**) the 21-27 km layer, (**e**) the 27-37 km layer, (**f**) the 37-43 km layer, (**g**) the 43-53 km layer and (**h**) the 0-80 km (total column) layer. The mean variation in the OMI Ret – CAMS x AK differences as a function of the scattering angle (°), as resolved on a 1° basis, is additionally overlaid (solid blue line) together with the standard deviation (1σ) calculated over all profiles (red shading).

450 hPa layer, as a likely consequence of the dependencies introduced in the B1 step (between 21 and 27 km primarily) and compensated in the 5.5-12 km layer. The purpose here of evaluating possible layer Ret – CAMS x AK dependencies with respect to scattering angle is to discern an approximate influence from polarisation effects and/or forward model errors. Although, the forward model used for these two UV-nadir sounders uses a scalar approximation that does not take into account polarisation effects, a correction is implemented from look-up tables. Error associated with this approach could thus also influence the observed mean biases for each sensor.

Finally, the Ret – CAMS x AK differences with respect to the computed Rayleigh scattering phase function (RSCAT PF) are displayed for each instrument in this sub-section. The RSCAT PF is a nondimensional quantitative measure of the angular distribution of scattered radiation and is defined using the following equation:

$$RSCAT\ PF = 1 + \cos^2\left(scat \cdot \frac{\pi}{180}\right) \quad (4.2)$$

Where *scat* is the scattering angle (°) (the angle between the solar path and the instrument line-of-sight) as shown previously in section 4.3.3.3. This transformation of the scattering angle dependence helps to show layer associations of the Ret – CAMS x AK differences more clearly as a function of light intensity and also polarisation effects due to single scattering, which is particularly relevant for top-of-the-atmosphere backscattered radiances in B1 wavelengths (< 300 nm). In Figure 4.14, the layer Ret – CAMS x AK differences for GOME-2A with respect to the computed Rayleigh scattering phase function are shown. For the surface-450 hPa (0-5.5 km) layer, the mean bias is slightly positively biased between ~0-3 DU, particularly for more intermediate values (~1.3-1.5). For the 450-170 hPa (5.5-12 km) subcolumn, a general negative bias (1σ range consistently below zero) is found with the largest values for lower phase function values (up to ~5 DU). The mean Ret – CAMS x AK dependence is well behaved generally for the 170-50 hPa (12-21 km), but with an anticorrelated dependence to the 5.5-12 km layer evident for the above 50-20 hPa (21-27 km) region. This is consistent with the pattern identified for GOME-2A, with a general negative and positive bias of approximately opposing magnitude between the 5.5-12 km and 21-27 km subcolumns respectively. The mean bias shows a similar dependence for the 20-5 hPa (27-37 km) layer with respect to the 21-27 km layer, with close agreement maintained throughout for the above 5-2 hPa (37-43 km) and 2-0.5 hPa (43-53 km) layers for the Ret – CAMS x AK differences with respect to the Rayleigh scattering phase function. The total column (0-80 km) subplot reveals a general downward sloping mean dependence, such that a slight positive bias is evident at low values (~1-2 DU) and a more noticeable positive bias exists at high values (up to ~-5 DU). The presence of a slope for certain layer dependencies here implies that polarisation effects exert some influence over the mean Ret – CAMS x AK profile difference, as a phase function value of 1.0 indicates polarisation in only one component compared with two components for a phase function value of 2.0 in the Rayleigh single scattering regime from stratospheric altitudes.

The same Ret – CAMS x AK differences versus the computed Rayleigh single scattering phase function are next shown for OMI in Figure 4.15. For the surface-450 hPa (0-5.5 km) layer, a downward slope in the mean dependence is apparent, which largely mirrors that also seen for the 450-170 hPa (5.5-12 km) region. Whilst the mean dependence is negligible throughout for the 170-50 hPa (12-21 km) layer, behaviour anticorrelated to that seen for the 5.5-12 km layer is evident for the 50-20 hPa (21-27 km) subcolumn. This is supportive of the compensation for an induced bias in the B1 step (in association with

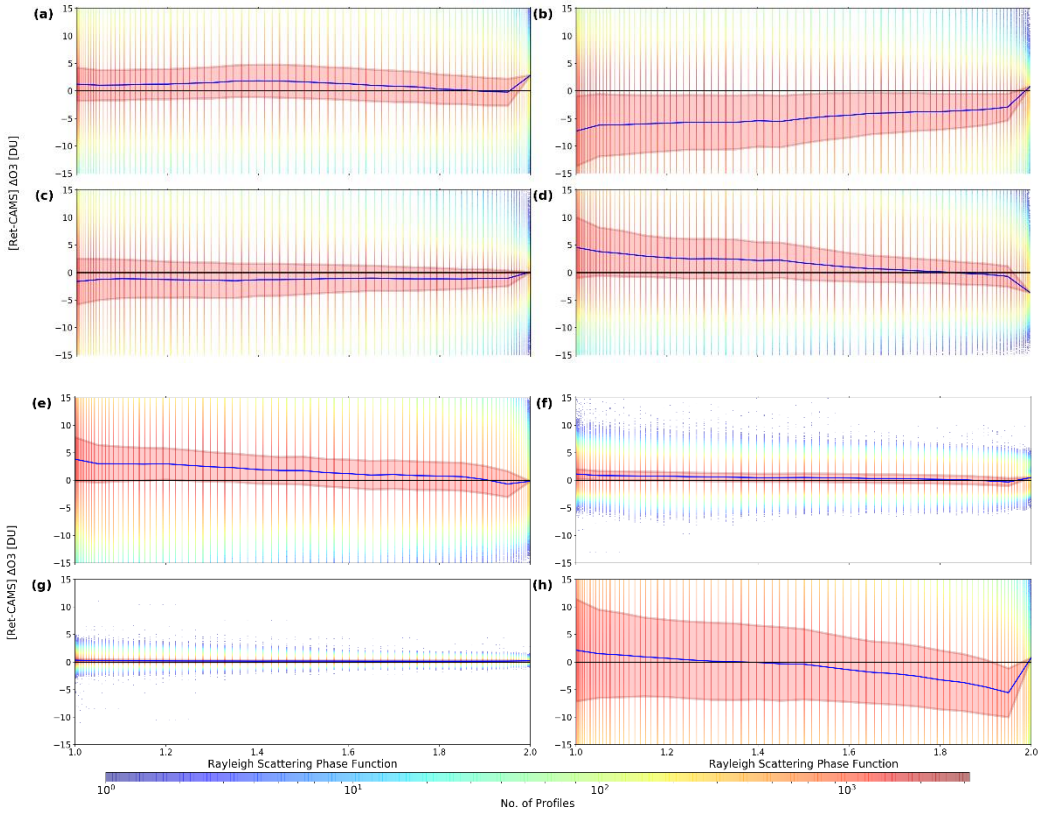

Figure 4.14 – Cloud density plots of the GOME-2A Ret – CAMS x AK tropospheric ozone (0-5.5 km) differences (y-axis) versus the GOME-2A (Ret) computed Rayleigh scattering phase function (x-axis) for (**a**) the 0-5.5 km layer, (**b**) the 5.5-12 km layer, (**c**) the 12-21 km layer, (**d**) the 21-27 km layer, (**e**) the 27-37 km layer, (**f**) the 37-43 km layer, (**g**) the 43-53 km layer and (**h**) the 0-80 km (total column) layer together with the standard deviation (1σ) calculated over all profiles (red shading).

the stratospheric ozone peak region) further down in the B2 step, as is also the case for GOME-2A and seen earlier for both sensors in section 4.3.1. The mean bias tendency for the 21-27 km layer also extends up to the 20-5 hPa (27-37 km) region, although no dependency is found for the higher layers; both 5-2 hPa (37-43 km) and 2-0.5 hPa (43-53 km) above the stratospheric ozone peak. For the total column (0-80 km) as a whole however, a general downward slope of the mean bias is evident for increasing phase function values, albeit with some oscillatory behaviour. For instance, a slight negative bias (up to ~-2 DU) is found for values between ~1.1 and 1.25, whereas a negligible mean bias is found for more intermediate phase function values (~1.3 and 1.5), before an increasing mean negative bias restabilises for higher values (> 1.5). Such complexity in these dependencies for the total column and other layers warrants further investigation, but could indicate issues with polarisation effects and scattering, even at more modest SZAs and/or lower latitude regions. Although the polarisation scrambler for the OMI instrument should in principle mean that any biases shown here are independent of polarisation state, the precision may be imperfect in the UV so some dependence could

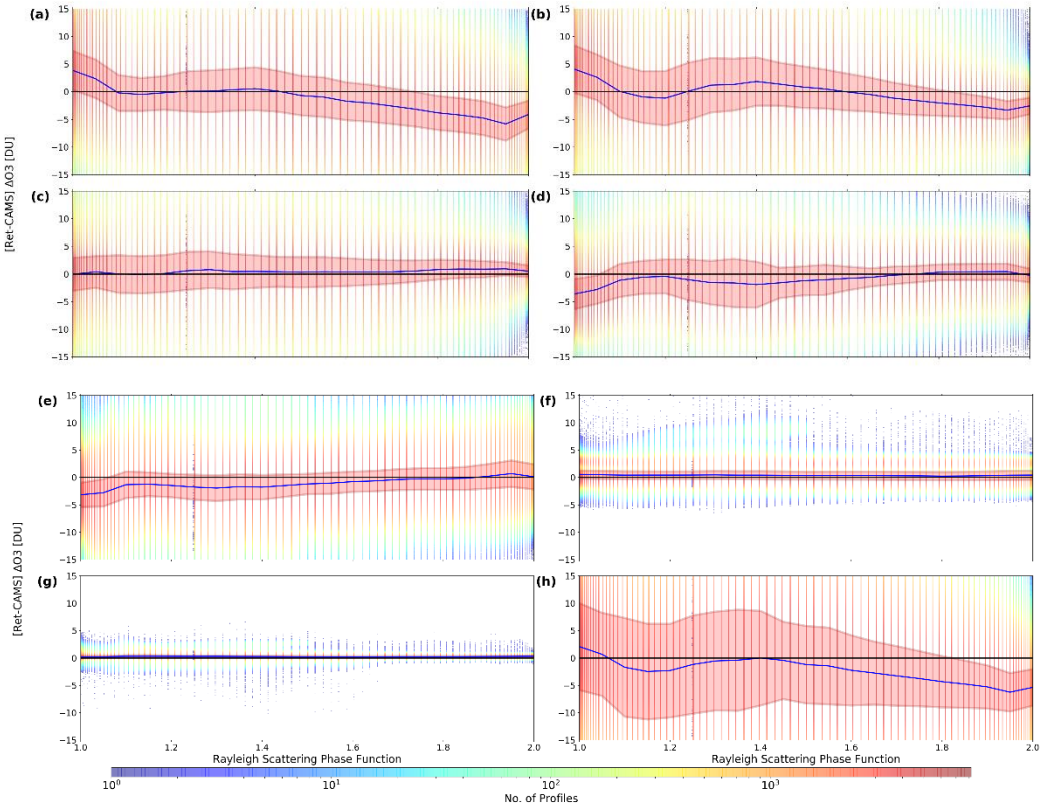

remain. Nonetheless however, the SZA and latitude appear to be most correlated with mean dependencies of the layer Ret – CAMS x AK differences, suggesting that scattering and polarisation effects are of lesser importance (although again this cannot be easily disentangled as these variables are intrinsically related).

4.4 Summary and Recommendations

Investigation of biases in the RAL ozone profile retrieval for two UV-nadir sounders (GOME-2A and OMI), as quantified with respect to the CAMS reanalysis, indicate potential deficiencies in handling of the B1 stratospheric profile retrieval. The B1 retrieval step involves extraction of information from the ~266-307 nm range of the Hartley band. Although CAMS cannot be regarded as a fully independent dataset for this application, as both OMI and GOME-2A total column information (together with height resolved information from OMI) are assimilated in this product, the OMI and GOME-2 data compared here have not been biased corrected and constitute only two of many satellite datasets that are assimilated. In particular, limb sounder information more strongly influences the spatial variability of stratospheric ozone within CAMS. The C-IFS representation of ozone formation, loss and transport is furthermore likely to significantly influence the representation of ozone in CAMS analyses (B. Kerridge, personal communication).

The main conclusions of the assessment undertaken here are listed below:

- A strong anticorrelation of the Ret – CAMS x AK mean bias is exists between the 450-170 hPa (5.5-12 km) and the 50-20hPa (21-27 km) layers in particular, for both the GOME-2A (2007-2017) and OMI (2004-2018) instruments.
- Having resolved multi-year mean differences with CAMS for each instrument on a latitude band (10° interval) versus month basis, Pearson (*r*) correlation coefficient values of -0.916 and -0.790 were calculated for GOME-2A and OMI, respectively, between the biases in these two subcolumns.
- Total columns derived by integration of profiles retrieved from the B2 step agree extremely well with CAMS, so the inference is that bias structure induced in the 21-27 km layer (and higher layers) in the B1 step (overall positive bias for GOME-2A and smaller negative bias in OMI), is largely compensated in the B2 step in the 5.5-12 km layer (as indicated by an overall negative bias pattern for GOME-2A and positive bias pattern for OMI of approximately equal and opposite magnitudes to those in the 21-27 km layer).
- The partial resemblance between the tropospheric (0-5.5 km) layer and the total column (0-80 km) biases for each instrument indicates however that propagation of a residual B1 bias might still contribute to the surface-450 hPa (0-5.5 km) layer biases, in addition to bias contribution induced during the B2 (Huggins band) step of the retrieval. Bias in the 0-5.5km layer will in part be due to compensation for residual stratospheric bias induced in the B1 step which has not been fully accommodated in the 5.5-12km layer and partly to bias inherent to the B2 (Huggins band) step itself.

It would be clearly desirable to improve handling of the stratospheric retrieval in the B1 step; both for its own sake and to eliminate the need for compensation in lower layers in the B2 step. Two retrieval tests are recommended to gain further insight:

1) Relaxation of ozone profiles to CAMS in the B1 step, to establish whether B1 spectra could be fitted solely in terms of the other geophysical and instrumental variables which are currently co-retrieved
2) Relaxation of stratospheric ozone profiles to CAMS in the B2 step, to quantify biases in tropospheric ozone arising from the B2 step alone.

This work has identified that the layer Ret – CAMS x AK residuals for each instrument, but most notably for GOME-2A, exhibit dependencies with respect to variables such as SZA

and latitude. Stratospheric biases arising during the B1 step could therefore originate from issues associated with SZA (and thereby also a function of latitude), such as radiometric throughput and calibration. Indeed, the dependence with latitude (section 4.3.3.2) highlights such issue to be specific to the extratropics. It is likely that improvement is needed for retrievals at higher SZAs where UV light levels are low and sensitivity to stray-light and detector dark current is high. The additional role of scattering dependence and polarisation effects was also presented in this chapter. Although further work is necessary to full understand the importance of these effects, individual layer dependencies imply some contribution, particularly for the GOME-2A sensor. Whilst OMI involves an onboard correction for polarisation to apply a correction, thus mitigating any raw dependencies minus any deficiencies from radiometric inprecision in the UV, GOME-2A adopts a more simplistic correction based on look-up tables. It is therefore perhaps not surprising that a greater dependence of the GOME-2A Ret – CAMS x AK differences is evident with respect to the computed Rayleigh scattering phase function in particular, compared with OMI. For scattering angles approaching 90°, which yields a Rayleigh scattering phase function value close to 1.0 (as derived by Equation 4.2), indications of a dependence may stem from the reduced light intensity registered, as only one polarised component of light is directed towards the instrument compared with two for phase function values approaching 2.0. The causes of biases induced in the B1 step need to be understood further, in relation to SZA and the suite of other geophysical and instrumental variables considered here, and potentially also those which have not been investigated so far. Rectification of deficiency in the B1 step and repeat of the analysis conducted here would then reveal potential issues with the retrieval in the B2 (Huggins band) step.

Chapter 5

The regional and seasonal aspects of the global tropospheric ozone climatology are explored and quantified in this chapter, through the use of a combined model-measurement approach. Near global, multi-year observations from the Ozone Monitoring Instrument (OMI), together with limited information from ozonesondes, are first used to verify the accuracy of simulated tropospheric ozone over a common baseline period (2005-

2010) from two state-of-the-art Chemistry-Climate Models (CCMs): EMAC and CMAM on a seasonally resolved basis. Noting the quantified model biases from this assessment, the simulated stratospheric influence is investigated and compared on a regional and seasonal basis, as facilitated using the model tagged stratospheric ozone (O_3S) tracers. Finally, recent changes in tropospheric ozone according to each model simulation are quantified over a 30-year climatological period (between 1980-1989 and 2001-2010). The seasonal influence of the stratosphere in influencing these recent changes is furthermore elucidated. The main chapter conclusions and wider discussion is then finally provided.

Characterising the Seasonal and Geographical Variability of Tropospheric Ozone (O_3), Stratospheric Influence and Recent Changes

This chapter contains results of a study (Williams et al., 2019) published in the journal Atmospheric Chemistry and Physics. A modified version of the results and discussion section is here presented, although the content and layout is very similar to that published. Please refer to the study for full context: Williams, R. S., Hegglin, M. I., Kerridge, B. J., Jöckel, P., Latter, B. G., and Plummer, D. A.: Characterising the seasonal and geographical variability in tropospheric ozone, stratospheric influence and recent changes, Atmos. Chem. Phys., 19, 3589–3620, https://doi.org/10.5194/acp-19-3589-2019, 2019.

In this chapter, a combined model-measurement approach is implemented to diagnose the regional and seasonal climatology of tropospheric ozone, which is known to be poorly constrained (Stevenson et al., 2006; Wu et al., 2007; Cooper et al., 2014; Gaudel et al., 2018). This study further serves to provide an update to earlier studies which quantify stratospheric influence on tropospheric ozone (e.g. Lamarque et al.,1999). Quantification of biases in hindcast specified-dynamics simulations from two state-of-the-art chemistry-climate models (CCMs) (EMAC and CMAM), which constitute two out of the 20 participating models as part of the Chemistry Climate Model Initiative (CCMI) (Morgenstern et al., 2017), is here provided with respect to satellite and in situ observations over a common baseline period (2005-2010). Using the knowledge derived from this model-measurement comparison assessment, the stratospheric influence on the regional distribution and seasonality of tropospheric ozone is then investigated with respect to in situ production from ozone precursor emissions over a much longer time period (1980-2010). The choice of the EMAC and CMAM CCMs for evaluations in this

chapter were selected on the basis of the definition of the stratospheric-tagged ozone (O_3S) tracers. Compared with other CCMI models, the model O_3S tracers contain the same interactive chemistry as the primary ozone simulations, except in the troposphere where ozone production reactions are neglected (see section 3.4.3 for the specific details for each model). In contrast, O_3S tracers (where available) are less robustly defined and are much more simplistic for other models as part of CCMI, and are therefore less suited to the application of this study. As a final component, both sets of ozone and O_3S hindcast simulations are then used to examine seasonal changes over the 34-year period, by comparing the last 10 years with the first 10 years of this period. Crucially, the contribution of the stratosphere to long-term changes in ozone, ranging from near the tropopause (~350 hPa) to the surface, is elucidated in each model and compared to highlight features of consistency. The overall findings and wider implications of this research are then discussed. Notably, the stratospheric influence is found to be larger than previously thought compared with earlier studies (e.g. Lamarque et al., 1999) and the importance of a well-resolved stratosphere is highlighted for accurate simulations of the stratospheric contribution to tropospheric ozone.

In order to evaluate the utility of the models in assessing tropospheric ozone and estimating stratospheric influence, the CCM simulations (EMAC and CMAM) are first validated here against the OMI observations, in addition to the spatially and temporally limited, height resolved ozonesonde measurements. This is achieved through a combined model-measurement characterisation of the seasonal and geographical variability of tropospheric ozone (section 5.1), together with the interannual variability (Section 5.2) over the 2005-2010 period. Lastly, a vertically resolved assessment of the CCMs is provided for three different mid-latitude regions (Europe, eastern North America and the Tasman Sea) from aggregated ozonesonde profile measurements between 1980 and 2010 (section 5.3).

5.1 Tropospheric Ozone (O_3) (Model-Measurement Comparison)

Seasonal composites of monthly mean surface-450 hPa (0-5.5 km) subcolumn ozone from OMI, together with available ozonesonde-derived AK-fitted subcolumns, and the respective differences for each AK-fitted CCM are shown in Figure 5.1. A seasonal maximum in tropospheric ozone is evident in each hemisphere during spring, which is more pronounced in the Northern Hemisphere and extended in many regions through to

summer (JJA). In contrast to the extratropics, tropospheric ozone remains low year-round (<20 DU) at low-latitudes although some seasonality is apparent; notably a northward shift in the region of lowest ozone from boreal winter into summer, and the reverse from boreal summer back to winter. This is likely associated with the seasonal migration of the Inter Tropical Convergence Zone (ITCZ) which closely follows the region of maximum solar insolation. In this region, strong upwelling occurs which leads to the transport of ozone depleted air from the tropical PBL upwards towards the tropopause. This is most pronounced across the Maritime Continent where convective activity is climatologically most intense (e.g. Thompson et al., 2012).

The Brewer-Dobson Circulation (BDC), which leads to meridional transport in ozone and other constituents in the stratosphere, is strongest during winter (weakest during summer) and it is this annual variability which exerts a major influence over the seasonality of free tropospheric ozone (through changes in stratosphere-troposphere exchange; STE), in regions of the extratropics where emissions of tropospheric ozone precursors are at a relatively low background level (Logan, 1985; Roscoe, 2006; Hegglin et al., 2006). This is invariably the case across much of the Southern Hemisphere, where anthropogenic precursor emissions are substantially lower and more spatially confined in comparison with the Northern Hemisphere. In some regions such as the South Atlantic, it is evident that tropospheric ozone is similarly high in winter (JJA) (~25-30 DU) but it is known that this is a result of biomass burning activity in western Africa and resultant plumes which are advected offshore during the dry season in particular (e.g. Mauzerall et al., 1998). Across Antarctica and the Southern Ocean however, halogen-induced stratospheric ozone depletion is likely the dominant driver of the seasonality; leading to a minimum in spring (SON), although no observations from OMI are available during the polar night (MAM and JJA). In the Northern Hemisphere, the strong influence of emission precursors from widespread anthropogenic activity serves to delay and broaden the maximum, since the peak in the in situ photochemical formation of ozone is driven by solar insolation. This is particularly apparent in subtropical regions such as the eastern

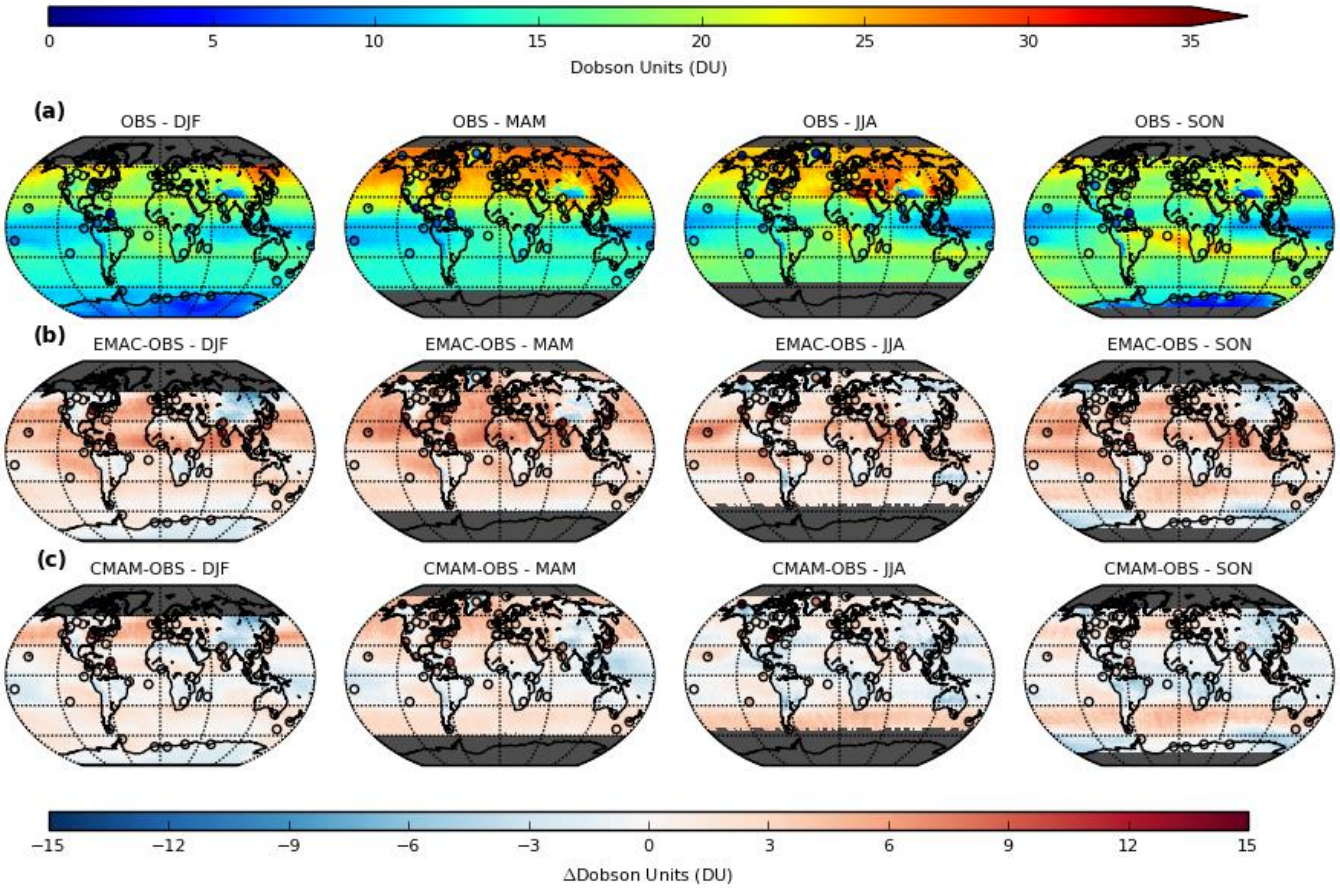

Figure 5.1 – Seasonal composites of monthly averaged surface-450 hPa (0-5.5 km) subcolumn O_3 (DU) for 2005-2010 (left to right) from (**a**) OMI, (**b**) EMAC minus OMI and (**c**) CMAM minus OMI. Circles denote (**a**) equivalent ozonesonde-derived subcolumn O_3 (DU), (**b**) EMAC minus ozonesonde differences and (**c**) CMAM minus ozonesonde differences. All data was regridded to 2.5° resolution (~275 km). All model and ozonesonde subcolumn data has been modified using AKs to ensure a direct comparison.

Mediterranean, due to favourable photochemical conditions for the production and subsidence of ozone during the summer months. It should be noted however, that the origins of the predominant springtime peak in the extratropics are still widely debated, particularly at a local to regional level due to the complex interplay between factors such as chemistry, deposition and the stratospheric influence which are inherently difficult to separate.

A corresponding zonally averaged monthly mean evolution, together with the respective differences for each CCM (both with and without AKs) is additionally shown in Figure 5.2 and further summarised as 30° latitude band averages in Table A1. Whilst the AK-fitted EMAC differences with respect to OMI (Figure 5.1b and Figure 5.2d) show an overall year-round, albeit seasonally varying positive bias, particularly within the 0° to 30° latitude band (~+2-8 DU), the difference is largely negative in CMAM (~0 to -4 DU), except during spring (MAM) in parts of the Northern Hemisphere (~0 to +4 DU) and within the 30°S to 60°S latitude band (~+2-6 DU). Although such differences on a zonally averaged basis are relatively small (on the order of 10-20 %), the systematic nature and seasonal dependence of such biases is important to consider. Regional differences are evidently larger however, with differences of up to 10 DU (50 %), such as over mid-latitude oceanic regions where both CCMs show a positive bias relative to OMI and also with respect to limited available ozonesonde data from maritime locations. Some continental regions such as eastern Asia on the other hand show a negative bias in most seasons; largest in winter (DJF) (5-10 DU or 20-40 %). A recent study by Hoesly et al. (2018) shows discrepancies between the CMIP5 NO_x emissions database (used in CCMI emission inventories) and an updated, refined database over the timeframe considered, the Community Emissions Data System (CEDS), which could explain the pattern of biases between the continental regions of the Northern Hemisphere. Whilst the CMIP5 emissions dataset is composed of "best available estimates" from many different sources, the dataset has limited temporal resolution (10-year intervals), contains inconsistent methods across emission species and lacks

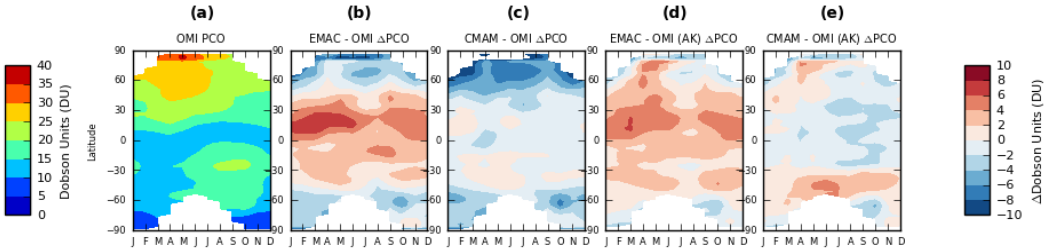

Figure 5.2 – Zonal-mean monthly averaged surface-450 hPa (0-5.5 km) subcolumn O_3 (DU) for 2005-2010 from (**a**) OMI, (**b**) EMAC minus OMI without AKs, (**c**) CMAM minus OMI without AKs, (**d**) EMAC minus OMI with AKs and (**e**) CMAM minus OMI with AKs.

uncertainty estimates and reproducibility. The CEDS dataset addresses some of these shortcomings by also factoring in activity data to estimate country, sector and fuel-specific emissions on an annual basis, which is further calibrated to existing inventories through emission factor scaling. The sign of the biases is more complex and spatially variable in summer (JJA) but are typically low (-3 to +3 DU), implying that the CCMs are reasonably consistent overall with the OMI measurements during this season. In the Southern Hemisphere, the general positive bias is weaker (particularly in austral winter and spring) and most regions show a negative bias in at least one season. Model-measurement agreement here is typically higher compared with the Northern Hemisphere, particularly for latitudes where O_3 precursor emissions are lower and in the less photochemically active seasons (i.e. autumn and winter). This could indicate that CCMs simulate excessive photochemical production of ozone in the Northern Hemisphere particularly (Young et al., 2013; Shepherd et al., 2014) or that the role of tropospheric sinks (e.g. through wet and dry deposition or other loss reactions within the wider O_x family) is underestimated (Revell et al., 2018), with our results indicating regionally differing magnitudes in these biases.

Both Figure 5.2 and Table A1 show the importance of applying AKs (on a monthly mean zonally-averaged basis) in order to diagnose the agreement between the two datasets, by enabling a like-for-like comparison, since it is clear that both CCMs significantly underestimate the amount of tropospheric ozone overall at both middle and high latitudes, relative to the OMI observations (Figure 5.2b,c). The effect of applying the AKs (Figure 5.2d,e) is shown to significantly reduce or even eradicate the negative bias (poleward of 30°N/S), and it is this difference which indicates the approximate magnitude of the influence vertical smearing has on the retrieved OMI subcolumn measurements. A residual negative bias (~ 2 to -6 DU) also exists in the Southern Hemisphere during spring (SON) over the Southern Ocean south of 60°S (adjacent to Antarctica). This might relate to differences in the representation of a transport barrier such as the edge of the wintertime polar vortex, which influences mixing in the surf zone region and is eradicated in this season, together with disparities in the magnitude of the Antarctic ozone hole, which has implications for vertical smearing, influencing the resultant tropospheric ozone burden. Indeed, a cold-pole bias which leads to a delayed onset in the seasonal breakdown of the polar vortex is an inherent bias common to most CCMs (McLandress et al., 2012). Biases in much of the tropics appear also to be connected to dynamics which favour long-range transport (e.g. trade wind circulations) originating from regions of

known precursor emissions (e.g. biomass burning from South America), although differences in the chemical schemes may also be influential and would require further analysis.

Differences with AKs show that EMAC is in slightly better agreement with OMI across the Southern Hemisphere extratropics, although CMAM is in closer or comparable agreement over the tropics and the Northern Hemisphere. The model is especially consistent during JJA and SON over the continents in particular (Figure 5.1b and 5.1c). Furthermore, a high level of agreement between the ozonesonde and OMI observations is apparent in all four seasons (Figure 5.1a), confirming that the OMI retrieval algorithm correctly captures the regional and seasonal climatological features in tropospheric ozone. Some sonde sites however show consistently smaller amounts of ozone (e.g. western North America and Greenland), although this may be attributed to the high elevation (e.g. mountain summit locations) of these sites relative to the average topographical elevation of a 2.5° grid cell within which the OMI observations are averaged over, which inherently leads to lower amounts of ozone within the partial column.

5.1.1 Ozone (O_3) Interannual Variability

As a metric of interannual variability, seasonal aggregates of the computed relative standard deviation (RSD) of the monthly mean ozone for OMI, each CCM and ozonesondes are shown in Figure 5.3, as calculated in equation 5.1 below:

$$RSD = \frac{1}{N}\sum_{i=0}^{N}\frac{\sigma_i}{\mu_i} \tag{5.1}$$

where N is the number of months in a season, σ_i is the standard deviation of each month calculated over all years and μ_i is the multiannual monthly mean of each month. Variability in the tropics is enhanced due to the significantly lower mean tropospheric ozone, in comparison with the extratropics. It should be noted that the calculated RSD is significantly lower for ozonesondes compared to each CCM and particularly the OMI measurements, which is currently being investigated further.

Although OMI shows much higher variability than the models, there is good agreement in regions of high RSD across much of the tropics (>10 %), which is largest during SON, at least from the OMI observations. The highest RSD is consistently found over the western Pacific and the Maritime Continent close to the equator, where it approaches 20 % for both OMI and the CCMs (particularly CMAM). The region is strongly influenced by some

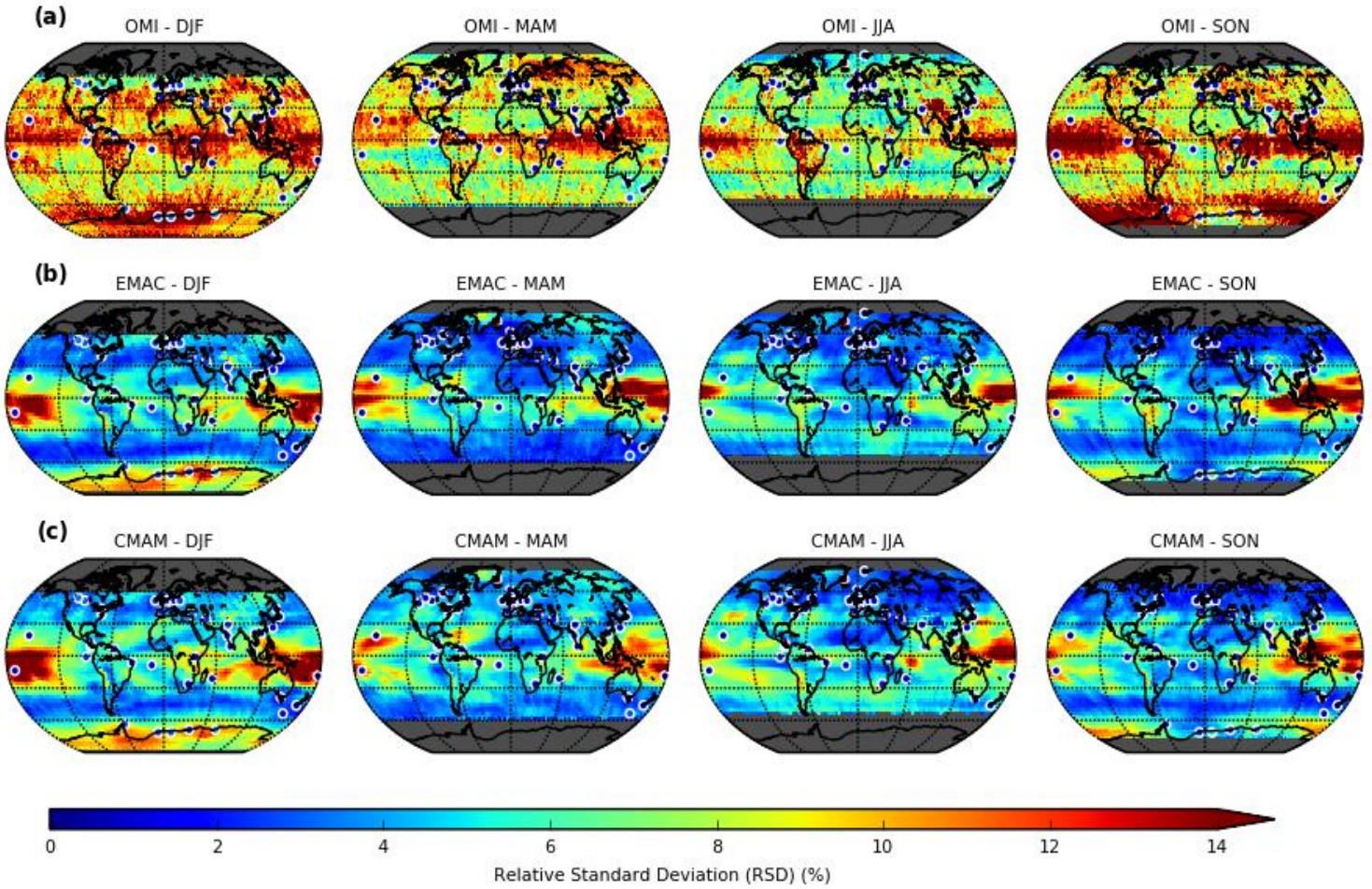

Figure 5.3 – Seasonal composites (left to right) of monthly 1000-450 hPa (0-5.5 km) subcolumn O_3 relative standard deviation (RSD) (%) for 2005-2010 for (**a**) OMI, **(b**) EMAC and (**c**) CMAM. Circles denote (**a-c**) the seasonal RSD calculated from ozonesonde measurements. Model and ozonesonde subcolumn data have again been modified using AKs to ensure a direct comparison.

of the main drivers of natural variability, including the El Niño Southern Oscillation (ENSO) and the Madden Julian Oscillation (MJO). Throughout the tropics, high variability may also be associated with the QBO. Although the QBO is a stratospheric phenomenon, studies show that the alternating phases of the zonal equatorial wind can influence tropospheric ozone by as much as 10-20 % (~8 ppbv) (e.g. Lee et al., 2010). The RSD is generally lower for OMI outside of the tropics, although significant variability (>10 %) is still evident for some regions in different seasons. The CCMs in contrast show very low RSD over much of the extratropics (<5 %), with only subtle spatial structure evident in the seasonal composites. Equivalent composites of the absolute standard deviation (not shown) show some variability however at mid-latitudes during winter and spring in each hemisphere (up to 2 DU), principally in oceanic regions, and this may indicate sensitivity to the main extratropical cyclone tracks. Higher RSD is however shown across Antarctica during the polar day and over the Southern Ocean (up to 10 %), which is collocated in the corresponding OMI seasonal composites. This may largely be a retrieval artefact caused by vertical smearing, which is highly dependent on the tropopause height, since comparative RSD fields from the CCMs without AKs show no such structure (not shown).

5.1.2 Ozone (O_3) Vertical Distribution Assessment

To evaluate the vertical agreement of the CCM O_3 VMR tracer simulations, monthly mean ozonesonde-derived measurements were interpolated and averaged between ±20 hPa of the 22 different model pressure levels between the surface (~1000 hPa) and the lower stratosphere (100 hPa) for three different extratropical regions. Figure 5.4 shows the monthly mean evolution averaged over all sites (left), together with the respective percentage differences relative to the nearest model grid columns in EMAC (middle) and CMAM (right), within each bounding box (region): (a) Europe (30° N - 65° N, 15° W - 35° E), (b) eastern North America (32.5° N - 60° N, 92.5° W - 55° W) and (c) the Tasman Sea (55° S - 15° S, 140° E - 180° E). The absolute differences are also shown in Figure A1 (see Appendix A). Tables A2a-c additionally provide a summary of this information on a seasonal basis for six selected pressure levels in each region. These regions were selected for the assessment due to the relatively high number of ozonesonde sites in close proximity. Furthermore, the variability in emissions of ozone precursors and stratospheric influence, due to varying UTLS dynamics in these predominantly extratropical regions, make these regions suitable for evaluating the realism to which the CCMs simulate these influences.

The seasonality in ozone VMR is shown to be very similar in both Europe (Figure 5.4a) and eastern North America (Figure 5.4b) as expected for two regions of similar latitude in the same hemisphere. In the stratosphere, a springtime maxima (autumn minima) is clear, although the timing is not synchronous at all pressure levels, with a tendency for a delayed maximum (minimum) in each region with increasing pressure (decreasing altitude). This is also apparent for the Tasman Sea region (Figure 5.4c), albeit the seasonality is reversed. This can be attributed to the BDC in the lower stratosphere, which leads to a gradual accumulation of ozone during wintertime in the lowermost stratosphere and a subsequent gradual depletion of ozone during summertime as the circulation weakens (Logan, 1985; Holton et al., 1995; Hegglin et al., 2006). For all regions, this delayed signal in the maximum (minimum) in ozone VMR propagates down into the troposphere (identified here as the region < 100 ppbv), with the exception of the springtime maximum over the Tasman Sea which peaks earlier with increasing pressure (decreasing altitude) from the tropopause (around late September) towards the surface (early August). Clearly though, there is a large difference in the climatological ozone VMR throughout the year between this region and both Europe and eastern North America; the Tasman Sea region reflecting only a very limited influence from emission precursors. The composite

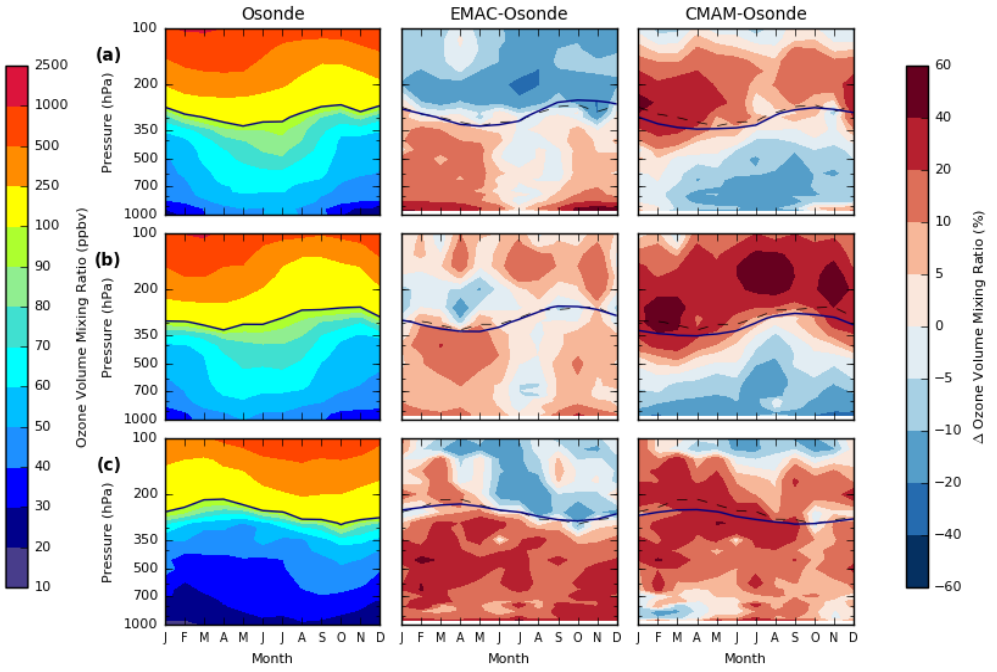

Figure 5.4 – Monthly evolution of the vertical distribution of mean O_3 volume mixing ratio (VMR) (ppbv) derived from ozonesonde measurements (left column); EMAC minus ozonesonde differences (%) (middle column) and CMAM minus ozonesonde differences (%) (right column) over the period 1980-2010 inclusive for three different world regions: (**a**) Europe (n = 18), (**b**) eastern North America (n = 14) and (**c**) Tasman Sea (n = 6). The ozonesonde/model 100 ppbv contour is additionally highlighted in bold (ozonesonde 100 ppbv contour indicated again by dashed line – middle and right column).

produced for this region likely provides a reasonable representation of the natural background influence of the stratosphere on tropospheric ozone in the extratropics, in contrast to the other two regions.

The computed model-ozonesonde monthly mean differences (Figure 5.4) reveal notable differences both between each model and each region in the troposphere (~300-1000 hPa); as high as 20-30 ppbv (>50 %). EMAC shows an almost universal positive bias between 0 and 40 % (0-20 ppbv) throughout the year for all three regions which contrasts with the overall negative bias in the stratosphere (~ 100-300 hPa) (except over eastern North America). Some seasonal dependence in the tropospheric bias is evident over Europe and eastern North America, with the largest (smallest) difference between September and May (June and August); on the order of ~+20-60 % (+10-20 ppbv) outside of boreal summer. In contrast, no obvious seasonal variation in the bias is apparent over the Tasman Sea region. For CMAM, a generally negative, seasonally dependent bias (~5-20 % or 5-10 ppbv) is apparent in the lower to middle troposphere over Europe and particularly eastern North America, most pronounced during summer (JJA), whereas an overall positive bias (up to 10-40 % or 5-20 ppbv) exists over the Tasman Sea, largest in the free troposphere. Both the seasonal character of the negative bias over Europe and eastern North America (largest during the most photochemically active months), together with the difference in the sign of the bias between the troposphere and the UTLS, strongly implies a difference in the implementation of the tropospheric chemistry scheme in CMAM compared with EMAC, since prescribed emissions are equivalent in both models. Specifically, the omission of non-methane VOCs (NMVOCs) in CMAM likely accounts for much of this underestimation.

The largest absolute differences (Figure A1) are however indeed evident in the lower stratosphere (100-300 hPa), with a systematic positive bias in CMAM in most seasons (widely between +50 and +200 ppbv, ranging from 10-50 %). A slight negative bias (~-10 to -50 ppbv or -0-10 %) is however apparent between 100 and 150 hPa over Europe, largely during summer (JJA), and also more pronounced over the Tasman Sea from March through to November (>50 ppbv or 5-20 %). Over eastern North America, a very large positive bias is evident in CMAM throughout the year ranging between 20 and 60 % (+50 to +200 ppbv), with a seasonal shift in the height of the largest differences, similarly to over Europe yet more pronounced. In contrast, the differences between EMAC and the ozonesonde measurements have a very different character, with a general negative bias over Europe, particularly in summer (JJA) (~-20 to -100 ppbv or -10-20 %). Over eastern

North America and the Tasman Sea, the pattern and magnitude of the biases is more complex with both pressure (altitude) and month. An overall positive bias is found over eastern North America (typically +20 to +50 ppbv or +5-20 %), except from January to May between ~170 and 250 hPa, whilst an overall negative bias (generally between -20 and -50 ppbv or 5-20 %) is evident over the Tasman Sea except between January and May and for a small region (120-180 hPa) during August-September. The general negative bias in EMAC (positive bias in CMAM) might indicate an underestimation (overestimation) in the strength of the BDC but the seasonal dependence of the bias, and in particular the complexity in EMAC, suggests influence from other factors.

5.1.3 Tropospheric Ozone Model-Measurement Comparison: Summary

In summary, the CCM simulations are broadly in agreement with both sets of observations, capturing both the extent and magnitude of geographical and seasonal features in tropospheric ozone over the concurrent period of data availability (2005-2010). Whilst it is found here that broad overall agreement in the global mean seasonal composites of tropospheric subcolumn (surface-450 hPa) ozone exists between both CCMs, although differences relative to OMI show that there is an overall significant, systematic positive bias in the EMAC model (Figure 5.1 and 5.2), particularly over the Northern Hemisphere (~2-8 DU), whereas no overall bias is apparent in CMAM despite some meridional and seasonal differences (~-4 to +4 DU). An evaluation of the model-ozonesonde differences in the vertical distribution of ozone VMRs (ppbv) over both Europe and eastern North America (Figure 5.4) indicates a different origin for the biases in each model compared with OMI. In EMAC, the positive bias is predominantly a result of excess in situ photochemical production from emission precursors, whereas biases in CMAM are largely determined by the relative influence of excessive vertical smearing of ozone (induced by applying the OMI AKs). This results from a large positive ozone bias in the lower stratosphere (not present in EMAC), as well as the much more simplified tropospheric chemistry scheme implementation. The additional smearing from AKs is concluded to overcompensate for the reduced in situ production of ozone to yield a larger positive or comparable bias in CMAM (poleward of 30°S/N) (Figure 5.2), where the application of AKs has a disproportionally larger effect on the estimated subcolumns. In contrast, a larger positive bias is found in EMAC over low latitudes (30°N-30°S) but primarily in the Northern Hemisphere where precursor emissions are more abundant, which is understandable due to the higher climatological mean position of the tropopause in this region (with respect to the extratropics), leading to less vertical smearing of

information from the stratosphere when AKs are applied. The zonal average monthly mean integrated subcolumn OMI-model differences without AKs (Figure 5.2b,c) would be consistent with this interpretation and it is obvious that application of the OMI AKs must have induced additional vertical smearing of ozone in CMAM in the equivalent latitude range (~30-65°N) compared with EMAC (Figure 5.2d,e) due to the likely presence of a high ozone bias in the lower stratosphere compared with both ozonesondes and EMAC. Such factor is also suspected to be influential in also explaining the transition from a negative to a positive bias after applying AKs in the Southern Hemisphere between May and December in the region between 30°S and 60°S in CMAM.

The sensitivity of the surface-450 hPa subcolumn to the lowermost stratosphere was earlier exemplified in a plot of the monthly mean AKs for August 2007 over the Southern Ocean (~47°S, 0°E) (Figure 3.9 in Chapter 3), which shows influence from the ~150-450 hPa pressure range. It is known that CCMs tend to have inherent biases in ozone in the lower stratosphere (e.g. Jöckel et al., 2006, 2016; Pendlebury et al., 2015; Kolonjari et al., 2017), so it is likely that the results found here are applicable hemisphere-wide but again further investigation is warranted, perhaps using an ozonesonde trajectory-based mapping approach (e.g. Liu et al., 2013b). The interannual variability (Figure 5.3) in the models seems to be consistent with that from the OMI measurements and as reported in the literature, at least in the equatorial region where the magnitude of interannual variability is typically on the order of ~ 10-20 %. In the extratropics, both ozonesondes and models show smaller variability (<5 %), in contrast to OMI. Whether such differences arise due to model inadequacies in capturing the magnitude of natural variability, or simply as a result of measurement noise in the OMI observations is a subject for further investigation.

5.2 Stratospheric Influence

Having assessed the ability of the CCMs to represent key features of the global climatology of tropospheric ozone with respect to both in situ and satellite observations, model simulations of the vertical distribution in ozone VMR are now investigated globally over the 1980-2010 climatological period, together with the role of stratospheric ozone in influencing both regional and seasonal variations.

5.2.1 O_3 Vertical Distribution, Seasonality and Stratospheric Contribution (O_3F)

Seasonal composites of the monthly mean, zonal-mean vertical distribution of ozone VMR in the troposphere and lower stratosphere (1000-80 hPa) are shown in Figure 5.5 for (a)

EMAC , (b) CMAM and (c) CMAM-EMAC , together with the percentage contribution of mean ozone of stratospheric origin (O_3F (%) = (O_3S / O_3) x 100: dashed lines). The equivalent seasonal composites of tagged-stratospheric ozone (O_3S) VMR are also shown in Figure A2. The meridional distribution in the tropospheric seasonal mean ozone VMR corresponds closely to the latitudinal variability in the integrated surface-450 hPa subcolumn seasonal composites produced from both the CCM and OMI data (Figure 5.1 and 5.2). The highest ozone VMR according to both CCMs can be found over mid-latitudes, with consistent seasonality to that identified in section 5.1; a maximum in the Northern Hemisphere during spring into summer (MAM and JJA) and in spring (SON) over the Southern Hemisphere. It is obvious that ozone VMR is significantly greater year-round in the Northern Hemisphere. This is due in part to the large difference in precursor emissions from the surface but also due to a stronger BDC in the Northern Hemisphere and subsequent enhanced STE of ozone, with the former clearly a greater influence near the surface, and the latter in the upper troposphere. As indicated by the dashed contours, the stratospheric influence increases with altitude for all latitudes across all seasons. However, there is a significant meridional gradient in the stratospheric influence, with values ranging from <30 % over the tropics in all four seasons throughout the troposphere, to maximum values between 40 and 75 % during the winter months at high latitudes in both hemispheres from the surface to 350 hPa. Towards summertime, this fraction decreases sharply across middle and high latitudes (particularly near the surface) due to a combination of reduced STE and increasing importance of precursor emissions during the photochemically active months. Thus in relative terms, the stratosphere has a smaller contribution outside the winter months (lowest in summer). Despite this, the stratosphere has the largest contribution during spring in absolute terms (see Figure A2), extended through to summer in the Northern Hemisphere upper troposphere, which is well established in the literature (e.g. Richards et al., 2013; Škerlak et al., 2014; Zanis et al., 2014). This further implies that the influence of the stratosphere becomes secondary to precursor emissions during the photochemically active months, away from the upper troposphere.

The inter-model difference in the zonal mean ozone VMR for each season is shown in Figure 5.5c. With respect to EMAC, CMAM shows lower values overall throughout the tropical troposphere, and also over the Northern Hemisphere lower and middle troposphere in all seasons (~0-30 % or between 0 and -20 ppbv). In contrast, CMAM shows much higher values in the extratropical upper troposphere (up to +50 ppbv or 50-100 %

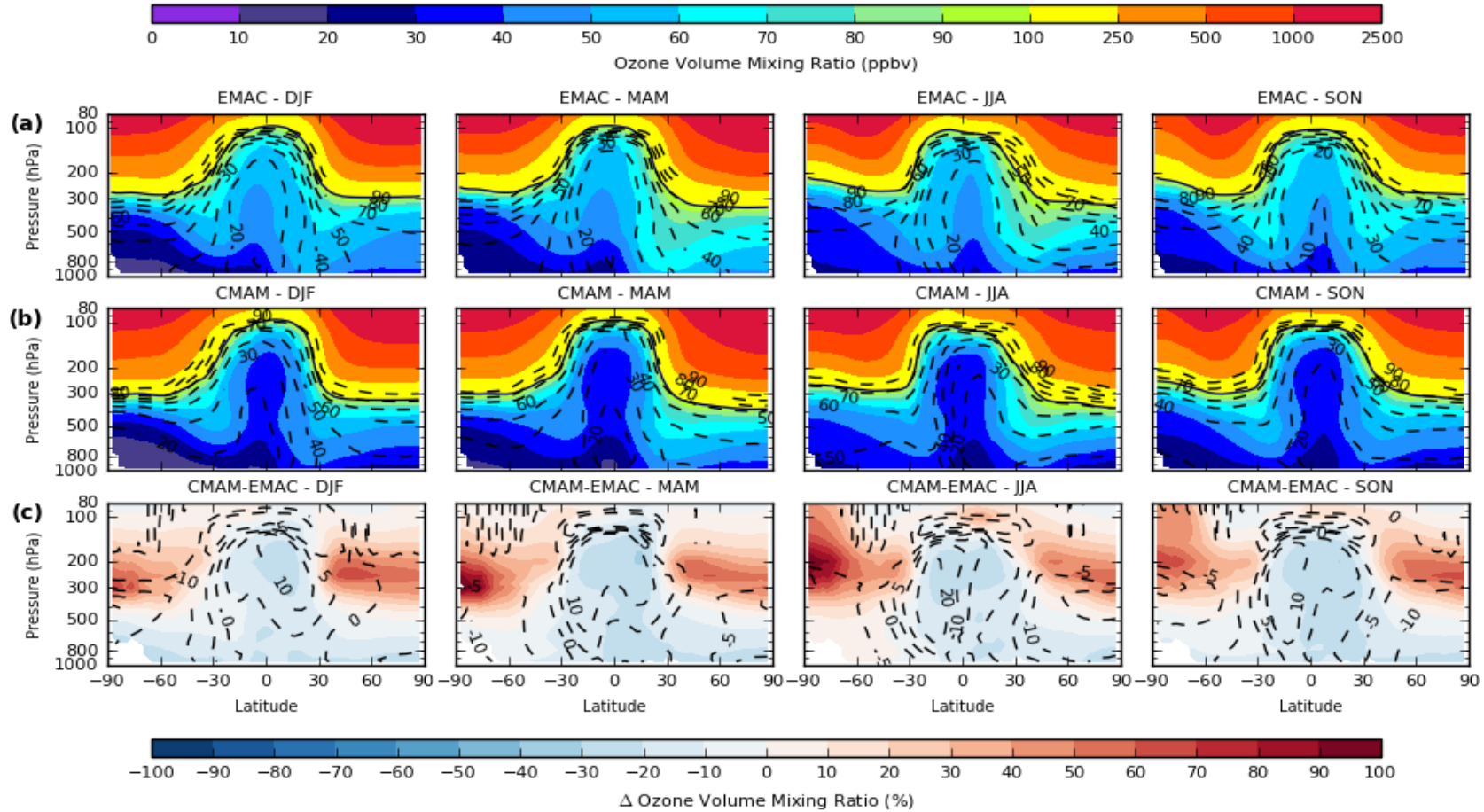

Figure 5.5 – Zonal mean seasonal composites of monthly mean O_3 VMR (ppbv) for the troposphere and lower stratosphere (1000-80 hPa) from (**a**) EMAC, (**b**) CMAM and (**c**) CMAM and EMAC (CMAM-EMAC) percentage differences over the period 1980-2010. Dashed lines indicate the stratospheric contribution (%) calculated using both ozone tracers in each model: O_3F (%) = (O_3S / O_3) x 100. The 100 ppbv contour (bold line) is included as a reference for the tropopause altitude (top and middle row).

in relative terms) in all seasons, with smaller positive differences extending towards the surface in the Southern Hemisphere, particularly in winter (JJA). The large difference in the extratropical upper troposphere, in conjunction with the vertically extensive negative bias in the tropics, may be partially attributed to a difference in the large scale dynamics in each model. Notably, a modest downward shift in the height of the extratropical tropopause would lead to such large differences apparent in Figure 5.5, due to the existence of a very sharp gradient in ozone VMR at this boundary. Indeed, it has been identified previously that tropopause pressures in EMAC are lower than CMAM (by as much as 30-50 hPa) in free running simulations, equating to a smaller total mass of the lowermost stratosphere (Hegglin et al., 2010), although the actual difference is likely smaller in the case of the specified dynamics simulations analysed here. Apart from over the Southern Hemisphere high latitudes, the negative difference in CMAM (relative to EMAC) throughout much of the troposphere would appear to be related to both a difference in the implementation of the tropospheric chemistry scheme in each model and the amount of simulated O_3S, which is evidently some 0-10 ppbv (up to 20 %) lower in CMAM despite a much larger ozone burden in the extratropical UTLS region (Figure A3c). An exception to this is over the Southern Hemisphere subtropics during wintertime (JJA) especially, where a significantly larger amount of O_3S (~0-20 %) is transported down towards the surface in CMAM compared with EMAC (indicative of greater STE). The absence of a positive difference in Figure 5.5c in this region however suggests an overwhelming influence of the reduced in situ photochemical formation of ozone in CMAM due to the simplicity of the tropospheric chemistry scheme in this model, despite an obvious larger stratospheric ozone fraction here (O_3F >20 % larger in CMAM in the mid-troposphere). It is important to stress that differences in the definition of the O_3S tracer within each model, notably that EMAC entails explicit chemical loss mechanisms of O_3S versus treatment within the wider O_x family in CMAM, together with possible differences in the lifetime of O_3S within the troposphere may also influence the results here. The same is true of differences in the tropopause height as mentioned above, although nudging to ERA-Interim should compensate for this factor to an extent. The individual and collective influence of these factors would require detailed investigation however to quantitatively diagnose this.

5.2.2 O_3F Global Distribution and Seasonality

The global distribution of ozone of stratospheric origin is next investigated, in order to quantify the relative contribution to tropospheric ozone, as well to help identify

preferential pathways of stratosphere-troposphere transport. The climatological fraction of stratospheric sourced ozone (O_3F) is shown globally for EMAC and CMAM, together with the difference between both models (CMAM-EMAC) in Figure 5.6 at (a) 350 hPa, (b) 500 hPa and (c) 850 hPa for both DJF and JJA (see Figure S4 for MAM and SON) over the period 1980-2010, when O_3F reaches a maximum in winter and minimum in summer. Both CCMs are broadly consistent at each pressure level, with a clear decrease in the O_3F towards the surface as already indicated in Figure 5.5. The meridional gradient is largest in the upper troposphere at 350 hPa with low values across the tropics (<40 % between 30°N and 30°S) associated with both convective upwelling and the short photochemical lifetime of ozone in the tropics, with higher values in the extratropics but particularly in gradient is largest, a planetary-scale wave pattern is evident (particularly at 350 hPa) which is consistent with longitudinal variability in the climatological positioning of the upper level jet streams induced by orography (e.g. the Rocky Mountains in North America) (Charney and Eliassen, 1949; Bolin, 1950), particularly in winter (DJF). Although the O_3F is relatively high during summer in each hemisphere at 350 hPa as well, the O_3F is much lower at 500 hPa and 850 hPa (which is consistent with Figure 5.5) and reflects the relative minimal role of the stratosphere during this season (with strong influence from precursor emissions instead). At 850 hPa, the stratospheric influence is typically largest over oceanic regions which further reflects the importance of emission precursors over continental the winter hemisphere (>70 %). In the Northern Hemisphere mid-latitudes where the regions, particularly in the Southern Hemisphere where biomass burning is prevalent over Africa and South America.

Large differences in O_3F are apparent at high latitudes (poleward of 60°N and 60°S) during summer in each hemisphere at 350 hPa, with CMAM showing a significantly smaller fraction in ozone of stratospheric origin (~40-50 %) compared with EMAC (~70-80 %). This is despite a positive bias of ~20-50 % (20-30 ppbv) in the seasonal mean ozone VMR in CMAM compared with EMAC (Figure 5.5c), although this bias exists across all seasons whereas the O_3F bias is seasonally dependent. Inspection of model tracer values (not shown) indicates slightly lower stratospheric ozone (O_3S) in CMAM compared with EMAC, along with higher O_3 values (ozone of non-stratospheric origin) at 350 hPa which gives rise to this difference; although the exact origin of this discrepancy would require further investigation. During wintertime in the Southern Hemisphere (JJA) subtropics, a large positive difference in O_3F also exists over a relatively narrow latitude range between 0°S and 30°S, which is indicative of an equatorward displacement in the position of the

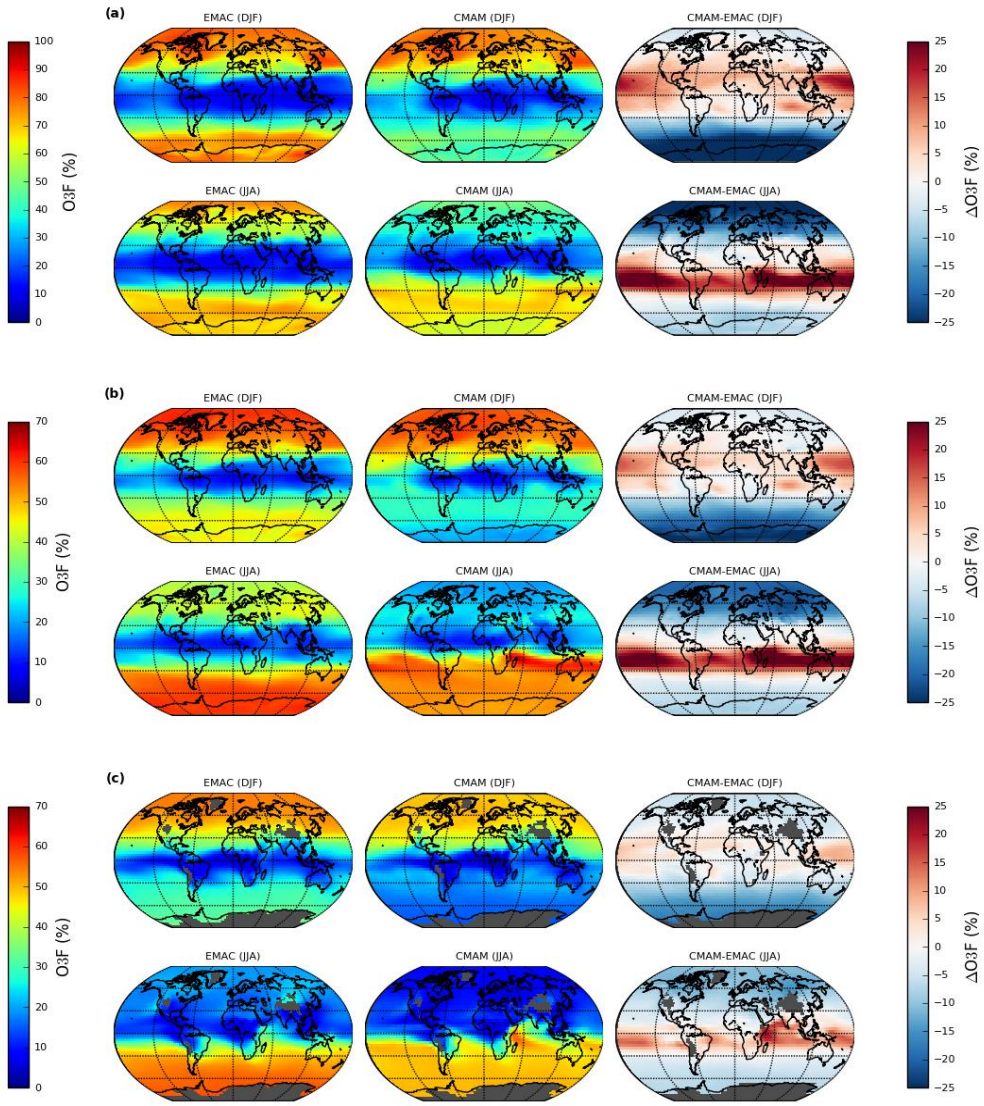

Figure 5.6 – Seasonal (DJF/JJA) composites of (**a**) 350 hPa, (**b**) 500 hPa and (**c**) 850 hPa monthly mean stratospheric ozone fraction (O_3F) for EMAC (left), CMAM (middle) and CMAM-EMAC (right) over the period 1980-2010. Note the scale difference between (**a**) and (**b-c**). Grey shaded regions represent regions where the surface pressure is lower than the plotted pressure level.

subtropical jet stream in CMAM compared with EMAC. The differences show some variation longitudinally, with the largest differences extending from east Africa towards Indonesia and northern Australia and out across the South Pacific. Reference to seasonal composites of the model O_3S VMR tracer (Figure A3) confirms that the positive bias is related to larger STE in CMAM relative to EMAC, at least over the Southern Hemisphere subtropics where it is on the order of 10-20 % in much of the free troposphere. The effect of greater STE, even locally across this latitude range, in CMAM would propagate eastwards due to the influence of upper level winds, leading to transport of ozone-rich air on intercontinental scales. Both the highest O_3S (not shown) and O_3F values in CMAM are apparent over a relatively small geographical area of the Indian Ocean north of

Madagascar (adjacent to the east African coastline) which signifies preferential stratosphere-to-troposphere transport in this region which extends deep into the lower troposphere (O_3F >50 % at 850 hPa). Although EMAC shows relatively high O_3F in the wider region during this season, evidence of a preferential STE pathway here is lacking in this model and indeed no such feature has been widely recognised in the literature. Such differences are non-existent during DJF, although CMAM shows generally higher O_3F over part of the Indian Ocean and the South Pacific and relatively lower O_3F over South America, the South Atlantic and over Africa. The differences described at 350 hPa are very similar at 500 hPa, albeit the negative difference at high latitudes during summer is lower (~10-20 %). Although the spatial distribution of the biases is broadly consistent at 850 hPa as well, there is much greater variability regionally in the tropics and the negative bias at high latitudes is relatively low (>10 %).

5.2.3 Monthly Evolution of Stratospheric Influence

The zonal-mean monthly evolution of mean ozone (O_3) VMR at 350, 500 and 850 hPa is shown in Figure 5.7 based on (a) the monthly mean aggregated in situ ozonesonde observations from the World Ozone and Ultraviolet Radiation Data Centre (WOUDC) database, interpolated and averaged for 10° latitude intervals and within ±20 hPa of each pressure level, (b) as simulated by EMAC, and (c) subsequently for EMAC O_3S and (d) EMAC O_3F. It should be noted therefore that this approach may be less accurate than if the model data was sampled only at the ozonesonde sites, although this impact be limited by the relatively coarse model resolution (~2.8° for EMAC and ~3.75° for CMAM). The ozonesonde measurements are in broad agreement with that simulated by EMAC (and CMAM; see Figure A5), in terms of both the seasonality and meridional variability in the climatological mean ozone VMR at each of the three different pressure levels. However, the ozone VMR across the Northern Hemisphere high latitudes at both 500 and 850 hPa during the broad spring and summer maximum is somewhat higher (~0-10 ppbv) in EMAC, whereas closer agreement with the ozonesonde climatology is apparent for CMAM (Figure A5). At the 350 hPa level on the other hand, CMAM overestimates ozone in the extratropics relative to both EMAC and ozonesondes by as much as 10-20 ppbv, which is consistent with the identified high ozone bias in the UTLS in CMAM over three different extratropical regions in section 5.1.3 (Figure 5.4), whereas EMAC is in closer agreement with the ozonesonde-derived composites. Furthermore, there is very high variability with latitude in the tropics compared with EMAC (and CMAM), although this is almost certainly an artefact of both the paucity and poor spatial representativeness of ozonesonde

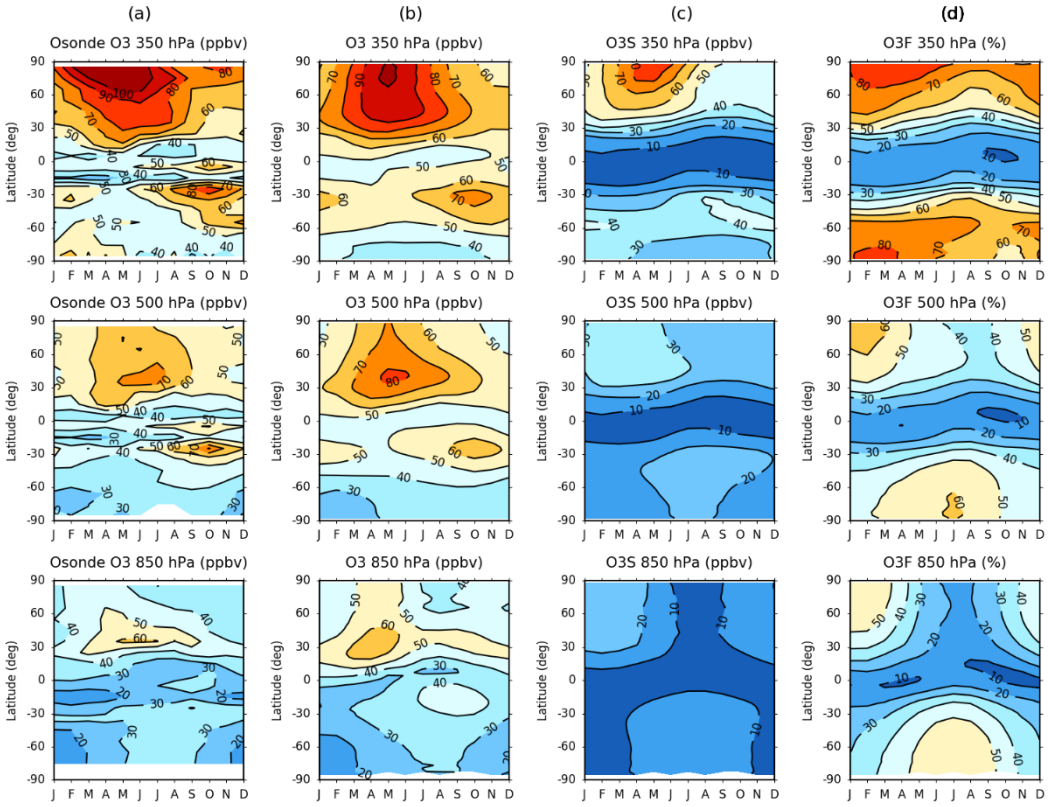

Figure 5.7 – Zonal-mean monthly mean evolution of O_3 VMR (ppbv) derived from (**a**) ozonesondes and (**b**) EMAC O_3 model tracer. The evolution of the (**c**) EMAC stratospheric O_3S tracer and (**d**) O_3F stratospheric fraction (%) are additionally included over the period 1980-2010 for 350 hPa (top row), 500 hPa (middle row) and 850 hPa (bottom row).

stations. This figure is similar to that produced by Lamarque et al. (1999, Figure 2, p. 26368) and their model results bear some resemblance to Figure 5.7 (Figure A5) in terms of the characterisation of the zonal mean evolution of ozone VMR and calculated O_3F, although significantly higher O_3 and O_3S VMRs are evident in the CCM simulations, as well as higher stratospheric fraction (O_3F) values in this study.

The EMAC O_3S evolution corresponds closely to the O_3 evolution at 350 hPa, reflecting the large contribution of the stratosphere in the upper troposphere ozone burden (shown also in the O_3F evolution), but this correspondence falls sharply towards the surface (850 hPa) as noted in section 5.2.2 from Figure 5.6. It is important to note that a pronounced spring maximum in O_3S (> 60 ppbv at 350 hPa) is only evident in the Northern Hemisphere, with a much smaller, short-lived maximum between 30° S and 60° S (~40 ppbv at 350 hPa), due to the combined influence of the springtime Antarctic ozone hole and a weaker BDC in the Southern Hemisphere which constrains the seasonality. The ozone hole influence is particularly apparent at 350 hPa in each model O_3F evolution fields (d), where the strong symmetry between each hemisphere is briefly interrupted during SON when the ozone hole readily develops over the Southern Hemisphere high-latitudes. The O_3F evolution

shows again the sharp meridional gradient in the stratospheric influence, particularly in the upper troposphere, which separates the tropical zone of convective upwelling from the region of net subsidence in both hemispheres where net STE is downward. The seasonality in extratropical O_3F is greater towards the surface due to the competing influence of precursor emissions. Despite this, Figure 5.7 (bottom row) shows that the stratosphere still contributes about half (~50 %) of the amount of ozone during winter at high latitudes at 850 hPa, implying that the stratosphere has a significant influence on near-surface ozone levels, and in turn air quality. This fraction is slightly higher in the Southern Hemisphere due to the lower abundance of precursors compared with the Northern Hemisphere.

5.2.4 Stratospheric Influence: Summary

In summary of this section, use of the model stratospheric ozone (O_3S) tracers reveals a significant difference in the strength and dominance of the shallow branch of the BDC in each model, which is intrinsically related to the burden of ozone in the extratropical lowermost stratosphere through transport from the primary ozone production (equatorial) region (Hegglin et al., 2006). This has implications for both the simulated downward flux of ozone from the stratosphere and its influence on the relative contribution of stratospheric ozone to tropospheric ozone. CMAM simulates a faster, shallower BDC as inferred from Figure 5.5 (section 5.2.1) which shows between 50-100 % more ozone in the extratropical UTLS region (equating to as much as a +50 ppbv difference), which contrasts with a negative difference in the tropics of between 0 and 30 % (0 to -20 ppbv difference) relative to EMAC within this region (~200-400 hPa). This inference is supported by a recent finding of a maximum decrease in the AoA between 1970 and 2100 in the mid-latitude lower stratosphere in CMAM, whereas EMAC shows a decrease in stratospheric mean AoA which is more pronounced with both latitude and altitude, due to acceleration of the BDC due to climate change (Eichinger et al., 2019).

It is inferred from characterisation of the vertical ozone distribution biases in Figure 5.4 (Section 5.1.2) that EMAC more accurately depicts the BDC and its effects on the meridional variation in stratospheric ozone, although it is likely that this model is still too conservative in this aspect compared to reality, given a smaller, but general negative stratospheric ozone bias (up to 10-20 %) in the extratropics with respect to ozonesondes. The same inference is in turn made for STE of ozone; a larger proportion of the downward flux of ozone is simulated over the subtropics in comparison with EMAC, which simulates

a larger flux in the extratropics (Figure 5.6 and Figure A3). The difference is particularly large in the Southern Hemisphere subtropics (0°-30°S), with a typically larger fraction of stratospheric ozone ranging from 10-25 % from the lower to upper troposphere in CMAM relative to EMAC during austral winter (JJA). There is indication of a preferential STE pathway over the western Indian Ocean and neighbouring east Africa which is active during this season as far down as the PBL according to CMAM, although any preferential pathway or STE 'hotspot' in this region is neither obvious in EMAC nor widely established in the literature. Further work is necessary to understand how realistic the representation of STE is in each model, together with the simulated in situ photochemical production of ozone from precursor emissions.

Reference to the earlier work of Lamarque et al. (1999) shows that the contemporary CCM simulations analysed in this study more closely match the ozonesonde-derived climatology, which is remarkably consistent in both this study and that produced by Lamarque et al. (1999, Figure 1, p. 26367), compared to the Intermediate Model of the Annual and Global Evolution of Species (IMAGES) chemistry transport model (CTM) selected in their study, which underestimated tropospheric ozone VMRs by as much as 20-50 %. Both the stratospheric ozone and derived stratospheric fraction fields in their study show very conservative numbers relative to that calculated in this study for both EMAC and CMAM, indicating that the stratosphere has a much larger influence than previously thought, although differences in the stratospheric tracer definitions might explain some of this difference. Both contemporary simulations suggest a significant stratospheric influence on tropospheric ozone, of over 50 % during wintertime in the extratropics (extending down into the lower troposphere), which is significantly higher than the 10-20 % estimated from the CTM in Lamarque et al. (1999) and still considerably higher than more recent studies, which imply an influence in the range of 30-50 % (e.g. Lelieveld and Dentener, 2000; Banerjee et al., 2016).

5.3 Recent Changes in Tropospheric O_3 and O_3S

Seasonal changes in the global mean tropospheric ozone distribution between 1980-1989 and 2001-2010 are next quantified using the CCM simulations, together with changes in attribution from the stratosphere. The changes in the simulated ozone (O_3) VMRs between these two periods are shown globally in Figure 5.8 at 350 hPa, 500 hPa and the surface model level, as well as throughout the troposphere for three different latitudinal cross sections (30°W, 30°E and 90°E) in Figure 5.9 for MAM/SON. Changes for DJF/JJA are

also shown globally in Figure A5 and for these latitude cross-sections in Figure A6. These latitudinal transects help show that regional changes in O_3 and O_3S are strongly height-dependent, particularly along these selected longitudes where notable features are observed, which differ in each model and season. The respective changes in the simulated stratospheric ozone (O_3S) VMRs are then shown globally in Figure 5.10 (Figure A7) for each level and as a function of pressure for each latitudinal cross section in Figure 5.11 for MAM/SON and Figure A8 for DJF/JJA. Zonal-mean changes in each model tracer are additionally summarised in Table A3 (O_3) and Table A4 (O_3S) for 30° latitude bands. Statistical significance is inferred where the paired t test p-value is less than 0.05 (stippled regions), although the distribution of such regions should be interpreted only as an approximation, in the absence of additional data (Waserstein and Lazar, 2016).

5.3.1 O_3 Change (1980-1989 to 2001-2010)

It is evident in Figure 5.8 that both models simulate an overall increase in ozone, which is typically largest (in absolute terms) and most robust (statistically significant) in the upper troposphere (350 hPa) and across the Northern Hemisphere in both seasons. The increase here in both MAM and SON is on the order of some 4-6 ppbv (5-10 %), although in excess of 6 ppbv across some regions during MAM and in CMAM especially, with only a slightly smaller overall increase evident at 500 hPa (mid-troposphere). Greater spatial variability is evident at 350 hPa (at least in MAM) due to enhanced sensitivity to changes in the tropopause altitude at this level. This can be inferred from Figure 5.9 in the Northern Hemisphere for the 30°W latitudinal cross section in particular, where relatively large apparent model disagreement at 350 hPa can be attributed to a slight downward shift in CMAM relative to EMAC; consistent with that found in sections 5.1 and 5.2. Relative to CMAM, the largest increases in EMAC are shifted equatorward (~10-40°N) and are collocated more closely with the region influenced by the subtropical jet stream (e.g. Manney and Hegglin, 2018), particularly in spring (MAM). In contrast, the largest changes in CMAM are generally poleward of 30°N, particularly at the 350 hPa level. The spatial distribution in the changes is also less zonally consistent than for EMAC, and this could reflect a greater influence in the eddy-driven (polar) jet stream in modulating such spatial variability.

Northern Hemisphere surface changes show greater regional variability due to the strong dependence of the surface environment as both a source of emission precursors and as a sink of ozone. In both seasons, the largest statistically significant increases can be found

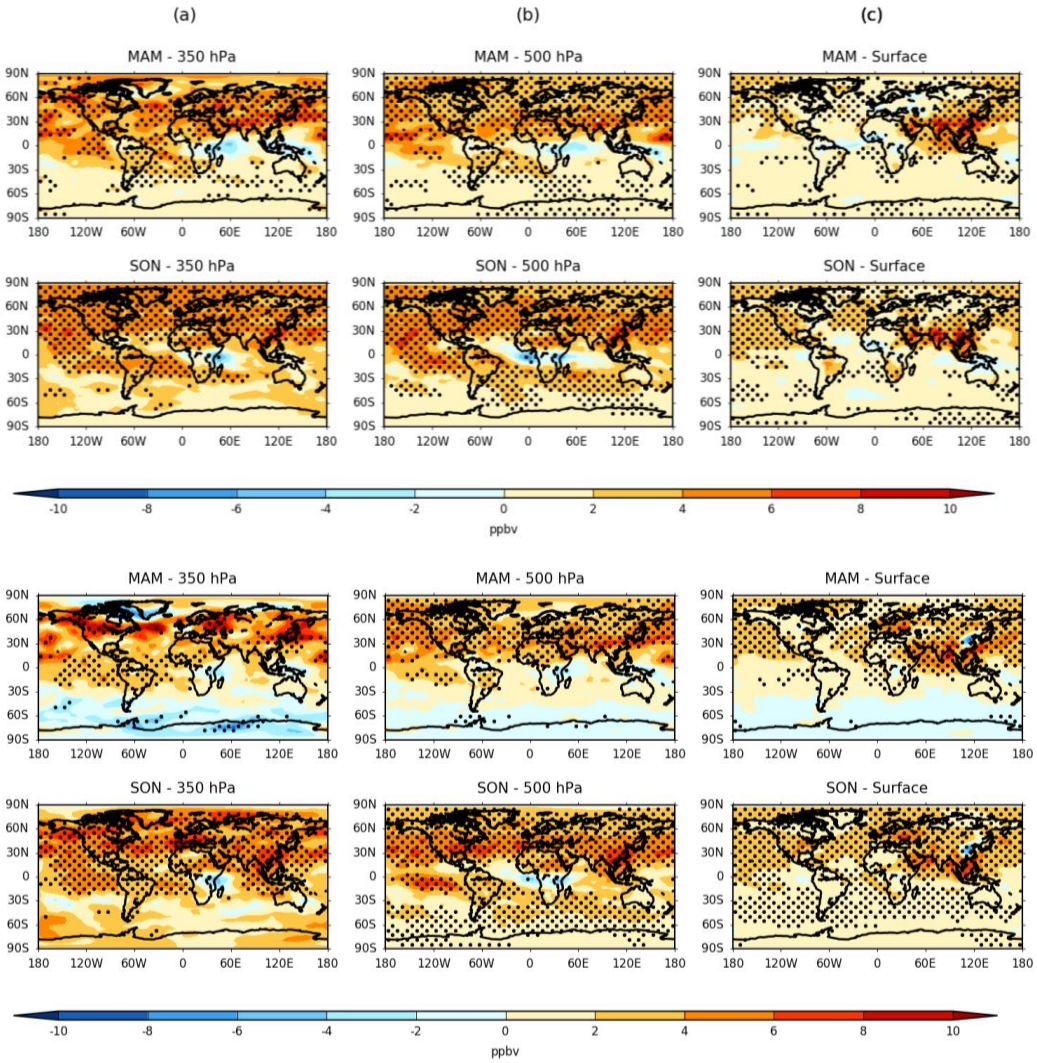

Figure 5.8 – Seasonal change in EMAC (top) and CMAM (bottom) ozone (O_3) VMR (ppbv) between 1980-1989 and 2001-2010 for MAM and SON at (**a**) 350 hPa, (**b**) 500 hPa and (**c**) the surface model level. Stippling denotes regions of statistical significance according to a paired two-sided t-test ($p < 0.05$).

over south east Asia (exceeding 6 ppbv locally), except for a small region of decrease over north-east China apparent only in CMAM. The 90°E latitudinal cross section in Figure 5.9 intersects this region, showing the largest increase close to the southern flank on the Himalayas in each model during both MAM (+6-10 ppbv) and SON (+4-6 ppbv), extending from the surface upwards towards the UTLS (350 hPa). A significant increase is also evident widely over oceanic regions, particularly in CMAM and in SON where values exceed 2 ppbv. This could be attributable to a number of factors, including increases in emissions from international shipping, long range transport from upstream precursor emission sources as well as enhanced subsidence in mid-latitudes due to the influence of subtropical high pressure systems (e.g. the Azores High and the North Pacific High) which may have expanded and intensified in recent decades (Li et al., 2011, 2012). For instance, the tropospheric burden of methane (CH_4) is known to have increased significantly over

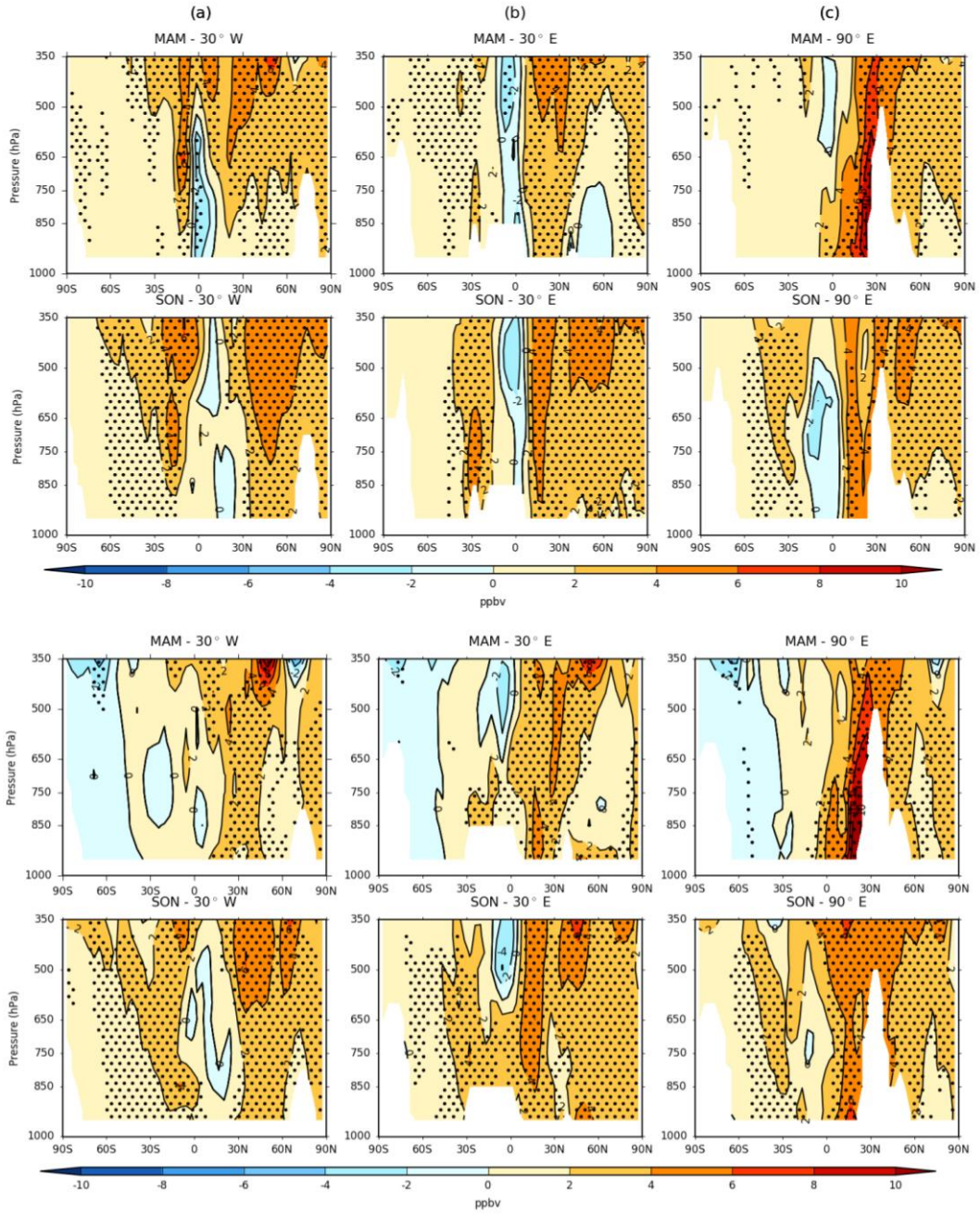

Figure 5.9 – Latitudinal cross-sections of the seasonal change in the vertical distribution of ozone (O_3) VMR (ppbv) from EMAC (top) and CMAM (bottom) between 1980-1989 and 2001-2010 for MAM and SON at (**a**) 30° W, (**b**) 30° E and (**c**) 90° E. Stippling denotes regions of statistical significance according to a paired two-sided t-test ($p < 0.05$).

this period (e.g. Young et al., 2013), with a substantial contribution to the globally averaged increase in tropospheric ozone during this period likely. Long range transport has a clear dominant influence over the Pacific sector, as expected due to the rapid advection from this region. Given recent emission controls in North America, and therefore smaller changes in surface ozone, this factor would be less influential over the Atlantic. Across Europe, there is a large discrepancy in the long term changes between the two models, with negligible change in EMAC (or even slightly negative in MAM) but

considerable increase (~2-6 ppbv) in CMAM in both seasons. Figure 5.10 later shows that this difference is at least partly related to the simulated downward flux of stratospheric ozone in each model during spring (MAM) but not in autumn (SON), with the remaining difference likely related to the chemistry schemes in each model. It is however noted from Jöckel et al. (2016), that the timing (seasonality) of road traffic emissions, as an input to the model chemistry scheme, was incorrectly implemented in this EMAC simulation. The result is a slight underestimation of tropospheric partial column ozone (up to ~1.5 DU in Northern Hemisphere mid-latitudes during boreal summer between 2000 and 2013; largest near primary source regions), but any impact on calculated ozone changes or trends has not yet been quantified.

Smaller, changes are typically found over the tropics and across parts of the Southern Hemisphere in both models (Figure 5.8), but particularly in CMAM and during autumn (MAM) when changes are near-zero or even negative. Between 0°N and 30°S, a continuous region of statistically significant increase in ozone (~2-6 ppbv) is however apparent along a north-west to south-east axis over the Pacific, South America and South Atlantic at both 350 and 500 hPa; largest and most coherent in EMAC and during SON, particularly over the Pacific Ocean. The geographical orientation of this feature is consistent with the climatological positioning of the Southern Hemisphere subtropical jet stream. Over Africa, a relatively small region of decrease (along or slightly south of the equator) is present in both seasons, in both models at 350 and 500 hPa. The largest decreases are evident in SON, where locally ozone has decreased at a rate of 4-6 ppbv. This feature is not always statistically significant, likely due to its small-scale and subsequent enhanced sensitivity to interannual variability. The latitudinal cross section through 30°E in Figure 5.9 shows this feature to be most pronounced in the mid- to upper-troposphere in each model (even absent in CMAM in the lower troposphere). The bimodal structure of the changes in ozone (with an increase to the south of this region) is again consistent with a poleward shift in the subtropical upper tropospheric jets as found by Manney and Hegglin (2018) and the location of STE. During autumn (MAM), CMAM shows a decrease over much of the extratropics (statistically significant in places at 350 hPa) which could be related to the effects of stratospheric ozone depletion, and the influence this may have on STE of ozone. Ozone depletion principally occurs however during spring (SON) so any apparent delayed impact on tropospheric ozone would need to be investigated further. Indeed, both models (but particularly CMAM) show widespread, statistically significant increases across much of the Southern Hemisphere extratropics

during this season at 500 hPa, and to a lesser extent at the surface, which appears related to the larger, regional increases in the subtropics, likely through long-range transport and entrainment around the hemisphere by upper level winds. The relatively insignificant changes at 350 hPa and changes in O_3S (section 5.3.2) imply that this increase is tropospheric driven.

5.3.2 O_3S Change (1980-1989 to 2001-2010)

The long term changes in the corresponding stratospheric ozone (O_3S) model tracers shown in Figure 5.10 and 5.11 for MAM/SON (and Figure A7 and A8 for DJF/JJA) help attribute the long term changes in O_3 described above primarily to either changes in STE or due to changes occurring in the troposphere, such as the photochemical production of ozone from precursors as well as changing tropospheric transport regimes. It is important to be aware that the role of STE is difficult to distinguish from other drivers such as emissions without dedicated sensitivity experiments however. Furthermore, a difference in O_3S lifetime between the two models may contribute to the differences presented here, as well as other influential factors such as convective transport. The latter is typically parameterised in models as a mass flux; either derived from the same analysis field as the large-scale flow fields used or recalculated online using the model's own convective parameterisation scheme which is more common for nudged simulations (Orbe et al., 2020). Indeed this is applicable for both EMAC and CMAM simulations evaluated here, albeit the two schemes are not equivalent between models (see Orbe et al., 2020 for details). Subsequently, it is important to note the differences in O_3S shown here between the two models in a relatively broad context (i.e. greater or lesser influence due to STE/emissions).

Similarly to the changes in O_3, both the largest spatial variability and changes in O_3S are evident towards the upper troposphere (350 hPa), particularly in the Northern Hemisphere where an overall increase can again be seen between both periods. The largest increases in O_3S span across the mid-latitudes in the Northern Hemisphere (particularly during MAM), with extensive regions of +3-5 ppbv or greater and +2-4 ppbv in both models during spring MAM) and autumn (SON) respectively, although statistical significance is often lacking in CMAM especially; indicating the high level of interannual variability in upper tropospheric dynamics. This can again be inferred from the spatial change patterns in the upper troposphere in the latitudinal cross sections in Figure 5.11 (Figure A8) but most notably along the 30°W meridian, where subtle shifts in the height

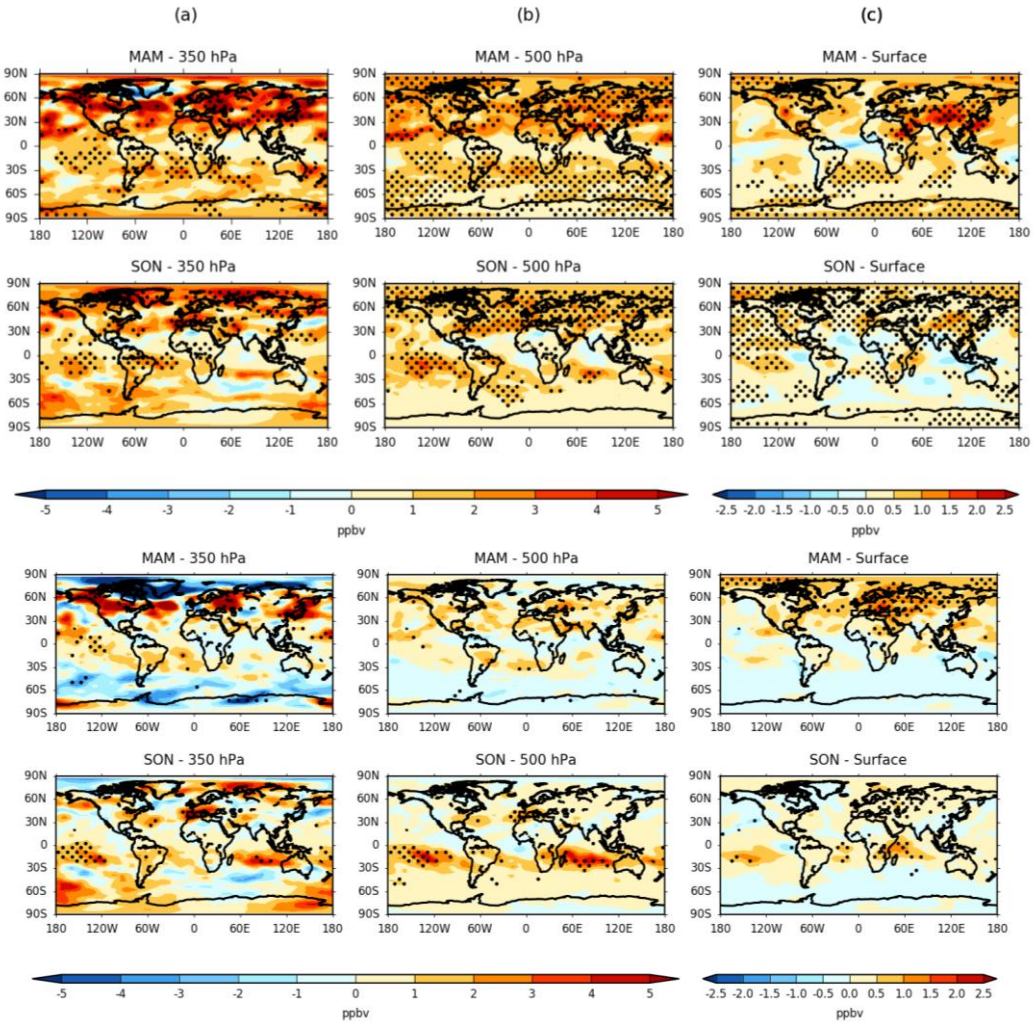

Figure 5.10 – Seasonal change in EMAC (top) and CMAM (bottom) stratospheric ozone (O_3S) VMR (ppbv) between 1980-1989 and 2001-2010 for MAM and SON at (**a**) 350 hPa, (**b**) 500 hPa and (**c**) the surface model level. Stippling denotes regions of statistical significance according to a paired two-sided t-test ($p < 0.05$). Note the scale difference between (**a-b**) and (**c**).

of tropopause, tropopause pressures of up to 30-50 hPa higher in CMAM (Hegglin et al., 2010), and associated sharp gradients in ozone VMR may at least partly explain the large discrepancies between the models in both the sign and magnitude of changes for any given region at the 350 hPa pressure level. Both models are however consistent in showing statistically significant increases in the regions of the subtropical jet, but particularly in EMAC, which is also evident in the mid-troposphere (500 hPa). In contrast, the models differ significantly at high latitudes, especially in MAM when CMAM shows a large decrease (>-5 ppbv) over parts of NE Canada, Southern Greenland and Northern Siberia.

Although EMAC shows a few localised regions of slight decrease, which are spatially collocated with CMAM, the model is dominated by an increase in O_3S at these latitudes. Together with intermodel discrepancies in tropopause height, the spatial distribution in

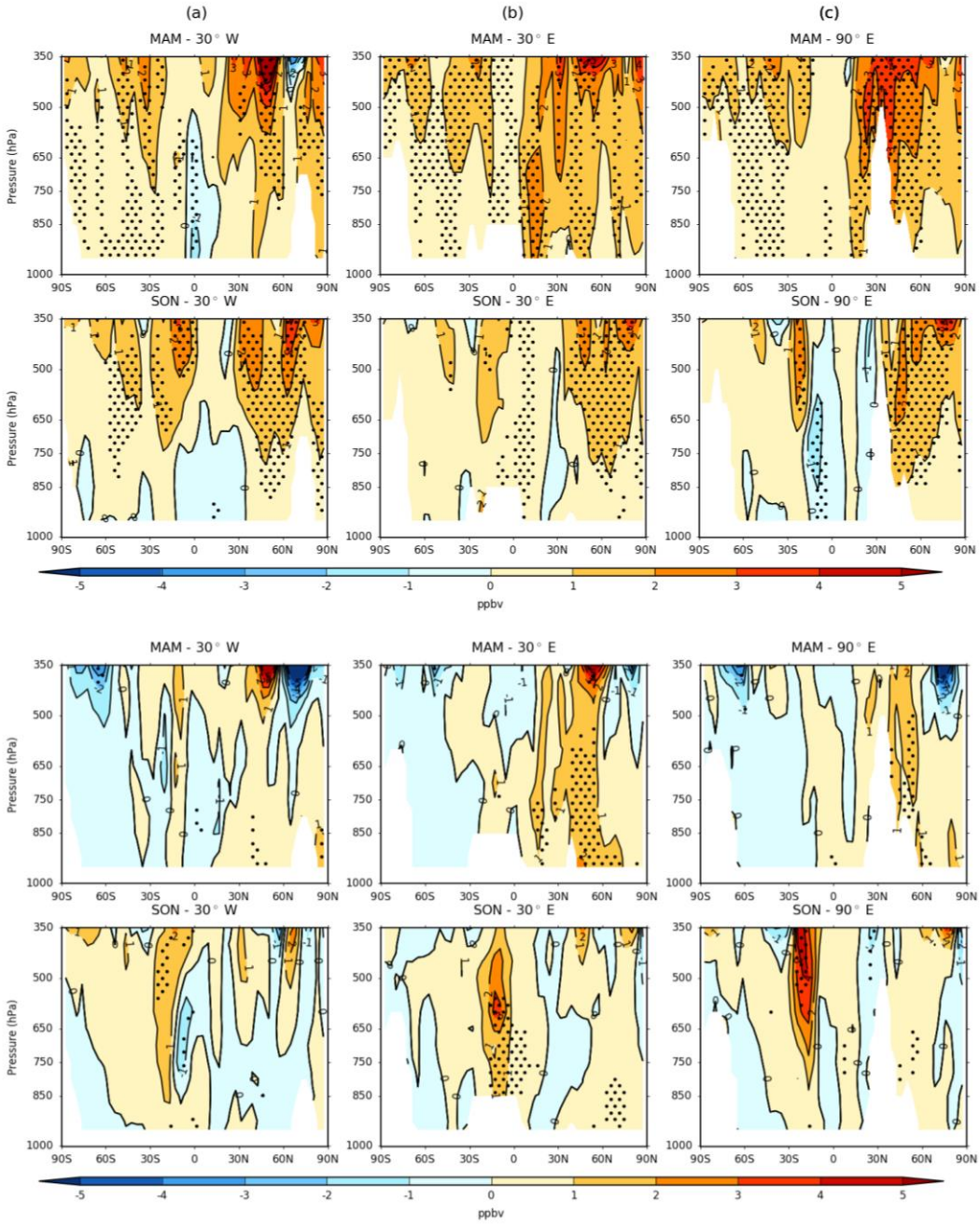

Figure 5.11 – Latitudinal cross-sections of the seasonal change in the vertical distribution of stratospheric ozone (O_3S) VMR (ppbv) from EMAC (top) and CMAM (bottom) between 1980-1989 and 2001-2010 for MAM and SON at (**a**) 30° W, (**b**) 30° E and (**c**) 90° E. Stippling denotes regions of statistical significance according to a paired two-sided t-test ($p < 0.05$).

changes during MAM (most notably in CMAM) could reflect an equatorward shift in the mean position of the eddy-driven polar jet stream over time, and the subsequent area of preferential downward STE, which has been identified through trend analyses using reanalysis datasets (Manney and Hegglin, 2018). Indeed, an equatorward trend of ~-0.4° dec^{-1} in the jet latitude has also been calculated for both models for the period 1960-2000 in a recent study by Son et al. (2018), as determined by the maxima in the 850 hPa zonal mean zonal wind, although this trend is typically poleward for most other CCMI models.

Conversely, changes at 500 hPa are much more spatially uniform, although large differences remain between the two models.

Surface changes in O_3S on the other hand are generally modest, with the large role of precursor emissions in contributing to the increase in O_3 (Figure 5.8) obvious across many regions, most notably over SE Asia, when comparing such changes with the calculated changes in the model O_3S tracers. Nonetheless, some regions (e.g. western North America and Eurasia) show an increase of 1-2 ppbv in MAM (locally significant), which represents a large fraction of the corresponding increase in O_3 (or even an offset of a slight negative change over parts of Europe in EMAC) as previously shown in Figure 5.8. The main difference between the two models is the larger relative increase in O_3S in EMAC across much of the Middle East and central southern Asia, and conversely across much of Europe and western Eurasia in CMAM. The former difference is additionally highlighted in the 90°E transect (Figure 5.11) which intersects the Himalayan region, although both models show a statistically significant increase (> 1 ppbv) in spring (MAM) along the northward flank of the mountain range which represents a minimum contribution of ~25-30 % to the surface ozone change of 2-4 ppbv (Figure 5.9) Regional discrepancies are smaller in SON with a general, albeit smaller, increase in O_3S (~+0-1 ppbv) apparent, which is most pronounced in EMAC.

Changes in O_3S across the tropics at both 350 and 500 hPa are generally small, consistent and of similar magnitude between each model, during both MAM and SON, reflecting the absence of influence from the stratosphere (typical tropical tropopause altitude of ~100 hPa in the tropics) and a general upwelling regime. In the Southern Hemisphere subtropics however, both models show hemispheric-wide, sometimes statistically increases in O_3S on the order of ~+1-4 ppbv centred between 10-30°S, except in CMAM during MAM when any increase is confined over South America and adjacent oceanic regions. Such zonal structure in the spatial trend patterns is strongly supportive of influence from the subtropical jet stream, with the largest changes offset slightly equatorward of the climatological mean position in both seasons as identified in the literature (Langford, 1999; Manney and Hegglin, 2018). Indeed, preferential transport from the stratosphere to the troposphere has a known tendency to occur on the equatorward side of the jet (Lamarque and Hess, 2003). The calculated changes in the O_3S tracer confirms that the O_3 changes (Figure 5.8) are primarily driven (>50 %) by an enhanced influence from the stratosphere, with the increase largest in CMAM during austral spring (SON) in likely association with an increased lower branch in the BDC in this

model, which is more pronounced in the Southern Hemisphere (Hegglin et al., 2014; Haenel et al., 2015). Poleward of 30°S, changes are weak and generally insignificant at 500 hPa, with CMAM exhibiting an overall slight decrease during MAM and also in SON over Antarctica, whilst EMAC displays a slight increase generally (only exceeding 1 ppbv on a local basis), most pronounced in MAM where changes are significant in places. The spatial change patterns are broadly similar at 350 hPa, although spatial variability is considerably larger and complex patterns emerge, with particularly large discrepancies during MAM between each model. The differential spatial change patterns in each model at this height could be attributable to a range of factors such as the simulation of stratospheric ozone depletion, changes in the BDC between the two time periods, as well as differences in tropopause altitude in each model. Surface changes in O_3S across the Southern Hemisphere are small (and insignificant in places), although two localised regions of statistically significant increase (locally >1 ppbv in CMAM) emerge in SON in the tropics; in the central South Pacific and over part of the western Indian Ocean and eastern Africa. The latter region is captured in the 30°E latitudinal cross section (Figure 5.11) in CMAM especially, with a clear downward pathway in evidence coupling changes in O_3S from the tropopause to the surface. Both regions are collocated spatially with the area of largest increase in O_3S at both 350 and 500 hPa in the Southern Hemisphere, indicating that the influence of enhanced STE of ozone during SON between 1980-1989 and 2001-2010 is able to penetrate deep into the PBL in these regions, explaining most of the increase in the model O_3 tracers locally here.

5.3.3 Recent Changes: Summary

To summarise, changes in seasonal mean tropospheric ozone are generally positive between 1980-1989 and 2001-2010 in both models, with a maximum increase of ~5-10 % corresponding to approximately 4-6 ppbv over the Northern Hemisphere and 2-6 ppbv over the Southern Hemisphere subtropics during springtime in both the middle (500 hPa) and upper troposphere (350 hPa). A significant stratospheric contribution to such increase is found here of up to 3-5 (1-4) ppbv during this season (~50-80 %), although significant intermodel disagreement exists in the magnitude and sometimes the sign of the attributable change in ozone due to the stratosphere for any given region or season. This is particularly the case in the extratropics, where different responses to transport likely arise in each model resulting from nudging to specified-dynamics as captured in ERA-Interim. Both the ozone (O_3) and stratospheric ozone (O_3S) tracers exhibit a preferential increase in the subtropics in EMAC and extratropics in CMAM) which may reflect the

relative importance of the subtropical and polar jet streams respectively. This difference is however larger in the former case, which implies that the higher amounts of simulated ozone from precursor emissions in EMAC, particularly in the Northern Hemisphere subtropics, propagates upward from the surface and longitudinally due to influence of these two jet streams, contributing to this difference. In the tropics and Southern Hemisphere extratropics on the other hand, estimated changes are typically small and insignificant, with some indication of a decrease over high-latitudes in CMAM. This could be attributable to the influence of stratospheric ozone depletion but this requires further investigation given the lack of model agreement and largest decrease in autumn (MAM), which is not consistent with the timing of the springtime stratospheric ozone hole.

Although surface ozone changes are dominated by regional changes in precursor emissions between the two periods – the largest, statistically significant increases (> 6 ppbv) over south-east Asia – the changing influence from the stratosphere is also implied to be potentially significant. Indeed, the global area of statistical significance in the calculated O_3S changes typically increases from the upper troposphere (350 hPa) to the surface. Increases in surface ozone driven by the stratosphere are inferred to be up to 1-2 ppbv between the two periods in the Northern Hemisphere, although this is highly variable both regionally and seasonally and between each model. In relative terms, the stratosphere may typically explain ~25-30 % of the surface change over some regions such as the Himalayas, although locally it could represent the dominant driver (> 50 %) where changes in emission precursors are negligible or even declining due to the enforcement of air quality regulations over regions such as Western Europe and Eastern North America. It should be noted however that isolating the role of the stratosphere in influencing recent changes in tropospheric ozone is not possible without performing detailed sensitivity experiments, due to interactions between chemistry and dynamics, including possible feedback mechanisms. Thus, the quantification provided here in terms of stratospheric attribution should be treated with caution. Of further note, is that that the significance patterns for the O_3 and O_3S changes calculated in each model, are very sensitive to the spatial correlation between the two time periods. Thus, regions of significance should be treated with caution, as the robustness of such signal should ideally be examined using multiple statistical tests.

The stratospheric influence over changes in tropospheric ozone could be overestimated in the case of CMAM, which has deficiencies in the representation of tropospheric chemistry, although both models contain a well resolved stratosphere and in the case of

EMAC, a comprehensive tropospheric chemistry scheme. It is claimed by Neu et al. (2014) that models without comprehensive tropospheric chemistry cannot be used to estimate stratospheric influence, since a much larger response to tropospheric ozone is found in such models. However the finding here that EMAC shows a larger increase in stratospheric-tagged ozone (O_3S), might imply otherwise for ozone change or trend assessments at least. The much smaller STE response found in their study, which shows only a modest 2 % change in northern hemisphere mid-latitude tropospheric ozone to a ~40 % variation in the strength of the stratospheric circulation, is also inferred from variability that occurs on interannual timescales due to ENSO and the QBO, which is used a proxy for the mean change in the stratospheric circulation this century. Therefore, the calculated changes presented here would perhaps question the assumption that interannual variations in ENSO and the QBO constitute a representative surrogate for long-term changes anticipated due to climate change.

5.4 Chapter 5 Conclusions

Seasonal variability, stratospheric influence and recent changes in tropospheric ozone are evaluated in this study using two state-of-the-art CCMs, which have the added provision of tagged stratospheric ozone (O_3S) tracer simulations. This study finds evidence that both CCMs are broadly consistent and agree with satellite (OMI) observations and limited in situ (ozonesonde) profile measurements over the 2005-2010 common baseline period in simulating both the geographical variability and seasonality in tropospheric subcolumn (surface-450 hPa) ozone. Inherent, systematic biases (with a strong seasonal dependence) are, however, shown to exist in each model. EMAC is characterised by an overall positive bias with respect to OMI, largest in Northern Hemisphere low latitudes during springtime (~2-8 DU or 10 -30 %). In contrast, CMAM shows no obvious overall bias (~±4 DU or ±20 %) but has significant regional, latitudinal and seasonal variability in both the sign and magnitude of the bias relative to OMI. In CMAM, the mid-latitude seasonal evolution of the biases relative to OMI (Figure 5.2) shows larger consistency prior to the application of the satellite (OMI) AKs, with respect to ozonesondes for three different extratropical regions (Figure 5.4), which is contrary to that expected through accounting for the observation geometry of the satellite. Whilst the application of AKs serves to slightly mitigate the positive tropospheric bias in mid-latitudes in EMAC, the negative bias in CMAM is generally converted to a positive bias in mid- to high latitudes. Comparisons with ozonesondes indicate that the low tropospheric bias in CMAM, likely related to the simplicity of the model chemistry scheme, is offset due to an inherent high ozone bias in

the lowermost stratosphere (as high as 40 to 60 %). This leads to excessive downward smearing of ozone into the troposphere as a result of applying satellite (OMI) AKs, necessary to compare both model simulation and OMI satellite measurements equivalently. This highlights an important limitation of the application of satellite AKs for model-measurement comparison analyses of tropospheric ozone where biases in UTLS ozone are known to exist. As discussed in section 3.5, AKs are necessary to apply to model or ozonesonde datasets to ensure like-for-like comparisons are made, but awareness of the potential impact of model UTLS ozone biases (which may propagate into such evaluations) is critical for accurate interpretations to be made when evaluating agreement between models and satellite measurements of tropospheric ozone.

The high bias in mid-latitudes in EMAC could be explained by an overestimation of emissions in MACCity (a CMIP5-based inventory) (Hoesly et al., 2018), which although used in both models, leads to a higher bias in EMAC due to the comparatively complex tropospheric chemistry scheme in this model. Given that the largest tropospheric biases are equatorward of the region influenced by vertical smearing from the lowermost stratosphere, the two influences are more independent in this model. The relative importance of these drivers is regionally and seasonally dependent but serves to yield an overall lower bias in CMAM compared with EMAC. The influence of applying AKs is typically to increase the subcolumn amount of tropospheric ozone (surface–450 hPa) in the extratropics by ~1-5DU and ~2-8DU in EMAC and CMAM respectively, depending on season, whereas a slight decrease (~0-1 DU) is induced in the tropics in all seasons. An exception to this is over the Southern Hemisphere high latitudes, where the increase is significantly lower due to influence of the ozone hole, particularly in austral spring (SON) when any increase is negligible (0-1 DU). It is important to note that like models, satellite retrieval platforms such as OMI have their own limitations, such as the susceptibility to instrument noise or retrieval errors (Levelt et al., 2006, 2018; Mielonen et al., 2015; Schenkeveld et al., 2017). It is suspected that this limitation is the cause of the large discrepancy in the seasonal composites of RSD, as a metric for the interannual variability, between OMI and the models, the latter of which is in closer agreement with that derived from ozonesondes. A general consensus on the interannual variability in tropical tropospheric ozone is, however, found, with RSD values of over 10 % in some regions and seasons, consistent with the known influence of different teleconnections, most notably the QBO, which is estimated to influence tropical tropospheric ozone anomalies by as much as 10 -20 % (8 ppbv) (Lee et al., 2010). Inconsistencies in a number of the model-

OMI and model-ozonesonde differences are also suspected to undermine the issue of resolution (in the case of models) and signal-to-noise ratio (in the case of OMI) in adequately resolving mesoscale features, such as local-scale pollution plumes or stratospheric intrusion (tropopause folding) events, although this would be an area warranting further investigation.

Taking the above information (from the model-measurement comparison in section 5.1) into account, the relatively long temporal span of the specified-dynamics CCM simulations was utilised to investigate the climatological stratospheric influence on tropospheric ozone and calculate estimated recent changes between 1980-1989 and 2001-2010. A clear difference in the strength and dominance of the shallow branch of the BDC is implied in each model, due to the large discrepancy in the burden of ozone in the extratropical lowermost stratosphere (~50-100% more ozone in CMAM compared with EMAC). The characterised biases with respect to ozonesondes indicate that CMAM has a faster, shallower BDC compared to actuality, which can be inferred from the large positive lower-stratospheric ozone bias (~20-60 %), whereas EMAC provides a more realistic simulation of the BDC, albeit perhaps one that is too conservative given a general negative ozone bias (up to 10-20 %) in the lower stratosphere. The difference in BDC simulation has implications for the simulated STE flux of ozone, with preferential downward transport in the subtropics in CMAM compared with the mid-latitudes in EMAC, particularly in the Southern Hemisphere subtropics and during springtime when the difference is as much as 10-25% from the lower to upper troposphere. Nonetheless, greater confidence cannot be placed in the overall results from either model. As explained previously, multiple factors (e.g. ozone lifetime, convective transport, chemical reaction budgets) influence both the representation of tropospheric ozone and potentially also the simulated stratospheric influence (at least over mid-latitudes). Without detailed model sensitivity evaluations, it is not possible to quantitatively claim that either model is more realistic in terms of representing the stratospheric influence on tropospheric ozone, or indeed the role of in situ photochemistry. Furthermore, it cannot be said whether either the EMAC or CMAM diagnoses STE using the O_3S tracers more accurately. Although this is defined similarly in each model, some differences are present (as highlighted earlier in section 3.4.3) which inhibits understanding here of whether one particular model represents this more accurately. The relative performance of each model concerning regional and seasonal aspects (e.g. the Eastern Mediterranean summer maximum in tropospheric ozone) also cannot be easily critiqued based on the limited evaluations undertaken here.

Compared to the model results of Lamarque et al. (1999), the CCM simulations examined here are in much closer agreement with ozonesonde measurements, with biases no larger than 20 %, as evidenced on a zonally averaged, monthly basis in Figure 5.7 (Figure A4). This contrasts with a systematic underestimation of tropospheric ozone VMR by as much as 20-50 % in the CTM analysed in their study. Despite a significant fall in the correspondence between the seasonal evolution of the simulated ozone and stratospheric ozone component in the CCMs from the upper to the lower troposphere, the results show a significant stratospheric influence on even lower tropospheric ozone – greater than 50 % in the wintertime extratropics, which contrasts with a modest 10 -20 % estimated from the CTM in Lamarque et al. (1999). Whilst the differences here with respect to this earlier study are likely to be real to a large extent, given that the CTM they used had a much less sophisticated chemistry scheme and relatively low vertical resolution (only 25 model levels and with a particularly simpler representation of the stratosphere), methodological differences with CCMs complicate the comparison here. As noted in section 3.4, CTMs are advantageous for the assessment of chemical drivers but the role of transport on the evolution of chemical fields cannot easily be evaluated as meteorological fields are assimilated (and thus feedbacks between dynamics and chemistry cannot be investigated). An important caveat of earlier CTMs, such as the IMAGES model used in the Lamarque et al. (1999) study, is that they are prone to issues arising as a by-product of the assimilation procedure (e.g. excess vertical mixing in the lower stratosphere). Furthermore, reanalyses that drive CTM fields were inherently noisier in the past (e.g. ERA-40), which has since been improved in later products (e.g. ERA-Interim) (Monge-Sanz et al., 2013). CCMs are thus more effective in evaluating the influence of transport on atmospheric chemistry (including feedbacks), and subsequent quantification of STE using these models is likely to be significantly more accurate. Consequently, greater confidence of the results presented here in relation to the role of stratospheric influence can be asserted compared to such studies.

Both models show an overall, statistically significant increase in ozone between 1980-1989 and 2001-2010, on the order of ~5-10 %, or some 4-6 ppbv over the Northern Hemisphere and 2-6 ppbv over the Southern Hemisphere subtropics, in the middle to upper troposphere, with a preferential increase over the subtropics in EMAC compared to the extratropics in CMAM (most pronounced in spring). As estimated using stratospheric tagged ozone tracers from each model, the stratosphere is found to provide a substantial contribution ranging between 1 and 3 ppbv (~20 %-50 %) in the mid-

troposphere (500 hPa) and over 5 ppbv (~50 -80 %) in the upper troposphere (350 hPa) across the Northern Hemisphere mid-latitudes, with a typical increase of 1-4 ppbv (~50 - 80 %) over the Southern Hemisphere subtropics at both pressure levels. Significant model disagreement, however, exists, particularly in the extratropical upper troposphere, likely due to known discrepancies in tropopause height and the variability in upper level dynamics, which may be further affected by the nudging applied to the models. The tropopause height in the extratropics was shown for instance in Hegglin et al. (2010) to be some 30-50 hPa greater (hence lower in altitude) on average in free running simulations of the CMAM model with respect to EMAC. Whilst the constraint of nudging in the specified-dynamics simulations would act to reduce this difference in such specified-dynamics simulations, this tendency would be expected to remain to an extent. Indeed, this would be consistent with the conclusion here that the extratropical tropopause is forced downwards by an enhanced lower branch of the BDC in CMAM relative to EMAC. Estimated changes in ozone and the stratospheric contribution, on the other hand, are generally small and insignificant in both equatorial and Southern Hemisphere extratropical regions. The spatial pattern of changes in surface ozone in contrast show a very different character, with the largest statistically significant increases over much of south-east Asia (> 6 ppbv) and a general increase of up to 2 ppbv or higher quite widely over Northern Hemisphere oceanic regions, but only very small, non-significant changes across the Southern Hemisphere. The influence from the stratosphere at the surface is seen to have a strong regional and seasonal dependence but is estimated to be as much as 1-2 ppbv during spring, which was estimated to be as large as ~25-30% along the northern flank of the Himalayan mountain range and greater than 50% over a localised, relatively unpolluted region of eastern Africa and the western Indian Ocean. The situation is complicated in some regions, however, where near-zero or slight negative changes in ozone VMR are apparent in places such as western Europe and eastern North America, corresponding to an observed hiatus or slight fall in precursor emissions.

This chapter highlights some of the shortcomings of both the EMAC and CMAM CCMs as part of the IGAC-SPARC CCMI activity, as validated with respect to satellite observations from OMI and in situ ozonesonde measurements, in simulating tropospheric ozone. In particular, the importance of a well-resolved stratosphere is clear in attaining a high level of model-measurement agreement and in terms of adequately representing stratospheric influence. For comparisons with satellite observational datasets, a well-resolved stratosphere is of paramount importance for the application of AKs, which smooth the

vertical distribution of model simulated ozone by smearing information down from the stratosphere to the troposphere. Using this derived knowledge, this study confirms the strong influence of the stratosphere in modulating tropospheric ozone and provides an indication that such influence may be larger than previously thought. Furthermore, recent changes in tropospheric ozone are shown to have a potentially significant attribution from the stratosphere, which is quantified here in relation to influence of changing precursor emissions. Understanding the importance of this aspect is however fraught with difficulty as changes in tropospheric ozone due to STE cannot easily be attributed without the aid of dedicated sensitivity experiments. Therefore, the quantitative estimates derived here may only serve as an indicator of the changing role of the stratosphere between these two decadal periods. A general increase in the amount of stratospheric ozone in the troposphere between 1980-1989 and 2001-2010 according to both CCMs, which is statistically significant in some regions of the world such as western Eurasia, eastern North America, the South Pacific and the southern Indian Ocean, would be expected from observed long-term changes in the shallow branch of the BDC (Hegglin et al., 2014). Transit times have been found to exhibit a steady decrease, primarily due to accelerated transport within this branch of the residual circulation (~75 %), with a smaller contribution from a shortening of the transit pathways (~25 %) (Bönisch et al., 2011). Indeed, a strengthening of the BDC is postulated to be the main mechanism for an expected increase in STE under future climate change scenarios (Hegglin and Shepherd, 2009; Butchart et al., 2010), in addition to stratospheric ozone recovery (Zeng et al., 2010), which further highlights the need for an improved understanding of the relationship between STE and tropospheric ozone and accurate quantitative estimates. These findings thus have important implications for the enforcement of both current and future air quality regulations as well as in constraining estimates of tropospheric ozone radiative forcing.

Chapter 6

Following on from the regional and seasonal assessment of tropospheric ozone, stratospheric influence and recent changes (Chapter 5), the potential influence of midwinter sudden stratospheric warmings (SSWs) on the interannual variability in Northern Hemisphere wintertime upper troposphere-lower stratosphere (UTLS) composition, namely ozone (O_3) and water vapour (H_2O), is investigated. The EMAC model signal in UTLS ozone and water vapour anomalies for a particular subclass of SSWs, so-called 'Polar-night Jet Oscillation' or PJO events which have a proportionately larger impact within the UTLS, is first verified against ozonesondes and the CAMS reanalysis over a multi-year period (2005-2013). Over a longer time period spanning the model specified-dynamics simulations (1980-2013), the stratosphere-troposphere evolution of ozone and water vapour following both PJO and other SSW (non-PJO) events is investigated. The radiative impacts of resultant perturbations to Arctic UTLS ozone and water vapour are subsequently examined for PJO events, followed by a series of sensitivity evaluations to determine the dependency of heating changes as a function of altitude and seasonality. The impact of such events on STE of ozone and resultant tropospheric ozone, extending across to mid-latitude regions, is then explored. The findings here of this novel study are then finally synthesised, with suggested actions provided for future work.

SSW Imprint in UTLS ozone (O_3) and water vapour (H_2O) Distributions: Radiative Effects and Impacts on STE

Sudden stratospheric warmings (SSWs) are abrupt disturbances to the wintertime stratospheric polar vortex (SPV) that can lead to pronounced regional changes in surface temperature and precipitation (Kidston et al., 2015). SSWs strongly impact the distribution of chemical constituents within the stratosphere (Tao et al., 2015), but the implications of these changes for stratosphere-troposphere exchange (STE) and radiative effects in the radiatively sensitive upper troposphere-lower stratosphere (UTLS) have not been extensively studied. In this chapter, hindcast specified-dynamics (RC1SD-base-10) simulations from the EMAC chemistry-climate model (CCM) (1979-2013) are primarily used to investigate changes in the chemical composition (both ozone and water vapour) over the Arctic polar-cap (60-90°N) region, with an emphasis on the UTLS and troposphere, following these events. The signature of SSWs on UTLS composition is first

Central date	dSSW/nSSW	NAM1000 (days 8–52)	Daily NAM1000 (%)	Daily NAM150 (%)	S/D	A/R	PJO/ nPJO
22.02.79	**dSSW**	**−1.1**	**78**	**87**	**S**	**R**	**nPJO**
29.02.80	**dSSW**	**−0.5**	**75**	**89**	**D**	**R**	**nPJO**
04.03.81	*nSSW*	*0.5*	*36*	*53*	*D*	*A*	*nPJO*
04.12.81	**dSSW**	**−0.9**	**82**	**80**	**D**	**A**	**nPJO**
24.02.84	**dSSW**	**−0.9**	**89**	**96**	**D**	**R**	**PJO**
01.01.85	**dSSW**	**−1.8**	**100**	**100**	**S**	**R**	**PJO**
23.01.87	**dSSW**	**−0.7**	**78**	**100**	**D**	**A**	**PJO**
08.12.87	*nSSW*	*0.3*	*44*	*62*	*S*	*A*	*PJO*
14.03.88	*nSSW*	*−0.1*	*49*	*38*	*S*	*R*	*nPJO*
21.02.89	*nSSW*	*0.8*	*11*	*78*	*S*	*R*	*nPJO*
15.12.98	*nSSW*	*−0.2*	*51*	*69*	*D*	*R*	*PJO*
26.02.99	**dSSW**	**−0.5**	**51**	**100**	**S**	**A**	**PJO**
20.03.00	*nSSW*	*0.2*	*33*	*40*	*D*	*R*[a]	*nPJO*
11.02.01	**dSSW**	**−0.8**	**69**	**91**	**S**	**A**	**nPJO**
30.12.01	*nSSW*	*1.1*	*11*	*31*	*D*	*A*	*nPJO*
18.01.03	*nSSW*	*0.0*	*44*	*57*	*S*	*A*	*nPJO*
05.01.04	**dSSW**	**−0.8**	**80**	**100**	**D**	**R**	**PJO**
21.01.06	**dSSW**	**−0.3**	**62**	**96**	**D**	**A**	**PJO**
24.02.07	*nSSW*	*0.3*	*47*	*42*	*D*	*R*	*nPJO*
22.02.08	*nSSW*	*−0.0*	*64*	*60*	*D*	*R*	*nPJO*
24.01.09	**dSSW**	**−0.6**	**69**	**100**	**S**	**A**	**PJO**
09.02.10	**dSSW**	**−0.3**	**58**	**96**	**S**	**A**	**PJO**
07.01.13	**dSSW**	**−0.6**	**73**	**98**	**S**	**A**	**PJO**[b]

Also shown are the three criteria used to define tropospheric impacts. dSSW events are highlighted in bold. nSSW events are marked with Italic.
[a]This event was not studied in Kodera *et al.* (2016).
[b]This event was not studied in Hitchcock *et al.* (2013).

Table 6.1 – List of all SSW events, as recorded by their central dates from the ERA-Interim reanalysis, during the 1979-2013 period which overlaps with the full length of the EMAC RC1SD-base-10 simulations. The major distinctions listed include split/displacement (S/D), absorptive/reflective (A/R) and PJO/nPJO events. Adapted from Table 1 in Karpechko et al. (2017).

identified in the CAMS reanalysis over a 9-year period (2005-2013) in section 6.1, with the robustness of the signal further verified from ozonesondes where available over a longer historical timespan (which is station dependent). Verification of the performance of the EMAC simulations is subsequently discussed in section 6.2, with respect to CAMS over the 2005-2013 common baseline period. This exercise is fundamental to investigation of the impact of SSWs on UTLS composition and STE of ozone, as the 35-year period (1979-2013) of the EMAC simulations used here yields a greater number of historical events than in the full CAMS record (2003-2018), which is necessary to obtain more statistically robust results. Note that the first two years from CAMS (2003 and 2004) are excluded for direct comparison with EMAC to remove any model spin up effects. Distinction of SSW events into two major subclasses, Polar-night Jet Oscillation (PJO) and non-PJO (nPJO) events, is then used to generate composite events over the 1980-2013 period which is evaluated in section 6.3. Here, the stratospheric-tagged ozone tracer (O_3S) simulation is fundamental to the elucidation and quantification of the impact of SSWs on STE and subsequent enhancement in tropospheric ozone. The radiative impacts of the simulated ozone and water vapour changes following PJO events, where the anomalies are much larger and more prolonged compared with nPJO events, are then investigated in section 6.4. In section 6.5, a series of artificial perturbations in ozone and water vapour are performed in three main experiments for the UTLS region (50-300 hPa) to assess the sensitivity of radiative impacts as a function of seasonality during the core of the stratospheric

dynamically active season (November to May). The implications of SSW events for the composition of the mid-latitude troposphere are later explored in section 6.6. Finally an overall summary of this chapter is then provided in section 6.7. A list of all recorded SSWs during this period is shown in Table 6.1, with each event categorised by three main distinctions, including that of the PJO/nPJO classification (Hitchcock et al., 2013).

6.1 Observational Signal

SSWs comprise the largest deviations from the mean state of the wintertime Northern Hemisphere extratropical stratosphere, with a frequency of ~6 events per decade (Charlton et al., 2007), and are defined by a reversal of the climatological polar temperature gradient and 60°N circumpolar mean wind from westerly to easterly at 10 hPa (~30 km) (Andrews, 1987). They can be categorised as either nPJO or PJO events, with a stronger impact on the composition of the lower stratosphere in the latter case given deeper propagation down to the lowermost stratosphere (LMS) (tropopause to 100 hPa) and known dynamical persistence timescales of up to 2-3 months (Hitchcock et al., 2013; De la Cámara et al., 2018a). Figure 6.1 shows observational evidence of the enhancement of ozone during the onset stage of a PJO-type polar vortex split event compared to climatology (Figure 6.1a); a time series of height-resolved ozone anomalies from the CAMS chemical reanalysis, including a few of these different event types (Figure 6.1b); and from mean ozonesonde profiles representing the climatology and SSW composites for three Arctic sites during the stratospheric dynamically active season (November-May) (Figure 6.1c). Although the signal is found to be insensitive to the choice of averaging in this analysis, a slightly stronger signal emerges by selecting only months from January to April when the influence from SSWs is most pronounced.

The increased incidence of major wintertime cold air outbreaks across the Northern Hemisphere, particularly over Eurasia (Kretschmer et al., 2018a), during either stratospheric weak vortex or SSW events has been a subject of much attention in recent years (Thompson et al., 2002; Kolstad et al., 2010; Kretschmer et al., 2018b) given the potential for significant advances in sub-seasonal predictive skill (Sigmond et al., 2013; Scaife et al., 2016). Intrinsic to such changes is the equatorward displacement of the tropospheric jet stream and associated storm tracks as the stratospheric jet weakens (Baldwin and Dunkerton, 1999; Baldwin and Dunkerton, 2001; Domeisen et al., 2013; Kidston et al., 2015). SSWs are often initiated by the upward propagation of planetary-

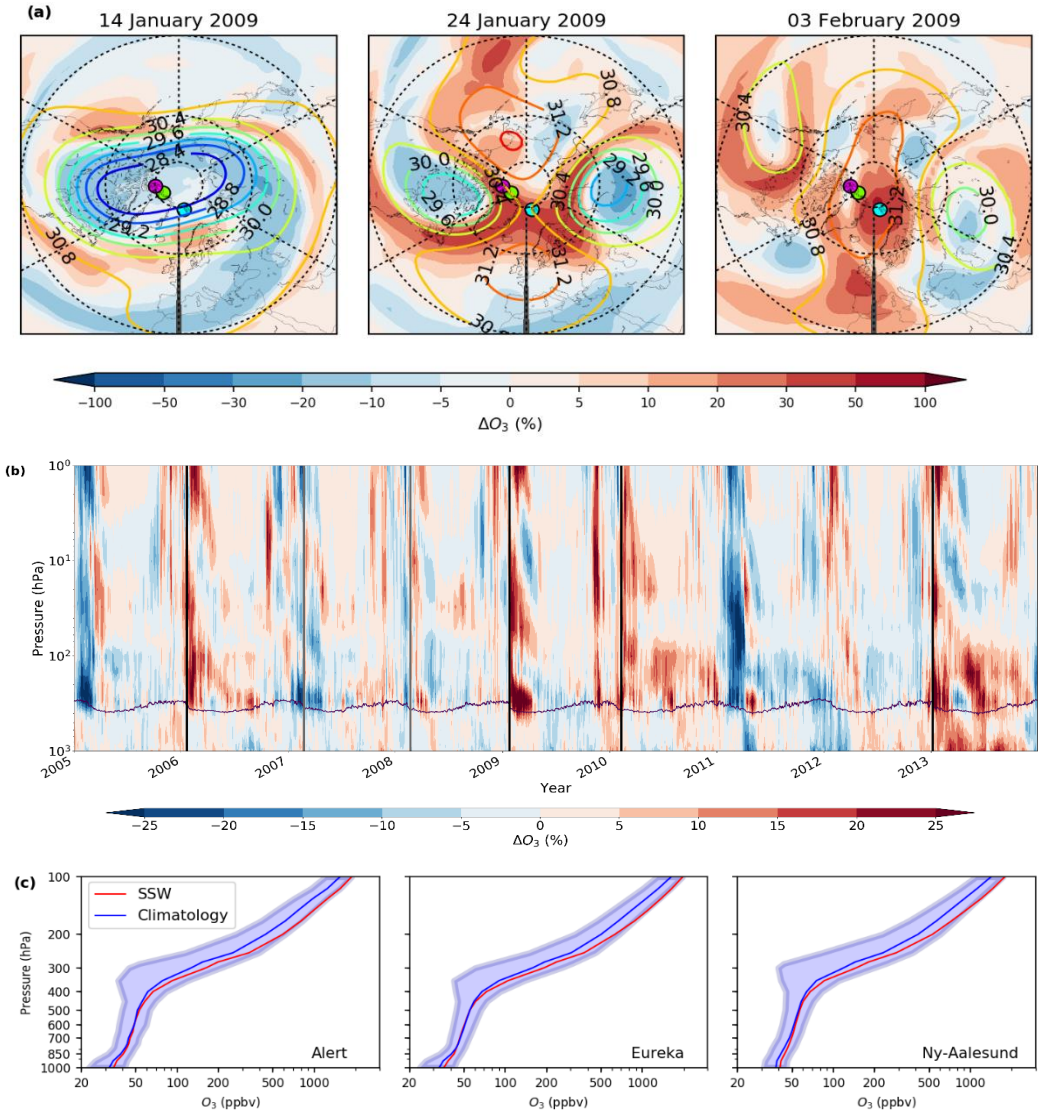

Figure 6.1 | Observational evidence for ozone changes during sudden stratospheric warmings (SSWs) **(a)** 10 hPa geopotential height (km) (contours) and deseasonalised ozone percentage anomalies (shading) over the Northern Hemisphere for (left) 10 days before, (centre) the SSW central warming date and (right) 10 days after a split vortex SSW event (January 2009) from the Copernicus Atmospheric Monitoring Service (CAMS) chemical reanalysis. Ozone anomalies are calculated with respect to the 2005-2013 baseline period. Contour intervals are 0.4 km. (**b**) CAMS time series of polar-cap averaged (60-90°N) deseasonalised ozone percentage anomalies for the 2005-2013 period. Black (grey) lines denote PJO (nPJO) SSWs central warming dates during the period. The 100 ppbv ozone contour (solid purple line) is shown as a proxy for the tropopause height. (**c**) Ozonesonde (100-1000 hPa) climatology (November-May) and SSW composite profiles for three long-running Arctic sites: Alert (green circle), Eureka (violet circle) and Ny-Aalesund (cyan circle) as marked on each map in (**a**). Mean SSW profiles were composited from all profiles within -20 to +70 days of an SSW central warming date with all remaining profiles used in compositing a mean climatology profile during the stratosphere dynamically active season (November to May). Blue shaded region represents 1σ around the climatological mean. The climatology is constructed excluding SSW events in each case.

scale waves from the troposphere which break, dissipate and deposit easterly momentum (Matsuno, 1971), although other factors such as stratospheric polar vortex internal

variability are also thought to be influential in determining the propensity for the occurrence of an SSW (Scott and Polavni, 2006; de la Cámara et al., 2017; White et al., 2019). The resulting enhanced poleward and downward transport during an SSW is also known to increase high-latitude stratospheric ozone, and lead to a breakdown of the polar vortex mixing barrier that leads to a flattening of tracer gradients in chemical species (Manney et al., 2009a; Manney et al., 2009b; Tao et al., 2015).

	Alert	**Eureka**	**Ny-Aalesund**
Location	82.5°N, 62.3°W	80.0°N, 86.4°W	78.9°N, 11.9°E
Date Range	1987-2013	1998-2013	1998-2013
SSW Profiles	257	371	402
Climatology Profiles	1305	1000	1217

Table 6.2 – The geographic latitude and longitude coordinates of the ozonesonde sites included in this study and date range, together with the number of profiles used in calculating station mean ozone vertical profiles (100-1000 hPa) during all SSW events (-20 to +70 days around an SSW central warming date) and for a station climatology (excluding SSW events) during the polar stratosphere dynamically active season (November to May). These profiles are shown in Figure 6.1c. All ozonesonde profiles were convolved (averaged ±20 hPa around the EMAC pressure levels) to reduce profile noise.

Whilst the timescales involved in relating LMS ozone anomalies to anomalous stratospheric circulation changes are well documented (Albers et al., 2018; Kiesewetter et al., 2010), the detailed vertical structure of the changes in the composition of the LMS (relevant for radiative forcing) and the implications for STE of ozone have however received little scientific attention thus far. The sensitivity of tropospheric ozone to variations in the Arctic and North Atlantic Oscillations has been widely discussed (Li et al., 2002; Creilson et al., 2003; Duncan and Bey, 2004), but these variations were explained by purely tropospheric mechanisms. A few studies have however provided evidence of a stratospheric influence (Sprenger and Wernli, 2003; Lamarque et al., 2004; Creilson et al., 2005; Ordóñez et al., 2007; Hess and Lamarque, 2007; Hsu and Prather, 2009; Pausata et al., 2012). The goal here is to provide a more comprehensive and quantitative assessment of the influence using state-of-the-art tools, namely using simulations from the EMAC CCM. Next assessed in section 6.2, is the realism and quantitative agreement of these simulations with respect to the CAMS reanalysis over a 9-year period of temporal overlap, for the chemical species ozone and water vapour.

6.2 EMAC-CAMS Validation

6.2.1 Ozone (O_3)

The correspondence between the CAMS reanalysis and the specified-dynamics (RC1SD-base-10) simulation from the EMAC CCM for deseasonalised (%) anomalies in ozone (O_3) is shown in Figure 6.2a-b over the common baseline period (2005-2013) for the Arctic (60-90°N) region. The EMAC-CAMS difference between each deseasonalised anomaly (%) time series is furthermore elucidated in Figure 6.2c. As quantification of the level of agreement between each dataset, the correspondence between each time series (on the vertical grid in which the CAMS data was retrieved), as quantified by Pearson correlation coefficient (r) values, for each pressure level (n = 25) and for all levels combined (1-1000 hPa) (n = 1), for the deseasonalised anomalies in O_3, are displayed in Table 6.3. Thus, the EMAC time series has been linearly interpolated both vertically and temporally to match the CAMS grid for this evaluation. Good overall agreement (1-1000 hPa) is evident between each time series (r = 0.776), with clear indication that EMAC accurately simulates both inter-seasonal and inter-annual variability in both stratospheric and tropospheric O_3 over the Northern Hemisphere polar-cap (60-90°N) region. As denoted by the correlation (r) values for individual pressure levels, agreement is greatest in the stratosphere (~1-300 hPa) (r = > 0.7), with the highest values in the mid-stratosphere (~10-30 hPa) where r values approach 0.95. In the troposphere (~400-1000 hPa), the correspondence is somewhat weaker (r = ~0.45-0.6), with indication of poorer agreement towards the surface. Nonetheless, these values are still supportive of reasonable agreement between each dataset in the troposphere, which is further apparent from visual inspection of each time series (Figure 6.3a-b) and the difference time series panel (Figure 6.3c).

Importantly, the key features of the evolution of the CAMS O_3 anomalies in the stratosphere following the major PJO-class of SSWs during the period, which notably includes the January 2009 and January 2013 vortex-split events, are well captured by EMAC. Moreover, EMAC-simulated variability in the evolution of stratosphere O_3 anomalies during wintertime (the core of the stratospheric dynamically active season) in years without SSWs also closely resembles CAMS. Of particular note is the remarkable agreement and antisymmetric pattern to the anomalies for both the two major SSW events during this period, January 2009 and January 2013, with respect to the pronounced strong SPV during the 2010/11 winter (Manney et al., 2011). Whilst, the key features of

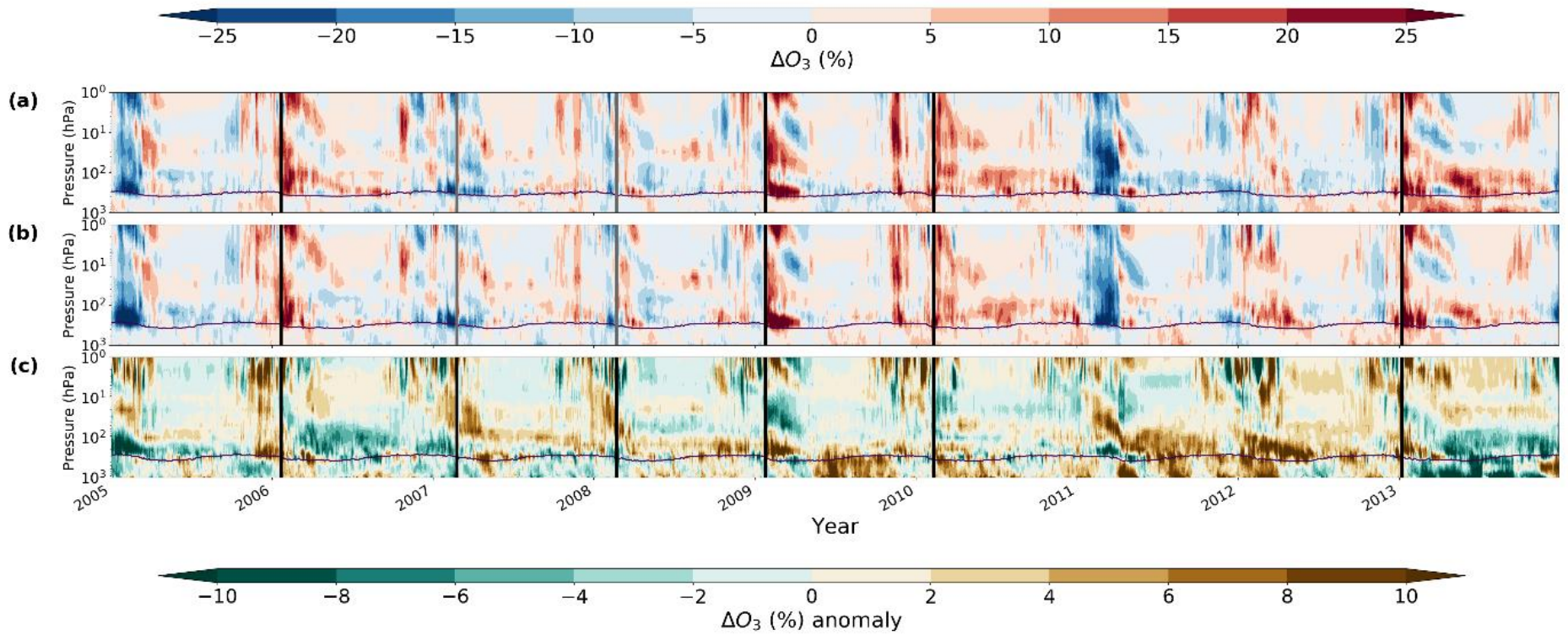

Figure 6.2 – Vertical-time evolution of polar-cap (60-90°N) deseasonalised ozone (%) anomalies for (**a**) the CAMS reanalysis and (**b**) from the EMAC CCM specified-dynamics (RC1SD-base-10) simulations relative to each respective climatology over the period 2005-2013. The differences between each anomaly time series (EMAC – CAMS) are additionally shown in (**c**). Black (grey) lines denote PJO (nPJO) SSW central warming dates during the period. The 100 ppbv ozone contour (purple line) is included as a proxy for the tropopause height.

Pressure (hPa)	Correlation (R)	Pressure (hPa)	Correlation (R)
1	0.782	**250**	0.902
2	0.713	**300**	0.861
3	0.707	**400**	0.614
5	0.826	**500**	0.551
7	0.892	**600**	0.535
10	0.924	**700**	0.516
20	0.922	**800**	0.503
30	0.942	**850**	0.514
50	0.895	**900**	0.534
70	0.861	**925**	0.531
100	0.870	**950**	0.518
150	0.864	**1000**	0.459
200	0.878	**1-1000**	0.776

Table 6.3 – Pearson (r) correlation coefficients between the EMAC and CAMS deseasonalised O_3 anomaly (%) time series (1-1000 hPa) over the 2005-2013 period. Values are shown for each CAMS pressure level (n = 25) and for all levels (n = 1). The EMAC time series was interpolated linearly both vertically and temporally to match the grid on which the CAMS data was retrieved.

the stratospheric O_3 anomaly evolution are in agreement with other studies in the literature (e.g. de la Cámara et al., 2018b), the anomalies in the UTLS region are not. Discrepancies of these findings with respect to the study by de la Cámara et al. (2018b) may however arise due to their choice of vertical coordinate system (potential temperature, θ), as well as expression of the anomalies in absolute (e.g. ppbv) as opposed to relative terms (i.e. %). Further constraint of their chosen vertical domain to between 1100 K and 350 K may further distort any association between the signal in O_3 anomalies shown here versus their findings. Interestingly however, a signal for an enhancement in UTLS O_3 anomalies following the January 2006 SSW event, as well as many other events between 1979 and 2007, is clearly captured in an evaluation by Kiesewetter et al. (2010, Figure 7) which uses a chemistry transport model (CTM) driven by sequentially assimilated SBUV satellite O_3 profile observations. Their evaluation also utilises potential temperature (θ) as a vertical coordinate system, which helps lend support to the EMAC and CAMS evolution shown here. Given remarkable agreement between the CAMS reanalysis and the EMAC simulation exists, confidence is ensured that EMAC performs well in this region.

This EMAC-CAMS difference panel (Figure 6.2c) in fact shows that the correspondence between each dataset is reasonable around and just after the SSW dates during the 2005-2013 period (solid lines), with the greatest disparity between the CAMS reanalysis and the EMAC simulation in the troposphere in fact evident during the summer of 2009, and throughout much of 2010 and 2011, which were both years devoid of SSWs. The evolution of the anomalies following the January 2013 SSW is however less consistently simulated between each dataset, although this is likely to be attributed to a change in the assimilated SBUV-2 data for O_3 in the CAMS reanalysis from this year onwards (Christophe et al., 2019), resulting in a known discontinuity in the CAMS record. The disparity is however largest in the troposphere region, which although may seem counterintuitive, is highly likely related to propagation effects from the change in stratospheric assimilated information from the SBUV-2 platform. This can be asserted on the basis that no direct information on the vertical distribution of O_3 in the troposphere region is assimilated into the reanalysis (Inness et al., 2019).

6.2.2 Water Vapour (H_2O)

The agreement between the CAMS reanalysis and the EMAC (RC1SD-base-10) specified-dynamics simulation of deseasonalised (%) anomalies in water vapour (H_2O) (1-1000 hPa) is next assessed in Figure 6.3, again for the period of concurrent data availability (2005-2013) over the Arctic (60-90°N) region. Pearson correlation (r) coefficient values of the correspondence between each dataset for each pressure level (hPa) (n = 25) and for all pressure levels combined (1-1000 hPa) (n = 1) are shown for deseasonalised anomalies in water vapour (H_2O) in Table 6.4. As for ozone (O_3), this assessment is achieved through linear interpolation of the EMAC time series with height and through time to match the grid on which the CAMS data was retrieved. A very high correlation (r = 0.808) is yielded over the time period as a whole, which is in fact slightly greater than that for O_3, and again signals remarkably close agreement between each dataset. Unlike for O_3 however, agreement between each dataset is generally weaker in the stratosphere (1-300 hPa) (r = ~0.0-0.7) but greater in the troposphere (400-1000 hPa (r = ~0.80-0.96). The weaker correlation for the stratosphere can likely be related to the fact that H_2O is not assimilated above the tropopause (~ 100-300 hPa), as taken from ERA-5 where specific humidity is assimilated from radiosondes, dropsondes and aircraft observations (Hersbach et al., 2020); instead relatively simplistic parameterisation of oxidation from methane (CH_4), that is directly assimilated from satellite observations from multiple sources (SCIAMACHY, TANSO and IASI) (Massart et al., 2014), is taken into account for the representation of

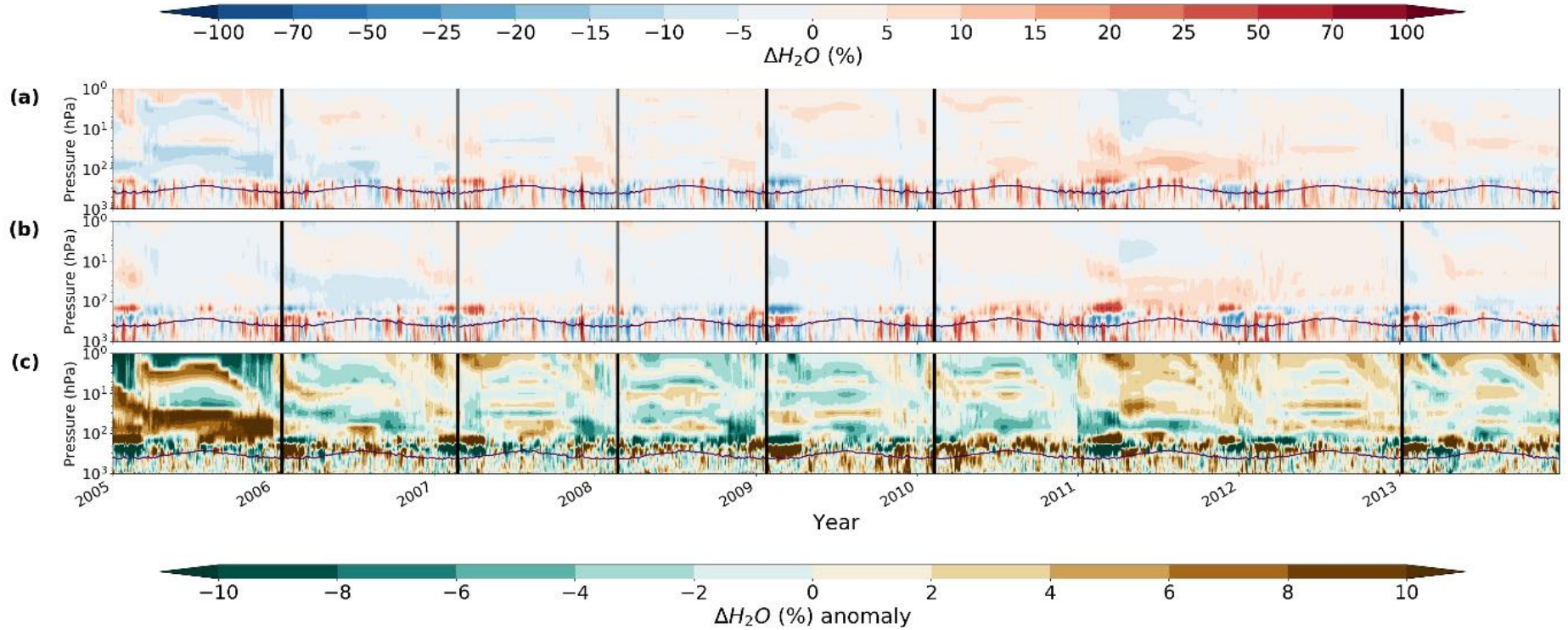

Figure 6.3 – Vertical-time evolution of polar-cap (60-90°N) deseasonalised water vapour (H_2O) (%) anomalies for (**a**) the CAMS reanalysis and (**b**) from the EMAC CCM specified-dynamics (RC1SD-base-10) simulations relative to each respective climatology over the period 2005-2013. The differences between each anomaly time series (EMAC – CAMS) are additionally shown in (**c**). Black (grey) lines denote PJO (nPJO) SSW central warming dates during the period. The 100 ppbv ozone contour (purple line) is included as a proxy for the tropopause height.

H_2O. Furthermore, it is more generally known that reanalyses are notoriously poor at accurately simulating H_2O within the extratropical UTLS, due to deficiencies in the simulation of cross-tropopause mixing, and often positively biased (too moist) (Davis et al., 2017). It is therefore reasonable to assume that EMAC has a better handle over the spatiotemporal variability of this species.

Throughout the bulk of the stratosphere, the correlation is however quite reasonable (~r = 0.50-0.75), but falls away slightly around the 50 hPa level (r = ~0.47) and more notably close or just above the tropopause at the 250 hPa level (r = ~0.25). The 50 hPa level appears throughout much of the time period in Figure 6.4 to be close to a inflexion point in which the sign of H_2O anomalies are opposite above and below this region. Thus, a slight deviation in the height of this critical layer or subtle timing differences in the onset of anomaly changes between the CAMS reanalysis and the EMAC simulation may account for the reduction of the correspondence for this level. Indeed, it is apparent that this even more true for the 250 hPa level, which is frequently close to the boundary between anomalously moist and dry conditions, particularly during winter. A dipole in this region is a common feature throughout the 9-year (2005-2013) period, with anomalies

Pressure (hPa)	Correlation (R)	Pressure (hPa)	Correlation (R)
1	-0.035	**250**	0.254
2	0.269	**300**	0.789
3	0.612	**400**	0.959
5	0.684	**500**	0.955
7	0.749	**600**	0.952
10	0.705	**700**	0.949
20	0.688	**800**	0.950
30	0.559	**850**	0.950
50	0.468	**900**	0.949
70	0.629	**925**	0.945
100	0.667	**950**	0.944
150	0.700	**1000**	0.928
200	0.504	**1-1000**	0.808

Table 6.4 – Pearson (r) correlation coefficients between the EMAC and CAMS deseasonalised H_2O anomaly (%) time series (1-1000 hPa) over the 2005-2013 period. Values are shown for each CAMS pressure level (n = 25) and for all levels (n = 1). The EMAC time series was interpolated linearly both vertically and temporally to match the grid on which the CAMS data was retrieved.

sometimes exceeding ±25 %. Following the major PJO-type SSWs over this period, which includes January 2006, January 2009 and January 2013, an anomalously dry region is found above the 250 hPa level, which overrides an anomalously moist region immediately below this level. This pattern is not consistent with the nPJO subclass of SSW events during this period (February 2007 and February 2008), nor other winters during this period such as in the 2010/11 winter which was characterised by an anomalously strong SPV. In the latter case however, a particularly strong H_2O dipole anomaly is present, with the sign of the anomalies inverted with respect to the three main PJO-type SSWs between 2005 and 2013. The fundamental reasons for the occurrence of a dipole in this region, which is most prevalent during winter, are unclear, but most likely relate to a vertical displacement in the mean tropopause height over the Arctic region and/or changes in poleward advection of moisture-rich air masses from lower latitudes.

6.3 SSW Composite Analysis

For every time series, each nPJO and PJO SSW event (-30 to +150 days of an event) is indexed for inclusion in the composites shown in this sub-section. In calculating the climatological composites, the indexing for each event is applied to all years in order to calculate an average over the 34-year time series (1980-2013). This procedure serves to remove all influence of seasonality in these evaluations when differencing each composite to produce the shown evolution of deseasonalised (%) anomalies.

6.3.1 Ozone (O_3) and Water Vapour (H_2O)

Having verified that trace gas distributions in the chemistry-climate model EMAC closely resemble the ozonesonde and CAMS reanalysis (Figure 6.1-6.3), with the caveat that agreement between the model and CAMS is lower below the tropopause for ozone (a larger impact is shown in CAMS for most events), the EMAC model is next used to examine composition changes during SSWs over an extended period to enhance the statistical signal. Figure 6.4a-c shows the composite evolution of deseasonalised anomalies of ozone (O_3), water vapour (H_2O) and the vertical residual velocity ($\overline{w}^*$), a metric for changes in the strength of polar downwelling, from the upper stratosphere to the surface (1-1000 hPa) over the period 1980-2013, split into nPJO (n = 11) and PJO (n = 11) events[1]. The relative anomalies in both O_3 and H_2O are more pronounced and protracted during PJO events, consistent with the resultant larger perturbation to the dynamical state of the

[1] An SSW event on 17 Feb 2002 is excluded in the nPJO/PJO classification from Karpechko et al. (2017).

lower and middle stratosphere (Hitchcock et al., 2013). The onset (taken as the central warming date (black line in Figure 6.4)) of a PJO-type SSW is characterised by the emergence of positive O_3 anomalies (5-20 %) in the middle and lower stratosphere (10-100 hPa), as well as in the upper stratosphere (1-3 hPa) just a few days later ($\Delta O_3 > 25$ %), which is well established from previous stratospheric ozone SSW composite analyses (de la Cámara et al., 2018b; Haase and Matthes, 2019). A larger, more prolonged relative enhancement ($\Delta O_3 > 25$ % persisting for ~50 days) is however seen in the LMS (tropopause to 100 hPa), which has so far received little attention. Concurrently, significant anomalies in H_2O are found around the timing of the SSW onset, albeit largely confined to the LMS region, which last for around 50-70 days. A clear drying signal (~25 %) is evident around 120-200 hPa, with a moistening signal of approximately equal magnitude immediately below, just above the tropopause (~200-350 hPa). Only a modest enhancement of up to ~10 % in O_3 and ~±10 % in H_2O is evident for nPJO events. Thus, whilst the patterns of the response in both O_3 and H_2O are consistent for each subclass of events, the magnitude and persistence appears to be strongly associated with the amplitude of the event within the lower stratosphere.

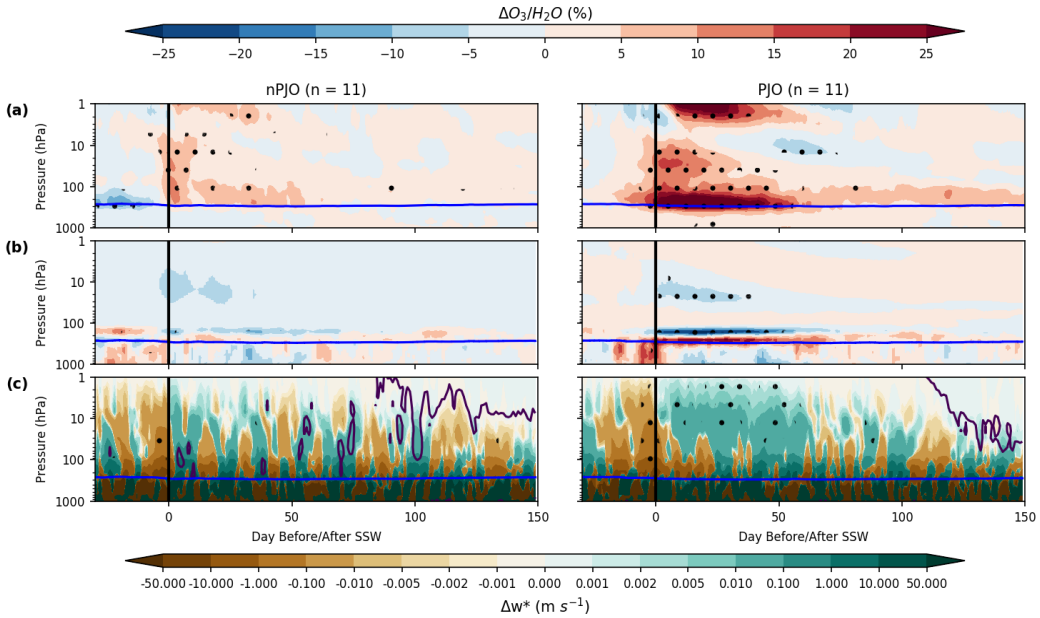

Figure 6.4 – Vertical-time composites of polar-cap (60-90°N) averaged (**a**) ozone (O_3), (**b**) water vapour (H_2O) and (**c**) the residual vertical velocity ($\overline{w}^*$) deseasonalised anomalies for nPJO SSWs (n = 11) and PJO SSWs (n = 11) (1980-2013) from EMAC for the time period 1980-2013. The anomalies are expressed as a percentage (%) with the exception of the residual vertical velocity ($\overline{w}^*$) anomalies which are given in units of m s^{-1} (0 m s^{-1} wind contour represented by purple solid line). Statistical significance at the 95 % level is indicated by stippling. The World Meteorological Organization (WMO) defined thermal tropopause is displayed for reference in each panel (blue solid line).

The long persistence timescales of the composition anomalies in the LMS reflects the dominant role of radiative processes, as the reversal of the stratospheric winds suppresses the propagation of planetary-waves into the stratosphere (Hitchcock et al., 2013). The evolution of polar downwelling ($\overline{w}^*$) anomalies shows a period of accelerated descent throughout the Arctic stratosphere immediately prior to an SSW in all cases. This is rapidly followed by a period of anomalously weak polar downwelling in the upper stratosphere that gradually propagates down as the SSW evolves (in the case of PJO events). This anomalous evolution in polar downwelling helps explain the establishment of the anomalies in O_3 and H_2O in the LMS and perhaps also influences their persistence, but this aspect would need to be studied further. The prolonged chemical changes in our observations are indeed consistent with the delayed recovery of the stratospheric polar vortex for PJO events, which are known to have larger impacts on the tropospheric circulation (Hitchcock et al., 2013; de la Cámara et al., 2018a). Although an increase in tropospheric ozone is shown during these events, the lack of statistical significance leads warrants further attempt to isolate the stratospheric influence.

6.3.2 Stratospheric Ozone (O_3S) and Ozone Fraction (O_3F)

In order to elucidate whether STE of ozone is enhanced as a result of the anomalous enrichment in LMS ozone, the tagged-stratospheric ozone (O_3S) tracer is next utilised. The tropospheric fraction of ozone of stratospheric origin (O_3F) using this tracer ($O_3F = O_3S/O_3$ x 100) is also derived to explore changes in the evolution of the stratospheric contribution. The deseasonalised (%) anomaly evolution for O_3S and O_3F are shown for both the nPJO is initially confined to the upper troposphere (300-500 hPa). Deeper penetration of O_3S into the troposphere, and more clearly shown in the anomalies of O_3F, is evident from around 20 days after the SSW central warming date, extending out to ~80 days. For both composites, a peak response around 50 days after the SSW onset date is apparent, with indication of an enhancement in ozone throughout the troposphere and elevated near-surface ozone which may impact air quality. The maximum increase in O_3S is on the order of ~5-10 % for PJO events, particularly near the surface, which equates to a change in the fraction of stratospheric ozone (O_3F) of > 5 %. In contrast, nPJO events show a minimal enhancement of O_3F (~ 1-2 %) for a much shorter duration. These findings support the notion that SSWs exert a downward influence not only dynamically on tropospheric circulation (Baldwin and Dunkerton, 1999; Scaife et al., 2016), but also chemically on tropospheric composition. The delay of this influence by 50-80 days after the SSW onset

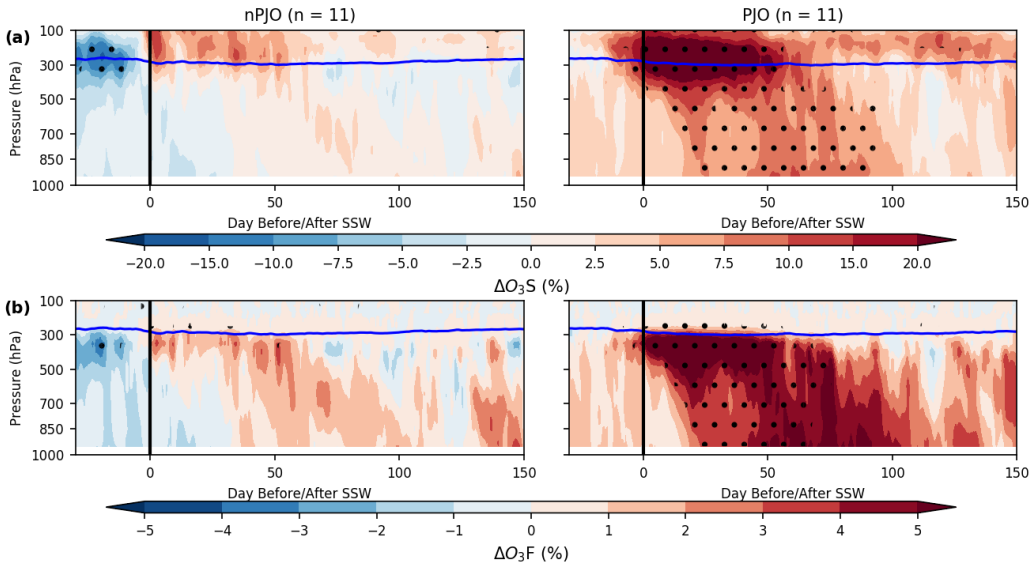

Figure 6.5 – Vertical-time composites of polar-cap (60-90°N) averaged (**a**) ozone of stratospheric origin (O_3S) and (b) the fraction of ozone of stratospheric origin ($O_3F = O_3S/O_3 \times 100$) deseasonalised anomalies for nPJO SSWs (n = 11) and PJO SSWs (n = 11) (1980-2013) from EMAC for the time period 1980-2013. The anomalies are expressed as a percentage (%) and statistical significance at the 95 % level is indicated by stippling. The World Meteorological Organization (WMO) defined thermal tropopause is displayed for reference in each panel (blue solid line).

ensures a maximum impact extending into the photochemically active season (spring) (Logan, 1985; Lelieveld and Dentener, 2000).and PJO event distinction (Figure 6.5a,b). A signal for enhanced STE is apparent for ~0-80 days following an SSW, although the entrainment of enhanced O_3S into the troposphere

6.3.3 Temperature

Since stratospheric temperatures serve as a good marker of anomalous changes in the strength of polar downwelling, consistent with variations in the magnitude of polar convergence attributable to alterations in the strength of the BDC or meridional circulation, temperature anomaly composites for each of the nPJO and PJO events are shown in Figure 6.6. In both cases, stratospheric warming occurs around the timing of an SSW onset, peaking between ~5 and 50 hPa, which was earlier shown in Figure 6.4c to coincide with a pulse of anomalously strong polar downwelling. An increase in temperature results as air warms adiabatically. For the nPJO composite, the region of warming, maximising around a 0-day lag at ~4-8 K, is confined to regions above 100 hPa and is short-lived (statistical significance is only inferred for approximately 10 days from the onset date). In contrast, temperature anomalies of up to 20 K are simulated in the few days prior to an event onset date for the PJO subclass of events between 1 and 10 hPa. For this region, a marked cooling subsequently follows (negative temperature anomalies

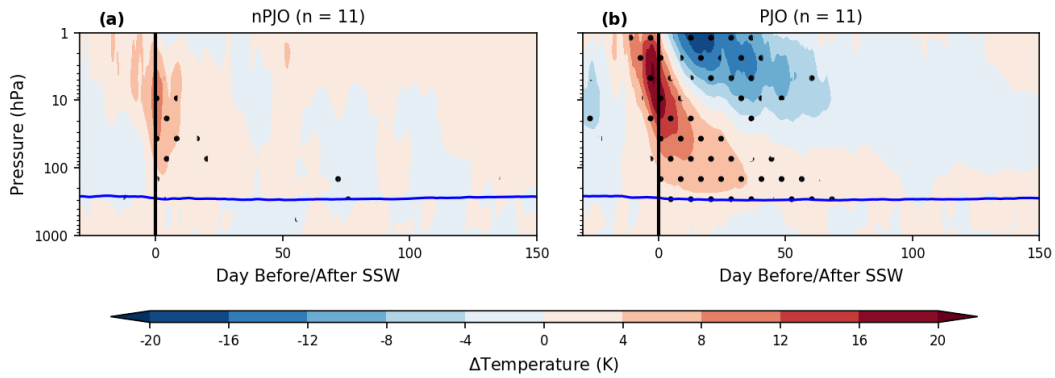

Figure 6.6 – Vertical-time composites of polar-cap (60-90°N) deseasonalised temperature (K) anomalies for (**a**) nPJO SSWs (n = 11) and (**b**) PJO SSWs (n = 11) (1980-2013) using specified-dynamics simulations from the EMAC CCM. Statistical significance at the 95 % level is indicated by stippling. The World Meteorological Organisation (WMO) defined thermal tropopause is displayed for reference in each panel (blue solid line).

of between ~-12 and -20 K between 1 and 5 hPa) which is relatively long-lasting. This feature is statistically significant between ~10 and 60 days following the SSW onset date and is characterised by a slow downward propagation of the signal. Below 10 hPa, the initial warming becomes increasingly prolonged but also weaker in magnitude as the signal propagates downward through the stratosphere. In the lower stratosphere (~100 hPa) for instance, a statistically significant positive temperature anomaly of ~4-8 K persists for up to 40 days from the SSW onset date. Although weaker still (~+0-4 K), the warming signal reaches down to the WMO-defined tropopause and is statistically significant between a ~0-30 day and a ~50-70 day lag. This leads to a fall in the mean tropopause height by ~20-30 hPa shortly after an event onset. Indeed, the significance of the PJO events is that the warming is maximised lower down in the stratosphere (Hitchcock et al., 2013), which invokes a much larger dynamical response following such events in the UTLS, and in turn the troposphere, via stratosphere-troposphere coupling mechanisms.

6.4 Radiative Impacts

A narrow band radiative transfer model is used to calculate temperature changes using the Fixed Dynamical Heating (FDH) method (Ramanathan and Dickinson, 1979; Fels et al., 1980); the model configuration is as given under UoR_NBM in Table 1 of Myhre et al. (2009). In terms of the general hierarchy of radiative transfer models, this model is considered to be of greater accuracy compared with radiative transfer code within a GCM, but less accurate than calculations using line-by-line models. The description of the FDH technique applied here is given in Table 1 of Myhre et al. (2009). The longwave (LW) radiative transfer code is a Malkmus random-band model at 10 cm^{-1} resolution (Forster and Shine, 1997; Chagas et al., 2001) and has been updated (see Shine and Myhre, 2020)

to include the HITRAN-2016 line parameters (Gordon et al., 2017) and the most recent version (MT_CKD3.2) of the MT_CKD water vapour continuum (Mlawer et al., 2019). The shortwave (SW) radiative transfer code consists of both a 4 stream discrete ordinate code, with a resolution of 5 nm in the UV and 10 nm in the visible, and a delta-Eddington code which contains exponential sum fitting in 14 bands in the near-IR (Forster and Shine, 1997; Chagas et al., 2001). The FDH calculations presented here assume clear-sky conditions and solar insolation for 70°N on the 27th January (lag +10 day calculation) and the 8th March (lag +50 day calculation). These dates represent the mean lag dates following the central warming (onset) date for all PJO-type SSW events (n = 11) during the period of the EMAC simulations (1980-2013). The FDH calculations are run to equilibrium and so may be slightly larger in magnitude than transient FDH calculations (Forster et al., 1997). Composited polar-cap (60-90°N) mean ozone (O_3), water vapour (H_2O) and temperature profiles, averaged at a lag of 10 (5-15) days and 50 (45-55) days after the central warming date of a PJO-type SSW, are extracted from EMAC as input to these calculations. The FDH calculations act upon all input EMAC model levels between 1 and 300 hPa, whilst the temperature profile remains fixed in the troposphere region (300-1000 hPa). By design, FDH calculations do not provide temperature changes in the troposphere (300-1000 hPa) and cloud responses to the SSW (and any additional rapid tropospheric adjustments) are not accounted for, which may amplify or dampen the induced radiative forcing impact. Background concentrations of the well-mixed trace gases: 3.89 ppmv for carbon dioxide (CO_2), 323 ppbv for nitrous oxide (N_2O) and 1800 ppbv for methane (CH_4) are specified for each calculation.

The O_3 and H_2O anomalies associated with SSWs will have radiative impacts which might not be well represented, for example in Numerical Weather Prediction (NWP) models that do not fully simulate these anomalies, which may hinder forecasting skill of the overall simulation and tropospheric response to such events. The radiatively-driven component of stratospheric temperature changes using the FDH technique is calculated for the subset of PJO-type SSW events (n = 11) during the period 1980-2013. Figure 6.7a-b shows the polar-cap (60-90°N) mean O_3 and H_2O anomaly profiles (1-1000 hPa) averaged 5-15 days after the central warming (onset) date, together with the calculated FDH temperature changes (ΔT), due to each species separately and the total change. The largest temperature changes after the SSW onset are found to occur in the LMS (tropopause to 100 hPa) in accordance with the largest changes in O_3 and H_2O with respect to climatology. A warming signal of ~1.5 K is evident around 150-200 hPa, mostly due to the reduction in

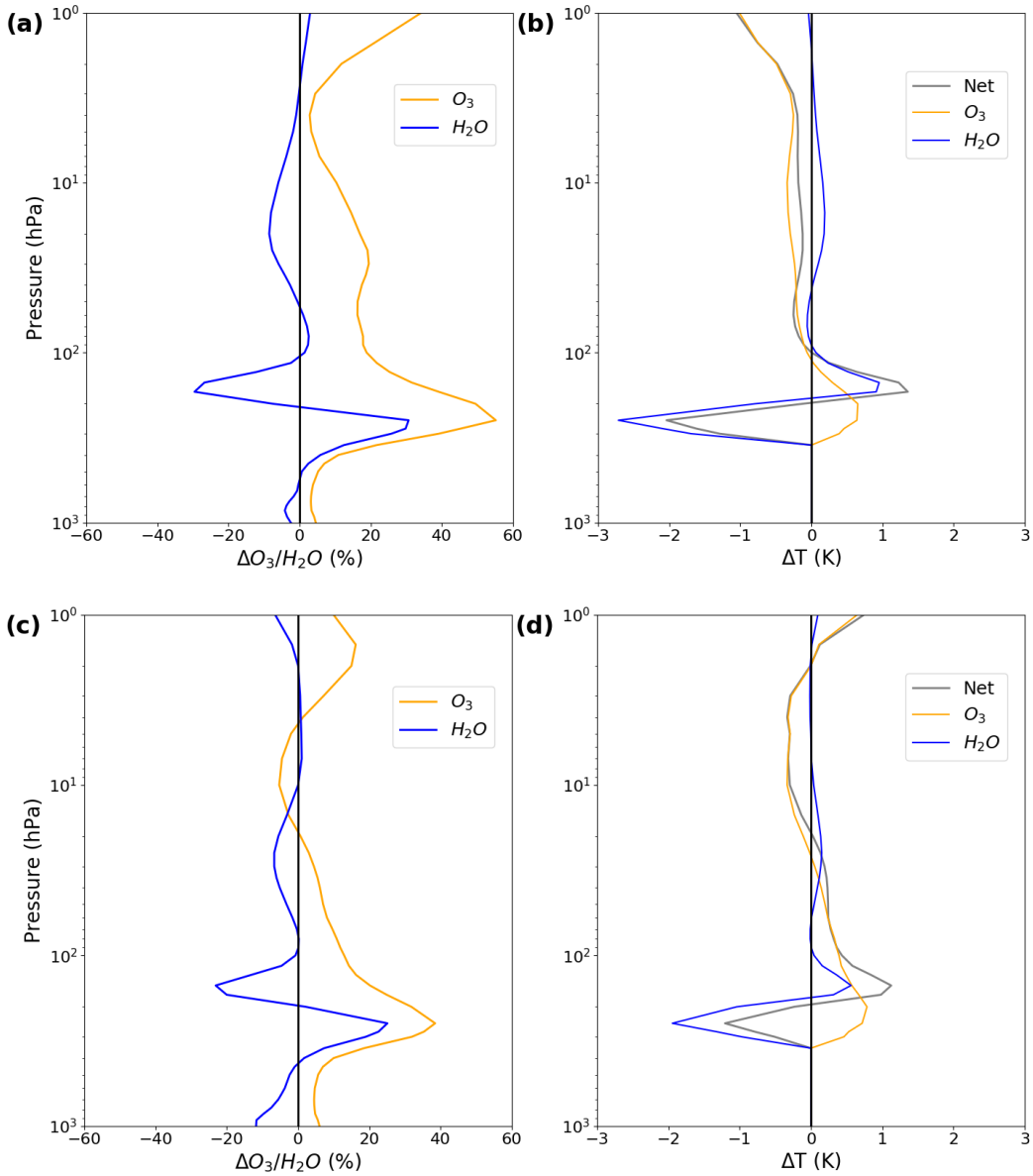

Figure 6.7 – (**a,c**) Polar-cap (60-90°N) averaged mean perturbations to the vertical profile of ozone and water vapour and (**b,d**) the resultant radiatively-driven stratospheric temperature changes averaged (**b**) 5-15 days and (**d**) 45-55 days after a PJO-type SSW (composite of 11 events over the period 1980-2013). The grey solid represents the net heating change due to these composition anomalies.

H_2O, with a cooling signal centred around 250-300 hPa of ~2 K, induced by the positive perturbation to H_2O, but moderated slightly by the radiative warming effect of O_3 in this region. Despite an enhancement of O_3 in the middle to lower stratosphere (10-100 hPa) however, a slight cooling (up to ~0.4 K) is found in this region, which is slightly offset by the radiative effect of H_2O (up to ~+0.1 K), leading to a net cooling of ~0.2-0.3 K. Above 10 hPa, O_3 changes alone lead to a cooling tendency that increases with altitude (~> 1 K at 1hPa). An additional set of calculations, averaged 45-55 days after the central warming (onset) date, yields similar results (Figure 6.7c-d), highlighting that such radiative effects may be relatively long-lasting. The FDH calculations yield changes in radiative fluxes in the

polar-cap due to the O_3 and H_2O changes which are of the order +0.76 W m^{-2} at the top of atmosphere, roughly equally due to the two gases and a change in surface radiative fluxes of -0.34 W m^{-2} due predominantly to O_3. These changes may be modulated by changes in atmospheric and surface dynamics, clouds, tropospheric H_2O, as well as surface albedo, and their wider significance would need to be assessed in coupled-climate simulations (Deng et al., 2013). It should be noted however that application of the FDH technique to investigate such radiative impacts has its limitations, and only serves as a useful first-order estimate of the stratospheric temperature response to perturbations in O_3 and/or H_2O.

Quantification of the sensitivity of the FDH calculations undertaken here, for different perturbations in O_3 and/or H_2O within the UTLS region (50-200 hPa), is next investigated through a series of sensitivity evaluations (Section 6.5). These idealised experiments are designed to provide further insight into the seasonality of the stratospherically adjusted radiative response over the Arctic region, together with the respective contributions from the LW and SW components, during the core of the stratospheric dynamically active season (taken here as the months from November to May inclusive). The range of perturbations to be artificially imposed in these evaluations take into account known variability in UTLS composition anomalies over the Arctic, as quantified in both CAMS and EMAC (2005-2013) in section 6.2, within the 50-200 hPa region where the largest relative (%) perturbations in O_3 and/or H_2O establish, not only following SSWs events, but more generally during wintertime in response to oscillations in the NAM index.

6.5 Radiative Importance of Arctic UTLS Ozone (O_3) and Water Vapour (H_2O)

To understand the stratospheric adjusted radiative impacts of perturbations in UTLS ozone (O_3) and water vapour (H_2O) in the Arctic stratosphere (70°N), a series of FDH calculations were performed in three main experiments. In a first experiment, monthly mean profiles of O_3 and H_2O were extracted from the EMAC RC1SD-base-10 model simulations over the period 1979-2013, together with monthly mean profiles of temperature which is used as an input in the calculations, from November to May inclusive (n = 7). A series of perturbations were then applied in the lower stratosphere (~ 50-200 hPa), with the five model levels above and below adjusted, based on a quadratic function centred around the 100 hPa level. The choice of this approach is informed from the anomaly profiles shown in Figure 6.7 for the 11 PJO SSW events between 1980 and 2013. The perturbation (multiplier) FDH calculations performed are 0.2, 0.4, 0.6, 0.8, 1.2, 1.4, 1.6, 1.8 and 2.0, which corresponds to an -80 %, -60 %, -40 %, -20 %, +20 %, +40 %,

+60 %, +80 % and +100% adjustment (m = 9) respectively for O_3 only calculations, H_2O only calculations and both O_3 and H_2O calculations combined (l = 3). Thus, a total of 189 FDH calculations (n*m*l) were performed in this experiment. Experiment two is setup identically to experiment one in terms of design, but only the LW aspects of the radiative transfer, in response to the artificially imposed perturbations in O_3 and/or H_2O, are accounted for in each calculations. By differencing the resultant temperature changes for this LW-only experiment from those performed in experiment one, which factors in both the SW and LW components, the SW only component can be elucidated. A residual approach to isolate the SW influence is taken, as the SW impact on temperature requires the LW response to calculate the temperature change, and thus a SW-only calculation cannot be performed. Unlike the LW calculations, while the SW changes induce temperature changes, the SW calculations are only very weakly dependent on that temperature change (K. Shine, personal communication). This residual approach however comes with the caveat that potential feedbacks between the SW and LW components would not be accounted for.

The first experiment therefore aims to quantify the altitudinal sensitivity of the radiative response to unit changes in O_3 and/or H_2O anomalies, which is known to be strongly height dependent in the UTLS region where the radiative importance is maximised, as a function of the seasonal cycle (from November to May inclusive). The second experiment expands on this by elucidating the LW and SW component changes in response to the applied perturbations, which again is highly sensitive to the seasonal cycle. Collectively, the derived understanding should help to understand the significance of chemical composition changes in the Arctic UTLS following PJO-type SSWs, which is not well constrained, but has been demonstrated to impact the downward coupling response into the troposphere (e.g. Haase and Matthes, 2019; Oehrlein et al., 2020).

6.5.1 Experiment One: Seasonal Dependence

6.5.1.1 Profile Temperature Changes

A selection of temperature change (ΔT [K]) profiles, as calculated using the FDH method in response to the artificially imposed perturbations in O_3 and/or H_2O between 50-200 hPa (also shown), are first plotted in Figures 6.8-6.10 for mid-December, mid-February and mid-April respectively. As illustrated in (a), negative perturbations are shown in each figure for a (b) 40 % reduction and a (c) 80 % reduction. In contrast, as illustrated in (d),

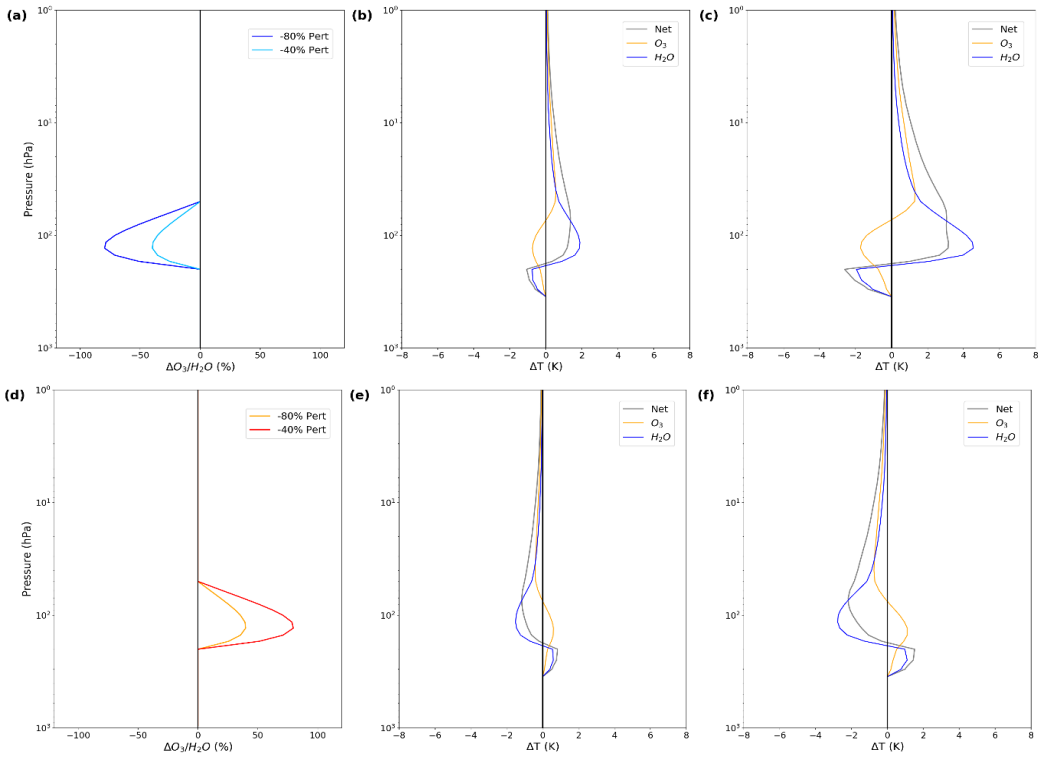

Figure 6.8 – Resultant radiatively-driven stratospheric temperature changes as a result of (**a**) an artificially imposed reduction in O_3 and/or H_2O by (**b**) 40 % and (**c**) 80 % and (**d**) an artificially imposed enhancement in O_3 and/or H_2O by (**e**) 40 % and (**f**) 80 % with respect to mid-December climatology.

positive perturbations are shown in each figure for a (e) 40 % enhancement and a (f) 80 % enhancement. The height-resolved ΔT shows clear sensitivity to the magnitude of the imposed perturbation for both chemical species, and in turn the net heating response. For each month shown, the profile ΔT are largely of opposite and equal magnitude between the -40 % perturbation and the +40 % run calculations. Although the ΔT response between the -80 % perturbation and the +80 % perturbation also exhibits a large degree of antisymmetry with respect to the ΔT = 0 line, the profile ΔT is typically larger for a negative perturbation of this magnitude within the 50-200 hPa region. This signifies a high degree of linearity in the FDH temperature response to changes in O_3 and/or H_2O, at least for perturbations up to ±40 %, with indications of an element of non-linearity in the ΔT response for much larger perturbations. This aspect will subsequently be more closely scrutinised in 6.5.1.2.

For the mid-December FDH calculations (Figure 6.8), the imposition of a negative (positive) 40 % perturbation in both O_3 and H_2O can be seen to induce a general warming (cooling) of the stratosphere (1-200 hPa), as denoted by the grey (Net) line, which is maximised between ~50 and 150 hPa by up to ~1.5 K. The magnitude of the ΔT gradually relaxes towards zero above 50 hPa, with negligible change in temperature in the

uppermost part of the stratosphere shown here (~1-2 hPa). The ΔT below 150 hPa sharply reverses in sign for each case, such that a cooling (warming) of ~1 K is evident around 200 hPa for a -40 % (+40 %) perturbation. Below 200 hPa, the ΔT profile quickly tends towards zero at 300 hPa, which marks the lower boundary of the calculated stratospheric adjusted temperature change using the FDH technique. By examining the profile ΔT changes for H_2O only (blue line), it is clear that H_2O dominates the heating response for this month, as determined by the close correspondence with the Net profile ΔT (grey line). This can be explained by the dominance of the LW radiative component during December for 70°N when solar insolation is zero, as H_2O is more radiatively important in the LW component. O_3 in contrast is a more radiatively active trace gas in the SW, and thus the profile ΔT for the O_3 only calculations in each case show a much smaller response. It can be inferred that the O_3 effect, especially, is subtly dependent on the balance between how the stratospheric absorption and emission change when each chemical species is perturbed (in the absence of appreciable SW effects) (K. Shine, personal communication). The ΔT due to O_3 is however similar in magnitude and sign to H_2O between 1 and 30 hPa, before diverging in sign between ~70 and 200 hPa, such that O_3 leads to a local cooling (warming) for a -40 % (+40 %) perturbation. This results in a dampening of the ΔT response in the Net case, when both O_3 and H_2O are perturbed, by as much as ~0.5 K near to the 150 hPa level. The radiative effect of O_3 gradually reduces beneath this level, where it converges with the ΔT = 0 line at 300 hPa.

The same response is evident for the -80 % and +80 % perturbation calculations for this month (Figure 6.8c,f). Whilst the magnitude of the response appears to be generally double that of the ±40 % cases, more close inspection shows a proportionally larger ΔT response for an 80 % reduction in O_3 and/or H_2O, compared with an 80 % enhancement. For instance, a Net ΔT between ~70 and 150 hPa of up to +3.5 K is calculated for the 80 % reduction case versus a ~-2.5 K for the 80 % enhancement case. This differential response would be anticipated due to the gradual saturation that occurs in gaseous absorption as concentrations increase, hence the system would on balance be expected to be more sensitive to negative perturbations than positive perturbations. Similarly for the region around 200 hPa, in which the ΔT response is inverse to the ~70-150 hPa region in each case, the -80 % perturbation case yields a ΔT of just over -2.5 K which compares with just over +1.5 K in the +80 % perturbation case. Calculations for each individual chemical species confirm an element of non-linearity of the FDH response for both O_3 and H_2O, although the largest differential ΔT response is evident for H_2O as this has the largest

impact on the Net profile ΔT. For the 70-150 hPa region, a warming (cooling) of ~4.5 K (~3 K) is shown and around 200 hPa, a cooling (warming) of ~2 K (~1-1.5 K) is shown for the H_2O only -80 % (+80 %) perturbation calculations.

In Figure 6.9, the same calculations are performed for a mid-February case, in which the SW component begins to influence the ΔT profile. Although the ΔT response as a function of height (pressure) is remarkably similar for each calculation, it is noticeable that the induced anomalies in O_3 have a significantly larger radiative effect, when compared with the mid-December case. The caveat with this statement however is that the absolute size of the imposed perturbation may differ between months due to seasonal changes in the initial climatological profiles, which is particularly relevant for O_3. This is particularly evident for the 150-300 hPa region, where the ΔT response is larger for each of the ±40 % and the ±80 % perturbations by a factor of ~1.5-2. The opposite tendency is however evident above 70 hPa, where the ΔT response due to O_3 is reduced. The impact on the Net ΔT profile is to moderate the region of warming (cooling) between 70 and 150 hPa and to locally enhance the region of cooling (warming) centred around 200 hPa for the positive (negative) perturbation calculations. Similarly to the ±40 % calculations

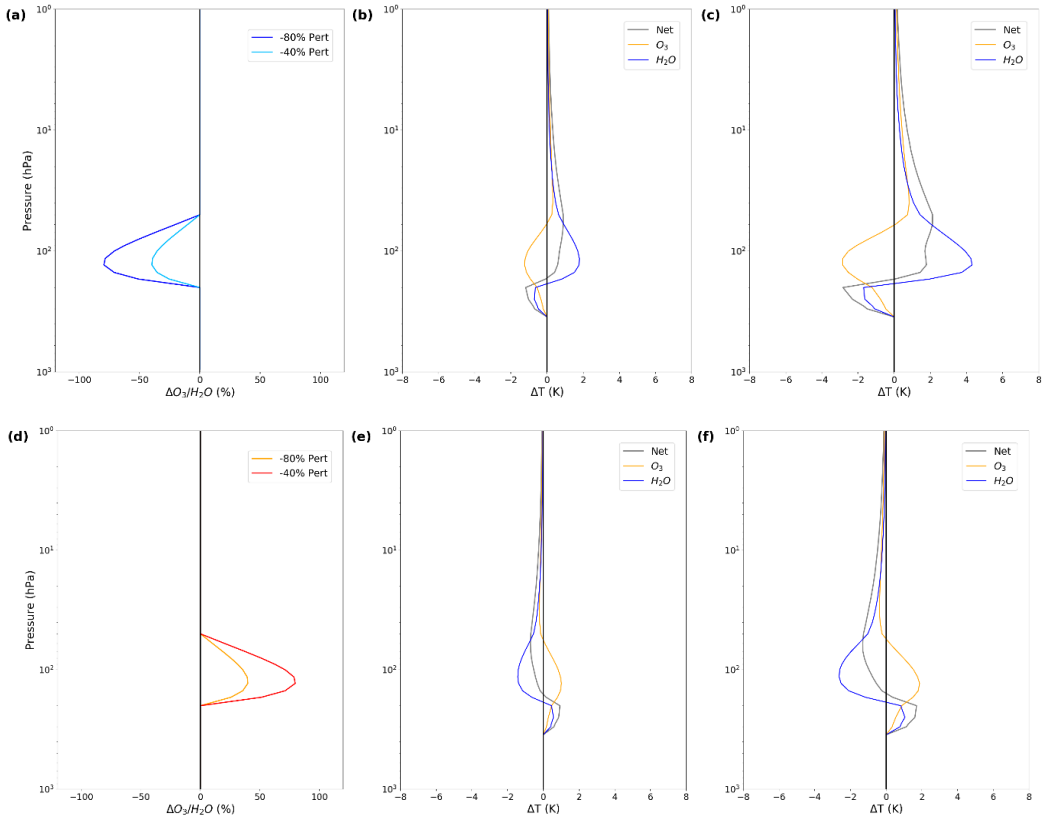

Figure 6.9 – Resultant radiatively-driven stratospheric temperature changes as a result of (**a**) an artificially imposed reduction in O_3 and/or H_2O by (**b**) 40 % and (**c**) 80 % and (**d**) an artificially imposed enhancement in O_3 and/or H_2O by **(e)** 40 % and **(f**) 80 % with respect to mid-February climatology.

performed for mid-December, the FDH response appears to be quite linear for each chemical species individually, as well as together combined, as evidenced by the largely antisymmetric changes with respect to ΔT = 0 line. For the ±80 % calculations, evidence of some non-linearity in the ΔT response becomes clearer (as was noted previously for mid-December). The enhanced radiative effect of O_3 for this month serves to reduce the region of warming (cooling) between 70 and 150 hPa to around ~2K (~-1.5 K) for the Net negative (positive) 80 % perturbation calculation. This compares with an induced warming (cooling) of up to ~4.5 K (~-2.5 K) for the H_2O only case and an induced cooling (warming) of up to ~-3 K (~2 K) for the O_3 only case. These numbers give indication that the radiative effects of both chemical species are not purely additive, which again supports the notion that some non-linearity in the FDH response exists when both chemical species are perturbed. It should be noted that the H_2O only ΔT profiles for each perturbation calculation are similar to that shown for the mid-December case (Figure 6.8), highlighting the relative importance of the LW component for H_2O, and its insensitivity to changes in the SW component.

Finally in Figure 6.10, the same ΔT profiles for each perturbation are again shown for a mid-April case. It is immediately apparent that the radiative effect of O_3 is further enhanced as the SW component becomes more influential. With respect to mid-February, the ΔT response is larger for each of the ±40 % and the ±80 % perturbations by around a factor of 1.5 for the 70-150 hPa region. A smaller enhancement in the ΔT response due to O_3 is evident below this region and in contrast, a reduction in the ΔT response is apparent above 70 hPa. These tendencies are consistent with those noted for the transition from a mid-December to a mid-February case. The radiative effect of O_3 for mid-April is now sufficiently large enough to change the sign of the ΔT response for much of the 70-150 hPa region in the Net case, such that a slight cooling (warming) is calculated for the negative (positive) perturbation calculations. For the ±40 % perturbation calculations, the ΔT response as a function of height (pressure) is again very similar in magnitude, albeit opposite in sign. As before, the ΔT profile structure remains similar for the ±80 % perturbation calculations, but with larger changes evident for an 80 % reduction compared with an 80 % enhancement in O_3 and/or H_2O. Between 70 and 150 hPa, the radiative effects of O_3 and H_2O largely offset each other to yield a slight cooling (warming) of up to ~1K (~1.5 K) for a -80 % (+80 %) perturbation of both chemical species. For the O_3 perturbed only calculation, a cooling (warming) of up to 5 K (3.5 K) is induced, with a calculated warming (cooling) of up to 4 K (2.5 K) for the H_2O only perturbed case, for a -

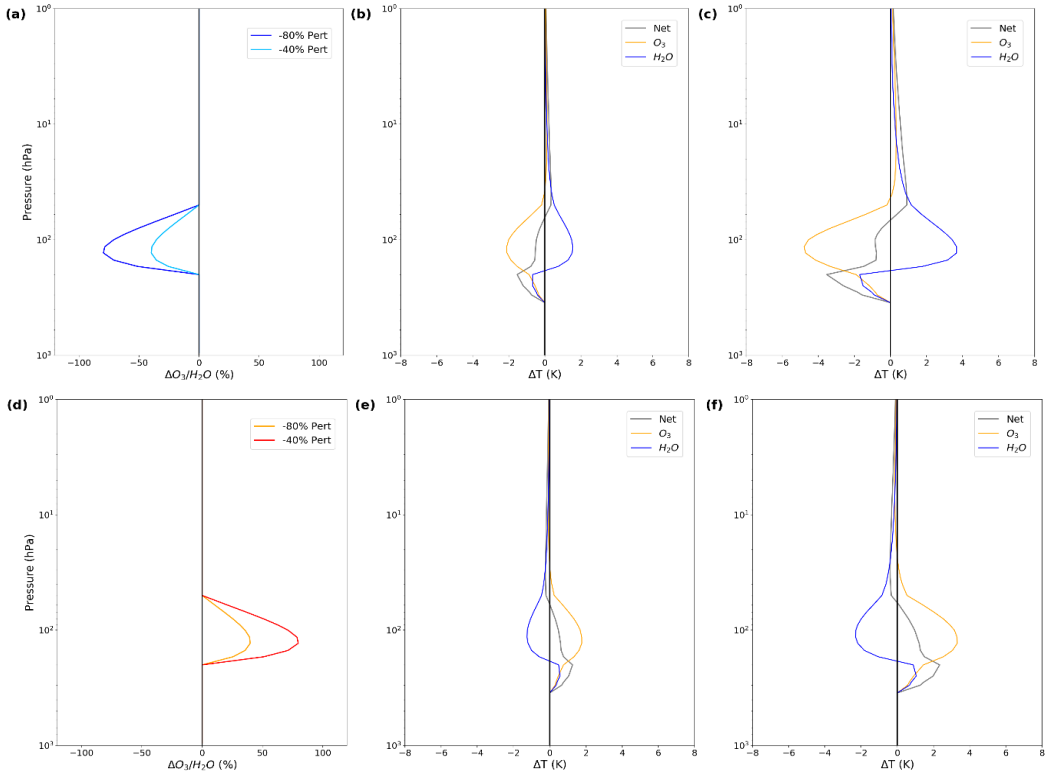

Figure 6.10 – Resultant radiatively-driven stratospheric temperature changes as a result of (**a**) an artificially imposed reduction in O_3 and/or H_2O by (**b**) 40 % and (**c**) 80 % and (**d**) an artificially imposed enhancement in O_3 and/or H_2O by (**e**) 40 % and (**f**) 80 % with respect to mid-April climatology.

80 % (+80 %) perturbation. The H_2O only ΔT response abruptly flips over in sign below 150 hPa, as seen before for the mid-December and mid-February cases, where the radiative impacts of both O_3 and H_2O become approximately equal around the 200 hPa level. This induces a cooling (warming) of ~1.5 K (1 K) in each case, which increases to a cooling (warming) of ~ 3.5 K (2.5 K) when both chemical species are perturbed in the Net case. As stated before, such implied non-linear aspects will next be assessed further in section 6.5.1.2 for this first experiment (experiment one).

Figure 6.11 provides a visual summary of the ΔT response across the three months shown here (December, February and April), as a function of the percentage perturbations (or multipliers) applied to the polar-cap mean (60-90°N) volume mixing ratio profiles in O_3 and/or H_2O from the EMAC climatology (1980-2013) within the UTLS region (50-200 hPa). The opposing ΔT response between the radiative effect of O_3 and H_2O across the range of perturbations applied is apparent in each month. The radiative effect of O_3 however increases markedly from December through until April, as evidenced by the more amplified ΔT response for larger perturbations especially, whereas the H_2O radiative effect reduces slightly in amplitude between the different perturbations from the mid-December to mid-April case. For the month of December, O_3 has a radiative effect of

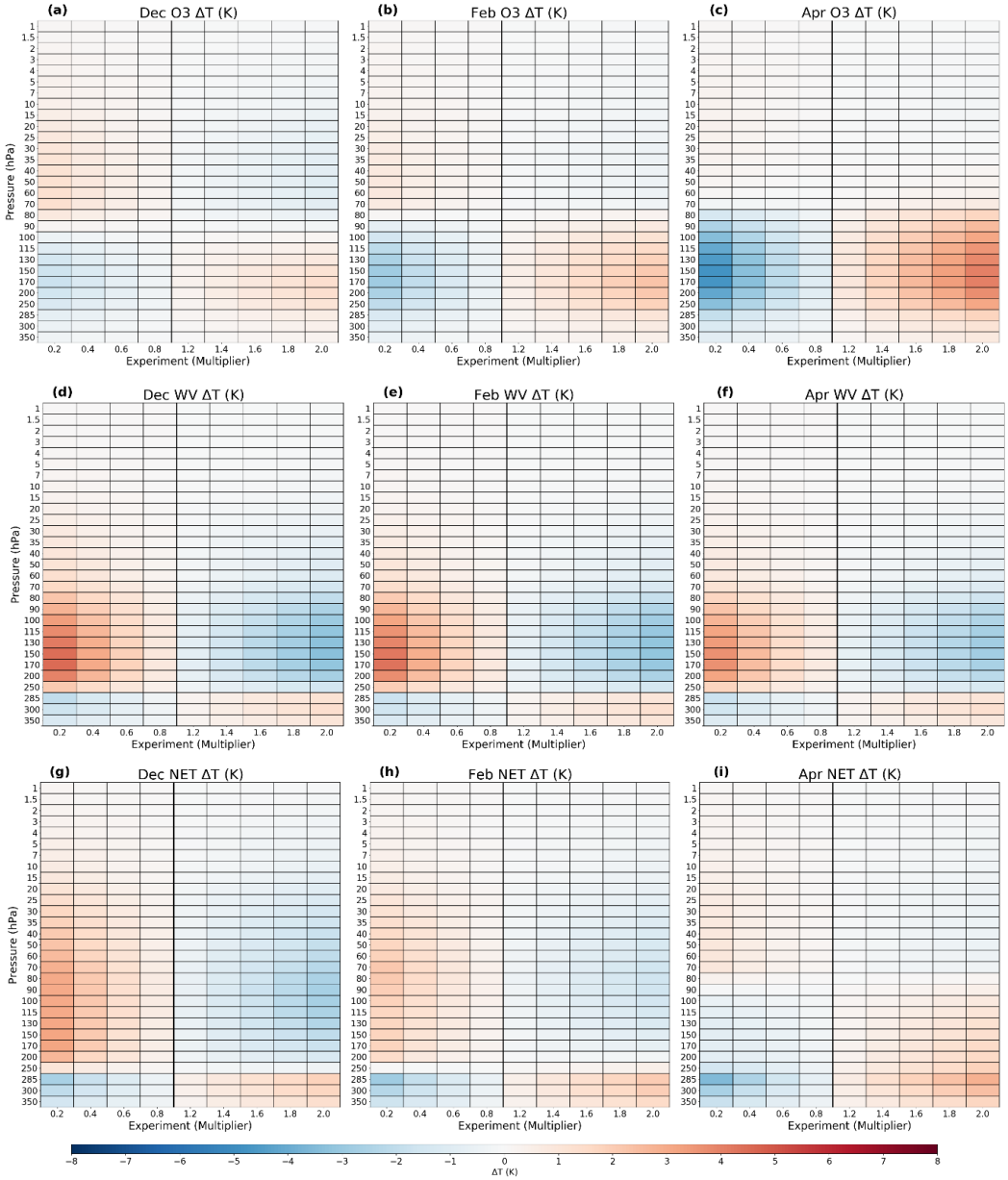

Figure 6.11 – Resultant radiatively-driven stratospheric temperature changes as a result of (**a-c**) ozone, (**d-f**) water vapour and (**g-i**) both O_3 and H_2O perturbations, with respect to mid-December (**a,d,g**), mid-February (**b,e,h**) and mid-April (**c,f,i**) climatology.

between ~-1.5 K and ~+1.5 K for an applied perturbation ranging between -80 % and +100 %. This increases to between ~-3 and ~+2 K for the month of February and between ~-5 and ~+4 K for the month of April. The radiative effect of H_2O on the other hand ranges from between ~+4.5 K and ~-3.5 K for the month of December, ~+4.5 K and ~-3 K for the month of February and ~+4 and ~-2.5 K for the month of April. The ΔT above ~70 hPa is inverse in sign to that of the UTLS region (70-150 hPa) for O_3 and is largest in December, when the magnitude of the radiative effect is similar to that of the lower stratospheric region, but is much more muted for February and particularly April. The H_2O radiative effect in this region is consistent in sign, but weaker still in magnitude, and is largely

insensitive to the change in seasonality (weakening only slightly from December through until April). The region between 250 hPa and 300 hPa is on the other hand of greater interest.

Whilst the O_3 radiative effect here is consistent with the UTLS region across the range of perturbations applied for each month, albeit weaker in magnitude, the H_2O radiative effect sharply opposes that within the UTLS region. This manifests as a dipole in the ΔT response, centred around the critical 250 hPa level, which becomes slightly less prominent from December through until April. The combined influence of perturbations in O_3 and H_2O for each of these three months is subsequently elucidated in Figure 6.11g-i. The resultant ΔT response between 1 and 300 hPa shows that the radiative effects of O_3 and H_2O cancel each other out to a large extent in the UTLS region (70-150 hPa), especially moving away from December through until April. This residual net radiative effect ranges from between ~+3.5 K and ~-3 K for December, ~+2.5 K and ~-2 K for February and ~-1 K and ~+1.5 K for April for an -80 % perturbation through to a +100 % perturbation in both chemical species. Note that the ΔT response flips over in sign for the month of April as the radiative importance of O_3 within this region is sufficient to overcompensate for the radiative effect of H_2O, as remarked upon previously. The ΔT response above 70 hPa is consistent with this region, gradually reducing in amplitude between the different perturbations with increasing height (decreasing pressure). A dipole response is also present for all three months in the Net response, centred around the 250 hPa level, which is qualitatively consistent with that shown for the H_2O only perturbations. The radiative effect of O_3 serves to enhance the net radiative impact in the region below 250 hPa, more especially into springtime. Although much of the Net ΔT response appears to be the product of linear, additive radiative effects from both O_3 and H_2O perturbations individually in Figure 6.11, it was demonstrated from the ΔT profile plots for each respective month (Figure 6.8-6.10) that some non-linearities, albeit fairly small for more modest perturbations in particular, in the radiative response exist when both O_3 and H_2O are perturbed. This aspect is next examined more closely in 6.5.1.2 and highlights the increasing importance of radiative feedbacks between O_3 and H_2O for larger perturbations.

6.5.1.2 Linearity Assessment

To investigate the degree of linearity of the ΔT response to the magnitude of the artificially imposed perturbations in UTLS (50-200 hPa) O_3 and/or H_2O, a linear regression

was performed for each pressure level in the EMAC model grid between 1 and 300 hPa over the range of percentage perturbations (multipliers) applied: -80 % to +100 % (0.2 to 2.0). Results for O_3 only perturbations are first shown in Figure 6.12 for the three months previously shown in 6.5.1.1 (December, February and April), for 11 select pressure levels between 1 and 300 hPa. Corresponding statistical output from each linear regression performed is subsequently shown in Table 6.5. For each of the three months, an opposing tendency in the local ΔT is found for the bottom three or four levels (150 hPa, 200 hPa, 250 hPa and 300 hPa), with respect to the other shown (higher) levels within the stratosphere. Most notably for levels 200 hPa and 250 hPa, a cooling (warming) is induced for reductions (enhancements) in the O_3 abundance with respect to the climatological values for EMAC averaged over the polar-cap region (60-90°N). As indicated by the slope values, which constitute the ΔT (K) per unit (20 %) change in the perturbation applied, a maximum local radiative sensitivity for O_3 is found at both the 200 hPa and 250 hPa level where ΔT = ~0.3 K for December, ~0.5 K for February and ~0.9 K for April per 20 % change in O_3 perturbation. This is clearly shown also in Figure 6.12. Above 150 hPa, a smaller inverse tendency is found for the ΔT response to perturbations in O_3. The region with the most sensitive ΔT response is found between ~50 and 100 hPa in December and to a lesser extent February. The ΔT response in April is however relatively insensitive to changes in O_3 above 150 hPa. A maximum change in ΔT per unit (20 %) perturbation in O_3 is on the order of -0.15 to -0.25 K for December, -0.10 to -0.13 K for February, with negligible change observed for April between 50 and 100 hPa. It is clear that the region of positive tendency (i.e. an increase in O_3 abundance leads to a positive ΔT) increases from December through to April as a function of seasonal changes in the radiative balance (as day length increases from 0 to over 12 hours).

For each linear regression performed for the levels between 1 and 300 hPa, high Pearson correlation coefficient (r) values combined with low standard error values, imply strong linearity in the ΔT response to perturbations in O_3. This is corroborated through inspection of each point and its relation to the position of the line of best fit for each level. Only for the levels with the greatest radiative sensitivity to O_3 changes (i.e. 200 hPa and 250 hPa) are there any indications of slight non-linearity in the ΔT response. As these calculations are for O_3 only perturbations, an element of non-linearity may arise due to non-local radiative mechanisms (i.e. the ΔT for each pressure level is determined by the ΔT for all other levels), in addition to the saturation absorption effect. These feedbacks are

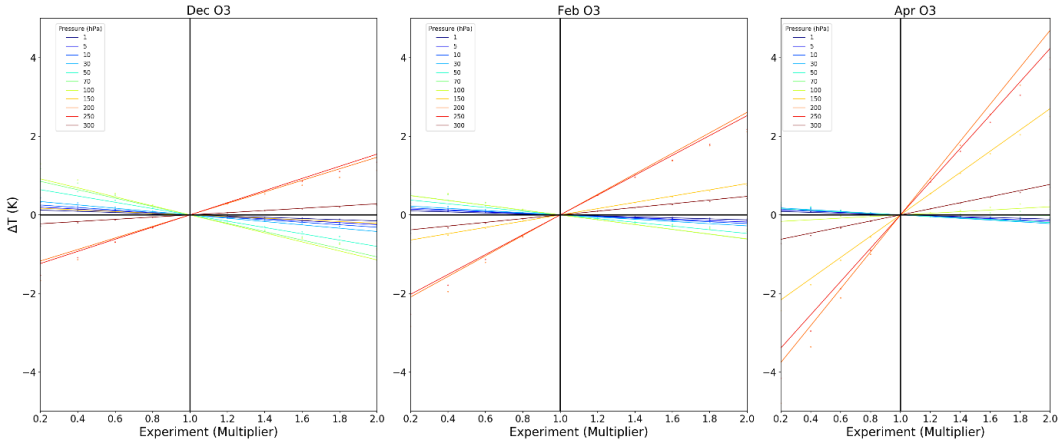

Figure 6.12 – Linear regression for the O_3 ΔT with respect to percentage perturbation (multiplier) magnitude for the months of December (**left**), February (**centre**) and April (**right**).

December			
Pressure (hPa)	**Slope**	**R**	**Std Err**
1	-0.031	-0.995	0.001
5	-0.050	-0.995	0.002
10	-0.064	-0.995	0.002
30	-0.087	-0.994	0.004
50	-0.165	-0.991	0.008
70	-0.220	-0.989	0.012
100	-0.237	-0.986	0.014
150	-0.043	-0.999	0.000
200	0.303	0.985	0.019
250	0.315	0.995	0.011
300	0.057	0.994	0.002
February			
Pressure (hPa)	**Slope**	**R**	**Std Err**
1	-0.026	-0.993	0.001
5	-0.037	-0.992	0.002
10	-0.045	-0.992	0.002
30	-0.057	-0.990	0.003
50	-0.098	-0.984	0.006
70	-0.129	-0.974	0.011
100	-0.129	-0.963	0.013
150	0.161	0.999	0.002
200	0.537	0.989	0.028
250	0.516	0.995	0.019
300	0.096	0.995	0.003
April			
Pressure (hPa)	**Slope**	**R**	**Std Err**
1	-0.222	-0.984	0.001
5	-0.033	-0.984	0.002
10	-0.040	-0.982	0.003
30	-0.046	-0.976	0.004
50	-0.042	-0.925	0.006
70	-0.007	-0.290	0.009
100	0.036	0.804	0.010
150	0.547	0.999	0.011
200	0.960	0.994	0.039
250	0.863	0.996	0.029
300	0.157	0.997	0.004

Table 6.5 – Linear regression output statistics for the resultant radiatively-driven stratospheric temperature changes as a function of the different artificially imposed perturbations applied within the UTLS region (70-150 hPa) for O_3. Results are shown for three out of the seven months as before (December, February and April) for a few select pressure levels from EMAC.

separate from those which may arise due to perturbations in more than one chemical species, which only become relevant when evaluating the Net ΔT response.

As shown in Figure 6.13, the results for the H_2O only perturbations yield different results as a function of height (pressure) across the range of perturbations in UTLS O_3 (50-200 hPa) applied. The different statistical parameters associated with each linear regression performed are shown separately for these calculations in Table 6.6. For all pressure levels shown, with the exception of the 300 hPa level, the ΔT response is characterised by a warming for negative perturbations and a cooling for positive perturbations for each of the three months. Interestingly and similarly to the O_3 only perturbations, the highest radiative sensitivity to changes in H_2O is shown for the 150 hPa, 200 hPa and 300 hPa levels. The slope values in Table 6.6 provide quantification of this, with a ΔT of between ~-0.5 and -0.8K per 20 % unit change in perturbation for each month. This negative tendency only weakens slightly with the seasonal change from December through to April. This contrasts with a positive tendency for the 300 hPa level, on the order of ΔT = ~0.2 K for each month per 20 % unit change in perturbation. As for O_3, the very high correlation (r) values and low standard error values for each pressure level shown, imply strong linearity in the radiative response to changes in H_2O. Whilst non-local radiative effects are clearly apparent as was found for O_3 (i.e. ΔT ≠0 outside of the artificially perturbed UTLS region – 50-200 hPa), any radiative feedbacks between different regions of the atmosphere do not serve to significantly influence the ΔT response for any given pressure level (either through amplification or dampening of the ΔT response). This is reflected by the distribution of points for each perturbation and the close relationship with the linear regression line of best fit.

The ΔT response for the range of perturbations applied in the Net case, where both O_3 and H_2O are perturbed between 50 and 200 hPa, are finally shown in Figure 6.14, together with the corresponding statistical output resulting from the linear regressions performed for the different pressure levels selected between 1 and 300 hPa (n = 11). As O_3 is radiatively sensitive in primarily the SW, the Net response in December strongly resembles that for H_2O. Only the 300 hPa level is characterised by a positive ΔT tendency for this month, a ΔT = ~0.28 K is calculated per 20 % unit change in perturbation, with respect to O_3 and H_2O abundance. A ΔT = ~-0.5 to -1 K is interpreted from the slope of the regression line for these levels, which markedly decreases with increasing height (decreasing pressure) above this region. The tendencies for February are furthermore very similar to that for December. A ΔT = ~0.32 K per 20 % unit change in perturbation is

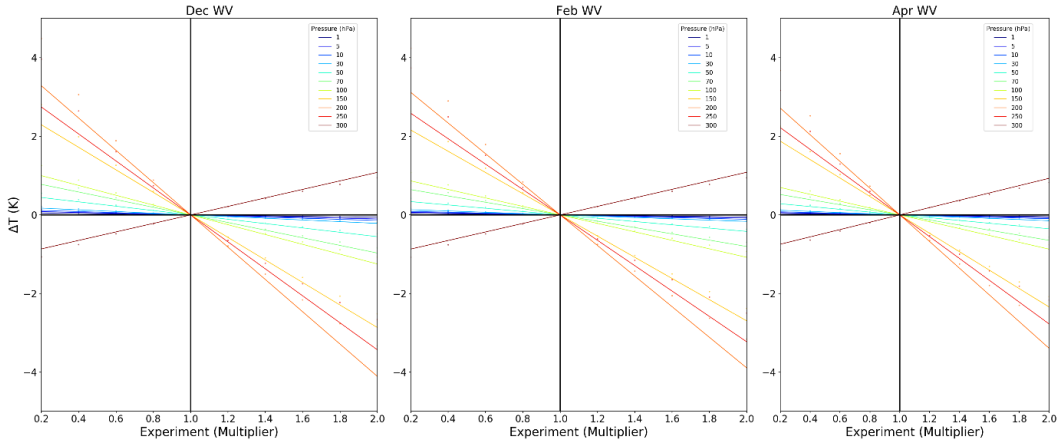

Figure 6.13 – Linear regression for the H_2O ΔT with respect to percentage perturbation (multiplier) magnitude for the months of December (**left**), February (**centre**) and April (**right**).

December			
Pressure (hPa)	**Slope**	**R**	**Std Err**
1	-0.012	-0.996	0.000
5	-0.021	-0.996	0.001
10	-0.029	-0.995	0.001
30	-0.044	-0.995	0.002
50	-0.113	-0.995	0.004
70	-0.198	-0.995	0.007
100	-0.255	-0.994	0.010
150	-0.584	-0.996	0.020
200	-0.845	-0.989	0.044
250	-0.710	-0.985	0.045
300	0.221	0.995	0.008
February			
Pressure (hPa)	**Slope**	**R**	**Std Err**
1	-0.010	-0.996	0.000
5	-0.017	-0.995	0.001
10	-0.023	-0.995	0.001
30	-0.034	-0.995	0.001
50	-0.086	-0.995	0.003
70	-0.164	-0.995	0.006
100	-0.220	-0.995	0.008
150	-0.549	-0.996	0.018
200	-0.801	-0.989	0.042
250	-0.669	-0.984	0.042
300	0.221	0.995	0.008
April			
Pressure (hPa)	**Slope**	**R**	**Std Err**
1	-0.009	-0.997	0.000
5	-0.014	-0.996	0.000
10	-0.020	-0.996	0.001
30	-0.030	-0.996	0.001
50	-0.072	-0.996	0.002
70	-0.132	-0.995	0.005
100	-0.178	-0.996	0.006
150	-0.477	-0.996	0.014
200	-0.698	-0.990	0.036
250	-0.573	-0.985	0.035
300	0.190	0.996	0.005

Table 6.6 – Linear regression output statistics for the resultant radiatively-driven stratospheric temperature changes as a function of the different artificially imposed perturbations applied within the UTLS region (70-150 hPa) for H_2O. Results are shown for three out of the seven months as before (December, February and April) for a few select pressure levels from EMAC.

additional importance of the SW component in February, through its relevance to the inferred for the 300 hPa level, with an opposing ΔT = ~-0.3 to -0.9 K per 20 % unit change in perturbation for 150-250 hPa. For remaining levels, the ΔT response is smaller again, not only with respect to these lower levels but also with the month of December. The radiative effects induced by O_3 in particular, can be inferred to reduce the Net ΔT response to perturbations in both chemical species, given that the H_2O ΔT tendencies were largely unchanged between December and February (but the O_3 ΔT tendencies increased). The O_3 ΔT tendencies however decreased for the region above 70 hPa, which has led to smaller Net ΔT tendencies as the response is largely additive (same sign tendencies both O_3 and H_2O) with H_2O, which again was characterised by only very small changes in the ΔT response between December and February. For the month of April, the region characterised by a positive tendency in the ΔT response to perturbations in both O_3 and H_2O has expanded beyond only the 300 hPa level to also include the above three levels: 150 hPa, 200 hPa and 250 hPa. The maximum radiative sensitivity has also shifted to the 250 hPa level where a ΔT = ~1 K is apparent per 20 % unit change in perturbation.

For pressure levels between 1 and 100 hPa, the ΔT tendency remains negative but is noticeably smaller with respect to February and more especially December throughout the vertical profile in this region. Although the radiative effect of H_2O was determined to reduce slightly from December through to April, the main reason for the change in the ΔT tendency between 100 and 300 hPa is a result of the increasing radiative importance of O_3 via the growing importance of the SW component. This confirms the earlier statement that the O_3 radiative effect begins to outweigh the H_2O radiative effect for the month of April, in contrast with both months December and February. The very high correlation (r) values and low standard error values in Table 6.7, together with the observation from

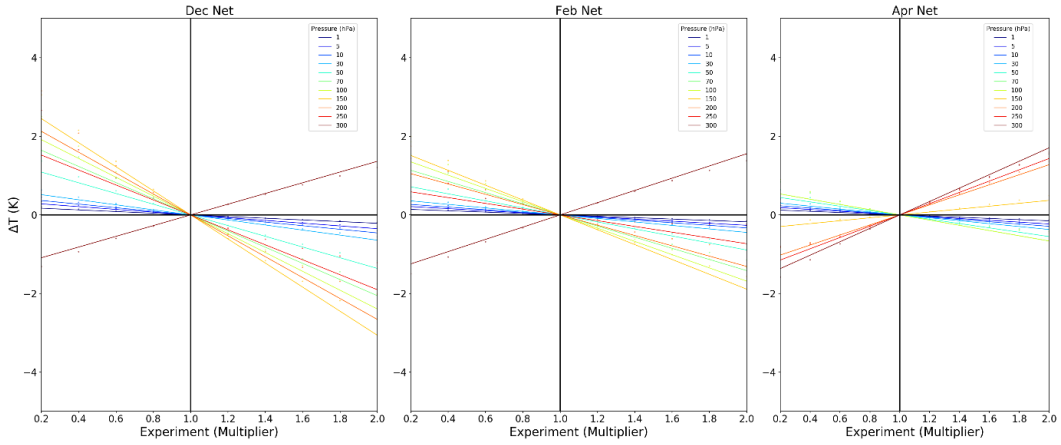

Figure 6.14 – Linear regression for the Net ΔT with respect to percentage perturbation (multiplier) magnitude for the months of December (**left**), February (**centre**) and April (**right**).

Pressure (hPa)	Slope	R	Std Err
1	-0.043	-0.996	0.001
5	-0.071	-0.996	0.002
10	-0.093	-0.996	0.003
30	-0.131	-0.995	0.005
50	-0.278	-0.994	0.011
70	-0.420	-0.994	0.017
100	-0.491	-0.992	0.022
150	-0.625	-0.995	0.023
200	-0.551	-0.982	0.038
250	-0.960	-0.960	0.041
300	0.277	0.996	0.009
February			
Pressure (hPa)	**Slope**	**R**	**Std Err**
1	-0.036	-0.995	0.001
5	-0.054	-0.994	0.002
10	-0.068	-0.994	0.003
30	-0.091	-0.993	0.004
50	-0.183	-0.991	0.009
70	-0.292	-0.989	0.015
100	-0.348	-0.988	0.019
150	-0.388	-0.991	0.018
200	-0.276	-0.968	0.025
250	-0.882	-0.882	0.031
300	0.317	0.996	0.010
April			
Pressure (hPa)	**Slope**	**R**	**Std Err**
1	-0.031	-0.991	0.002
5	-0.047	-0.990	0.002
10	-0.060	-0.990	0.003
30	-0.076	-0.989	0.004
50	-0.114	-0.983	0.008
70	-0.139	-0.974	0.012
100	-0.140	-0.964	0.014
150	0.070	0.964	0.007
200	0.252	0.997	0.007
250	0.993	0.993	0.012
300	0.346	0.998	0.008

Table 6.7 – Linear regression output statistics for the resultant radiatively-driven stratospheric temperature changes as a function of the different artificially imposed perturbations applied within the UTLS region (70-150 hPa) for the Net. Results are shown for three out of the seven months as before (December, February and April) for a few select pressure levels from EMAC.

Figure 6.14 that the calculated values in ΔT are close to the linear regression line of best fit for each level, again indicates strong linearity in the radiative response. As both O_3 and H_2O are perturbed for this set of calculations, this implies that the radiative effect of each chemical species can be added to yield the Net ΔT response to a good approximation of that shown. Nonetheless, an element of non-linearity can be discerned from Figure 6.14 centrally within the UTLS region (150-250 hPa), particularly for the month of December, in that the calculated ΔT begins to deviate from that predicted by the linear regression for increasingly larger perturbations. This seemingly originates from the slightly larger degree of non-linearity noted for H_2O compared to O_3, but is indeed possible that radiative feedback mechanisms between O_3 and H_2O may modulate the ΔT response to an extent. Further investigation would however be required to disentangle and quantify the role of

this factor further, together with any non-local radiative effects which may locally amplify or dampen the ΔT response away from the linear approximations. The relative role of the LW and SW components to the ΔT response quantified here, for the range of percentage perturbations (-80 % to +100 %) in O_3 and/or H_2O applied here, is next assessed in section 6.5.2.

6.5.2 Experiment Two: LW and SW Components

As before in section 6.5.2.1, profile temperature changes (ΔT [K]) in response to artificially introduced percentage perturbations in the UTLS (50-200 hPa) O_3 and/or H_2O, are depicted in Figures 6.15 and 6.17 for the LW only and Figures 6.16 and 6.18 for the SW only component (the latter taken as the LW+SW minus LW residual), but only for mid-February and mid-April respectively. The absence of the SW component in mid-December, as the sun stays below the horizon all day for the input latitude (70°N), means that the LW profile ΔT response for the month of December is equal to the total ΔT response shown earlier in Figure 6.8 (section 6.5.1.1). As before, the negative perturbations applied are illustrated (panel a), for a (b) 40 % reduction and an (c) 80 % reduction. Correspondingly, the positive perturbations applied are then depicted (d) for a (e) 40 % enhancement and an (f) 80 % enhancement. During the month of February, the cooling (warming) effect of O_3 for negatively (positively) imposed perturbations within the UTLS region is reduced for the LW only ΔT response, from up to ~-3 K (+ 2K) for an 80 % reduction (enhancement) to ~-2 K (+1 K) between ~100 and 200 hPa. This contrasts with an enhancement in the region of warming (cooling) associated with negative (positive) imposed perturbations between ~1 and 70 hPa. For the region of greatest sensitivity here (~50-70 hPa), the warming (cooling) increases from ~0.75 K (~-0.5 K) to ~1.25 K (~1.0 K) for the ± 80 % perturbation calculations. Below 200 hPa, the radiative effect of O_3 in the LW only is further reduced as the calculated ΔT approaches 0 at the critical 300 hPa level (lowest boundary of the calculated FDH temperature changes). For the H_2O only perturbations however, the ΔT response changes very little for the LW only experiment. A slight amplification of the magnitude of the ΔT response is discernible throughout the profile (1-300 hPa), maximising within the UTLS region for the ±80 % perturbation calculations. Thus, the changes in the Net profile ΔT response must be attributed to the isolation of the SW radiative component for O_3 almost entirely. Gradually increasing in magnitude from 1 hPa to the UTLS region (50-200 hPa), the Net ΔT increases (decreases) ~2 K (~1.5 K) to ~>3 K (~2.5 K) in the UTLS between the initial LW+SW calculations (Figure 6.9 in section 6.5.1.1) and the LW only calculations shown here for the +80 % (-80 %)

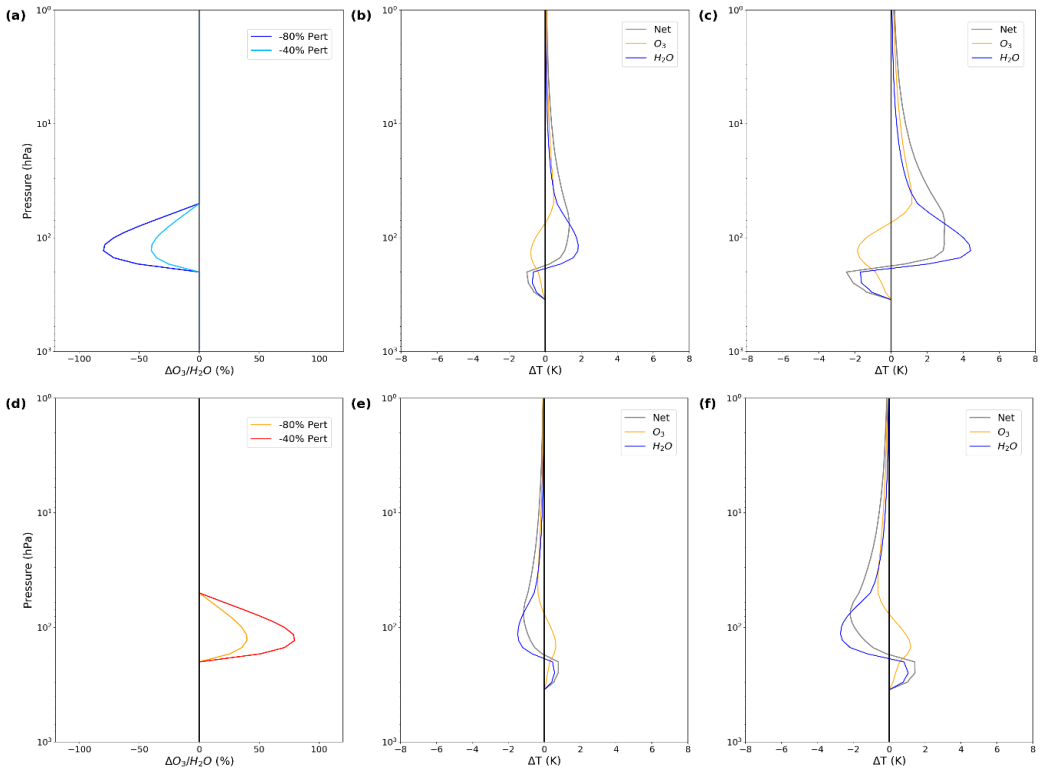

Figure 6.15 – Resultant radiatively-driven stratospheric temperature changes as a result of (**a**) an artificially imposed reduction in O_3 and/or H_2O by (**b**) 40 % and (**c**) 80 % and (**d**) an artificially imposed enhancement in O_3 and/or H_2O by (**e**) 40 % and (**f**) 80 % with respect to mid-February climatology. Results are shown for the LW component only.

perturbations. In contrast, the opposing region of cooling (warming) with to negatively (positively) imposed perturbations, which peaks between ~200 and 250 hPa, reduces by ~0.5 K between the LW+SW calculations and the LW only calculations for this month.

These results are equivalently shown through inference of the SW only component, taken as a residual (LW+SW – LW), in Figure 6.16. The radiative impact of O_3 drives almost all of the imposed cooling (warming) evident in the Net case for the negative (positive) perturbation SW calculations, as evidenced by the exceptionally close agreement for the ΔT profiles. For an -80 % (+80 %) perturbation, the ΔT due to O_3 maximises at ~-1 K (~+ 0.8 K) around the 100 hPa level (exactly where the perturbation is largest). A tiny radiative impact from H_2O is just about discernible for these larger perturbation calculations, slightly amplifying the LW+SW ΔT response in each case (but by less than 0.1 K in either direction). The similarity in the ΔT profile structure for O_3 in both the LW only and inferred SW only calculations, shows that the larger ΔT response in the earlier calculations for the LW+SW originates from almost solely the perturbation in O_3. The SW and LW radiative

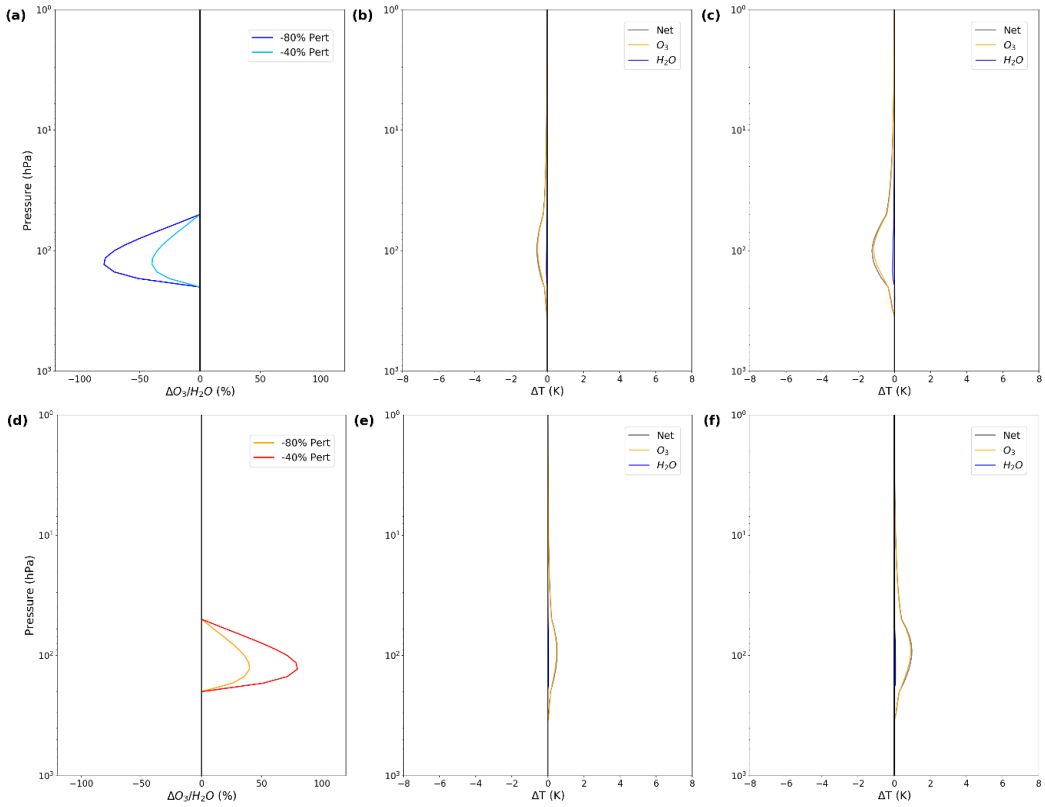

Figure 6.16 – Resultant radiatively-driven stratospheric temperature changes as a result of (**a**) an artificially imposed reduction in O_3 and/or H_2O by (**b**) 40 % and (**c**) 80 % and (**d**) an artificially imposed enhancement in O_3 and/or H_2O by (**e**) 40 % and (**f**) 80 % with respect to mid-February climatology. Results are shown for the residual SW component only (LW+SW – LW).

effects disentangled here show that the LW and SW radiative components are by in large linear and additive, serving to shift reduce the Net ΔT in the UTLS region from ~+ 3 K to +2 K for an 80 % reduction case, and from a ~-2.5 K to an -1.7 K for the 80 % enhancement case, for the LW only versus the LW+SW calculations respectively. This compensation effect is a result of the contrasting radiative effect of the imposed (same sign) perturbation in H_2O. Between ~200 and 250 hPa however, the radiative effect of O_3 and H_2O reinforce each other, such that addition of both LW and SW components for O_3 enhance the Net ΔT response (with the H_2O ΔT response almost entirely driven by the LW component).

The same LW only and SW only perturbation calculations for mid-April, when the importance of the SW component in association with solar heating is greatly enhanced for this month (day length >12 hours), are subsequently shown in Figure 6.17 and Figure 6.18 respectively. For O_3, the LW induced radiative cooling (warming) for negative (positive) perturbations is further reduced with respect to mid-February in the UTLS region primarily. With respect to the earlier shown LW+SW calculations for this month (Figure 6.10), it is clear that the O_3 SW component has now overtaken the LW component

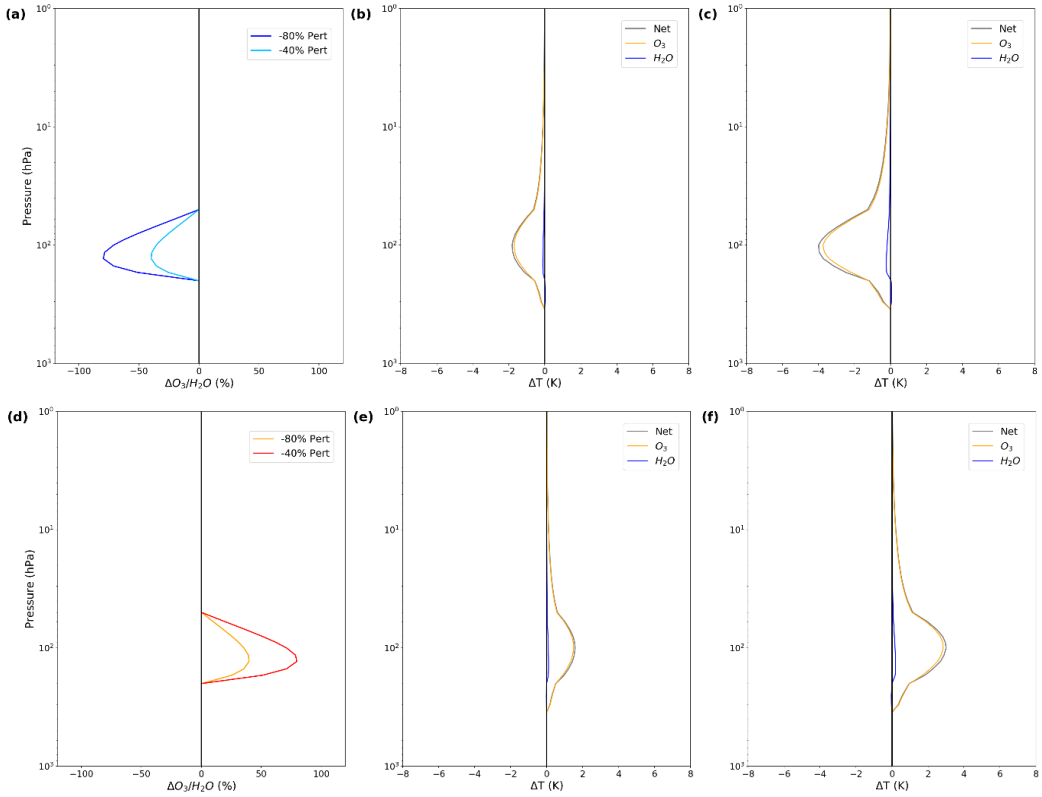

Figure 6.17 – Resultant radiatively-driven stratospheric temperature changes as a result of (**a**) an artificially imposed reduction in O_3 and/or H_2O by (**b**) 40 % and (**c**) 80 % and (**d**) an artificially imposed enhancement in O_3 and/or H_2O by (**e**) 40 % and (**f**) 80 % with respect to mid-April climatology. Results are shown for the LW component only.

in terms of magnitude. This is indeed confirmed for the ΔT profile plots the inferred SW only calculations shown next (Figure 6.19). The LW induced radiative cooling (warming) for a -80 % (+ 80 %) perturbation is reduced to ~-1.5 K (+1 K) between ~100 and 200 hPa. In contrast, the LW induced radiative warming (cooling) above 70 hPa for negative(positive) perturbations in O_3 is enhanced and so must be offset by the SW radiative component (which can indeed be seen to be the case in Figure 6.18). Compared with mid-February, the LW only H_2O radiative effect for mid-April shows very similar profile characteristics, only with only a slight reduction in magnitude. A slightly bigger difference emerges between Figure 6.10 (shown in section 6.5.1.1) for the combined LW+SW calculations and the LW only calculations shown here. A slight reduction in the LW radiative effect can be inferred due to a very small offset from the increasing SW influence (shown next in Figure 6.19). Below 200 hPa however, the H_2O ΔT profile is essentially unchanged between both LW+SW and LW only calculations. Finally, the Net ΔT response for these LW only calculations shows that the radiative effect of H_2O is dominant for this component, as interpreted from the remarkable relationship between the H_2O and Net ΔT profiles shown. In the earlier LW+SW calculations shown earlier for

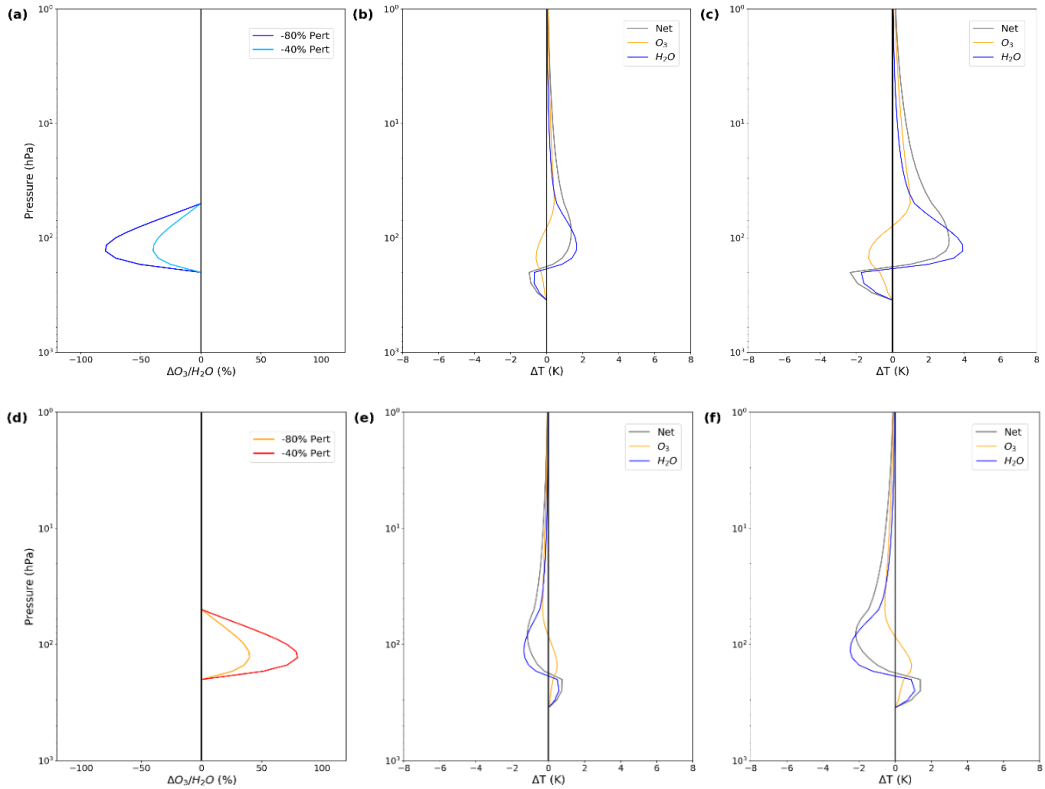

Figure 6.18 – Resultant radiatively-driven stratospheric temperature changes as a result of (**a**) an artificially imposed reduction in O_3 and/or H_2O by (**b**) 40 % and **(c**) 80 % and (**d**) an artificially imposed enhancement in O_3 and/or H_2O by (**e**) 40 % and (**f**) 80 % with respect to mid-April climatology. Results are shown for the residual SW component only (LW+SW – LW).

mid-April, the Net ΔT profiles had different characteristics for both positive and negative perturbations; indicating that the net warming (cooling) shown here for the UTLS region for the -80 % (+80 %) perturbation calculations is completely compensated for (even overcompensated for) by the SW radiative effects due to O_3 (now shown as a residual in Figure 6.19 where it is confirmed to be the case). This invoked a slight net cooling (warming) for these imposed perturbations by ~-1 K (+1.5 K) in the UTLS (50-200 hPa) region. Whilst the competing effects of the LW and SW components in the case can further be seen extend higher up in the stratosphere, albeit steadily decreasing in magnitude above 70 hPa, the two components again reinforce each other in the LMS (p > 200 hPa).

Quantified for the inferred SW only component in the perturbation calculations (Figure 6.19), is the imposed cooling of up to ~-1.5 to -2.0 K and ~-3.5 to -4.0 K for the -40 % and -80 % negative perturbation calculations respectively (centred around the 125 hPa level) for O_3. This contrasts with a SW-induced warming of up to ~+1.5 K and ~+3 K for the 40 % and 80 % positive perturbation calculations respectively. In each case, a very small SW radiative effect is induced when H_2O is perturbed by these respective amounts. For the -

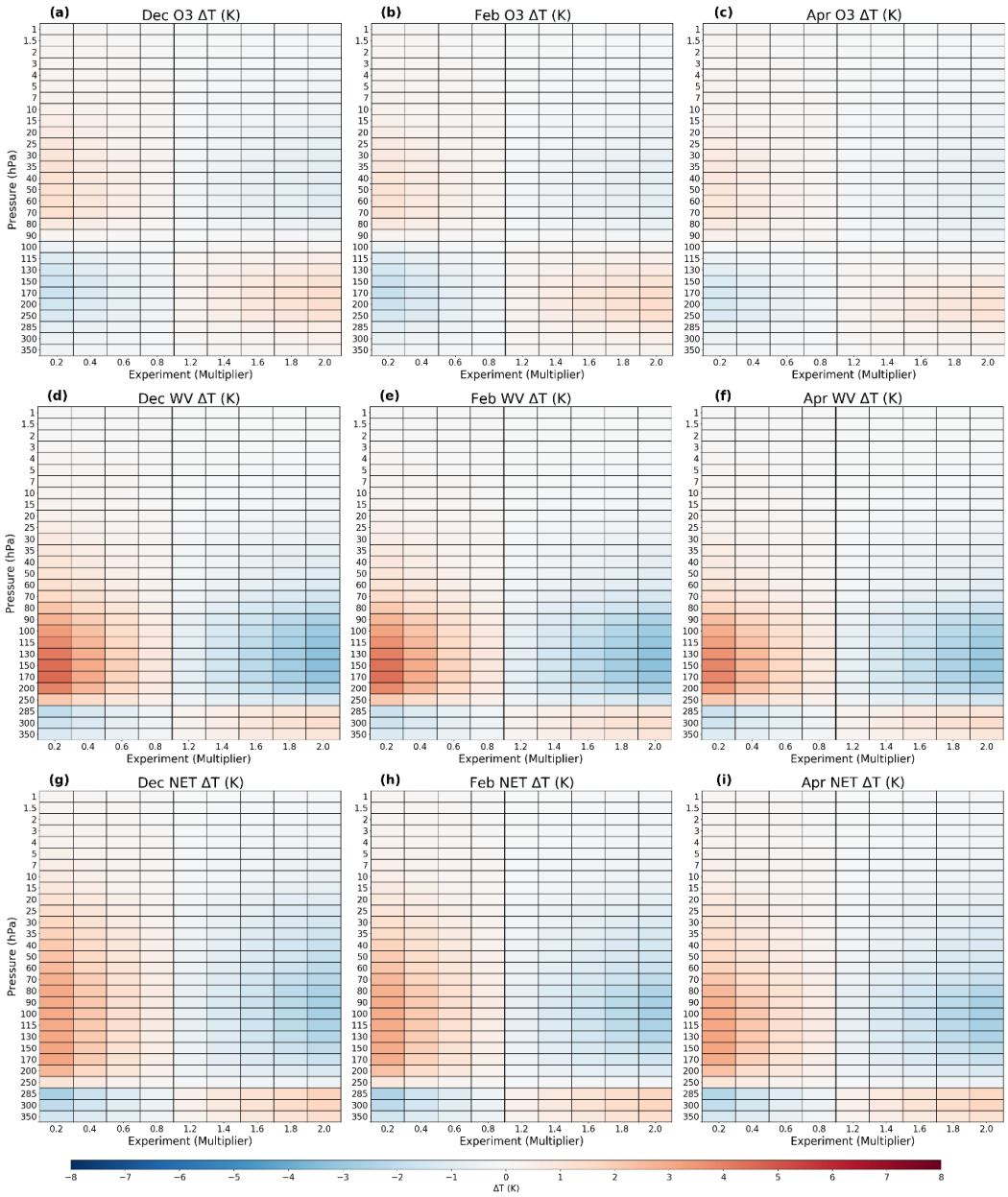

Figure 6.19 – Resultant radiatively-driven stratospheric temperature changes as a result of (**a-c**) O_3, (**d-f**) H_2O and (**g-i**) both O_3 and H_2O perturbations, with respect to mid-December (**a,d,g**), mid-February (**b,e,h**) and mid-April (**c,f,i**) climatology. Results are shown for the LW component only.

80 % (+80 %) perturbation, a maximum cooling (warming) between ~100 and 200 hPa is calculated on the order of ~0.1 to 0.2 K in each direction. This slightly enhances the Net radiative ΔT response for the different perturbations shown. It should be noted that a non-local SW contribution from O_3 exists outside of the perturbed region (50-200 hPa), that gradually reduces in magnitude with distance from the perturbed region.

As in section 6.5.1.1, the ΔT due to O_3 (Figure 6.19a-c), H_2O (Figure 6.19d-f) and the Net case (Figure 6.19g-i) is shown across the full range of perturbations (multipliers) applied within the UTLS region (50-200 hPa), first for the LW only calculations. Note that in the

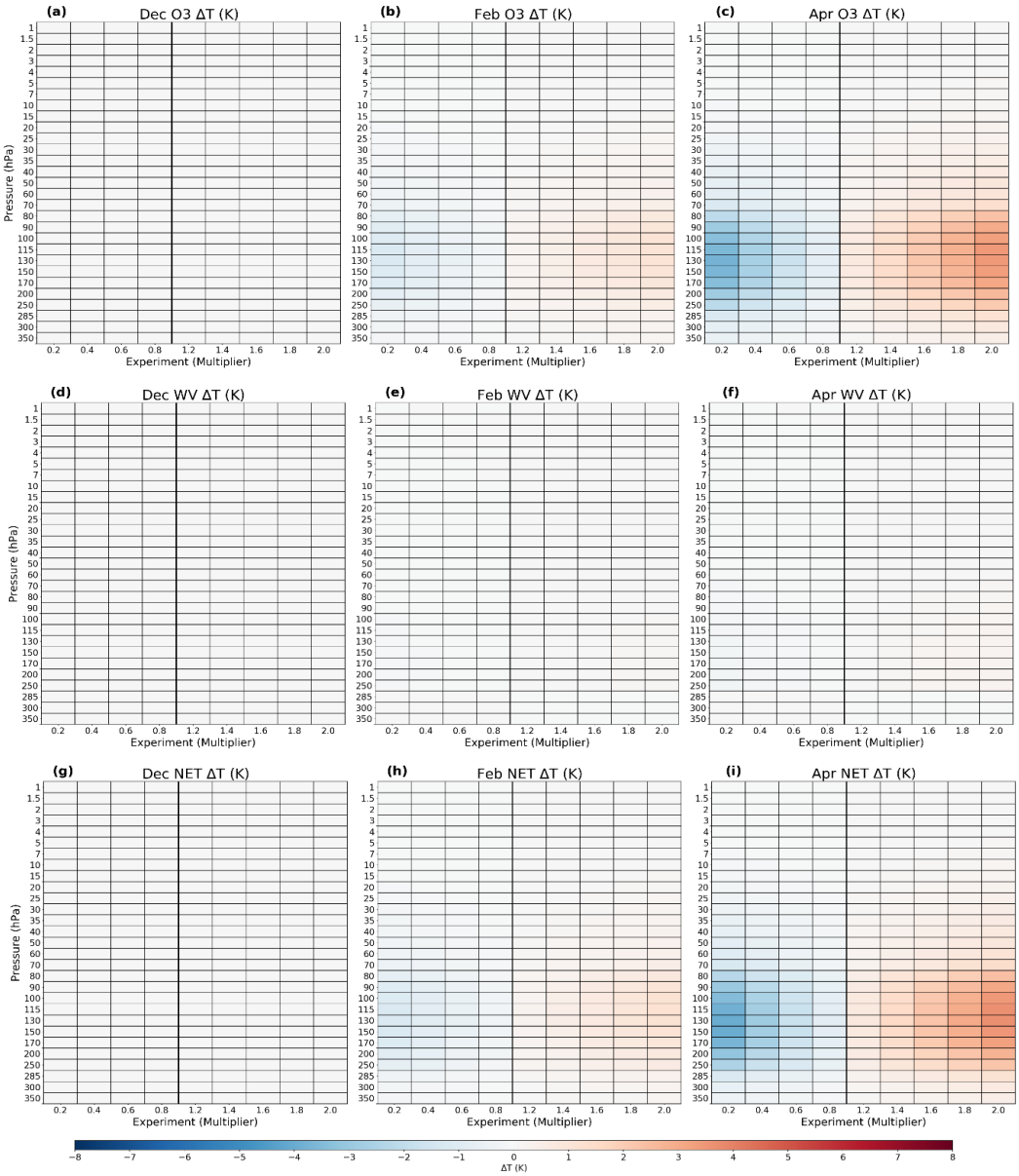

Figure 6.20 – Resultant radiatively-driven stratospheric temperature changes as a result of (**a-c**) O_3, (**d-f**) H_2O and (**g-i**) both O_3 and H_2O perturbations, with respect to mid-December (**a,d,g**), mid-February (**b,e,h**) and mid-April (**c,f,i**) climatology. Results are shown for the residual SW component only (LW+SW – LW).

case of December, the results are identical to that shown in Figure 6.11 for the LW+SW case, as the SW component is irrelevant for this month. For O_3, the LW induced temperature changes reduce slightly in magnitude from December through to April, throughout the profile across the range of perturbations applied. This is also true for H_2O, with a slightly larger change in ΔT over this seasonal transition. This leads to an overall subtle decrease in the ΔT response in the Net case, when both O_3 and H_2O are perturbed in the calculations. With respect to the LW+SW calculations shown earlier (Figure 6.11), the radiative effect of O_3 transitions from being LW dominant in December, and to a lesser extent February, to being largely SW dependent in April. Examination of the SW induced

temperature changes reveals a contribution of this component by ΔT = ~± 4 K for a ≥ ±80 % perturbation between 100 and 150 hPa, whilst the LW-induced component contributes a ΔT = ~± 1.5 K for a ≥ ±80 % perturbation around 200-250 hPa) below ~70 hPa. The H_2O radiative effect can be seen to be largely trivial in the SW, but was shown earlier to rise to ~0.1-0.2 K in Figure 6.18 for this month. Whilst the Net radiative effect in the LW is a product of a slight dampening of the LW radiative effect due to H_2O by the LW radiative effect of O_3, except below 250 hPa where the LW radiative effects become additive, the SW radiative effects are almost entirely driven by the ΔT due to O_3.

6.6 Regional Tropospheric Ozone Enhancement

To ascertain changes in LMS and tropospheric ozone following PJO-type SSWs over different mid-latitude regions of the Northern Hemisphere (Europe, North America and Asia), where enhanced stratospheric influx has the potential to affect air quality, distributions of the integrated quantity of ozone (Dobson Units, DU) are calculated from the model for different pressure ranges (subcolumns). Distributions of ozone for each region are calculated using a standard histogram binning approach for the PJO subclass of SSW events (n = 11). With respect to the 34-year time series of the EMAC simulations, every nPJO and PJO SSW event (-30 to +150 days of an event) is first indexed for inclusion in the composites generated. Subsequently, each event is averaged over the following 30-day lags: 0-30 day, 30-60 day and 60-90 day. In calculating the climatological composites, the indexing for each event is first applied to artificially remove the effects of all SSWs (-30 to +150 days of an event) over the 34-year time series (1980-2013), before a multi-year average is computed (non-SSW climatology). The indexing is then reapplied to this new array to remove any influence of seasonality in our evaluations.

For each subcolumn, the integrated amount of ozone (in Dobson Units, DU) at every 10-hourly model timestep within each 30-day period analysed (n = 72), multiplied by the number of model grid points in each selected domain, is used in generating a histogram of the data (which is divided in to 20 bins). This yields a total number of data points of n = 392,040 for North America, n = 261,360 for Europe and n = 629,640 for Asia. The SSW and climatological distributions (excluding SSW events as defined within -30 to +150 days of an event) are then compared. SSW (solid lines) and climatology (dashed lines) composite distributions are included for the LMS (100-300 hPa), upper troposphere (300-500 hPa), planetary boundary layer (900-1000 hPa) and the model surface level, averaged over the 0-30 day, 30-60 day, and 60-90 day period following the SSW central warming date (Figure 6.21).

To evaluate the statistical robustness of the differences between the SSW and corresponding climatological distributions (displayed in Figure 6.21), a bootstrapping (resampling with replacement) procedure was furthermore employed. This entailed resampling over a standard number of permutations (10000) from an original pool of values, to yield 95% confidence intervals around the median, 90th percentile and 95th percentile of each distribution. Note that each event was considered to be an independent sample only (resulting in 11 SSW and 11 climatological cases) to remove any effects of spatial and temporal autocorrelation. The null hypothesis of this test was that the calculated 95 % confidence intervals around each statistic overlap for each pair of

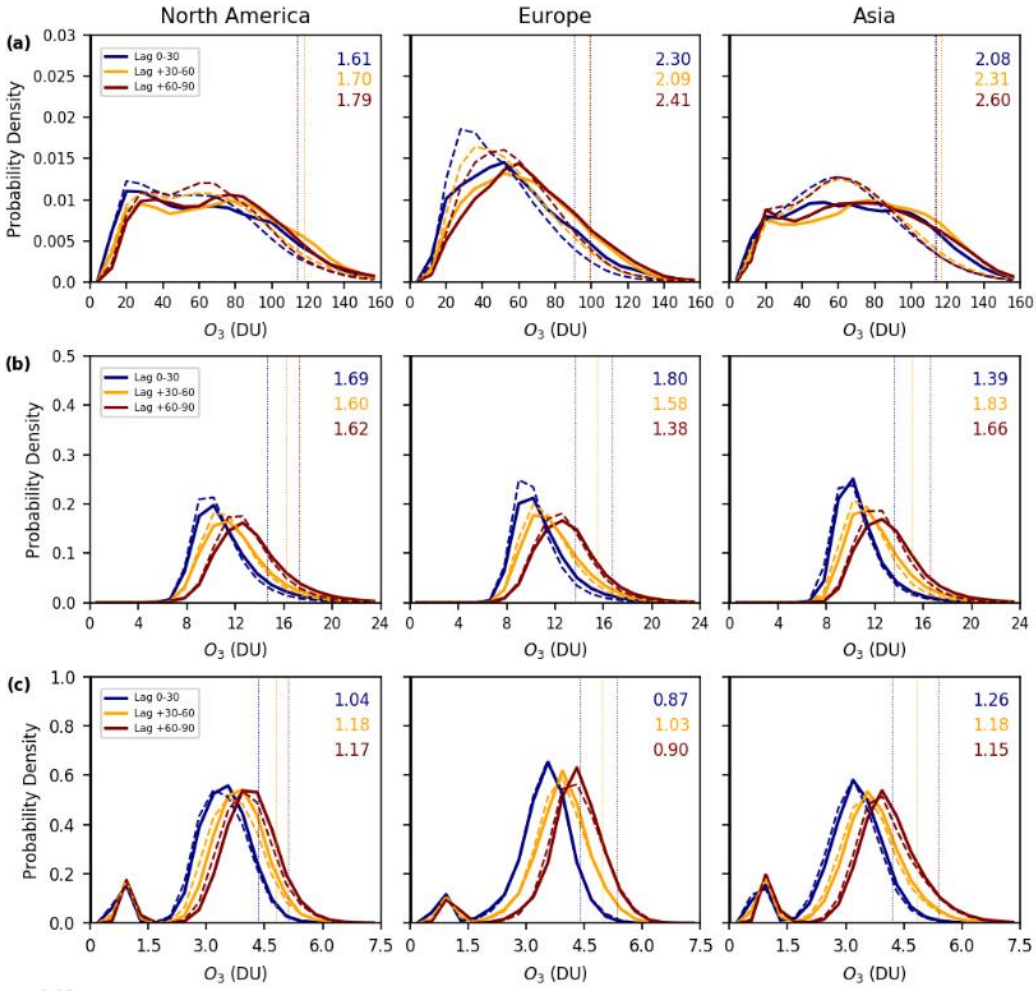

Figure 6.21a - Time-area averaged distributions for North America (30°N-70°N, 150°W-60°W), Europe (30°N-70°N, 30°W-30°E) and Asia (30°N-70°N, 30°E-180°E) for (**a**) the LMS (100-300 hPa), (**b**) upper troposphere (300-500 hPa) and (**c**) the planetary boundary layer (900-1000 hPa) subcolumn (DU) ozone for lags 0-30 days (blue lines), 30-60 days (orange lines) and 60-90 days (red lines) following the SSW central warming date. Solid lines represent SSW composite distributions and dashed lines represent the composite generated from the EMAC climatology (1980-2013) excluding SSW events. Risk ratio (RR) values of the probability of an exceedance in the 95-percentile level of each climatological distribution (dashed vertical lines) are indicated.

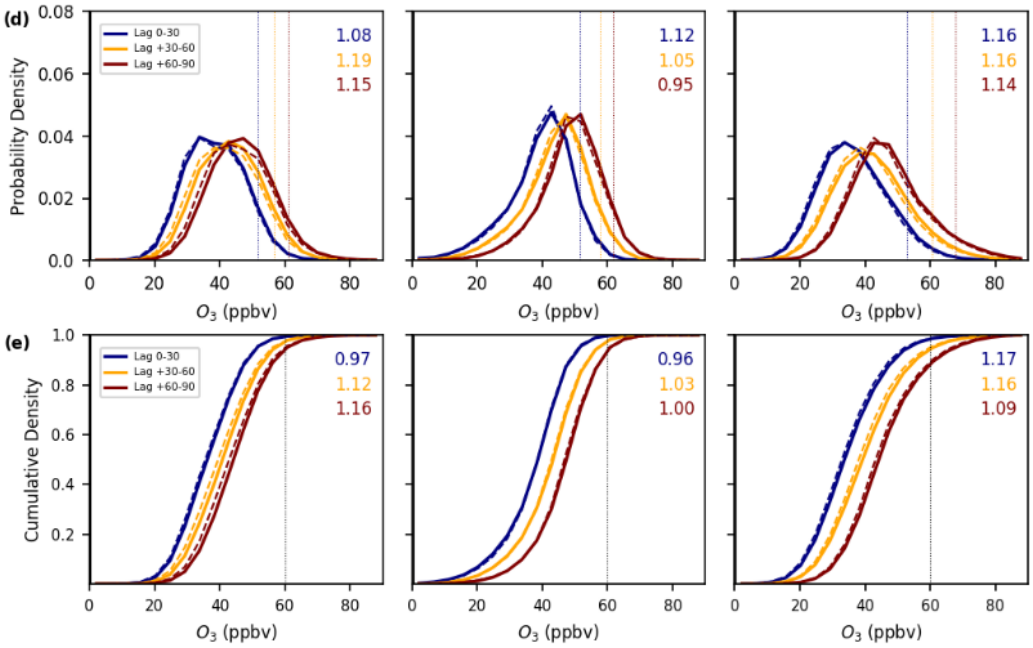

Figure 6.21b - Time-area averaged distributions for North America (30°N-70°N, 150°W-60°W), Europe (30°N-70°N, 30°W-30°E) and Asia (30°N-70°N, 30°E-180°E) for (**d**) modelled surface ozone mixing ratios (ppbv) for lags 0-30 days (blue lines), 30-60 days (orange lines) and 60-90 days (red lines) following the SSW central warming date. Solid lines represent SSW composite distributions and dashed lines represent the composite generated from the EMAC climatology (1980-2013) excluding SSW events. The cumulative ozone distributions with respect to climatology for the model surface level are additionally shown (**e**) to highlight the overall shift towards anomalously high ozone values even near the surface. Risk ratio (RR) values of the probability of an exceedance in the 95-percentile level of each climatological distribution (dashed vertical lines) are indicated in (**d**), and again in (**e**) where the values represent a RR increase in the likelihood of an exceedance in the 60 ppbv threshold (a typical surface air quality standard). Note that the RR values for (**e**) are particularly sensitive to the seasonal cycle in ozone, in that the values indicate the relative increase in exceedances above 60 ppbv. Thus, when the number of climatological samples exceeding the 60 ppbv ozone threshold is very small early in the year, only a small shift in the distribution can yield a very large RR.

distributions. Thus, the alternative hypothesis is that the confidence intervals do not overlap for this test, which would signify a statistically significant difference.

From this approach, the confidence intervals were only largely found to not overlap for each of the three statistics (median, 90th and 95th percentile) for the UTLS (100-300 hPa) subcolumn over each region. The detailed results of this analysis are therefore not here shown. To explore the possibility of statistical robustness further, a two sample t-test was additionally performed as inference of statistical significance based on rejection of the null hypothesis that the confidence intervals for each distribution overlap may not always be a valid assumption (e.g. Schenker and Gentelman, 2001; Payton et al., 2003). The alternative hypothesis for this measure is that the associated p values are less than 0.05.

Region	Statistic	Lag (days from onset)		
		0-30	30-60	60-90
North America	Clim	1.1 ± 0.5 (0.4, 2.0)	4.1 ± 1.1 (2.4, 6.0)	7.6 ± 1.1 (5.5, 9.5)
	SSW	1.0 ± 0.5 (0.2, 2.1)	4.2 ± 1.3 (1.9, 6.8)	8.5 ± 1.3 (6.0, 11.0)
	RR	1.2 ± 1.2 (0.2, 4.2)	1.1 ± 0.5 (0.4, 2.4)	1.2 ± 0.3 (0.7, 1.8)
Europe	Clim	0	4.1 ± 1.5 (1.8, 6.8)	10.8 ± 2.2 (7.1, 14.2)
	SSW	0.6 ± 0.5 (0.1, 1.6)	4.2 ± 1.8 (1.1, 8)	10.2 ± 2.1 (6.0, 14.3)
	RR	infinite	1.2 ± 0.9 (0.2, 3.5)	1.0 ± 0.3 (0.5, 1.7)
Asia	Clim	2.0 ± 0.6 (1.0, 3.1)	7.0 ± 2.0 (3.9, 10.4)	14.6 ± 2.5 (10.5, 18.7)
	SSW	2.3 ± 0.7 (1.1, 3.9)	7.6 ± 2.0 (3.9, 11.7)	15.0 ± 2.6 (9.9, 19.8)
	RR	1.3 ± 0.7 (0.4, 3.0)	1.2 ± 0.5 (0.5, 2.6)	1.1 ± 0.3 (0.6, 1.7)

Table 6.8 – Exceedances (± 1σ) (%) in surface ozone above the EU air quality standard (60 ppbv) for each climatological (clim) and PJO-type SSW composited (n = 11) distributions (as determined through bootstrap sampling with replacement over 10000 iterations). Values in parentheses represent the 95% confidence intervals around each value. The risk ratio (RR ± 1σ) values denote the relative change in the number of cases in exceedance of this threshold, again with values in parentheses representative of the 95 % confidence intervals around each value (as determined through bootstrap sampling with replacement over 10000 iterations). Note however that inference of statistical significance can be problematic earlier in the season, as there are fewer cases in exceedance of this threshold, particularly in the climatological cases. Note that RRs are 'infinite' in cases where the climatological distributions do not show any (i.e. zero) exceedances of the 60 ppbv ozone threshold. Values in grey denote reductions in exceedance risk of the 60 ppbv ozone standard following these events.

However use of this test was found to broadly match the results of that from the bootstrapping analysis and is thus again not shown here.

Additionally, risk ratios (RR) (displayed values) are calculated to indicate the likelihood of an exceedance of the 95-percentile for each SSW distribution, with respect to each corresponding climatological distribution at each lag, with the exception of the model surface level where the 60 ppbv threshold is substituted in place of the 95-percentiles. The 60 ppbv (120 μg m^3) threshold constitutes the recognised ozone air quality standard for the European Union, which is set slightly higher at 70 ppbv (140 μg m^3) for North America (EEA, 2018; US EPA, 2015), although this threshold has recently been lowered (Cooper et al., 2015). The latter is shown for the corresponding cumulative ozone distributions for the surface (Figure 6.21b), and bootstrapping is again undertaken for this case to further quantify the significance, and with it the robustness, of the results (note that the calculated RR values deviate slightly from those displayed in Figure 6.21b: see Table 6.8).

The risk ratio of a 95-percentile exceedance in the ozone distributions for a PJO-type SSW, with respect to climatology, is calculated for the three 30-day periods following the central warming (onset) date (lag 0: 0 to +30 days, lag 1: +30 to +60 days and lag 2: +60 to +90 days) following the approach by Zhang and Wang (2019, Figure 1). From the derived cumulative ozone distributions, the 95-percentile (0.95) level is identified for each climatological distribution at each lag. The corresponding value of ozone (DU) is used to identify the change in the proportion of the SSW distribution above and below this 0.95 level. This value (X_{ssw}) is used in determining the risk ratio (RR) of an exceedance in ozone above this level as calculated in Equation 6.1:

$$RR = \frac{1-X_{ssw}}{1-0.95} \quad (6.1)$$

The risk ratio may also be calculated by substituting in a threshold value (e.g. the 60 ppbv ozone standard) in place of the 95th percentile, as used in Figure 6.21b for the model surface. Using this threshold, we additionally calculate RR values using the bootstrapping (resampling with replacement) approach (Table 6.8), as previously described, to assign confidence intervals and evaluate the extent to which the confidence intervals overlap. Inference of statistical significance ($p < 0.05$) is again corroborated by also performing a one sample t-test.

A clear difference in the ozone SSW distributions is apparent for the LMS (100-300 hPa) over each region with respect to all corresponding climatological distributions (Figure 6.21a). An overall statistically significant shift towards higher values of ozone in all cases, according to the p-value metric associated with a paired two-sided t-test was found. In most cases, the 95% confidence intervals around the mean, 90th percentile and 95th percentile statistics also do not overlap, which further corroborates the presence of a statistically significant signal, that the overall enhancement in ozone evident from the polar-cap composites (Figure 6.4 in section 6.3) indeed extends over mid-latitude regions (not shown). The changes in the upper troposphere (300-500 hPa) are qualitatively similar to those in the LMS, which would further support this assertion (Figure 6.21a), although the differences between the composites are smaller and statistical significance is borderline at best. Whilst the p-value threshold implied statistical significance in most cases, inspection of the confidence intervals for this subcolumn reveals a considerable amount of overlap in the majority of cases. The frequency of a 95-percentile exceedance in the SSW distributions is typically on the order of a 1.6 to 2.6 fold increase to a 1.4 to

1.8 fold increase relative to climatology for the LMS and upper troposphere respectively, as evidenced by the displayed RR values in Figure 6.21a for each region and lag.

A much less conclusive signal is found for the approximation of the planetary boundary layer (here defined as 900-1000 hPa) (Figure 6.21a), which is consistent with model estimates of the depth of this layer (McGrath-Sprangler et al., 2015). In almost all cases, the SSW and climatological distributions are largely indistinguishable from each other. Indeed, both the bootstrapping and two sided t-test evaluation confirmed the lack of statitiscal significance (as determined from the presence of strongly overlapping confidence intervals and p values > 0.05). This is despite modest indications of overall elevated ozone abundances following such events in most cases over North America and Asia. The calculated RR values for this layer indicate a slight enhancement in the risk of an exceedance of the 95-percentiles following the PJO subclass of SSWs, with respect to the computed climatology (excluding SSWs), for both North America and Asia (RR = 1.0 to 1.2). This is however not the case over Europe where the RR value drops to between 0.85 and 1.05, which instead indicates a slight reduction in the probability of an exceedance relative to this threshold. The overall signal is the same when the model surface level is instead analysed (Figure 6.21b). The RR values of a 95-percentile exceedance for the surface are again between 1.0 and 1.2 for each region (highest for each lag over North America and Asia). Assessment of changes in the median, 90^{th} and 95^{th} percentiles of each SSW distribution versus each corresponding climatological distribution, again confirmed the absence of any statistically significant signal. Nonetheless, a very slight overall shift towards higher near-surface regional ozone values is illustrated in the cumulative ozone distributions for the model surface level (Figure 6.21b). The RR values displayed, calculated with respect to the substituted typical ozone air quality standard (60 ppbv), are again between ~1.0 and 1.2 for both North America and Asia at each lag (but between 0.95 and 1.05 for each lag over Europe).

The RR values for each region at each lag were additionally calculated through the same bootstrapping (resampling with replacement) procedure applied to obtain the median, 90^{th} and 95^{th} percentile statistics of each distribution, to further evaluate the statistical robustness of any signal for an enhanced risk in the exceedance of a typical surface ozone air quality standard (60 ppbv) (Table 6.10). An overall slight shift towards a greater number of exceedances of this threshold is again derived using this approach (RR = 1.0 to 1.2), with the exception of the 60-90 day lag over Europe and the 0-30 day lag over North America. Once more, this corresponds to an increased probability of ozone air quality

exceedance, using the 60 ppbv threshold as a benchmark, of between ~10 and 20 %. Despite this, no such cases are found to be statistically significant due to the largely overlapping 95 % confidence intervals (values shown in brackets). The inferred coincidence of this increased likelihood of high surface ozone events during the springtime ozone maximum is of potential importance, as studies show that boundary layer processes (e.g. turbulent mixing) can entrain ozone with a stratospheric source origin well in excess of these air quality standards (Langford et al., 2017; Lefohn et al., 2011).

To further assess the role of direct stratospheric influence following these events, to remove any influence from redistribution of tropospheric produced ozone due to circulation anomalies (as captured by the NAM index), the ozone distributions (as shown in Figure 6.21) are replotted for the stratospheric tagged ozone (O_3S) tracer in Figure 6.22. The ozone distributions and displayed RR values appear very similar to those shown before for the LMS (100-300 hPa) and the upper troposphere (300-500 hPa) (Figure 6.22a), as the stratosphere contributes significantly to the total ozone abundance at these altitudes. For the planetary boundary layer (900-1000 hPa) and surface model level however (Figure 6.22b), the O_3S values are as much as 50 % or more smaller and the corresponding distributions are much tighter. Despite this, an overall shift towards higher O_3S values is more easily discernible than before (in Figure 6.21) and as quantified through the RR metric, using the climatological 95-percentile as a benchmark in each case. A significant enhanced risk of the exceedance of the 95-percentiles for each case is computed for the O_3S tracer (~1.5 to 3.0), which highlights that enhanced downward transport of ozone from the stratosphere is simulated by the EMAC model following such events. However, the impacts on surface air quality are nonetheless found to be small and largely statistically insignificant from the evaluations shown in this section. Further investigation is therefore imperative to understanding the role enhanced STE of ozone may have on mid-latitude surface air quality following midwinter PJO-type SSWs. Although examples of direct stratospheric influence on surface air quality have been documented for individual events (e.g. Lefohn et al., 2011), it is nevertheless perhaps not surprising that a statistically significant signal for an overall background enhancement in tropospheric and surface level ozone is not found here following the PJO subclass of SSW events. The 34-year period of the EMAC specified-dynamics simulations used here (1980-2013), at a coarse resolution of 2.75°, only encompass 11 individual events. As well as this very small sample size, the variability in the dynamical impact of each SSW event is likely

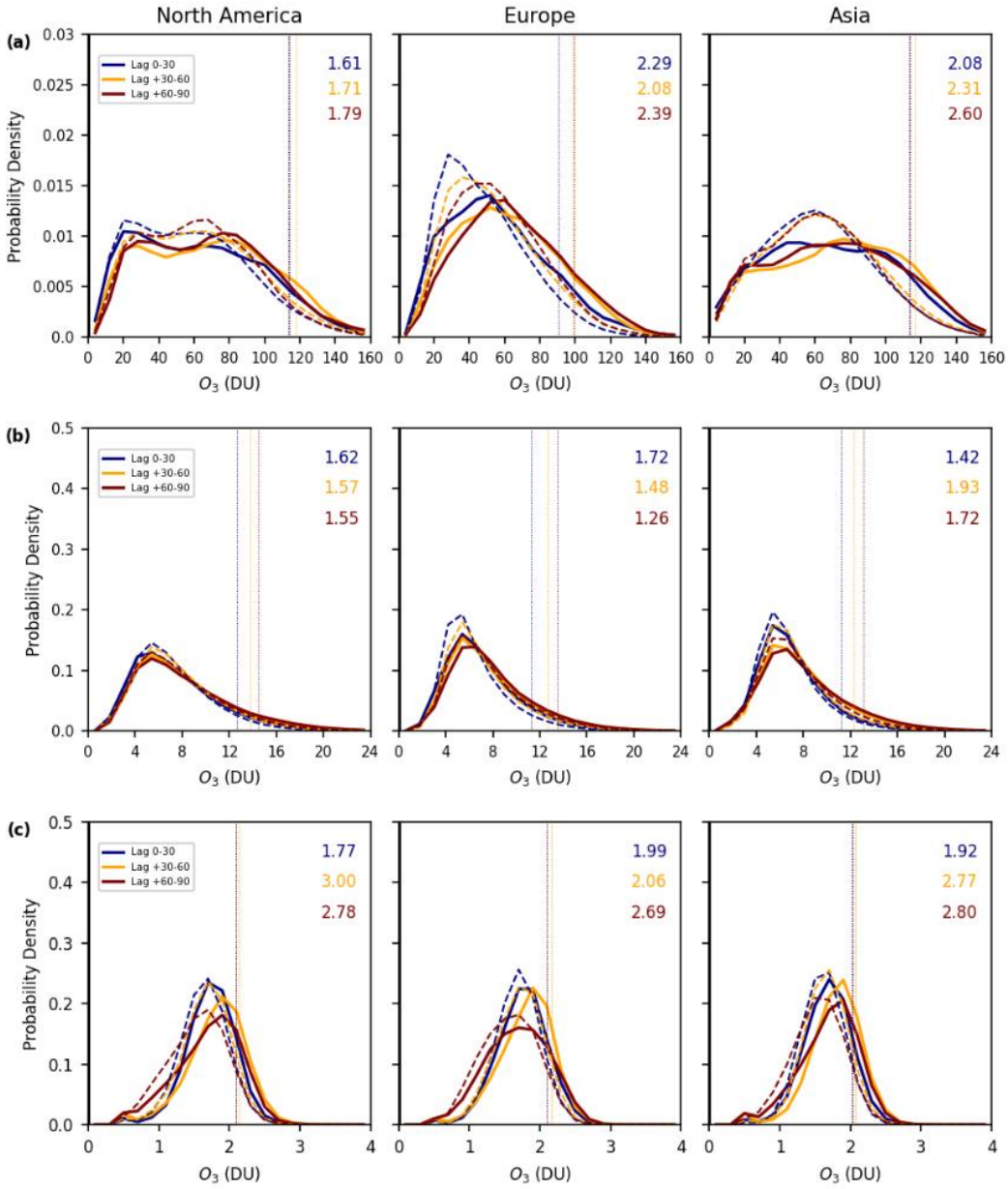

Figure 6.22a – Time-area averaged distributions for North America (30°N-70°N, 150°W-60°W), Europe (30°N-70°N, 30°W-30°E) and Asia (30°N-70°N, 30°E-180°E) for (**a**) the LMS (100-300 hPa), (**b**) upper troposphere (300-500 hPa) and (**c**) the planetary boundary layer (900-1000 hPa) subcolumn ozone (DU) of stratospheric origin (O_3S) for lags 0-30 days (blue lines), 30-60 days (orange lines) and 60-90 days (red lines) following the SSW central warming date. Solid lines represent SSW composite distributions and dashed lines represent the composite generated from the EMAC climatology (1980-2013) excluding SSW events. Risk ratio (RR) values of the probability of an exceedance in the 95-percentile level of each climatological distribution (dashed vertical lines) are indicated.

to be large. Therefore, this initial investigation would benefit strongly from usage of higher resolution data covering a longer timeframe to help discern any robust, statistically signal that may emerge following such events.

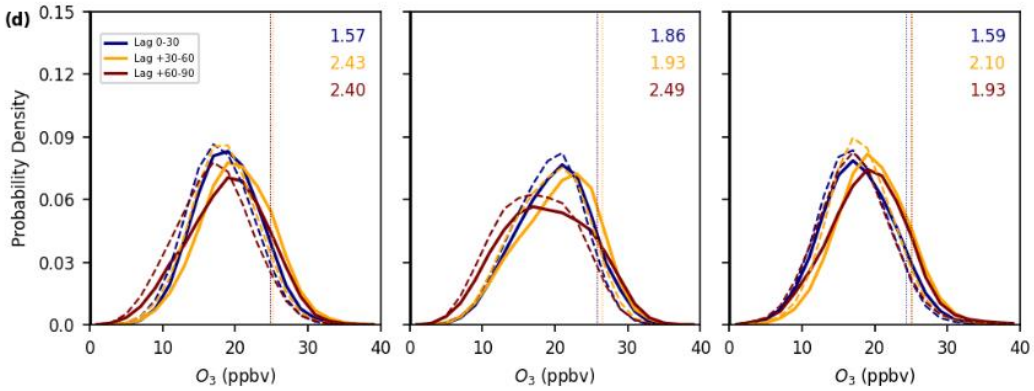

Figure 6.22b – Time-area averaged distributions for North America (30°N-70°N, 150°W-60°W), Europe (30°N-70°N, 30°W-30°E) and Asia (30°N-70°N, 30°E-180°E) for (**d**) modelled surface O_3S mixing ratios (ppbv) for lags 0-30 days (blue lines), 30-60 days (orange lines) and 60-90 days (red lines) following the SSW central warming date. Solid lines represent SSW composite distributions and dashed lines represent the composite generated from the EMAC climatology (1980-2013) excluding SSW events. Risk ratio (RR) values of the probability of an exceedance in the 95-percentile level of each climatological distribution (dashed vertical lines) are indicated.

6.7 Summary and Future Work

Using the EMAC CCM, along with observational evidence from both ozonesondes and the CAMS reanalysis, it is shown that PJO-type SSWs are associated with significant composition changes in the UTLS that persist for extended timescales of up to 2-3 months, which is consistent with dynamical recovery timescales in this region (Hitchcock et al., 2013). The establishment of anomalies in UTLS ozone (O_3) of > 25 % and water vapour (H_2O) anomalies of ~± 25 %, within days of the SSW central warming (onset) date, appear to be instigated by a short, pronounced period of anomalous polar downwelling that extends vertically throughout the depth of the stratosphere. Variability in polar downwelling during wintertime is known to be associated with variations in the strength of the BDC, as air is forced to converge and subside over high latitudes, which strongly influences the temperature of the polar stratosphere through modulation of adiabatic heating (Calvo et al., 2017; Kawatani et al., 2019). The resulting enhancement in lower stratospheric ozone is seen to subsequently propagate into the Arctic troposphere on a timescale of 50-80 days; leading to a peak impact on near-surface ozone during spring when photochemistry becomes increasingly important (Logan, 1985) for a typical event in January or February. The chemical perturbations in both ozone and water vapour are furthermore postulated to have a significant influence on the polar tropospheric thermodynamic response to such events, consistent with the known radiative forcing sensitivity to the structure and composition of the UTLS (Riese et al., 2012; Randel and Wu, 2010; Gilford et al., 2016). The inferred UTLS temperature changes of ±2 K identified

here may contribute to shortcomings in NWP models to accurately represent dynamical downward coupling after an SSW, given the inadequate representation of atmospheric composition (including ozone chemistry) in these models. It is therefore concluded that the representation of such constituents is pertinent to improving NWP forecasts on weekly to sub-seasonal timescales.

The radiative impacts of perturbations in ozone and/or water vapour more generally in the polar UTLS (50-200 hPa) were further investigated though a series of FDH calculations, to quantify profile stratospheric adjusted temperature changes, as a function of both seasonality (during the core of the stratospheric dynamically active season; taken as November to May inclusive) and contributions from each of the LW and SW radiative components. With emphasis on the results for a mid-December, mid-February and mid-April case, a clear seasonal aspect to the FDH-calculated profile temperature response is apparent, as day length increases from 0 to over 12 hours. The radiative importance of ozone significantly increases during this time, whilst the radiative importance of water vapour reduces slightly, across the range of different perturbations applied (-80 to +100 %). Investigation of the calculated LW and residual SW component temperature response confirms that ozone is a more radiatively active trace gas in the SW, whereas water vapour is strongly dominant in the LW. The increase importance of solar heating over this period leads to a shift in the Net temperature response due to primarily water vapour in December, to a slightly greater contribution from ozone compared with water vapour by April. The UTLS temperature response for the Net case is subsequently found to reverse in sign in April, compared to both December and February. Although the radiative response is found to be highly linear for each month (across each of the ozone, water vapour and Net perturbations), a small element of non-linearity exists, particularly for the water vapour only calculations. Most notably, the temperature response is proportionally larger for negative perturbations, as might be expected due to increasing saturation of gaseous absorption for positive perturbations. A potential role from both non-local radiative effects and possible radiative feedbacks between ozone and water vapour (in the Net case) may contribute to the observed non-linear aspect but cannot be discerned here and would require further investigation. A first step would be to systematically perturb individual levels to determine regions of the UTLS conducive to the occurrence of non-local radiative effects. It is important to consider the limitations of the FDH technique here in calculating such radiatively induced temperature changes. Both atmospheric and surface dynamics, together with variables such as surface albedo, clouds and tropospheric

water vapour may all transpire to modulate induced temperature changes in the real atmosphere, as demonstrated from studies investigating coupled-climate feedbacks (e.g. Deng et al., 2013), which are not captured in this approach. To explore the additional role of dynamical feedbacks following on from this study, GCM simulations in which ozone and water vapour are fixed could be compared to equivalent simulations in which both chemical species are fully interactive.

Finally in section 6.6, influence from anomalous changes in polar UTLS ozone and water vapour, in response to PJO-type SSWs, is confirmed to extend across the major continents of the Northern Hemisphere mid-latitudes (North America, Europe and Asia). An overall shift towards higher EMAC-simulated ozone abundances is shown for both the LMS and the upper troposphere, not just in a mean sense, but also in terms of the upper percentiles of each distribution for the three 30-day lags following the composite SSW onset date examined: 0-30 days, 30-60 days and 60-90 days. As further quantification of this aspect, the RR of a 95-percentile exceedance of each climatological distribution is calculated to be between a factor of 1.6 and 2.6 fold increase for the LMS, and between a factor of 1.4 and 1.8 fold increase for the upper troposphere; with these values largest over Europe and Asia and with longer lag times more generally. Nearer to the surface, the influence of any enhancement in ozone following these events cannot be confirmed here, despite a very slight tendency towards higher ozone values, particularly over North America and Asia. Although not statistically significant, a ~10-20 % enhancement in the RR of an exceedance of the 95-percentile of each climatological distribution is calculated for the planetary boundary layer (900-1000 hPa) and model surface level, which remains true when the 60 ppbv threshold (typical ozone air quality standard) is substituted in place of this benchmark for the calculations. However, this finding has to be placed in the context of the confidence intervals shown in Figure 6.10, which are very wide and overlap significantly with an RR of 1 (i.e. no change in the probability of a surface exceedance of ozone above 60 ppbv).

Use of the ozone of stratospheric origin (O_3S) model tracer to isolate effects that may arise due to redistribution of ozone of tropospheric origin, resulting from induced circulation anomalies such as captured by the NAM index, confirms that a tendency towards higher O_3S occurs following the PJO-type subclass of events (with respect to the constructed climatologies in each case). The differences and calculated RRs are significantly larger for the planetary boundary layer and surface level, which signals that EMAC does simulate influence from enhanced STE of ozone over mid-latitudes that

penetrates down into the lower troposphere, with resultant ramifications potentially for surface air quality during spring (which marks the start of the photochemically active season). An increased risk of near-surface ozone threshold exceedances could therefore be anticipated in the weeks following an event, with implications for mitigation interventions, if further evaluations of higher resolution data indeed corroborate these findings further. Another limiting factor of the approach here is the small sample of events considered; only 11 PJO events during the 1980-2013 period of the EMAC specified-dynamics simulations. This aspect could be addressed by substituting in usage of free-running simulations, which in the case of EMAC, would extend the time period considered significantly (available from as early as the 1950s; Jöckel et al., 2016). Further investigation is also required in verifying that such quantitative estimated impacts on surface air quality are supported by observations more widely; such as captured from networks of air quality monitoring stations. Although the data hinted that North America may be a region for preferential downward transport of ozone-rich air following these events (though not discussed as statistical significance is lacking), it is also important to consider that large regional asymmetries may arise when individual events are considered (Lin et al., 2012; Lin et al., 2015), as each event may be dynamically unique in terms of evolution (vortex split versus vortex displacement events).

Chapter 7

The main findings of this project are highlighted and discussed in this final chapter. The motivation, aim and research questions set out in Chapter 1 is first reiterated, before the progress made in this thesis, in attaining new knowledge and insights, is evaluated. The conclusions from results presented in each scientific working chapter (Chapters 4 to 6 inclusive) are both then discussed in turn and collectively. In a final section, a series of remarks are made in regard to the advance to science this thesis contributes. An advisory summary of the recommended next steps for the research area is here too provided.

Summary and Discussion

Whilst the distribution of ozone in the stratosphere (where ~90 % of the column total resides) is largely characterised by gradual seasonal changes and large-scale meridional gradients driven by the strength of the Brewer-Dobson Circulation (BDC) and photochemical production, the distribution and relative abundance of ozone throughout the troposphere is in contrast much more variable in both space and time. The wide range of different ozone sources and sinks (as covered in Chapter 1 and Chapter 2.1), as well as a relatively short global mean lifetime (~3 weeks), has meant that the regional and seasonal climatology of tropospheric ozone has long been poorly constrained. It is only in recent decades that more globally expansive, near continuous measurements (most notably from satellite platforms), together with new tools such as simulations from chemistry-climate models (CCMs) (which include fully interactive chemistry schemes), have enabled us to further advance our understanding in such detail. In terms of attribution of the tropospheric ozone burden, the latter can facilitate detailed characterisation of the relative influence of both tropospheric precursor emissions (e.g. NOx, CO and VOCs) and the contribution from the stratosphere (as quantified through the stratosphere-troposphere exchange (STE) of ozone flux) on such spatial and temporal scales. Such tools are furthermore useful for determining past, present and future changes in tropospheric ozone, as well as understanding how the influence from these drivers has evolved over time.

Knowledge of the regional and seasonal variability in tropospheric ozone (O_3), including its variability on timescales ranging from hours, to months, to years, has been limited by

both the paucity of observations and modelling capabilities. A number of studies have however attempted to characterise the spatiotemporal distribution, variability and trends in tropospheric ozone, as well as its drivers from different data sources (e.g. Logan, 1985; Lamarque et al., 1999; Oltmans et al., 2006; Lelieveld and Dentener, 2000; Cooper et al., 2014; Banerjee et al., 2016; Gaudel et al., 2018). Whilst such examples include efforts to disentangle contributions from in situ photochemical production from ozone precursor emissions, with respect to the downward flux of ozone from the stratosphere, knowledge of these two main competing drivers has remained somewhat elusive, particularly at a regional level and on a seasonal basis. Another confounding factor in assessments of tropospheric ozone drivers is that models have been primarily used to investigate either the stratosphere or troposphere separately, thus resulting in only a relatively simplistic representation of the component not studied. Enhancing our understanding of each influence is highly relevant for air quality, which can impact both human (Paoletti et al., 2014; WHO, 2019) and ecosystem health (Paoletti, 2007; Monks et al., 2015), radiative forcing estimates (e.g. Lacis et al., 1990; IPCC, 2014; Checa-Garcia et al., 2018) and insight into the oxidation capacity of the troposphere (Seinfeld and Pandis, 2006).

The aim of this research project was to provide a more comprehensive, quantitative update over the regional and seasonal characterisation of tropospheric ozone with respect to earlier studies in the literature (e.g. Lamarque et al., 1999), by utilising both new tools and measurements in a combined approach (Chapter 5). As a pre-requisite to this, the retrieval limitations of globally extensive, near continuous measurements from UV-nadir sounders were to be investigated (Chapter 4). As a follow-up study to Chapter 5, focus on a potential understudied driver of interannual variability in STE and tropospheric ozone was examined, which entailed investigation into possible connections resulting from midwinter sudden stratospheric warmings (SSWs) (Chapter 6). As outlined in Chapter 1, the following research questions (numbered 1 to 3) were posed to help motivate each study (which corresponds chronologically to each scientific working chapter; Chapters 4 to 6) within this research project:

1) *"What are the limitations of satellite-retrieved tropospheric ozone measurements from UV-nadir sounders? What are the sources of potential retrieval error that may contribute towards such limitations? How can such retrieval errors be mitigated, thus reducing associated uncertainty and retrospectively improving the accuracy of the satellite datasets?"*

In response to the first question, the work undertaken in Chapter 4 uncovers a notable deficiency in the first stage of the Rutherford Appleton Laboratory (RAL) ozone profile retrieval scheme, associated with inference of stratospheric ozone from the Hartley band (266-307 nm) region within the UV part of the electromagnetic spectrum, for both the GOME-2A and OMI nadir-viewing sounders. All indication is that this deficiency influences the retrieval globally, with possible implications for the accuracy of the retrieval also in the second step, concerning discrimination of ozone amounts in the troposphere from spectral structure in the Huggins band region (323-335 nm). However, the issue seems to disproportionately impact retrievals associated with increasing latitude and solar zenith angle (SZA). The cause of this dependency may therefore be related in part to defective radiometric throughput and calibration at relatively low-light levels. Despite some instrumental differences in this dependency observed for the different layers investigated, likely attributed to sensor-specific factors, the underlying principal cause seems to be inherent to the retrieval scheme.

Further work is next needed to identify the exact issue(s) concerning the stratospheric retrieval step. It is possible that other co-retrieved geophysical or instrumental variables are associated with the magnitude of the retrieval bias, as determined from use of the CAMS reanalysis, although this so far remains unclear following this preliminary investigation. Whilst error induced in this retrieval step is compensated strongly at lower altitudes, it is conceivable that the impact of this deficiency may indeed propagate into the second, tropospheric stage of the retrieval. This and other factors influencing bias in the retrieved tropospheric and lower stratospheric amounts have not yet been elucidated, so this would be another prioritised focus for future work. As mentioned in section 4.4, a couple of retrieval tests have been identified to address mitigation of retrieval error, which should help pave way for the development of a geophysically meaningful bias correction scheme that can be applied on a profile-by-profile basis, as a long-term target. This would replace the existing bias correction scheme, derived from latitude-month binned ozonesonde observations, and would hopefully facilitate retrospective reconciliation of the UV-nadir satellite datasets of tropospheric ozone from OMI, GOME-2A and other sounders (e.g. SCIAMACHY and GOME-2B).

2) *"What are the regional and seasonal characteristics of tropospheric ozone, according to both models and measurements? How does the role of the stratosphere compare with influence from in situ formation of ozone? What are*

the recent changes in tropospheric ozone and how is this influenced by changes in STE?"

The seasonally resolved, near-present day global climatology of tropospheric ozone was characterised in detail in Chapter 5 using satellite measurements from OMI, ozonesonde observations and the EMAC and CMAM CCMs. The origin of the model biases was closely examined and the different factors that lead to these were highlighted. This evaluation invoked a message of caution when interpreting the level of model-measurement agreement of tropospheric ozone and drawing comparisons between models. This derived knowledge was then taken into account when later diagnosing the simulated stratospheric influence on a regional and seasonal basis in each model, together with calculation of recent changes in tropospheric ozone and attribution from the stratosphere. This study therefore addresses these research questions, providing an update to earlier studies (e.g. Lamarque et al., 1999) using contemporary models and measurements.

3.) "What are the sources of interannual variability in tropospheric ozone and STE? Which teleconnections or drivers are understudied in relation to such impacts? What are the radiative implications of resultant composition changes in response to such sources of internal variability? What are the ramifications for STE of ozone and tropospheric ozone, including potential impacts on surface air quality?"

It was identified in Chapter 2, that midwinter SSW events have a significant impact on the stratospheric BDC, and thus, interannual variability in meridional stratospheric ozone transport during Northern Hemisphere wintertime. It is known that changes in the BDC can impact STE of ozone, although studies examining the impact of such events on STE of ozone appeared to be lacking. Subsequently, evaluations undertaken in Chapter 6 were tailored to addressing the potential role of SSWs on, at first, Arctic UTLS chemical composition (namely ozone and water vapour). It was found that following long-lived PJO-type SSW events, in which the lower stratosphere becomes significantly perturbed, large positive anomalies in ozone of > 25 % and water vapour anomalies of up to ±25 % may lead to temperature changes of up to 2 K in this region. A series of sensitivity evaluations show the radiative response to changing perturbations in ozone and/or water vapour to be strongly linear irrespective of seasonality. The sign and magnitude of the radiative response however differs significantly between December and April, during the months

examined. This is strongly associated with changes to shortwave heating resulting from the shift in day length from 0 to over 12 hours between these two months. Although, this study provides a quantitative insight into the radiative significance of such changes in UTLS composition, the implications this may have for Numerical Weather Prediction (NWP) will require a much more detailed investigation. Finally, the impacts on STE, tropospheric ozone and surface air quality following this subset of SSW events are explored using the EMAC CCM over the three primary mid-latitude regions (North America, Europe and Asia). Although the enhancement in UTLS ozone following SSW events also impacts these regions, a statistically robust signal for an increase in tropospheric and surface level ozone is not here found. However, it is understood that a number of caveats exist with the approach undertaken here (see section 6.6 and 6.7) and a number of additional approaches could indeed help to determine whether any signal is indeed present (involving higher resolution and much longer datasets). In short, the conclusions from this chapter provide answers to the questions set out above, but much further work is needed to quantify the different impacts arising from such events.

A further discussion of each scientific working chapter is provided here for each chapter in turn. In section 7.1, the insights derived in Chapter 4: '**Reconciliation of UV-Nadir Satellite Tropospheric Ozone Datasets**' are first discussed and next steps for future work are summarised. The findings of the combined model-measurement approach and subsequent applied model evaluations in Chapter 5: '**Characterising the Seasonal and Geographical Variability of Tropospheric Ozone (O_3), Stratospheric Influence and Recent Changes'** are then discussed and summarised in the context of the wider literature (section 7.2). As a manifestation of interannual variability during the Northern Hemisphere stratospheric dynamically active season, the influence of SSWs on UTLS composition and STE of ozone assessed in Chapter 6: **SSW Imprint in UTLS ozone (O_3) and water vapour (H_2O) distributions: Radiative Effects and Impacts on STE** are finally summarised in section 7.3. The wider implications of this research and intended future directions are discussed. Finally, section 7.4 will serve to highlight the scientific advances made during this research project and its contribution to the wider field of research.

7.1 Limitations of UV-Nadir Tropospheric Ozone Datasets

This thesis set out to first investigate the accuracy of vertically resolved satellite observations of ozone from the OMI and GOME-2A UV-nadir sounders, over their mission lifetimes, as retrieved using the RAL-OMI optimal estimation retrieval scheme. This

scheme differs from other retrieval algorithms, as applied to the raw satellite measurements (sun-normalised backscattered radiances from Earth reflectance), in that sensitivity to the tropospheric part of the retrieval is enhanced. A precision of ~4 DU is yielded for the surface-450 hPa (~0-5.5 km) layer for a typical instrument sounding (Gaudel et al., 2018). Accurate retrieval of the stratospheric part of the profile is however a necessary pre-requisite for accurate inference of tropospheric ozone from these sounders. In recent years, scientific evaluations of the various different versions of globally gridded (L3) satellite data from the GOME-2A and OMI instruments using the RAL optimal estimation scheme, as made available for the wider user community, have involved application of a post-hoc bias correction to correct for suspected deficiencies in the retrieval scheme. This bias correction consists of quantified differences for each retrieved layer, up to 50-30 hPa (~27-37 km) altitude, with respect to aggregated ozonesonde measurements. The correction was resolved on a month versus latitude (30° interval) basis, averaged over each sounder mission period. Although this correction is deemed an effective measure to limit potential error in the retrieved subcolumn ozone abundances, that may result from deficiencies of either geophysical or instrumental origin, it is far from an ideal solution. This motivated investigation here (Chapter 4) of retrieval differences with respect to the CAMS reanalysis dataset, which overlaps with the mission periods of GOME-2A and OMI, and has the advantage of providing continuous global coverage compared with ozonesondes. The CAMS reanalysis has been extensively validated and has been demonstrated to provide accurate information on the spatiotemporal distribution of ozone in both the stratosphere and troposphere. An additional advantage of the use of CAMS for this purpose is that global coverage helped to facilitate analysis of the bias evolution in the UV-nadir sounders, as quantified by computed differences between the retrieval and CAMS multiplied by the satellite AK (Ret – CAMS x AK), which is necessary to account for the observation geometry of the satellite when directly comparing CAMS with each satellite, on a profile-by-profile basis. Subsequent investigation of dependencies in the Ret – CAMS x AK differences, in relation to a number of different co-retrieved instrumental and geophysical variables, yielded insight into possible causes for inferred deficiencies in the retrieval. Crucially, investigation of both the GOME-2A and OMI sensors enabled both sensor specific issues and those common to UV-nadir sounding to be identified.

An initial comparison of retrieval minus ozonesonde x AK (Ret – Sonde x AK) and Ret – CAMS x AK differences, as resolved on a month versus latitude (30° interval) basis for the

GOME-2A instrument, indicated remarkably close agreement. This lended confidence to the realism of biases in the retrieved subcolumn amounts and provided assurance that CAMS is a suitable dataset to investigate bias dependencies. For both sensors, a strong anticorrelation between the 50-20 hPa (~21-27 km) and 450-170 hPa (~5.5-12 km) retrieved layer amounts over the extratropics indicated a potential issue in the retrieval of the stratospheric ozone profile, which constitutes the first step of the three-stage sequential approach of the RAL retrieval scheme, entailing extraction of vertical information from the Band 1 (B1) or Hartley band retrieval step at wavelengths between ~266 and 307 nm. Although this pattern was evident for both sounders over their respective missions, an inverse pattern was noted between each sensor. For GOME-2A, a largely positive (negative) bias was found for the 21-27 km (5.5-12 km) layer, whereas a smaller, albeit negative (positive) overall bias was calculated for the ~21-27 km (5.5-12 km) layer in the case of OMI, with respect to the CAMS reanalysis. The most likely explanation for this anticorrelation would be the presence of deficiencies associated with radiometric calibration in the B1 step, that appears to be both partly sensor independent and partly sensor-specific, which first affects the retrieval in the region coincident with the stratospheric ozone peak; between 50 and 20 hPa (21-27 km). It is clear that such bias induced in this region then propagates downward into the extended tropospheric part of the retrieval, where the magnitude of biases are largely compensated for (as indicated by biases of opposing sign but of approximate equal magnitude) within the 450-170 hPa (5.5-12 km) layer. Within this region lies the boundary between the retrieval under the B1 step and the subsequent B2 (Huggins band) step. The relatively high agreement between the bias patterns for the troposphere or surface-450 hPa (0-5.5 km) region and for the total column (~0-80 km) is further testament to this compensatory effect.

Further investigation of the bias dependencies, for each of these two respective regions of atmosphere in particular, confirmed significant association of the Ret – CAMS x AK differences as a function of both increasing SZA and latitude. This association supports a physical basis for potential radiometric calibration errors which may arise due to the increased importance of stray-light and dark current correction at increasingly low-light levels. It was then inferred that rectification of deficiencies in the B1 step of the retrieval based on these findings, would help to elucidate the origin of biases that may arise in the B2 step, which currently cannot be easily discerned due to the downward propagation of the induced bias in the 50-20 hPa (~21-27 km) region. These next steps would help develop a physically meaningful bias correction for each instrument, that involves

statistical modelling of dependencies with respect to a more comprehensive range of geophysical and instrumental variables, that can be applied on a profile-by-profile to replace the existing post-hoc bias correction, which may not account for retrieval error effectively.

7.2 Seasonal and Regional Drivers of Tropospheric Ozone

Having rigorously evaluated the performance of the UV-nadir sounders with respect to CAMS, globally gridded (L3) data from OMI, alongside vertically resolved profile measurements from limited available ozonesondes contained within the WOUDC database, were both in turn selected to verify the robustness of the representation of seasonally resolved tropospheric ozone from the EMAC and CMAM CCMs over a short period of concurrent data availability (2005-2010). Results of this model-measurement validation revealed a widespread systematic positive bias in tropospheric subcolumn ozone for the EMAC model, betweensurface-450 hPa (~0-5.5 km), on the order ~2-8 DU. This contrasted with a less systematic, more spatially and seasonally complex bias pattern in subcolumn tropospheric ozone for the CMAM model (~± 4 DU). Importantly however, it was shown using ozonesondes that model-measurement differences in tropospheric ozone could likely be explained by both model biases in lower stratospheric ozone, as manifestation of suspected biases in the strength of the lower branch of the BDC which has direct implications for the simulated downward STE flux of ozone, as well as in the simulated in situ photochemical production from ozone precursor emissions which depends on the model-specific implementation of these chemistry schemes (the same emission inventories are utilised in both models). The former influence becomes relevant when vertical smearing of information is induced upon applying the satellite AKs to each model dataset, to ensure like-for-like comparisons with UV-nadir retrieved satellite data. Thus, biases in lower stratospheric ozone can imprint onto the troposphere in such comparisons. In EMAC, extratropical lower stratospheric ozone was characterised by a general negative bias year round, which contrasted with a positive bias in the troposphere region. This was in direct contrast with CMAM, which had a strong positive bias in lower stratospheric ozone of between ~ 10 and 50 % and a general negative bias in lower tropospheric ozone (~ 5-20 %). The observed biases between each model and OMI for the tropospheric subcolumn were thus deduced to result from compensation between these opposing differences between the lower stratosphere and the troposphere. In CMAM, the omission of non-methane VOCs (NMVOCs) in the interactive chemistry scheme can likely explain the negative differences in lower tropospheric ozone, whereas the positive

bias in tropospheric ozone in EMAC can be attributed to the implementation of the tropospheric ozone chemistry scheme.

Taking on board these findings, both the vertically well-resolved CCMs were then used to examine the regional and seasonal contribution of the stratosphere to the abundance of tropospheric ozone, before further evaluating recent changes over the full period of the hindcast, specified-dynamics simulations (1980-2010). In support of the earlier model-measurement comparison findings, a faster shallow branch of the BDC was inferred to be simulated in the CMAM model, upon examination of differences in extratropical UTLS ozone between each model (~50-100 % more ozone with respect to EMAC). This has implications for the downward STE flux of ozone in each model, as quantified using the model stratospheric-tagged ozone tracers (O_3S). In CMAM, STE is focussed more towards the subtropics, whereas STE preferentially occurs more towards the extratropics in the EMAC model. Largest disparities were observed over the Southern Hemisphere subtropics, with some ~10-25 % more ozone of stratospheric origin in CMAM compared to EMAC during austral winter (JJA) in the troposphere. Overall, both models imply a larger stratospheric influence than previously thought compared with earlier studies (e.g. Lamarque et al., 1999; Lelieveld and Dentener, 2000; Banerjee et al., 2016); exceeding 50 % during wintertime in the extratropics as far down as the lower troposphere, when photochemistry is relatively quiescent. Recent changes in tropospheric ozone at different altitudes were then subsequently calculated over the 35-year period, by subtracting the periods 2001-2010 and 1980-1989 inclusive. A widespread increase in tropospheric ozone was derived for each model, with a maximum increase of ~5-10 % or approximately ~4-6 ppbv (~2-6 ppbv) in the Northern Hemisphere (Southern Hemisphere subtropics) during springtime in the middle to upper troposphere, and > 6 ppbv over south-east Asia at ground level. The stratosphere is estimated to have contributed up to ~50-80 % of this change, which decreases to a still significant ~25-30 % near to the surface.

To attain both a high level of model-measurement agreement and accurate representation of the stratospheric influence on tropospheric ozone, it is clear that a well-resolved stratosphere is critical to achieving this. However, it is important to realise that UV-nadir retrieved information of tropospheric also has its limitations, as investigated more deeply in chapter 4, and it is shown with the aid of ozonesondes that caution is required when interpreting the level of agreement between satellite observations and models, as biases can arise from multiple sources. There are indications from this study that the stratospheric influence has increased in recent decades and this trend might be

anticipated to continue through the 21st century, as the BDC is projected to accelerate due to climate change (Hegglin and Shepherd, 2009; Butchart et al., 2010) and as stratospheric ozone recovers (Zeng et al., 2010).

7.3 SSW Driven Chemical Composition Changes: UTLS and Tropospheric Ozone

As discussed in Chapter 5, interannual variability in tropospheric ozone can arise due to a number of factors. Teleconnections, or long distance interactions within the climate system, can collectively influence both meteorological variables (e.g. temperature and precipitation) and distributions of trace gases such as ozone. Examples include ENSO, the QBO, the MJO and variability associated with the 11-year solar cycle, which have all been shown to modulate tropospheric ozone levels globally, via both tropospheric and stratospheric pathways. The mechanisms for such modulation can involve redistribution of ozone within the troposphere due to dynamics, as well as variations in the in situ photochemical production of ozone from surface based emissions and lightning NO_x at a regional level. This can again be related to induced dynamical changes in part, but also as a result of modification to the formation of emissions that may be controlled by factors such as precipitation changes due to these drivers (e.g. biomass burning). The 11-year solar cycle may additionally impact tropospheric photochemistry due to relatively large insolation changes at UV wavelengths that occur between solar minimum and maximum conditions. In addition to these influences, changes in the strength of the stratospheric residual circulation, or BDC, have been demonstrated to impact the downward STE flux of ozone from the stratosphere which can further influence tropospheric ozone levels. Modulation of upward propagating wave activity from the troposphere can further influence the STE flux of ozone in more complex ways. Such influence may however be captured by indices such as the Northern and Southern annular modes, which have been demonstrated to be correlated with changes in STE and tropospheric ozone.

A largely understudied potential source of interannual variability in UTLS composition and tropospheric ozone that was identified and selected for further investigation using the EMAC model comprises midwinter SSWs, that occur almost exclusively in the Northern Hemisphere on average 6 times per decade (Charlton et al., 2007). Although SSWs have been investigated in relation to the dynamical impacts on the troposphere and changes in the distributions of trace gases within the stratosphere, less focus has been devoted to understanding the impact on UTLS composition and STE of ozone. Chapter 6 aimed to quantify this influence based on a distinction of events based on the depth to which the

warming descends within the stratosphere. The validity of the use of EMAC for this purpose was again first tested with respect to the CAMS reanalysis, in terms of capturing and representing accurately anomalies in ozone and water vapour, and found to adequate for such investigation. It was then found that in the case of Polar-night Jet Oscillation (PJO) events, in which the warming is maximised in the lower stratosphere (~ 60 hPa) (Hitchcock et al., 2013), anomalies in polar-cap (60-90°N) ozone (> 25 %) and water vapour (~ ± 25 %) may establish and persist in the UTLS for up to 2-3 months, which is consistent with the length of known dynamical recovery timescales in this region (Hitchcock et al., 2013; De la Cámara et al., 2018a). The radiative impacts of such perturbations are calculated using the Fixed Dynamical Heating (FDH) technique, which yields an estimate of the stratospheric adjusted temperatures, and are found to be highly significant (up to ~ ± 2 K). To understand this response in greater detail, a series of sensitivity evaluations involving an artificially imposed change in UTLS (50-200 hPa) ozone and water vapour were undertaken as a function of the seasonal cycle during the core of the stratospheric dynamically active season (November-May inclusive). The influence of ozone on the FDH temperature changes is shown to markedly increase between December and May, as the importance of the SW radiative component greatly increases, due to its primary radiative effect in this component. This contrasts with the dominance of water vapour in impacting the profile temperature changes (ΔT) earlier in winter, when the long-wave (LW) radiative component dominates. The radiative response is largely linear to the perturbation in ozone and/or water vapour applied, but some indications of non-linearity manifest at particularly higher perturbations. This is especially true for water vapour, in which negative perturbations have a slightly more pronounced response with to imposed positive perturbations as a consequence of the saturation effect of gaseous absorption at higher concentrations.

Finally, the potential influence on STE of ozone is investigated more widely over the main populated centres of the Northern Hemisphere (Europe, North America and Asia), extending into mid-latitudes (30-70°N). A clear enhancement in UTLS and upper tropospheric ozone indeed extends into mid-latitudes following the PJO subclass of events, but the impacts appear to be significantly muted towards the surface. The implications for air quality thus warrant more detailed investigation, although it is emphasised that such enhancements likely result from episodic, transient events, as denoted from shifts in calculated ozone distributions with respect to climatology. An inferred 10 to 20 % increase in the likelihood of an exceedance at the 95-percentile of the

climatological ozone distributions in both planetary boundary layer and surface ozone is nonetheless calculated, which is also found when substituting this threshold with a typical ozone air quality standard (taken here as 60 ppbv). The importance of UTLS composition for NWP on weekly to sub-seasonal timescales is illustrated from this work and as a potential early indicator for surface ozone exceedances during springtime, when tropospheric ozone reaches a seasonal maximum, following such events.

7.4 Wider Findings and Future Work

Whilst it is clear that both observations and CCMs have their limitations when used to understand regional and seasonal variability in tropospheric ozone, it is demonstrated in this thesis that insights can be maximised when combining knowledge from these different sources. To achieve this, it is shown that an in depth understanding of the origin of biases in each dataset is fundamental to making correct interpretations, before ascertaining the level of agreement between datasets. The limitations of the UV-nadir retrieval using the RAL ozone optimal estimation scheme for the GOME-2A and OMI instruments were in part elucidated in Chapter 4, which will help pave way to the development of a physically meaningful bias correction scheme that can be applied on a profile-by-profile basis in the future. This will retrospectively improve the record of tropospheric ozone over the mission lifetimes of each sounder, and may be adapted for future satellite missions in years to come. The biases in the CCMs was later shown, with respect to ozonesondes and satellite data from OMI, to originate from both dynamical and chemical causes in Chapter 5, before each model was utilised to quantify the stratospheric influence and recent changes in tropospheric ozone, resolved at a regional and seasonal level. Combining this knowledge, the robustness of quantitative estimates on the stratospheric influence was demonstrated and it could be discerned with confidence that the stratospheric influence on tropospheric ozone is larger than thought compared to earlier studies. Nonetheless, this study is limited in regard to the use of only two CCMs when a whole suite of such models are available (e.g. Stevenson et al., 2006; Young et al., 2013). It would therefore be informative to apply such evaluations (in Chapter 5) to other such models. However, other such models do not have the provision of a tagged stratospheric ozone (O_3S) tracer, or involve the use of a different and invariably more simplistic formulation.

Noting the overall better performance for the EMAC model, compared with CMAM, in this study with respect to OMI and ozonesondes observations, as well as consistency with

respect to CAMS in regard to the representation of both ozone and water vapour, this model was subsequently utilised to understand possible influence from midwinter SSWs on Arctic UTLS composition and in turn, STE of ozone which may have important radiative impacts and surface air quality implications (Chapter 6). Whilst profound, relatively long-lasting impacts were found in terms of both UTLS composition changes and enhanced STE following such events, the potential impacts on surface air quality appear to comparatively small but with a large degree of uncertainty due to the limited number of events available for the composite based approach adopted here. In further understanding such possible influence, evaluation of higher resolution data sources would be required over a much longer timespan to encompass a greater number of SSW events, in order to constrain such possible impacts and to derive as statistically robust signal. The implications for Numerical Weather Prediction (NWP) on weekly to sub-seasonal timescales, in terms of chemical-radiative impacts and tropospheric ozone forecasts, can in contrast be better appreciated here but further work is nonetheless required to quantify the importance of each aspect. Ultimately, this research project has served to elucidate the regional and seasonal characterisation of tropospheric ozone in greater detail than was hitherto possible, using new tools and measurements in a combined manner that additionally accounts for the various limitations associated with independent data sources, to aid interpretations of the relative importance of the stratosphere against the role of in situ formed ozone from precursor emission sources.

Appendix A

DJF	OMI	EMAC-OMI	CMAM-OMI	EMAC-OMI (AK)	CMAM-OMI (AK)	Δ EMAC-OMI	Δ CMAM-OMI
60°N-90°N	26.47	-6.92	-9.92	-3.58	-3.71	3.34	6.21
30°N-60°N	20.78	0.04	-3.24	1.41	-0.09	1.36	3.15
0°N-30°N	16.51	5.32	-0.03	4.55	-0.70	-0.86	-0.68
30°S-0°N	14.13	2.16	-0.76	1.91	-0.82	-0.25	-0.06
60°S-30°S	13.96	-0.51	-2.14	1.45	1.16	1.96	3.31
90°S-60°S	9.60	-2.86	-3.83	-0.46	0.57	2.40	4.40
MAM	**OMI**	**EMAC-OMI**	**CMAM-OMI**	**EMAC-OMI (AK)**	**CMAM-OMI (AK)**	**Δ EMAC-OMI**	**Δ CMAM-OMI**
60°N-90°N	28.44	-3.65	-8.22	1.07	0.14	4.72	8.36
30°N-60°N	25.03	1.71	-3.37	3.70	0.58	2.00	3.95
0°N-30°N	18.10	5.58	-0.94	4.83	-1.21	-0.75	-0.27
30°S-0°N	13.33	2.48	-0.63	2.29	-0.61	-0.19	0.02
60°S-30°S	14.11	0.55	-0.66	1.90	2.22	1.35	2.88
90°S-60°S	13.06	-2.89	-3.26	-1.18	0.34	1.71	3.59
JJA	**OMI**	**EMAC-OMI**	**CMAM-OMI**	**EMAC-OMI (AK)**	**CMAM-OMI (AK)**	**Δ EMAC-OMI**	**Δ CMAM-OMI**
60°N-90°N	25.88	-4.93	-7.96	-1.10	-1.22	4.08	6.73
30°N-60°N	24.09	0.29	-3.55	1.36	-1.55	1.32	2.00
0°N-30°N	15.22	3.73	-0.72	3.20	-1.85	-0.64	-1.12
30°S-0°N	16.54	2.76	-0.54	1.97	-1.35	-0.63	-0.81
60°S-30°S	17.07	-0.25	-0.50	1.21	2.78	2.71	3.28
90°S-60°S	16.48	-2.76	-2.42	-1.74	-1.23	1.68	1.19
SON	**OMI**	**EMAC-OMI**	**CMAM-OMI**	**EMAC-OMI (AK)**	**CMAM-OMI (AK)**	**Δ EMAC-OMI**	**Δ CMAM-OMI**
60°N-90°N	22.99	-4.04	-6.95	-2.17	-2.08	2.44	4.87
30°N-60°N	20.14	1.71	-2.34	2.02	-1.37	0.50	0.97
0°N-30°N	14.83	4.56	-0.85	4.06	-2.09	-0.64	-1.24
30°S-0°N	17.60	2.80	-1.02	2.21	-1.75	-0.60	-0.73
60°S-30°S	17.28	-0.07	-1.61	2.12	2.02	2.19	3.63
90°S-60°S	11.52	-1.93	-2.58	-1.54	-1.87	0.39	0.71

Table A1 – Seasonal mean 1000-450 hPa (0-5.5 km) subcolumn O_3 (DU) for 2005-2010 from OMI and differences with respect to both EMAC and CMAM both with and without AKs, together with the change (Δ) in bias through applying the OMI AKs on a zonal mean 30° latitude band basis.

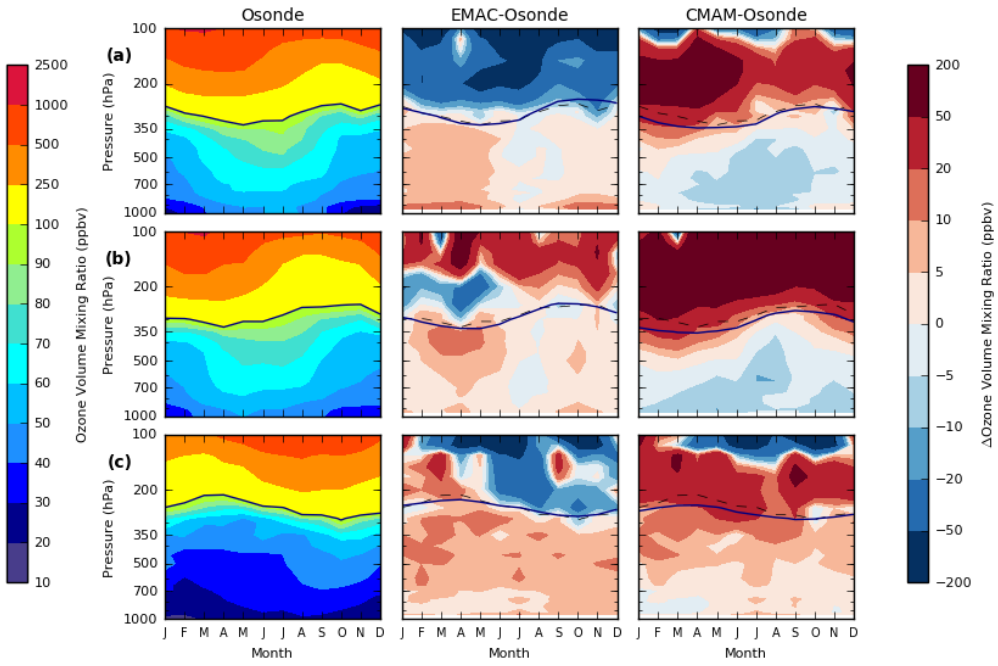

Figure A1 – Monthly evolution of the vertical distribution of mean O_3 volume mixing ratio (VMR) (ppbv) derived from ozonesonde measurements (left column); EMAC minus ozonesonde differences (ppbv) (middle column) and CMAM minus ozonesonde differences (ppbv) (right column) over the period 1980-2010 inclusive for three different world regions: (a) Europe (n = 18), (b) eastern North America (n = 14) and (c) Tasman Sea (n = 6). The ozonesonde/model 100 ppbv contour (the ozone defined extratropical tropopause as identified in Bethan et al. (1996)) is additionally highlighted in bold (ozonesonde 100 ppbv contour indicated again by dashed line – middle and right column).

Pressure (hPa)	DJF Osonde (ppbv)	DJF EMAC-Osonde (ppbv)	DJF CMAM-Osonde (ppbv)	MAM Osonde (ppbv)	MAM EMAC-Osonde (ppbv)	MAM CMAM-Osonde (ppbv)
100	958.1	-86.7 (-9.1 %)	-47.6 (-4.9 %)	1009.8	-60.2 (-5.9%)	-28.3 (-2.7 %)
200	591.4	-48.5 (-8.3 %)	+28.6 (+4.9 %)	677.2	-27.3 (-4.0 %)	+48.9 (+7.3 %)
350	62.3	+4.9 (+7.7 %)	+10.8 (+17.1 %)	83.7	+5.8 (+7.1 %)	+11.8 (+14.6 %)
500	51.2	+5.4 (+10.6 %)	+0.8 (+1.5 %)	67.0	+7.1 (+10.5 %)	-1.8 (-2.7 %)
850	45.6	+4.5 (+9.9 %)	-2.3 (-5.0 %)	57.8	+5.9 (+10.2 %)	-6.1 (-10.5 %)
1000	27.4	+12.2 (+45.3 %)	+1.4 (+5.6 %)	44.7	+10.6 (+24.1 %)	-5.2 (-11.5 %)
Pressure (hPa)	**JJA Osonde (ppbv)**	**JJA EMAC-Osonde (ppbv)**	**JJA CMAM-Osonde (ppbv)**	**SON Osonde (ppbv)**	**SON EMAC-Osonde (ppbv)**	**SON CMAM-Osonde (ppbv)**
100	738.3	-85.6 (-11.7 %)	-34.6 (-4.7 %)	712.7	-86.7 (-12.1 %)	-6.6 (-0.7 %)
200	453.5	-60.0 (-13.6 %)	+16.2 (+3.3 %)	377.0	-41.5 (-10.8 %)	+30.2 (+8.4 %)
350	88.0	+1.2 (+1.3 %)	+2.0 (+2.3 %)	65.9	+1.6 (+2.6 %)	+0.1 (+0.2 %)
500	75.2	-1.0 (-1.2 %)	-6.8 (-8.9 %)	57.9	+2.0 (+3.7 %)	-5.3 (-8.9 %)
850	59.4	-0.2 (-0.3%)	-8.6 (-14.4 %)	48.2	+3.9 (+8.3 %)	-4.9 (-10.2 %)
1000	50.1	+1.7 (+3.4 %)	-8.8 (-17.4 %)	33.3	+11.0 (+37.0 %)	-1.8 (-3.3 %)

Table A2a – Seasonally averaged ozone VMR (ppbv) values for six pressure levels between the surface (1000 hPa) and the lower stratosphere (100 hPa) derived from available ozonesondes measurements across Europe (30° N - 65° N, 15° W - 35° E) (n = 18) over the period 1980-2010 inclusive, together with the differences with respect to both EMAC and CMAM (also expressed in percentage terms).

Pressure (hPa)	DJF Osonde (ppbv)	DJF EMAC-Osonde (ppbv)	DJF CMAM-Osonde (ppbv)	MAM Osonde (ppbv)	MAM EMAC-Osonde (ppbv)	MAM CMAM-Osonde (ppbv)
100	939.5	+35.0 (+3.8 %)	+56.6 (+6.2 %)	906.6	+27.6 (+3.8 %)	+57.9 (+7.6 %)
200	608.0	+16.5 (+2.4 %)	+81.7 (+13.3 %)	615.5	+32.4 (+5.7 %)	+104.1 (+17.7 %)
350	67.1	+4.0 (+6.0 %)	+17.5 (+25.9 %)	80.8	+11.3 (+14.1 %)	+19.7 (+25.0 %)
500	52.9	+3.1 (+5.8 %)	+0.6 (+1.0 %)	65.5	+8.7 (+13.3 %)	+1.3 (+2.2 %)
850	46.6	+2.8 (+6.0 %)	-3.8 (-8.2 %)	58.5	+4.4 (+7.5 %)	-5.8 (-9.9 %)
1000	33.5	+4.6 (+13.6 %)	-7.6 (-22.6 %)	47.0	+4.8 (+10.2 %)	-8.1 (-17.3 %)
Pressure (hPa)	**JJA Osonde (ppbv)**	**JJA EMAC-Osonde (ppbv)**	**JJA CMAM-Osonde (ppbv)**	**SON Osonde (ppbv)**	**SON EMAC-Osonde (ppbv)**	**SON CMAM-Osonde (ppbv)**
100	611.1	+23.5 (+3.7 %)	+96.0 (+15.8 %)	581.8	+24.4 (+4.0 %)	+99.4 (+17.2 %)
200	330.5	+34.0 (+10.8 %)	+125.6 (+39.3 %)	299.7	+33.1 (+10.8 %)	+97.2 (+32.4 %)
350	83.5	+2.1 (+2.5 %)	+0.7 (+0.7 %)	63.8	+4.1 (+6.5 %)	+3.5 (+5.8 %)
500	70.4	+1.8 (+2.6 %)	-5.1 (-7.3 %)	54.8	+4.6 (+8.5 %)	-1.9 (-3.5 %)
850	58.4	-1.4 (-2.5 %)	-6.8 (-11.7 %)	49.5	+2.9 (+5.9 %)	-4.8 (-9.8 %)
1000	46.4	+2.1 (+4.4 %)	-4.6 (-9.9 %)	36.2	+6.2 (+17.2 %)	-6.6 (-18.6 %)

Table A2b – Same as for Table A2a but for eastern North America (32.5° N - 60° N, 92.5° W - 55° W) (n = 14).

Pressure (hPa)	Osonde (ppbv)	DJF EMAC-Osonde (ppbv)	CMAM-Osonde (ppbv)	Osonde (ppbv)	MAM EMAC-Osonde (ppbv)	CMAM-Osonde (ppbv)
100	485.3	+13.2 (+3.0 %)	+36.5 (+7.9 %)	544.0	-44.7 (-8.1 %)	-13.2 (-2.1 %)
200	294.1	-9.4 (-2.7 %)	+19.4 (+7.2 %)	270.3	+6.3 (+3.4 %)	+41.0 (+16.3 %)
350	52.7	+7.8 (+15.0 %)	+9.3 (+17.9 %)	42.5	+11.1 (+26.5 %)	+10.5 (+25.1 %)
500	40.1	+9.1 (+22.9 %)	+6.6 (+16.6 %)	36.2	+9.6 (+26.6 %)	+5.9 (+16.4 %)
850	26.9	+6.0 (+22.5 %)	+0.5 (+2.1 %)	29.5	+4.9 (+17.6 %)	+1.0 (+3.8 %)
1000	18.6	+6.1 (+32.9 %)	+1.2 (+6.8 %)	22.7	+5.7 (+25.0 %)	+2.0 (+8.5 %)
Pressure (hPa)	**Osonde (ppbv)**	**JJA EMAC-Osonde (ppbv)**	**CMAM-Osonde (ppbv)**	**Osonde (ppbv)**	**SON EMAC-Osonde (ppbv)**	**CMAM-Osonde (ppbv)**
100	807.3	-72.7 (-9.1 %)	-84.7 (-10.5 %)	848.8	-64.9 (-7.6 %)	-83.3 (-9.7 %)
200	486.1	-45.6 (-9.5 %)	-20.0 (-4.1 %)	463.9	-5.8 (-1.2 %)	+5.4 (+1.3 %)
350	50.4	+6.5 (+13.7 %)	+8.9 (+18.5 %)	61.2	+6.1 (+10.2 %)	+7.7 (+12.9 %)
500	40.8	+7.8 (+19.3 %)	+5.0 (+12.2 %)	46.6	+8.8 (+18.9 %)	+5.3 (+11.5 %)
850	36.6	+3.3 (+8.9 %)	+2.2 (+5.9 %)	35.5	+6.7 (+18.8 %)	+2.6 (+7.1 %)
1000	25.8	+8.0 (+31.5 %)	+6.9 (+27.3 %)	26.3	+7.8 (+29.7 %)	+3.1 (+11.3 %)

Table A2c – Same as for Table A2a/A2b but for the Tasman Sea region (15° S - 55° S, 140° E - 180° E) (n = 6).

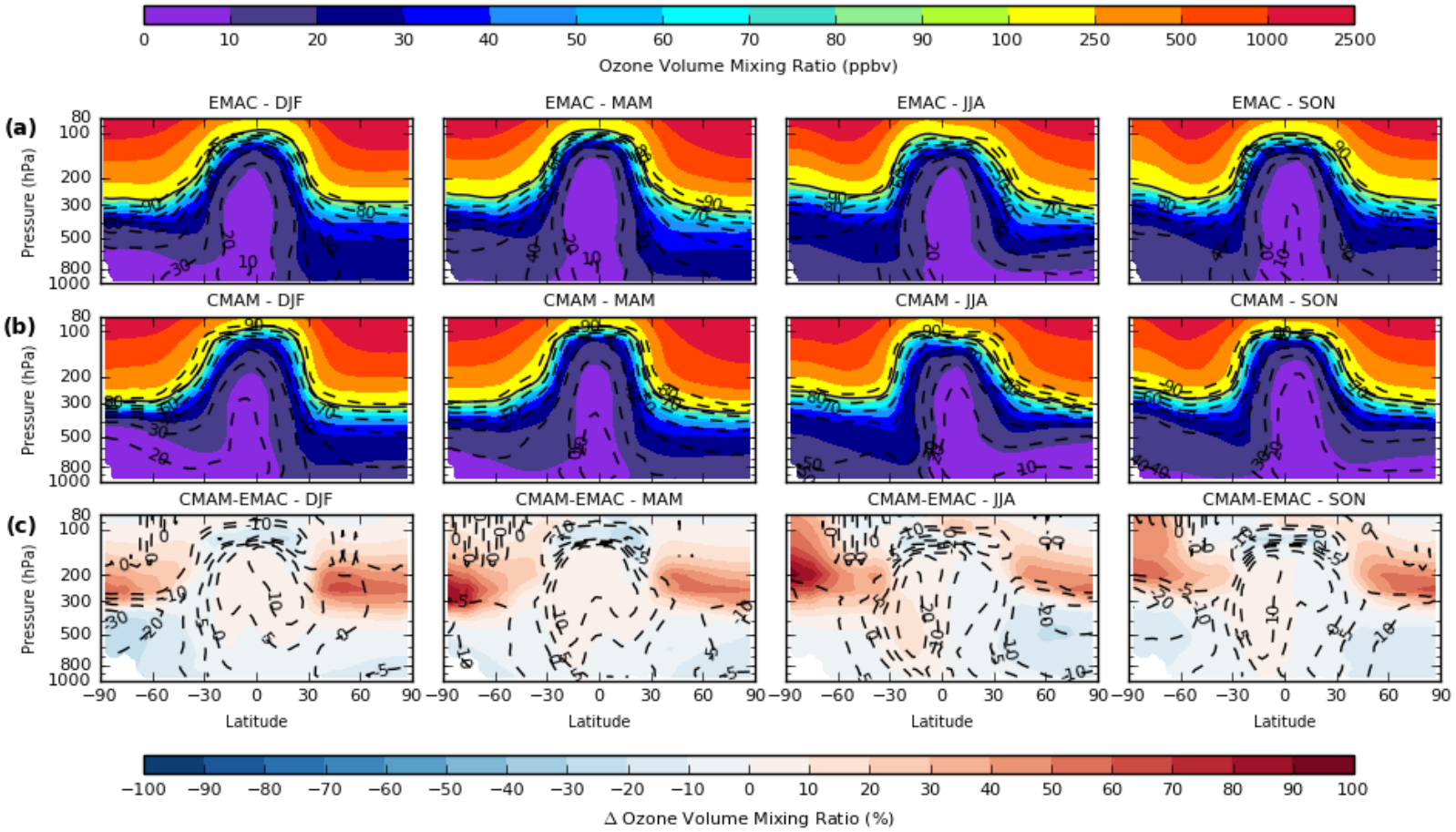

Figure A2 – Zonal mean seasonal composites of monthly mean O_3S concentration (ppbv) for the troposphere and lower stratosphere (1000-80 hPa) from (a) EMAC, (b) CMAM and (c) CMAM and EMAC (CMAM-EMAC) percentage differences over the period 1980-2010. Dashed lines indicate the stratospheric contribution (%) calculated using both ozone tracers in each model: O_3F (%) = (O_3S / O_3) x 100. The 100 ppbv contour (bold line) is included as a reference for the tropopause altitude (top and middle row).

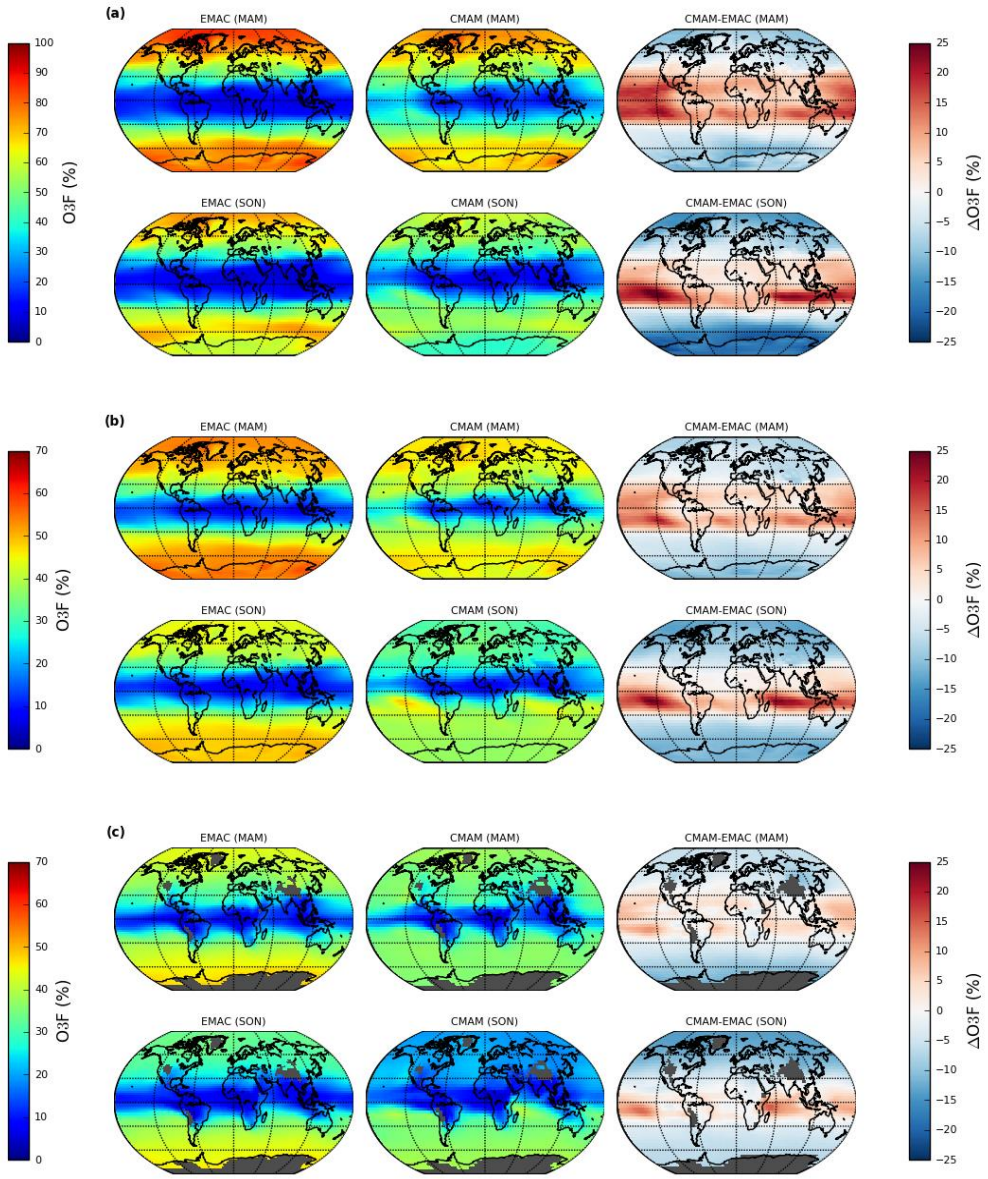

Figure A3 – Seasonal (MAM/SON) composites of (a) 350 hPa, (b) 500 hPa and (c) 850 hPa monthly mean stratospheric ozone fraction (O_3F) for EMAC (left), CMAM (middle) and CMAM-EMAC (right) over the period 1980-2010. Note the scale difference between (a) and (b-c).

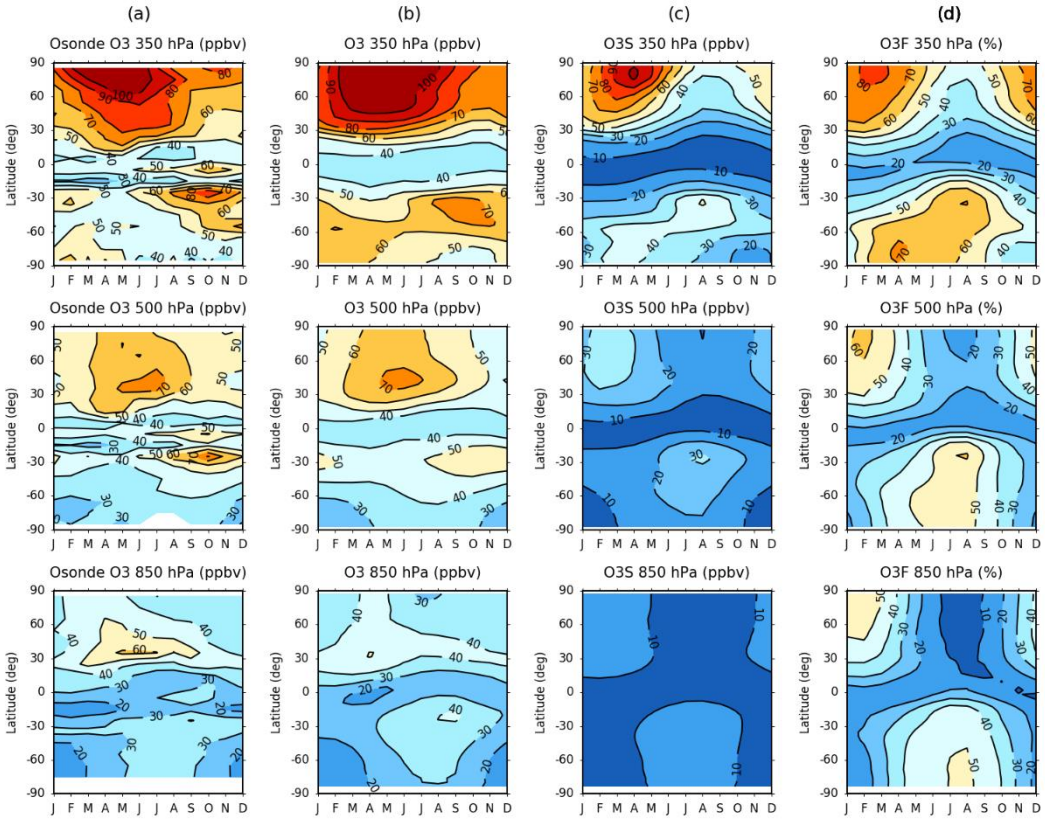

Figure A4 – Zonal-mean monthly mean evolution of O_3 VMR concentration (ppbv) derived from (a) ozonesondes and (b) CMAM O_3 model tracer. The evolution of the (c) CMAM stratospheric O_3S tracer and (d) O_3F stratospheric fraction (%) are additionally included over the period 1980-2010 for 350 hPa (top row), 500 hPa (middle row) and 850 hPa (bottom row).

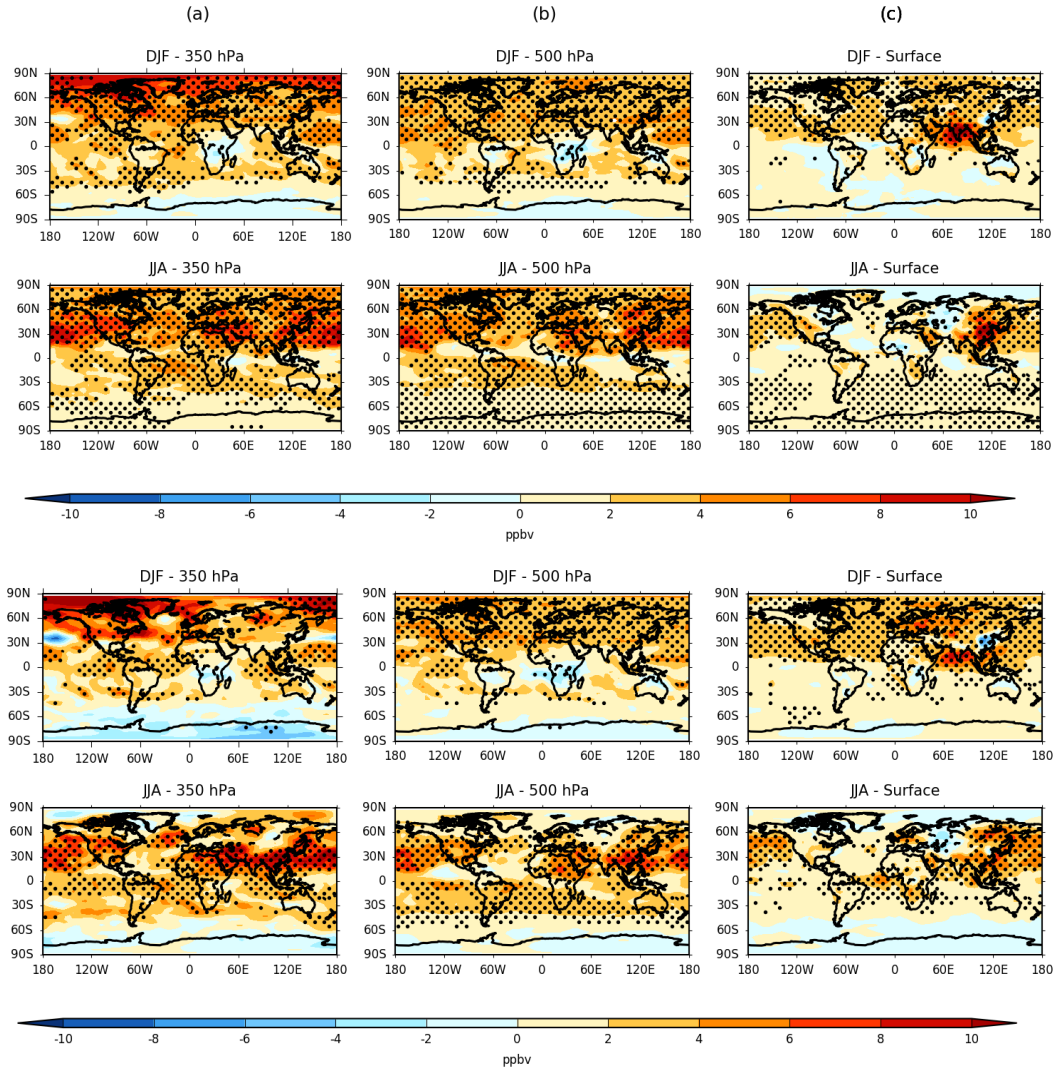

Figure A5 – Seasonal change in EMAC (top) and CMAM (bottom) ozone (O_3) VMR concentration (ppbv) between 1980-89 and 2001-10 for DJF and JJA at (a) 350 hPa, (b) 500 hPa and (c) the surface model level. Stippling denotes regions of statistical significance according to a paired two-sided t-test ($p < 0.05$).

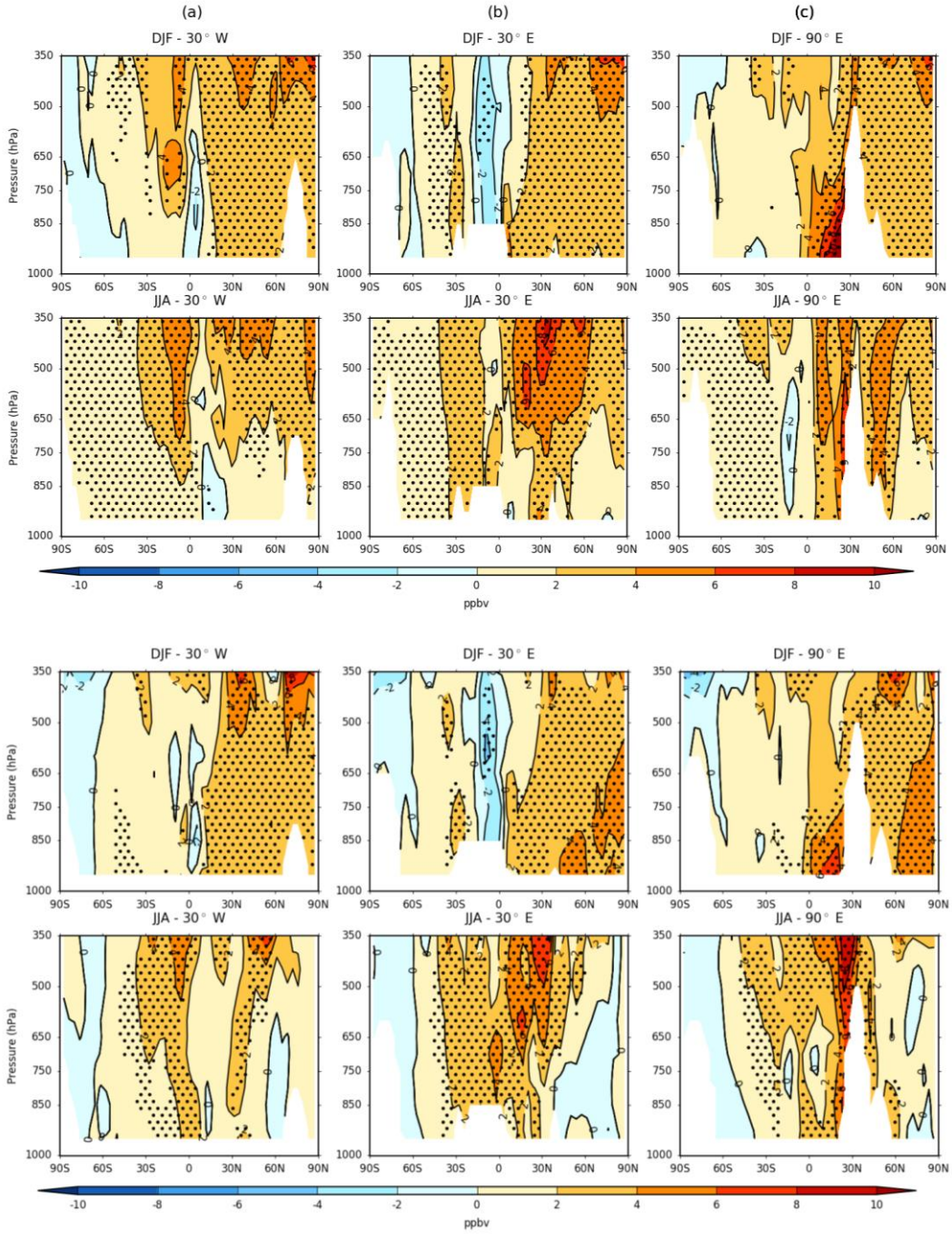

Figure A6 – Longitudinal cross-sections of the seasonal change in the vertical distribution of ozone (O_3) VMR (ppbv) from EMAC (top) and CMAM (bottom) between 1980-89 and 2001-10 for DJF and JJA at (a) 30° W, (b) 30° E and (c) 90° E. Stippling denotes regions of statistical significance according to a paired two-sided t-test ($p < 0.05$).

DJF	EMAC O3			CMAM O3		
	350 hPa	500 hPa	Surface	350 hPa	500 hPa	Surface
60°N-90°N	+7.0 (+11.3 %)*	+3.6 (+7.4 %)*	+2.0 (+7.0 %)*	+7.1 (+8.7 %)	+3.6 (+7.5 %)*	+2.7 (+13.3 %)*
30°N-60°N	+4.4 (+6.6 %)*	+3.7 (+6.8 %)*	+2.0 (+5.8 %)*	+3.6 (+4.9 %)	+3.5 (+6.9 %)*	+2.8 (+13.4 %)*
0°N-30°N	+2.7 (+5.4 %)	+2.7 (+5.4 %)	+2.7 (+6.4 %)	+2.5 (+6.4 %)	+2.1 (+5.1 %)	+2.6 (+8.0 %)
30°S-0°N	+1.9 (+3.9 %)	+1.5 (+3.1 %)	+0.7 (+2.7 %)	+1.5 (+4.0 %)	+0.9 (+2.4 %)	+0.8 (+4.0 %)
60°S-30°S	+1.7 (+2.9 %)	+1.3 (+3.0 %)	+0.2 (+1.0 %)	+0.4 (+0.8 %)	+0.9 (+2.0 %)	+0.4 (+2.4 %)
90°S-60°S	-0.4 (-0.9 %)	+0.1 (+0.3 %)	+0.1 (+0.9 %)	-2.3 (-3.5 %)	-0.2 (-0.9 %)	+0.1 (+ 0.7%)
MAM	EMAC O3			CMAM O3		
	350 hPa	500 hPa	Surface	350 hPa	500 hPa	Surface
60°N-90°N	+3.4 (+3.7 %)	+3.4 (+5.2 %)*	+1.6 (+4.5 %)	+1.6 (+1.4 %)	+3.0 (+4.8 %)	+1.9 (+6.8 %)*
30°N-60°N	+4.8 (+5.4 %)*	+3.7 (+5.2 %)*	+1.8 (+3.6 %)	+5.0 (+5.3 %)	+4.1 (+6.4 %)*	+2.4 (+6.7 %)
0°N-30°N	+3.2 (+5.3 %)	+3.4 (+5.7 %)	+2.1 (+4.8 %)	+2.9 (+6.6 %)	+3.0 (+6.4 %)	+2.7 (+8.7 %)
30°S-0°N	+1.6 (+3.3 %)	+1.3 (+2.8 %)	+1.0 (+3.6 %)	+1.5 (+4.3 %)	+0.9 (+2.7 %)	+0.9 (+4.3 %)
60°S-30°S	+1.2 (+2.4 %)	+1.2 (+2.8 %)	+0.4 (+1.7 %)	-0.6 (-0.9 %)	+0.1 (+0.1 %)	-0.0 (-0.2 %)
90°S-60°S	+1.0 (+2.4 %)	+0.8 (+2.8 %)	+0.5 (+2.4%)	-2.2 (-3.4 %)	-0.5 (-1.4 %)	-0.3 (-1.5 %)
JJA	EMAC O3			CMAM O3		
	350 hPa	500 hPa	Surface	350 hPa	500 hPa	Surface
60°N-90°N	+4.0 (+4.7 %)*	+3.7 (+6.1 %)*	+0.3 (+0.9 %)	+1.8 (+1.7 %)	+1.1 (+1.9 %)	+0.2 (+0.8 %)
30°N-60°N	+5.4 (+6.5 %)*	+4.5 (+6.5 %)*	+1.8 (+5.0 %)	+4.6 (+5.7 %)	+3.2 (+5.1 %)	+2.0 (+6.6 %)
0°N-30°N	+3.9 (+6.9 %)	+3.5 (+6.5 %)	+1.7 (+5.6 %)	+4.3 (+10.1 %)	+3.2 (+7.9 %)	+2.1 (+8.5 %)
30°S-0°N	+2.3 (+4.2 %)	+2.1 (+4.0 %)	+0.9 (+2.8 %)	+2.5 (+6.7 %)	+2.6 (+6.4 %)	+1.3 (+4.7 %)
60°S-30°S	+1.9 (+3.5 %)	+1.7 (+3.8 %)*	+0.7 (+2.4 %)*	+1.9 (+3.0 %)	+1.5 (+3.4 %)	+0.1 (+0.4 %)
90°S-60°S	+1.0 (+2.4 %)	+1.1 (+3.1 %)*	+0.8 (+3.2 %)*	-0.7 (-1.3 %)	-0.1 (-0.3 %)	-0.2 (-0.9 %)
SON	EMAC O3			CMAM O3		
	350 hPa	500 hPa	Surface	350 hPa	500 hPa	Surface
60°N-90°N	+4.4 (+7.3 %)*	+3.7 (+7.3 %)*	+2.0 (+7.1 %)*	+4.1 (+5.4 %)	+3.0 (+6.1 %)*	+2.1 (+10.5 %)*
30°N-60°N	+4.5 (+6.9 %)*	+4.4 (+7.7 %)*	+2.1 (+5.7 %)	+5.3 (+8.4 %)*	+4.8 (+9.4 %)*	+2.7 (10.7 %)*
0°N-30°N	+3.4 (+6.7 %)	+3.3 (+6.6 %)	+2.3 (+6.6 %)	+3.8 (+10.2 %)*	+3.2 (+8.9 %)	+2.7 (+10.3 %)*
30°S-0°N	+2.6 (+4.6 %)	+2.3 (+4.2 %)	+0.8 (+2.6 %)	+2.6 (+6.6 %)	+2.3 (+5.5 %)	+1.3 (+5.3 %)
60°S-30°S	+2.0 (+3.1 %)	+1.7 (+3.6 %)	+0.4 (+1.6 %)	+1.7 (+2.4 %)	+1.9 (+4.1 %)*	+0.7 (+2.7 %)*
90°S-60°S	+1.4 (+3.3 %)	+0.9 (+2.6 %)	+0.6 (+2.5 %)	+2.4 (+4.7 %)	+1.3 (+3.8 %)	+0.5 (+2.1 %)

Table A3 - 30° latitude band changes in seasonal mean ozone (O_3) VMR (ppbv) (also expressed in percentage (%) terms) between 1980-89 and 2001-10 at 350 hPa, 500 hPa and the surface (left to right for each model). Values denoted with an asterisk (*) represent statistical significance at the 95% confidence level ($p < 0.05$) as determined by a two-sided paired t-test.

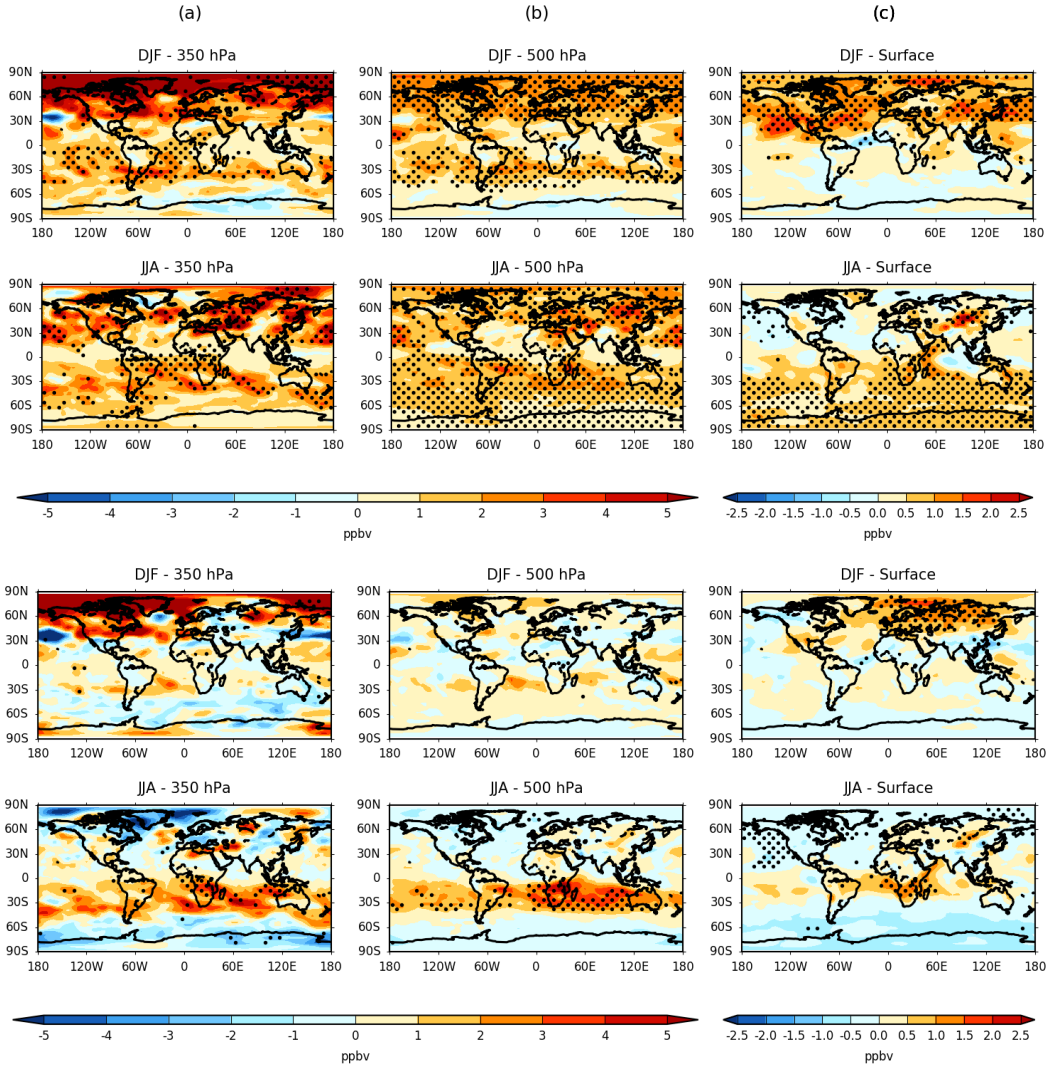

Figure A7 – Seasonal change in EMAC (top) and CMAM (bottom) stratospheric ozone (O_3S) VMR concentration (ppbv) between 1980-89 and 2001-10 for DJF and JJA at (a) 350 hPa, (b) 500 hPa and (c) the surface model level. Stippling denotes regions of statistical significance according to a paired two-sided t-test ($p < 0.05$). Note the scale difference between (a-b) and (c).

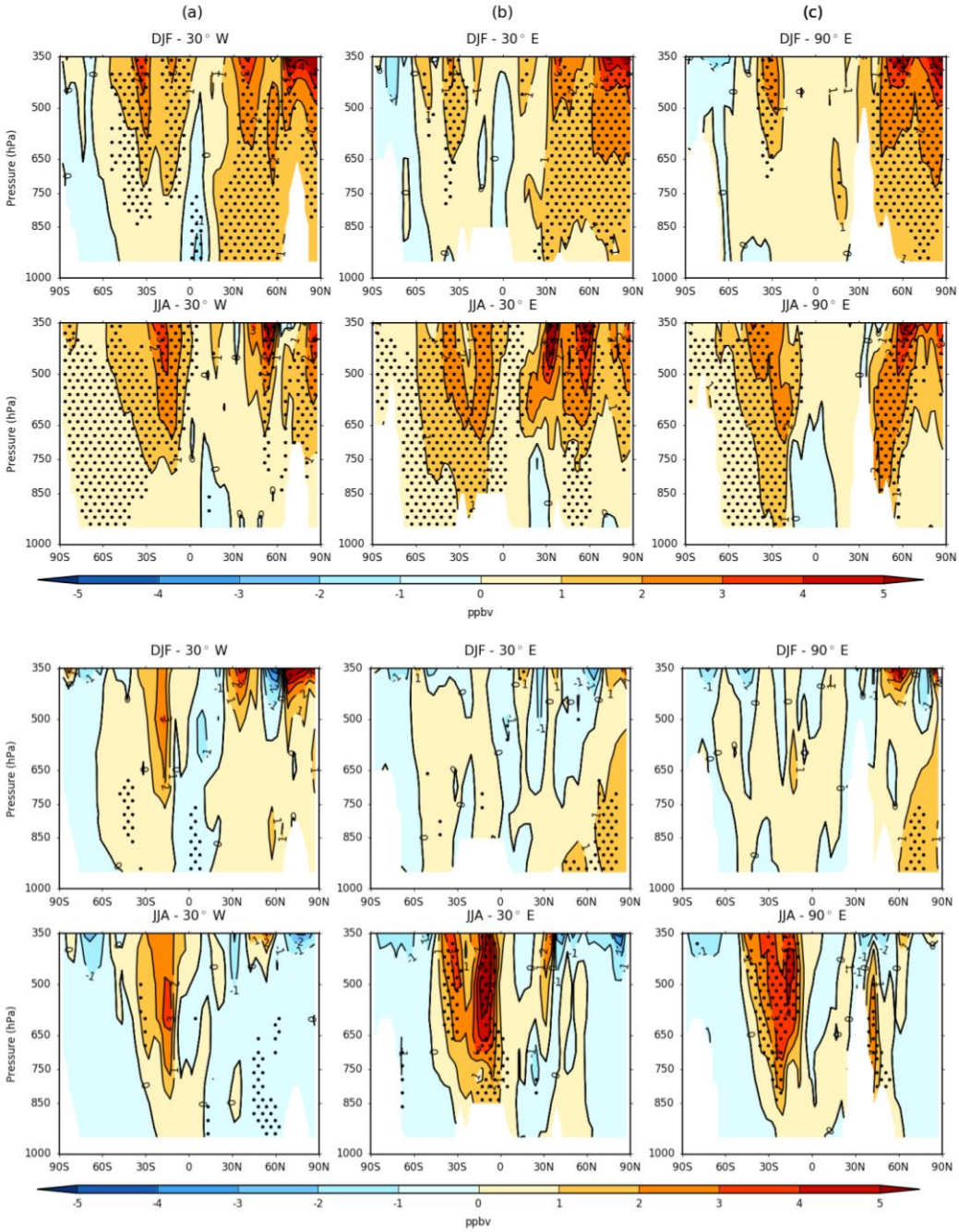

Figure A8 – Longitudinal cross-sections of the seasonal change in the vertical distribution of stratospheric ozone (O_3S) VMR (ppbv) from EMAC (top) and CMAM (bottom) between 1980-89 and 2001-10 for DJF and JJA at (a) 30° W, (b) 30° E and (c) 90° E. Stippling denotes regions of statistical significance according to a paired two-sided t-test ($p < 0.05$).

DJF	EMAC O3S			CMAM O3S		
	350 hPa	500 hPa	Surface	350 hPa	500 hPa	Surface
60°N-90°N	+6.9 (+14.0 %)	+2.4 (+8.4 %)*	+0.9 (+6.1 %)	+5.3 (+8.1 %)	+0.5 (+1.8 %)	+0.5 (+5.9 %)
30°N-60°N	+2.8 (+6.2 %)	+1.9 (+6.7 %)*	+1.0 (+5.9 %)	+0.7 (+1.5 %)	+0.0 (+0.1 %)	+0.3 (+3.4 %)
0°N-30°N	+0.9 (+8.1 %)	+1.0 (+7.9 %)	+0.5 (+5.1 %)	+0.2 (+2.1 %)	-0.0 (-0.1 %)	-0.1 (-1.3 %)
30°S-0°N	+1.2 (+13.2 %)	+1.1 (+11.6 %)	+0.1 (+4.2 %)	+0.3 (+3.0 %)	+0.3 (+2.7 %)	+0.0 (+0.8 %)
60°S-30°S	+1.2 (+4.4 %)	+0.9 (+5.1 %)	-0.0 (-0.0 %)	-0.5 (-1.4 %)	+0.2 (+2.0 %)	+0.0 (+0.2 %)
90°S-60°S	+0.1 (+0.1 %)	-0.0 (-0.2 %)	+0.0 (-0.4 %)	+0.1 (+0.2 %)	-0.1 (-1.0 %)	-0.1 (-2.9 %)
MAM	EMAC O3S			CMAM O3S		
	350 hPa	500 hPa	Surface	350 hPa	500 hPa	Surface
60°N-90°N	+1.8 (+2.5 %)	+1.9 (+5.5 %)	+0.8 (+5.1 %)	-2.7 (-2.4 %)	+0.2 (+0.7 %)	+0.7 (+6.7 %)
30°N-60°N	+3.3 (+6.2 %)	+2.1 (+6.4 %)	+0.8 (+4.5 %)	+1.6 (+2.7 %)	+0.8 (+2.9 %)	+0.5 (+5.0 %)
0°N-30°N	+1.6 (+11.7 %)	+1.6 (+12.5 %)	+0.5 (+7.4 %)	+0.4 (+2.1 %)	+0.4 (+1.7 %)	+0.2 (+2.0 %)
30°S-0°N	+1.1 (+13.1 %)	+1.0 (+11.6 %)	+0.3 (+5.0 %)	+0.4 (+4.0 %)	+0.2 (+1.8 %)	+0.0 (+0.2 %)
60°S-30°S	+1.3 (+4.7 %)	+1.1 (+6.2 %)*	+0.4 (+4.0 %)	-0.9 (-2.3 %)	-0.3 (-1.5 %)	-0.2 (-2.5 %)
90°S-60°S	+1.5 (+5.0 %)	+0.9 (+5.9 %)*	+0.5 (+5.5 %)*	-0.9 (-2.0 %)	-0.3 (-1.9 %)	-0.1 (-1.7 %)
JJA	EMAC O3S			CMAM O3S		
	350 hPa	500 hPa	Surface	350 hPa	500 hPa	Surface
60°N-90°N	+2.1 (+3.5 %)	+1.8 (+7.3 %)	+0.0 (+0.2 %)	-1.4 (-2.7 %)	-0.5 (-3.9 %)	-0.1 (-6.0 %)
30°N-60°N	+2.5 (+6.3 %)	+1.8 (+6.5 %)	+0.1 (+0.7 %)	-0.2 (-0.3 %)	-0.2 (-1.1 %)	-0.1 (-2.4 %)
0°N-30°N	+1.1 (+9.9 %)	+0.9 (+9.4 %)	+0.1 (+2.9 %)	+0.1 (+1.5 %)	+0.0 (+0.0 %)	+0.0 (-0.6 %)
30°S-0°N	+1.4 (+11.2 %)	+1.5 (+12.3 %)	+0.5 (+4.4 %)	+1.5 (+8.7 %)	+1.8 (+8.9 %)	+0.3 (+3.6 %)
60°S-30°S	+1.7 (+5.0 %)	+1.4 (+6.1 %)*	+0.6 (+3.7 %)*	+1.0 (+2.4 %)	+0.7 (+2.8 %)	-0.4 (-2.5 %)
90°S-60°S	+0.8 (+3.0 %)	+0.9 (+4.2 %)*	+0.6 (+4.3 %)*	-1.5 (-4.2 %)	-0.7 (-3.3 %)	-0.5 (-3.9 %)
SON	EMAC O3S			CMAM O3S		
	350 hPa	500 hPa	Surface	350 hPa	500 hPa	Surface
60°N-90°N	+2.8 (+6.6 %)	+1.5 (+7.0 %)*	+0.5 (+5.9 %)	+0.3 (+0.8 %)	+0.0 (+0.1 %)	+0.2 (+4.9 %)
30°N-60°N	+1.7 (+5.2 %)	+1.5 (+6.8 %)	+0.4 (+4.0 %)	+0.5 (+2.0 %)	+0.3 (+2.3 %)	+0.1 (+1.9 %)
0°N-30°N	+0.7 (+8.9 %)	+0.6 (+8.2 %)	+0.1 (+3.7 %)	+0.1 (+2.4 %)	+0.1 (+1.8 %)	+0.1 (+1.7 %)
30°S-0°N	+1.2 (+11.8 %)	+1.2 (+11.5 %)	+0.1 (+2.4 %)	+1.2 (+9.7 %)	+1.5 (+10.0 %)	+0.3 (+4.2 %)
60°S-30°S	+1.1 (+2.7 %)	+0.8 (+3.5 %)	+0.0 (+0.2 %)	+0.2 (+0.6 %)	+0.6 (+3.1 %)	-0.1 (-0.5 %)
90°S-60°S	+1.2 (+4.3 %)	+0.4 (+2.5 %)	+0.2 (+1.8 %)	+1.2 (+5.2 %)	+0.1 (+1.0 %)	-0.1 (-0.8 %)

Table A4 - 30° latitude band changes in seasonal mean stratospheric ozone (O_3S) VMR (ppbv) (also expressed in percentage (%) terms) between 1980-89 and 2001-10 at 350 hPa, 500 hPa and the surface (left to right for each model). Values denoted with an asterisk (*) represent statistical significance at the 95% confidence level ($p < 0.05$) as determined by a two-sided paired t-test.

References

Akritidis, D., Zanis, P., Pytharoulis, I., Mavrakis, A. and Karacostas, T. (2010). A deep stratospheric intrusion event down to the earth's surface of the megacity of Athens. *Meteorology and atmospheric physics*, *109*(1-2), 9-18.

Akritidis, D., Pozzer, A., Zanis, P., Tyrlis, E., Škerlak, B., Sprenger, M., and Lelieveld, J. (2016). On the role of tropopause folds in summertime tropospheric ozone over the eastern Mediterranean and the Middle East, Atmos. Chem. Phys., 16, 14025–14039, https://doi.org/10.5194/acp-16-14025-2016.

Akritidis, D., Pozzer, A. and Zanis, P. (2019). On the impact of future climate change on tropopause folds and tropospheric ozone. *Atmospheric Chemistry and Physics*, *19*(22), 14387-14401.

Albers, J. R., Perlwitz, J., Butler, A. H., Birner, T., Kiladis, G. N., Lawrence, Z. D. et al. (2018). Mechanisms Governing Interannual Variability of Stratosphere-to-Troposphere Ozone Transport. *Journal of Geophysical Research: Atmospheres*, *123*(1), 234–260. https://doi.org/10.1002/2017JD026890.

Allen, D. J. and Pickering, K. E. (2002). Evaluation of lightning flash rate parameterizations for use in a global chemical transport model, J. Geophys. Res.-Atmos., 107, 4711, https://doi.org/10.1029/2002JD002066.

American Meteorological Society (AMS) (2012). *Glossary of Meteorology: Teleconnection.* Retrieved from: https://glossary.ametsoc.org/wiki/Teleconnection.

Anderson, J. G., Brune, W. H. and Proffitt, M. H. (1989). Ozone destruction by chlorine radicals within the Antarctic vortex: The spatial and temporal evolution of ClO-O3 anticorrelation based on in situ ER-2 data. *Journal of Geophysical Research: Atmospheres*, *94*(D9), 11465-11479.

Andrews, D. G. and Mcintyre, M. E. (1976). Planetary waves in horizontal and vertical shear: The generalized Eliassen-Palm relation and the mean zonal acceleration. *Journal of the Atmospheric Sciences*, *33*(11), 2031-2048.

Andrews, D. G. and McIntyre, M. E. (1978a). An exact theory of nonlinear waves on a Lagrangian-mean flow. *Journal of fluid Mechanics*, *89*(4), 609-646.

Andrews, D. G. and McIntyre, M. E. (1978b). Generalized Eliassen-Palm and Charney-Drazin theorems for waves on axismmetric mean flows in compressible atmospheres. *Journal of the Atmospheric Sciences*, *35*(2), 175-185.

Andrews, D. G. and McIntyre, M. E. (1978). On wave-action and its relatives. *Journal of Fluid Mechanics*, *89*(4), 647-664.

Andrews D. G., Holton J. R. and Leovy C. B (1987). *Middle Atmosphere Dynamics* (Academic, San 398 Diego, CA).

Arblaster, J. M. and Meehl, G. A. (2006). Contributions of external forcings to southern annular mode trends. *Journal of climate*, *19*(12), 2896-2905.

Assmann, R. (1902). Über die Existenz eines wärmeren Luftstromes in der Höhe von 10 bis 15 km. (On the existence of a warmer airflow at heights from 10 to 15 km). Sitzungsber. K. Preuss. Akad. Wiss., 24, 495–504.

Austin, J., Shindell, D., Beagley, S. R., Brühl, C., Dameris, M., Manzini, E. et al. (2003). Uncertainties and assessments of chemistry-climate models of the stratosphere.

Avery, M. A., Davis, S. M., Rosenlof, K. H., Ye, H. and Dessler, A. E. (2017). Large anomalies in lower stratospheric water vapour and ice during the 2015–2016 El Niño. *Nature Geoscience*, *10*(6), 405-409.

Ayarzagüena, B., Polvani, L. M., Langematz, U., Akiyoshi, H., Bekki, S., Butchart, N. et al. (2018). No robust evidence of future changes in major stratospheric sudden warmings: A multi-model assessment from CCMI. *Atmospheric Chemistry and Physics*, *18*(15), 11277–11287. https://doi.org/10.5194/acp-18-11277-2018.

Baldwin, Mark P. and Dunkerton, T. J. (1999). Propagation of the Arctic Oscillation from the stratosphere to the troposphere. *Journal of Geophysical Research Atmospheres*, *104*(D24), 30937–30946. https://doi.org/10.1029/1999JD900445

Baldwin, M. P. and Dunkerton, T. J. (2001). Stratospheric harbingers of anomalous weather regimes. *Science*, *294*(5542), 581–584. https://doi.org/10.1126/science.1063315.

Baldwin, M. P., Gray, L. J., Dunkerton, T. J., Hamilton, K., Haynes, P. H., Randel, W. J. et al. (2001). The quasi-biennial oscillation. *Reviews of Geophysics*, *39*(2), 179-229.

Baldwin, M. P., Birner, T., Brasseur, G., Burrows, J., Butchart, N., Garcia, R. et al. (2019).

100 Years of Progress in Understanding the Stratosphere and Mesosphere. *Meteorological Monographs*, *59*, 27-1.

Banerjee, A., Maycock, A. C., Archibald, A. T., Abraham, N. L., Telford, P., Braesicke, P., and Pyle, J. A.: Drivers of changes in stratospheric and tropospheric ozone between year 2000 and 2100, Atmos. Chem. Phys., 16, 2727–2746, https://doi.org/10.5194/acp-16-2727-2016, 2016.

Baray, J. L., Daniel, V., Ancellet, G. and Legras, B. (2000). Planetary-scale tropopause folds in the southern subtropics. *Geophysical Research Letters*, *27*(3), 353-356.

Beekmann, M., Ancellet, G., Megie, G., Smit, H. G. J., and Kley, D. (1994). Intercomparison campaign of vertical ozone profiles including electrochemical sondes of ECC and Brewer-Mast type and a ground based UV-differential absorption lidar, J. Atmos. Chem., 19, 259–288, https://doi.org/10.1007/BF00694614.

Beekmann, M., Ancellet, G., Blonsky, S., De Muer, D., Ebel, A., Elbern, H. et al. (1997). Regional and global tropopause fold occurrence and related ozone flux across the tropopause. *Journal of Atmospheric Chemistry*, *28*(1-3), 29-44.

Bell, C. J., Gray, L. J. and Kettleborough, J. (2010). Changes in Northern Hemisphere stratospheric variability under increased CO2 concentrations. *Quarterly Journal of the Royal Meteorological Society*, *136*(650), 1181-1190.

Bellenger, H., Guilyardi, É., Leloup, J., Lengaigne, M. and Vialard, J. (2014). ENSO representation in climate models: From CMIP3 to CMIP5. *Climate Dynamics*, *42*(7-8), 1999-2018. doi: 10.1007/s00382-013-1783-z

Best, N., Havens, R., and LaGow, H. (1947). Pressure and Temperature of the Atmosphere to 120 km. *Physical Review*, *71*(12), 915.

Bhartia, P. K., McPeters, R. D., Mateer, C. L., Flynn, L. E. and Wellemeyer, C. (1996). Algorithm for the estimation of vertical ozone profiles from the backscattered ultraviolet technique. *Journal of Geophysical Research: Atmospheres*, *101*(D13), 18793-18806.

Bhartia P.K. (2009) Role of Satellite Measurements in the Discovery of Stratospheric Ozone Depletion. In: Zerefos C., Contopoulos G., Skalkeas G. (eds) Twenty Years of Ozone Decline. Springer, Dordrecht.

Birner, T. and Bönisch, H. (2011). Residual circulation trajectories and transit times into the extratropical lowermost stratosphere. *Atmospheric Chemistry and Physics*, *11*(2), 817.

Black, R. X., McDaniel, B. A. and Robinson, W. A. (2006). Stratosphere–troposphere coupling during spring onset. *Journal of climate*, *19*(19), 4891-4901.

Bojkov, R. D. (1986). Surface ozone during the second half of the nineteenth century. *Journal of climate and applied meteorology*, *25*(3), 343-352.

Bönisch, H., Engel, A., Curtius, J., Birner, T. and Hoor, P. (2009). Quantifying transport into the lowermost stratosphere using simultaneous in-situ measurements of SF 6 and CO 2. *Atmospheric Chemistry and Physics*, *9*(16), 5905-5919.

Bönisch, H., Engel, A., Birner, Th., Hoor, P., Tarasick, D. W., and Ray, E. A. (2011). On the structural changes in the Brewer-Dobson circulation after 2000, Atmos. Chem. Phys., 11, 3937–3948, https://doi.org/10.5194/acp-11-3937-2011.

Boville, B. A. (1984). The influence of the polar night jet on the tropospheric circulation in a GCM. *Journal of the atmospheric sciences*, *41*(7), 1132-1142.

Boyd, J. P. (1976). Planetary waves and the semiannual wind oscillation in the tropical upper stratosphere. *PhDT*.

Brasseur, G. and Solomon, S. (1995). Aeronomy of the Middle Atmosphere, D. Reidel.

Brewer A. W. (1949). Evidence for a world circulation provided by measurements of helium and water vapor distribution in the stratosphere. Quart. J. Roy. Meteor. Soc., 75, 351–363, https://doi.org/10.1002/qj.49707532603.

Brinkop, S., Dameris, M., Jöckel, P., Garny, H., Lossow, S., and Stiller, G.: The millennium water vapour drop in chemistry– climate model simulations, Atmos. Chem. Phys., 16, 8125–8140, https://doi.org/10.5194/acp-16-8125-2016, 2016.

Brion, J., Chakir, A., Daumont, D., Malicet, J. and Parisse, C. (1993). High-resolution laboratory absorption cross section of O3. Temperature effect. *Chemical physics letters*, *213*(5-6), 610-612.

Brion, J., Chakir, A., Charbonnier, J., Daumont, D., Parisse, C. and Malicet, J. (1998). Absorption spectra measurements for the ozone molecule in the 350–830 nm region. *Journal of atmospheric chemistry*, *30*(2), 291-299.

Browell, E. V., Ismail, S. and Grant, W. B. (1998). Differential absorption lidar (DIAL) measurements from air and space. *Applied Physics B*, *67*(4), 399-410.

Bunzel, F. and Schmidt, H. (2013). The Brewer–Dobson circulation in a changing climate: Impact of the model configuration. *Journal of the atmospheric sciences*, *70*(5), 1437-1455.

Butchart, N. and Scaife, A. A. (2001). Removal of chlorofluorocarbons by increased mass exchange between the stratosphere and troposphere in a changing climate. *Nature*, *410*(6830), 799-802.

Butchart, N., Scaife, A. A., Bourqui, M., De Grandpré, J., Hare, S. H. E., Kettleborough, J. et al. (2006). Simulations of anthropogenic change in the strength of the Brewer–Dobson circulation. *Climate Dynamics*, *27*(7-8), 727-741.

Butchart, N., Cionni, I., Eyring, V., Shepherd, T. G., Waugh, D. W., Akiyoshi, H. et al. (2010). Chemistry–climate model simulations of twenty-first century stratospheric climate and circulation changes. *Journal of Climate*, *23*(20), 5349-5374.

Butchart, N., Charlton-Perez, A. J., Cionni, I., Hardiman, S. C., Haynes, P. H., Krüger, K. et al. (2011). Multimodel climate and variability of the stratosphere. *Journal of Geophysical Research: Atmospheres*, *116*(D5).

Butchart, N. (2014). Reviews of Geophysics The Brewer-Dobson circulation. *Rev. Geophys*, *52*, 157–184. https://doi.org/10.1002/2013RG000448.

Butler, A. H., Seidel, D. J., Hardiman, S. C., Butchart, N., Birner, T. and Match, A. (2015). Defining sudden stratospheric warmings. *Bulletin of the American Meteorological Society*, *96*(11), 1913-1928.

Butler, A. H., Sjoberg, J. P., Seidel, D. J. and Rosenlof, K. H. (2017). A sudden stratospheric warming compendium.

Calvo, N. and Garcia, R. R. (2009). Wave forcing of the tropical upwelling in the lower stratosphere under increasing concentrations of greenhouse gases. *Journal of the atmospheric sciences*, *66*(10), 3184-3196.

Calvo, N., Giorgetta, M. A., Garcia-Herrera, R. and Manzini, E. (2009). Nonlinearity of the combined warm ENSO and QBO effects on the Northern Hemisphere polar vortex in MAECHAM5 simulations. *Journal of Geophysical Research: Atmospheres*, *114*(D13).

Calvo, N., Garcia, R. R., Randel, W. J. and Marsh, D. R. (2010). Dynamical mechanism for the increase in tropical upwelling in the lowermost tropical stratosphere during warm ENSO events. *Journal of the Atmospheric Sciences*, *67*(7), 2331-2340.

Camp, C. D., Roulston, M. S. and Yung, Y. L. (2003). Temporal and spatial patterns of the interannual variability of total ozone in the tropics. *Journal of Geophysical Research: Atmospheres*, *108*(D20).

de la Cámara, A. D. L., Albers, J. R., Birner, T., Garcia, R. R., Hitchcock, P., Kinnison, 433 D. E. et al. Sensitivity of sudden stratospheric warmings to previous stratospheric 434 conditions. J. Atmos. Sci., ***74***, 2857-2877 (2017).

de la Cámara, A., Abalos, M. and Hitchcock, P. Changes in stratospheric transport and mixing during sudden stratospheric warmings. *J. Geophys. Res-Atmos.* ***123***, 3356-3373 (2018a).

de La Cámara, A., Abalos, M., Hitchcock, P., Calvo, N., and Garcia, R. R. (2018b). Response of Arctic ozone to sudden stratospheric warmings. *Atmospheric Chemistry and Physics*, *18*(22), 16499–16513. https://doi.org/10.5194/acp-18-16499-2018.

Castanheira, J. M. and Barriopedro, D. (2010). Dynamical connection between tropospheric blockings and stratospheric polar vortex. *Geophysical research letters*, *37*(13).

Cagnazzo, C., Manzini, E., Fogli, P. G., Vichi, M. and Davini, P. (2013). Role of stratospheric dynamics in the ozone–carbon connection in the Southern Hemisphere. *Climate dynamics*, *41*(11-12), 3039-3054.

Callies, J., Corpaccioli, E., Eisinger, M., Hahne, A. and Lefebvre, A. (2000). GOME-2-Metop's second-generation sensor for operational ozone monitoring. *ESA bulletin*, *102*, 28-36.

Chagas, J. C., Newnham, D. A., Smith, K. M. and Shine, K. P. (2001). Effects of improvements in near-infrared water vapour line intensities on short-wave atmospheric absorption. *Geophysical research letters*, *28*(12), 2401-2404.

Chance, K. V., Burrows, J. P., Perner, D. and Schneider, W. (1997). Satellite measurements of atmospheric ozone profiles, including tropospheric ozone, from ultraviolet/visible measurements in the nadir geometry: a potential method to retrieve tropospheric ozone. *Journal of Quantitative Spectroscopy and Radiative Transfer*, *57*(4), 467-476.

Chance, K. and Kurucz, R. L. (2010). An improved high-resolution solar reference spectrum for earth's atmosphere measurements in the ultraviolet, visible, and near infrared. *Journal of quantitative spectroscopy and radiative transfer*, *111*(9), 1289-1295.

Chandra, S., Ziemke, J. R., Min, W. and Read, W. G. (1998). Effects of 1997–1998 El Nino on tropospheric ozone and water vapor. *Geophysical Research Letters*, *25*(20), 3867-3870.

Chandra, S., Ziemke, J. R., Duncan, B. N., Diehl, T. L., Livesey, N. J. and Froidevaux, L. (2009). Effects of the 2006 El Niño on tropospheric ozone and carbon monoxide: Implications for dynamics and biomass burning. *Atmospheric Chemistry and Physics*, *9*(13), 4239-4249.

Chapman, S. (1930). A theory of upper atmospheric ozone. Mem. Roy. Meteor. Soc.. 3. 103–125.

Charlton, A. J., Polvani, L. M., Perlwitz, J., Sassi, F., Manzini, E., Shibata, K. et al. (2007). A new look at stratospheric sudden warmings. Part II: Evaluation of numerical model simulations. *J. Climate*, ***20***, 470-488.

Charlton-Perez, A. J., Baldwin, M. P., Birner, T., Black, R. X., Butler, A. H., Calvo, N. et al. (2013). On the lack of stratospheric dynamical variability in low-top versions of the CMIP5 models. *Journal of Geophysical Research: Atmospheres*, *118*(6), 2494-2505.

Charney, J. G. and Eliassen, A. (1949). A Numerical Method for Predicting the Perturbations of the Middle Latitude Westerlies, Tellus, 1, 38–54, https://doi.org/10.3402/tellusa.v1i2.8500.

Charney, J. G. and Drazin, P. G. (1961). Propagation of planetary scale waves from the lower atmosphere to the upper atmosphere. *J Geophys Res*, *66*, 83-109.

Checa-Garcia, R., Hegglin, M. I., Kinnison, D., Plummer, D. A. and Shine, K. P. (2018). Historical tropospheric and stratospheric ozone radiative forcing using the CMIP6 database. *Geophysical Research Letters*, *45*(7), 3264-3273.

Chipperfield, M. P., Gray, L. J., Kinnersley, J. S. and Zawodny, J. (1994). A two-dimensional model study of the QBO signal in SAGE II NO2 and O3. *Geophysical research letters*, *21*(7), 589-592.

Chipperfield, M. P. (2003). A three-dimensional model study of long-term mid-high latitude lower stratosphere ozone changes.

Christophe, Y., Bennouna, Y., Schulz, M., Eskes, H. J., Basart, S., Benedictow, A. M. et al. (2019). Validation report of the CAMS global Reanalysis of aerosols and reactive gases, years 2003-2018.

Clerbaux, C., Boynard, A., Clarisse, L., George, M., Hadji-Lazaro, J., Herbin, H. et al. (2009). Monitoring of atmospheric composition using the thermal infrared IASI/MetOp sounder.

Cohen, J., Screen, J. A., Furtado, J. C., Barlow, M., Whittleston, D., Coumou, D. and Jones, J. (2014). Recent Arctic amplification and extreme mid-latitude weather. *Nature geoscience*, *7*(9), 627-637.

Colette, A. and Ancellet, G. (2005). Impact of vertical transport processes on the tropospheric ozone layering above Europe: Part II: climatological analysis of the past 30 years, Atmos. Environ, 39, 5423– 5435, https://doi.org/10.1016/j.atmosenv.2005.06.015.

Collimore, C. C., Martin, D. W., Hitchman, M. H., Huesmann, A. and Waliser, D. E. (2003). On the relationship between the QBO and tropical deep convection. *Journal of climate*, *16*(15), 2552-2568.

Collins, W. J., Lamarque, J. F., Schulz, M., Boucher, O., Eyring, V., Hegglin, M. I. et al. (2017). AerChemMIP: quantifying the effects of chemistry and aerosols in CMIP6. *Geoscientific Model Development*, *10*(2), 585-607.

Cooper, O. R., Parrish, D. D., Stohl, A., Trainer, M., Nédélec, P., Thouret, V. et al. (2010). Increasing springtime ozone mixing ratios in the free troposphere over western North America. *Nature*, *463*(7279), 344–348. https://doi.org/10.1038/nature08708

Cooper, O. R., Parrish, D. D., Ziemke, J., Balashov, N. V., Cupeiro, M., Galbally, I. E. et al. (2014). Global distribution and trends of tropospheric ozone: An observation-based review. *Elementa*. https://doi.org/10.12952/journal.elementa.000029

Cooper, O. R., Langford, A. O., Parrish, D. D. & Fahey, D. W. (2015). Challenges of a lowered US ozone standard. *Science*, ***348***, 1096-1097.

Coy, L., Eckermann, S. and Hoppel, K. (2009). Planetary wave breaking and tropospheric forcing as seen in the stratospheric sudden warming of 2006. *Journal of the atmospheric sciences*, *66*(2), 495-507.

Creilson, J. K., Fishman, J. and Wozniak, A. E. (2003). Intercontinental transport of tropospheric ozone a study of its seasonal variability across the North Atlantic utilizing tropospheric ozone residuals and its relationship to the North Atlantic Oscillation. *Atmos. Chem. Phys.* ***3****,* 2053–2066 .

Creilson, J. K., Fishman, J. and Wozniak, A. E. (2005). Arctic Oscillation–induced variability in satellite-derived tropospheric ozone. *Geophys. Res. Lett*. ***32,*** L1482.

Cristofanelli, P., Bonasoni, P., Collins, W., Feichter, J., Forster, C., James, P. et al. (2003). Stratosphere-to-troposphere transport: A model and method evaluation. *Journal of Geophysical Research: Atmospheres*, *108*(D12).

Cristofanelli, P., Bracci, A., Sprenger, M., Marinoni, A., Bonaf'e, U., Calzolari, F. et al. (2010). Tropospheric ozone variations at the Nepal Climate Observatory- Pyramid (Himalayas, 5079ma.s.l.) and influence of deep stratospheric intrusion events, Atmos. Chem. Phys., 10, 6537–6549, https://doi.org/10.5194/acp-10-6537-2010.

Crutzen, P. J. (1988). Tropospheric ozone: An overview. *Tropospheric ozone*, 3-32.

Crutzen, P. J., Lawrence, M. G. and Pöschl, U. (1999). On the background photochemistry of tropospheric ozone. *Tellus B: Chemical and Physical Meteorology*, *51*(1), 123-146.

Cuesta, J., Eremenko, M., Liu, X., Dufour, G., Cai, Z., Höpfner, M. et al. (2013). Satellite observation of lowermost tropospheric ozone by multispectral synergism of IASI thermal infrared and GOME-2 ultraviolet measurements over Europe. *Atmospheric Chemistry and Physics*, *13*(19), 9675.

Dafka, S., Akritidis, D., Zanis, P., Pozzer, A., Xoplaki, E., Luterbacher, J. et al. (2020). On the link between the Etesian winds, tropopause folds and tropospheric ozone over the Eastern Mediterranean during summer. *Atmospheric Research*, *248*, 105161.

Danielsen, E. F. (1968). Stratospheric-tropospheric exchange based on radioactivity, ozone and potential vorticity. *Journal of the Atmospheric Sciences*, *25*(3), 502-518.

Danielsen, E. F. (1980). Stratospheric source for unexpectedly large values of ozone measured over the Pacific Ocean during Gametag, August 1977. *Journal of Geophysical Research: Oceans*, *85*(C1), 401-412.

Das, S. S., Ratnam, M. V., Uma, K. N., Subrahmanyam, K. V., Girach, I. A., Patra, A. K. and Sijikumar, S. (2016). Influence of tropical cyclones on tropospheric ozone: possible implications. *Atmospheric Chemistry & Physics*, *16*(8).

Daumont, D., Brion, J., Charbonnier, J. and Malicet, J. (1992). Ozone UV spectroscopy I: Absorption cross-sections at room temperature. *Journal of Atmospheric Chemistry*, *15*(2), 145-155.

Davis, S. M., Hegglin, M. I., Fujiwara, M., Dragani, R., Harada, Y., Kobayashi, C. et al. (2017). Assessment of upper tropospheric and stratospheric water vapor and ozone in reanalyses as part of S-RIP. *Atmospheric Chemistry and Physics*, *17*(20), 12743-12778.

Deng, Y., Park, T. W. and Cai, M. (2013). Radiative and dynamical forcing of the surface and atmospheric temperature anomalies associated with the northern annular mode. *J. Climate* ***26***, 5124-5138.

Derwent, R. G., Manning, A. J., Simmonds, P. G., Spain, T. G. and O'Doherty, S. (2013). Analysis and interpretation of 25 years of ozone observations at the Mace Head Atmospheric Research Station on the Atlantic Ocean coast of Ireland from 1987 to 2012. *Atmospheric Environment*, *80*, 361-368.

DeWeaver, E. and Nigam, S. (2002). Linearity in ENSO's atmospheric response. *Journal of climate*, *15*(17), 2446-2461.

Diallo, M., Legras, B. and Chédin, A. (2012). Age of stratospheric air in the ERA-Interim.

Diallo, M., Riese, M., Birner, T., Konopka, P., Muller, R., Hegglin, M. I. et al. (2018). Response of stratospheric water vapor and ozone to the unusual timing of El Niño and the QBO disruption in 2015–2016. *Atmospheric Chemistry and Physics*, *18*(17), 13055-13073.

Dibb, J. E., Meeker, L. D., Finkel, R. C., Southon, J. R., Caffee, M. W., and Barrie, L. A.: Estimation of stratospheric input to the Arctic troposphere: 7Be and 10Be in aerosols at Alert, Canada, J. Geophys. Res., 99, 12855–12864, https://doi.org/10.1029/94JD00742, 1994.

Ding, A. J., Wang, T., Thouret, V., Cammas, J. P. and Nédélec, P. (2008). Tropospheric ozone climatology over Beijing: analysis of aircraft data from the MOZAIC program. *Atmospheric Chemistry and Physics*, *8*(1), 1-13.

Dhomse, S. S., Kinnison, D., Chipperfield, M. P., Salawitch, R. J., Cionni, I., Hegglin, M. I. et al. (2018). Estimates of ozone return dates from Chemistry-Climate Model Initiative simulations. *Atmospheric Chemistry and Physics*, *18*(11), 8409-8438.

Dobson G. M. B. (1956). Origin and distribution of the polyatomic molecules in the atmosphere. *Proceedings of the Royal Society of London. Series A. Mathematical and Physical Sciences*, *236*(1205), 187-193.

Dobson, G. M. B. (1963). Exploring the Atmosphere. Clarendon Press, 228 pp.

Doherty, R. M., Stevenson, D. S., Johnson, C. E., Collins, W. J. and Sanderson, M. G. (2006). Tropospheric ozone and El Niño–Southern Oscillation: Influence of atmospheric dynamics, biomass burning emissions, and future climate change. *Journal of Geophysical Research: Atmospheres*, *111*(D19).

Domeisen, D. I. V., Sun, L. and Chen, G. (2013). The role of synoptic eddies in the tropospheric response to stratospheric variability. *Geophysical Research Letters*, *40*(18), 4933–4937. https://doi.org/10.1002/grl.50943

Duncan, B. N. and Bey, I. A modeling study of the export pathways of pollution from Europe: Seasonal and interannual variations (1987–1997). *J. Geophys. Res-Atmos.* ***109***, D08301 (2004).

Dunkerton, T. (1978). On the mean meridional mass motions of the stratosphere and mesosphere. *Journal of the Atmospheric Sciences*, *35*(12), 2325-2333.

Ebel, A., Hass, H., Jakobs, H. J., Laube, M., Memmesheimer, M., Oberreuter, A. et al. (1991). Simulation of ozone intrusion caused by a tropopause fold and cut-off low. *Atmospheric Environment. Part A. General Topics*, *25*(10), 2131-2144.

Ebojie, F., Burrows, J. P., Gebhardt, C., Ladstätter-Weißenmayer, A., Von Savigny, C., Rozanov, A. et al. (2016). Global tropospheric ozone variations from 2003 to 2011 as seen by SCIAMACHY. *Atmospheric Chemistry and Physics*, *16*(2), 417.

Eichinger, R., Dietmüller, S., Garny, H., Šácha, P., Birner, T., Bönisch, H. et al. (2019). The influence of mixing on the stratospheric age of air changes in the 21st century, Atmos. Chem. Phys., 19, 921–940, https://doi.org/10.5194/acp-19-921-2019.

Elbern, H., Hendricks, J. and Ebel, A. (1998). A climatology of tropopause folds by global analyses. *Theoretical and Applied Climatology*, *59*(3-4), 181-200.

Emmons, L. K., Hauglustaine, D. A., Müller, J. F., Carroll, M. A., Brasseur, G. P., Brunner, D. et al. (2000). Data composites of airborne observations of tropospheric ozone and its precursors. *Journal of Geophysical Research: Atmospheres*, *105*(D16), 20497-20538.

Engel, A., Bönisch, H., Brunner, D., Fischer, H., Franke, H., Günther, G. et al. (2006). Highly resolved observations of trace gases in the lowermost stratosphere and upper troposphere from the Spurt project: an overview. *Atmospheric chemistry and physics*, *6*(2), 283-301.

Engel, A., Möbius, T., Bönisch, H., Schmidt, U., Heinz, R., Levin, I. et al. (2009). Age of stratospheric air unchanged within uncertainties over the past 30 years. *Nature Geoscience*, *2*(1), 28-31.

Ermolli, I., Matthes, K., de Wit, T. D., Krivova, N. A., Tourpali, K., Weber, M. et al. (2013). Recent variability of the solar spectral irradiance and its impact on climate modelling. *arXiv preprint arXiv:1303.5577*.

Eskes, H., Huijnen, V., Arola, A., Benedictow, A., Blechschmidt, A. M., Botek, E. and Engelen, R. (2015). Validation of reactive gases and aerosols in the MACC global analysis and forecast system. *Geoscientific model development*, *8*, 3523-3543.

Eskes, H. J., Clark, H., Schulz, M., Christophe, Y., Ramonet, M., Basart, S. et al. (2018). Validation report for the CAMS global reanalyses of aerosols and reactive trace gases, year 2003.

European Environment Agency (EEA) (2018). Air quality in Europe – 2018 report. Available at https://www.eea.europa.eu/publications/air-quality-in-europe-2018/download.

European Space Agency (ESA) (2020). *UV nadir viewing galleries: Overview.* Retrieved from: https://earth.esa.int/web/sppa/recover.

Eyring, V., Harris, N. R. P., Rex, M., Shepherd, T. G., Fahey, D. W., Amanatidis, G. T. et. al. (2005). A strategy for process-oriented validation of coupled chemistry–climate models. *Bulletin of the American Meteorological Society*, *86*(8), 1117-1134.

Eyring, V., Butchart, N., Waugh, D. W., Akiyoshi, H., Austin, J., Bekki, S. et al. (2006). Assessment of coupled chemistry-climate models: Evaluation of dynamics, transport and ozone. *J. Geophys. Res*, *111*, D22308.

Eyring, V., Lamarque, J-F., Hess, P., Arfeuille, F., Bowman, K., Chipperfield, M. P., Duncan, B. et al. (2013). Overview of IGAC/SPARC Chemistry-Climate Model Initiative (CCMI) community simulations in support of upcoming ozone and climate assessments, SPARC Newsletter, 40 (January), 48–66, available at: http://oceanrep.geomar.de/ 20227/ (last access: 1 March 2019).

Fabian, P. and Pruchniewicz, P. G. (1977). Meridional distribution of ozone in the troposphere and its seasonal variations. *Journal of Geophysical Research*, *82*(15), 2063-2073.

Fadnavis, S. and Beig, G. (2009). Quasi-biennial oscillation in ozone and temperature over tropics. *Journal of atmospheric and solar-terrestrial physics*, *71*(2), 257-263.

Fahey, D. W., Kelly, K. K., Kawa, S. R., Tuck, A. F., Loewenstein, M., Chan, K. R. et al. (1990). Observations of denitrification and dehydration in the winter polar stratospheres. *Nature*, *344*(6264), 321-324.

Fahey, D. W., Gao, R. S., Carslaw, K. S., Kettleborough, J., Popp, P. J., Northway, M. J. et al. (2001). The detection of large HNO3-containing particles in the winter Arctic stratosphere. *Science*, *291*(5506), 1026-1031.

Farman, J. C., Gardiner, B. G. and Shanklin, J. D. (1985). Large losses of total ozone in Antarctica reveal seasonal ClOx/NOx interaction. *Nature*, *315*(6016), 207-210.

Farmer, C. B., Toon, G. C., Schaper, P. W., Blavier, J. F. and Lowes, L. L. (1987). Stratospheric trace gases in the spring 1986 Antarctic atmosphere. *Nature*, *329*(6135), 126-130.

Feister, U. and Warmbt, W. (1987). Long-term measurements of surface ozone in the German Democratic Republic. *Journal of Atmospheric Chemistry*, *5*(1), 1-21.

Fels, S. B., Mahlman, J. D., Schwarzkopf, M. D. and Sinclair, R. W. (1980). Stratospheric sensitivity to perturbations in ozone and carbon dioxide: Radiative and dynamical response. *Journal of the Atmospheric Sciences*, *37*(10), 2265-2297.

Fioletov, V. E. and Shepherd, T. G. (2003). Seasonal persistence of midlatitude total ozone anomalies. *Geophysical Research Letters*, *30*(7).

Fiore, A. M., Jacob, D. J., Field, B. D., Streets, D. G., Fernandes, S. D., and Jang, C.: Linking ozone pollution and climate change: The case for controlling methane, Geophys. Res. Lett., 29, 1919, https://doi.org/10.1029/2002GL015601, 2002a.

Fiore, A. M., Jacob, D. J., Bey, I., Yantosca, R. M., Field, B. D., Fusco, A. C. and Wilkinson, J. G. (2002b). Background ozone over the United States in summer: Origin, trend, and contribution to pollution episodes. *Journal of Geophysical Research Atmospheres*, *107*(15). https://doi.org/10.1029/2001JD000982.

Fishman, J., Solomon, S. and Crutzen, P. J. (1979). Observational and theoretical evidence in support of a significant in-situ photochemical source of tropospheric ozone. *Tellus*, *31*(5), 432-446.

Fishman, J. and Larsen, J. C. (1987). Distribution of total ozone and stratospheric ozone in the tropics: Implications for the distribution of tropospheric ozone. *Journal of Geophysical Research: Atmospheres*, *92*(D6), 6627-6634.

Fishman, J., Watson, C. E., Larsen, J. C. and Logan, J. A. (1990). Distribution of tropospheric ozone determined from satellite data. *Journal of Geophysical Research*. https://doi.org/10.1029/JD095iD04p03599.

Flury, T., Wu, D. L. and Read, W. G. (2013). Variability in the speed of the Brewer–Dobson circulation as observed by Aura/MLS. *Atmospheric Chemistry and Physics*, *13*(9), 4563-4575.

Foret, G., Eremenko, M., Cuesta, J., Sellitto, P., Barré, J., Gaubert, B. et al. (2014). Ozone pollution: What can we see from space? A case study, J. Geophys. Res.-Atmos., 119, 8476–8499, https://doi.org/10.1002/2013JD021340.

Forster P. M. de F. and Shine K.P. (1997). Radiative forcing and temperature trends from stratospheric ozone changes. *J. Geophys. Res-Atmos.*, ***102***, 10841-10855.

Forster P. M. de F., Freckleton R. S. and Shine K.P (1997). On the concept of radiative forcing. *Clim. Dynam.* ***13***, 547-560.

Forster, P. et al., 2007: Changes in Atmospheric Constituents and in Radiative Forcing. In: Climate Change 2007: The Physical Science Basis. Contribution of Working Group I to the Fourth Assessment Report of the Intergovernmental Panel on Climate Change [Solomon, S., D. Qin, M. Manning, Z. Chen, M. Marquis, K. B. Averyt, M. Tignor and H. L. Miller (eds.)] Cambridge University Press, Cambridge, United Kingdom and New York, NY, USA, 129-234.

Frey, W., Schofield, R., Hoor, P., Kunkel, D., Ravegnani, F., Ulanovsky, A. et al. (2015). The impact of overshooting deep convection on local transport and mixing in the tropical upper troposphere/lower stratosphere (UTLS). *Atmospheric Chemistry and Physics*, *15*(11), 6467-6486.

Folkins, I., Loewenstein, M., Podolske, J., Oltmans, S. J. and Proffitt, M. (1999). A barrier to vertical mixing at 14 km in the tropics: Evidence from ozonesondes and aircraft measurements. *Journal of Geophysical Research: Atmospheres*, *104*(D18), 22095-22102.

Fröhlich, C. (2006). Solar irradiance variability since 1978. In *Solar Variability and Planetary Climates* (pp. 53-65). Springer, New York, NY.

Fu, D., Worden, J. R., Liu, X., Kulawik, S. S., Bowman, K. W. and Natraj, V. (2013). Characterization of ozone profiles derived from Aura TES and OMI radiances. *Atmospheric Chemistry and Physics*, *13*(6), 3445-3462.

Fueglistaler, S., Dessler, A. E., Dunkerton, T. J., Folkins, I., Fu, Q. and Mote, P. W. (2009). Tropical tropopause layer. *Reviews of Geophysics*, *47*(1).

Fujiwara, M., Kita, K., Kawakami, S., Ogawa, T., Komala, N., Saraspriya, S. and Suripto, A. (1999). Tropospheric ozone enhancements during the Indonesian forest fire events in 1994 and in 1997 as revealed by ground-based observations. *Geophysical Research Letters*, *26*(16), 2417-2420.

Fusco, A. C. and Salby, M. L. (1999). Interannual variations of total ozone and their relationship to variations of planetary wave activity. *Journal of Climate*, *12*(6), 1619-1629.

Gao, X. H. and Stanford, J. L. (1990). Low-frequency oscillations in total ozone measurements. *Journal of Geophysical Research: Atmospheres*, *95*(D9), 13797-13806.

Garcia, R. R., Stordal, F., Solomon, S. and Kiehl, J. T. (1992). A new numerical model of the middle atmosphere: 1. Dynamics and transport of tropospheric source gases. *Journal of Geophysical Research: Atmospheres*, *97*(D12), 12967-12991.

García-Herrera, R., Calvo, N., Garcia, R. R. and Giorgetta, M. A. (2006). Propagation of ENSO temperature signals into the middle atmosphere: A comparison of two general circulation models and ERA-40 reanalysis data. *Journal of Geophysical Research: Atmospheres*, *111*(D6).

Garcia, R. R. and Randel, W. J. (2008). Acceleration of the Brewer–Dobson circulation due to increases in greenhouse gases. *Journal of the Atmospheric Sciences*, *65*(8), 2731-2739.

Garcia, R. R., Smith, A. K., Kinnison, D. E., Cámara, Á. D. L. and Murphy, D. J. (2017). Modification of the gravity wave parameterization in the Whole Atmosphere Community Climate Model: Motivation and results. *Journal of the Atmospheric Sciences*, *74*(1), 275-291.

Garfinkel, C. I. and Hartmann, D. L. (2007). Effects of the El Niño–Southern Oscillation and the quasi-biennial oscillation on polar temperatures in the stratosphere. *Journal of Geophysical Research: Atmospheres*, *112*(D19).

Garfinkel, C. I., Feldstein, S. B., Waugh, D. W., Yoo, C. and Lee, S. (2012). Observed connection between stratospheric sudden warmings and the Madden-Julian Oscillation. *Geophysical Research Letters*, *39*(18).

Gaudel, A., Cooper, O. R., Ancellet, G., Barret, B., Boynard, A., Burrows, J. P. et al. (2018). Tropospheric Ozone Assessment Report: Present-day distribution and trends of tropospheric ozone relevant to climate and global atmospheric chemistry model evaluation, Elementa, 6, 1–58, https://doi.org/10.1525/elementa.291.

Gerber, E. P., Butler, A., Calvo, N., Charlton-Perez, A., Giorgetta, M., Manzini, E. et al. (2012). Assessing and understanding the impact of stratospheric dynamics and variability on the Earth system. *Bulletin of the American Meteorological Society*, *93*(6), 845-859.

Gettelman, A., Hegglin, M. I., Son, S. W., Kim, J., Fujiwara, M., Birner, T. et al. (2010). Multimodel assessment of the upper troposphere and lower stratosphere: Tropics and global trends. *Journal of Geophysical Research: Atmospheres*, *115*(D3).

Gettelman, A., Pan, L. L., Randel, W. J., Hoor, P., Birner, T. and Hegglin, M. I. (2011). The Extratropical Upper Troposphere and Lower Stratosphere. *Reviews of Geophysics*, *49*(3), 1–31. https://doi.org/10.1029/2011RG000355.1.INTRODUCTION

Gilford, D. M., Solomon, S. and Portmann, R. W. (2016). Radiative impacts of the 2011 abrupt drops in water vapor and ozone in the tropical tropopause layer. *Journal of Climate*, *29*(2), 595–612. https://doi.org/10.1175/JCLI-D-15-0167.1

Gilge, S., Plass-Duelmer, C., Fricke, W., Kaiser, A., Ries, L., Buchmann, B. and Steinbacher, M. (2010). Ozone, carbon monoxide and nitrogen oxides time series at four alpine GAW mountain stations in central Europe. *Atmospheric Chemistry and Physics*, *10*(24), 12295-12316.

Gille, J. C., Bailey, P. L., Russell, J. M. and Russell, J. M. (1980). Temperature and composition measurements from the LRIR and LIMS experiments on Nimbus 6 and 7. *Philosophical Transactions of the Royal Society of London. Series A, Mathematical and Physical Sciences*, *296*(1418), 205-218.

Glanville, A. A. and Birner, T. (2017). Role of vertical and horizontal mixing in the tape recorder signal near the tropical tropopause. *Atmospheric Chemistry & Physics*, *17*(6).

Gómez-Escolar, M., Calvo, N., Barriopedro, D. and Fueglistaler, S. (2014). Tropical response to stratospheric sudden warmings and its modulation by the QBO. *Journal of*

Geophysical Research: Atmospheres, *119*(12), 7382-7395.

Gordon, I. E., Rothman, L. S., Hill, C., Kochanov, R. V., Tan, Y., Bernath, P. F. et al. (2017). The HITRAN2016 molecular spectroscopic database. *Journal of Quantitative Spectroscopy and Radiative Transfer*, *203*, 3-69.

Götz, F. W. P., A. R. Meetham, and G. M. B. Dobson (1934). The vertical distribution of ozone in the atmosphere. Proc. Phys. Soc. London, A145, 416, https://doi.org/10.1098/rspa.1934.0109.

Grainger, J. F. and Ring, J. (1962). Anomalous Fraunhofer line profiles. *Nature*, *193*(4817), 762-762.

Granier, C., Bessagnet, B., Bond, T., D'Angiola, A., van Der Gon, H. D., Frost, G. J. et al. (2011). Evolution of anthropogenic and biomass burning emissions of air pollutants at global and regional scales during the 1980–2010 period. *Climatic Change*, *109*(1-2), 163.

Grant, W. B., Browell, E. V., Fishman, J., Brackett, V. G., Veiga, R. E., Nganga, D. and Long, C. S. (1994). Aerosol-associated changes in tropical stratospheric ozone following the eruption of Mount Pinatubo. *Journal of Geophysical Research: Atmospheres*, *99*(D4), 8197-8211.

Gray, L. J. and Pyle, J. A. (1989). A two-dimensional model of the quasi-biennial oscillation of ozone. *Journal of the atmospheric sciences*, *46*(2), 203-220.

Gray, L. J., Beer, J., Geller, M., Haigh, J. D., Lockwood, M., Matthes, K. et al. (2010). Solar influences on climate. *Reviews of Geophysics*, *48*(4).

Gray, L. J., Scaife, A. A., Mitchell, D. M., Osprey, S., Ineson, S., Hardiman, S. et al. (2013). A lagged response to the 11 year solar cycle in observed winter Atlantic/European weather patterns. *Journal of Geophysical Research: Atmospheres*, *118*(24), 13-405.

Gray, L. J., Woollings, T. J., Andrews, M. and Knight, J. (2016). Eleven-year solar cycle signal in the NAO and Atlantic/European blocking. *Quarterly Journal of the Royal Meteorological Society*, *142*(698), 1890-1903.

Greenslade, J. W., Alexander, S. P., Schofield, R., Fisher, J. A., and Klekociuk, A. K. (2017). Stratospheric ozone intrusion events and their impacts on tropospheric ozone in the Southern Hemisphere, Atmos. Chem. Phys., 17, 10269–10290, https://doi.org/10.5194/acp-17-10269-2017.

Guenther, A., Hewitt, C. N., Erickson, D., Fall, R., Geron, C., Graedel, T. et al. (1995). A global model of natural volatile organic compound emissions, J. Geophys. Res., 100, 8873–8892, https://doi.org/10.1029/94JD02950.

Haase, S. and Matthes, K. (2019). The importance of interactive chemistry for stratosphere–491 troposphere coupling. *Atmos. Chem. Phys.* ***19***, 3417-3432.

Haenel, F. J., Stiller, G. P., von Clarmann, T., Funke, B., Eckert, E., Glatthor, N. et al. (2015). Reassessment of MIPAS age of air trends and variability, Atmos. Chem. Phys., 15, 13161–13176, https://doi.org/10.5194/acp-15-13161-2015.

Haigh, J. D. (1994). The role of stratospheric ozone in modulating the solar radiative forcing of climate. *Nature*, *370*(6490), 544-546.

Hall, T. M. and Plumb, R. A. (1994). Age as a diagnostic of stratospheric transport. *Journal of Geophysical Research: Atmospheres*, *99*(D1), 1059-1070.

Harada, Y., Goto, A., Hasegawa, H., Fujikawa, N., Naoe, H. and Hirooka, T. (2010). A major stratospheric sudden warming event in January 2009. *Journal of the Atmospheric Sciences*, *67*(6), 2052–2069. https://doi.org/10.1175/2009JAS3320.1

Hartley, W. N. (1880). On the probable absorption of solar radiation by atmospheric ozone. *Chem. News*, *42*(268).

Hauchecorne, A., Bertaux, J. L., Dalaudier, F., Keckhut, P., Lemennais, P., Bekki, S. et al. (2010). Response of tropical stratospheric O 3, NO 2 and NO 3 to the equatorial Quasi-Biennial Oscillation and to temperature as seen from GOMOS/ENVISAT.

Hauglustaine, D. A., Brasseur, G. P., Walters, S., Rasch, P. J., Müller, J. F., Emmons, L. K. et al. (1998). MOZART, a global chemical transport model for ozone and related chemical tracers: 2. Model results and evaluation. *Journal of Geophysical Research: Atmospheres*, *103*(D21), 28291-28335.

Haynes, P. H., McIntyre, M. E., Shepherd, T. G., Marks, C. J. and Shine, K. P. (1991). On the "downward control" of extratropical diabatic circulations by eddy-induced mean zonal forces. *Journal of the Atmospheric Sciences*, *48*(4), 651-678.

Haynes, P. and Shuckburgh, E. (2000). Effective diffusivity as a diagnostic of atmospheric transport: 2. Troposphere and lower stratosphere. *Journal of Geophysical Research: Atmospheres*, *105*(D18), 22795-22810.

Heath, D. F., Mateer, C. L. and Krueger, A. J. (1973). The Nimbus-4 Backscatter Ultraviolet (BUV) atmospheric ozone experiment—tow years' operation. *Pure and Applied Geophysics*, *106*(1), 1238-1253.

Hegglin, M. I., Brunner, D., Peter, T., Hoor, P., Fischer, H., Staehelin, J., Krebsbach, M., Schiller, C., Parchatka, U., andWeers, U. (2006). Measurements of NO, NOy, N2O, and O3 during SPURT: implications for transport and chemistry in the lowermost stratosphere, Atmos. Chem. Phys., 6, 1331–1350, https://doi.org/10.5194/acp-6-1331-2006.

Hegglin, M. I. and Shepherd, T. G. (2007). O3-N2O correlations from the Atmospheric Chemistry Experiment: Revisiting a diagnostic of transport and chemistry in the stratosphere. *Journal of Geophysical Research: Atmospheres*, *112*(D19).

Hegglin, M. I. and Shepherd, T. G. (2009). Large climate-induced changes in ultraviolet index and stratosphere-to-troposphere ozone flux, Nat. Geosci., 2, 687–691, https://doi.org/10.1038/NGEO604.

Hegglin, M. I., Gettelman, A., Hoor, P., Krichevsky, R., Manney, G. L., Pan, L. L. et al. (2010). Multimodel assessment of the upper troposphere and lower stratosphere: Extratropics, J. Geophys. Res.-Atmos., 115, D00M09, https://doi.org/10.1029/2009JD013638, 2010.

Hegglin, M. I., Plummer, D. A., Shepherd, T. G., Scinocca, J. F., Anderson, J., Froidevaux, L. et al. (2014). Vertical structure of stratospheric water vapour trends derived from merged satellite data. *Nature Geoscience*, *7*(10), 768–776. https://doi.org/10.1038/NGEO2236

Hegglin, M. I. and Lamarque, J.-F. (2015). The IGAC/SPARC Chemistry-Climate Model Initiative Phase-1 (CCMI-1) model data output, NCAS British Atmospheric Data Centre, 24 September 2018, available at: http://catalogue.ceda.ac.uk/uuid/9cc6b94df0f4469d8066d69b5df879d5 (last access: 24 September 2018).

Helland-Hansen, B. and Nansen, F. (1920). *Temperature Variations in the North Atlantic Ocean and in the Atmosphere: Introductory Studies on the Cause of Climatological Variations (with Forty-eight Plates)* (Vol. 2537). Smithsonian institution.

Hersbach, H., Bell, B., Berrisford, P., Hirahara, S., Horányi, A., Muñoz-Sabater, J. et al. (2020). The ERA5 global reanalysis. *Quarterly Journal of the Royal Meteorological Society*, *146*(730), 1999-2049.

Hess, P.G. and Lamarque, J.F. (2007). Ozone source attribution and its modulation by the Arctic oscillation during the spring months. *J. Geophys. Res-Atmos., **112***.

Hess, P. G. and Zbinden, R. (2013). Stratospheric impact on tropospheric ozone variability and trends: 1990–2009, Atmos. Chem. Phys., 13, 649–674, https://doi.org/10.5194/acp-13-649-2013.

Hess, P., Kinnison, D. and Tang, Q. (2015). Ensemble simulations of the role of the stratosphere in the attribution of northern extratropical tropospheric ozone variability. *Atmospheric Chemistry and Physics (Online)*, *15*(LLNL-JRNL-655965; LLNL-JRNL-653917).

Hitchcock, P., Shepherd, T. G. and Manney, G. L. (2013). Statistical characterization of Arctic polar-night jet oscillation events. *J. Climate*, ***26***, 2096-2116.

Hitchman, M. H. and Huesmann, A. S. (2007). A seasonal climatology of Rossby wave breaking in the 320–2000-K layer. *Journal of the Atmospheric sciences*, *64*(6), 1922-1940.

Hoesly, R. M., Smith, S. J., Feng, L., Klimont, Z., Janssens-Maenhout, G., Pitkanen, T. et al. (2018). Historical (1750–2014) anthropogenic emissions of reactive gases and aerosols from the Community Emissions Data System (CEDS), Geosci. Model Dev., 11, 369–408, https://doi.org/10.5194/gmd-11-369-2018.

Hoinka, K. P. (1997). The tropopause: Discovery, definition and demarcation. Meteor. Z., 6, 281–303, https://doi.org/10.1127/metz/6/1997/281.

Holloway, A. M. and Wayne, R. P. (2010). Atmospheric Chemistry, ISBN: 978-1-84755-807-7.

Holton, J. R. and Tan, H. C. (1980). The influence of the equatorial quasi-biennial oscillation on the global circulation at 50 mb. *Journal of the Atmospheric Sciences*, *37*(10), 2200-2208.

Holton, J. R. and Tan, H. C. (1982). The quasi-biennial oscillation in the Northern Hemisphere lower stratosphere. *Journal of the Meteorological Society of Japan. Ser. II*, *60*(1), 140-148.

Holton, J. R. (1990). On the global exchange of mass between the stratosphere and troposphere. *Journal of the atmospheric sciences*, *47*(3), 392-395.

Holton, J. R., Haynes, P. H., McIntyre, M. E., Douglass, A. R., Rood, R. B. and Pfister, L.

(1995). Stratosphere-troposphere exchange. *Reviews of Geophysics*, *33*(4), 403–439. https://doi.org/10.1029/95RG02097.

Holton, J. R. and Lelieveld, J. (1996). Stratosphere-troposphere exchange and its role in the budget of tropospheric ozone, in: Clouds, chemistry and climate Springer, Berlin, Heidelberg, 173–190.

Hood, L. L. (1997). The solar cycle variation of total ozone: Dynamical forcing in the lower stratosphere. *Journal of Geophysical Research: Atmospheres*, *102*(D1), 1355-1370.

Hoskins, B. J., McIntyre, M. E. and Robertson, A. W. (1985). On the use and significance of isentropic potential vorticity maps. *QJR Meteorol. Soc.*, *111*, 877-946, https://doi.org/10.1002/qj.49711147002.

Hoskins, B. J. (1991). Towards a PV-θ view of the general circulation. *Tellus A: Dynamic Meteorology and Oceanography*, *43*(4), 27-36.

Hossaini, R., Chipperfield, M. P., Feng, W., Breider, T. J., Atlas, E., Montzka, S. A. et al. (2012). The contribution of natural and anthropogenic very short-lived species to stratospheric bromine. *Atmospheric Chemistry and Physics*, *12*(1), 371-380.

Hsu J. and Prather, M. J. (2009). Stratospheric variability and tropospheric ozone. *J. Geophys. Res-Atmos.* ***114***, D06102.

HTAP (Hemispheric Transport of Air Pollution): Hemispheric Transport of Air Pollution 2010 Part A: Ozone And Particulate Matter, Air Pollution Studies No. 17, available at: http://www.htap.org/publications/2010_report/2010_Final_Report/HTAP%202010%20Part%20A%20110407.pdf (last access: 5 March 2019), 2010.

Hu, D., Tian, W., Guan, Z., Guo, Y. and Dhomse, S. (2016). Longitudinal asymmetric trends of tropical cold-point tropopause temperature and their link to strengthened walker circulation. *Journal of Climate*, *29*(21), 7755-7771.

Hudman, R. C., Jacob, D. J., Cooper, O. R., Evans, M. J., Heald, C. L., Park, R. J. et al. (2004). Ozone production in transpacific Asian pollution plumes and implications for ozone air quality in California, J. Geophys. Res.-Atmos., 109, D23S10, https://doi.org/10.1029/2004JD004974.

Huijnen, V., Miyazaki, K., Flemming, J., Inness, A., Sekiya, T. and Schultz, M. G. (2020). An intercomparison of tropospheric ozone reanalysis products from CAMS, CAMS interim, TCR-1, and TCR-2. *Geoscientific Model Development*, *13*(3).

Ineson, S., Scaife, A. A., Knight, J. R., Manners, J. C., Dunstone, N. J., Gray, L. J. and Haigh, J. D. (2011). Solar forcing of winter climate variability in the Northern Hemisphere. *Nature Geoscience*, *4*(11), 753-757.

Inness, A., Ades, M., Agusti-Panareda, A., Barré, J., Benedictow, A., Blechschmidt, A. M. V. et al. (2019). The CAMS reanalysis of atmospheric composition. *Atmospheric Chemistry and Physics*, *19*(6), 3515-3556.

Inness A., Engelen, R. and Flemming, J. (2019). The new CAMS global reanalysis of atmospheric composition. Retrieved from: https://ecmwf.net/en/newsletter/158/meteorology/new-cams-global-reanalysis-atmospheric-composition.

IPCC: Climate Change 2013: The Physical Science Basis. Contribution of Working Group I to the Fifth Assessment Report of the Intergovernmental Panel on Climate Change, edited by: Stocker, T. F., Qin, D., Plattner, G.-K., Tignor, M., Allen, S. K., Boschung, J., Nauels, A., Xia, Y., Bex, V., and Midgley, P. M., Cambridge University Press, Cambridge, United Kingdom and New York, NY, USA, 1535 pp., https://doi.org/10.1017/CBO9781107415324, 2013.

Iwasaki, T., Hamada, H. and Miyazaki, K. (2009). Comparisons of Brewer-Dobson circulations diagnosed from reanalyses. *Journal of the Meteorological Society of Japan. Ser. II*, *87*(6), 997-1006.

Jacob, D. J. (1999). *Introduction to Atmospheric Chemistry.* Princeton University Press. Retrieved from: http://acmg.seas.harvard.edu/people/faculty/djj/book.

Jensen, E. and Pfister, L. (2004). Transport and freeze-drying in the tropical tropopause layer. *Journal of Geophysical Research: Atmospheres*, *109*(D2).

Jensen, A. A., Thompson, A. M. and Schmidlin, F. J. (2012). Classification of Ascension Island and Natal ozonesondes using self-organizing maps. *Journal of Geophysical Research: Atmospheres*, *117*(D4).

Jöckel, P., Tost, H., Pozzer, A., Brühl, C., Buchholz, J., Ganzeveld, L. et al. (2006). The atmospheric chemistry general circulation model ECHAM5/MESSy1: consistent simulation of ozone from the surface to the mesosphere, Atmos. Chem. Phys., 6, 5067–5104, https://doi.org/10.5194/acp-6-5067-2006.

Jöckel, P., Tost, H., Pozzer, A., Kunze, M., Kirner, O., Brenninkmeijer, C. A. M. et al. (2016). Earth System Chemistry integrated Modelling (ESCiMo) with the Modular Earth Submodel System (MESSy) version 2.51, Geosci. Model Dev., 9, 1153–1200, https://doi.org/10.5194/gmd-9-1153-2016.

Joiner, J. and Bhartia, P. K. (1995). The determination of cloud pressures from rotational Raman scattering in satellite backscatter ultraviolet measurements. *Journal of Geophysical Research: Atmospheres*, *100*(D11), 23019-23026.

Jones, R. L. and Pyle, J. A. (1984). Observations of CH4 and N2O by the Nimbus 7 SAMS: A comparison with in situ data and two-dimensional numerical model calculations. *Journal of Geophysical Research: Atmospheres*, *89*(D4), 5263-5279.

Jones, R. L., Pyle, J. A., Harries, J. E., Zavody, A. M., Russell III, J. M. and Gille, J. C. (1986). The water vapour budget of the stratosphere studied using LIMS and SAMS satellite data. *Quarterly Journal of the Royal Meteorological Society*, *112*(474), 1127-1143.

Kalabokas, P., Hjorth, J., Foret, G., Dufour, G., Eremenko, M., Siour, G. et al. (2017). An investigation on the origin of regional springtime ozone episodes in the western Mediterranean. *Atmospheric Chemistry & Physics*, *17*(6).

Kang, W. and Tziperman, E. (2017). More frequent sudden stratospheric warming events due to enhanced MJO forcing expected in a warmer climate. *Journal of Climate*, *30*(21), 8727–8743. https://doi.org/10.1175/JCLI-D-17-0044.1

Kar, J., Deeter, M. N., Fishman, J., Liu, Z., Omar, A., Creilson, J. K. et al. (2010). Wintertime pollution over the Eastern Indo-Gangetic Plains as observed from MOPITT, CALIPSO and tropospheric ozone residual data. *Atmospheric Chemistry and Physics*, *10*(24), 12273.

Karpechko, A. Y., Hitchcock, P., Peters, D. H. and Schneidereit, A. (2017). Predictability of downward propagation of major sudden stratospheric warmings. *Q. J. Royal Meteorol. Soc*, ***143***, 1459-1470.

Kentarchos, A. S. and Roelofs, G. J. (2003). A model study of stratospheric ozone in the troposphere and its contribution to tropospheric OH formation. *Journal of Geophysical Research: Atmospheres*, *108*(D12).

Kerkweg, A., Sander, R., Tost, H., and Jöckel, P. (2006). Technical note: Implementation of prescribed (OFFLEM), calculated (ONLEM), and pseudo-emissions (TNUDGE) of chemical

species in the Modular Earth Submodel System (MESSy), Atmos. Chem. Phys., 6, 3603–3609, https://doi.org/10.5194/acp-6-3603-2006.

Keppens, A., Lambert, J. C., Granville, J., Miles, G., Siddans, R., van Peet, J. C. A. et al. (2014). Round-robin evaluation of nadir ozone profile retrievals: methodology and application to MetOp-A GOME-2. *Atmospheric Measurement Techniques Discussions*, *7*(11).

Kida, H. (1983). General circulation of air parcels and transport characteristics derived from a hemispheric GCM-II: Very long-term motions of air parcels in the troposphere and stratosphere. *Journal of the Meteorological Society of Japan*, *61*(4), 510-523.

Kidston, J., Scaife, A. A., Hardiman, S. C., Mitchell, D. M., Butchart, N., Baldwin, M. P. et al. (2015). Stratospheric influence on tropospheric jet streams, storm tracks and surface weather. *Nature Geoscience*, *8*(6), 433–440. https://doi.org/10.1038/NGEO2424

Kiesewetter, G., Sinnhuber, B. M., Vountas, M., Weber, M. and Burrows, J. P. (2010). A long-term stratospheric ozone data set from assimilation of satellite observations: High-latitude ozone anomalies. *Journal of Geophysical Research Atmospheres*, *115*(10), 1–17. https://doi.org/10.1029/2009JD013362.

Kinnersley, J. S. and Tung, K. K. (1999). Mechanisms for the extratropical QBO in circulation and ozone. *Journal of the atmospheric sciences*, *56*(12), 1942-1962.

Kivi, R., Kyrö, E., Turunen, T., Harris, N. R. P., von der Gathen, P., Rex, M. et al. (2007). Ozonesonde observations in the Arctic during 1989–2003: Ozone variability and trends in the lower stratosphere and free troposphere. *Journal of Geophysical Research: Atmospheres*, *112*(D8).

Klenk, K. F., Bhartia, P. K., Kaveeshwar, V. G., McPeters, R. D., Smith, P. M. et al. (1982). Total ozone determination from the backscattered ultraviolet (BUV) experiment. *Journal of Applied Meteorology*, *21*(11), 1672-1684.

Kolonjari, F., Plummer, D. A., Walker, K. A., Boone, C. D., Elkins, J. W., Hegglin, M. I. et al. (2017). Assessing stratospheric transport in the CMAM30 simulations using ACE-FTS measurements, Atmos. Chem. Phys., 18, 6801–6828, https://doi.org/10.5194/acp-18-6801-2018.

Kolstad, E. W., Breiteig, T. and Scaife, A. A. (2010). The association between stratospheric weak polar vortex events and cold air outbreaks in the Northern Hemisphere. *Q. J. Roy. Meteor*. Soc. ***136***, 886-893.

Komhyr, W. D., Grass, R. D. and Leonard, R. K. (1986). Total ozone decrease at South Pole, Antarctica, 1964-1985. *Geophysical research letters*, *13*(12), 1248-1251.

Konopka, P., Ploeger, F., Tao, M., Birner, T. and Riese, M. (2015). Hemispheric asymmetries and seasonality of mean age of air in the lower stratosphere: Deep versus shallow branch of the Brewer-Dobson circulation. *Journal of Geophysical Research: Atmospheres*, *120*(5), 2053-2066.

Kravitz, B., Caldeira, K., Boucher, O., Robock, A., Rasch, P. J., Alterskjær, K. et al. (2013). Climate model response from the geoengineering model intercomparison project (GeoMIP). *Journal of Geophysical Research: Atmospheres*, *118*(15), 8320-8332.

Krebsbach, M., Schiller, C., Brunner, D., Günther, G., Hegglin, M. I., Mottaghy, D., Riese, M., Spelten, N., and Wernli, H. (2006). Seasonal cycles and variability of O3 and H2O in the UT/LMS during SPURT, Atmos. Chem. Phys., 6, 109–125, https://doi.org/10.5194/acp-6-109-2006.

Kretschmer, M., Cohen, J., Matthias, V., Runge, J. and Coumou, D. (2018a). The different stratospheric influence on cold-extremes in Eurasia and North America. *Npj. Climat.* 406 *Sci.* ***1***, 44.

Kretschmer, M., Coumou, D., Agel, L., Barlow, M., Tziperman, E. and Cohen, J. (2018b). More persistent weak stratospheric polar vortex states linked to cold extremes. *Bull. Am. Meteorol. Soc.* ***99***, 49-60.

Kroon, M., De Haan, J. F., Veefkind, J. P., Froidevaux, L., Wang, R., Kivi, R. and Hakkarainen, J. J. (2011). Validation of operational ozone profiles from the Ozone Monitoring Instrument. *Journal of Geophysical Research: Atmospheres*, *116*(D18).

Kunz, T. and Greatbatch, R. J. (2013). On the northern annular mode surface signal associated with stratospheric variability. *Journal of the atmospheric sciences*, *70*(7), 2103-2118.

Kunze, M., Godolt, M., Langematz, U., Grenfell, J. L., Hamann-Reinus, A., and Rauer, H.: Investigating the early Earth faint young Sun problem with a general circulation model, Planet. Space Sci., 98, 77–92, https://doi.org/10.1016/j.pss.2013.09.011, 2014.

Kodera, K. and Kuroda, Y. (2002). Dynamical response to the solar cycle. *Journal of Geophysical Research: Atmospheres*, *107*(D24), ACL-5.

Kuroda, Y. and Kodera, K. (2004). Role of the Polar-night Jet Oscillation on the formation of the Arctic Oscillation in the Northern Hemisphere winter. *Journal of Geophysical Research: Atmospheres*, *109*(D11).

Kusuma, L., Lubis, S. W. and Setiawan, S. (2019, May). Unprecedented Quasi-Biennial Oscillation (QBO) disruption in 2015-2016: Implications for tropical waves and ozone. In *IOP Conference Series: Earth and Environmental Science* (Vol. 284, No. 1, p. 012016). IOP Publishing.

Lacis, A. A., Wuebbles, D. J. and Logan, J. A. (1990). Radiative forcing of climate by changes in the vertical distribution of ozone. *Journal of Geophysical Research*, *95*(D7), 9971–9981. https://doi.org/10.1029/JD095iD07p09971

Lamarque, J. F., Hess, P. G., and Tie, X. X. (1999). Three-dimensional model study of the influence of stratosphere-troposphere exchange and its distribution on tropospheric chemistry, J. Geophys. Res.-Atmos., 104, 26363–26372, https://doi.org/10.1029/1999JD900762.

Lamarque, J. F. and Hess, P. G. (2003). Local Processes, Encyclopedia of Atmospheric Sciences, 4, 262–268.

Lamarque, J. F. and Hess, P. G. Arctic Oscillation modulation of the Northern Hemisphere spring tropospheric ozone. *Geophys. Res. Lett.,* ***31***, L06127 (2004).

Lamarque, J.-F., Bond, T. C., Eyring, V., Granier, C., Heil, A., Klimont, Z. et al. (2010). Historical (1850–2000) gridded anthropogenic and biomass burning emissions of reactive gases and aerosols: methodology and application, Atmos. Chem. Phys., 10, 7017–7039, https://doi.org/10.5194/acp-10-7017-2010.

Langford, A. O., T. J. O'Leary, C. D. Masters, K. C. Aikin, and M. H. Proffitt (1998), Modulation of middle and upper tropospheric ozone at northern midlatitudes by the El Niño/Southern Oscillation, Geophys. Res. Lett., 25, 2667–2670.

Langford, A. O. (1999). Stratosphere-troposphere exchange at the subtropical jet: Contribution to the tropospheric ozone budget at midlatitudes, Geophys. Res. Lett., 26, 2449–2452, https://doi.org/10.1029/1999GL900556.

Langford, A. O., Alvarez, R. J., Brioude, J., Fine, R., Gustin, M. S., Lin, M. Y. et al. (2017). Entrainment of stratospheric air and Asian pollution by the convective boundary layer in the southwestern US. *J. Geophys. Res-Atmos.*, ***122*****,** 1312-1337.

Langematz, U., Tully, M. (Lead Authors), Calvo, N., Dameris, M., de Laat, A. T. J., Klekociuk, A., Müller, R. and Young, P. (2018). *Polar stratospheric ozone: Past, present, and future, chapter 4 in scientific assessment of ozone depletion: 2018, global ozone research and monitoring project–Report No. 58*. Geneva, Switzerland: World Meteorological Organization.

Laube, J. C., Engel, A., Bönisch, H., Möbius, T., Worton, D. R., Sturges, W. T. et al. (2008). Contribution of very short-lived organic substances to stratospheric chlorine and bromine in the tropics–a case study. *Atmospheric Chemistry and Physics*, *8*(23), 7325-7334.

Law, K. (2010). More ozone over North America. *Nature*, *463*(7279), 307-308.

Lee, S., Shelow, D. M., Thompson, A. M., and Miller, S. K. (2010). QBO and ENSO variability in temperature and ozone from SHADOZ, 1998–2005, J. Geophys. Res., 115, D18105, https://doi.org/10.1029/2009JD013320, 2010.77.

Lefohn, A. S., Shadwick, D. and Oltmans, S. J. (2010). Characterizing changes in surface ozone levels in metropolitan and rural areas in the United States for 1980–2008 and 1994–2008. *Atmospheric Environment*, *44*(39), 5199-5210.

Lefohn, A. S., Wernli, H., Shadwick, D., Limbach, S., Oltmans, S. J. and Shapiro, M. (2011). The importance of stratospheric–tropospheric transport in affecting surface ozone concentrations in the western and northern tier of the United States. *Atmos. Environ.*, ***45***, 4845-4857.

Lelieveld, J. and Dentener, F. J. (2000). What controls tropospheric ozone?, J. Geophys. Res.-Atmos., 105, 3531–3551, https://doi.org/10.1029/1999JD901011.

Lelieveld, J., Hoor, P., Jöckel, P., Pozzer, A., Hadjinicolaou, P., Cammas, J. P. and Beirle, S. (2009). Severe ozone air pollution in the Persian Gulf region. *Atmospheric Chemistry and Physics*. https://doi.org/10.5194/acp-9-1393-2009

Lelieveld, J., Berresheim, H., Borrmann, S., Crutzen, P. J., Dentener, F. J., Fischer, H. et al. (2002). Global air pollution crossroads over the Mediterranean. *Science*, *298*(5594), 794-799.

Lelieveld, Jos, Gromov, S., Pozzer, A. and Taraborrelli, D. (2016). Global tropospheric

hydroxyl distribution, budget and reactivity. *Atmospheric Chemistry and Physics*. https://doi.org/10.5194/acp-16-12477-2016.

Lenton, A., Codron, F., Bopp, L., Metzl, N., Cadule, P., Tagliabue, A. et al. (2009). Stratospheric ozone depletion reduces ocean carbon uptake and enhances ocean acidification. *Geophysical Research Letters*, *36*(12).

Leovy, C. B., Sun, C. R., Hitchman, M. H., Remsberg, E. E., Russell III, J. M., Gordley, L. L. et al. (1985). Transport of ozone in the middle stratosphere: Evidence for planetary wave breaking. *Journal of the atmospheric sciences*, *42*(3), 230-244.

Levelt, P. F., van den Oord, G. H., Dobber, M. R., Malkki, A., Visser, H., de Vries, J. et al. (2006). The ozone monitoring instrument, IEEE T. Geosci. Remote., 44, 1093–1101, https://doi.org/10.1109/TGRS.2006.872333.

Levelt, P. F., Joiner, J., Tamminen, J., Veefkind, J. P., Bhartia, P. K., Stein Zweers, D. C. et al. (2018). The Ozone Monitoring Instrument: overview of 14 years in space, Atmos. Chem. Phys., 18, 5699–5745, https://doi.org/10.5194/acp-18-5699-2018.

Leventidou, E., Weber, M., Eichmann, K. U., Burrows, J. P., Heue, K. P., Thompson, A. M. et al. (2018). Harmonisation and trends of 20-year tropical tropospheric ozone data. *Atmospheric Chemistry and Physics*, *18*(13), 9189-9205.

Li, Q., Jacob, D. J., Bey, I., Palmer, P. I., Duncan, B. N., Field, B. D. et al. (2002). Transatlantic transport of pollution and its effects on surface ozone in Europe and North America. *J. Geophys. Res-Atmos. 107, 4166*.

Li, F., Stolarski, R. S. and Newman, P. A. (2009). Stratospheric ozone in the post-CFC era. *Atmospheric Chemistry and Physics*, *9*(6), 2207-2213.

Li, W., Li, L., Fu, R., Deng, Y., and Wang, H. (2011). Changes to the North Atlantic Subtropical High and Its Role in the Intensification of Summer Rainfall Variability in the Southeastern United States, J. Climate, 24, 1499–1506, https://doi.org/10.1175/2010JCLI3829.1.

Li, W., Li, L., Ting, M., and Liu, Y (2012). Intensification of Northern Hemisphere subtropical highs in a warming climate, Nat. Geosci., 5, 830–834, https://doi.org/10.1038/NGEO1590.

Libby, W. F. (1959). Radioactive fallout particularly from the Russian October series. *Proceedings of the National Academy of Sciences of the United States of America*, *45*(7), 959.

Lin, S. and Rood, R. B. (1996). Multidimensional Flux-Form Semi-Lagrangian Transport Schemes, Mon. Weather Rev., 124, 2046–2070, https://doi.org/10.1175/1520-0493(1996)124<2046:MFFSLT>2.0.CO;2.

Lin, M., Fiore, A. M., Cooper, O. R., Horowitz, L. W., Langford, A. O., Levy II, H. et al. (2012). Springtime high surface ozone events over the western United States: Quantifying the role of stratospheric intrusions, J. Geophys. Res.-Atmos., 117, D00V22, https://doi.org/10.1029/2012JD018151.

Lin, M., Horowitz, L. W., Oltmans, S. J., Fiore, A. M., and Fan, S. (2014). Tropospheric ozone trends at Mauna Loa Observatory tied to decadal climate variability, Nat. Geosci., 7, 136–143, https://doi.org/10.1038/NGEO2066.

Lin, M., Fiore, A. M., Horowitz, L. W., Langford, A. O., Oltmans, S. J., Tarasick, D. et al. (2015). Climate variability modulates western US ozone air quality in spring via deep stratospheric intrusions, Nat. Commun., 6, 7105, https://doi.org/10.1038/ncomms8105.

Lindemann, F. A., and G. Dobson (1923). A theory of meteors and the density and temperature of the outer atmosphere to which it leads. Proc. Roy. Soc. London, 102, 411–437, https://doi.org/10.1098/rspa.1923.0003.

Lindzen, R. S. and Holton, J. R. (1968). A theory of the quasi-biennial oscillation. *Journal of the Atmospheric Sciences*, *25*(6), 1095-1107.

Linvill, D. E., Hooker, W. J. and Olson, B. (1980). Ozone in Michigan's environment 1876–1880. *Monthly Weather Review*, *108*(11), 1883-1891.

Limpasuvan, V., Thompson, D. W. J. and Hartmann, D. L. (2004). The life cycle of the Northern Hemisphere sudden stratospheric warmings. *Journal of Climate*, *17*(13), 2584–2596. https://doi.org/10.1175/1520-0442(2004)017<2584:TLCOTN>2.0.CO;2

Lisac, I. and Grubišić, V. (1991). An analysis of surface ozone data measured at the end of the 19th century in Zagreb, Yugoslavia. *Atmospheric Environment. Part A. General Topics*, *25*(2), 481-486.

Liu, X., Bhartia, P. K., Chance, K., Froidevaux, L., Spurr, R. J. D., and Kurosu, T. P. (2010). Validation of Ozone Monitoring Instrument (OMI) ozone profiles and stratospheric ozone columns with Microwave Limb Sounder (MLS) measurements, Atmos. Chem. Phys., 10, 2539–2549, https://doi.org/10.5194/acp-10-2539-2010, 2010.

Liu, X., Bhartia, P. K., Chance, K., Spurr, R. J. D., and Kurosu, T. P. (2010). Ozone profile retrievals from the Ozone Monitoring Instrument. *Atmospheric Chemistry & Physics*, *10*(5).

Liu, J., Tarasick, D. W., Fioletov, V. E., McLinden, C., Zhao, T., Gong, S. et al. (2013). A global ozone climatology from ozone soundings via trajectory mapping: a stratospheric perspective, Atmos. Chem. Phys., 13, 11441–11464, https://doi.org/10.5194/acp-13-11441-2013.

Liu, J., Rodriguez, J. M., Oman, L. D., Douglass, A. R., Olsen, M. A. and Hu, L. (2020). Stratospheric impact on the Northern Hemisphere winter and spring ozone interannual variability in the troposphere. *Atmospheric Chemistry and Physics*, *20*(11), 6417-6433.

Logan, J. A. (1985). Tropospheric ozone: Seasonal behavior, trends, and anthropogenic influence, J. Geophys. Res., 90, 10463–10482, https://doi.org/10.1029/JD090iD06p10463.

Logan, J. A., Jones, D. B. A., Megretskaia, I. A., Oltmans, S. J., Johnson, B. J., Vömel, H. et al. (2003). Quasibiennial oscillation in tropical ozone as revealed by ozonesonde and satellite data. *Journal of Geophysical Research: Atmospheres*, *108*(D8).

Logan, J. A., Staehelin, J., Megretskaia, I. A., Cammas, J. P., Thouret, V., Claude, H. et al. (2012). Changes in ozone over Europe: Analysis of ozone measurements from sondes, regular aircraft (MOZAIC) and alpine surface sites. *Journal of Geophysical Research: Atmospheres*, *117*(D9).

Lorenz, D. J. and Hartmann, D. L. (2003). Eddy-zonal flow feedback in the Northern Hemisphere winter. *Journal of Climate*, *16*(8), 1212–1227. https://doi.org/10.1175/1520-0442(2003)16<1212:EFFITN>2.0.CO;2.

Loyola, D. G., Koukouli, M. E., Valks, P., Balis, D. S., Hao, N., Van Roozendael, M. and Lambert, J. C. (2011). The GOME-2 total column ozone product: Retrieval algorithm and ground-based validation. *Journal of Geophysical Research: Atmospheres*, *116*(D7).

Lubis, S. W., Matthes, K., Harnik, N., Omrani, N. E. and Wahl, S. (2018). Downward wave coupling between the stratosphere and troposphere under future anthropogenic climate change. *Journal of Climate*, *31*(10), 4135-4155.

Mahieu, E., Chipperfield, M. P., Notholt, J., Reddmann, T., Anderson, J., Bernath, P. F. et al. (2014). Recent Northern Hemisphere stratospheric HCl increase due to atmospheric

circulation changes. *Nature*, *515*(7525), 104-107.

Manatsa, D. and Mukwada, G. (2017). A connection from stratospheric ozone to El Niño-Southern Oscillation. *Scientific reports*, *7*(1), 1-10.

Malicet, J., Daumont, D., Charbonnier, J., Parisse, C., Chakir, A.. and Brion, J. (1995). Ozone UV spectroscopy. II. Absorption cross-sections and temperature dependence. *Journal of atmospheric chemistry*, *21*(3), 263-273.

Malley, C. S., Henze, D. K., Kuylenstierna, J. C., Vallack, H. W., Davila, Y., Anenberg, S. C. et al. Ashmore, M. R. (2017). Updated global estimates of respiratory mortality in adults≥ 30 years of age attributable to long-term ozone exposure. *Environmental health perspectives*, *125*(8), 087021.

Manney, G. L. et al. (2009a). Aura Microwave Limb Sounder observations of dynamics and transport during the record-breaking 2009 Arctic stratospheric major warming. *Geophys. Res. Lett.* ***36***, L12815.

Manney, G. L. et al. (2009b). Satellite observations and modeling of transport in the upper troposphere through the lower mesosphere during the 2006 major stratospheric sudden warming. *Atmos. Chem. Phys.* **9**, 4775–4795.

Manney, G. L., Santee, M. L., Rex, M., Livesey, N. J., Pitts, M. C., Veefkind, P. et al. (2011). Unprecedented Arctic ozone loss in 2011. *Nature*, *478*(7370), 469-475.

Manney, G. L. and Hegglin, M. I. (2018). Seasonal and Regional Variations of Long-Term Changes in Upper-Tropospheric Jets from Reanalyses, J. Climate, 31, 423–448, https://doi.org/10.1175/JCLI-D- 17-0303.1.

Marenco, A., Gouget, H., Nédélec, P., Pagés, J. P. and Karcher, F. (1994). Evidence of a long-term increase in tropospheric ozone from Pic du Midi data series: Consequences: Positive radiative forcing. *Journal of Geophysical Research: Atmospheres*, *99*(D8), 16617-16632.

Martius, O., Polvani, L. M. and Davies, H. C. (2009). Blocking precursors to stratospheric sudden warming events. *Geophysical Research Letters*, *36*(14).

Massart, S., Agusti-Panareda, A., Aben, I., Butz, A., Chevallier, F., Crevosier, C. et al. (2014). Assimilation of atmospheric methane products into the MACC-II system: from SCIAMACHY to TANSO and IASI.

Matsuno, T. (1971). A Dynamical Model of the Stratospheric Sudden Warming. *Journal of*

the Atmospheric Sciences. https://doi.org/10.1175/1520-0469(1971)028<1479:admots>2.0.co;2

Matthes, K., Kuroda, Y., Kodera, K. and Langematz, U. (2006). Transfer of the solar signal from the stratosphere to the troposphere: Northern winter. *Journal of Geophysical Research: Atmospheres*, *111*(D6).

Mauzerall, D. L., Logan, J. A., Jacob, D. J., Anderson, B. E., Blake, D. R., Bradshaw, J. D., Heikes, B., Sachse, G. W., Singh, H., and Talbot, B. (1998). Photochemistry in biomass burning plumes and implications for tropospheric ozone over the tropical South Atlantic, J. Geophys. Res.-Atmos., 103, 8401–8423, https://doi.org/10.1029/97JD02612.

Maycock, A., Matthes, K., Tegtmeier, S., Thiéblemont, R. and Hood, L. (2016). The representation of solar cycle signals in stratospheric ozone–Part 1: A comparison of recently updated satellite observations. *Atmospheric Chemistry and Physics*, *16*, 10021-10043.

McElroy, M. B., Salawitch, R. J., Wofsy, S. C. and Logan, J. A. (1986). Reductions of Antarctic ozone due to synergistic interactions of chlorine and bromine. *Nature*, *321*(6072), 759-762.

McGrath-Spangler, E. L., Molod, A., Ott, L. E. and Pawson, S (2015). Impact of planetary boundary layer turbulence on model climate and tracer transport. *Atmos. Chem. Phys.*, ***15***, 7269–7286.

McIntyre, M. E. (1982). How well do we understand the dynamics of stratospheric warmings?. *Journal of the Meteorological Society of Japan. Ser. II*, *60*(1), 37-65.

McLandress, C. and Shepherd, T. G. (2009). Simulated anthropogenic changes in the Brewer–Dobson circulation, including its extension to high latitudes. *Journal of Climate*, *22*(6), 1516-1540.

McLandress, C., Jonsson, A. I., Plummer, D. A., Reader, M. C., Scinocca, J. F. and Shepherd, T. G. (2010). Separating the dynamical effects of climate change and ozone depletion. Part I: Southern Hemisphere stratosphere. *Journal of Climate*, *23*(18), 5002-5020.

McLandress, C., Shepherd, T. G., Polavarapu, S., and Beagley, S. R. (2012). Is missing orographic gravity wave drag near 60° S the cause of the stratospheric zonal wind biases in chemistry–climate models?, J. Atmos. Sci., 69, 802–818, https://doi.org/10.1175/JAS-D-11-0159.1.

McLandress, C., Scinocca, J. F., Shepherd, T. G., Reader, M. C. and Manney, G. L. (2013). Dynamical Control of the Mesosphere by Orographic and Nonorographic Gravity Wave Drag during the Extended Northern Winters of 2006 and 2009, J. Atmos. Sci., 70, 2152–2169, https://doi.org/10.1175/JAS-D-12-0297.1.

McLandress, C., Plummer, D. A. and Shepherd, T. G. (2014). A simple procedure for removing temporal discontinuities in ERA-Interim upper stratospheric temperatures for use in nudged chemistry-climate model simulations. *Atmospheric Chemistry and Physics*, *14*(3), 1547-1555.

McLinden, C. A., Olsen, S. C., Hannegan, B., Wild, O., Prather, M. J. and Sundet, J. (2000). Stratospheric ozone in 3-D models: A simple chemistry and the cross-tropopause flux. *Journal of Geophysical Research: Atmospheres*, *105*(D11), 14653-14665.

McPeters, R. D., Labow, G. J. and Logan, J. A. (2007). Ozone climatological profiles for satellite retrieval algorithms. *Journal of Geophysical Research: Atmospheres*, *112*(D5).

Meehl, G. A., Arblaster, J. M., Branstator, G. and Van Loon, H. (2008). A coupled air–sea response mechanism to solar forcing in the Pacific region. *Journal of Climate*, *21*(12), 2883-2897.

Meloen, J., Siegmund, P., Van Velthoven, P., Kelder, H., Sprenger, M., Wernli, H. et al. (2003). Stratosphere-troposphere exchange: A model and method intercomparison. *Journal of Geophysical Research: Atmospheres*, *108*(D12).

Merryfield, W. J., McFarlane, N., and Lazare, M. (2003). A generalised hybrid transformation for tracer advection, Research Activity in Atmospheric and Oceanic Modelling, CAS/JSC WGNE Blue Book, Report, report No. 33, WMO/TD 1161, World Meteorological Organization, Geneva, 13–14.

Meul, S., Langematz, U., Kröger, P., Oberländer-Hayn, S. and Jöckel, P. (2018). Future changes in the stratosphere-to-troposphere ozone mass flux and the contribution from climate change and ozone recovery. *Atmospheric Chemistry and Physics (ACP)*, *18*(10), 7721-7738.

Mielonen, T., de Haan, J. F., van Peet, J. C. A., Eremenko, M., and Veefkind, J. P. (2015). Towards the retrieval of tropospheric ozone with the Ozone Monitoring Instrument (OMI), Atmos. Meas. Tech., 8, 671–687, https://doi.org/10.5194/amt-8-671-2015.

Miles, G. M., Siddans, R., Kerridge, B. J., Latter, B. G., and Richards, N. A. D. (2015). Tropospheric ozone and ozone profiles retrieved from GOME-2 and their validation, Atmos. Meas. Tech., 8, 385–398, https://doi.org/10.5194/amt-8-385-2015.

Misios, S., Gray, L. J., Knudsen, M. F., Karoff, C., Schmidt, H. and Haigh, J. D. (2019). Slowdown of the Walker circulation at solar cycle maximum. *Proceedings of the National Academy of Sciences*, *116*(15), 7186-7191.

Mitchell, D. M., Gray, L. J., Anstey, J., Baldwin, M. P. and Charlton-Perez, A. J. (2013). The influence of stratospheric vortex displacements and splits on surface climate. *Journal of Climate*, *26*(8), 2668–2682. https://doi.org/10.1175/JCLI-D-12-00030.1.

Mitchell, D. M., Misios, S., Gray, L. J., Tourpali, K., Matthes, K., Hood, L. and Shindell, D. (2015). Solar signals in CMIP-5 simulations: The stratospheric pathway. *Quarterly Journal of the Royal Meteorological Society*, *141*(691), 2390-2403.

Mlawer, E. J., Turner, D. D., Paine, S. N., Palchetti, L., Bianchini, G., Payne, V. H. et al. (2019). Analysis of water vapor absorption in the far-infrared and submillimeter regions using surface radiometric measurements from extremely dry locations. *Journal of Geophysical Research: Atmospheres*, *124*(14), 8134-8160.

Monge-Sanz, B. M., Chipperfield, M. P., Dee, D. P., Simmons, A. J. and Uppala, S. M. (2013). Improvements in the stratospheric transport achieved by a chemistry transport model with ECMWF (re) analyses: Identifying effects and remaining challenges. *Quarterly Journal of the Royal Meteorological Society*, *139*(672), 654-673.

Molina, L. T. and Molina, M. J. (1987). Production of chlorine oxide (Cl2O2) from the self-reaction of the chlorine oxide (ClO) radical. *Journal of Physical Chemistry*, *91*(2), 433-436.

Monks, P. S., Granier, C., Fuzzi, S., Stohl, A., Williams, M. L., Akimoto, H. et al. (2009). Atmospheric composition change–global and regional air quality. *Atmospheric environment*, *43*(33), 5268-5350.

Monks, P. S., Archibald, A. T., Colette, A., Cooper, O., Coyle, M., Derwent, R. et al. (2015). Tropospheric ozone and its precursors from the urban to the global scale from air quality to short-lived climate forcer. *Atmospheric Chemistry and Physics*, *15*(15), 8889–8973. https://doi.org/10.5194/acp-15-8889-2015

Morgenstern, O., Hegglin, M. I., Rozanov, E., O'Connor, F. M., Abraham, N. L., Akiyoshi, H. et al. (2017). Review of the global models used within phase 1 of the Chemistry–Climate

Model Initiative (CCMI), Geosci. Model Dev., 10, 639–671, https://doi.org/10.5194/gmd-10-639-2017.

Mote, P. W., Rosenlof, K. H., McIntyre, M. E., Carr, E. S., Gille, J. C., Holton, J. R. et al. (1996). An atmospheric tape recorder: The imprint of tropical tropopause temperatures on stratospheric water vapor. *Journal of Geophysical Research: Atmospheres*, *101*(D2), 3989-4006.

Mount, G. H., Sanders, R. W., Schmeltekopf, A. L. and Solomon, S. (1987). Visible spectroscopy at Mcmurdo Station, Antarctica: 1. Overview and daily variations of NO2 and O3, Austral Spring, 1986. *Journal of Geophysical Research: Atmospheres*, *92*(D7), 8320-8328.

Munro, R., Siddans, R., Reburn, W. J. and Kerridge, B. J. (1998). Direct measurement of tropospheric ozone distributions from space. *Nature*, *392*(6672), 168-171.

Munro, R., Lang, R., Klaes, D., Poli, G., Retscher, C., Lindstrot, R. and Kokhanovsky, A. (2016). The GOME-2 instrument on the Metop series of satellites: instrument design, calibration, and level 1 data processing-an overview. *Atmospheric Measurement Techniques*, *9*(3).

Murgatroyd, R. J. and Singleton, F. S. (1961). Possible meridional circulations in the stratosphere and mesosphere. *Quarterly Journal of the Royal Meteorological Society*, *87*(372), 125-135.

Myhre G, Kvalevåg M, Rädel G, Cook J, Shine KP, Clark H. et al. (2009). Intercomparison of radiative forcing calculations of stratospheric water vapour and contrails *Meteorologische Zeitschrift* 18:585-596.

Myhre, G., Shindell, D., Bréon, F.-M., Collins, W., Fuglestvedt, J., and Huang, J. (2013). Anthropogenic and Natural Radiative Forcing, in: Climate Change 2013: The Physical Science Basis. Contribution of Working Group I to the Fifth Assessment Report of the Intergovernmental Panel on Climate Change, edited by: Stocker, T. F., Qin, D., Plattner, G.-K., Tignor, M., Allen, S. K., Boschung, J., Nauels, A., Xia, Y., Bex, V., and Midgley, P. M., Cambridge University Press, Cambridge, United Kingdom and New York, NY, USA, 659–740, https://doi.org/10.1017/CBO9781107415324.018.

Nakagawa, K. I. and Yamazaki, K. (2006). What kind of stratospheric sudden warming propagates to the troposphere? *Geophysical Research Letters*, *33*(4), 3–6.

https://doi.org/10.1029/2005GL024784

Nassar, R., Logan, J. A., Worden, H. M., Megretskaia, I. A., Bowman, K. W., Osterman, G. B. et al. (2008). Validation of Tropospheric Emission Spectrometer (TES) nadir ozone profiles using ozonesonde measurements, J. Geophys. Res.-Atmos., 113, D15S17, https://doi.org/10.1029/2007JD008819.

Neu, J. L., Sparling, L. C. and Plumb, R. A. (2003). Variability of the subtropical "edges" in the stratosphere. *Journal of Geophysical Research: Atmospheres*, *108*(D15).

Neu, J. L., Flury, T., Manney, G. L., Santee, M. L., Livesey, N. J. and Worden, J. (2014). Tropospheric ozone variations governed by changes in stratospheric circulation. *Nature Geoscience*, *7*(5), 340–344. https://doi.org/10.1038/ngeo2138.

Newman, P. A., Nash, E. R. and Rosenfield, J. E. (2001). What controls the temperature of the Arctic stratosphere during the spring?. *Journal of Geophysical Research: Atmospheres*, *106*(D17), 19999-20010.

Nishii, K., Nakamura, H. and Orsolini, Y. J. (2011). Geographical dependence observed in blocking high influence on the stratospheric variability through enhancement and suppression of upward planetary-wave propagation. *Journal of Climate*, *24*(24), 6408-6423.

Oberländer, S., Langematz, U. and Meul, S. (2013). Unraveling impact factors for future changes in the Brewer-Dobson circulation. *Journal of Geophysical Research: Atmospheres*, *118*(18), 10-296.

Oberländer-Hayn, S., Gerber, E. P., Abalichin, J., Akiyoshi, H., Kerschbaumer, A., Kubin, A. et al. (2016). Is the Brewer-Dobson circulation increasing or moving upward?. *Geophysical Research Letters*, *43*(4), 1772-1779.

Oehrlein, J., Chiodo, G. and Polvani, L. M. (2020). The effect of interactive ozone chemistry on weak and strong stratospheric polar vortex events. *Atmospheric Chemistry and Physics*, *20*(17), 10531-10544.

Okamoto, K., Sato, K. and Akiyoshi, H. (2011). A study on the formation and trend of the Brewer-Dobson circulation. *Journal of Geophysical Research: Atmospheres*, *116*(D10).

Olsen, S. C., McLinden, C. A. and Prather, M. J. (2001). Stratospheric N2O–NO y system: Testing uncertainties in a three-dimensional framework. *Journal of Geophysical Research: Atmospheres*, *106*(D22), 28771-28784.

Olsen, M. A., Wargan, K. and Pawson, S. (2016). Tropospheric column ozone response to ENSO in GEOS-5 assimilation of OMI and MLS ozone data. *Atmospheric Chemistry and Physics*, *16*(11), 7091.

Oltmans, S. J., Lefohn, A. S., Shadwick, D., Harris, J. M., Scheel, H. E., Galbally, I. et al. (2013). Recent tropospheric ozone changes–A pattern dominated by slow or no growth. *Atmospheric Environment*, *67*, 331-351.

Oman, L. D., Ziemke, J. R., Douglass, A. R., Waugh, D. W., Lang, C., Rodriguez, J. M. and Nielsen, J. E. (2011). The response of tropical tropospheric ozone to ENSO. *Geophysical Research Letters*, *38*(13).

Oman, L. D., Douglass, A. R., Ziemke, J. R., Rodriguez, J. M., Waugh, D. W., & Nielsen, J. E. (2013). The ozone response to ENSO in Aura satellite measurements and a chemistry-climate simulation. *Journal of Geophysical Research: Atmospheres*, *118*(2), 965-976.

Orbe, C., Plummer, D. A., Waugh, D. W., Yang, H., Jöckel, P., Kinnison, D. E. et al. (2020). Description and Evaluation of the specified-dynamics experiment in the Chemistry-Climate Model Initiative. *Atmospheric Chemistry and Physics*, *20*(6), 3809-3840.

Ordóñez, C., Brunner, D., Staehelin, J., Hadjinicolaou, P., Pyle, J.A., Jonas, M. et al. (2007). Strong influence of lowermost stratospheric ozone on lower tropospheric background ozone changes over Europe. *Geophys. Res. Lett., **34**,* L07805.

Orphal, J. (2003). A critical review of the absorption cross-sections of O3 and NO2 in the ultraviolet and visible. *Journal of Photochemistry and Photobiology A: Chemistry*, *157*(2-3), 185-209.

Orsolini, Y. J. and Doblas-Reyes, F. J. (2003). Ozone signatures of climate patterns over the Euro-Atlantic sector in the spring. *Quarterly Journal of the Royal Meteorological Society: A journal of the atmospheric sciences, applied meteorology and physical oceanography*, *129*(595), 3251-3263.

O'Sullivan, D. and Salby, M. L. (1990). Coupling of the quasi-biennial oscillation and the extratropical circulation in the stratosphere through planetary wave transport. *Journal of the atmospheric sciences*, *47*(5), 650-673.

O'Sullivan, D. and Young, R. E. (1992). Modeling the quasi-biennial oscillation's effect on the winter stratospheric circulation. *Journal of the atmospheric sciences*, *49*(24), 2437-2448.

Ott, L. E., Duncan, B. N., Thompson, A. M., Diskin, G., Fasnacht, Z., Langford, A. O. et al. (2016). Frequency and impact of summertime stratospheric intrusions over Maryland during DISCOVER-AQ (2011): New evidence from NASA's GEOS-5 simulations. *Journal of Geophysical Research*. https://doi.org/10.1002/2015JD024052

Pan, L., Solomon, S., Randel, W., Lamarque, J. F., Hess, P., Gille, J. et al. (1997). Hemispheric asymmetries and seasonal variations of the lowermost stratospheric water vapor and ozone derived from SAGE II data. *Journal of Geophysical Research: Atmospheres*, *102*(D23), 28177-28184.

Pan, L. L., Wei, J. C., Kinnison, D. E., Garcia, R. R., Wuebbles, D. J. and Brasseur, G. P. (2007). A set of diagnostics for evaluating chemistry-climate models in the extratropical tropopause region. *Journal of Geophysical Research: Atmospheres*, *112*(D9).

Paoletti, E. (2007). Ozone impacts on forests. *CAB Reviews: Perspectives in Agriculture, Veterinary Science, Nutrition and Natural Resources*. https://doi.org/10.1079/PAVSNNR20072068

Paoletti, E., De Marco, A., Beddows, D. C. S., Harrison, R. M. and Manning, W. J. (2014). Ozone levels in European and USA cities are increasing more than at rural sites, while peak values are decreasing. *Environmental Pollution*, *192*(x), 295–299. https://doi.org/10.1016/j.envpol.2014.04.040

Parrish, D. D., Law, K. S., Staehelin, J., Derwent, R., Cooper, O. R., Tanimoto, H. et al. (2012). Long-term changes in lower tropospheric baseline ozone concentrations at northern mid-latitudes. *Atmospheric Chemistry and Physics*, *12*(23), 11485-11504.

Parrish, D. D., Lamarque, J.-F., Naik, V., Horowitz, L., Shindell, D. T., Staehelin, J. et al. (2014). Long-term changes in lower tropospheric baseline ozone concentrations: Comparing chemistry-climate models and observations at northern midlatitudes, J. Geophys. Res.-Atmos., 119, 5719–5736, https://doi.org/10.1002/2013JD021435

Pausata, F. S. R., Pozzoli, L., Vignati, E. & Dentener, F. J. North Atlantic Oscillation and tropospheric ozone variability in Europe: model analysis and measurements intercomparison. *Atmos. Chem. Phys.* ***12***, 6357-6376 (2012).

Pavelin, E. G., Johnson, C. E., Rughooputh, S. and Toumi, R. (1999). Evaluation of pre-industrial surface ozone measurements made using Schönbein's method. *Atmospheric Environment*, *33*(6), 919-929.

Pawson, S., Kodera, K., Hamilton, K., Shepherd, T. G., Beagley, S. R., Boville, B. A. et al. (2000). The GCM-Reality Intercomparison Project for SPARC (GRIPS): Scientific issues and initial results. *Bulletin of the American Meteorological Society*, *81*(4), 781-796.

Payton, M. E., Greenstone, M. H. and Schenker, N. (2003). Overlapping confidence intervals or standard error intervals: what do they mean in terms of statistical significance?. *Journal of Insect Science*, *3*(1).

Pendlebury, D., Plummer, D., Scinocca, J., Sheese, P., Strong, K., Walker, K. et al. Comparison of the CMAM30 data set with ACE-FTS and OSIRIS: polar regions, Atmos. Chem. Phys., 15, 12465–12485, https://doi.org/10.5194/acp-15-12465-2015.

Perl, G. (1965). Das bodennahe Ozon in Arosa, seine regelmässigen und unregelmässigen Schwankungen. *Archiv für Meteorologie, Geophysik und Bioklimatologie, Serie A*, *14*(4), 449-458.

Pittock, A. B. (1978). A critical look at long-term Sun-weather relationships. *Reviews of Geophysics*, *16*(3), 400-420.

Plumb, R. A. (2002). Stratospheric transport. *Journal of the Meteorological Society of Japan. Ser. II*, *80*(4B), 793-809.

Plumb, R. A. and Bell, R. C. (1982). A model of the quasi-biennial oscillation on an equatorial beta-plane. *Quarterly Journal of the Royal Meteorological Society*, *108*(456), 335-352.

Plumb, R. A. and Eluszkiewicz, J. (1999). The Brewer–Dobson circulation: Dynamics of the tropical upwelling. *Journal of the atmospheric sciences*, *56*(6), 868-890.

Plummer, D., Lamarque, J.-F., and Hegglin, M. (2014). Chemistry-Climate Model Initiative (CCMI) Model Output Requirements and Data Reference Syntax, available at: http://www.met.reading.ac.uk/~qr903932/CCMI-website/Wordpress_PDFs/CCMI1_DRS_20140422.pdf (last access: 7 March 2019).

Pope, R. J., Chipperfield, M. P., Arnold, S. R., Glatthor, N., Feng, W., Dhomse, S. S. et al. (2018). Influence of the wintertime North Atlantic Oscillation on European tropospheric composition: an observational and modelling study. *Atmospheric Chemistry and Physics*, *18*(11), 8389-8408.

Poulida, O., Dickerson, R. R. and Heymsfield, A. (1996). Stratosphere-troposphere exchange in a midlatitude mesoscale convective complex: 1. Observations. *Journal of Geophysical Research: Atmospheres*, *101*(D3), 6823-6836.

Prather, M. J. and Remsberg, E. E. (1993). The atmospheric effects of stratospheric aircraft. Report of the 1992 Models and Measurements Workshop. Volume 3: Special diagnostic studies.

Prather, M. J., Zhu, X., Tang, Q., Hsu, J., and Neu, J. L. (2011). An atmospheric chemist in search of the tropopause, J. Geophys. Res.-Atmos., 116, D04306, https://doi.org/10.1029/2010JD014939.

Price, J. D. and Vaughan, G. (1993). The potential for stratosphere-troposphere exchange in cut-off-low systems. *Quarterly Journal of the Royal Meteorological Society*, *119*(510), 343-365.

Ramanathan, V. and Dickinson, R. E. (1979). The role of stratospheric ozone in the zonal and seasonal radiative energy balance of the earth-troposphere system. *Journal of the Atmospheric Sciences*, *36*(6), 1084-1104.

Randel, W. J. (1993). Global variations of zonal mean ozone during stratospheric warming events. *Journal of the atmospheric sciences*, *50*(19), 3308-3321.

Randel, W. J. and Wu, F. (1996). Isolation of the ozone QBO in SAGE II data by singular-value decomposition. *Journal of the atmospheric sciences*, *53*(17), 2546-2559.

Randel, W. J., Wu, F. and Stolarski, R. (2002). Changes in column ozone correlated with the stratospheric EP flux. *Journal of the Meteorological Society of Japan. Ser. II*, *80*(4B), 849-862.

Randel, W. J. and Wu, F. (2007). A stratospheric ozone profile data set for 1979–2005: Variability, trends, and comparisons with column ozone data. *Journal of Geophysical Research: Atmospheres*, *112*(D6).

Randel, W. J., Garcia, R. R., Calvo, N. and Marsh, D. (2009). ENSO influence on zonal mean temperature and ozone in the tropical lower stratosphere. *Geophysical Research Letters*, *36*(15).

Randel, W. J. and Wu, F. (2010). The polar summer tropopause inversion layer. *Journal of the Atmospheric Sciences*, *67*(8), 2572–2581. https://doi.org/10.1175/2010JAS3430.1.

Ray, E. A., Moore, F. L., Elkins, J. W., Dutton, G. S., Fahey, D. W., Vömel, H. et al. (1999). Transport into the Northern Hemisphere lowermost stratosphere revealed by in situ tracer measurements. *Journal of Geophysical Research: Atmospheres*, *104*(D21), 26565-26580.

Ray, E. A., Portmann, R. W., Yu, P., Daniel, J., Montzka, S. A., Dutton, G. S. et al. (2020). The influence of the stratospheric Quasi-Biennial Oscillation on trace gas levels at the Earth's surface. *Nature Geoscience*, *13*(1), 22-27.

Rayner, N. A., Parker, D. E., Horton, E. B., Folland, C. K., Alexander, L. V., Rowell, D. P., Kent, E. C., and Kaplan, A.: Global analyses of sea surface temperature, sea ice, and night marine air temperature since the late nineteenth century, J. Geophys. Res.-Atmos., 108, 4407, https://doi.org/10.1029/2002JD002670, 2003.

Reed, R. J. and Danielsen, E. F. (1958). Fronts in the vicinity of the tropopause. *Archiv für Meteorologie, Geophysik und Bioklimatologie, Ser. A, Meteorologie und Geophysik*, *11*(1), 1-17.

Reichler, T., Kim, J., Manzini, E. and Kröger, J. (2012). A stratospheric connection to Atlantic climate variability. *Nature Geoscience*, *5*(11), 783-787.

Reutter, P., Škerlak, B., Sprenger, M. and Wernli, H. (2015). Stratosphere-troposphere exchange (STE) in the vicinity of North Atlantic cyclones. *Atmospheric Chemistry and Physics*, *15*(19), 10939-10953.

Revell, L. E., Stenke, A., Tummon, F., Feinberg, A., Rozanov, E., Peter, T. et al. (2018). Tropospheric ozone in CCMI models and Gaussian process emulation to understand biases in the SOCOLv3 chemistry–climate model, Atmos. Chem. Phys., 18, 16155–16172, https://doi.org/10.5194/acp-18-16155-2018.

Richards, N. A. D., Arnold, S. R., Chipperfield, M. P., Miles, G., Rap, A., Siddans, R., Monks, S. A., and Hollaway, M. J. (2013). The Mediterranean summertime ozone maximum: global emission sensitivities and radiative impacts, Atmos. Chem. Phys., 13, 2331–2345, https://doi.org/10.5194/acp-13-2331-2013.

Riese, M., Ploeger, F., Rap, A., Vogel, B., Konopka, P., Dameris, M. and Forster, P. (2012). Impact of uncertainties in atmospheric mixing on simulated UTLS composition and related radiative effects. *Journal of Geophysical Research: Atmospheres*, *117*(D16).

Rind, D., Suozzo, R., Balachandran, N. K. and Prather, M. J. (1990). Climate change and the middle atmosphere. Part I: The doubled CO2 climate. *Journal of the Atmospheric Sciences*, *47*(4), 475-494.

Rodgers, C. D. (1976). Retrieval of atmospheric temperature and composition from remote measurements of thermal radiation. *Reviews of Geophysics*, *14*(4), 609-624.

Rodgers, C. D. (2000). *Inverse methods for atmospheric sounding: theory and practice* (Vol. 2). World scientific.

Roelofs, G. J. and Lelieveld, J. O. S. (1997). Model study of the influence of cross-tropopause O3 transports on tropospheric O3 levels, Tellus B, 49, 38–55, https://doi.org/10.3402/tellusb.v49i1.15949.

Roelofs, G. J., Kentarchos, A. S., Trickl, T., Stohl, A., Collins, W. J., Crowther, R. A. et al. (2003). Intercomparison of tropospheric ozone models: Ozone transport in a complex tropopause folding event. *Journal of Geophysical Research: Atmospheres*, *108*(D12).

Rood, R. B., Douglass, A. R., Cerniglia, M. C., Sparling, L. C. et al. (2000). Seasonal variability of middle-latitude ozone in the lowermost stratosphere derived from probability distribution functions. *Journal of Geophysical Research: Atmospheres*, *105*(D14), 17793-17805.

Roscoe, H. K. (2006). The Brewer–Dobson circulation in the stratosphere and mesosphere – Is there a trend?, Adv. Space. Res., 38, 2446–2245, https://doi.org/10.1016/j.asr.2006.02.078.

The Royal Society (2008). Ground-level ozone in the 21st century: future trends, impacts and policy implications. Retrieved from: https://royalsociety.org/-/media/Royal_Society_Content/policy/publications/2008/7925.pdf

Rosenlof, K. H. and Holton, J. R. (1993). Estimates of the stratospheric residual circulation using the downward control principle. *Journal of Geophysical Research: Atmospheres*, *98*(D6), 10465-10479.

Rosenlof, K. H. (1995). Seasonal cycle of the residual mean meridional circulation in the stratosphere. *Journal of Geophysical Research: Atmospheres*, *100*(D3), 5173-5191.

Rosenlof, K. H., Tuck, A. F., Kelly, K. K., Russell III, J. M. and McCormick, M. P. (1997). Hemispheric asymmetries in water vapor and inferences about transport in the lower stratosphere. *Journal of Geophysical Research: Atmospheres*, *102*(D11), 13213-13234.

Rozanov, V. V., Diebel, D., Spurr, R. J. D. and Burrows, J. P. (1997). GOMETRAN: A radiative transfer model for the satellite project GOME, the plane-parallel version. *Journal of Geophysical Research: Atmospheres*, *102*(D14), 16683-16695.

Sander, R., Baumgaertner, A., Gromov, S., Harder, H., Jöckel, P., Kerkweg, A. et al. (2011). The atmospheric chemistry box model CAABA/MECCA-3.0, Geosci. Model Dev., 4, 373–380, https://doi.org/10.5194/gmd-4-373-2011.

Salawitch, R. J., Fahey, D. W., Hegglin M. I., McBride, L. A., Tribett, W. R. and Doherty, S. J. (2019). Twenty Questions and Answers About the Ozone Layer: 2018 Update, Scientific Assessment of Ozone Depletion: 2018, 84 pp., World Meteorological Organization, Geneva, Switzerland.

Salby, M. L. and Callaghan, P. F. (2002). Interannual changes of the stratospheric circulation: Relationship to ozone and tropospheric structure. *Journal of Climate*, *15*(24), 3673-3685.

Salby, M. L. (2011). Interannual changes of stratospheric temperature and ozone: Forcing by anomalous wave driving and the QBO. *Journal of the atmospheric sciences*, *68*(7), 1513-1525.

Sander, R., Jöckel, P., Kirner, O., Kunert, A. T., Landgraf, J., and Pozzer, A. (2014). The photolysis module JVAL-14, compatible with the MESSy standard, and the JVal PreProcessor (JVPP), Geosci. Model Dev., 7, 2653–2662, https://doi.org/10.5194/gmd-7-2653-2014.

Sanderson, M. G., Collins, W. J., Hemming, D. L. and Betts, R. A. (2007). Stomatal conductance changes due to increasing carbon dioxide levels: Projected impact on surface ozone levels. *Tellus B: Chemical and Physical Meteorology*, *59*(3), 404-411.Santer, B. D., Sausen, R., Wigley, T. M. L., Boyle, J. S., Achutarao, K., Doutriaux, C. et al. (2003a). Behavior of tropopause height and atmospheric temperature in models, reanalyses, and observations: Decadal changes, J. Geophys. Res.-Atmos., 108, 4002, https://doi.org/10.1029/2002JD002258.

Santer, B. D., Wehner, M. F., Wigley, T. M. L., Sausen, R., Meehl, G. A., Taylor, K. E. (2003b). Contributions of Anthropogenic and Natural Forcing to Recent Tropopause Height Changes, Science, 301, 479–483, https://doi.org/10.1126/science.1084123.

Sassi, F., Kinnison, D., Boville, B. A., Garcia, R. R. and Roble, R. (2004). Effect of El Niño–Southern Oscillation on the dynamical, thermal, and chemical structure of the middle atmosphere. *Journal of Geophysical Research: Atmospheres*, *109*(D17).

Sátori, G., Williams, E. and Lemperger, I. (2009). Variability of global lightning activity on the ENSO time scale. *Atmospheric Research*, *91*(2-4), 500-507.

Sauvage, B., Martin, R. V., Van Donkelaar, A. and Ziemke, J. R. (2007). Quantification of the factors controlling tropical tropospheric ozone and the South Atlantic maximum. *Journal of Geophysical Research: Atmospheres*, *112*(D11).

Scaife, A. A., Ineson, S., Knight, J. R., Gray, L., Kodera, K. and Smith, D. M. (2013). A mechanism for lagged North Atlantic climate response to solar variability. *Geophysical Research Letters*, *40*(2), 434-439.

Scaife, A. A., Karpechko, A. Y., Baldwin, M. P., Brookshaw, A., Butler, A. H., Eade, R. et al. (2016). Seasonal winter forecasts and the stratosphere. *Atmospheric Science Letters*, *17*(1), 51-56.

Schenker, N. and Gentleman, J. F. (2001). On judging the significance of differences by examining the overlap between confidence intervals. *The American Statistician*, *55*(3), 182-186.

Schenkeveld, V. M. E., Jaross, G., Marchenko, S., Haffner, D., Kleipool, Q. L., Rozemeijer, N. C. et al. (2017). In-flight performance of the Ozone Monitoring Instrument, Atmos. Meas. Tech., 10, 1957–1986, https://doi.org/10.5194/amt-10-1957-2017.

Scherhag, R. (1952). Die explosionartigen Stratospharenwarmungen des Spatwinters 1951-1952. *Ber. Deut. Wetterd.*, *6*, 51-63.

Schoeberl, M. R., Ziemke, J. R., Bojkov, B., Livesey, N., Duncan, B., Strahan, S. et al. (2007). A trajectory-based estimate of the tropospheric ozone column using the residual method. *Journal of Geophysical Research: Atmospheres*, *112*(D24).

SCIAMACHY Measurement Models (n.d.). Retrieved from https://www.iup.uni-bremen.de/sciamachy/instrument/modes/.

Scinocca, J. F., McFarlane, N. A., Lazare, M., Li, J., and Plummer, D. (2008). Technical Note: The CCCma third generation AGCM and its extension into the middle atmosphere, Atmos. Chem. Phys., 8, 7055–7074, https://doi.org/10.5194/acp-8-7055-2008.

Scott, R. K. and Polvani, L. M. (2006). Internal variability of the winter stratosphere. Part I: Time-independent forcing. *J. Atmos. Sci.*, ***63***, 2758-2776.

Seinfeld, J. H. and Pandis, S. N. (2006). Atmospheric chemistry and physics: from air pollution to climate change. John Wiley & Sons.

Sellitto, P., Bojkov, B. R., Liu, X., Chance, K., and Del Frate, F. (2011).Tropospheric ozone column retrieval at northern mid-latitudes from the Ozone Monitoring Instrument by means of a neural network algorithm, Atmos. Meas. Tech., 4, 2375–2388, https://doi.org/10.5194/amt-4-2375-2011.

Sellitto, P., Di Noia, A., Del Frate, F., Burini, A., Casadio, S. and Solimini, D. (2012). On the role of visible radiation in ozone profile retrieval from nadir UV/VIS satellite measurements: An experiment with neural network algorithms inverting SCIAMACHY data. *Journal of Quantitative Spectroscopy and Radiative Transfer*, *113*(12), 1429-1436.

Seviour, W. J., Butchart, N. and Hardiman, S. C. (2012). The Brewer–Dobson circulation inferred from ERA-Interim. *Quarterly Journal of the Royal Meteorological Society*, *138*(665), 878-888.

Shapiro, M. A. (1980). Turbulent mixing within tropopause folds as a mechanism for the exchange of chemical constituents between the stratosphere and troposphere. *Journal of the Atmospheric Sciences*, *37*(5), 994-1004.

Shepherd, T. G. (2007) Transport in the middle atmosphere, J. Meteorol. Soc. Jpn., 85B, 165–191, https://doi.org/10.2151/jmsj.85B.165.

Shepherd, T. G., Plummer, D. A., Scinocca, J. F., Hegglin, M. I., Fioletov, V. E., Reader, M. C., Remsburg, E., von Clarmann, T., and Wang, H. J. (2014). Reconciliation of halogen-induced ozone loss with the total-column ozone record, Nat. Geosci., 7, 443–449, https://doi.org/10.1038/NGEO2155.

Sheppard, P. A. (1963). Atmospheric tracers and the study of the general circulation of the atmosphere. *Reports on progress in physics*, *26*(1), 213.

Shindell, D., Rind, D., Balachandran, N., Lean, J. and Lonergan, P. (1999). Solar cycle variability, ozone, and climate. *Science*, *284*(5412), 305-308.

Shine KP and Myhre G (2020). The spectral nature of stratospheric temperature adjustment and its application to halocarbon radiative forcing *Journal of Advances in Modeling Earth Systems 12:e2019MS001951 doi: 10.1029/2019MS001951.*

Shuckburgh, E., d'Ovidio, F. and Legras, B. (2009). Local mixing events in the upper troposphere and lower stratosphere. Part II: Seasonal and interannual variability. *Journal of the atmospheric sciences*, *66*(12), 3695-3706.

Sigmond, M., Scinocca, J. F., Kharin, V. V. and Shepherd, T. G. (2013). Enhanced seasonal forecastskill following stratospheric sudden warmings. *Nature Geosci.* ***6***, 98-102.

Sissala, J. E. (1975). The Nimbus-6 user's guide. *STIN*, *76*, 31256.

Škerlak, B., Sprenger, M., and Wernli, H. (2014). A global climatology of stratosphere–troposphere exchange using the ERA-Interim data set from 1979 to 2011, Atmos. Chem. Phys., 14, 913–937, https://doi.org/10.5194/acp-14-913-2014.

Smit, H. G. J. and Kley, D. (1998). JOSIE: The 1996 WMO International intercomparison of ozonesondes under quasi flight conditions in the environmental simulation chamber at Jülich, WMO Global Atmosphere Watch report series, No. 130 (Technical Document No. 926), World Meteorological Organization, Geneva.

Smit, H. G. J. and Straeter, W.: JOSIE-1998, Performance of ECC Ozone Sondes of SPC-6A and ENSCI-Z Type, WMO Global Atmosphere Watch report series, No. 157 (Technical Document No. 1218), World Meteorological Organization, Geneva, 2004a.

Smit, H. G. J. and Straeter,W.: JOSIE-2000, Jülich Ozone Sonde Intercomparison Experiment 2000, The 2000 WMO international intercomparison of operating procedures for ECC-ozonesondes at the environmental simulation facility at Jülich, WMO Global Atmosphere Watch report series, No. 158 (Technical Document No. 1225), World Meteorological Organization, Geneva, 2004b.

Solomon, S., Crutzen, P. J. and Roble, R. G. (1982). Photochemical coupling between the thermosphere and the lower atmosphere: 1. Odd nitrogen from 50 to 120 km. *Journal of Geophysical Research: Oceans*, *87*(C9), 7206-7220.

Solomon, S., Garcia, R. R., Rowland, F. S. and Wuebbles, D. J. (1986). On the depletion of Antarctic ozone. *Nature*, *321*(6072), 755-758.

Solomon, S. (1999). Stratospheric ozone depletion: A review of concepts and history. *Reviews of Geophysics*, *37*(3), 275-316.

Solomon, S., Thompson, D. W. J., Portmann, R. W., Oltmans, S. J. and Thompson, A. M. (2005). On the distribution and variability of ozone in the tropical upper troposphere:

Implications for tropical deep convection and chemical-dynamical coupling. *Geophysical Research Letters*, *32*(23).

Solomon, S., Manning, M., Marquis, M. and Qin, D. (2007). *Climate change 2007-the physical science basis: Working group I contribution to the fourth assessment report of the IPCC* (Vol. 4). Cambridge university press.

Son, S. W., Han, B. R., Garfinkel, C. I., Kim, S. Y., Park, R., Abraham, N. L. et al. (2018). Tropospheric jet response to Antarctic ozone depletion: An update with Chemistry-Climate Model Initiative (CCMI) models, Environ. Res. Lett., 13, 054024, https://doi.org/10.1088/1748-9326/aabf21.

Song, Y. and Robinson, W. A. (2004). Dynamical mechanisms for stratospheric influences on the troposphere. *Journal of the Atmospheric Sciences*, *61*(14), 1711-1725.

Soukharev, B. E. and Hood, L. L. (2006). Solar cycle variation of stratospheric ozone: Multiple regression analysis of long-term satellite data sets and comparisons with models. *Journal of Geophysical Research: Atmospheres*, *111*(D20).

SPARC (1998). SPARC/IOC/GAW Assessment of Trends in the Vertical Distribution of Ozone, edited by: Harris, N., Hudson, R., and Phillips, C., SPARC Report No. 1, WMO Ozone Research and Monitoring Project Report No. 43, available at: https://www.sparc-climate.org/publications/sparc-reports/ (last access: 4 March 2019).

SPARC (2010). SPARC CCMVal Report on the Evaluation of Chemistry-Climate Models. V. Eyring, T. Shepherd and D. Waugh (Eds.), SPARC Report No. 5, WCRP-30/2010, WMO/TD – No. 40, available at www.sparc-climate.org/publications/sparc-reports/.

Sprenger, M. and Wernli, H. (2003). A northern hemispheric climatology of cross-tropopause exchange for the ERA15 time period (1979–1993). *J. Geophys. Res-Atmos.,* ***108*** (2003).

Staley, D. O. (1962). On the mechanism of mass and radioactivity transport from stratosphere to troposphere, J. Atmos. Sci., 19, 450–467, https://doi.org/10.1175/1520-0469(1962)019<0450:OTMOMA>2.0.CO;2.

Stevenson, D., Doherty, R., Sanderson, M., Johnson, C., Collins, B. and Derwent, D. (2005). Impacts of climate change and variability on tropospheric ozone and its precursors. *Faraday discussions*, *130*, 41-57.

Stevenson, D. S., Dentener, F. J., Schultz, M. G., Ellingsen, K., Van Noije, T. P. C., Wild, O. et al. (2006). Multimodel ensemble simulations of present-day and near-future tropospheric ozone. *Journal of Geophysical Research: Atmospheres*, *111*(D8).

Stevenson, D. S., Young, P. J., Naik, V., Lamarque, J.-F., Shindell, D. T., Voulgarakis, A. et al. (2013). Tropospheric ozone changes, radiative forcing and attribution to emissions in the Atmospheric Chemistry and Climate Model Intercomparison Project (ACCMIP), Atmos. Chem. Phys., 13, 3063–3085, https://doi.org/10.5194/acp-13-3063-2013.

Stohl, A., Spichtinger-Rakowsky, N., Bonasoni, P., Feldmann, H., Memmesheimer, M., Scheel et al. (2000). The influence of stratospheric intrusions on alpine ozone concentrations, Atmos. Environ., 34, 1323–1354, https://doi.org/10.1016/S1352-2310(99)00320-9.

Stohl, A., Bonasoni, P., Cristofanelli, P., Collins, W., Feichter, J., Frank, A. et al. (2003). Stratosphere-troposphere exchange: A review, and what we have learned from STACCATO. *Journal of Geophysical Research Atmospheres*, *108*(12). https://doi.org/10.1029/2002jd002490

Stolarski, R. S., Krueger, A. J., Schoeberl, M. R., McPeters, R. D., Newman, P. A. and Alpert, J. C. (1986). Nimbus 7 satellite measurements of the springtime Antarctic ozone decrease. *Nature*, *322*(6082), 808-811.

Strahan, S. E., Douglass, A. R., Stolarski, R. S., Akiyoshi, H., Bekki, S., Braesicke, P. et al. (2011). Using transport diagnostics to understand chemistry climate model ozone simulations. *Journal of Geophysical Research: Atmospheres*, *116*(D17).

Sturges, W. T., Oram, D. E., Carpenter, L. J., Penkett, S. A. and Engel, A. (2000). Bromoform as a source of stratospheric bromine. *Geophysical Research Letters*, *27*(14), 2081-2084.

Sudo, K. and Takahashi, M. (2001). Simulation of tropospheric ozone changes during 1997–1998 El Nino: Meteorological impact on tropospheric photochemistry. *Geophysical research letters*, *28*(21), 4091-4094.

Taguchi, M. and Hartmann, D. L. (2006). Increased occurrence of stratospheric sudden warmings during El Niño as simulated by WACCM. *Journal of climate*, *19*(3), 324-332.

Taguchi, M. (2010). Wave driving in the tropical lower stratosphere as simulated by WACCM. Part II: ENSO-induced changes for northern winter. *Journal of the atmospheric sciences*, *67*(2), 543-555.

Tang, Q. and Prather, M. J. (2012). Five blind men and the elephant: what can the NASA Aura ozone measurements tell us about stratosphere-troposphere exchange?. *Atmospheric Chemistry and Physics*, *12*(5), 2357-2380.

Tao, M. et al. (2015). Impact of the 2009 major sudden stratospheric warming on the composition of the stratosphere. *Atmos. Chem. Phys.* ***15***, 8695-8715.

Tarasick, D. W., Carey-Smith, T. K., Hocking, W. K., Moeini, O., He, H., Liu, J. et al. (2019). Quantifying stratosphere-troposphere transport of ozone using balloon-borne ozonesondes, radar windprofilers and trajectory models, Atmos. Environ., 198, 496–509, https://doi.org/10.1016/j.atmosenv.2018.10.040.

Tarasova, O. A., Senik, I. A., Sosonkin, M. G., Cui, J., Staehelin, J. and Prévôt, A. S. (2009). Surface ozone at the Caucasian site Kislovodsk High Mountain Station and the Swiss Alpine site Jungfaujoch: Data analysis and trends (1990–2006). *Atmospheric Chemistry and Physics*, *9*(12), 4157-4175.

Taylor KE, Stouffer RJ, Meehl GA. (2012). An overview of CMIP5 and the experiment design. Bull. Amer. Meteor. Soc. 2012; 93:485–498.

Tegtmeier, S., Rex, M., Wohltmann, I. and Krüger, K. (2008). Relative importance of dynamical and chemical contributions to Arctic wintertime ozone. *Geophysical Research Letters*, *35*(17).

Tegtmeier, S., Hegglin, M. I., Anderson, J., Bourassa, A., Brohede, S., Degenstein, D. and Jones, A. (2013). SPARC Data Initiative: A comparison of ozone climatologies from international satellite limb sounders. *Journal of Geophysical Research: Atmospheres*, *118*(21), 12-229.

Teisserenc de Bort, L. (1902). Variations de la température de l'air libre dans la zone comprise entre 8 km et 13 km d'altitude. *Compt. Rend. Seances Acad. Sci. Paris*, *134*, 987-989.

Thompson, D. W. and Wallace, J. M. (2000). Annular modes in the extratropical circulation. Part I: Month-to-month variability. *Journal of climate*, *13*(5), 1000-1016.

Thompson, C. J. and Battisti, D. S. (2001). A linear stochastic dynamical model of ENSO. Part II: Analysis. *Journal of Climate*, *14*(4), 445-466.

Thompson, D. W., Baldwin, M. P. & Wallace, J. M. (2002). Stratospheric connection to Northern Hemisphere wintertime weather: Implications for prediction. *J. Climate* ***15***, 1421-1428.

Thompson, D. W. and Solomon, S. (2002). Interpretation of recent Southern Hemisphere climate change. *Science*, *296*(5569), 895-899.

Thompson, D. W., Baldwin, M. P. and Solomon, S. (2005). Stratosphere–troposphere coupling in the Southern Hemisphere. *Journal of the atmospheric sciences*, *62*(3), 708-715.

Thompson, D. W. (n.d.). *Annular Modes Website*. Retrieved from: https://atmos.colostate.edu/~davet/ao/introduction.html.

Thompson, A. M., Stone, J. B., Witte, J. C., Miller, S. K., Pierce, R. B., Chatfield, R. B. et al. (2007a). Intercontinental Chemical Transport Experiment Ozonesonde Network Study (IONS) 2004: 1. Summertime upper troposphere/lower stratosphere ozone over northeastern North America, J. Geophys. Res.-Atmos., 112, D12S12, https://doi.org/10.1029/2006JD007441.

Thompson, A. M., Stone, J. B., Witte, J. C., Miller, S. K., Oltmans, S. J. Kucsera, T. L., Ross, et al. (2007b). Intercontinental chemical transport experiment ozonesonde network study (IONS) 2004: 2. Tropospheric ozone budgets and variability over northeastern North America, J. Geophys. Res.-Atmos., 112, D12S13, https://doi.org/10.1029/2006JD007670.

Thompson, A. M., Miller, S. K., Tilmes, S., Kollonige, D.W., Witte, J. C. Oltmans, S. J. et al. (2012). Southern Hemisphere Additional Ozonesondes (SHADOZ) ozone climatology (2005–2009): Tropospheric and tropical tropopause layer (TTL) profiles with comparisons to OMI-based ozone products, J. Geophys. Res.-Atmos., 117, D23301, https://doi.org/10.1029/2011JD016911.

Tian, B., Yung, Y. L., Waliser, D. E., Tyranowski, T., Kuai, L., Fetzer, E. J. et al. (2007). Intraseasonal variations of the tropical total ozone and their connection to the Madden-Julian Oscillation. *Geophysical Research Letters*, *34*(8).

Tost, H., Jöckel, P., Kerkweg, A., Sander, R., and Lelieveld, J. (2006). Technical note: A new comprehensive SCAVenging submodel for global atmospheric chemistry modelling, Atmos. Chem. Phys., 6, 565–574, https://doi.org/10.5194/acp-6-565-2006.

Trenberth, K. E., Caron, J. M., Stepaniak, D. P. and Worley, S. (2002). Evolution of El Niño–Southern Oscillation and global atmospheric surface temperatures. *Journal of Geophysical Research: Atmospheres*, *107*(D8), AAC-5.

Trenberth, K. E. and Smith, L. (2006). The vertical structure of temperature in the tropics: Different flavors of El Nino. *Journal of climate*, *19*(19), 4956-4973.

Trepte, C. R. and Hitchman, M. H. (1992). Tropical stratospheric circulation deduced from satellite aerosol data. *Nature*, *355*(6361), 626-628.

Trickl, T., Feldmann, H., Kanter, H. J., Scheel, H. E., Sprenger, M., Stohl, A. and Wernli, H. (2010). Forecasted deep stratospheric intrusions over Central Europe: case studies and climatologies. *Atmospheric Chemistry and Physics*, *10*(2), 499-524.

Trickl, T., Vogelmann, H., Giehl, H., Scheel, H. E., Sprenger, M. and Stohl, A. (2014). How stratospheric are deep stratospheric intrusions?. *Atmospheric Chemistry and Physics*, *14*(18), 9941-9961.

Tripathi, O. P., Baldwin, M., Charlton-Perez, A., Charron, M., Eckermann, S. D., Gerber, E. et al. (2015). The predictability of the extratropical stratosphere on monthly time-scales and its impact on the skill of tropospheric forecasts. *Quarterly Journal of the Royal Meteorological Society*, *141*(689), 987-1003.

Tung, K. K., Ko, M. K., Rodriguez, J. M. and Sze, N. D. (1986). Are Antarctic ozone variations a manifestation of dynamics or chemistry?. *Nature*, *322*(6082), 811-814.

Tung, K. K. and Yang, H. (1994). Global QBO in circulation and ozone. Part I: Reexamination of observational evidence. *Journal of the atmospheric sciences*, *51*(19), 2699-2707.

Turner, M. C., Jerrett, M., Pope III, C. A., Krewski, D., Gapstur, S. M., Diver, W. R. et al. Long-term ozone exposure and mortality in a large prospective study. *American journal of respiratory and critical care medicine*, *193*(10), 1134-1142.

UCAR (2008). *Stratosphere-Troposphere Analyses of Regional Transport.* Retrieved from: https://www.acom.ucar.edu/start/.

U.S. Environmental Protection Agency. National Ambient Air Quality Standards for Ozone - Proposed Rule, Federal Register. **80**, 65292-65498, available at http://www.gpo.gov/fdsys/pkg/FR-2015-10-26/pdf/2015-26594.pdf (2015).

Valks, P. J. M., Koelemeijer, R. B. A., Van Weele, M., Van Velthoven, P., Fortuin, J. P. F. and Kelder, H. (2003). Variability in tropical tropospheric ozone: Analysis with Global Ozone Monitoring Experiment observations and a global model. *Journal of Geophysical Research: Atmospheres*, *108*(D11).

Valks, P., Hao, N., Gimeno Garcia, S., Loyola, D., Dameris, M., Jöckel, P. and Delcloo, A. (2014). Tropical tropospheric ozone column retrieval for GOME-2. *Atmospheric Measurement Techniques*, *7*(8), 2513-2530.

Van Dingenen, R., Dentener, F. J., Raes, F., Krol, M. C., Emberson, L. and Cofala, J. (2009). The global impact of ozone on agricultural crop yields under current and future air quality legislation. *Atmospheric Environment*. https://doi.org/10.1016/j.atmosenv.2008.10.033.

Van Roozendael, M., Spurr, R., Loyola, D., Lerot, C., Balis, D., Lambert, J. C. et al. (2012). Sixteen years of GOME/ERS-2 total ozone data: The new direct-fitting GOME Data Processor (GDP) version 5—Algorithm description. *Journal of Geophysical Research: Atmospheres*, *117*(D3).

Varotsos, C. (2002). The southern hemisphere ozone hole split in 2002. *Environmental Science and Pollution Research*, *9*(6), 375-376.

Vaughan, G., Price, J. D. and Howells, A. (1994). Transport into the troposphere in a tropopause fold. *Quarterly Journal of the Royal Meteorological Society*, *120*(518), 1085-1103.

Very Short-lived substances (n.d.). Retrieved from https://www.iup.uni-bremen.de/atmospheric/research/veryshortlivedsubstances/index.html.

Vigouroux, C., Blumenstock, T., Coffey, M. T., Errera, Q., Garcia, O. E., Jones, N. B. et al. (2015). Trends of ozone total columns and vertical distribution from FTIR observations at eight NDACC stations around the globe.

Vingarzan, R. (2004). A review of surface ozone background levels and trends. *Atmospheric environment*, *38*(21), 3431-3442.

Volk, C. M., Elkins, J. W., Fahey, D. W., Salawitch, R. J., Dutton, G. S., Gilligan, J. M. et al. (1996). Quantifying transport between the tropical and mid-latitude lower stratosphere. *Science*, *272*(5269), 1763-1768.

Volz, A. and Kley, D. (1988). Evaluation of the Montsouris series of ozone measurements made in the nineteenth century. *Nature*, *332*(6161), 240-242.

Voulgarakis, A., Hadjinicolaou, P. and Pyle, J. A. (2011). Increases in global tropospheric ozone following an El Nino event: examining stratospheric ozone variability as a potential driver. *Atmospheric Science Letters*, *12*(2), 228-232.

Vountas, M., Rozanov, V. V. and Burrows, J. P. (1998). Ring effect: Impact of rotational Raman scattering on radiative transfer in Earth's atmosphere. *Journal of Quantitative Spectroscopy and Radiative Transfer*, *60*(6), 943-961.

Wang, Y. and Jacob, D. J. (1998). Anthropogenic forcing on tropospheric ozone and OH since preindustrial times. *Journal of Geophysical Research: Atmospheres*, *103*(D23), 31123-31135.

Wang, Y., Jacob, D. J. and Logan, J. A. (1998). Global simulation of tropospheric O3-NO^-hydrocarbon chemistry 3. Origin of tropospheric ozone and effects of nonmethane hydrocarbons. *Journal of Geophysical Research*, *103*(D9), 10-757.

Wang, Y., Hao, J., McElroy, M. B., Munger, J. W., Ma, H., Chen, D. and Nielsen, C. (2009). Ozone air quality during the 2008 Beijing Olympics: effectiveness of emission restrictions. *Atmospheric Chemistry and Physics*.

Wang, Y., Konopka, P., Liu, Y., Chen, H., Müller, R., Plöger, F. et al. (2012). Tropospheric ozone trend over Beijing from 2002–2010: ozonesonde measurements and modeling analysis. *Atmospheric Chemistry and Physics*, *12*(18), 8389-8399.

Wang, Y., Ma, Y. F., Eskes, H., Inness, A., Flemming, J. and Brasseur, G. P. (2020). Evaluation of the CAMS global atmospheric trace gas reanalysis 2003-2016 using aircraft campaign observations. *Atmospheric Chemistry and Physics*, *20*, 4493-4521.

Wasserstein, R. L. and Lazar, N. A. (2016). The ASA's statement on pvalues: context, process, and purpose, Am. Stat., 70, 129–133, https://doi.org/10.1080/00031305.2016.1154108.

Waugh, D. and Hall, T. (2002). Age of stratospheric air: Theory, observations, and models. *Reviews of Geophysics*, *40*(4), 1-1.

Wernli, B. H. and Davies, H. C. (1997). A Lagrangian-based analysis of extratropical cyclones. I: The method and some applications. *Quarterly Journal of the Royal Meteorological Society*, *123*(538), 467-489.

Wespes, C., Hurtmans, D., Emmons, L. K., Safieddine, S., Clerbaux, C., Edwards, D. P. and Coheur, P. F. (2016). Ozone variability in the troposphere and the stratosphere from the first 6 years of IASI observations (2008–2013).

Wirth, V. (1995). Diabatic heating in an axisymmetric cut-off cyclone and related stratosphere-troposphere exchange. *Quarterly Journal of the Royal Meteorological Society*, *121*(521), 127-147.

WMO (2014). Scientific Assessment of Ozone Depletio, Global Ozone Research and Monitoring Project-Report No. 55, WMO (World Meteorological Organization), Geneva, Switzerland, available at: https://www.esrl.noaa.gov/csd/assessments/ozone/, 2014.

WMO/GAW Ozone Monitoring Community. (2015). World Meteorological Organization-Global Atmosphere Watch Program (WMOGAW)/World Ozone and Ultraviolet Radiation Data Centre (WOUDC) [Data], available at: https://woudc.org (last access: 20 January 2018), https://doi.org/10.14287/10000008.

Worden, H. M., Logan, J. A., Worden, J. R., Beer, R., Bowman, K., Clough, S. A. et al. (2007). Comparisons of Tropospheric Emission Spectrometer (TES) ozone profiles to ozonesondes: Methods and initial results, J. Geophys. Res.-Atmos., 112, D03309, https://doi.org/10.1029/2006JD007258.

Weber, M., Dhomse, S., Wittrock, F., Richter, A., Sinnhuber, B. M. and Burrows, J. P. (2003). Dynamical control of NH and SH winter/spring total ozone from GOME observations in 1995–2002. *Geophysical Research Letters*, *30*(11).

Weber, M., Dikty, S., Burrows, J. P., Garny, H., Dameris, M., Kubin, A. et al. (2011). The Brewer-Dobson circulation and total ozone from seasonal to decadal time scales. *Atmospheric Chemistry and Physics*, *11*(21), 11221–11235. https://doi.org/10.5194/acp-11-11221-2011

White, I., Garfinkel, C. I., Gerber, E. P., Jucker, M., Aquila, V. and Oman, L. D. (2019). The downward influence of sudden stratospheric warmings: Association with tropospheric precursors. *J. Climate*, ***32***, 85-108.

Wild, O., 2007. Modelling the global tropospheric ozone budget: Exploring the variability in current models. *Atmos. Chem. Phys., 7*, 2643–2660.

Woollings, T., Charlton-Perez, A., Ineson, S., Marshall, A. G. and Masato, G. (2010). Associations between stratospheric variability and tropospheric blocking. *Journal of Geophysical Research: Atmospheres*, *115*(D6).

World Health Organisation (WHO). (2019). Ten threats to global health in 2019. In *World Health Organisation (WHO)*.

WMO, 1957: Definition of the tropopause. *WMO Bull.*, **6**, 136.

Wu, S., Mickley, L. J., Jacob, D. J., Logan, J. A., Yantosca, R. M. and Rind, D. (2007). Why are there large differences between models in global budgets of tropospheric ozone?. *Journal of Geophysical Research: Atmospheres*, *112*(D5).

Xian, T. and Homeyer, C. R. (2019). Global tropopause altitudes in radiosondes and reanalyses. *Atmos. Chem. Phys*, *19*, 5661-5678.

Yang, H., Chen, G., Tang, Q., and Hess, P. (2016). Quantifying isentropic stratosphere-troposphere exchange of ozone, J. Geophys. Res.-Atmos., 121, 3372–3387, https://doi.org/10.1002/2015JD024180.

Yeung, L. Y., Murray, L. T., Martinerie, P., Witrant, E., Hu, H., Banerjee, A.. et al. (2019). Isotopic constraint on the twentieth-century increase in tropospheric ozone. *Nature*, *570*(7760), 224-227.

Young, P. J., Archibald, A. T., Bowman, K. W., Lamarque, J.-F., Naik, V., Stevenson, D. S. et al. (2013). Preindustrial to end 21st century projections of tropospheric ozone from the Atmospheric Chemistry and Climate Model Intercomparison Project (ACCMIP), Atmos. Chem. Phys., 13, 2063–2090, https://doi.org/10.5194/acp-13-2063-2013.

Yulaeva, E., Holton, J. R. and Wallace, J. M. (1994). On the cause of the annual cycle in tropical lower-stratospheric temperatures. *Journal of the atmospheric sciences*, *51*(2), 169-174.

Yvon-Lewis, S. and Butler, J. H. (2015). Halogen sources, natural (methyl bromide and related gases). *Encyclopedia of atmospheric sciences, 5*, 228-232.

Zahn, A., Brenninkmeijer, C. A. M. and Van Velthoven, P. F. J. (2004). Passenger aircraft project CARIBIC 1997–2002, Part I: the extratropical chemical tropopause. *Atmospheric Chemistry and Physics Discussions*, *4*(1), 1091-1117.

Zanis, P., Gerasopoulos, E., Priller, A., Schnabel, C., Stohl, A., Zerefos, C. et al. (2003). An estimate of the impact of stratosphere-to-troposphere transport (STT) on the lower free tropospheric ozone over the Alps using 10Be and 7Be measurements, J. Geophys. Res., 108, 8520, https://doi.org/10.1029/2002JD002604.

Zanis, P., Hadjinicolaou, P., Pozzer, A., Tyrlis, E., Dafka, S., Mihalopoulos, et al. (2014). Summertime free-tropospheric ozone pool over the eastern Mediterranean/Middle East, Atmos. Chem. Phys., 14, 115–132, https://doi.org/10.5194/acp-14-115-2014.

Zeng, G. and Pyle, J. A. (2003). Changes in tropospheric ozone between 2000 and 2100 modeled in a chemistry-climate model. *Geophysical Research Letters*, *30*(7).

Zeng, G. and Pyle, J. A. (2005). Influence of El Nino Southern Oscillation on stratosphere/troposphere exchange and the global tropospheric ozone budget. *Geophysical research letters*, *32*(1).

Zeng, G., Morgenstern, O., Braesicke, P., and Pyle, J. A. (2010). Impact of stratospheric ozone recovery on tropospheric ozone and its budget, Geophys. Res. Lett., 37, L09805, https://doi.org/10.1029/2010GL042812.

Zhang, L., Jacob, D. J., Boersma, K. F., Jaffe, D. A., Olson, J. R., Bowman, K. W. et al. (2008). Transpacific transport of ozone pollution and the effect of recent Asian emission increases on air quality in North America: an integrated analysis using satellite, aircraft, ozonesonde, and surface observations, Atmos. Chem. Phys., 8, 6117–6136, https://doi.org/10.5194/acp-8-6117-2008.

Zhang, J. and Wang, F. (2019). Changes in the Risk of Extreme Climate Events over East 557 Asia at Different Global Warming Levels. *Water*, ***11***, 2535.

Ziemke, J. R., Chandra, S. and Bhartia, P. K. (1998). Two new methods for deriving tropospheric column ozone from TOMS measurements: Assimilated UARS MLS/HALOE and convective-cloud differential techniques. *Journal of Geophysical Research: Atmospheres*, *103*(D17), 22115-22127.

Ziemke, J. R., Chandra, S., Oman, L. D. and Bhartia, P. K. (2010). A new ENSO index derived from satellite measurements of column ozone. *Atmospheric Chemistry & Physics Discussions*, *10*(2).

Ziemke, J. R., Chandra, S., Labow, G. J., Bhartia, P. K., Froidevaux, L., and Witte, J. C. (2011). A global climatology of tropospheric and stratospheric ozone derived from Aura OMI and

MLS measurements, Atmos. Chem. Phys., 11, 9237–9251, https://doi.org/10.5194/acp-11-9237-2011.

Ziemke, J. R. and Chandra, S. (2012). Development of a climate record of tropospheric and stratospheric column ozone from satellite remote sensing: evidence of an early recovery of global stratospheric ozone, Atmos. Chem. Phys., 12, 5737–5753, https://doi.org/10.5194/acp-12-5737-2012.

Ziemke, J. R., Douglass, A. R., Oman, L. D., Strahan, S. E. and Duncan, B. N. (2015). Tropospheric ozone variability in the tropics from ENSO to MJO and shorter timescales. *Atmospheric Chemistry & Physics*, *15*(14).